Technische Universität München

TUM School of Engineering and Design

Parameter Identification and Controller Optimization for Electrical Drives

Xinyue Li

Vollständiger Abdruck der von der TUM School of Engineering and Design der Technischen Universität München zur Erlangung des akademischen Grades einer

Doktorin der Ingenieurwissenschaften

genehmigten Dissertation.

Vorsitzender: Prof. Dr.-Ing. /Univ. Tokio habil. Martin Buss
Prüfer der Dissertation:

1. Prof. Dr.-Ing. Dr. h. c. Ralph Kennel
2. Prof. Dr. ir. Dr. h. c. Rik W. De Doncker (RWTH Aachen)

Die Dissertation wurde am 04.08.2021 bei der Technischen Universität München eingereicht und durch TUM School of Engineering and Design am 03.05.2022 angenommen.

To Those Whom I Love and
Those Who Love Me

Acknowledgements

The journey that brought me here writing this thesis has been an exciting and truly wonderful one. Many people have helped me reach this important milestone in my life and have contributed to this thesis as well as to my development as an engineer and researcher by sharing their expertise, knowledge, passion and fresh perspective. I will try to thank them in a few words.

First and foremost, I would like to express my sincere gratitude to my advisor Professor Ralph Kennel for giving me the opportunity of joining the Institute for Electrical Drive Systems and Power Electronics (EAL) at the Technical University of Munich and pursuing my PhD. I have always admired the breadth and depth of his knowledge in the fields of power electronics and electrical drives. The amount of academic freedom, trust and support he has shown me is exceptional. Furthermore, I want to thank Professor Rik W. De Doncker for agreeing to be my co-examiner and for carefully evaluating my doctorate dissertation. The first time I met him was during my master study at RWTH Aachen University, when I attended his course "Electrical Drives". I was deeply impressed by the insight of his lectures and his willingness to share his extensive knowledge.

I am grateful to Dr. Heiko Peter for offering me the opportunity to work at Bosch Rexroth AG and for his mentorship, support. He motivates me to keep the practical applications and their limitations in mind. His abundant industrial experience combined with his outstanding ability of motivating people has heavily influenced me. I would not be the engineer and researcher that I am today without you. I wish you a brilliant career as you deserve. I would also like to thank my wonderful colleagues at Bosch Rexroth AG. Dr. Christian Fahrbach has taught me how to organize my work and provided me opportunities to share opinions with experts, receive inspiring feedbacks. Thomas Reulbach gave me the possibility to quickly learn the basics of the embedded system IndraDrive and guided me through my first steps in validating the algorithms on it. I am grateful for having worked with Xinmei Zhang, Dong Wang, Yi Zhu and Gerhard Fröhlich. The profitable interaction with them have given rise to a great part of my work.

Besides the aforementioned people, I would like to acknowledge my other collaborators, Wei Tian, Qifan Yang and Xiaonan Gao at EAL. Xiaonan has explored with me the topic of model predictive control and helped me with formulating the problems in a mathematically concise way. Wei, the expert in multilevel modular converters, has always discussed and shared with me about the research and other topics, from which I have benefited considerably. He has been a close friend since my master study and offered me a lot of help. Qifan is not only an office

mate, but also a brilliant friend providing me with his unique perspective on research and life. Special thanks goes to Dehao Kong, for the dinners we had, for the comfort and encouragement you brought me.
My deepest thanks go to my parents, who have always been unconditionally supportive and guided me on a personal level. Despite the distance separating Germany and China, they have kept company with me for this journey. I couldn't have done it without everything you gave me.

Stuttgart, in September 2020
Xinyue Li

Abstract

In control of electrical drives, actuating the physical systems in order to minimize losses or to track a specific reference is the ultimate goal. In most applications, the knowledge of the system parameters is essential for the precise and dynamic control of the closed-loop system, especially for the system under the model-based control. However, parameters may vary during the operation. Additionally, several disturbances and uncertainties can still be noticed in the drive system. The challenge to motivate the work of this thesis prescribes its two parts: the first part addresses the parameter identification problem within the framework of the electrical drive, while the second part of this thesis concerns the optimization of the control performance.

On the basis of the introduction to the main components of an electrical drive system, we firstly study the offline parameter identification procedures for it, where the electrical parameters of the machine and the distorted voltage caused by the inverter are primarily discussed. The offline determined results are suitable for the implementation at the start-up or for the drive system with relatively low control requirements. However, the parameter variation problem can not be completely tackled by implementing the offline determined parameters, since the affecting factors of the parameter variation are complex, diverse and the offline measurements have limited capability to describe these highly nonlinear, multidimensional characteristics. As a promising solution, the online parameter identification methods have been proposed to obtain the real-time value of the parameters of interest. Prior to the identification, the parameter identifiability of the PMSM drive system is analysed based on the local observability theory for the nonlinear system. Subsequently, the state-of-the-art online estimation methods and the auspicious moving horizon estimator are introduced, where the principles and the implementations are explicitly given. A comprehensive comparison among the aforementioned methods is carried out based on the experimental results regarding different testing scenarios. The comparing results are then summarized in terms of various aspects, namely the computational burden, the identification accuracy, the robustness, the speed of convergence and the memory allocation. Furthermore, as it is addressed previously, the distorted voltage of the inverter significantly affects the identification results. Therefore, an online parameter estimation framework including the inverter distortion is proposed, where the dual Kalman filter and extended Kalman filter have been deployed for the verification. A considerable improvement in terms of the accuracy can be observed by implementing the proposed scheme.

In the second part of this thesis, the main focus is the optimization of the model-based predictive control (MPC) under the existence of the disturbances and the uncertainties, where both

the continuous-control-set MPC (CCS-MPC) and the finite-control-set MPC (FCS-MPC) are discussed. As the name suggests, one of the main drawbacks of the MPC is its sensitivity to the model accuracy, which has a larger impact on the CCS-MPC than on the FCS-MPC. In this thesis, the effects of the model uncertainties and the disturbances on the CCS-MPC and the FCS-MPC are individually studied via simulations and experiments. In the context of the CCS-MPC, a novel robust control scheme is proposed, where the disturbance observer is integrated into the design of the controller. The closed-loop stability is studied and proved to be input-to-state stable, if several prerequisites are satisfied, which known to the author is the first proof for such a control framework. The effectiveness of the proposed control scheme is verified under various test scenarios. The experimental results demonstrate its superior performance over the conventional CCS-MPC. In the framework of the FCS-MPC, one of the mainly raised concerns is the computational burden of the control with a long prediction horizon, which can be reduced by employing the sphere decoding algorithm. After observing the matrices of the surface-mounted PMSM, a formulation of the FCS-MPC in the stationary reference frame is proposed to further reduce the computational burden for the SPMSM. Different to the CCS-MPC, FCS-MPC inherits the discrete nature of the inverter. Therefore, the model uncertainty and the disturbance do not necessarily lead to the non-optimal solution of the controller. A probability study is carried out to show the impacts of the parameter variation. Moreover, the discrete constraint of the FCS-MPC impedes the analytical analysis of the parameter variation effects. Thus, they are quantified with the help of simulations. It can be concluded from the investigations that the FCS-MPC is also affected by the parameter mismatch problem. Analogously to the CCS-MPC, a control scheme considering the system uncertainties and the disturbances is developed to improve the control performance of the FCS-MPC, where a disturbance observer is employed. The proposed control approach is then verified and compared with the conventional FCS-MPC under several testing cases. It outperforms the conventional FCS-MPC in all cases regarding the tracking accuracy and in most cases regarding the total demand distortion. However, the deployment of the disturbance observer can only eliminate the steady-state offset. The harmonics still exist in the drive system and degrade the control performance. This thesis focuses on the harmonics caused by the inverter. Nonetheless, the methods are generally formulated and can be modified, applied to eliminate harmonics resulted from the other sources. As discussed previously, the influence of the inverter can be eliminated by employing the aforementioned parameter estimation scheme. However, after examining the observability of the system including both the inverter nonlinear effect and the model uncertainty, it is impossible to estimate them simultaneously. Therefore, they need to be treated separately. The steady-state error is then compensated by the implementation of the disturbance observer, while the harmonics are eliminated by employing the fractional-repetitive-control based method. The proposed fractional-repetitive-control based compensation method is adaptive to the machine speed and can be easily implemented. It is furthermore compared with the state-of-the-art methodologies and shows its capability to deal with the harmonics. Furthermore, it can also improve the system robustness against parameter mismatch to a certain level.

Zusammenfassung

Bei der Regelung von elektrischen Antrieben geht das um die Verlustminimierung oder die Erreichung eines gewünschten Sollwertes. In den meisten Anwendungen benötigt man für die präzise und dynamische Regelung die Parameter der Regelstrecke — dies gilt auch für die modellbasierte Regelung. Allerdings können die Parameter während des Betriebs variieren. Außerdem können noch unterschiedliche Störungen und Unsicherheiten im Antriebssystem auftreten. Die Aufgabe, die diese Doktorarbeit motiviert, besteht aus zwei Bestandteilen: Der erste Teil behandelt das Problem der Parameteridentifikation innerhalb des elektrischen Antriebs während des Betriebs, während der zweite Teil sich mit der Optimierung des Reglers beschäftigt.

Ausgehend von der Einführung in die Hauptbestandteile eines elektrischen Antriebssystems werden zunächst die Offline-Parameter-Identifikationsverfahren für elektrische Antriebe betrachtet — mit besonderem Augenmerk auf die elektrischen Parameter der Maschine und die durch den Umrichter verursachte verzerrte Spannung. Offline ermittelten Parameter eignen sich für die Inbetriebnahme eines Antriebssystems oder für Antriebssysteme mit relativ niedriger Anforderung. Dieses Konzept kann allerdings das Problem der Parameteränderung nicht vollständig durch die Implementierung der offline ermittelten Parametern lösen, da die Parameter von komplexen und vielfältigen Faktoren beeinflusst sind und die Offline-Messungen nur begrenzt in der Lage sind, diese hochgradig nichtlinearen, mehrdimensionalen Eigenschaften zu beschreiben. Als vielversprechende Lösungen werden die Online-Parameteridentifikationsmethoden vorgeschlagen, um die aktuelle Werte der betreffenden Parameter zu erhalten. Die modernsten Online-Schätzverfahren sowie der neuartige Moving Horizon Estimator werden nach Analyse der Parameteridentifizierbarkeit vorgestellt: in Details erläutert und in Anwendung gezeigt. Ein umfassender Vergleich zwischen den theoretischen Ansätzen und den Realitäten wird anhand der experimentellen Ergebnisse bezüglich unterschiedlicher Testszenarien durchgeführt. Die Vergleichsergebnisse werden dann in Bezug auf unterschiedliche Aspekte zusammengefasst, in Hinblick auf den Rechenaufwand, die Genauigkeit, die Robustheit, die Konvergenzgeschwindigkeit und die Speicherbelegung. Die bereits erwähnten Identifikationsergebnisse werden von der verzerrten Spannung des Wechselrichters erheblich beeinträchtigt. Daher wird ein Online-Parameterschätzverfahren vorgestellt, das die Wechselrichterverzerrung berücksichtigt — hierzu wurden das duale Kalman Filter und das erweiterte Kalman Filter eingesetzt. Durch das vorgeschlagene Schema kann eine beträchtliche Verbesserung hinsichtlich der Genauigkeit erzielt werden.

Als zweiter Beitrag werden in dieser Dissertation Optimierungen der modellbasierten prädik-

tiven Regelung (MPC) unter der Berücksichtigung von Störungen und Ungenauigkeiten betrachtet, wobei sowohl die Continuous-Control-Set-MPC (CCS-MPC) als auch die Finite-Control-Set-MPC (FCS-MPC) behandelt werden. Wie der Name schon andeutet, ist einer der Hauptnachteile der MPC die Empfindlichkeit gegenüber der Genauigkeit der Parameter, die bei der CCS-MPC größere Auswirkung hat als bei der FCS-MPC. In dieser Dissertation werden die Auswirkung der Modellungenauigkeiten und der Störungen auf die CCS-MPC und die FCS-MPC jeweils anhand der Simulationen und Experimenten untersucht. Im Kontext der CCS-MPC wird ein neuartiges robustes Regelungsschema vorgeschlagen, bei dem der Störungsbeobachter integriert ist. Die Stabilität des geschlossenen Regelkreises wird untersucht. Es wird nachgewiesen, dass das System bei Erfüllung einiger Voraussetzungen Input-to-State stabil ist. Die Funktion des vorgeschlagenen Regelungsschemas wird unter unterschiedlichen Szenarien überprüft. Die experimentellen Ergebnisse demonstrieren eine gegenüber der konventionellen CCS-MPC verbesserte Funktionsfähigkeit. Bei Anwendung der FCS-MPC ist eines der Hauptschwierigkeit die Rechenbelastung des Prozessors mit einem langen Prädiktionshorizont — diese könnte durch den Einsatz des Sphere-Decoding-Algorithmus reduziert werden. Außerdem wird nach Betrachtung aus der Matrizen des Modells der oberflächenmontierten PMSM eine Formulierung der FCS-MPC im stationären Bezugssystem vorgeschlagen, um den Rechenaufwand für die SPMSM weiter zu reduzieren. Im Unterschied zur CCS-MPC übernimmt die FCS-MPC die diskrete Eigenschaft des Umrichters. Daher führen die Modellungenauigkeit und die Störung nicht unbedingt zu einer sub-optimalen Lösung des Reglers. Mit Hilfe einer Wahrscheinlichkeitsbetrachtung werden die Auswirkungen der Parameterveränderung verdeutlicht. Das diskrete Verhalten der FCS-MPC erschwert die analytische Beschreibung der Auswirkung der Parameterveränderungen. Deshalb werden diese mit Hilfe von Simulationen untersucht und quantifiziert. Aus den Untersuchungen lässt sich schlussfolgern, dass die FCS-MPC ebenfalls von Parameterabweichungen beeinflusst wird. Analog zur CCS-MPC wird ein Regelverfahren entworfen, das die Systemungenauigkeiten und die Störungen in Betracht zieht, um die Regelungsverfahren der FCS-MPC zu verbessern — hierbei wird ein Störungsbeobachter eingesetzt. Das vorgeschlagene Regelungskonzept wird anschließend verifiziert und mit meheren Testszenarien mit der konventionellen FCS-MPC in mehreren Testfällen verglichen. Es übertrifft die konventionelle FCS-MPC in allen Fällen hinsichtlich der Regelungsgenauigkeit und in den meisten Fällen hinsichtlich der Oberschwingungen. Ein zusätzliche Störungsbeobachters kann jedoch nur den stationären Offset eliminieren. Oberschwingungen existieren nach wie vor im Antriebssystem und beeinflussen das Regelverhalten. Diese Dissertation konzentriert sich auf die durch den Umrichter verursachten Oberschwingungen. Dennoch sind die Methoden allgemein formuliert und können so modifiziert und angewendet werden, um die von anderen Quellen stammende Oberschwingungen zu untersuchen. Wie bereits erklärt, kann der Einfluss des Umrichters durch die Verwendung des oben beschriebenen Parameterschätzungsschemas kompensiert werden. Die Beobachtbarkeit des Systems stellt dar, dass man nicht gleichzeitig den nichtlinearen Effekt des Umrichters und die Modellungenauigkeiten schätzen kann. Deswegen müssen sie separat behandelt werden. Der stationäre Fehler wird dann durch die Implementierung des Störungsbeobachters ausgeglichen, während die Oberschwingungen durch den Einsatz der auf einer Fractional-Repetitive-Regelung basierenden Methode eliminiert werden. Die vorgestellte Kompensationsmethode ist an die Maschinendrehzahl anpassbar und kann einfach implementiert werden. Außerdem wird sie mit dem Stand der Technik verglichen. Sie stellt die Möglichkeit her-

aus, die Oberschwingungen zu minimieren. Die Robustheit des Systems gegenüber Parameterfehlanpassungen kann mit der vorgeschlagenen Methode deutlich verbessern.

Contents

Part I

PRELIMINARIES

CHAPTER 1

Introduction

The electrical drive system is widely utilized in a large number of industrial and domestic applications, such as transportation systems (electric vehicles and trains), home appliances (air conditioners and heat pumps) and industrial utilizations (fans and pumps). It is complex, nonlinear and typically assembled with three major parts, namely the electrical machine, the power electronic converter and the control system.

In general, the electrical machines can be categorized into two groups: direct current (DC) machines and alternating current (AC) machines. Even though the DC machines, thanks to the separation of field and torque production, require a relatively low complexity for the control system, they have been gradually replaced by the AC machines nowadays. Comparing to the DC machines, the AC machines can achieve higher speed and has lower maintenance effort as well as longer life expectancy [1].

As the actuator of the electrical drive systems, the power converters actuate the command from the control system and deliver the energy to the electrical machine. As a result of the discrete nature of the power converters, only discrete-valued outputs can be produced. In particular, a voltage source inverter (VSI) is utilized for delivering the energy to the AC machines, which is consisted by power electronic devices, e.g. insulated gate bipolar transistor (IGBT) and metal oxide semiconductor field effect transistor (MOSFET). Many topologies are available to realize the energy transfer, for example the two-level VSI, the multi-level VSI and the modular multi-level inverter, among which the two-level VSI, because of its simplicity of the topology and simpleness to control, is mostly applied in a wide range of industries. The inverter is fed by a DC link, which can provide and absorb electric energy. The DC link is typically connected to a larger system, e.g. a power grid or a distributed DC source, and realized by a DC-link capacitor. The voltage command delivered to the inverter is computed by the control system, which ensures that the electrical drive system actuates as expected. The utilization of microprocessors enables the fully digital implementation of the control methods. Moreover, the technology advances have facilitated an increase in the availability of the computational resources in the last few decades. Thanks to this development, applications over a large range of domain are able

to deploy advanced control methods for complex systems and various control targets, which realizes precise and dynamic control for diverse systems.

1.1 Background and Motivation

The control of the electrical drive systems are tasked with the guarantee for the operational safety and the fulfilment of the performance expectations. Generally speaking, the following requirements on the controller design need to be considered [2]:

- **Control accuracy**: the error between the reference and the controlled variables should be minimized.
- **Dynamic response**: the control loop has fast dynamics for the reference tracking and has the ability of disturbance rejection.
- **Harmonics**: the discrete nature of the power converters provokes harmonics in the control loop, which is normally evaluated with the metrics such as the total harmonic distortion (THD) and the total demand distortion (TDD). The harmonic content is normally restricted by specified standards.
- **System constraints**: the constraints of the plant, e.g. the current and speed limitation, and of the actuator, such as the maximum voltage and current, must be included.
- **Efficiency**: the control methods should guarantee high efficiency of the converter as well as of the machine.
- **Applicability**: the control methods need to maintain the control performance over a wide range of operating area.
- **Complexity**: the complexity of the control methods is tolerable for the hardware resources with only limited computational power.

One of the most popular control methods in the industrial applications is the field oriented control (FOC), which controls the electrical machines in a cascaded manner and realizes the control with the linear proportional-integral-derivative (PID) controller. The classic FOC is easy to implement and has low computational burden. Nonetheless, the constraints in the electrical drive system, the discrete nature of the inverter and many other nonlinearities in the system degrades the performance of the FOC. Moreover, in the framework of the cascaded control, the inner control loop is required to be much faster than the outer loop, which limits the bandwidth of the controller and impedes the design of the control parameters. In order to tackle these drawbacks, more sophisticated control approaches have been proposed. One of the promising methods is the model predictive control (MPC), which formulates the control problem as an optimization problem and includes the constraints into the problem formulation. Regarding various control objects, the application of MPC can be roughly sorted into three groups: model predictive current control (MPCC), model predictive speed control (MPSC) and model predictive torque control (MPTC). In terms of the constraints on the control voltage, MPC

can be categorized into continuous-control-set model predictive control (CCS-MPC) and finite-control-set model predictive control (FCS-MPC), where CCS-MPC delivers the control voltage as a continuous value and FCS-MPC outputs directly the switching signals.

However, an accurate, dynamic and stable design of the control further requires the capability to understand and manipulate the individual elements within the electrical drive systems. In many applications, the values from the data sheets of the manufacturers are employed as the baseline of the drive system. However, since the accurate parameter values of the electrical machine over the whole operating range are essential for the control performance, the standstill frequency response (SSFR) test is normally conducted before the start-up. It has become the standard method for identifying the machines, where the response on the test signal with a single frequency is evaluated. Nonetheless, the identified parameters are time-varying and affected by numerous factors, such as the temperature and the saturation effect. Moreover, in almost all the practical applications, the uncertainty exists in the model of the electrical drive system, which may come from various sources, for example unmodelled system elements and external disturbances. The combination of the observer and the model-based control method yields a powerful and versatile framework for advanced control. The system states as well as the parameters are adapted based on the measurements, which further benefits the controller in a way that the prediction accuracy as well as the control performance is improved.

1.2 Outline and Contributions

This thesis consists of three main parts. In the first part, the background material that is essential to this thesis is introduced. The second part concentrates on the offline as well as the online identification methods for the electrical drive system. This is followed by the third part, which lays the focus on optimizing the predictive control methods under the existence of uncertainties and disturbances.

Part I: Preliminaries The permanent-magnet synchronous machine drive system comprises mainly three components, namely the PMSM, the inverter and the control system. In Chapter 2, a brief introduction to the PMSM is given, including the construction as well as the mathematical modeling of the PMSM. Several assumptions are deployed to simplify the establishment of its three-phase mathematical model. It can be further simplified and transformed into the two-axis system, of which two different reference frames, i.e. the stationary reference frame and the rotating reference frame can be employed depending on the application field. As the actuator in the drive system, VSI is furthermore discussed. The basic mathematical definitions relevant for the optimization problems are reviewed, which is followed by the overview on the state-of-the-art control strategies for the PMSM drive system. The uncertainties and the disturbances existing in the drive system are summarized as a closure of this part.

Part II: Parameter identification Part II of this thesis concentrates on the parameter identification for the PMSM drive system. Firstly, the observability of the PMSM electrical parameters is analyzed. The local observability theory is employed to achieve this goal. Subsequently, the offline determination procedures for the PMSM parameters are developed, where both the

linear and nonlinear flux linkage interpretation are investigated. In order to complete the computational results from the discrete measurement points, an appropriate interpolation method is required. The most applied interpolation methods are introduced and employed to complete the results of offline determined parameters as a smoothed map. Besides the offline determination procedures, the estimation methods with current injection can also be applied to identify all electrical parameters of PMSM. In this thesis, the square-wave-form and the sinusoidal-wave-form current are applied. The amplitude as well as the frequency of the injected current is determined by the simulations. Related experiments are furthermore conducted to compare and justify the estimation performance. However, the offline determination procedures are normally time-consuming and may increase the instrument costs as well as the implementation complexity. Although, the current injection method can proceed during the operation, the injected current may result in the current distortion and the torque pulsation problem. Thus, the online parameter estimation method is proposed as a more proper solution for the real-time parameter identification. Five methods are explicitly studied in this work, namely model reference adaptive system (MRAS), recursive least squares (RLS), extended Kalman filter (EKF), unscented Kalman filter (UKF) and moving horizon estimator (MHE). Their theoretical foundations are parsed at first. Subsequently, the aforementioned methods are implemented on an embedded system to estimate the identifiable parameter combinations for PMSM. The corresponding experimental results are shown and compared in terms of various aspects. Furthermore, the former investigation shows that the voltage distortion caused by the VSI affects the estimation results. Therefore, a dual-EKF-based estimator and a EKF-based estimator are deployed for the parameter estimation considering the influence of the VSI, of which the distorted voltage is included as an extended term into the system model. One of the attractiveness of the dual EKF is that the parameter filter can be deactivated. This characteristic provides the possibility of the computational burden reduction and the memory release.

Part III: Controller optimization In Part III, we leave the realm of the parameter estimation problem and investigate the control problems considering the model uncertainties and the disturbances. Chapter 4 elaborates the framework of the continuous-control-set model predictive control, including the formulation of the optimization problem and the computation, implementation for the real-time applications. To eliminate the impacts of the model uncertainties and the disturbances, an observer-based robust control strategy is proposed. This proposal is unifying formulated and can be applied to any AC drive system. Moreover, the stability of the closed loop is furthermore analyzed by employing the input-to-state stability theory, which can be analogously mapped onto other drive systems. The impacts of the parameter mismatches on the control performance of the CCS-MPC are investigated via experiments and subsequently quantified. The effectiveness of the proposed solution is verified with different testing scenarios, where disparate uncertainties and disturbances are discussed. The FCS-MPC also suffers from the effects of system uncertainties and disturbances. In Chapter 5, the basic concepts of the FCS-MPC are firstly given. The establishment of the optimization problem and the corresponding solving methods are furthermore introduced. Instead of applying the exhaustive enumeration method, the sphere decoding algorithm is employed to reduce the online computational burden and enable a long-horizon prediction during the operation. A formulation of the FCS-MPC for SPMSM on the stationary reference frame can further reduce the computational burden by allocating a large portion of the matrix computation to offline preparation. On the

contrary to the CCS-MPC, the model uncertainties and disturbances do not necessarily affect the solution of the FCS-MPC, which can be traced back to the mixed-integer characteristic of the underlying optimization problem associating with the FCS-MPC. The simulations on the probability of acquiring the optimal solutions under the existence of the parameter mismatches are carried out to justify this statement. An incremental MHE is applied as the disturbance observer to improve the tracking ability and system stability. Nonetheless, the disturbance observer has limited bandwidth and filter effects. Therefore, the periodic disturbances remain in the PMSM drive system, even though the disturbance observer is implemented. In Chapter 6, the topic of attenuation of the periodic disturbance is investigated, where the main effort lies on compensating the distorted voltage caused by the VSI. The state-of-the-art approaches for eliminating the disturbances caused by the VSI are reviewed and explained. Then, a novel approach based on the fractional repetitive control is proposed to compensate the distorted voltage. The proposed compensation method tackles the problem of shifted high control gains at the target frequency, which is caused by the fractional ratio between the target frequency and the sampling frequency and often encountered during the implementation on a digital control platform. Since the target frequency varies with the fundamental frequency of the PMSM, the compensating values adapts to the eventual motor speed. In order to limit the control gain and improve the system stability, a moving average filter is furthermore deployed. The compensation performance is determined by investigating the individual parameters via simulations and experiments, while the stability of the overall system is guaranteed through theoretical analysis. The proposed method is furthermore verified with experiments, of which the results are furthermore compared with the state-of-the-art approaches for the distorted voltage compensation. More experimental investigations are also provided regarding the performance evaluation of the proposed method at the steady state and during the transient.

Concluding remarks of this thesis are given in Chapter 7, where an outlook to the possible future works derived from this thesis is also presented.

CHAPTER 2

Permanent Magnet Synchronous Machine Drive System

This chapter lays theoretical foundations for the further analysis and development of this thesis. In this chapter, the composition of the permanent magnet synchronous machine drive system are introduced, namely the permanent magnet synchronous machine, the inverter and the controller. A general structure of the electrical drive system can be represented by the Fig. 2.1.

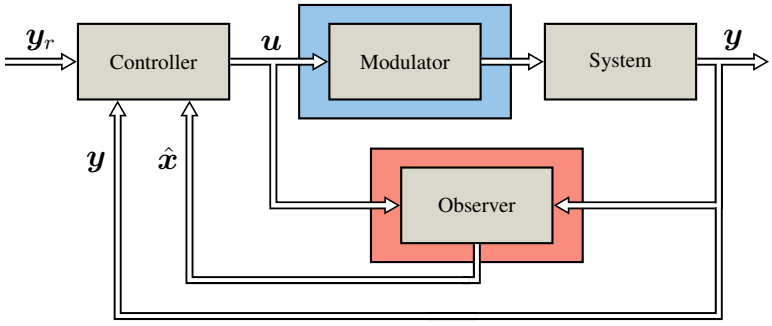

Figure 2.1: Typical control structure in the field of power electronics and electrical drives.

Depending on the control methods, the modulator is optional for the drive system, which translates the voltage commands from the control system into the switching commands for the semiconductor switches. The most applied modulation methods are the carrier-based pulse width modulator (PWM) and the space vector modulator (SVM). The controller denotes the control unit, where the design and the computation of the control, the planning for realizing a specified task or minimizing the losses take place. The control approaches are normally implemented on an embedded computing platform such as microcontrollers and reconfigurable hardware, where field-programmable gate array (FPGA) and programmable logic controller (PLC) are mostly used in practice, respectively. The system in Fig. 2.1 represents the plant to be controlled, which can be the electric machines or the combination of the power electronics and

the electric machines. Considering different types of machines, the observer can be required by the electrical drives. For example, the flux observer is mandatory for the control of the induction machine, since the flux can not be directly measured but is essential for the precise control. Furthermore, some control methods also employ the observer to improve the control performance.

2.1 Permanent Magnet Synchronous Machine

In this thesis, the drive system with the permanent-magnet synchronous machine (PMSM) is investigated. The PMSM gained popularity with the development of permanent magnets, especially the rare-earth magnets, e.g. the Neodymium (NeFeB) and the Samarium-Cobalt (SmCo) magnets. The implementation of the permanent magnets enables a compact construction of the rotor. It also leads to the advantages such as high efficiency and high torque density of PMSM. In this section, the construction of the PMSM, including the stator and rotor, is firstly introduced. Subsequently, the PMSM modeling is established in different reference frames. For the PMSM drive system, two reference frames are normally deployed, namely the stationary reference frame and the rotating reference frame. Once the reference frame is determined, the electrical drive system can be modelled correspondingly. At last, the formulation for describing the mechanical system is also given.

2.1.1 Construction of PMSM

2.1.1.1 Stator

The stator of a PMSM, which is also called armature, is made of thin laminations of highly permeable steel aiming to reduce the core losses [3]. The air-gap flux density is limited by the saturation of the stator core. In particular, the peak flux density is limited by the width of the teeth, while the stator back determines the maximum total flux. The armature windings are constructed in the stator slots and symmetrically distributed so that the flux linkage produced by the stator current is allocated as sinusoidally as possible. There are two main categories of the construction of armature windings, the distributed windings and the concentrated windings. Details about the difference between them can be found in [4]. The three-phase windings are exactly alike in shape as well as in form and can be connected as a star (Y) form or as a delta (Δ) form. They are displaced from each other by an electrical angle of 120° and repeated n_p times along the circumference, where $n_\mathrm{p} \in \mathbb{Z}^+$ denotes the number of pole pairs.

2.1.1.2 Rotor

Considering the way how magnets are installed into the rotor, PMSM can be basically divided into surface permanent-magnet synchronous machine (SPMSM) and interior permanent-magnet synchronous machine (IPMSM). As the name suggests, the magnets of SPMSM are mounted directly onto/into the rotor surface. There are in general two types of SPMSM, surface-mounted permanent magnet synchronous machine and surface-insert permanent magnet synchronous machine. Their constructions are shown in Fig. 2.2. A surface-mounted PMSM, e. g. in Fig. 2.2a, has a magnetically isotropic rotor and is typically not suitable for field-weakening. A

surface-inset PMSM, e.g. in Fig. 2.2b has high saliency ratio, where the saliency ratio indicates the difference in magnetic paths between with and without magnets. The saliency effect, which indicates the saliency ratio, can be neglected in the surface-mounted PMSM [5]. The saliency is also an indicator of magnetic interaction and reluctance torque production capabilities. Moreover, the air-gap flux density is distributed smoothly in surface-mounted PMSM. The torque ripples are therefore small [6].

Figure 2.2: General structure of SPMSMs. (a) Surface-mounted permanent magnet synchronous machine. (b) Surface-inset permanent magnet synchronous machine.

Different from SPMSM, IPMSM integrates magnets in the interior of the rotor, of which the typical structures are presented in Fig. 2.3. The magnets are therefore physically protected by the rotor. In these machines, the saliency cannot be neglected. This characteristic enables IPMSM to produce reluctance torque even in the field-weakening operation region. Therefore, IPMSMs are usually employed for a higher speed operation than SPMSMs. IPMSM in Fig. 2.3a is magnetized tangentially, with alternating directions, where the interior permanent magnets act as flux barriers and therefore can achieve high saliency ratio. The IPMSM in Fig. 2.3b is magnetized radially, which can benefit the PMSM for achieving high air-gap induction or for employing weaker, cheaper magnets.

In general, the surface-mounted PMSM configuration is popular in many application domains, because it is easy to manufacture and has low production costs. A more detailed discussion over IPMSM and SPMSM lies beyond the scope of this thesis. The comprehensive comparison between SPMSM and IPMSM has been conducted in researches such as [7, 8].

Figure 2.3: General structure of IPMSMs. (a) Interior permanent magnet synchronous machine. (b) Interior permanent magnet synchronous machine (with circumferential orientation).

The permanent magnet flux linkage is important for the induced magnetic flux of PMSM and has the ability to sustain its own magnetic flux within a magnetic field excited by external

sources [9]. It supports the magnetic flux passing from rotor to stator through the air gap. The permanent magnet flux linkage reflects the characteristic of the permanent magnet, which means that its value is determined by the magnet material, the shape and the attached magnetic circuit. Therefore, it is mainly affected by the temperature and the ageing effect [9].

2.1.2 PMSM Modeling

PMSM has been intensively studied in many works, such as [10] and [11]. In most PMSM drive systems, the linearised equations with constant parameters are applied for modeling the current loop dynamics. Nonetheless, the nonlinear model of PMSM that includes the self-inductance and meanwhile the cross-inductance has also been implemented for some applications [12]. Normally, only the fundamental model is applied for the most applications, where the modeling of harmonics is ignored. In practice, the PMSMs are considerably complicated, therefore several assumptions are normally accepted in order to simplify the physical system of the PMSM and to establish a relatively reasonable, acceptable mathematical model. These assumptions are shown in the following:

- The machine induced magnetic field is sinusoidal.
- The eddy current and the hysteresis losses are negligible.
- The armature windings are symmetrically constructed and the influence from winding head is neglected.
- The saturation effect will be taken into account in the parameter variations.

The PMSM is then simplified as a symmetrical three-phase system, which is shown in Fig. 2.4. The phase voltages, u_a, u_b and u_c, are obtained by subtracting the zero voltage u_0 from the

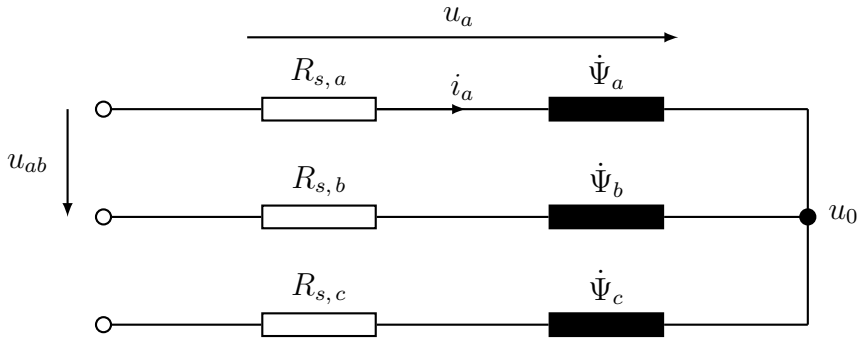

Figure 2.4: Three-phase system of the PMSM.

terminal voltage u_{a0}, u_{b0} and u_{c0}, respectively. It can be given as

$$\begin{bmatrix} u_a \\ u_b \\ u_c \end{bmatrix} = \begin{bmatrix} u_{a0} \\ u_{b0} \\ u_{c0} \end{bmatrix} - u_0 \boldsymbol{I} \,, \tag{2.1}$$

where $\boldsymbol{I} \in \mathbb{R}^{3\times 1}$ is a three-dimensional vector of all ones. The zero voltage u_0 represents the voltage between the neutral point of the electric machine and the neutral potential of the drive

system [4]. Furthermore, the phase voltage consists of two parts, the resistance voltage drop caused by the phase resistance R_s and the by flux linkage induced voltage, which is denoted by $\dot{\boldsymbol{\Psi}}_{abc}$ [13]. Therefore, the phase voltage $\boldsymbol{u}_{abc} = (u_a,\ u_b,\ u_c)^T$ can be calculated by

$$\boldsymbol{u}_{abc} = R_\mathrm{s}\, \boldsymbol{i}_{abc} + \frac{\mathrm{d}}{\mathrm{d}\,t}\boldsymbol{\Psi}_{abc}\ , \tag{2.2}$$

where $\boldsymbol{i}_{abc} = (i_a,\ i_b,\ i_c)^T$ is the phase current and $\boldsymbol{\Psi}_{abc} = (\Psi_a,\ \Psi_b,\ \Psi_c)^T$ denotes the total flux linkage associated with the corresponding phase. In order to simplify the analysis and the control of the three-phase system described in (2.2), the equation is normally further transformed into a two-axis orthogonal reference frame.

2.1.2.1 Reference Frames

The reference frame, which is also called the coordinate system, can be chosen for the transformation from the three-phase system to the two-axis system. A general presentation of the reference frame transformation is shown in Fig. 2.5. An arbitrary vector $\boldsymbol{z}$ can be regarded

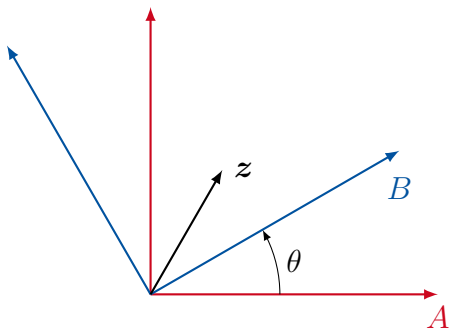

Figure 2.5: General reference frame representation and transformation. $\boldsymbol{z}$ is an arbitrary vector. Two different reference frames are represented as A in red and as B in blue.

as a vector in the coordinate system A and also in the coordinate system B, as it is shown in Fig. 2.5. The transformation from the reference frame A to the reference frame B is realized by rotating the quantity with the relative angle θ. The angle can be computed by integrating the relative speed or directly obtained from the corresponding measurement. The mathematical interpretation for a general manner of the transformation is given by

$$\boldsymbol{z}^B = \boldsymbol{z}^A \cdot e^{-j\theta}\ . \tag{2.3}$$

2.1.2.2 Stationary Reference Frame

In general, there are two different orthogonal reference frames for the control of PMSM drive systems, i.e. the stationary and the rotating reference frame, as it is shown in Fig. 2.6.

The stationary reference frame is also called $\alpha\beta0$ reference frame, where the α-axis, β-axis and 0-axis are perpendicular to each other. The vector $\boldsymbol{z}_{abc}$ in the three-phase system is transformed into the stationary reference frame with the so-called Clarke transformation $\boldsymbol{T}_{\alpha\beta0}$ via

$$\boldsymbol{z}^S = \boldsymbol{T}_{\alpha\beta0} \cdot \boldsymbol{z}_{abc}\ , \tag{2.4}$$

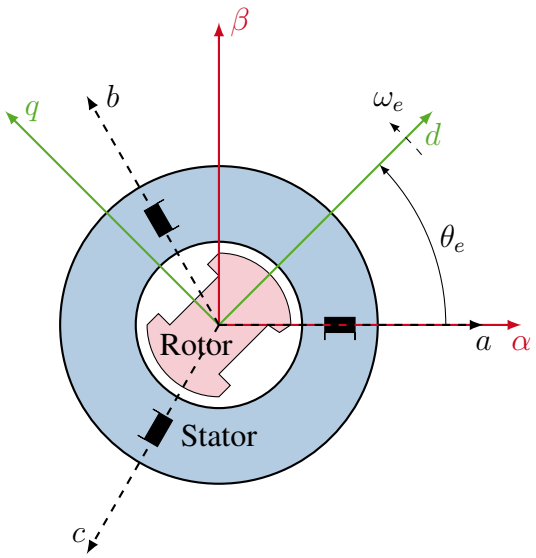

Figure 2.6: Visualization of the reference frame representations and the transformation for the PMSM. Black dashed line denotes the three-phase reference frame. Red solid line denotes $\alpha\beta$ domain. Green solid line represents the rotating dq domain, which rotates with the rotor angular speed.

where z^S denotes the quantity in the stationary reference frame and

$$\boldsymbol{T}_{\alpha\beta0} = A_T \cdot \begin{bmatrix} 1 & -\frac{1}{2} & -\frac{1}{2} \\ 0 & \frac{\sqrt{3}}{2} & -\frac{\sqrt{3}}{2} \\ \frac{1}{2} & \frac{1}{2} & \frac{1}{2} \end{bmatrix} . \tag{2.5}$$

A_T is a coefficient indicating the principle of the transformation, which is equal to $2/3$ in the case of the amplitude-invariant principle and is $\sqrt{2/3}$ with the power-invariant principle. The amplitude-invariant principle retains the amplitude of the currents and the voltages, e.g. the magnitude of the current vector is equivalent to the amplitude of the phase current. The power-invariant principle scales the magnitude of the current vector, which becomes 1.5 times of the phase current amplitude, while the energy and the power can be directly computed from the vectorial quantities and remain unchanged.

The transformed quantity $\boldsymbol{z}^S$ rotates with the angular velocity ω_e in the plane spanned by the two orthogonal coordinates ($\alpha\beta$ domain). Moreover, under the assumption that the three-phase system is balanced, the zero system of PMSM can be neglected. The transformation in (2.4) is then simplified as

$$\boldsymbol{z}^S = \boldsymbol{T}_{\alpha\beta} \cdot \boldsymbol{z}_{abc} , \tag{2.6}$$

with

$$\boldsymbol{T}_{\alpha\beta} = A_T \cdot \begin{bmatrix} 1 & -\frac{1}{2} & -\frac{1}{2} \\ 0 & \frac{\sqrt{3}}{2} & -\frac{\sqrt{3}}{2} \end{bmatrix} . \tag{2.7}$$

The simplified Clarke transformation in (2.6) is more often used than (2.4). The inverse matrix of $T_{\alpha\beta0}$ and the pseudo-inverse of $T_{\alpha\beta}$ are denoted by $T^{-1}_{\alpha\beta0}$ and $T^{-1}_{\alpha\beta}$, respectively. The voltage equation of PMSM in (2.2) is then transformed into the stationary reference frame as

$$\boldsymbol{u}^S = R_\mathrm{s}\, \boldsymbol{i}^S + \frac{\mathrm{d}}{\mathrm{d}t} \boldsymbol{\Psi}^S , \tag{2.8}$$

where $\boldsymbol{u}^S = (u_\alpha,\ u_\beta)^T$, $\boldsymbol{i}^S = (i_\alpha,\ i_\beta)^T$ and $\boldsymbol{\Psi}^S = (\Psi_\alpha,\ \Psi_\beta)^T$. R_s represents the phase resistance, since the armature windings of three phases are assumed to be identical.

2.1.2.3 Rotating Reference Frame

The rotating reference frame employs the rotor rotating frame as the reference, which is shown in Fig. 2.6 in green. More specifically, the reference domain rotates with the rotor angular speed ω_e. The transformation from the three-phase system to the rotor reference frame is called Park transformation or dq transformation. The dq transformation maps the vector $\boldsymbol{z}_{abc}$ from the three-phase system to the vector $\boldsymbol{z}^R$ in the dq reference frame via the following equation:

$$\boldsymbol{z}^R = A_T \cdot \begin{bmatrix} \cos(\theta_e) & \cos(\theta_e - \frac{2\pi}{3}) & \cos(\theta_e + \frac{2\pi}{3}) \\ -\sin(\theta_e) & -\sin(\theta_e - \frac{2\pi}{3}) & -\sin(\theta_e + \frac{2\pi}{3}) \\ \frac{1}{2} & \frac{1}{2} & \frac{1}{2} \end{bmatrix} \cdot \boldsymbol{z}^{abc} = \boldsymbol{T}_{dq0} \cdot \boldsymbol{z}_{abc}\ , \tag{2.9}$$

where θ_e denotes the rotor position. Moreover, the vector in the dq reference frame can be derived from the $\alpha\beta$ reference frame with

$$\boldsymbol{z}^R = \boldsymbol{z}^S \cdot e^{-j\theta_e}\ . \tag{2.10}$$

Analogously to Clarke transformation, the 0-component can be omitted in the dq reference frame, which leads to the reduced Park transformation with the transforming matrix $\boldsymbol{T}_{dq}$ given as

$$\boldsymbol{T}_{dq} = \begin{bmatrix} \cos(\theta_e) & \cos(\theta_e - \frac{2\pi}{3}) & \cos(\theta_e + \frac{2\pi}{3}) \\ -\sin(\theta_e) & -\sin(\theta_e - \frac{2\pi}{3}) & -\sin(\theta_e + \frac{2\pi}{3}) \end{bmatrix}\ . \tag{2.11}$$

The corresponding inverse matrix of $\boldsymbol{T}_{dq0}$ and the pseudo-inverse of $\boldsymbol{T}_{dq}$ are denoted by $\boldsymbol{T}_{dq0}^{-1}$ and $\boldsymbol{T}_{dq}^{-1}$, respectively.

With the relationship given in (2.10), the voltage equation in (2.8) can be transformed into the dq reference frame by substituting the relationship (2.10) into (2.8) as

$$\begin{aligned} \boldsymbol{u}^R \cdot e^{j\theta_e} &= R_\mathrm{s}\, \boldsymbol{i}^R \cdot e^{j\theta_e} + \frac{\mathrm{d}}{\mathrm{d}\,t}(\boldsymbol{\Psi}^R \cdot e^{j\theta_e}) \\ &= R_\mathrm{s}\, \boldsymbol{i}^R \cdot e^{j\theta_e} + \frac{\mathrm{d}}{\mathrm{d}\,t}\boldsymbol{\Psi}^R \cdot e^{j\theta_e} + j\omega_e \cdot \boldsymbol{\Psi}^R \cdot e^{j\theta_e}\ , \end{aligned} \tag{2.12}$$

which can be more compactly written as

$$\boldsymbol{u}^R = R_\mathrm{s}\, \boldsymbol{i}^R + \frac{\mathrm{d}}{\mathrm{d}\,t}\boldsymbol{\Psi}^R + j\omega_e \cdot \boldsymbol{\Psi}^R\ , \tag{2.13}$$

where $\boldsymbol{u}^R = (u_d,\ u_q)^T$, $\boldsymbol{i}^R = (i_d,\ i_q)^T$ and $\boldsymbol{\Psi}^R = (\Psi_d,\ \Psi_q)^T$. Equation (2.13) can also be written as the most applied formulation:

$$\begin{aligned} u_d &= R_\mathrm{s}\, i_d + \frac{\mathrm{d}}{\mathrm{d}\,t}\Psi_d - \omega_e \Psi_q\ , \\ u_q &= R_\mathrm{s}\, i_q + \frac{\mathrm{d}}{\mathrm{d}\,t}\Psi_q + \omega_e \Psi_d\ . \end{aligned} \tag{2.14}$$

The main advantage of transforming the quantities into the rotating reference frame is that the transformation simplifies the sinusoidal time-varying currents and voltages to complex numbers, i.e. DC signals. The computation for the control system is meanwhile simplified. The inverse transformation can be performed afterwards to recover the actual three-phase values.

2.1.2.4 Electrical System

The electrical system of the PMSM is successfully formulated and derived in different reference frames. The formulations are given in (2.2), (2.8) and (2.13). They can be used for describing the steady state as well as the transient behavior of the machine. However, in many cases, it is necessary to replace the flux linkage $\boldsymbol{\Psi}$ by corresponding currents and inductances. The parameters of the two-axis model, especially the inductances, vary nonlinearly with the operating conditions, which is primarily a result of the saturation and cross-saturation effects [12]. The saturation effect refers to the effect that the current saturates the magnetic material on the same axis, while the cross-saturation effect denotes the effect that the current causes the variation of the flux on the other axis. More related information can be found in Section 2.4. A general function describing the relationship between flux and current in d- and q-axis can be given as [14]

$$\begin{bmatrix} \Psi_d \\ \Psi_q \end{bmatrix} = \begin{bmatrix} l_{dd}(i_d) & l_{dq}(i_d,\, i_q) \\ l_{qd}(i_d,\, i_q) & l_{qq}(i_q) \end{bmatrix} \begin{bmatrix} i_d \\ i_q \end{bmatrix} + \begin{bmatrix} \Psi_\mathrm{m} \\ 0 \end{bmatrix} , \tag{2.15}$$

where l_{dd} and l_{qq} denote the self-inductance in d- and q-axis, respectively. They are solely dependent on the own current. On the other hand, $l_{dq}(i_d,\, i_q)$ and $l_{qd}(i_d,\, i_q)$ represent the cross-coupling inductances, which are caused by the other current. In summary, the self-inductance is only related to the current of the same axis and the cross-coupling inductance depend on both currents. In some works, the self-inductance is considered as a function of both i_d and i_q [15]. Then, different inductances are introduced to interpret the nonlinearities of the fluxes. A general formulation of the PMSM electrical system with inductances, where the fluxes of the voltage equation in (2.14) is substituted by the inductances, can be written as

$$\begin{bmatrix} u_d \\ u_q \end{bmatrix} = \begin{bmatrix} R_\mathrm{s} & -\omega_e\, L_q \\ \omega_e\, L_d & R_\mathrm{s} \end{bmatrix} \begin{bmatrix} i_d \\ i_q \end{bmatrix} + \begin{bmatrix} L_{dd} & L_{dq} \\ L_{qd} & L_{qq} \end{bmatrix} \begin{bmatrix} \dfrac{\mathrm{d}}{\mathrm{d}\,t} i_d \\ \dfrac{\mathrm{d}}{\mathrm{d}\,t} i_q \end{bmatrix} + \begin{bmatrix} \dfrac{\mathrm{d}}{\mathrm{d}\,t} \Psi_\mathrm{m} \\ \omega_e\, \Psi_\mathrm{m} \end{bmatrix} , \tag{2.16}$$

where L_d and L_q are the so-called absolute inductance, which corresponds to the linearised model of the flux in the latter section. L_{dd}, L_{qq}, L_{dq} and L_{qd} denote the differential inductances, which describe the partial derivatives of the flux linkages, of which the definition is given by

$$L_{dd} = \frac{\partial \Psi_d}{\partial i_d} , \quad L_{dq} = \frac{\partial \Psi_d}{\partial i_q} , \quad L_{qq} = \frac{\partial \Psi_q}{\partial i_q} , \quad L_{qd} = \frac{\partial \Psi_q}{\partial i_d} . \tag{2.17}$$

L_{dd} and L_{qq} denote the same characteristics of the flux linkage as the absolute inductance. L_{dq} and L_{qd} are the measures to represent the influence of the cross-coupling for PMSM. From a mathematical perspective, the absolute inductance corresponds to the gradient of the flux maps, while the differential inductance complies with the partial derivative of the function at individual operating point. It is worth mentioning that in the general model in (2.16), the permanent magnet flux linkage Ψ_m is also time-varying. Therefore, the term $\dot{\Psi}_\mathrm{m}$ can not be omitted in the equation (2.16).

Although the general model in (2.16) is preferred to precisely describe the global relationship between the flux and the current, deploying it will significantly increase the complexity of the

analysis and the design of the control system for PMSM. Furthermore, the determination of the nonlinear model characteristics is sophisticated and requires certain laboratory setups as well as measuring procedures, as introduced in [16–18]. Therefore, the linearised PMSM model is more commonly applied in practice, which simplifies the function that describing the relationship between the flux and the current in (2.15) and approximates the PMSM behaviour locally with a linear function as

$$\begin{bmatrix} \Psi_d \\ \Psi_q \end{bmatrix} = \begin{bmatrix} L_d & 0 \\ 0 & L_q \end{bmatrix} \begin{bmatrix} i_d \\ i_q \end{bmatrix} + \begin{bmatrix} \Psi_\mathrm{m} \\ 0 \end{bmatrix} . \tag{2.18}$$

The permanent magnet flux linkage Ψ_m, which aligned with the d-axis, is also regarded as constant in the linearised model (2.18). As a result, the voltage equation in (2.16) can be simplified as

$$\begin{bmatrix} u_d \\ u_q \end{bmatrix} = \begin{bmatrix} R_\mathrm{s} & -\omega_e L_q \\ \omega_e L_d & R_\mathrm{s} \end{bmatrix} \begin{bmatrix} i_d \\ i_q \end{bmatrix} + \begin{bmatrix} L_d & 0 \\ 0 & L_q \end{bmatrix} \begin{bmatrix} \frac{\mathrm{d}}{\mathrm{d}t} i_d \\ \frac{\mathrm{d}}{\mathrm{d}t} i_q \end{bmatrix} + \begin{bmatrix} 0 \\ \omega_e \Psi_\mathrm{m} \end{bmatrix} . \tag{2.19}$$

2.1.2.5 Mechanical System

The mechanical differential equations tie the electrical system of PMSM with the mechanical system. The mechanical angular speed can be calculated with

$$\frac{\mathrm{d}}{\mathrm{d}t} \omega_\mathrm{m} = \frac{1}{J} \cdot (T_\mathrm{e} - T_\mathrm{r}) , \tag{2.20}$$

where T_r is the resistive torque, which including the friction of the shaft and the load torque T_l. J is the inertia of the system and T_e denotes the inertial torque, which can be computed with the electrical quantities by

$$T_\mathrm{e} = \frac{3}{2} n_p \cdot \Im\{\boldsymbol{\Psi}^* \cdot \boldsymbol{i}\} , \tag{2.21}$$

where n_p denotes the number of the pole pairs. The electrical rotor speed can be given by

$$\omega_e = n_p \, \omega_\mathrm{m} . \tag{2.22}$$

Subsequently, the operating principles of the inverter is introduced.

2.2 Inverter

2.2.1 Introduction

An inverter in the drive system serves as a link between the power grid and the associated motors. In Fig. 2.7, a two-level inverter with DC-link is connected to the motor. Conventionally, the inverter consists of six controllable switches or solid-state valves [19]. Two switches connected to the same phase are called the leg of the inverter. In Fig. 2.7, the switches are represented as IGBTs with anti-parallel diodes. Another prominent example of the active switch is the MOSFET. The controllable switches conducts or blocks the current flow depending on the control signals. More specifically, a positive current between the collector (C) and emitter (E) of IGBT is conducted or blocked if a control signal applied to the gate (G). The corresponding status of

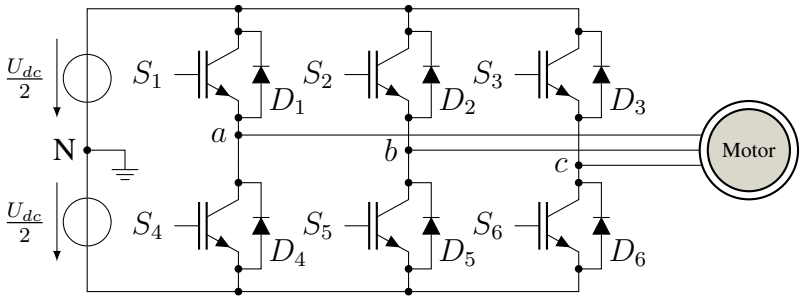

Figure 2.7: PMSM drive system with a three-phase two-level VSI.

the switches is called on or off. Each of the six switches can either be on or off, which leads to 2^6 combinations of the switching patterns. However, some of them are fatal for the devices, e.g. turn on the both switches of the same leg will cause short circuit. Some are not really contributing, such as the scenario when the resulting voltage relies on the current direction. In order to guarantee a safe operation of the inverter, two switches of a leg are conversely commanded, i.e. if the switch of the upper leg is on, then the one of the lower leg is off and vice versa. It is sufficient to analyze the current paths of a leg for further discussion. The conclusions about the other legs can be readily deduced from this analysis. Fig. 2.8 shows the possible transitions of the switching on a leg, where the current flow path regarding the current direction and the states of the switch S_1 are shown.

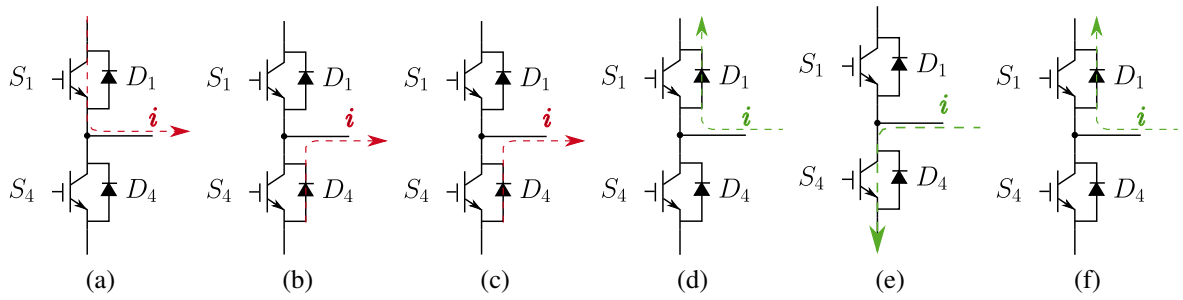

Figure 2.8: The flow path of the phase current regarding the current direction as well as the states of the switches S_1 and S_4. i in red denotes the positive phase current, while the green one represents the negative phase current. (a) S_1 is on, S_4 is off. (b) S_1 is off, S_4 is on. (c) S_1 is off, S_4 is off. (d) S_1 is on, S_4 is off. (e) S_1 is off, S_4 is on. (f) S_1 is off, S_4 is off.

- For the situation, where S_1 is on and S_4 is off, the positive current flows from the upper DC-link rail through the upper switch (in Fig. 2.8a) and the negative current flows through the upper freewheeling diode (in Fig. 2.8d).

- For the situation, where S_1 is off and S_4 is on, the positive current flows through the lower freewheeling diode (in Fig. 2.8b) and the negative current flows through the lower switch (in Fig. 2.8e).

- For the situation, where both switches are off, the positive current flows through the lower freewheeling diode (in Fig. 2.8c) and the negative current flows through the upper freewheeling diode (in Fig. 2.8f).

As a result, the VSI has in total 2^3 switching states. The switching state as well as the voltage level of a leg can be then represented with $v \in \mathbb{V}$, where $\mathbb{V}$ can be given as

$$\mathbb{V} := \{0,\, 1\}\ . \tag{2.23}$$

The set $\mathbb{V}$ is the constraint set for each phase of a two-level inverter. The values 0 and 1 correspond to the applied voltage for u_{aN}, u_{bN} and u_{cN}, which denote $-\frac{U_{dc}}{2}$ and $\frac{U_{dc}}{2}$, respectively. U_{dc} denotes the DC link voltage. As it is shown in Fig. 2.4, the neutral point potential is given by u_0. Therefore, the phase voltage can be derived as

$$u_x = \frac{U_{dc}}{2}\,(2\,v_x - 1) - u_0\ , \tag{2.24}$$

where the subscript x denotes an arbitrary phase of the three phases, i.e. $x \in \{a,\, b,\, c\}$. Considering the relationship between the phase voltage u_a and u_{aN} as

$$u_{aN} = u_a + u_{0N}\ , \tag{2.25}$$

and the assumption that

$$i_{a0} + i_{b0} + i_{c0} = 0\ , \tag{2.26}$$

The phase voltage vector $\boldsymbol{u}_{abc} = (u_a,\, u_b,\, u_c)^T$ is then derived from $(u_{aN},\, u_{bN},\, u_{cN})^T$, and can be written as

$$\begin{bmatrix} u_a \\ u_b \\ u_c \end{bmatrix} = \frac{1}{3}\begin{bmatrix} 2 & -1 & -1 \\ -1 & 2 & -1 \\ -1 & -1 & 2 \end{bmatrix}\begin{bmatrix} u_{aN} \\ u_{bN} \\ u_{cN} \end{bmatrix}\ . \tag{2.27}$$

The voltage vector $\boldsymbol{u}_{abc}$ can be furthermore transformed into the $\alpha\beta$ domain with the Clarke transformation in (2.6). The resulting possible voltage vectors $\boldsymbol{u}_{\alpha\beta} = (u_\alpha,\, u_\beta)^T$ spans a hexagon, which is shown in Fig. 2.9. Therefore, the switching state vectors in $\alpha\beta$ reference

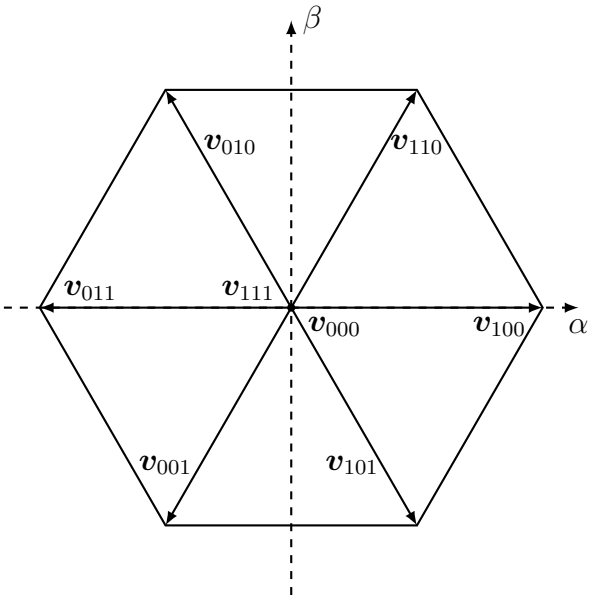

Figure 2.9: Switching states in the $\alpha\beta$ domain, which span a hexagon.

frame $\boldsymbol{v}_{\alpha\beta}$ can be denoted as a vector in the set $\mathcal{S}_v$, i.e. $\boldsymbol{v}_{\alpha\beta} \in \mathcal{S}_v$, where

$$\mathcal{S}_v := \left\{ \underbrace{\begin{bmatrix} 0 \\ 0 \end{bmatrix}}_{\boldsymbol{v}_{000}}, \underbrace{\begin{bmatrix} \frac{2}{3} \\ 0 \end{bmatrix}}_{\boldsymbol{v}_{100}}, \underbrace{\begin{bmatrix} \frac{1}{3} \\ \frac{1}{\sqrt{3}} \end{bmatrix}}_{\boldsymbol{v}_{110}}, \underbrace{\begin{bmatrix} -\frac{1}{3} \\ \frac{1}{\sqrt{3}} \end{bmatrix}}_{\boldsymbol{v}_{010}}, \underbrace{\begin{bmatrix} -\frac{2}{3} \\ 0 \end{bmatrix}}_{\boldsymbol{v}_{011}}, \underbrace{\begin{bmatrix} -\frac{1}{3} \\ -\frac{1}{\sqrt{3}} \end{bmatrix}}_{\boldsymbol{v}_{001}}, \underbrace{\begin{bmatrix} \frac{1}{3} \\ -\frac{1}{\sqrt{3}} \end{bmatrix}}_{\boldsymbol{v}_{101}} \right\}. \tag{2.28}$$

The sphere spanned by the vectors in $\mathcal{S}_v$, as shown in Fig. 2.9, can be defined by $\mathcal{S}_u := \text{conv}\, \mathcal{S}_v$, where conv denotes the convex hull operator [20]. Thus, $\mathcal{S}_u$ can be given as

$$\mathcal{S}_u = \left\{ \boldsymbol{u}_{\alpha\beta} \in \mathbb{R}^{2\times 1} \;\middle|\; \begin{bmatrix} \frac{\sqrt{3}}{2} & 0 & -\frac{\sqrt{3}}{2} & -\frac{\sqrt{3}}{2} & 0 & \frac{\sqrt{3}}{2} \\ \frac{1}{2} & 1 & \frac{1}{2} & -\frac{1}{2} & -1 & -\frac{1}{2} \end{bmatrix}^T \boldsymbol{u}_{\alpha\beta} \leq \frac{U_{dc}}{\sqrt{3}} \right\}. \tag{2.29}$$

2.2.2 Actuation Scheme

The inverter requires a direct gating signal to actuate the voltage command from the controller. Depending on the control methods, a modulator is optional for the electrical drive systems, which is however required when a duty cycle is generated from the controller. Mostly deployed modulation schemes are PWM and SVM. Besides, some alternative modulation schemes have also been proposed regarding specific applications with different topologies, power levels and requirements on switching frequency and dynamic response [21–23]. However, regardless of the actuation scheme, the discrete nature of the inverter introduces undesired harmonics into the electrical drive system.

2.2.2.1 Direct Actuation

Some control methods compute directly the gating signal for the inverter, i.e. the output signal satisfies $\mathbb{V}$. Therefore, the modulator is omitted for the direct actuation scheme. The switching signals is uniquely defined by $\boldsymbol{v} \in \{0,\, 1\}^3$. A typical strategy for choosing the optimal switching signals is to minimize on the one hand the tracking error, on the other hand the overall switching transitions. The direct actuation strategies are normally employed for the medium- and high-voltage drives in order to reduce the switching losses, since the losses of these drives are dominated by the switching losses whereas the ripples of the controlled ripples, e.g. currents, are less relevant [2].

2.2.2.2 Modulation Schemes

Besides the direct actuation, the actuation through modulator is widely applied in industry, since the dominance of the PI controllers emphasizes the application of a modulator to translate the real-valued voltage command into the switching signals. The modulator is normally applied in the low-voltage drives, of which the switching frequency is relatively constant and in general higher than the direct control strategies.

2.2.2.2.1 Pulse Width Modulation PWM translates the real-valued voltage command u_x^* of the phase x into a discrete switching signal by intersecting the duty cycle with a triangular or sawtooth carrier signal [19] and generating pulses of fixed amplitude, variable width [24].

Therefore, PWM is also called the carrier-based PWM. As it is shown in Fig. 2.7, an inverter produces discrete voltages of the values $\frac{U_{dc}}{2}$ and $-\frac{U_{dc}}{2}$. The first step of PWM is to scale the voltage command by half of the DC-link voltage, which yields

$$\bar{u}_x^* = \frac{u_x}{U_{dc}/2} \,. \tag{2.30}$$

The magnitude of the modulating signal $\bar{u}_x^*$ is referred as the modulation index and defined by

$$m = \bar{U}_x^* \,, \tag{2.31}$$

where $\bar{U}_x^*$ is the magnitude of the scaled voltage $\bar{u}_x^*$, i.e. $\bar{U}_x^* := |\max \bar{u}_x^*|$. Three working regions are defined for the modulation index m [19]:

- $m \in [0,\, 1]$: linear modulation region.
- $m \in [1,\, 2/\sqrt{3}]$: extended linear modulation region. The injection of the harmonic and its multiples is required.
- $m \in [2/\sqrt{3},\, m_{max}]$: overmodulation region. Relatively high harmonics are injected. The voltage as well as the current quality decreases. m_{max} with a value of $4/\pi$ denotes the six-step operation, which fully uses the available DC-link voltage but further worsens the voltage as well as the current quality.

For the two-level inverter, the typical realization of the PWM is shown in Fig. 2.10, where a triangular carrier signal is employed [25]. The carrier signal is defined by the carrier frequency

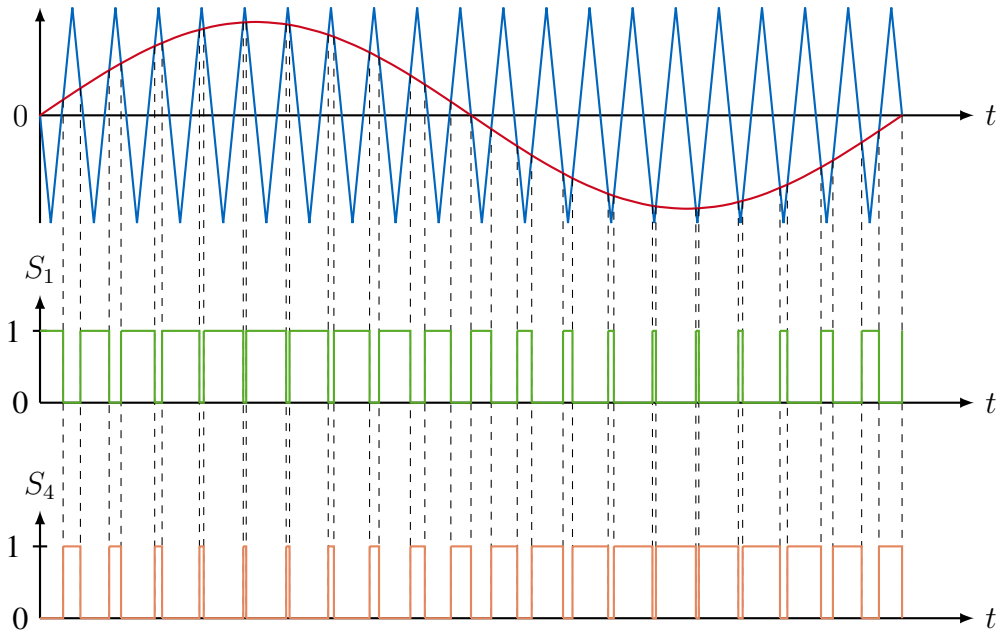

Figure 2.10: PWM generating principle with a sinusoidal reference and a triangular carrier signal.

f_c that is normally much higher than the fundamental frequency. As it is indicated in Fig. 2.10, the upper switch will be on, if the reference voltage is greater than the carrier signal, and vice versa. The principle of PWM can be realized either by analog implementation or by digital

implementation. However, the control precision and reliability of the analog implementation are less satisfying because of the complex circuit structure as well as the varying parameters of the analog devices. Therefore, the digital implementation is mostly adopted nowadays. Readers can refer to [25] for deeper explanation and analysis about the PWM.

2.2.2.2.2 Space Vector Modulation Fig. 2.9 demonstrates the switching vectors in the $\alpha\beta$ domain, which divide the sphere S_u into six sectors. Instead of comparing the reference voltage to the carrier signal as in PWM, SVM chooses switching vectors based on the location of the reference voltage in the $\alpha\beta$ reference frame.

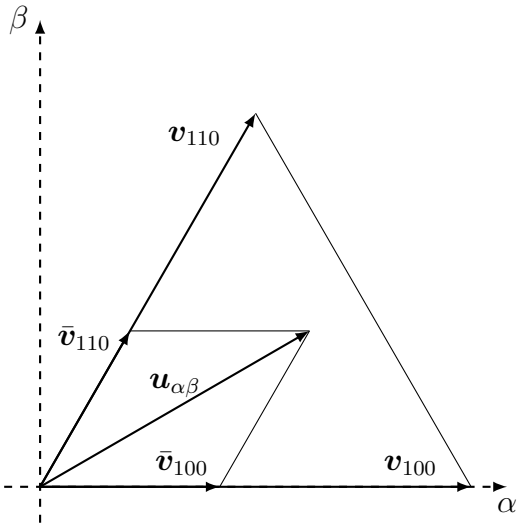

Figure 2.11: SVM generating principle with a reference voltage vector $\boldsymbol{u}_{\alpha\beta}$ in the sector consisting of the switching vectors $\boldsymbol{v}_{100}$ and $\boldsymbol{v}_{110}$.

In Fig. 2.11, an example for applying SVM is presented, of which the reference voltage vector $\boldsymbol{u}_{\alpha\beta}$ lies in the sector consisting of the two adjacent switching vectors $\boldsymbol{v}_{100}$ and $\boldsymbol{v}_{110}$. The reference voltage $\boldsymbol{u}_{\alpha\beta}$ is then synthesized by combing the two adjacent active switching vectors $\boldsymbol{v}_{100}$, $\boldsymbol{v}_{110}$ and one or two of the passive vectors $\boldsymbol{v}_{000}$, $\boldsymbol{v}_{111}$. There are several alternatives of SVM regarding different requirements on current quality and computational burden. The computational principle of the SVM is briefly introduced as follows. The active time of $\boldsymbol{v}_{000}$, $\boldsymbol{v}_{111}$ and the passive vectors are defined as t_1, t_2 and t_0, respectively. Since the t_1 and t_2 in one switching period T_c are proportional to the length of the corresponding vectors $\bar{\boldsymbol{v}}_{100}$ and $\bar{\boldsymbol{v}}_{110}$, the active times can be computed as [26]

$$t_1 = \frac{\|\bar{\boldsymbol{v}}_{100}\|}{\|\boldsymbol{v}_{100}\|} T_c \,, \quad t_2 = \frac{\|\bar{\boldsymbol{v}}_{110}\|}{\|\boldsymbol{v}_{100}\|} T_c \,, \quad t_0 = T_c - t_1 - t_2 \,. \tag{2.32}$$

The reference voltage $\boldsymbol{u}_{\alpha\beta}$ can be rewritten as a combination of $\boldsymbol{v}_{100}$, $\boldsymbol{v}_{110}$ and the passive vectors as

$$\boldsymbol{u}_{\alpha\beta} = \bar{\boldsymbol{v}}_{100} + \bar{\boldsymbol{v}}_{110} = \frac{t_1}{T_c} \cdot \boldsymbol{v}_{100} + \frac{t_2}{T_c} \cdot \boldsymbol{v}_{110} + \frac{t_0}{T_c} \cdot (\boldsymbol{v}_{000} \text{ or } \boldsymbol{v}_{111}) \,. \tag{2.33}$$

The reference voltage vector $\boldsymbol{u}_{\alpha\beta}$ can be represented in the phasor form as $\boldsymbol{u}_{\alpha\beta} = \|\boldsymbol{u}_{\alpha\beta}\| \angle\theta_{\boldsymbol{u}}$, where $\|\boldsymbol{u}_{\alpha\beta}\|$ and $\theta_{\boldsymbol{u}}$ are the amplitude and the angle of $\boldsymbol{u}_{\alpha\beta}$, respectively. The relationship be-

tween $\boldsymbol{u}_{\alpha\beta}$ and $\boldsymbol{v}_{000}$, $\boldsymbol{v}_{111}$ can be derived by means of the Fig. 2.11 and the law of trigonometric function in the following

$$\begin{aligned} \|\boldsymbol{u}_{\alpha\beta}\| \cdot \sin\left(\frac{\pi}{3} - \theta_{\boldsymbol{u}}\right) &= \|\bar{\boldsymbol{v}}_{100}\| \sin\frac{\pi}{3} , \\ \|\boldsymbol{u}_{\alpha\beta}\| \cdot \sin\frac{\pi}{3} &= \|\bar{\boldsymbol{v}}_{110}\| \sin\frac{\pi}{3} . \end{aligned} \tag{2.34}$$

Substitute (2.34) into (2.32), the active times can be obtained as

$$t_1 = \frac{2}{\sqrt{3}} T_c\, m \sin\left(\frac{\pi}{3} - \theta_{\boldsymbol{u}}\right) , \quad t_2 = \frac{2}{\sqrt{3}} T_c\, m \sin\theta_{\boldsymbol{u}} , \tag{2.35}$$

where m is the modulation index. Higher value of m leads to the overmodulation, where (2.35) is no longer valid. In order to reduce the number of commutation and switching losses, a state sequence with adjacent successive states is preferred. Only one commutation should occur during the state change of the switching vectors. The generated duty cycles of the three phases via symmetric SVM regarding different modulation index are shown in Fig. 2.12.

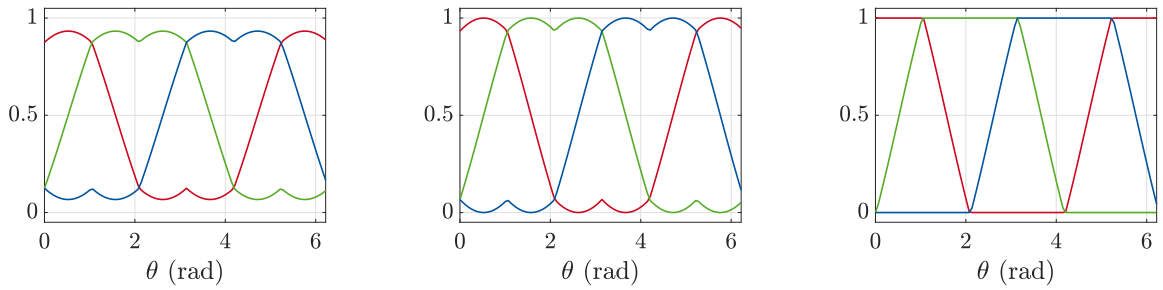

(a) $m = 1$ (b) $m = 2/\sqrt{3}$ (c) $m = \pi/4$

Figure 2.12: The duty cycle of three-phases via symmetric SVM regarding different modulation index m. The duty cycles of the phase a, b and c are denoted with red, green and blue, respectively.

2.2.2.2.3 Optimized Pulse Patterns The intuition of the optimized pulse patterns (OPP) is to find the optimal switching angles and switch positions in a fundamental period and allocates the computational burden offline [24]. The concept of OPP was widely adopted in 1970s for the slow switched power semiconductors [25]. Nowadays the main goal of applying OPP is to achieve the optimization criterion, e.g. minimizing the THD, since the current harmonics cause considerable losses in the machine. The pulse patterns are calculated offline over the operating range of the machine and stored in a look-up table for the online searching. For details regarding OPP, readers can refer to [24].

2.3 Control of Electrical Drive Systems

This section firstly overviews the theoretical foundations of the control and optimization problem. The control problem of the electrical drive systems denotes high complexity and subjects to multiple objectives. As stated in Section 1.1, there are many requirements for the performance

of the controller, which need to be considered during the controller design. Subsequently, an introduction to the state-of-the-art control strategies for the electrical drive system is presented. The system model as well as the system constraint in the context of PMSM drive system control is furthermore presented.

2.3.1 Prerequisite

An optimization problem consists of a cost function $J(x)$ and a constraint set $\mathbb{X}$. Solving the optimization problem is to find a feasible solution that minimizes the cost function $J(x)$. The feasible solution with the minimum cost is defined as a minimizer x^*. The solution is called feasible if the constraint is satisfied. In this section, several basic convex optimization problems as well as one special case related to the direct control of the power electronics is introduced. Subsequently, the Lagrangian duality and Karush-Kuhn-Tucker optimality conditions are also briefly discussed. However, the systems in real applications are normally complicated and demonstrate the nonlinear characteristics, which leads to a formulation of the nonlinear optimization problem.

2.3.1.1 Convex Optimization Problems

Convex optimization belongs to the mathematical optimization and has received considerable attention due to its theoretical and practical properties. Besides the well-established theoretical foundations, the convex optimization problems arising in the practical applications can be solved efficiently with numerous maturely developed solvers. Its definition is given in the following.

Definition 2.1 (Convex set [20])
A set $\mathbb{S}$ is convex if for any two points x_1, $x_2 \in \mathbb{S}$, all convex combinations of them also lie in the set $\mathbb{S}$, i.e.

$$(1-\theta)\, x_1 + \theta\, x_2 \in \mathbb{S}, \qquad \forall \theta \in [0,\, 1],\, \forall x_1,\, x_2 \in \mathbb{S}\,. \tag{2.36}$$

A significant characteristic of convex optimization problems is the equivalence of any local minimizer and the global minimizer. Some relevant convex optimization problems to this thesis are introduced as follows. Readers can refer to [20] for deeper explanation and analysis.

2.3.1.1.1 Linear Programming The simplest and mostly implemented convex optimization problem is the linear programming (LP), which describes the problem with linear affine cost functions and constraints. The general formulation of a LP can be given as

$$\begin{aligned} \min \quad & \boldsymbol{c}^T \boldsymbol{x} + d \\ \text{s.t.} \quad & \boldsymbol{G}\,\boldsymbol{x} \leq \boldsymbol{h} \\ & \boldsymbol{A}\,\boldsymbol{x} = \boldsymbol{b}\,, \end{aligned} \tag{2.37}$$

where $\boldsymbol{x} \in \mathbb{R}^n$ is the variable vector. $\boldsymbol{c} \in \mathbb{R}^n$, $\boldsymbol{h} \in \mathbb{R}^m$ and $\boldsymbol{b} \in \mathbb{R}^m$ are given vectors. $\boldsymbol{G} \in \mathbb{R}^{m\times n}$ and $\boldsymbol{A} \in \mathbb{R}^{m\times n}$ are given matrices. d is a scalar, which does not affect the feasible set. The feasible set of the problem in (2.37) is a polyhedron, where the linear cost function is minimized.

2.3.1.1.2 Quadratic Programming A quadratic programming (QP) has a quadratic cost function and subjects to affine constraints. The standard QP is defined as

$$\begin{aligned} \min \quad & \frac{1}{2}\boldsymbol{x}^T \boldsymbol{Q}\, \boldsymbol{x} + \boldsymbol{c}^T \boldsymbol{x} + d \\ \text{s.t.} \quad & \boldsymbol{G}\, \boldsymbol{x} \leq \boldsymbol{h} \\ & \boldsymbol{A}\, \boldsymbol{x} = b\,, \end{aligned} \tag{2.38}$$

where $\boldsymbol{Q} = \boldsymbol{Q}' \in \mathbb{R}^{n\times n}$, $\boldsymbol{c} \in \mathbb{R}^n$. The constant d can be omitted if only the optimizer is interested. Obviously, the quadratic programming is an extension or a generalization of the linear programming, where the matrix $\boldsymbol{Q} = \boldsymbol{0}$ in quadratic programming will lead to a linear programming. An widely applied example of the quadratic programming is the so-called linear-least-squares problem, where $\boldsymbol{Q}$ is symmetric positive definite and d is omitted. QP can be solved by using the interior point method [27], the active set [28] and the gradient methods [29].

2.3.1.1.3 Mixed-Integer Quadratic Programming One of the goals in this work is to improve the robustness as well as the performance of the direct current control, which is mainly related to the direct control of the inverter under the consideration of motor dynamics. This optimization problem is often referred as the mixed-integer programming (MIP), which includes the integer variables as the optimization variable and contains a discrete feasible set. Solving MIPs imposes a substantial computational burden on the computing hardware. The problem is generally non-deterministic polynomial-time hard (NP-hard), of which the solution time grows exponentially with the number of integer optimization variables [30]. More specifically, the problem invoked in this work is called mixed-integer quadratic programming (MIQP), which is necessarily to be introduced here. Besides, it is also a special case of QP. Generally, the MIQP can be formulated as

$$\begin{aligned} \min_{\boldsymbol{x}_c,\, \boldsymbol{x}_b} \quad & \frac{1}{2}\boldsymbol{x}^T \boldsymbol{Q}\, \boldsymbol{x} + \boldsymbol{c}^T\, \boldsymbol{x} + d \\ \text{s.t.} \quad & \boldsymbol{G}_c\, \boldsymbol{x}_c + \boldsymbol{G}_b\, \boldsymbol{x}_b \leq \boldsymbol{h} \\ & \boldsymbol{A}_c\, \boldsymbol{x}_c + \boldsymbol{A}_b\, \boldsymbol{x}_b = \boldsymbol{b} \\ & \boldsymbol{x}_c \in \mathbb{R}^{n_c},\, \boldsymbol{x}_b \in \{0,1\}^{n_b} \\ & \boldsymbol{x} = [\boldsymbol{x}_c,\, \boldsymbol{x}_b]^T\,, \end{aligned} \tag{2.39}$$

where $\boldsymbol{Q} \geq \boldsymbol{0} \in \mathbb{R}^{(n_c+n_b)\times(n_c+n_b)}$. n_c and n_b are the dimension number of continuous and integer variable, respectively. The problem is a mixed integer linear program (MILP), if $\boldsymbol{Q} = \boldsymbol{0}$. The constant term d is often omitted, since it has no influence on the optimizer. The most direct method to solve a MIQP is to enumerate all the possible integer values of the integer variable $\boldsymbol{x}_b$ and solve the corresponding QPs, which aggregates 2^{n_b} possibilities. This method is widely utilized in the direct current control with a short prediction horizon. However, by using this method, the solving of MIQP becomes NP hard, which means that in worst case the computational burden grows exponentially with the number of binary variables. In [31], several efficient algorithms are introduced and applied for solving the MIQP, such as branch-and-bound method, decomposition method, cutting-plane method and logic-based method.

2.3.1.2 Lagrangian Duality

Duality is essential for solving the optimization problem. It provides optimality certificates and has been studied in various directions. In this thesis, the Lagrangian duality is introduced, which is widely applied for the convex optimization problems [20]. In general, the optimization problem can be expressed as

$$\begin{aligned} \min_{\boldsymbol{x}} \quad & J\left(\boldsymbol{x}\right) \\ \text{s.t.} \quad & g_i\left(\boldsymbol{x}\right) \leq 0, \quad i = 1, \ldots, m \\ & h_j(\boldsymbol{x}) = 0, \quad j = 1, \ldots, n\ , \end{aligned} \tag{2.40}$$

where $J(\boldsymbol{x}) : \mathbb{R}^n \to \mathbb{R}$ is the cost function, $g_i(\boldsymbol{x}) : \mathbb{R}^n \to \mathbb{R}$ is the inequality constraint functions and $h_j(\boldsymbol{x})$ denotes the equality constraint functions, i.e. $h_j(\boldsymbol{x}) = \boldsymbol{a}_j^T\, \boldsymbol{x} - \boldsymbol{b}_j$. The Lagrangian function of (2.40) is defined as

$$\mathcal{L}(\boldsymbol{x},\, \boldsymbol{\lambda},\, \boldsymbol{\nu}) = J(\boldsymbol{x}) + \sum_{i=1}^{m} \lambda_i\, g_i(\boldsymbol{x}) + \sum_{i=1}^{n} \nu_i\, h_i(\boldsymbol{x})\ , \tag{2.41}$$

where $\boldsymbol{\lambda}$ and $\boldsymbol{\nu}$ are referred as Lagrange multipliers or dual multiplier vectors. The correlated Lagrangian dual problem is given as [20]

$$\begin{aligned} \max_{\boldsymbol{\lambda},\boldsymbol{\nu}} \quad & d\left(\boldsymbol{\lambda},\, \boldsymbol{\nu}\right) \\ \text{s.t.} \quad & \boldsymbol{\lambda} \succeq 0\ , \end{aligned} \tag{2.42}$$

where

$$d(\boldsymbol{\lambda},\, \boldsymbol{\nu}) = \min_{\boldsymbol{x}} \mathcal{L}(\boldsymbol{x},\, \boldsymbol{\lambda},\, \boldsymbol{\nu})\ , \tag{2.43}$$

which gives a lower bound on the optimal value of the primal optimization problem in (2.40). Since the cost function to be maximized is concave and the constraint is convex, the Lagrangian dual problem in (2.43) is a convex optimization problem.

2.3.1.3 Karush-Kuhn-Tucker conditions

Assume all equations in the optimization problem (2.40) are differentiable, then the gradient of $\mathcal{L}(\boldsymbol{x},\, \boldsymbol{\lambda}^*,\, \boldsymbol{\nu}^*)$ vanishes at $\boldsymbol{x} = \boldsymbol{x}^*$. Therefore, for any optimization problem that strong duality holds, the triplet $(\boldsymbol{x},\, \boldsymbol{\lambda},\, \boldsymbol{\nu})$ can only be optimal if the following set conditions are satisfied,

$$\begin{aligned} \nabla J(\boldsymbol{x}^*) + \sum_{i=1}^{m} \lambda_i^*\, \nabla g_i(\boldsymbol{x}^*) + \sum_{i=1}^{n} \nu^*\, \nabla h_i(\boldsymbol{x}^*) = 0, & \\ g_i(\boldsymbol{x}^*) \leq 0, \qquad & i = 1,\, 2,\, \cdots,\, m\ , \\ h_i(\boldsymbol{x}^*) = 0, \qquad & i = 1,\, 2,\, \cdots,\, n\ , \\ \lambda_i^* \geq 0, \qquad & i = 1,\, 2,\, \cdots,\, m\ , \\ \lambda_i^*\, g_i(\boldsymbol{x}^*) = 0, \qquad & i = 1,\, 2,\, \cdots,\, m\ , \end{aligned} \tag{2.44}$$

which are also known as Karush-Kuhn-Tucker (KKT) optimality conditions. The KKT conditions are the first order necessary conditions for optimality of the constrained optimization problem (2.40). They are also the necessary and sufficient optimality conditions for the QPs.

2.3.1.4 Nonlinear Optimization Problem

If the cost function or some of the constraints are nonlinear, then the optimization problem is called a nonlinear programming (NLP) problem. The general nonlinear optimization problem can be difficult to solve, even if the cost functions and the constraints are smooth. However, with the help of efficient numerical solving techniques, such as multiple shooting, a good local optima or even the global optimum can be obtained. Depending on the requirement about the convergent rate and the robustness, the available memory resource, the adequate computing methods can be determined.

In this work, the NLP is solved with Newton type methods, which use the first- or second-order derivatives for the solution. The reference [32] has given an elaborate overview for solving a NLP. The Newton's methods can be classified into two families: sequential quadratic programming (SQP) type methods and interior point (IP) type methods. In this thesis, we will only cover the SQP methods. SQP is a general technique for finding the local optimum of the original problem by iteratively linearizing the NLP at the current step. It applies in every iteration a Newton step to the KKT system of the NLP. Therefore, it demonstrates a fast rate of convergence. More details can be found in Section 3.5.4.

2.3.2 Control Strategies

Many control methods have been proposed to realize the precise control of electrical drives. The most commonly used control methods for the electrical drive systems can be roughly sorted into the scalar-based control and the vector-based control. The scalar-based control method utilizes the steady-state model of the PMSM and computes the magnitude as well as the frequency of the command voltage accordingly. The vector-based control schemes are established based on the dynamic model of the machine and therefore enable a fast transient during the change of the reference or the occurrence of the disturbances. They can be further divided into two subcategories, i.e. the field oriented control and the predictive control. FOC was developed in the 1970s [34], which decouples the control for the air-gap flux and the electromagnetic torque. As its name suggests, FOC aligns the reference frame with the flux linkage and decoupled the system. However, because of the reference transformation, an encoder or an observer is required for obtaining the rotor position. The principle of the predictive control is to predict the system behavior in the future via deploying the model of the system. The predictions are then used to compute the command signal based on the predefined optimizing criterion. According to different optimizing criteria, the predictive control for the electrical drive system can be commonly classified into deadbeat control, hysteresis-based control, trajectory-based control and model predictive control [33]. The hysteresis-based control defines the boundaries of the controlled variables. The trajectory-based control actuates the command in such a way that the controlled variables follow the predefined trajectory. The deadbeat control minimizes the tracking error for the next time instant. Thanks to the development of the numerical optimization and advances in the computational power of microcontrollers, more complex control strategies from the predictive control category have received more attentions in the recent years. In MPC, a cost function regarding the predefined criteria is formulated within the prediction horizon N_p, which is then optimized under the consideration of the associating constraints. Therefore, MPC offers a more flexible framework for the control purpose. It is also worth mentioning that the deadbeat

control can be considered as a special case of MPC, where the cost function includes only the reference tracking within one prediction step and the constraints are omitted. The individual control method is introduced in the following.

2.3.2.1 V/f Control

The V/f control is based on the current dynamics of the machine in the steady state, which is short for Volts/Hertz. It is the most applied and simplest control scheme for the drive control. The control scheme is in general a feed-forward controller and has no feedback mechanism. The current loop of a PMSM in steady state is simplified from (2.13) and omits the differential term, which can be given by

$$\boldsymbol{u}^R = R_\mathrm{s}\, \boldsymbol{i}^R + j\omega_e \cdot \boldsymbol{\Psi}^R \,. \tag{2.45}$$

It can be observed from (2.45) that the resistive voltage drop can be ignored, if the speed ω_e is high enough. Then the output voltage of the current controller is proportional to the rotor angular speed. At low speed, the voltage drop on the stator resistance is a considerable term and may become comparable to the back electromotive force in the current dynamics, an additional voltage is applied to compensate the resistive part. The simpleness of V/f control on the other hand comes with drawbacks [37]. One of them is the instability of the system after exceeding a certain frequency. Damper windings are constructed with the rotor to assure the synchronization of the rotor to the electrical frequency, which would limit the design of the PMSM. Moreover, the control method delivers a relatively poor dynamic performance and further limits its application. Besides, it provides deficient fault protection mechanism against stall detection and over-currents.

2.3.2.2 FOC

In this thesis, the term **FOC** denotes the control realized with the PID control strategy. The PID controller is widely used in almost all industrial applications. As the name suggests, the PID control consists of a proportional, an integral and a derivative part, which belongs to linear control strategy. The overall control output of the PID controller in the continuous-time domain is given as

$$u = K_P\, e + K_I \int e \,\mathrm{d}t + K_D \,\frac{\mathrm{d}}{\mathrm{d}t} e \,, \tag{2.46}$$

where e denotes the tracking error between the reference y^* and the measurement y, i.e. $e = y^* - y$. However, because of the limitation on the output control value u as well as the anti-windup strategy, which is normally implemented for the integral term of the PID control to improve the stability of the closed-loop system, the PID controller may demonstrates nonlinear effects for the overall control loop. The tuning of the coefficients K_P, K_I and K_D is normally based on the system model of the drive system. Nonetheless, they can also be designed without any knowledge of the system. FOC can deliver high steady state control precision and is carried out with fixed switching frequency. However, its dynamic performance is in general unsatisfactory. Furthermore, the control bandwidth of FOC is limited.

2.3.2.3 Hysteresis-Based Control

The principle of the hysteresis-based control is to constrain the controlled variables within the boundaries of a hysteresis area. Therefore, the hysteresis control is also called bang-bang controller. No modulator is necessary in the hysteresis-based control. However, the hysteresis-based controller requires very high sampling rates to avoid the violation of the boundary and to achieve an acceptable control performance. In [38], the hysteresis-based predictive current controller was proposed. The block diagram of this proposal is shown in Fig. 2.13 [38]. The hysteresis area is defined by a circle, which evaluates whether the error between the reference value and the actual value is acceptable or not. A crossover of the boundary line actives the computation of the next switching state. The switching state vector that minimizes the switching frequency is selected [38]. Other optimization criteria can be likewise chosen for the hysteresis-based control, e.g. low current distortion and low electromagnetic inferences [33]. Moreover, the error boundary rotates with the reference value, as it is shown in Fig. 2.13.

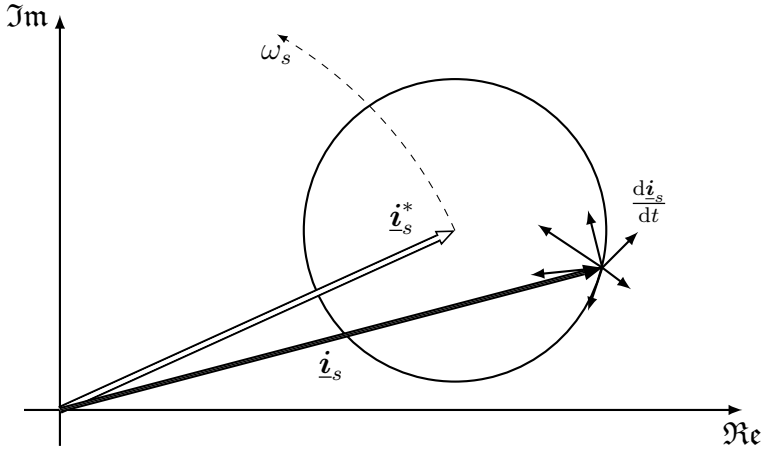

Figure 2.13: Principle of the hysteresis-based control.

2.3.2.4 Trajectory-Based Control

The trajectory-based control directly computes the command value to force the controlled variables to travel along the predefined trajectory. In Fig. 2.14, an example of the trajectory-based control from [39] is shown, where it is applied to the direct speed control problem. The parabolas in Fig. 2.17 are computed by classifying the switching states into three groups, i.e. torque increasing, slowly torque decreasing and rapidly torque decreasing, and investigating the relationship between e and a with the consideration of the system dynamics, where e denotes the tracking error of the speed and a represents the acceleration. The initial state is given as e_k/a_k. The adjacent state e_{k+1}/a_{k+1} is reached by choosing the switching state S_k, which is the torque increasing voltage vector. Analogously, the states at $k+2$ and subsequently at $k+3$ are achieved by choosing the switching states S_{k+1} and S_{k+2}, respectively. Then the tracking error e is controlled within the hysteresis band defined by $-H_y$ and H_y.

Nonetheless, the calculation of the trajectories requires a foreknowledge of the system. Moreover, the switching frequency is limited.

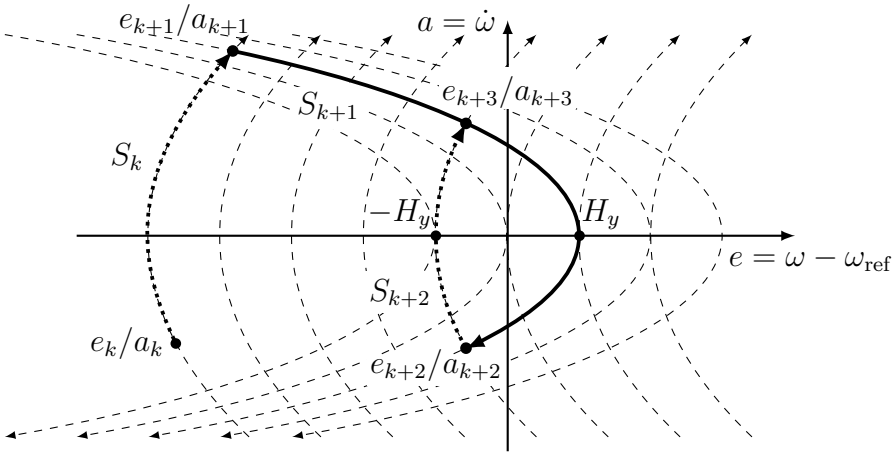

Figure 2.14: Principle of the trajectory-based control.

2.3.2.5 Deadbeat Control

The deadbeat control proceeds based on the system model and computes the command signals with the intuition of reaching the reference value at the next time instant. An example of the deadbeat control is shown in Fig. 2.15. Ideally the controlled value can reach the reference at the next time instant, which contributes to the advantage of the deadbeat control, i.e. fast dynamic response. However, because of the model uncertainties and disturbances in the system, the deadbeat control may exhibit steady-state errors, ripples or even cause instability of the closed-loop system.

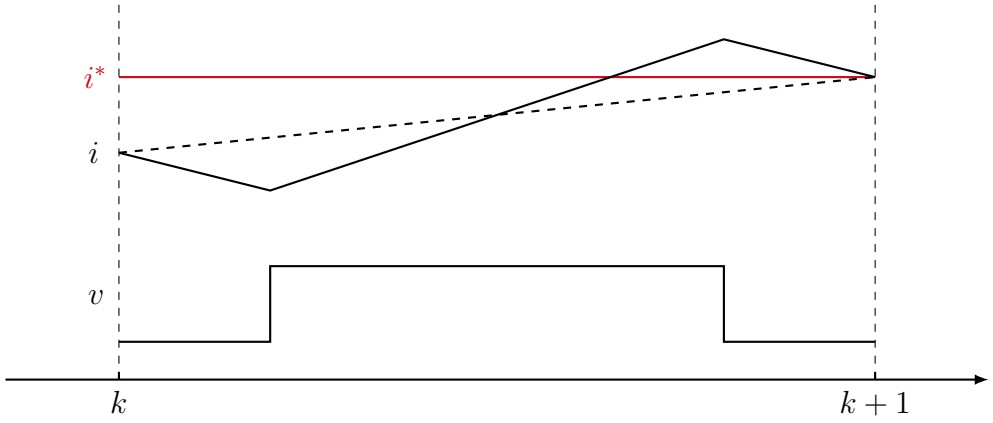

Figure 2.15: Principle of the deadbeat control.

2.3.2.6 Model Predictive Control

Model predictive control (MPC) has been a topic of research and application for several decades. It was originally introduced in the process industry [40]. MPC has received widespread attention both in academia and industry because of its capability of satisfying constraints and fast dynamic response. In [38] the possibility of applying MPC in the domain of power electronics was presented. The computational issues of solving the MPC problem and the obstacle of constructing parametric solutions have restricted the application of MPC in practice, especially for

complex systems and sophisticated control problems. However, thanks to the vast developments in numerical optimization and the advances in the computational power of microprocessors, MPC has been studied and applied as a promising control strategy for various power electronics and electrical drive systems [41, 42]. MPC solves a constrained finite time optimal control (CFTOC) problem at each sampling time instant, i.e. it uses the model of the system to predict the system behaviour of the controlled system states over N_p steps in the future and computes the problem based on certain criteria. Moreover, MPC provides the possibility of including the system constraints into the optimization problem. The optimizing criteria are designed as a cost function for the optimization. N_p is called the prediction horizon for the optimization problem. Nonetheless, MPC implements only the first element of the solution sequence, i.e. the optimal control sequence, into the plant. Subsequently, at the next time instant, the CFTOC is computed with the most recent measurements over the shifted horizon. This control policy is called the receding horizon policy, which introduces dynamic control input into the system. Its working methodology is shown in Fig. 2.16, where N_p denotes the prediction horizon and N_u represents the control horizon.

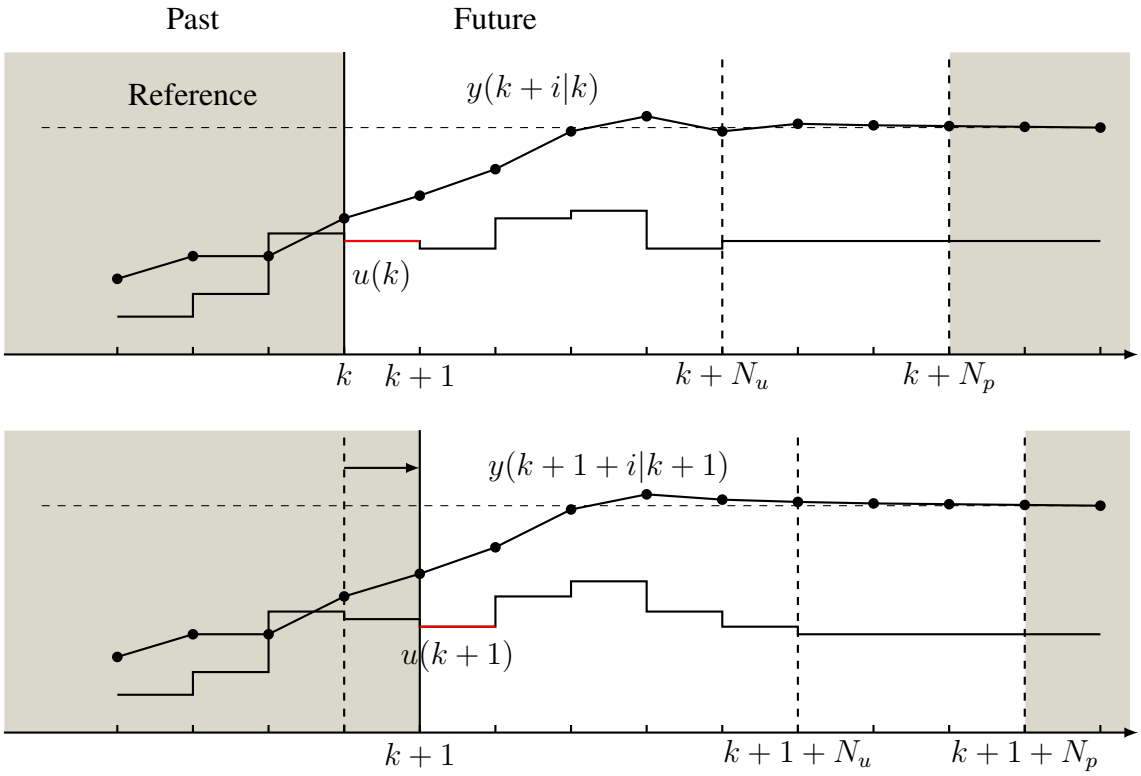

Figure 2.16: The principle of the model predictive control with receding horizon policy.

Depending on the optimizer of the control problem, MPC for the power electronics and the electrical drives can be roughly divided into two groups: continuous-control-set model predictive control (CCS-MPC) and finite-control-set model predictive control (FCS-MPC). CCS-MPC considers the control voltage as a continuous quantity. Therefore, a modulator is mandatory for the CCS-MPC to actuate the voltage command and delivers switching signals to the inverter. On the contrary to that, FCS-MPC directly considers the discrete nature of the power electronics

and includes it into the control problem. Therefore, the modulator is omitted in the context of FCS-MPC. Because that FSC-MPC directly computes the switching signals for the converter, it is also called the direct MPC. Among numerous FCS-MPC variants, the prediction horizon is commonly set to one [2], because a long prediction horizon is believed to cause explosion of the number of solutions, which further increases the computational burden.

2.3.3 Control Structure

Fig. 2.17 shows a classical cascaded control structure for the indirect control of the electrical drive system via the aforementioned vector-based control methods [43]. This structure decomposes the stator current of PMSM into the field-generating component and torque-generating component, which simplifies the control problem to almost identical as the operation with the DC machine. Firstly, the measurements of the three-phase stator currents are carried out. Nonetheless, only currents of two phases (normally i_a and i_b) are measured in practice, since the sum of the currents of three phases is zero. By applying the Clarke transformation $T_{\alpha\beta}$ in (2.7), the three-phase currents are transformed into the $\alpha\beta$ coordinates. Subsequently, the Park transformation T_{dq} in (2.11) is applied to further transform the currents into the dq reference frame, where the measured (with encoder) or estimated rotor angle is deployed. The outer loop of the cascaded control is the speed loop, which generates the torque reference T^* and subsequently the current references $\boldsymbol{i}^*$. The current reference generator can be realized with simple proportional-integral (PI) technique or the efficiency optimizing strategies, e.g. maximum torque per ampere (MTPA) concept. The current reference is then delivered to the current controller, where the control task can be accomplished by the control methods introduced in the former section. The output command voltage from the current controller is then transformed back into the three-phase reference frame via the pseudo inverse of the Park transformation and of the Clarke transformation. This continuous-valued voltage command $\boldsymbol{u}^*_{abc}$ passes through the modulator, e.g. with the aforementioned PWM and SVM, and are translated into the discrete-valued switching states $\boldsymbol{S}_{abc}$, which are then forwarded to the power inverter.

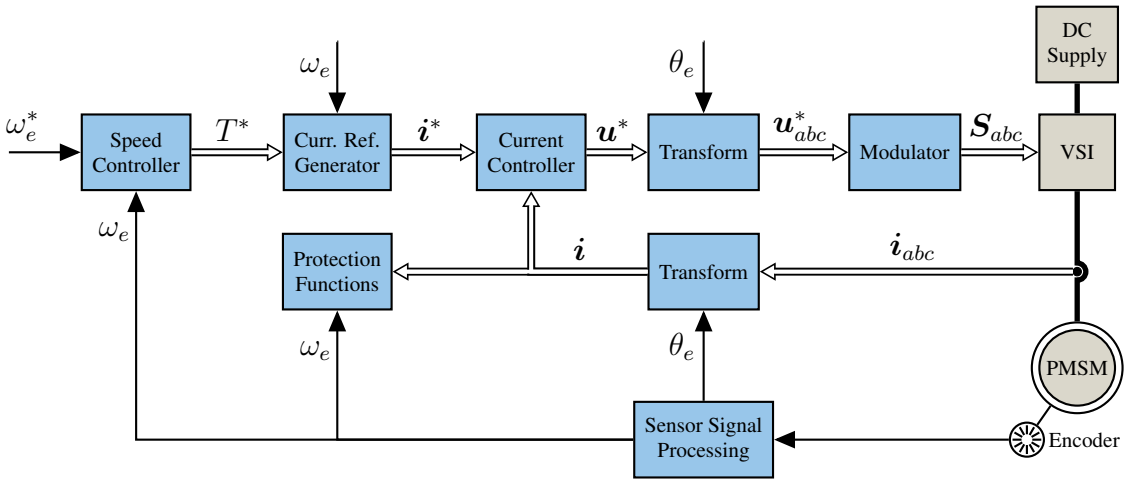

Figure 2.17: General control structure of vector-based control for PMSM.

2.3.4 System Model

As it is stated previously, the system model for the current control can be chosen either in the $\alpha\beta$ reference frame or in the dq reference frame. Depending on the control input, the control input of the system model can be the continuous-valued voltage command $\boldsymbol{u}$ or the switching signals of three-phases $\boldsymbol{v}$. However, they can be generally formulated into the state-space form and discretized with a selected method.

2.3.4.1 Continuous-Time Model

A linear time-invariant system is characterized by differential equations, which can be compactly reformulated into the state-space form as

$$\begin{aligned} \frac{\mathrm{d}}{\mathrm{d}\,t}\,\boldsymbol{x}(t) &= \boldsymbol{A}_c\,\boldsymbol{x}(t) + \boldsymbol{B}_c\,\boldsymbol{u}(t)\;, \\ \boldsymbol{y}(t) &= \boldsymbol{C}_c\,\boldsymbol{x}(t) + \boldsymbol{D}_c\,\boldsymbol{u}(t)\;, \end{aligned} \tag{2.47}$$

where $\boldsymbol{x}$ denotes the state vector, $\boldsymbol{u}$ denotes the input vector and $\boldsymbol{y}$ denote the output vector. $\boldsymbol{A}_c$ is the state or system matrix, $\boldsymbol{B}_c$ is the input matrix, $\boldsymbol{C}_c$ is the output matrix and $\boldsymbol{D}_c$ is the feedthrough matrix. The state-space formulation exhibits a convenient and compact manner to model and analyze the system with multiple inputs and outputs.

2.3.4.2 Discrete-Time Model

The continuous system needs to be discretized, in order to realize the implementation of the control algorithms on digital control systems. For a linear system in (2.47), the general formulation of the discretized state space with a constant sampling time T_s can be written as

$$\begin{aligned} \boldsymbol{x}_{k+1} &= \boldsymbol{A}\,\boldsymbol{x}_k + \boldsymbol{B}\,\boldsymbol{u}_k\;, \\ \boldsymbol{y}_k &= \boldsymbol{C}\,\boldsymbol{x}_k + \boldsymbol{D}\,\boldsymbol{u}_k\;, \end{aligned} \tag{2.48}$$

where k denotes the current time step. The discrete-time system (2.48) is restricted to change its state variables at the sampling instant $t = k\,T_s$.

2.3.4.3 Discretization Methods

The discretization of a continuous system can be realized with many methods, which can be selected according to the requirements of the discretization accuracy and the available computational resources.

2.3.4.3.1 Exact Discritization The most accurate discretization method is the so-called exact discretizaion, which is given as

$$\boldsymbol{A} = e^{\boldsymbol{A}_c\,T_s}, \quad \boldsymbol{B} = \Big(\int_0^{T_s} e^{\boldsymbol{A}_c\,\tau}\mathrm{d}\tau\Big)\,\boldsymbol{B}_c\;. \tag{2.49}$$

The output matrix $\boldsymbol{C}_c$ and the feedthrough matrix $\boldsymbol{D}_c$ are given same as the continuous form by

$$\boldsymbol{C} = \boldsymbol{C}_c\;, \quad \boldsymbol{D} = \boldsymbol{D}_c\;. \tag{2.50}$$

Although the exact discretization offers an exact solution to the differential equations, the information of inter-sampling behaviour is still lost by the discretization. Moreover, for nonlinear system, it is difficult to derive the exact solution.

2.3.4.3.2 Euler Discretization As the simplest discretization method, the Euler's method is most commonly applied in practice. Euler's method is based on a truncated Taylor series expansion and approximates the ordinary differential equations in a first-order manner. Regarding the computation procedure of the differentiation, Euler's method can be roughly divided into two different methods, namely the Euler-forward discretization and the Euler-backward discretization. The forward Euler discretization approximates the differentiation at $t = k\,T_s$ with

$$\frac{\mathrm{d}}{\mathrm{d}\,t}\boldsymbol{x}(t) \approx \frac{\boldsymbol{x}(k+1) - \boldsymbol{x}(k)}{T_s}\,. \tag{2.51}$$

The implicit analogue of the forward Euler discretization method is the backward Euler discretization, which approximates the differentiation with

$$\frac{\mathrm{d}}{\mathrm{d}\,t}\boldsymbol{x}(t) \approx \frac{\boldsymbol{x}(k) - \boldsymbol{x}(k-1)}{T_s}\,. \tag{2.52}$$

The backward Euler discretization is numerically more stable than the forward Euler discretization. But it is more time-consuming and not always available. Therefore, the forward Euler method is mostly applied, which transforms the continuous-time system in (2.47) into the discrete form via

$$\boldsymbol{A} = \boldsymbol{I} + \boldsymbol{A}_c\,T_s, \quad \boldsymbol{B} = \boldsymbol{B}_c\,T_s\,. \tag{2.53}$$

The output matrix $\boldsymbol{C}_c$ and the feedthrough matrix $\boldsymbol{D}_c$ still remain unchanged for deriving the matrices for the discrete-time system, i.e.

$$\boldsymbol{C} = \boldsymbol{C}_c\,, \quad \boldsymbol{D} = \boldsymbol{D}_c\,. \tag{2.54}$$

2.3.4.3.3 High-Order Discretization Besides the aforementioned discretization methods, methods such as Heun's method, Runge-Kutta methods provide higher-order discretization. Therefore, comparing to the Euler's method, they can approximate the differentiation more accurately and correct to a higher-order term in the Taylor series expansion. More details about the high-order discretization can be found in [44]. Nonetheless, the forward Euler discretization is sufficient enough for short sampling intervals of up to several tens of microseconds [24]. Therefore, it is deployed for the rest of this work.

2.3.5 System Constraints

A physical system is always limited by certain constraints, which guarantee the safe operation of the system. The electrical drive system is also no exception. There are many limits need to be considered in the electrical drive system, e.g. the limitation of the DC-link voltage and the limitation from the inverter as well as from the machine. However, the most restrictive limits are imposed by the DC-link voltage, the applied modulation method and the maximum allowed current of the machine as well as of the inverter [45]. Moreover, for the direct control, the voltage limitation is not a continuous space, but a set comprised by the discrete values.

2.3.5.1 Current Limit

The magnitude of the stator current is limited considering that only a restricted amount of heat can be produced during the operation, which is mainly determined by the maximum operating temperature and given as the maximum allowed current of the machine $I_{\max}$. The maximum allowed current is then represented in the two-axis reference frame, i.e. $\alpha\beta$ reference frame or dq reference frame, as a circle centered at the origin and with a radius of $I_{\max}$. Therefore, the current vector is constraint by the current limit and can be written as

$$\boldsymbol{i} \in \mathbb{I} := \{\boldsymbol{i} \in \mathbb{R}^2 | \ \|\boldsymbol{i}\| \leq I_{\max}\}, \tag{2.55}$$

where $\boldsymbol{i}$ denotes the current vector in either $\alpha\beta$ reference frame or dq reference frame. The transient violation of the current constraint is actually acceptable, since the thermal time constants are much larger than the electric ones.

2.3.5.2 Voltage Limit

Another operation limit that needs to be considered is the maximum output voltage provided by the DC-link. As it is introduced previously, the output voltage of the inverter is a function of the DC-link voltage U_{dc}. For the indirect control problem, the voltage limit is given in (2.29), i.e.

$$\boldsymbol{u}_{\alpha\beta} \in \mathbb{U} := \left\{ \boldsymbol{u}_{\alpha\beta} \in \mathbb{R}^{2\times 1} \ \middle| \ \begin{bmatrix} \frac{\sqrt{3}}{2} & 0 & -\frac{\sqrt{3}}{2} & -\frac{\sqrt{3}}{2} & 0 & \frac{\sqrt{3}}{2} \\ \frac{1}{2} & 1 & \frac{1}{2} & -\frac{1}{2} & -1 & -\frac{1}{2} \end{bmatrix}^T \boldsymbol{u}_{\alpha\beta} \leq \frac{U_{dc}}{\sqrt{3}} \right\}. \tag{2.56}$$

For the direct control problem, the control variable is the switching states. Therefore, the voltage limit becomes integer-valued input constraint as in (2.23), i.e.

$$\boldsymbol{u}_{abc} \in \mathbb{V}^3 \ . \tag{2.57}$$

The constraints resulted from the physical nature of the system, e.g. $\mathbb{U}$ and $\mathbb{V}$, can not be violated. Therefore, they are called hard constraints. On the contrary, the constraints that are established to guarantee the safe operation of the system, e.g. the current limit $\mathbb{I}$, can be violated bearing the risk of failure. Thus, they are denoted as soft constraints.

2.4 Uncertainties and Disturbances in Drive System

The AC machine drive system is complicated and intrinsically nonlinear, as presented previously. It contains various uncertainties and disturbances, which include both low-frequency components, such as the back EMF and the parameter variation phenomenon, and the high-frequency components, for example the disturbances induced by the VSI nonlinearities and flux harmonics. Thus, one of the essential tasks for realizing the precise control of the drive system is to reject the various external disturbances and improve the system robustness under the existence of various uncertainties. In this section, the two main sources of the disturbances and the uncertainties, i.e. the parameter variation and the VSI nonlinear effects, are explained and analyzed. Furthermore, the other uncertainties and disturbances are also introduced, such as the digital delay and the flux harmonics. Their impacts can be concluded as causing a degradation

of the control performance and invoking instability of the closed-loop system. The deterioration of the control performance can be denoted by steady-state errors and periodic disturbances. The static error, which is mainly caused by the parameter variation during the operation or the other slow varying disturbances in the drive system, affects the control accuracy. The periodic disturbances degrades the control performance, e.g. fluctuation in the current control loop as well as in the speed control loop, toque pulsation and more losses. Moreover, authors in [46] addressed the detection of performance degradation from an incipient stage can substantially reduce the unscheduled downtime as well as the repairing cost, and further increase the production efficiency.

2.4.1 Parameter Variation

A precise knowledge of the machine parameters is required for the control system design [47, 48], condition monitoring and fault detection. As it is indicated in [49], the machine condition variation can cause lower efficiency, worse current regulation performance and disturbed speed control. Besides, the machine electrical parameters are frequently used as an indicator of the machine conditions. In the following, the parameter variation problem is comprehensively analyzed. The factors causing the parameter variation are elaborated.

2.4.1.1 Temperature

The main external affecting factor of the parameter variation is the temperature. It has a great influence on both electrical and magnetic properties of the material. However, in many drive systems, the temperature sensor is omitted considering the fact that it will increase the manufacturing cost as well as the maintenance expenses. Furthermore, most modern drives apply the PWM to produce the voltage, which can cause electrical noise and may affect the accuracy of the dynamically measured temperature. The variation of the thermal condition can be caused by the external environment and the machine itself. As it is explained in [50], there are many factors contributing to the increase of the temperature in the PMSM, but the main internal sources can be concluded as the PM eddy current loss, the PM hysteresis loss, the copper loss and the aluminium loss. Besides, the mechanical losses on account of the friction in the bearings may associate the internal sources. The impacts of the temperature on the individual components are further analyzed in following.

2.4.1.1.1 Stator Resistance The relationship between the stator resistance and the temperature can be simplified as the thermal behaviour of the copper, since the most electrical machines are constructed with copper windings. The general formulation of the resistance in conductors can be given as a function of the temperature in the following

$$R_{\mathrm{s}}(T) = R_0 \left(1 + \alpha \left(T - T_0\right)\right) , \tag{2.58}$$

where R_0 is the resistance at the room temperature T_0 and α is the temperature coefficient of the material. The temperature coefficient α is given as $\alpha_{Cu} = 0.004\,041\,^{\circ}\mathrm{C}^{-1}$ for copper conductors and $\alpha_{Al} = 0.004\,308\,^{\circ}\mathrm{C}^{-1}$ for aluminum conductors. Normally, T_0 is considered as $20\,^{\circ}\mathrm{C}$. PMSM usually have an operating temperature range of $100\,^{\circ}\mathrm{C}$. The resistance consisting of copper conductors can vary under the thermal effects by 40% (with $\alpha_{Cu} = 0.004\,041\,^{\circ}\mathrm{C}^{-1}$).

2.4.1.1.2 Permanent Magnet Flux Linkage The permanent magnet flux linkage is also temperature dependent [51]. Its temperature coefficient, which can roughly describe the thermal characteristics of the magnet, can be provided by the permanent magnet manufacturers. The function of the permanent magnet flux linkage to the temperature can be written similarly to (2.58) and given as

$$\Psi_{\mathrm{m}}(T) = \Psi_{\mathrm{m},0}\left(1 + \beta\left(T - T_0\right)\right), \tag{2.59}$$

where $\Psi_{\mathrm{m},0}$ is the permanent magnet flux linkage value at the room temperature T_0, T is the rotor temperature and β is the thermal coefficient of the permanent magnets. Neodymium Iron Boron (NdFeB) and Samarium Cobalt (SmCo) magnets are the most popular commercialized permanent magnet materials for constructing PMSMs. They have a temperature coefficient of $\beta = -0.11\,\%/°\mathrm{C}$ and $\beta = -0.03\,\%/°\mathrm{C}$, respectively. Besides, most permanent magnet materials have an approximate Curie temperature, which indicates the temperature causing permanent demagnetization [9]. Therefore, an operation of PMSMs above the Curie temperature should be avoided. In general, the influence of the temperature on the permanent magnets can be sorted into three main categories: the permanent change of the magnetic material, the irreversible change and the reversible change. They are further explained in following [9]:

- The permanent change: the change persist even if the magnet is fully remagnetized.
- The irreversible change: the change persist even after the cause has been removed. But the original demagnetization curve can be restored by remagnetizing the magnet.
- The reversible change: the change is reversible. For example, the field weakening, which enables the motor to run in the high-speed area (above the basic speed area).

2.4.1.1.3 Inductance The temperature changes also influence the inductances of the PMSM, since the temperature affects characteristics of the magnetic material and further causes a change of the inductances.

2.4.1.2 Saturation Effect

The saturation effect is considered as the primary affecting factor for the inductances and describes the characteristic parameters of ferromagnetic as well as ferrimagnetic materials. It indicates the state, from which the applied external magnetic field increases the magnetization of the material slowly and the magnetization remains nearly constant. A typical saturation curve can be described as a function between the current and the corresponding flux linkage, which is demonstratively presented in Fig. 2.18, where the points P_1 and P_2 are selected as two representative points for further specification. L_1 and L_2 denote their gradient, respectively.

In PMSM machines, the magnetic characteristic of the magnetic paths associated with the d- and the q-axis are different. The magnetic flux linkage in the d-axis includes the permanent magnet flux linkage. Therefore, a certain level of magnetic field is already built by the permanent magnet even before the machine is excited, as it is shown at P_2 in Fig. 2.18. The corresponding inductance is approximated as the gradient L_2. As a result, a zero or negative current is normally applied in the d-axis. In comparison to the d-axis, the magnetic flux linkage in q-axis can be considered within the linear region in Fig. 2.18, which is represented with the

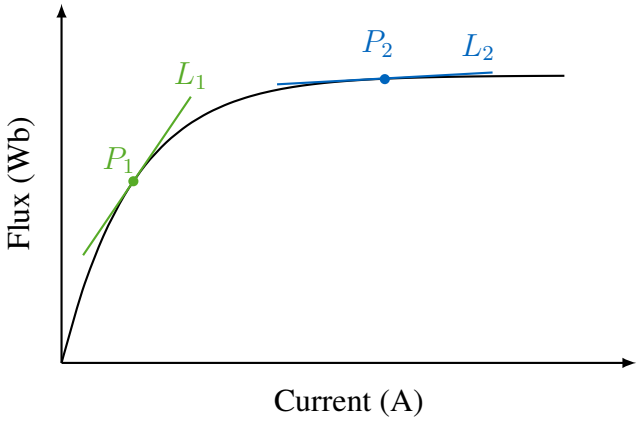

Figure 2.18: Saturation effect of the flux linkage.

point P_1 and denoted by the gradient L_1. Furthermore, because of the saturation effect, the d-axis inductance of permanent magnet synchronous machines is considered to vary more slowly than the q-axis inductance.

2.4.1.3 Other Causes

Besides the aforementioned main causes, the parameters of the PMSM drive system can be furthermore affected by the following factors:

- **Aging Effect** There are two main types of magnetic aging, namely structural aging and thermally activated magnetization processes [52]. For example, the permanent magnets loose a small fraction of their remanence each decade [52].

- **Oxidation** All types of rare earth magnet are vulnerable to oxidation, dominated by the corrosion on the surface. The oxidation causes a permanent metallurgical change in their structure [9]. The oxidized surface layer possesses a lower intrinsic coercivity, which accelerates demagnetization of this region, especially for the thin magnet.

- **Pressure** The pressure will cause a undesirable structural change, which will further affects the parameters in the drive system.

2.4.2 Influence from Inverter

In most applications, the command voltage of the current controller is employed as the terminal voltage of the machine, since the terminal voltage is normally unavailable during the operation. However, due to the nonlinearities of the VSI, the terminal voltage of the machine differs from the commanded output voltage. However, the distorted voltage has a great influence on the control as well as on the estimation performance of the PMSM. In this section, the nonlinear effects of the VSI are firstly comprehensively analyzed. Then, the nonlinearities are approximated in order to simplify its inclusion into the estimation model and furthermore the compensation of the distorted voltage.

2.4.2.1 Analysis of the Nonlinearities

One of the main problems accompanying the real inverters in the AC machine drive systems is the error voltage between the command voltage given by the controller and the real output voltage of the inverter [53,54]. It is affected by several factors, the DC-link voltage, the inserted dead-time and the nonlinear properties of the power inverter. The nonlinear characteristics of the inverter consist of the turn-on/-off time of the power switches, the voltage drops on the switches as well as on the freewheeling diodes and the parasitic effects. One of the several issues caused by the inverter nonlinearities is the zero-clamping phenomenon, which occurs during the dead time at the small-current region (normally near zero). However, because of the applied gross compensation for the distorted voltage in practice, the undercompensation or the overcompensation often occurs, which would further elevate the significance of the current clamping [55]. In order to realize an accurate compensation of the distorted voltage, the sophisticated analysis is firstly required, which is elaborated in the following.

2.4.2.1.1 Voltage Drops Firstly, the analysis on the voltage drops across the power devices is carried out. The voltage drops of power devices, including the forward voltage drop of the active switch U_{ce} and the voltage drop of the anti-parallel diode U_d, are relatively small but still not negligible [56]. The current pathway of a phase leg is shown in Fig. 2.8. The current flows through S_1 or D_4 if the current $i_a > 0$, while the current flows through S_4 or D_1 if the phase current i_a is negative. The voltage drops are related to the conducting current i and can be approximated as a linear function of i, as indicated in [57]. The approximation of the voltage drop is composed of a threshold voltage and an equivalent on-state slope resistance as

$$\begin{aligned} U_{ce} &= U_{ce,\,th} + R_{ce} \cdot |i| \,, \\ U_d &= U_{d,\,th} + R_d \cdot |i| \,, \end{aligned} \tag{2.60}$$

where $U_{ce,\,th}$, R_{ce} are the threshold voltage and the equivalent resistance of the active switch, respectively. Accordingly, $U_{d,\,th}$ and R_d denote the threshold voltage and equivalent resistance of the anti-parallel diode, respectively. They are normally available in the data sheets. The distorted voltage caused by the voltage drops is additionally related to the current direction, i.e. the voltage drop reduces the output voltage when the current is positive and boosts the output voltage when the phase current is negative. More specifically, the error voltage induced by the voltage drops, which is denoted by $u_{e,\,1} := u^*_{aN} - u_{aN}$, can be approximately given as [57]

$$u_{e,\,1} = \begin{cases} U_{ce} \cdot d + U_d \cdot (1-d) \,, & \text{for } i_a > 0 \,, \\ -U_{ce} \cdot (1-d) - U_d \cdot d \,, & \text{for } i_a < 0 \,, \end{cases} \tag{2.61}$$

where d is the duty cycle.

2.4.2.1.2 Turn-on/-off Times Besides the voltage drops, the power devices demonstrate non-ideal switching behaviours with the so-called turn-on and turn-off times. The turn-on time T_{on} is the actual turn-on time and established as the sum of the turn-on delay and the rising time. Correspondingly, the turn-off time T_{off} is the real turn-off time and defined as the amount of turn-off delay and the falling time. A schematic presentation of the real switching behaviour

of the active switch is shown in Fig. 2.19. The voltage u_{S_1} denotes the voltage on the switch S_1 and the red solid line denotes the gating signal of S_1. t_1 denotes the turn-on delay and t_2 is the rising time. t_3 and t_4 represent the turn-off delay and the falling time, respectively. The

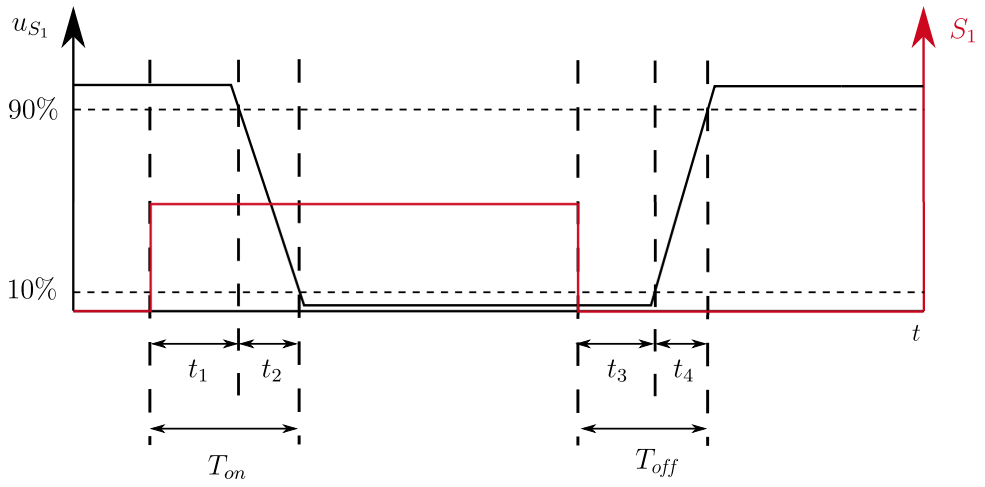

Figure 2.19: Schematic presentation of the switching transient with the consideration of turn-on/-off times.

turn-on and turn-off delay are mostly determined by the threshold voltage and the time constant regarding the equivalent circuit of the gate-source (MOSFET) or gate-emitter (IGBT) terminal, while the rising and falling time are associated with the DC-link voltage, the characteristics of the parasitic elements and the phase current [58, 59]. In terms of the effects from the parasitic elements, we can roughly divided them into the effect from the parasitic capacitance and the one from the parasitic inductance.

The parasitic capacitance is a capacitor-like behaviour in power devices, which is resulted from the packaging and the electrical wiring [60]. There are in general two types of parasitic capacitance, the input capacitance that causes the time delay during the switching, and the output capacitance, which affects the rising as well as the falling edge of the output voltage during commutation. They will be charged and discharged during the turn-on and the turn-off of the switches. In Fig. 2.20, the influence of the output capacitance on the output voltage at different levels of phase currents are shown. If the time to charge or discharge the equivalent output capacitance is smaller than the T_{dead}, i.e. the absolute value of the phase current is sufficiently large, the commutation will be finished within the dead time, which is shown in Fig. 2.20a. On the contrary, if the absolute value of the phase current is too small to fully charge/discharge the parasitic capacitance, the commutation will be forced to conduct after the switching, as presented in Fig. 2.20b.

Analogously to the parasitic capacitances, the output voltage of the inverter is also affected by the parasitic inductances. The switching transient can be simplified and approximated as a resistor-inductor-capacitor (RLC) circuit, which is a second-order switching circuit and normally underdamped. Therefore, hard switching may cause a voltage overshoot or even the oscillation. In order to tackle this problem, a snubber circuit is typically deployed to convert the output equivalent circuit into a third-order circuit, i.e. from underdamped to critically damped or overdamped [59]. A simulation is carried out to demonstrate the effectiveness of the snubber circuit. The simulation results of the step response of the equivalent output circuits are shown in Fig. 2.21. The red solid line and the blue solid line denote the step response of the transfer

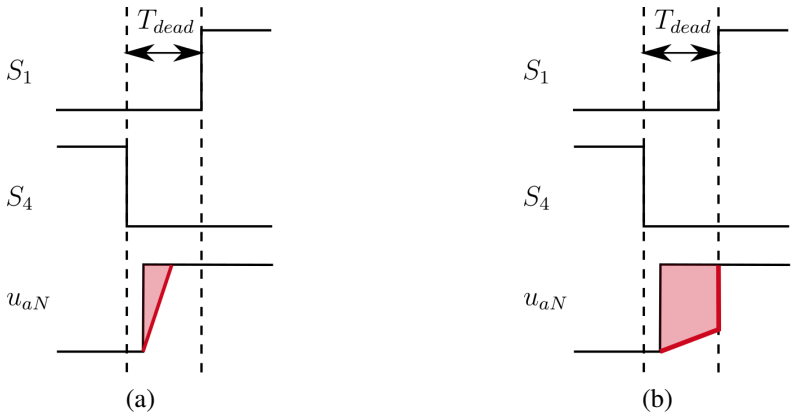

Figure 2.20: The output voltage at different current level with $i_a < 0$. The red solid line illustrates the real transition of u_{aN}. (a) represents the scenario, where the absolute value of i_a is relatively large and (b) denotes the situation, at which the absolute value of i_a is relatively small.

function without and with snubber circuit, respectively. As it is shown in Fig. 2.21, the snubber

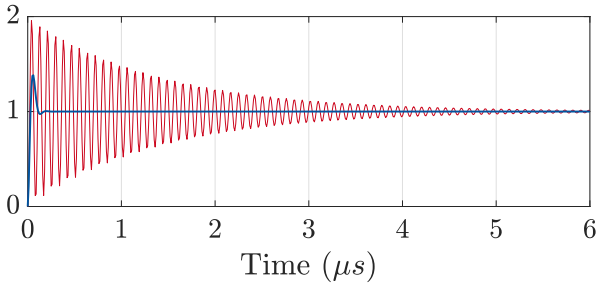

Figure 2.21: Demonstration of the comparison of the voltage on the switches during the turning off with and without snubber circuit, where the red solid line and the blue solid line denote the step response of the transfer function without and with snubber circuit, respectively.

circuit has suppressed the oscillation phenomenon with a significant reduction of the voltage overshoot. However, an overshoot of the phase voltage can still be observed based on the RLC model, which needs to be considered as part of the distorted voltage. The error voltage evoked by the turn-on/-off time can be approximately written as

$$u_{e,2} = \begin{cases} -\dfrac{U_{dc}}{2} \cdot \dfrac{T_{off} - T_{on}}{T_c} , & \text{for } i_a > 0 , \\ \dfrac{U_{dc}}{2} \cdot \dfrac{T_{off} - T_{on}}{T_c} , & \text{for } i_a < 0 . \end{cases} \tag{2.62}$$

2.4.2.1.3 Dead-Time Effect As it is explained previously, the switching behaviour of the VSI in practice is non-ideal and actuates a gate signal with turn-on/-off times. Thus, a time delay is required, which is called the dead-time or interlock time and denoted by T_{dead} in this thesis. The insertion of this time delay can prevent the simultaneous conduction of two power devices on the same phase leg (e.g. S_1 and S_4) and ensure a reliable current switchover. During the dead time, both switches on the same leg are switched off and the current flows through the corresponding diode, as shown in Fig. 2.8. The voltage error caused by the dead-time can be

approximated as

$$u_{e,3} = \begin{cases} \frac{U_{dc}}{2} \cdot \frac{T_{dead}}{T_c} , & \text{for } i_a > 0 , \\ -\frac{U_{dc}}{2} \cdot \frac{T_{dead}}{T_c} , & \text{for } i_a < 0 . \end{cases} \tag{2.63}$$

Even though the dead time is in general very short and essential to guarantee a safe operation of the inverter, it deteriorates the output voltage and degrades the motor performance, especially at the low-current region. If the current is crossing the zero during the dead time, it will clamp to zero and stay there for the rest of the dead time [61].

2.4.2.1.4 Summary The aforementioned factors compose the voltage distortion of the VSI output voltage. They are summarized and shown in Fig. 2.22, where the switching transients including the nonlinear effects are shown in two cases, i.e. with the positive and the negative current. The voltage distortion caused by the dead-time and the voltage drops has the opposite phase with the phase current, while the distortion caused by the switching time, the parasitic effects is in phase with the current.

In Fig. 2.22, T_c denotes the switching period. Furthermore, the practical behaviour of the switches is investigated with the experiments. The experimental measurements of u_{S_1} were conducted with various current levels and the turn-off signal is given to the gate at $t = 0\,\mathrm{s}$. The experimental results are shown in Fig. 2.23.

In Fig. 2.23, the turn-off behaviour of S_1 in practice is shown, which also represents the falling edge of the output voltage for the phase a. The turn-off signal is commanded to the switch S_1 at $t = 0\,\mathrm{s}$. It can be concluded from Fig. 2.23 that the current level has a great impact on the switching behaviour. More explicitly, a higher phase current can significantly reduce the switching time. The voltage at $i_a = 0\,\mathrm{A}$ stays low until around $t = 2.4\,\mathrm{s}$, which denotes the turn-on of the lower switch S_4.

2.4.2.2 Approximation of the Nonlinearities

The nonlinear effects are complicated for their inclusion into the design of the controller or the compensation, since they are time variant and depend on the working points. In order to tackle this problem, the nonlinear effects are simplified and approximated in the following. Firstly, the error caused by the dead time, the turn-on time and the turn-off time can be approximately calculated as

- Positive current:
$$T_{a,e}^{+} = T_a^{*} - T_a^{+} = T_{dead} + T_{on} - T_{off} . \tag{2.64}$$
- Negative current:
$$T_{a,e}^{-} = T_a^{*} - T_a^{-} = -(T_{dead} + T_{on} - T_{off}) . \tag{2.65}$$

T_a^{*} and $T_{a,r}$ denote the active time of the ideal switch and of the real switch, respectively. $T_{a,e}^{+}$ and $T_{a,e}^{-}$ represent the time difference between the active time and the ideal time at the positive current and the negative current, respectively. The error active time from (2.64) and (2.65) can be concluded into a function and is given as

$$T_{a,e} = T_a^{*} - T_{a,r} = \mathrm{sgn}(i_a)(T_{dead} + T_{on} - T_{off}) , \tag{2.66}$$

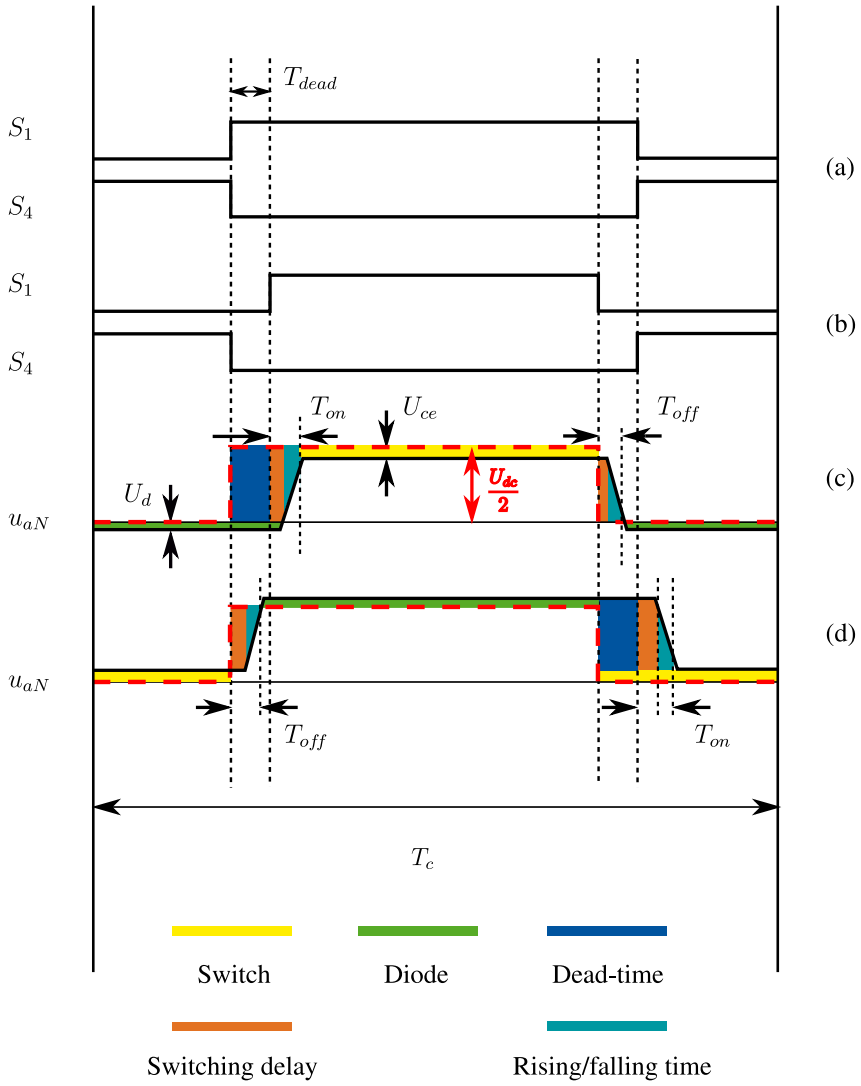

Figure 2.22: Illustration for the nonlinearities of the switch S_1. (a) represents the ideal gating pulse signals. (b) shows the insertion of the dead time into the ideal gating pulse signals. (c) demonstrates the actual output voltage with the positive current, i.e. $i_a > 0$. (d) demonstrates the actual output voltage with the negative current, i.e. $i_a < 0$.

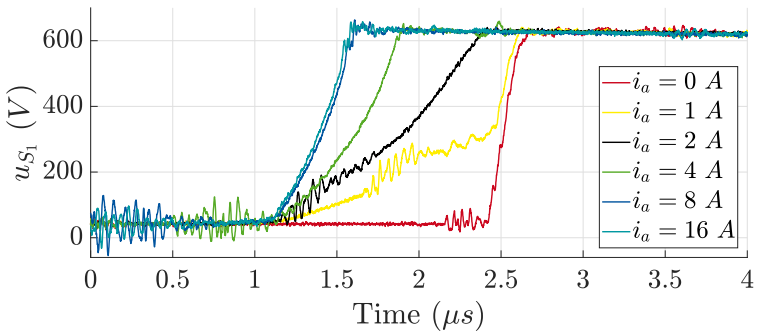

Figure 2.23: Experimental measurements of u_{S_1} at various current levels.

where $\mathrm{sgn}(i_\mathrm{a})$ is the sign function and defined as:

$$\mathrm{sgn}(i_\mathrm{a}) = \begin{cases} 1, & i_\mathrm{a} > 0\ , \\ -1, & i_\mathrm{a} < 0\ . \end{cases} \tag{2.67}$$

It can be observed from the Fig. 2.22 that the average terminal voltage including VSI nonlinearties over one PWM step can be given as follows [62]

$$u_{aN} = (U_{dc} - U_{ce} + U_d)(\frac{T_{a,r}}{T_c} - \frac{1}{2}) - \frac{1}{2}(U_{ce} + U_d)\mathrm{sgn}(i_a)\ . \tag{2.68}$$

Substitute the approximation of the voltage drops in (2.60) into the terminal voltage formulation in (2.68), it can be obtained that

$$u_{aN} = (U_{dc} - U_{ce} + U_d)(\frac{T_{a,r}}{T_c} - \frac{1}{2}) - \frac{1}{2}(U_{ce,th} + U_{d,th})\mathrm{sgn}(i_a) - \frac{1}{2}(R_{ce} + R_d)\, i_a\ . \tag{2.69}$$

Similar results can be derived for u_{bN} and u_{cN}. With the relationship in (2.27), u_a can be further derived as

$$\begin{aligned} u_a =& (U_{dc} - U_{ce} + U_d)\ \frac{2\,T_{a,r} - T_{b,r} - T_{c,r}}{3\,T_c} \\ & - \frac{1}{6}(U_{ce,th} + U_{d,th})\left[2\,\mathrm{sgn}(i_a) - \mathrm{sgn}(i_b) - \mathrm{sgn}(i_c)\right] - \frac{1}{2}(R_{ce} + R_d)\, i_a\ . \end{aligned} \tag{2.70}$$

On the other hand, the ideal phase voltage u_a^* is computed with

$$u_a^* = U_{dc}\ \frac{2\,T_a^* - T_b^* - T_c^*}{3\,T_c}\ . \tag{2.71}$$

Subtract (2.70) from (2.71) the distorted voltage caused by the VSI nonlinearities is then given by

$$\begin{aligned} \Delta u_a &= u_a^* - u_a \\ &= A_d\left[2\,\mathrm{sgn}(i_a) - \mathrm{sgn}(i_b) - \mathrm{sgn}(i_c)\right] + (U_{ce} - U_d)\ \frac{2\,T_a^* - T_b^* - T_c^*}{3\,T_c} + \frac{R_{ce} + R_d}{2} i_a\ , \end{aligned} \tag{2.72}$$

where the intermediate parameter A_d is defined as

$$A_d = (U_{dc} - U_{ce} + U_d)\ \frac{T_{dead} + T_{on} - T_{off}}{3\,T_c} + \frac{U_{ce,th} + U_{d,th}}{6}\ . \tag{2.73}$$

As a result, the distorted voltage of $\boldsymbol{u}_{abc}$ can be given as

$$\begin{aligned} \begin{bmatrix} \Delta u_a \\ \Delta u_b \\ \Delta u_c \end{bmatrix} &= A_d \begin{bmatrix} 2 & -1 & -1 \\ -1 & 2 & -1 \\ -1 & -1 & 2 \end{bmatrix} \begin{bmatrix} \mathrm{sgn}(i_a) \\ \mathrm{sgn}(i_b) \\ \mathrm{sgn}(i_c) \end{bmatrix} + \frac{U_\mathrm{ce} - U_d}{3\,T_c} \begin{bmatrix} 2 & -1 & -1 \\ -1 & 2 & -1 \\ -1 & -1 & 2 \end{bmatrix} \begin{bmatrix} T_a^* \\ T_b^* \\ T_c^* \end{bmatrix} + \frac{R_{ce} + R_d}{2} \begin{bmatrix} i_a \\ i_b \\ i_c \end{bmatrix} \\ &= A_d \begin{bmatrix} 2 & -1 & -1 \\ -1 & 2 & -1 \\ -1 & -1 & 2 \end{bmatrix} \begin{bmatrix} \mathrm{sgn}(i_a) \\ \mathrm{sgn}(i_b) \\ \mathrm{sgn}(i_c) \end{bmatrix} + \frac{U_{ce} - U_d}{U_{dc}} \begin{bmatrix} u_a^* \\ u_b^* \\ u_c^* \end{bmatrix} + \frac{R_{ce} + R_d}{2} \begin{bmatrix} i_a \\ i_b \\ i_c \end{bmatrix}\ . \end{aligned} \tag{2.74}$$

where u_a^*, u_b^* and u_c^* denote the commanded voltage of the phase a, b and c, respectively. Furthermore, (2.74) can be transformed into the dq reference frame with the aid of the Park transformation $\boldsymbol{T}_{dq}$ and its pseudo inverse $\boldsymbol{T}_{dq}^{-1}$ as [63]

$$\begin{aligned}\begin{bmatrix}\Delta u_d\\ \Delta u_q\end{bmatrix} &= \boldsymbol{T}_{dq}\begin{bmatrix}\Delta u_a\\ \Delta u_b\\ \Delta u_c\end{bmatrix}\\ &= 3\,A_d\,\boldsymbol{T}_{dq}\,\mathrm{sgn}\left(\boldsymbol{T}_{dq}^{-1}\begin{bmatrix}i_d\\ i_q\end{bmatrix}\right) + \frac{U_{ce}-U_d}{U_{dc}}\begin{bmatrix}u_d^*\\ u_q^*\end{bmatrix} + \frac{R_{ce}+R_d}{2}\begin{bmatrix}i_d\\ i_q\end{bmatrix}\end{aligned} \tag{2.75}$$

In (2.75), the second and the third term are straightforward. The first term can be explicitly explained by the Table 2.1, which shows the relationship between the signs of the phase currents as well as the electrical angle and the distorted voltage of VSI. In the Table 2.1, $A_d' := 4A_d$ and

State	$\theta_e + \theta_{\boldsymbol{i}}$	$\mathrm{sgn}(i_a)$	$\mathrm{sgn}(i_b)$	$\mathrm{sgn}(i_c)$	$\Delta u_{d,1}$	$\Delta u_{q,1}$
1	$(-\frac{\pi}{6},\ \frac{\pi}{6}]$	1	-1	-1	$A_d'\cos(\theta_e)$	$-A_d'\sin(\theta_e)$
2	$(\frac{\pi}{6},\ \frac{\pi}{2}]$	1	1	-1	$A_d'\cos(\theta_e-\frac{\pi}{3})$	$-A_d'\sin(\theta_e-\frac{\pi}{3})$
3	$(\frac{\pi}{2},\ \frac{5\pi}{6}]$	-1	1	-1	$A_d'\cos(\theta_e-\frac{2\pi}{3})$	$-A_d'\sin(\theta_e-\frac{2\pi}{3})$
4	$(\frac{5\pi}{6},\ \frac{7\pi}{6}]$	-1	1	1	$A_d'\cos(\theta_e-\pi)$	$-A_d'\sin(\theta_e-\pi)$
5	$(\frac{7\pi}{6},\ \frac{3\pi}{2}]$	-1	-1	1	$A_d'\cos(\theta_e-\frac{4\pi}{3})$	$-A_d'\sin(\theta_e-\frac{4\pi}{3})$
6	$(\frac{3\pi}{2},\ \frac{11\pi}{6}]$	1	-1	1	$A_d'\cos(\theta_e-\frac{5\pi}{3})$	$-A_d'\sin(\theta_e-\frac{5\pi}{3})$

Table 2.1: The distorted voltage of the VSI $\Delta\boldsymbol{u}$ in (2.75) as a function of electrical angle θ_e, where $\Delta u_{d,1}$ and $\Delta u_{q,1}$ denote the first term of (2.75).

$\theta_{\boldsymbol{i}}$ denotes the angle of the current in dq reference frame. It can be concluded from the Table 2.1 that the first term of distorted voltage $[\Delta u_d,\ \Delta u_q]$ rotates discontinuously with electrical angle θ_e and its trajectory is a hexagon [64].

In order to illustrate the waveform of the error voltage $\Delta\boldsymbol{u}$, a simulation has been carried out and the corresponding results are shown in Fig. 2.24, which demonstrates the waveform of the $\Delta\boldsymbol{u}$ and its relationship with the electrical angle θ_e under the $i_d = 0$ control, i.e. $\theta_{\boldsymbol{i}} = \frac{\pi}{2}$. Fig. 2.24 shows that the distorted voltage caused by the VSI is periodic and related to the electrical angle as well as the present current vector. Furthermore, in the simplified model in (2.74) and (2.75), the amplitude of the distorted voltage A_d is considered as a constant, which varies in practice depending on the operating points and environmental conditions.

2.4.3 Other Uncertainties and Disturbances

Besides the aforementioned two sources of uncertainties and disturbances, i.e. the parameter variation and the nonlinearities of the VSI, there are many other uncertainties and disturbances

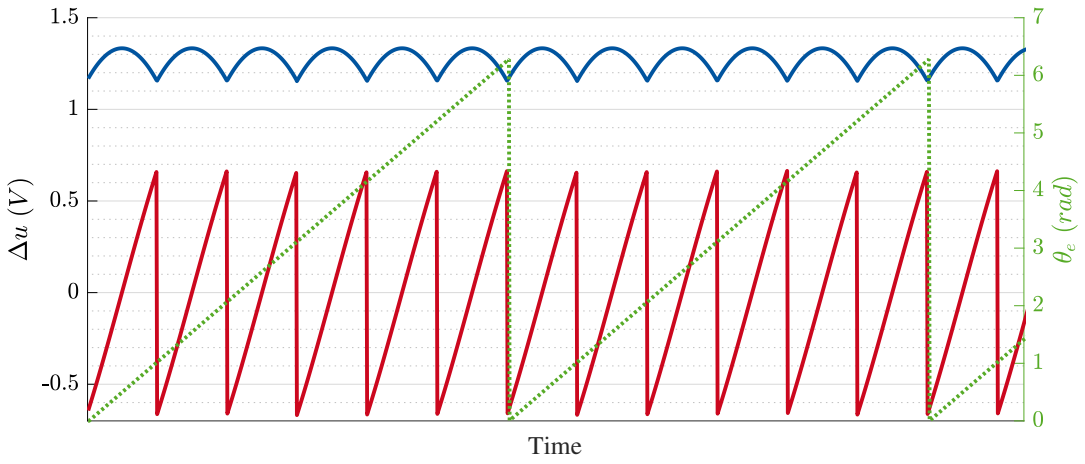

Figure 2.24: Ideal distorted voltages with a constant U_{dead} in the rotor reference frame, where the red solid line represents the distorted voltage in d-axis, the blue solid line denotes the distorted voltage in q-axis and the green dotted line is θ_e .

in the PMSM drive system, which also affect the control performance as well as the motor condition.

2.4.3.1 Digital Delay

The modern control approaches are commonly implemented on a digital control platform, where the controller computes the command signals based on the measurements from the most recent time instant. Particularly for the sophisticated control methods, such as MPC, a large number of computations need to be completed. It may lead to a considerable time delay between the acquisition of the measurement at the sampling instant and the actuation of the manipulated command value to the drive system. Moreover, the assumption of a constant reference value can also cause a delay effect for the predictive control. In general, the references are assumed to be constant within the prediction horizon, which is valid under the circumstances that the real reference is constant or the sampling time is relatively small. However, for some control scenarios, e.g. the current control in $\alpha\beta$ reference frame, as well as the control during the transitions, the delay effects are emphasized.

Compensation of the digital delay has been covered in several works, such as [65, 66]. For the digital-delay effect resulted from the discrete nature of the digital platform, a prediction based on the current measurements need to be carried out, which is then employed for the computation of the manipulated command values. On the other hand, the digital delay effects from the varying reference value can be compensated by extrapolating the references.

2.4.3.2 Cogging Torque

The cogging torque is produced by the magnetic interaction between the permanent magnets and the stator slots. It refers to the circumferential component of the attractive force that attempts to maintain the alignment between the stator teeth and the permanent magnets [67]. Therefore, the cogging torque depends on the position, the number of magnetic poles and the number of teeth on the stator. Its impact is especially prominent in the low-speed region and even exists

in a from power source disconnected system [68]. As it is given in [69], the resultant cogging torque T_{ct} can be written as a Fourier series as

$$T_{ct} = \sum_{i=1,2,3,\cdots}^{\infty} T_{ct,\,i}\, \sin(i\, N_{\mathrm{m}}\, \theta_e)\ , \tag{2.76}$$

where N_{m} denotes the least common multiples between the slots number and the pole pairs, θ_e denotes the electrical angle and $T_{ct,\,i}$ is the amplitude of the i-th harmonic.

2.4.3.3 Flux Harmonics

In the real PMSMs, a perfect sinusoidal flux density distribution is difficult to be built in the air gap. The developed flux linkage between the permanent magnet and the stator currents consists of the harmonics of the order 5, 7, 11 and higher [70]. In the dq reference frame, they appear as 6-th, 12-th and the multiples of 6-th harmonic, which can then be denoted as [70, 71]

$$\Psi_d = \sum_{i=0}^{\infty} \Psi_{dh,\,i} \cos(6i\, \theta_e)\ , \Psi_q = \sum_{i=1}^{\infty} \Psi_{qh,\,i} \cos(6i\, \theta_e)\ , \tag{2.77}$$

where $\Psi_{dh,\,i}$ and $\Psi_{qh,\,i}$ are the amplitudes of the $6i$-th order harmonic flux in d- and q-axis, respectively. The flux harmonics further affect the control performance of the electrical drive system. For example, they can generate $6i$-th periodic ripples on the electromagnetic torque as well as on the speed. Moreover, in the current control loop, the flux harmonics induce the harmonics in the back EMF and further influence the current quality.

2.4.3.4 Measurement Errors

Measurement errors can be referred to as current measurement errors and position measurement errors. The current measurement error is analyzed firstly. Normally the current measurement procedure includes a sampling mechanism, a low-pass filter and an A/D converter, where the sampling is finished by the current sensors, the low-pass filter and the A/D converter transform the transduced voltage signals into the digital values. The error that exists in the current measurement procedure can be classified into the offset error and the scaling error [72]. The offset error is resulted from an unbalanced supply voltage of the current sensor and the analogue devices in the measurement path. Another error is the scaling error, which is generated during the process of the scaling from the current sensor to the A/D converter and the calibration from the A/D converter to the current controller [72]. Without loss of generality, the acquired current value neglecting the nonideal factors in the filter and the A/D converter can be given as [71]

$$\bar{i} = \frac{R_{\mathrm{sr}}}{R_{\mathrm{sN}}}\, i + \frac{u_{\mathrm{ov}} - u_{\mathrm{oN}}}{r\, R_{\mathrm{sN}}}\ , \tag{2.78}$$

where $\bar{i}$ and i denotes the measured value and the real value of the current, respectively. R_{sr} is the sampling resistance. u_{ov} is the offset voltage applied for the polarity conversion. R_{sN} and u_{oN} denote the nominal value of the sample resistance and the offset voltage, respectively. r is the transducer ratio of the current sensor. It can be observed from (2.78), the current measurement

error is mainly affected by two factors, the deviation of $u_{\mathrm{ov}} - u_{\mathrm{oN}}$ and the varying sampling resistance R_{sr}. As a result, the offset error causes a current ripple oscillating at the fundamental frequency and the scaling error induces a current ripple oscillating at the frequency of twice of the fundamental frequency [71].

Analogously, the position measurement can also be erroneous and further affect the performance of the drive system. The most applied position sensors are resolver, absolute encoder and incremental encoder, which can be selected regarding different requirements, for example, robustness, price and accuracy. Similar to the current measurement error, the position measurement error can be categorized into the offset error, the harmonic error and the phase shift error. More details can be found in works such as [73].

2.4.3.5 Phase Unbalancing

In a three-phase motor, the phase characteristics, e.g. the resistances, should be as balanced as possible. However, due to the corrosion, contamination or other problems mentioned in 2.4.1, the phase unbalancing occurs frequently during the operation of the PMSM. It generates the negative sequence voltages and currents that may impair the motor efficiency and deteriorates its performance. Furthermore, it can result in an unbalancing heating of the stator, which may further cause the excessive thermal stress and increase the impedance unbalance.

2.4.3.6 Noise

In most applications, the process as well as the measurement noise is assumed to be white. However, in reality the most encountered noise is the coloured noise. The coloured process/measurement noise is denoted as $\boldsymbol{w}^c$ and $\boldsymbol{v}^c$, respectively. Their propagation can be given as

$$\begin{aligned} \boldsymbol{w}_{k+1}^c &= \boldsymbol{A}_{\boldsymbol{w}} \boldsymbol{w}_k^c + \boldsymbol{B}_{\boldsymbol{w}} \boldsymbol{w}_k \,, \\ \boldsymbol{v}_{k+1}^c &= \boldsymbol{A}_{\boldsymbol{v}} \boldsymbol{v}_k^c + \boldsymbol{B}_{\boldsymbol{v}} \boldsymbol{v}_k \,, \end{aligned} \tag{2.79}$$

where $\boldsymbol{w}_k$ and $\boldsymbol{v}_k$ are the zero-mean white noise with the covariance matrices $\boldsymbol{Q}$ and $\boldsymbol{R}$, respectively. They are uncorrelated. The colored noise can be comprised into the state space and modelled as a new state as

$$\begin{aligned} E[\boldsymbol{w}_{k+1}^c \boldsymbol{w}_k^{cT}] &= \boldsymbol{A}_{\boldsymbol{w}} E[\boldsymbol{w}_k^c \boldsymbol{w}_k^{cT}] \,, \\ E[\boldsymbol{v}_{k+1}^c \boldsymbol{v}_k^{cT}] &= \boldsymbol{A}_{\boldsymbol{v}} E[\boldsymbol{v}_k^c \boldsymbol{v}_k^{cT}] \,. \end{aligned} \tag{2.80}$$

2.4.3.7 External Disturbances

In addition to the aforementioned uncertainties and disturbances in the PMSM drive system, the system is also affected by the external disturbances, such as the load torque and the friction torque. The load torque is considered as one of the most severe external disturbances of the drive system, since the coupling of the load motor and the drive motor is a nonideal rigid body and the add of a load torque may cause the mechanical resonance [74]. Other mechanical factors, such as the friction torque [75] and torsional vibrations [76], are also unavoidable in the servo systems.

2.4.4 Impacts

The uncertainties and the disturbances of the electrical drive system have multiple impacts on the system. On the one hand, they can impinge on the control performance of the control methods. On the other hand, they may affect the motor condition. The impacts from the parameter mismatch are investigated and presented in details as follows.

2.4.4.1 Impacts on the Control Performance

Different control methods can be applied to the current control of the PMSM drive system. However, the uncertainties as well as the disturbances influence the control performance in various way and to different extent. For example, the parameter mismatch has less effects on the FOC than on the model-based methods. It changes the dynamic behaviour of the FOC method, while it can result in a steady-state error or even instability for the model-based control methods. The impacts of the parameter mismatches are analyzed in the following.

2.4.4.1.1 Impacts on the Reference Generator Based on the torque reference and the measurement of the rotor speed, the current reference vector $\boldsymbol{i}^*$ is generated in the reference generator. The current reference is then delivered into the current controller. The reference is generated based on several criteria. Firstly, the measurements are checked to determine the existence of a suitable reference, e.g. the speed is restricted by the maximum speed. Then, the operation strategy is determined, namely MTPA, maximum current, field weakening and maximum torque per voltage (MTPV). The algorithm to generate the reference current is shown in Algorithm 2.1 [77].

Algorithm 2.1 MTPX

Input T^*, ω_e
Output $\boldsymbol{i}^*$
if $\omega_e \leq \omega_A$ **then**
  MTPA
else
  if $\omega_e \leq \omega_V$ **then**
    if $T^* \leq T_U$ **then**
      $\mathbb{E}_U := \{\boldsymbol{i} \in \mathbb{R}^2 |\ \|\boldsymbol{u}(\boldsymbol{i})\|^2 \leq U_{\max}^2\}$
    else
      $\mathbb{E}_I := \{\boldsymbol{i} \in \mathbb{R}^2 |\ \|\boldsymbol{i}\|^2 \leq I_{\max}^2\}$
    end if
  else
    if $T^* \leq T_V$ **then**
      $\mathbb{E}_U$
    else
      MTPV
    end if
  end if
end if

The sets $\mathbb{E}_U$ and $\mathbb{E}_I$ are the voltage and the current limitation, respectively. Moreover, ω_A is the maximally feasible MTPA angular velocity for the given torque reference and ω_V is the constant MTPV cut-in angular velocity, which is computed from the maximum current and the maximum voltage. T_U denotes the maximally feasible field weakening torque and T_V denotes the MTPV cut-in torque. They are determined by the electrical angular velocity, as given in [77]. Firstly, the measurements and the torque reference are delivered as input into the algorithm MTPX in Algorithm 2.1. The feasibility of the current reference will be examined based on the input. Then the rotor speed ω_e is compared with the two offline determined speeds ω_A and ω_V and the torque reference T^* is compared with the T_U and T_V. The mechanism to generate the current reference $\boldsymbol{i}^*$ is then selected accordingly.

A simulation about the impact of the parameter variation on the reference generator, more specifically on the MTPX stated in the Algorithm 2.1, has been carried out. The corresponding results are shown in Fig. 2.25, where the isotorque loci based on the constant inductance value and the inductance as a nonlinear function of the currents are compared.

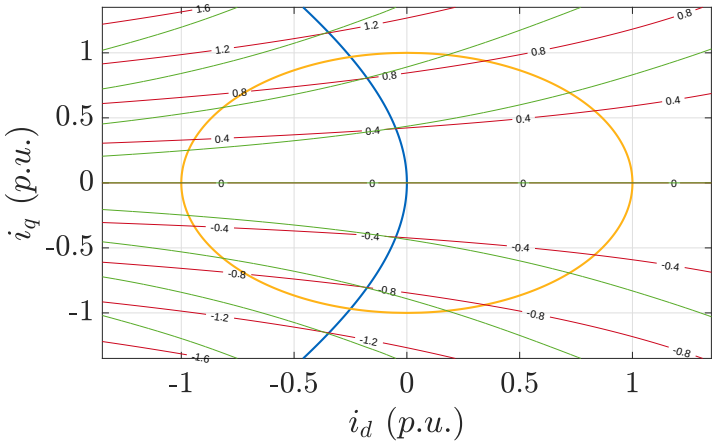

Figure 2.25: PMSM characteristics in the state-space with isotorque loci. The MTPA trajectory, which is offline computed with the constant inductance values, is denoted by the blue. It is derived from the isotorque loci in green. The isotorque loci computed from the real inductance map, which is nonlinear and a function of currents, are presented in red. The yellow circle presents the current limit $\mathbb{E}_I$.

The Fig. 2.25 shows that the parameter mismatch of the inductances can cause an obvious deviation from the real isotorque loci, i.e. the difference between the read solid line and the green solid line. In some applications, the model based on the offline parameters, i.e. the constant inductances, can be improved by deploying correcting factors, which provides an approximation for the global nonlinear model and improves the model accuracy locally [78].

2.4.4.1.2 Impacts on the FOC The most applied control method for the PMSM electrical drive system is the FOC (with PI technique). Although FOC is less sensitive to the parameter variation problem than MPC, its performance can also be affected. The PI technique is implemented in the dq reference frame, of which the transfer function can be generally given as

$$G_{PI} = K_p + K_i \frac{1}{s} . \tag{2.81}$$

Depending on the design criterion, the magnitude optimum (to obtain a largest possible bandwidth) or the symmetric optimum technique (examine both the input and disturbance transfer function) [79] can be deployed to determine the coefficients of the FOC. Particularly, the closed-loop control system designed with the magnitude optimum technique only optimizes the closed-loop transfer function between the reference input and the controlled variable. The existence of disturbances may change the system behaviour. The coefficients of FOC are designed based on the parameters and via the pole-zero cancellation principle, which no longer holds. Therefore, the disturbances may deteriorate the control performance. Since the controller is designed based on the classical linear control theory, the impacts of the parameter mismatch can be evaluated with the localization of the system poles.

The pole-zero maps showing the influence of the parameter mismatches, i.e. from the variation of the stator resistance and of the inductances, are illustrated in Fig. 2.26, where the closed-loop stability under the parameter variation is furthermore denoted. The transfer func-

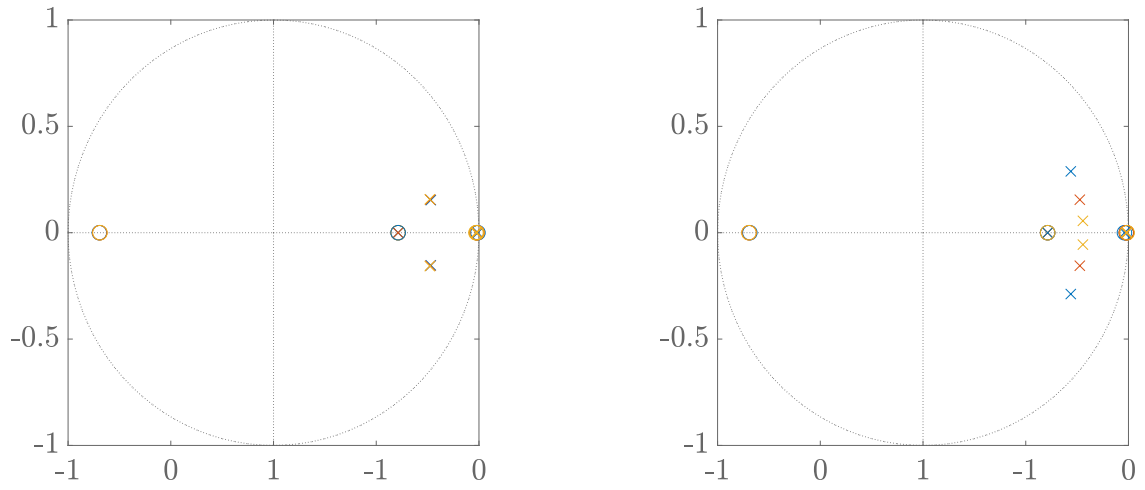

(a) (b)

Figure 2.26: Discrete pole-zero map of the FOC current controller at a sampling frequency of 10 kHz. (a) Simulation results of the resistance value variation, where $r_p = 50\%$ is denoted in blue, $r_p = 100\%$ is denoted in red and $r_p = 150\%$ is denoted in yellow. (b) Simulation results of the inductance value variation.

tion for the open loop of the current control in the d-axis can be simplified by eliminating the interdependent term relating to the q-axis current and is given as

$$G_{i,d} = \frac{1}{s\,L_d + R_s}\,, \tag{2.82}$$

where the coupling term of the current loop is excluded from the transfer function and assumed that it can be compensated afterwards. The transfer function of the current control in q-axis can be analogously formulated. Therefore, the analysis focuses on the d-axis. Besides the PMSM current loop of d-axis, a digital delay is furthermore included into the open loop function, which is selected as two sampling time period and given as a first order time lag system. The parameter mismatch is simulated by changing the parameter values of the PMSM current model and

quantified by a ratio r_p , which is defined by

$$r_p = \frac{p_m}{p_c} \times 100\% \,, \tag{2.83}$$

where p_m is the parameter value deployed in the current model of PMSM and p_c is the value of the parameter employed in the controller. As it is presented in Fig. 2.26, the variation of the inductance may have a great impact on the closed-loop stability, which can be explained by the position of the inductance in the transfer function in (2.82). However, the pole-zero maps reveal that the poles remains within the unit circle. Thus, the FOC stabilizes the system even under the parameter mismatches. The variation of the inductance shifts the poles away or closer to the real axis, which indicates that the damping behaviour of the PI controller is changed. The variation of the resistance, as it is shown in Fig. 2.26a, has slight influence on the pole placement.

2.4.4.1.3 Impacts on the Predictive Control In this work, two predictive control methods are investigated, i.e. CCS-MPC and FCS-MPC. The deadbeat control is also included and regarded as a special case of the CCS-MPC. The predictive current control methods are all set up based on the system model and have proven to be effective as well as powerful for the control of systems with accurate models and small disturbances. However, if the model uncertainties and the external disturbances are not ignorable, the performance of the predictive control can deteriorate or even the system may exhibit instability. MPC gains robustness from a long prediction horizon, but the obvious error can still be noted for the reference tracking under the impact of the model uncertainties and the disturbances. In order to analyze the impacts of the parameter-mismatch phenomenon, let us recall the simplified nominal current prediction model in dq reference frame, which is given as

$$\begin{bmatrix} u_d \\ u_q \end{bmatrix} = \begin{bmatrix} R_\mathrm{s} & -\omega_e\, L_q \\ \omega_e\, L_d & R_\mathrm{s} \end{bmatrix} \begin{bmatrix} i_d \\ i_q \end{bmatrix} + \begin{bmatrix} L_d & 0 \\ 0 & L_q \end{bmatrix} \begin{bmatrix} \dfrac{\mathrm{d}}{\mathrm{d}\,t} i_d \\ \dfrac{\mathrm{d}}{\mathrm{d}\,t} i_q \end{bmatrix} + \begin{bmatrix} 0 \\ \omega_e\, \Psi_m \end{bmatrix} \,. \tag{2.84}$$

The current prediction model of the real PMSM including the parameter variation effect is given by

$$\begin{bmatrix} u_d - \Delta u_d^p \\ u_q - \Delta u_q^p \end{bmatrix} = \begin{bmatrix} R_\mathrm{s} & -\omega_e\, L_q \\ \omega_e\, L_d & R_\mathrm{s} \end{bmatrix} \begin{bmatrix} i_d \\ i_q \end{bmatrix} + \begin{bmatrix} L_d & 0 \\ 0 & L_q \end{bmatrix} \begin{bmatrix} \dfrac{\mathrm{d}}{\mathrm{d}\,t} i_d \\ \dfrac{\mathrm{d}}{\mathrm{d}\,t} i_q \end{bmatrix} + \begin{bmatrix} 0 \\ \omega_e\, \Psi_m \end{bmatrix} \,, \tag{2.85}$$

where Δu_d^p and Δu_q^p denote the error voltage caused by the parameter variation and can be represented as

$$\begin{aligned} \Delta u_d^p &= \Delta R_\mathrm{s}\, i_d + \Delta L_d \frac{\mathrm{d}}{\mathrm{d}\,t} i_d - \Delta L_q\, \omega_e\, i_q \,, \\ \Delta u_q^p &= \Delta R_\mathrm{s}\, i_q + \Delta L_q \frac{\mathrm{d}}{\mathrm{d}\,t} i_q + \Delta L_d\, \omega_e\, i_d + \Delta \Psi_\mathrm{m}\, \omega_e \,. \end{aligned} \tag{2.86}$$

The simulation results as well as the experimental results to quantify the impacts of the parameter mismatch are given in details in the Chapter 4 and the Chapter 5.

2.4.4.2 Impacts on the Motor Condition

The PMSM has been moreover applied in mission- and safety-critical systems, such as military and medical systems. A reliable operation and timely maintenance is essential for these application domains. Therefore, a novel condition monitoring method is necessary for identifying the degradation at its incipient stage, which can substantially reduce the maintenance cost as well as the machine downtime [46]. The impacts of the uncertainties and disturbances on the motor condition are shown in the following.

2.4.4.2.1 Magnetic Faults The permanent magnet is the most critical component in the PMSM. As explained in Section 2.4.1, various reasons can cause the irreversible demagnetization of the permanent magnet, e.g. the thermal stress [51], the oxidation and the unbalanced load. The demagnetization can further lead to a reduction of the efficiency, poor performance and even a motor fault [46]. On the one hand, the demagnetization causes higher copper losses for the motor operated at a given torque, which heats the motor, reduces the efficiency and stability. On the other hand, the demagnetization disturbs the air-gap flux distribution. It further causes magnetic pull and current harmonics. They are responsible for bearing erosion, rotor bending as well as vibration and acoustic noise, respectively.

2.4.4.2.2 Electrical Faults The disturbances and uncertainties in the electrical drive systems can cause the stator winding insulation failures. The materials used for the insulation in electric machines are related to the deterioration from a combination of thermal overloading and cycling, voltage stresses on the insulating material and mechanical stresses, etc. Nonetheless, the thermal stresses account for the main reason for the degradation of the stator winding insulation. The disturbances and uncertainties induce more losses and increase the thermal stresses on the stator windings. Moreover, the implementation of the VSI introduces transient voltages with a high slope rate, which further adds the electrical stresses at the machine terminals. It is the main reason of the electrical stresses and provokes the insulation degradation.

2.5 Summary

In this chapter, the basic concepts of the permanent magnet synchronous machine drive system are introduced, including the main components of the permanent magnet synchronous machine, the inverter as well as its operating principle and the control of the drive system. The drive system in practice is much more complex and contains many nonlinear effects, which can be simplified and approximated under several assumptions. The mathematical models of the PMSM in the continuous-time domain are furthermore presented, both in the stationary reference frame and the rotating reference frame. They are further discretized with the preselected discretization methods, which is determined based on the requirement for the model accuracy and the availability of the computational resources. The working principle of the inverter as well as the relevant actuation schemes are presented. The switching commands for the inverter can be directly computed by the control algorithm or modulated through the corresponding modulator, where the PWM, the SVM and the OPP are introduced. Furthermore, the control of the electrical drive system is systematically established. The fundamental concepts of the

optimization problem are given, which are followed by the classical control approaches of the electric drive system. Subsequently, the control structure of the most applied cascaded control is illustrated and introduced. The system model and the constraints involved in the electric drive system are furthermore presented. In the end, the uncertainties and the disturbances that exist in the electrical drive system are explicitly introduced, especially the parameter variations and the nonlinear effects of the VSI. Their impacts on the control performance and the motor conditions are further investigated and analyzed. These foundations play an essential role for the further studies and development of this thesis.

Part II

PARAMETER IDENTIFICATION

CHAPTER 3

Parameter Determination and Estimation

In this chapter, the observability of the PMSM is firstly examined, where the persistent excitement is absent. Then, the offline determination procedures regarding the parameters of the simplified model and those of the general model for the PMSM are investigated. The VSI nonlinearities are furthermore quantified via the measurements, where two methods for the offline determination of the error voltage that is resulted from the nonlinear effects are introduced. As it is mentioned in the previous chapter, the nonlinear effects are affected by several factors. Therefore, their impacts are validated through the experiments. However, the offline determination of the parameters may require extra hardware and sophisticated determination procedure. The online identification can be regarded as an alternative for obtaining the parameters in real time, which can be realized with or without current injection. The current injection can be expected as a persistent excitement and overcomes the rank deficient problem of the PMSM parameter identification. Thus, the associated methods are capable to simultaneously identify all the electrical parameters of the simplified model, while the methods without current injection can estimate up to two electrical parameters at the same time. Moreover, several online identification methods are studied and compared via the experimental results. Conclusions about the advantages as well as the disadvantages can be drawn in terms of various criteria, which can be further served as a reference for choosing a proper observer under different circumstances. Furthermore, the influence of the VSI nonlinearities on the identification results is shown. A promising method based on the dual extended Kalman filter (DEKF) is proposed, in which the nonlinear effects of the VSI is included and identified. Its effectiveness is verified via experimental investigations.

3.1 Introduction

The parameters of a system can be directly solved from sufficient equations. Ignoring the disturbance, the parameter estimation problem is an inverse problem, which can be directly solved in the linear system and requires solving approaches in the nonlinear system. The parameters

can also be treated as the system states, which transforms the parameter estimation problem into a state estimation problem. As it is analyzed in the previous chapter, there exist multiple disturbances and noises in practice. Different from the discrete linear system presented in (2.48), a more general and practical system model includes moreover the state or the process disturbance $\boldsymbol{w}(k)$ and the measurement, output disturbance $\boldsymbol{v}(k)$, which can be then given as

$$\begin{aligned} \boldsymbol{x}_{k+1} &= \boldsymbol{A}\,\boldsymbol{x}_k + \boldsymbol{B}\,\boldsymbol{u}_k + \boldsymbol{w}_k\ , \\ \boldsymbol{y}_k &= \boldsymbol{C}\,\boldsymbol{x}_k + \boldsymbol{v}_k\ , \end{aligned} \tag{3.1}$$

where $\boldsymbol{w}(k)$ denotes the unmodelled uncertainties, modeling errors and process variations and $\boldsymbol{v}(k)$ represents sensor errors, disturbances and modeling errors of the outputs. The matrix $\boldsymbol{D}$ in the general formulation (2.48) is omitted. The parameter estimation as well as the state estimation problem can be defined in different representations regarding the deployment of the available measurements.

Definition 3.1 (State Estimation [80])
Given a sequence of measurements $\boldsymbol{Y}_m = [\boldsymbol{y}_0^T, \boldsymbol{y}_1^T, \cdots, \boldsymbol{y}_m^T]^T$ for the system in (3.1)*, the state estimation problem describes a retrieving procedure of state $\boldsymbol{x}_k$ from $\boldsymbol{Y}_m$. The estimation problem is called a filtering problem if $k = m$, a prediction problem if $k > m$ and a smoothing problem if $k < m$.*

In general, the parameter estimation methods can be roughly classified into two categories, i.e. offline and online parameter estimation. The offline estimation methods, as its name suggests, are carried out offline before the operation of the motor or at the start-up. There are several variants. The first one is to compute the parameters from the motor construction data, which is the most straightforward way to obtain the motor parameters. The motor construction data can be the geometrical and material data. It is relatively accurate, since the parameters are acquired from the physical data. However, it is computationally expensive, since the computation is based on field calculation methods, e.g. the finite element method [81]. The second option is to conduct the standstill frequency response (SSFR) test, where the response on a test signal with a certain signal frequency is evaluated. It has become a standard method for identifying synchronous machines [16]. Extensions and improvements of SSFR are moreover given in [82], [83], to name but a few. The last variant is to perform the time-domain motor measurements and adjust the parameters to reconstruct the measurements, which requires a simplification of the motor models [84]. However, the electrical drive system is complex, nonlinear and time-variant. The parameters may vary during the operation, as it is clarified in Chapter 2, and solely the accurate motor parameters can not guarantee a satisfactory control performance. Moreover, an accurate offline determination of the motor parameters may require sophisticated measuring procedures. Even though the self-commissioning procedure can be deployed for automatically determining the parameters, additional instruments may be required and the implementation complexity is increased. Thus, the online parameter estimation method is a more proper solution for identifying the actual parameters in real time. In this chapter, five online estimation methods are covered, namely the recursive least squares, the model reference adaptive system, the extended Kalman filter, the unscented Kalman filter and the moving horizon estimator. They are implemented and compared for the parameter estimation problem of the PMSM. The corresponding analysis and the subsequent experimental results are compared in terms of different metrics.

However, most of the previous studies ignore the influence of the voltage source inverter nonlinearities, which has been introduced in Chapter 2. To compensate the VSI nonlinearities, several methods have been proposed. Authors in [62] suggested to compensate the nonlinearities with the results from offline experimental measurements. Nonetheless, the switching times and the voltage drops vary with operating conditions. Authors in [85] proposed an online averaging technique including a feedforward and a feedback loop to adjust the compensation. But this method still needs offline measurements to set up a look-up table. Authors in [86] applied a disturbance observer to observe the output voltage errors and fed the error back to voltage references in order to compensate the dead-time effects. Reference [87] also used a disturbance observer to identify the disturbance voltage in q-axis, which was further applied to compensate the error voltage caused by the dead time. Reference [88] utilized a simple vector operator, which consists of the inner and outer products of the rotor flux linkage increment and the unit back electromotive force, to estimate the disturbance voltage. In [89], the reference voltage in d-axis and low pass filters are used to calculate the distorted voltage for the $i_d = 0$ control of the PMSM. In this chapter, the VSI nonlinearity is included into the system model of the estimation problem and regarded as a system state of PMSM. EKF and DEKF are investigated for the online estimation problem of the PMSM electrical parameters and the VSI nonlinearities. Comparisons between the proposed methods and EKF without VSI nonlinearity compensation have been furthermore carried out on an industrial embedded system with various scenarios.

3.2 Observability Analysis

The observability is concerned with the feasibility of reconstructing system states from the measurements of the previous times, which are constrained within a finite period of time. The most straightforward methodology for the observability analysis is to algebraically evaluate the estimated quantities from the machine model equations [90]. However, the results obtained can not be easily adopted for the similar problems, e.g. for other types of machines. Moreover, the to be estimated values, for example the electrical parameters and the rotor speed, vary much more slowly than the currents and are normally regarded as a constant during one sampling period. Under this assumption, the to be estimated parameters can be considered as the system states and then included into the system model, which furthermore transforms the underlying linear time-variant (LTV) system into a nonlinear time-invariant (NTI) system. The global observability analysis for NTI system is difficult to carry out [91]. One possible approach is to linearise the system model in a certain subspace, where a linear system observability analysis can be conducted accordingly [92]. Nonetheless, this approach is therefore localized in the certain subspace and loses the general observability for the entire state trajectories. Another possibility is to apply a local observability analysis to the nonlinear system [93]. The main advantage of this concept is that the observability analysis becomes a relatively simple algebraic problem.

3.2.1 Observability for Nonlinear System

The local observability for a nonlinear system is briefly introduced as follows.

Definition 3.2 (Lie Derivative [93])
Let $\boldsymbol{f} : \mathbb{R}^n \to \mathbb{R}^n$ be a vector field in $\mathbb{R}^n$, and $h : \mathbb{R}^n \to \mathbb{R}$ be a smooth scalar function. Then, the ***Lie derivative*** *of h with respect to $\boldsymbol{f}$ is*

$$\mathcal{L}_{\boldsymbol{f}} h = \nabla_h \boldsymbol{f} = \frac{\partial h}{\partial \boldsymbol{x}} \boldsymbol{f} = \sum_{i=1}^{n} \frac{\partial h}{\partial x_i} f_i \,, \tag{3.2}$$

where $\boldsymbol{f} = [f_1,\, f_2,\, \cdots,\, f_n]^T$ and $\boldsymbol{x} = [x_1,\, x_2,\, \cdots,\, x_n]^T$.

Theorem 3.1 (Local Observability [93])
For a nonlinear system described by the system equation $\dot{\boldsymbol{x}} = \boldsymbol{f}(\boldsymbol{x},\, \boldsymbol{u})$ and the measurement equation $\boldsymbol{y} = \boldsymbol{h}(\boldsymbol{x})$, if n linearly independent vectors can be found within $\mathcal{O}$ at a state $\boldsymbol{x}_0 \in \mathbb{X}$, then the system is locally observable at state $\boldsymbol{x}_0$, where $\mathcal{O}$ is the Jacobian of $\boldsymbol{O}$ at $\boldsymbol{x}_0$ and $\boldsymbol{O}$ denotes the Lie derivative vector of $\boldsymbol{h}$ with respect to $\boldsymbol{f}$, i.e.

$$\mathcal{O} = \frac{\partial \boldsymbol{L}}{\partial \boldsymbol{x}}\Big|_{\boldsymbol{x}_0} \,, \tag{3.3}$$

with $\boldsymbol{L} = [\mathcal{L}_{\boldsymbol{f}}^0 \boldsymbol{h},\, \mathcal{L}_{\boldsymbol{f}}^1 \boldsymbol{h},\, \cdots,\, \mathcal{L}_{\boldsymbol{f}}^n \boldsymbol{h}]$, where $\mathcal{L}_{\boldsymbol{f}}^k \boldsymbol{h}$ denotes the k-th order Lie derivative.

By applying the local observability theorem in Theorem 3.1, the examination of observability for nonlinear system is transformed into a rank examination problem of the observability matrix $\mathcal{O}$.

3.2.2 Observability of PMSM

The to be estimated parameters are the stator resistance R_s, inductances of d- as well as of q-axis and the permanent magnet flux linkage Ψ_m. Revisit the analysis about the parameter variations in Section 2.4.1, it can be concluded that the variations of the stator resistance and the permanent magnet flux linkage are much slower than the current dynamics, since they are mainly affected by the temperature. The inductances of d- and q-axis are related to the currents, and we assume that they can be regarded as constant within one sampling period, in order to simplify the analysis. Moreover, a state is most likely observable for fast variation if a slow variation is observable [91]. Thus, the observability matrix $\mathcal{O}$ for examining the nonlinear system with $\boldsymbol{x} = [i_d,\, i_q,\, R_\mathrm{s},\, L_d,\, L_q,\, \Psi_\mathrm{m}]$ is derived from $\mathcal{O} = \frac{\partial \boldsymbol{L}}{\partial \boldsymbol{x}}$, where

$$\boldsymbol{L} = \begin{bmatrix} \mathcal{L}_{\boldsymbol{f}}^0 \boldsymbol{h} \\ \mathcal{L}_{\boldsymbol{f}}^1 \boldsymbol{h} \\ \mathcal{L}_{\boldsymbol{f}}^2 \boldsymbol{h} \\ \mathcal{L}_{\boldsymbol{f}}^3 \boldsymbol{h} \\ \mathcal{L}_{\boldsymbol{f}}^4 \boldsymbol{h} \\ \mathcal{L}_{\boldsymbol{f}}^5 \boldsymbol{h} \end{bmatrix}, \quad \boldsymbol{f} = \begin{bmatrix} -\dfrac{R_\mathrm{s}}{L_d} i_\mathrm{d} + \dfrac{L_q}{L_d} \cdot \omega_e \cdot i_q + \dfrac{u_d}{L_d} \\ -\dfrac{R_\mathrm{s}}{L_q} i_q - \dfrac{L_d}{L_q} \cdot \omega_e \cdot i_d + \dfrac{u_q}{L_q} - \dfrac{\Psi_\mathrm{m}}{L_q} \omega_e \\ 0 \\ 0 \\ 0 \\ 0 \end{bmatrix}, \quad \boldsymbol{h} = \begin{bmatrix} i_d \\ i_q \end{bmatrix} . \tag{3.4}$$

More specifically, the observability matrix $\mathcal{O} \in \mathbb{R}^{12\times 6}$ can be expanded regarding to $\boldsymbol{x}$ as

$$\mathcal{O} = \begin{bmatrix} \frac{\partial \mathcal{L}_{\boldsymbol{f}}^0 h_1}{\partial i_d} & \frac{\partial \mathcal{L}_{\boldsymbol{f}}^0 h_1}{\partial i_q} & \frac{\partial \mathcal{L}_{\boldsymbol{f}}^0 h_1}{\partial R_\mathrm{s}} & \frac{\partial \mathcal{L}_{\boldsymbol{f}}^0 h_1}{\partial L_d} & \frac{\partial \mathcal{L}_{\boldsymbol{f}}^0 h_1}{\partial L_q} & \frac{\partial \mathcal{L}_{\boldsymbol{f}}^0 h_1}{\partial \Psi_\mathrm{m}} \\ \frac{\partial \mathcal{L}_{\boldsymbol{f}}^0 h_2}{\partial i_d} & \frac{\partial \mathcal{L}_{\boldsymbol{f}}^0 h_2}{\partial i_q} & \frac{\partial \mathcal{L}_{\boldsymbol{f}}^0 h_2}{\partial R_\mathrm{s}} & \frac{\partial \mathcal{L}_{\boldsymbol{f}}^0 h_2}{\partial L_d} & \frac{\partial \mathcal{L}_{\boldsymbol{f}}^0 h_2}{\partial L_q} & \frac{\partial \mathcal{L}_{\boldsymbol{f}}^0 h_2}{\partial \Psi_\mathrm{m}} \\ \frac{\partial \mathcal{L}_{\boldsymbol{f}}^1 h_1}{\partial i_\mathrm{d}} & \frac{\partial \mathcal{L}_{\boldsymbol{f}}^1 h_1}{\partial i_\mathrm{q}} & \frac{\partial \mathcal{L}_{\boldsymbol{f}}^1 h_1}{\partial R_\mathrm{s}} & \frac{\partial \mathcal{L}_{\boldsymbol{f}}^1 h_1}{\partial L_d} & \frac{\partial \mathcal{L}_{\boldsymbol{f}}^1 h_1}{\partial L_q} & \frac{\partial \mathcal{L}_{\boldsymbol{f}}^1 h_1}{\partial \Psi_\mathrm{m}} \\ \frac{\partial \mathcal{L}_{\boldsymbol{f}}^1 h_2}{\partial i_d} & \frac{\partial \mathcal{L}_{\boldsymbol{f}}^1 h_2}{\partial i_q} & \frac{\partial \mathcal{L}_{\boldsymbol{f}}^1 h_2}{\partial R_\mathrm{s}} & \frac{\partial \mathcal{L}_{\boldsymbol{f}}^1 h_2}{\partial L_d} & \frac{\partial \mathcal{L}_{\boldsymbol{f}}^1 h_2}{\partial L_q} & \frac{\partial \mathcal{L}_{\boldsymbol{f}}^1 h_2}{\partial \Psi_\mathrm{m}} \\ \vdots & \vdots & \vdots & \vdots & \vdots & \vdots \\ \frac{\partial \mathcal{L}_{\boldsymbol{f}}^5 h_1}{\partial i_d} & \frac{\partial \mathcal{L}_{\boldsymbol{f}}^5 h_1}{\partial i_q} & \frac{\partial \mathcal{L}_{\boldsymbol{f}}^5 h_1}{\partial R_\mathrm{s}} & \frac{\partial \mathcal{L}_{\boldsymbol{f}}^5 h_1}{\partial L_d} & \frac{\partial \mathcal{L}_{\boldsymbol{f}}^5 h_1}{\partial L_q} & \frac{\partial \mathcal{L}_{\boldsymbol{f}}^5 h_1}{\partial \Psi_\mathrm{m}} \\ \frac{\partial \mathcal{L}_{\boldsymbol{f}}^5 h_2}{\partial i_d} & \frac{\partial \mathcal{L}_{\boldsymbol{f}}^5 h_2}{\partial i_q} & \frac{\partial \mathcal{L}_{\boldsymbol{f}}^5 h_2}{\partial R_\mathrm{s}} & \frac{\partial \mathcal{L}_{\boldsymbol{f}}^5 h_2}{\partial L_d} & \frac{\partial \mathcal{L}_{\boldsymbol{f}}^5 h_2}{\partial L_q} & \frac{\partial \mathcal{L}_{\boldsymbol{f}}^5 h_2}{\partial \Psi_\mathrm{m}} \end{bmatrix} . \tag{3.5}$$

According to the Theorem 3.1, the system is weakly locally observable, if rank$\{\mathcal{O}\} = 6$. This condition can be examined with a matrix constructed by any six rows of $\mathcal{O}$ [94]. We choose the first six rows of the matrix $\mathcal{O}$ and define it as $\mathcal{O}_1 \in \mathbb{R}^{6\times 6}$ for verification, which can be given as

$$\mathcal{O}_1 = \begin{bmatrix} 1 & 0 & 0 & 0 & 0 & 0 \\ 0 & 1 & 0 & 0 & 0 & 0 \\ -\frac{R_\mathrm{s}}{L_d} & \frac{L_q}{L_d}\omega_e & -\frac{i_d}{L_d} & -\frac{1}{L_d}f_1 & \frac{\omega_e}{L_d}i_q & 0 \\ -\frac{L_d}{L_q}\omega_e & -\frac{R_\mathrm{s}}{L_q} & -\frac{i_q}{L_q} & -\frac{\omega_e}{L_q}i_d & -\frac{1}{L_q}f_2 & -\frac{\omega_e}{L_q} \\ \frac{{R_\mathrm{s}}^2}{L_d^2} - \omega_e^2 & -\frac{R_\mathrm{s}L_q}{L_d^2} - \frac{R_\mathrm{s}\omega_e}{L_d} & \Omega_1 & \Omega_2 & -\frac{R_\mathrm{s}\omega_e}{L_d^2}i_q & -\frac{\omega_e^2}{L_d} \\ \frac{R_\mathrm{s}L_d}{L_q^2} + \frac{R_\mathrm{s}\omega_e}{L_q} & \frac{{R_\mathrm{s}}^2}{L_q^2} - \omega_e^2 & \Omega_3 & \frac{R_\mathrm{s}\omega_e}{L_q^2}i_d & \Omega_4 & \frac{R_\mathrm{s}\omega_e}{L_q^2} \end{bmatrix} , \tag{3.6}$$

with

$$\Omega_1 = \frac{2R_\mathrm{s}}{L_d^2}i_d - \frac{L_q}{L_d^2}\omega_e i_q - \frac{u_d}{L_d^2} - \frac{\omega_e}{L_d}i_q \, , \qquad \Omega_2 = \frac{2R_\mathrm{s}}{L_d^2}f_1 - \frac{L_q}{L_d^2}\omega_e f_2 - \frac{\omega_e^2}{L_d}i_d \, ,$$
$$\Omega_3 = \frac{2R_\mathrm{s}}{L_q^2}i_q + \frac{\omega_e}{L_q}i_d + \frac{L_d}{L_q^2}\omega_e i_d - \frac{u_q}{L_q^2} + \frac{\omega_e}{L_q^2}\Psi_\mathrm{m} \, , \qquad \Omega_4 = \frac{2R_\mathrm{s}}{L_q^2}f_2 + \frac{L_d}{L_q^2}\omega_e f_1 - \frac{\omega_e^2}{L_q}i_q \, .$$

There are several predefined conditions for the identification problem of PMSM. On the one hand, no additional sensor is required, which means only the available measurements can be used, i.e. the currents of d-, q- axis and the rotor position. On the other hand, the conclusions of the observability should be globally applicable, i.e. valid for both at the steady state and during the transitions. For the identification problem, the steady state is the worst-case scenario. Therefore, the rank of $\mathcal{O}_1$ at steady state will be assessed. It can be obtained that the rank of $\mathcal{O}_1$ at steady state is four, which means that up to two parameters can be identified simultaneously without a persistent excitement. In order to find out the observable parameter combinations, the sub-matrices of $\mathcal{O}_1$ regarding various parameter combinations are evaluated. The observability matrix of the parameter combination $[R_\mathrm{s},\, L_d]$ is defined as $\mathcal{O}_{1,1}$. Analogously, the observability matrices of parameter combinations of $[R_\mathrm{s},\, L_d]$, $[R_\mathrm{s},\, L_q]$, $[R_\mathrm{s},\, \Psi_\mathrm{m}]$, $[L_d,\, L_q]$, $[L_d,\, \Psi_\mathrm{m}]$,

$[L_q,\ \Psi_\mathrm{m}]$ are defined as $\mathcal{O}_{1,2}, \cdots, \mathcal{O}_{1,6}$, respectively. Their determinant is calculated and can be given as

$$\begin{aligned} |\mathcal{O}_{1,1}| &= \omega_e\, i_d^2 - i_q\, f_1\ , & |\mathcal{O}_{1,2}| &= \frac{R_\mathrm{s}\,\omega_e}{L_d^2}\, i_d\, i_q - \Omega_1\, \omega_e\, i_q\ , \\ |\mathcal{O}_{1,3}| &= -\frac{R_\mathrm{s}\,\omega_e}{L_q^2} i_d\ , & |\mathcal{O}_{1,4}| &= \frac{R_\mathrm{s}\,\omega_e^2}{L_d^2\, L_q}\, i_d\, i_q + \frac{\Omega_2}{L_q}\, f_2\ , \\ |\mathcal{O}_{1,5}| &= 0\ , & |\mathcal{O}_{1,6}| &= -\frac{{R_\mathrm{s}}^2\,\omega_e^2}{L_d^2\, L_q^2}\, i_q + \frac{\omega_e^2}{L_d}\, \Omega_4\ . \end{aligned} \tag{3.7}$$

Based on the results in (3.7), several conclusions can be drawn.

- L_d and Ψ_m can not be simultaneously identified at the steady state.
- For many applications of PMSM, the direct current i_d is fixed to zero with the aim of minimizing the machine loss. However, this control method furthermore restricts the observability of copious parameter combinations, i.e. $[R_\mathrm{s},\ L_d]$, $[R_\mathrm{s},\ \Psi_\mathrm{m}]$ and $[L_d,\ L_q]$.
- The operating points of PMSM have also great influence on the observability. More specifically, the motor speed ω_e can determine the observability. All parameter combinations become unobservable at $\omega_e = 0$.

However, the conclusions drawn above are based on two conditions: no additional sensors and no persistent excitement. The four electrical parameters can be simultaneously observable, as long as the persistent transition takes place.

3.3 Offline Determination of Parameters

The offline approaches follow the measuring procedure and compute the corresponding parameters with the measurements. Normally, look-up tables or interpolating functions are built to serve the online application of the estimates. They are easy to implement, but the determination procedure is time consuming, since the whole working area needs to be covered. However, the measuring and determining procedures can also be completed by the self-commissioning process, where the procedures run automatically and the computational results are then saved as a look-up table or interpolated as a function. Traditionally, short-circuit and/or low-voltage tests are carried out to capture the machine characteristics, such as the transient as well as subtransient reactances and time constants. However, the SSFR test has become an alternative to the aforementioned tests [16]. It can be performed at a relatively modest expense, poses a low probability of the risk to the motor and requires low effort for the test setup. In the following, the offline procedures regarding determining individual electrical parameters as well as the distorted voltage caused by the VSI nonlinearities are introduced.

3.3.1 Stator Resistance

The stator resistance R_s is a relevant quantity for the operation of the electrical machines. For example, in traction applications, despite the torque control is required, the torque at the motor shaft is often not measured, which not only is for the purpose of cost savings in the purchase, but

also denotes a significant reduction for maintenance and a lower susceptibility to faults. Thus, in order to realize highly precise control, the torque needs to be derived from the available signals, which is then given by the equation in (2.21). The flux map that is considered as a function of the currents can be obtained by the introduced procedure or deploying the substitution of the inductance-like functions, i.e. the explicit nonlinear function in (2.15) or the approximated linear function in (2.18). The details about the determination procedure are shown in Section 3.3.2. Moreover, the stator resistance is relevant for the determination of the flux maps. Furthermore, the precise acquisition of the stator resistance is also important for the sensorless control methods, especially for the low-speed region [95]. A lower rotor speed of the PMSM results in a smaller value of the induced voltage, which furthermore increases the relevance of the stator resistance accuracy.

In general, the stator resistance R_s can be identified with various methods. The most straightforward method is to directly measure the resistance of each phase and compute the average value of the measurements. However, the to be identified motor is normally implemented in the electrical drive system and connected to other components of the drive system, which impedes the direct measurements of the stator resistance. Another option for identifying the stator resistance is to inject testing signals in d- and q-axis and evaluate the voltage as well as the current response [96]. Normally, a DC current is injected, either into the terminal or into the neutral point of the star-connected machine with a capacitor bank. In this thesis, the former method is implemented for the offline stator resistance determination. To obtain an accurate value, several voltage values are applied in d-axis and the computational results are averaged. To take the possible asymmetries of the motor into account, different angle points are evaluated. It is worth mentioning that because of the nonlinearities of the inverter, the voltage command of the current controller is not equivalent to the terminal voltage of the motor. The distorted voltage can be either compensated by the offline measured values of VSI nonlinearities or approximated as a linear function under the assumption that the error voltage resulted from the VSI nonlinear effects increase linearly with the current. If the distorted voltage can be directly compensated, the value of the command voltage is applied. Otherwise, the stator resistance is computed via

$$R_s = \frac{u_{d,\,1} - u_{d,\,2}}{i_{d,\,1} - i_{d,\,2}}\,, \tag{3.8}$$

where $u_{d,\,1}$ and $i_{d,\,1}$ denote the average voltage and current in the d-axis at the steady state of the first operating point, respectively. Analogously, $u_{d,\,2}$ and $i_{d,\,2}$ denote the average voltage and current of the d-axis of the second operating point. The identification results for the PMSMs in Section B.1.3 are shown in Table 3.1.

Table 3.1: Identification results of the stator resistance for the PMSMs

Description	PMSM I	PMSM II
Data Sheet Value	$4.2\ \Omega$	$6.5\ \Omega$
Measured Value	$4.35\ \Omega$	$6.25\ \Omega$

3.3.2 Inductances

As mentioned in Section 2.1.2.4, various inductances can be defined in the context of different machine models. They can be applied for different usages, e.g. the absolute inductances is important for the FOC to calculate the command voltage [10], the absolute as well as the differential inductances are both necessary for the sensorless control [14] and the reference generator [97]. Since the most applications employ the inductance in the dq reference frame, the identification of the inductances is carried out in this reference.

3.3.2.1 Interpolation Methods

The flux maps $\Psi_d(i_d,\, i_q)$, $\Psi_q(i_d,\, i_q)$ and the further derived inductances are computed from the measurements of limited working points. It may cause problems at the intermediate points between two measured working points. Therefore, the interpolation methods significantly affect the computational results. They determine the way of generating the intermediate values. The most applied interpolation methods are the linear interpolation, the polynomial interpolation and the spline interpolation. In order to explain the principle of each method, an example with random points is employed, which is shown in Fig. 3.1a.

3.3.2.1.1 Piecewise Constant Interpolation The most straightforward and simplest way is to deploy the value from the nearest points, which is called piecewise constant interpolation and shown in Fig. 3.1b. Thanks to its simpleness, it can be used for high dimensional interpolation. However, a step is generated between two points, which introduces discontinuous derivatives and furthermore causes problem in the control applications.

3.3.2.1.2 Linear Interpolation One of the simplest interpolation methods is the linear interpolation, which is shown in Fig. 3.1c. It can be generally formulated as follows

$$y = a_0 + a_1 \cdot x \,, \tag{3.9}$$

where a_1 is the slope of two adjacent points. The linear interpolation reduces the discontinuity provoked in piecewise constant interpolation and constrains it within a certain range. It is also simple and quick, but it has limited precision.

3.3.2.1.3 Polynomial Interpolation The polynomial interpolation is a more general form of the linear interpolation, which can be given as

$$y = a_0 + a_1 \cdot x + \cdots + a_n \cdot x^n \,, \tag{3.10}$$

where $n \in \mathbb{Z}$ denotes the degree of the polynomial function. It is worth mentioning that the degree of the polynomial function n is always smaller than the number of the available data points. In Fig. 3.1d and Fig. 3.1e, a third degree polynomial and a sixth degree polynomial are employed for the interpolation, respectively. The third degree polynomial interpolation is much more accurate than the linear interpolation function. Nonetheless, the inaccuracy can be observed at several points. On the contrary, the sixth degree polynomial function adequately

describes the raw data and provides more precise results than the third degree polynomial interpolation. Moreover, since the interpolation is a polynomial, it is infinitely differentiable. However, a higher accuracy on the other hand means higher computational burden. Another disadvantage associating with the high-degree polynomial interpolation is that it tends to oscillate, especially when the points are not in a smooth sequence [98].

3.3.2.1.4 Spline Interpolation Another relatively precise interpolation method is the spline interpolation, where low-degree function (higher than first-degree) polynomials are formulated between each two adjacent points and the polynomial functions with smooth conjunctions are chosen. Normally, a third degree polynomial is employed. As it is shown in Fig. 3.1f, a high accuracy can be achieved through the spline interpolation.

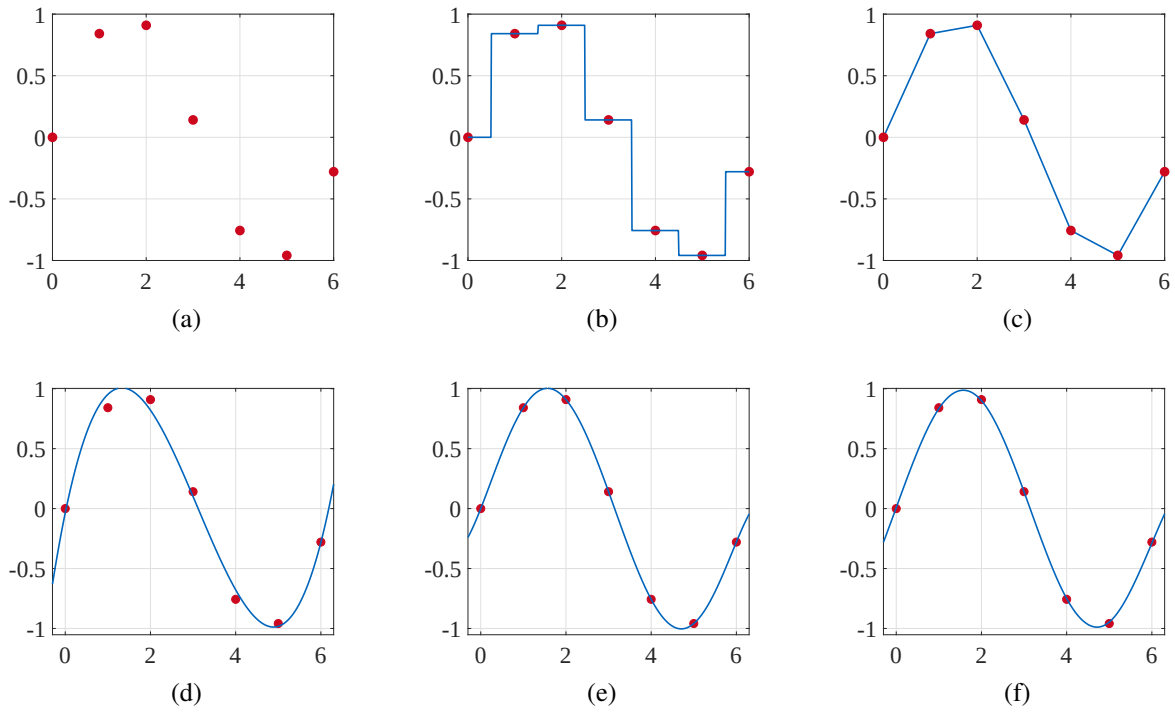

Figure 3.1: Demonstrations of the various interpolation methods. (a) represents the raw data points. (b) denotes the simple piecewise constant interpolation. (c) gives the results of the linear interpolation. (d) and (e) are the interpolation results via the polynomial interpolation methods of a third degree polynomial and a sixth degree polynomial, respectively. (f) demonstrates the interpolation results with the spline interpolation method.

However, besides the accuracy, the computational burden needs to be considered during the interpolating process. The piecewise constant interpolation requires least computational expenses, since only the interval of present value needs to be determined. A higher precision brings higher computational burdens as well as higher memory requirements. Therefore, the choice of the interpolation methods depends on the available computational resource and the requirement of the accuracy. The interpolated measurement results are afterwards implemented for the control system synthesis. It is usually helpful if the interpolated curves can omit any discontinuities in the function itself or even in the derivatives, since the discontinuities may deteriorate the control performance [99]. Thus, the cubic spline interpolation (third order) is

implemented in this thesis to approximate the intervals between two adjacent points.

3.3.2.2 Flux Linkage

Recall the voltage equation in (2.14), the flux can be computed at the steady state with $\dot{\boldsymbol{\Psi}} = \mathbf{0}$. Then the flux linkage Ψ_d and Ψ_q can be obtained with the equation given in the following

$$\begin{aligned} \Psi_d(i_d,\, i_q) &= \frac{u_q(i_d,\, i_q) - R_\mathrm{s}\, i_q}{\omega_e}\,, \\ \Psi_q(i_d,\, i_q) &= \frac{u_d(i_d,\, i_q) - R_\mathrm{s}\, i_d}{\omega_e}\,. \end{aligned} \tag{3.11}$$

The individual operating points over the space of $(i_d,\, i_q)$ is measured to obtain the flux map. An adequate rotor speed is chosen, in order to guarantee the feasibility of (3.11). For each operating points, the corresponding voltages u_d, u_q and the real rotor speed ω_e are recorded. As it is indicated in (3.11), the stator resistance is essential for the identification of the inductances. However, as revealed in Section 2.4.1, the resistance is mainly influenced by the temperature. During the flux determination procedure, the current is injected for a short time, which meanwhile is long enough to reach the steady state. Furthermore, a temperature sensor is mounted on the motor and monitors the motor temperature, which is used for the adjustment of the stator resistance by deploying (2.58) with the temperature coefficient $\alpha_{Cu} = 0.004\,041\,^{\circ}\mathrm{C}^{-1}$ for the copper conductors. The measuring procedure is introduced as follows.

Procedure 3.1 (Flux Map Determination)

1. *The current control loop of the to be identified motor need to be tuned so that any working points $(i_d,\, i_q)$ can be reached. The load motor is controlled under constant speed and robust against various load conditions.*

2. *The motor rotates within mid-speed region, in order to avoid the dominance of the VSI nonlinear effects at the low-speed area and the speed-related effects, e.g. the iron loss, at high speed.*

3. *The measurements, i.e. the rotor speed ω_m and the current of d- as well as q-axis, voltage commands u_d^*, u_q^* and the motor temperature T, are collected and saved.*

4. *After the measurements are completed, they are evaluated. The flux map is furthermore computed via* (3.11).

The aforementioned determining procedure are carried out for the determination of the flux maps for the two PMSMs described by the Table B.2 and the Table B.3. The stator resistances R_s are obtained through the method described in previous section. The test benches for the flux map determination share the same basic structure. The to be identified motor is connected to an inverter and coupled with a PMSM as the load motor. Both motors as well as the inverters are controlled by the IndraDrive Cs (from Bosch Rexroth AG), which is an industrial embedded system equipped with a microprocessor from Renesas (SH7750R). At the beginning of the measurement, a constant speed is selected and realized by the load machine. The choice of the rotor speed affects the accuracy of the identified flux map and furthermore the inductances. If a

relatively low speed is chosen, the nonlinear effects of the inverter can have a great impact on the measurement. The compensation of the nonlinearities can be performed with sophisticated measurements introduced in Section 3.3.4 or online compensated method proposed in Section 3.6. If a high speed is chosen, the electro-motive force (EMF) term of the voltage equation is relatively large, while the nonlinear effect of the VSI has less contribution to the terminal voltage and is less relevant for the identification accuracy. Regarding this perspective, the highest possible speed for the measuring is desirable. However, a high speed test can have some speed-dependent disturbances, e.g. the iron losses, for the identification. Therefore, a speed of approximately half the rated speed is selected for the determination procedure. The experimental results of two PMSMs, i.e. PMSM I in Table B.2 and PMSM II in Table B.3, are shown in Fig. 3.2 and Fig. 3.3, respectively. Once the determination of the flux map is completed, the determination procedure of the inductances can be further carried out.

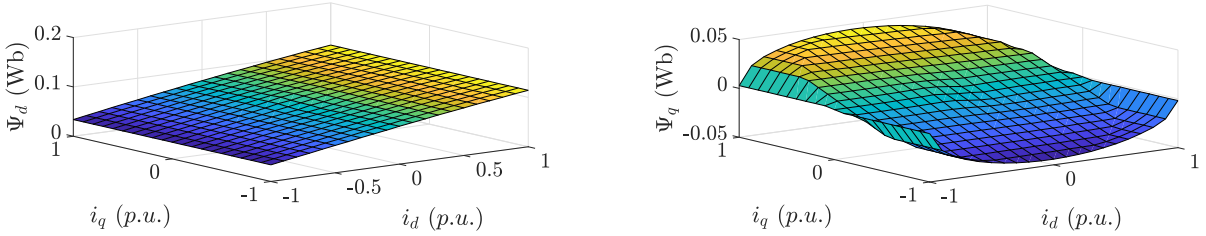

Figure 3.2: The flux linkage maps Ψ_d and Ψ_q as functions of i_d, i_q for the PMSM I in Table B.2.

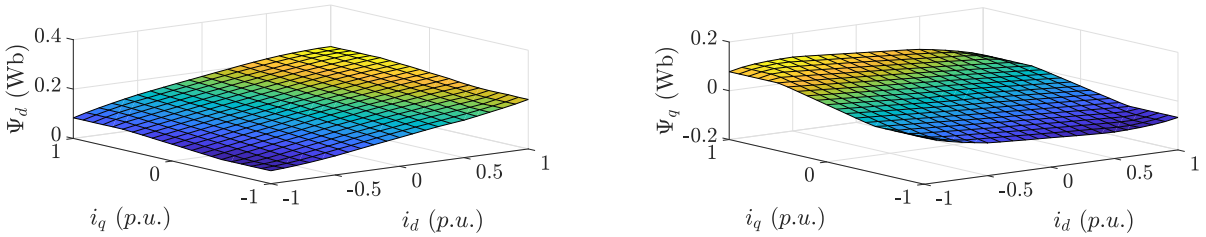

Figure 3.3: The flux linkage maps Ψ_d and Ψ_q as functions of i_d, i_q for the PMSM II in Table B.3.

3.3.2.3 Absolute Inductance

The inductance can be correspondingly derived on the basis of the flux maps. The flux maps in Fig. 3.2 and Fig. 3.3 is obtained via the procedure described in Procedure 3.1. Therefore, the steady-state equation is investigated. The absolute inductance can be then computed with the determination results of the flux linkage and via the following formulations:

$$\begin{aligned} L_d &= \frac{\Psi_{d,i} - \Psi_{d,0}}{i_d} \,, \\ L_q &= \frac{\Psi_{q,i} - \Psi_{q,0}}{i_q} \,, \end{aligned} \tag{3.12}$$

where $\Psi_{d,i}$ and $\Psi_{q,i}$ denote an arbitrary measurement point on the flux map $\Psi_d(i_d,\, i_q)$ and $\Psi_q(i_d,\, i_q)$, respectively. $\Psi_{d,0}$ represent the values of the flux map Ψ_d with $i_d = 0$. Analogously, $\Psi_{q,0}$ represent the values of the flux map Ψ_q with $i_q = 0$.

Procedure 3.2 (Absolute Inductance Determination)

1. *Compute the absolute inductances L_d as well as L_q by means of the formulas in* (3.12).

2. *The computational results from the previous step are smoothed via the methods mentioned in Section 3.3.2.1.*

The computational results after the step 1 in Procedure 3.2 derived from the flux maps presented in Fig. 3.2 is shown in Fig. 3.4. It can be observed from Fig. 3.4 that the discontinuity mostly

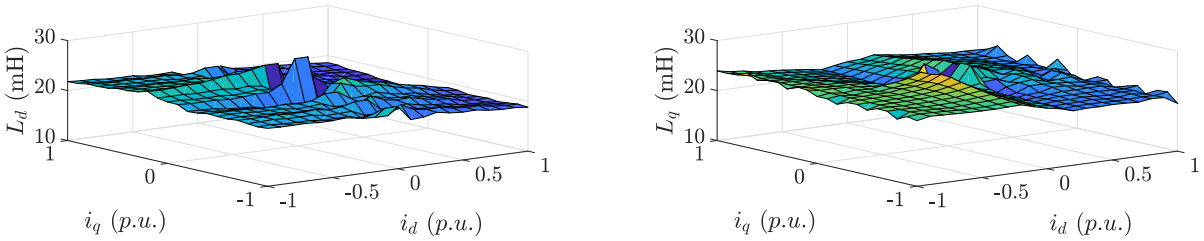

(a) (b)

Figure 3.4: The computational results after the step 1 in Procedure 3.2 derived from the flux map shown in Fig. 3.2 for the PMSM I.

appears around the $i_d = 0$ and $i_q = 0$, as well as at the edge of the flux map. Thus, the interpolation is necessary for the derivation of the absolute inductance from the flux maps. The results of the PMSM I after the interpolation with the spline interpolation method is shown in Fig. 3.5. It can be concluded from the Fig. 3.5 that the absolute inductance in the d-axis, i.e.

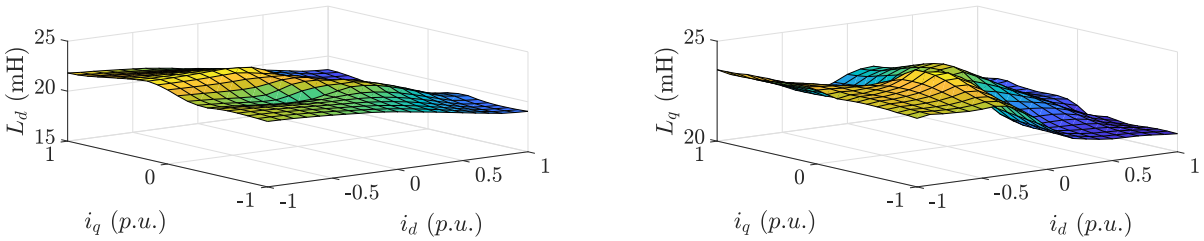

(a) (b)

Figure 3.5: The derived and interpolated absolute inductance map from the flux map shown in Fig. 3.2 for the PMSM I.

L_d, of PMSM I is always smaller than L_q and decreases further with positive field current i_d. The derived and interpolated results of the PMSM II after the absolute inductance determination procedure in Procedure 3.2 is shown in Fig. 3.6. The analogous conclusion can be drawn from the results presented in Fig. 3.6.

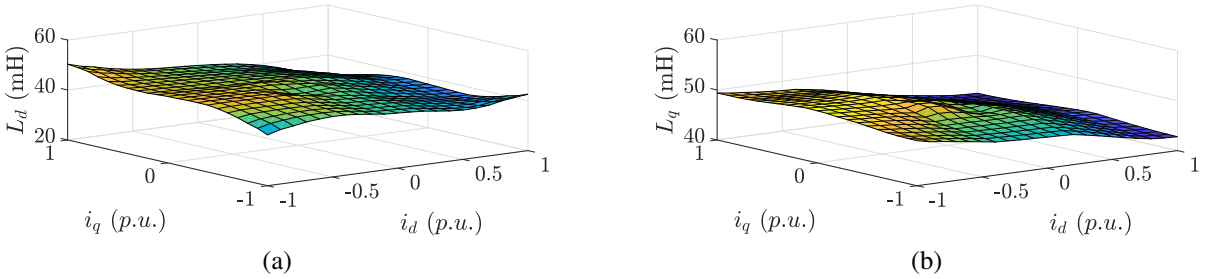

Figure 3.6: The determined absolute inductance map from the flux map shown in Fig. 3.3 for the PMSM II.

3.3.2.4 Differential Inductance

The differential inductance, defined in (2.17), is solely relevant for the operation of PMSM if the current is changing, i.e. during the transient. Therefore, the determination of the differential inductance requires a dynamic operation to create transitions for the measurement. A promising approach is to inject an additional high frequency test current into the PMSM at an arbitrary working point [100, 101]. The differential inductance can be computed from the voltage and current values of the corresponding frequency. As previously mentioned, the voltage equation can be written with the differential inductance as (2.16). The identification procedure is conducted at standstill of the PMSM, i.e. $\omega_e = 0$, and the permanent magnet flux linkage is regarded as a constant during the identification procedure, i.e. $\dot{\Psi}_\mathrm{m} = 0$. Therefore, the voltage equation can be simplifies during the identification procedure as

$$\begin{bmatrix} u_d \\ u_q \end{bmatrix} = R_\mathrm{s} \begin{bmatrix} i_d \\ i_q \end{bmatrix} + \begin{bmatrix} L_{dd} & L_{dq} \\ L_{qd} & L_{qq} \end{bmatrix} \begin{bmatrix} \dfrac{\mathrm{d}}{\mathrm{d}\,t} i_d \\ \dfrac{\mathrm{d}}{\mathrm{d}\,t} i_q \end{bmatrix} . \tag{3.13}$$

In order to obtain the differential inductance map for all working points, the identification procedure on individual working point consisting of i_d and i_q is conducted. Subsequently, the high frequency signal with a relatively small amplitude is injected into the constant currents. The voltage equation in (3.13) is then rewritten as [101]

$$\begin{bmatrix} u_d + u_{d,hf} \\ u_q + u_{q,hf} \end{bmatrix} = R_\mathrm{s} \begin{bmatrix} i_d + i_{d,hf} \\ i_q + i_{q,hf} \end{bmatrix} + \begin{bmatrix} L_{dd} & L_{dq} \\ L_{qd} & L_{qq} \end{bmatrix} \begin{bmatrix} \dfrac{\mathrm{d}}{\mathrm{d}\,t} i_d + \dfrac{\mathrm{d}}{\mathrm{d}\,t} i_{d,hf} \\ \dfrac{\mathrm{d}}{\mathrm{d}\,t} i_q + \dfrac{\mathrm{d}}{\mathrm{d}\,t} i_{q,hf} \end{bmatrix} , \tag{3.14}$$

where the subscript hf denotes the component of the high frequency. Moreover, it can be given that $\frac{\mathrm{d}}{\mathrm{d}\,t}\boldsymbol{i} = 0$ for the steady state. In order to obtain the differential inductances, the high frequency signal is firstly injected into the d-axis current. Therefore, it can be given that

$$u_d + u_{d,hf} = R_\mathrm{s} \left(i_d + i_{d,hf}\right) + L_{dd} \frac{\mathrm{d}}{\mathrm{d}\,t} i_{d,hf} . \tag{3.15}$$

The aforementioned equation (3.15) can be divided into the constant and high-frequency part. In order to achieve this goal, an adequate filter is implemented, e.g. the Goertzel algorithm [102], the band-pass filter [103] and the neural network [104], to separate the DC part and high-frequency part of the signals. In this thesis, the Goertzel algorithm is employed, of which the

functions are similar to the fast Fourier transform (FFT) but analyze only the selected frequency. In contrast to FFT, which is computationally expensive and difficult for the real-time computation, the Goetzel algorithm has relatively lower computational cost. However, the Goetzel algorithm also has disadvantages. On the one hand, it can only be applied to the steady state problem and causes a phase shift if the amplitude or the phase of the to be filtered signal varies. Nonetheless, the phase and amplitude of the determination process are constant. Therefore, there is no phase shift for the determination process. On the other hand, the ratio between the sampling frequency and the frequency of the to be filtered signal needs to be an integer [105]. As a result, the selected frequency of the injected signal should satisfy this requirement. In latter chapter, the filter for fractional ratio is introduced.

The voltage equation of d-axis can be further separated as

$$\begin{aligned} u_d &= R_\mathrm{s}\, i_d \ , \\ u_{d,\,hf} &= R_\mathrm{s}\, i_{d,\,hf} + L_{dd}\, \frac{\mathrm{d}}{\mathrm{d}\, t} i_{d,\,hf} \ . \end{aligned} \tag{3.16}$$

The high-frequency component is generated as a sinusoidal signal. Therefore, the high-frequency component of (3.16) can be rewritten as

$$u_{d,\,hf} = R_\mathrm{s}\, i_{d,\,hf} + j\omega_{hf}\, L_{dd}\, i_{d,\,hf} \ , \tag{3.17}$$

where ω_{hf} denotes the frequency of the injected high frequency current. As a result, the differential inductance L_{dd} can be derived from (3.17) by

$$L_{dd} = \frac{1}{\omega_{hf}} \sqrt{\frac{u_{d,\,hf}^2}{i_{d,\,hf}^2} - R_\mathrm{s}^2} \ . \tag{3.18}$$

Subsequently, the similar procedure is applied in q-axis, i.e. the high frequency current is injected in i_q and the voltage equation of u_q is reformulated. The differential equation of L_{qq} can be computed with

$$L_{qq} = \frac{1}{\omega_{hf}} \sqrt{\frac{u_{q,\,hf}^2}{i_{q,\,hf}^2} - R_\mathrm{s}^2} \ . \tag{3.19}$$

For the cross-coupling differential inductance L_{dq}, a current of q-axis is given and the voltage equation of u_d is applied. The high frequency term is then given as

$$u_{d,\,hf} = L_{dq}\, \frac{\mathrm{d}}{\mathrm{d}\, t} i_{q,\,hf} \ . \tag{3.20}$$

Analogously to the aforementioned computation procedure, the cross-coupling inductance L_{dq} can be given as

$$L_{dq} = \frac{u_{d,\,hf}}{\omega_{hf}\, i_{q,\,hf}} \ . \tag{3.21}$$

In the similar manner, the cross-coupling inductance L_{qd} can be computed by

$$L_{qd} = \frac{u_{q,\,hf}}{\omega_{hf}\, i_{d,\,hf}} \ . \tag{3.22}$$

In principle, it is also possible to inject a testing voltage instead of a testing current for the evaluation process. The corresponding voltage equation consists of the DC term and the high-frequency term. If a testing voltage is injected, the voltage equation for the high-frequency part is then given as

$$\begin{bmatrix} u_{d,hf} \\ u_{q,hf} \end{bmatrix} = R_{\mathrm{s}} \begin{bmatrix} i_{d,hf} \\ i_{q,hf} \end{bmatrix} + \begin{bmatrix} L_{dd} & L_{dq} \\ L_{qd} & L_{qq} \end{bmatrix} \begin{bmatrix} \frac{\mathrm{d}}{\mathrm{d}\,t} i_{d,hf} \\ \frac{\mathrm{d}}{\mathrm{d}\,t} i_{q,hf} \end{bmatrix} . \tag{3.23}$$

Even though it is assumed that $L_{dq} = L_{qd}$, there are still three variables remained for solving out of two equations in (3.23). Therefore, the injection of the testing current provokes more accurate results. The desired characteristics of the differential inductances are determined at each operating point within the operation range. The identification procedure is summarized in the following.

Procedure 3.3 (Differential Inductance Determination)

1. *The current control loop of the to be identified motor need to be so tuned that any working point consisting of arbitrary current pair* $(i_d,\, i_q)$ *can be reached. The load motor stays at standstill and is firmly locked.*

2. *A high frequency signal with a relatively small amplitude and the predetermined frequency is injected into the* d*-axis current* i_d*.*

3. *The measurements, i.e. currents of* d*- as well as* q*-axis, the voltage commands and the motor temperature* T*, are collected and saved.*

4. *A high frequency signal with a relatively small amplitude and the predetermined frequency is injected into the* q*-axis current* i_q*.*

5. *The measurements, i.e. currents of* d*- as well as* q*-axis, the voltage commands and the motor temperature* T*, are collected and saved.*

6. *The differential inductance can be computed via* (3.18), (3.19), (3.21) *and* (3.22)*.*

During the identification procedure, the temperature of the motor should be kept constant, so that the impact from the variation of the resistance can be ignored. Otherwise, the temperature model of the stator resistance and the actual temperature need to be considered. The aforementioned determination procedure is applied to both PMSM I and PMSM II. The experimental results of self differential inductances L_{dd} and L_{qq} as well as the cross-coupling differential inductances L_{dq} and L_{qd} for the PMSM I are shown in Fig. 3.7 and Fig. 3.8, respectively.

It can be observed from the figures that the absolute inductances L_d , L_q have similar surface development to the differential inductances L_{dd} , L_{qq}. The cross-coupling differential inductances L_{dq} and L_{qd} are much smaller than them. Moreover, L_{dq} and L_{qd} are symmetric and can hardly differ from each other. In the context of different control requirements and computational resources, the corresponding inductance map can be deployed.

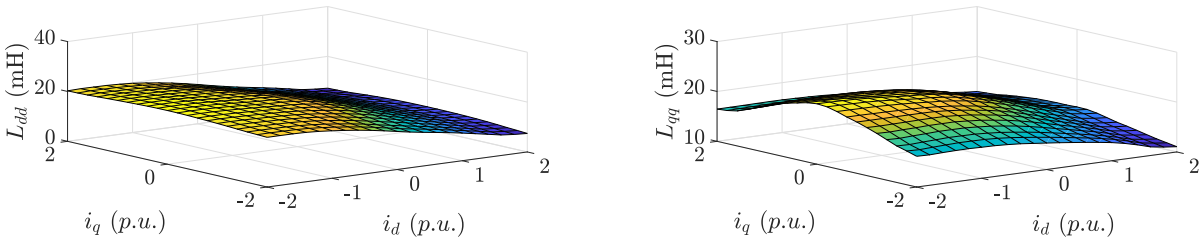

(a) (b)

Figure 3.7: The determined self differential inductance maps, i.e. L_{dd} and L_{qq}, for the PMSM I.

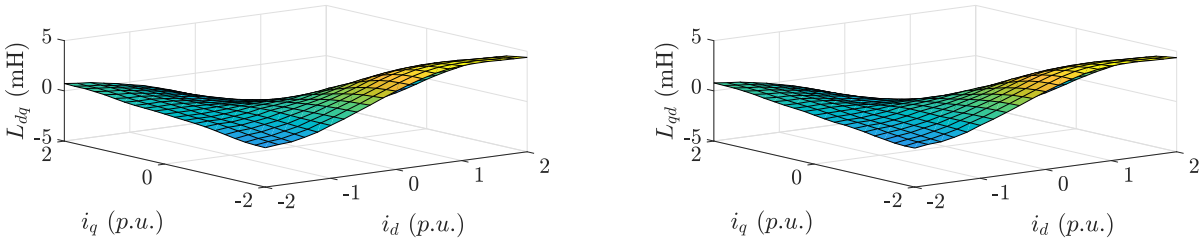

(a) (b)

Figure 3.8: The determined cross-coupling differential inductance maps, i.e. L_{dq} and L_{qd}, for the PMSM I.

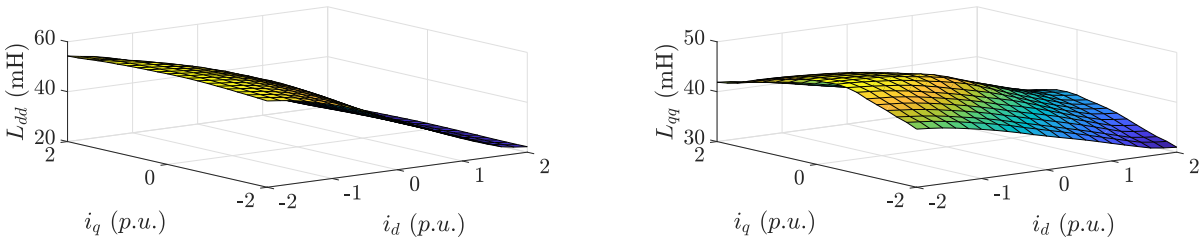

(a) (b)

Figure 3.9: The determined self differential inductance maps, i.e. L_{dd} and L_{qq}, for the PMSM II.

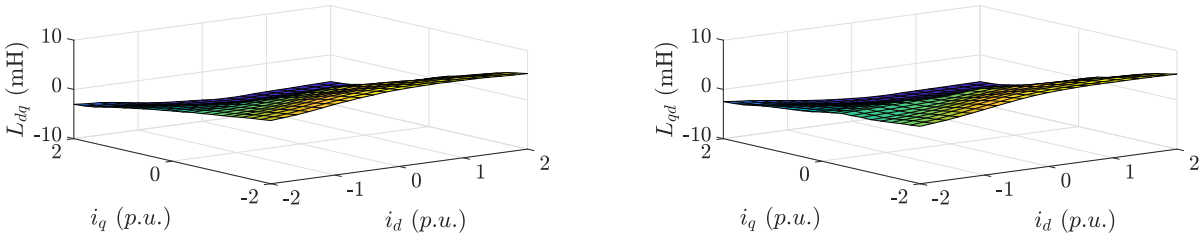

(a) (b)

Figure 3.10: The determined cross-coupling differential inductance maps, i.e. L_{dq} and L_{qd}, for the PMSM II.

3.3.3 Permanent Magnet Flux Linkage

The permanent magnet flux linkage Ψ_m, as the name suggests, relates to the flux linkage excited by the permanent magnet. Depends on the machine type, different operating strategies for the PMSM are implemented. For example, it is possible that the flux of the permanent magnets in the surface-inserted PMSM is completely absorbed by the surrounding iron and therefore the machine can be operated under the field weakening, while the surface-mounted PMSM faces a much higher danger of an irreversible demagnetization at a comparable field-weakening operation. For identifying the permanent magnet flux linkage Ψ_m , the linearised voltage equation in (2.19), more specifically the equation of q-axis, is deployed, since the permanent magnet flux linkage Ψ_m only related to the quantities in q-axis. Conventionally, a no-load test is carried out to determine the EMF. The to be identified motor is driven under a constant speed. The effective value of the terminal voltage and the motor speed are measured and then used for calculation of the permanent magnet flux linkage Ψ_m by

$$\Psi_\mathrm{m} = \sqrt{\frac{2}{3}}\,\frac{U_l}{\omega_e}\,, \tag{3.24}$$

where U_l denotes the effective value of the line voltage. The coefficient $\sqrt{2}/\sqrt{3}$ is derived under the assumption that the terminal voltage is sinusoidal. Another possibility is to identify the permanent magnet flux linkage Ψ_m with a procedure that is analogously to the identification procedure of the stator resistance R_s in Section 3.3.1. The principle of the stator resistance identification is to create two current states and compute the difference of the voltages as well as the currents to alleviate the influence of the disturbances. This intuition can also be applied to identify the permanent magnet flux linkage Ψ_m . For some applications, for example the traction applications, the identification can be realized online, since the variation of i_q may happen during the operation. It is worth mentioning that different from the identification of R_s , Ψ_m can not be determined at the standstill, which can be simply concluded from the voltage equation of u_q that the zero speed excludes the term Ψ_m from the equation. The permanent magnet flux linkage Ψ_m can be computed from two different working points by [105]

$$\Psi_\mathrm{m} = \frac{1}{\bar{\omega}_e}\left[\frac{u_{q,1}+u_{q,2}}{2} - R_\mathrm{s}\,\frac{i_{q,1}+i_{q,2}}{2} - \bar{\omega}_e\,\bar{L}_d\,\frac{i_{d,1}+i_{d,2}}{2}\right], \tag{3.25}$$

where

$$\begin{aligned} \bar{\omega}_e &= \frac{\omega_{e,1}+\omega_{e,2}}{2}\,, \\ \bar{L}_d &= \frac{1}{\omega_e}\,\frac{u_{q,1}-u_{q,2}}{i_{d,1}-i_{d,2}}\,. \end{aligned} \tag{3.26}$$

The computational method presented in (3.25) corresponds to the averaging of the two alternated operating points, which are generated by injecting a predetermined test signal. The aforementioned procedure is subsequently applied for the PMSM I and PMSM II. The identification results are accordingly listed in Table 3.2.

It is worth mentioning that the flux maps from the former section can be directly deployed for obtaining the values of the permanent magnet flux linkage.

Table 3.2: Identification results of the permanent magnet flux linkage for the PMSMs

Description	PMSM I	PMSM II
Data Sheet Value	$0.1108\,\mathrm{Wb}$	$0.212\,\mathrm{Wb}$
Measured Value	$0.114\,\mathrm{Wb}$	$0.212\,\mathrm{Wb}$

3.3.4 VSI Nonlinearities

Besides the parameters of the motors, the inverter of the drive system also requires identification, since the voltage command is distorted by the nonlinear effects of the inverter and the terminal voltage of the motor is normally not directly measurable. The most simple way to include the VSI nonlinearities is to carry out an approximation from the values of the data sheet. However, the data from manufacturer is difficult to approximate. On the one hand, multiple segments are required for accurately interpreting the characteristics of the VSI. On the other hand, a complex function for the deployment will increase the computational cost of the compensation mechanism. Nonetheless, the simplified approximation, as it is shown previously, can not guarantee the accuracy of the compensation. Furthermore, the variability during the production is also noteworthy and the characteristics of the inverter are not always available. Therefore, the offline determination of the VSI nonlinearities is still desired for the precise control of the PMSM drive system.

In general, the most applied offline methods for determining the nonlinearities of VSI are:

1. Direct measuring the terminal voltage and computing the voltage error as a function of the phase current. The function is then implemented into the drive system as a look-up table.

2. Deriving the nonlinearities with the aid of the motor parameters.

3. Approximating the nonlinearities via identifying the individual components (characteristics of semiconductors) [59].

Considering the complexity of the engaged experimental facilities, the direct measuring method and the derivation with the help of the motor parameters are preferred. Many developers of the drive system conduct offline measurements and feed the results back into the system to compensate the distorted voltage. The choice of the method normally depends on the budget as well as the available experimental facilities. The first engaged method is determining the nonlinear effect with the help of the motor parameters. The determination procedure is described in the following.

Procedure 3.4 (VSI Nonlinearities Determination Method I)

- *Define the maximum value and the rising as well as the falling slope of the test voltage.*
- *Gradually deliver the command voltage in the d-axis, of which the step voltage is determined by the slope and the maximum voltage. The voltage of the q-axis keeps constant at zero.*
- *Measure the current and save the measurements as well as the voltage commands.*

- *Compute the error voltage.*

The procedure is conducted at standstill. After obtaining the current i_d and the voltage u_d, the error voltage can be computed as

$$\Delta u = \bar{U}_{x,i} - \bar{I}_{x,i}\, R_\mathrm{s}\ , \tag{3.27}$$

where $\bar{U}_{x,i}$ denotes the phase voltage at the measuring point i of the phase x and $\bar{I}_{x,i}$ represents the averaged phase current at the measuring point i of the phase x. $\bar{I}_{x,i}$ is computed as the mean value of the currents from both the rising and falling slope, where the same voltage command is applied. The experimental as well as the computational results are shown in Fig. 3.11.

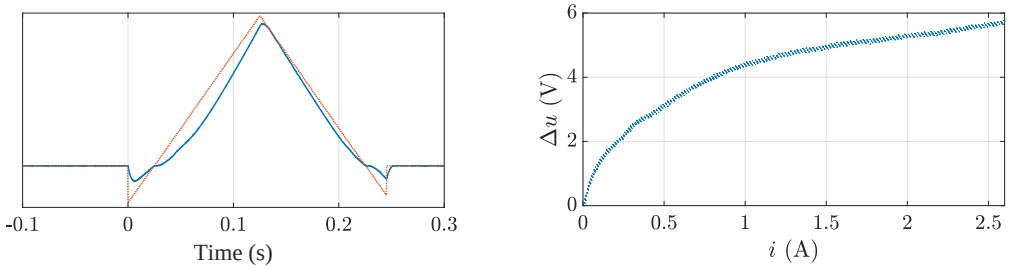

Figure 3.11: The measurement and computational results of implementing the VSI nonlinearities determination method I. (a) shows the measured phase current in solid blue and the command phase voltage in solid red. (b) denotes the computational results of the VSI nonlinearities via the determination method I.

Another method is the direct measuring method, which substrates the output voltage from the real measured voltage. The output voltage u_{xN} can be measured by applying a resistor-capacitor (RC) circuit or computed by the multiplication of the corresponding duty cycle and the DC-link voltage. In this work, the output voltage is measured by deploying a RC circuit, where $R = 20\,\mathrm{k\Omega}$ and $C = 10\,\mathrm{nF}$. Its cutoff frequency is therefore $795\,\mathrm{Hz}$. The determination method II is stated in the following.

Procedure 3.5 (VSI Nonlinearities Determination Method II)

- *Define the maximum value and the rising as well as the falling slope of the test voltage.*
- *Gradually deliver the command voltage to the d-axis, which is determined by the slope and the maximum voltage. The voltage of the q-axis keeps constant at zero.*
- *Measure the current and the voltage.*
- *Compute the error voltage.*

With the aforementioned procedure, the measurements are conducted accordingly. The corresponding experimental and computational results are shown in Fig. 3.12. It can be concluded from Fig. 3.11 and Fig. 3.12 that the identified error voltage Δu from both methods are similar, although small differences can be observed. The error voltage increases with the rise of the phase current. However, the rate of the growing decreases as the phase current increases. The identification of the VSI nonlinearities is important for the control and normally conducted once

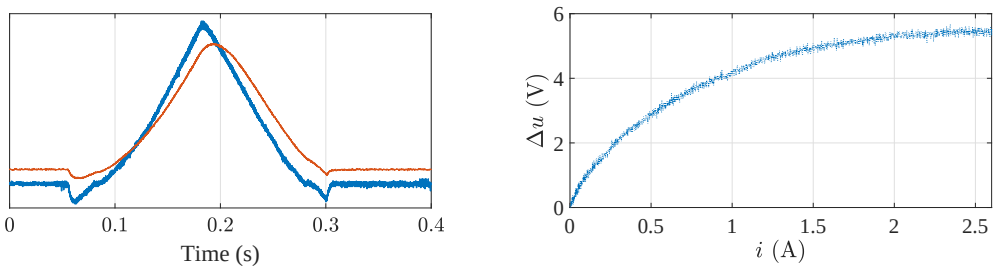

Figure 3.12: The measurement and computation results of implementing the VSI nonlinearities determination method II. (a) shows the measured phase current in solid blue and the measured phase voltage in solid red. (b) denotes the computational results of the VSI nonlinearities determination method II.

before the operation of the PMSM. But the nonlinear effects can be affected by multiple factors. In the following, the possible affecting factors are elaborated. The related measurements are carried out to present their relationships.

3.3.4.1 Affecting Factors

3.3.4.1.1 Output Parasitic Capacitance As introduced in Section 2.4.2, the VSI introduces nonlinear effects at the machine terminal and causes voltage distortions. The nonlinear phenomenon is complex and difficult to quantify. Even though the offline identification methods can be applied to determine the distorted voltage, it can be influenced by many factors. In this section, several experiments have been carried out to study the affecting factors for the nonlinearities. Fig. 3.13 demonstrates the influence of the equivalent output parasitic capacitance on the error voltage, which further affects the switching behaviour of the inverter. As presented in Fig. 3.13, the increase of the equivalent output parasitic capacitance would decelerate the development of the error voltage [60].

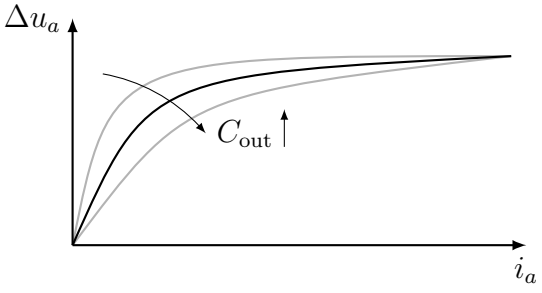

Figure 3.13: Influence of the equivalent output parasitic capacitance on distorted voltage.

3.3.4.1.2 Phase Current Measurements have been conducted to investigate the influence of the current level on the switching behaviour. The corresponding experimental results at the room temperature (around $25\,^{\circ}\mathrm{C}$) are shown in Fig. 3.14, where the turn-on and turn-off behaviour are separately established. T_d denotes the delay time at turn-on or turn-off, T_r denotes the rising time and T_{on} represents the sum of the turn-on delay and rising time. T_f denotes the falling time and T_{off} is defined as the sum of turn-off delay and the falling time. As it is justified

in Section 2.4.2, the turn-on and turn-off delay are associated with the threshold voltage and the time constant of the gate-emitter (gate-source) terminal. The rising and falling time are mostly affected by the bus voltage, the parasitic-element effects and the phase current [106].

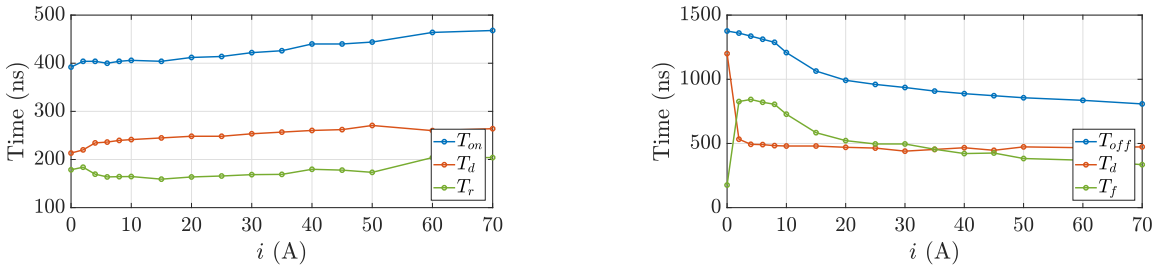

(a) (b)

Figure 3.14: Influence of the current level on the switching behaviour. (a) represents the influence of the current on the turn-on behaviour and (b) demonstrates the impact of the current on the turn-off behaviour.

It can be noted from Fig. 3.14 that in comparison to the turn-off time, the turn-on time is less affected by the current level. However, an increase of the turn-on time can still be observed as the current grows. The turn-off time is heavily influenced by the current value, where the turn-off delay and the falling time both show a significant change at $i = 2\,\mathrm{A}$. Afterwards, the falling time continuously decreases as the current increases, while the turn-off delay is relatively steady. It can be explained by the fact that the falling time is caused by the parasitic-element and therefore more sensitive to the current.

3.3.4.1.3 Cable Length Besides the influence from the current level, the effect of the cable length is also investigated. In practice, a power cable of an arbitrary length is utilized to connect the inverter and the motor. However, because of the impedance of the cable, which is normally related to its characteristics, e.g. length and diameter, the terminal voltage is also affected by the cable. It is in general difficult to quantify its effects [107]. Normally, the connector between the inverter and the motor is already determined and the choice of the cable is also limited. Thus, the most relevant factor is the cable length. In Fig. 3.15, two cable lengths of $75\,\mathrm{m}$ and $5\,\mathrm{m}$ are compared at different switching frequency, namely $4\,\mathrm{kHz}$ and $8\,\mathrm{kHz}$.

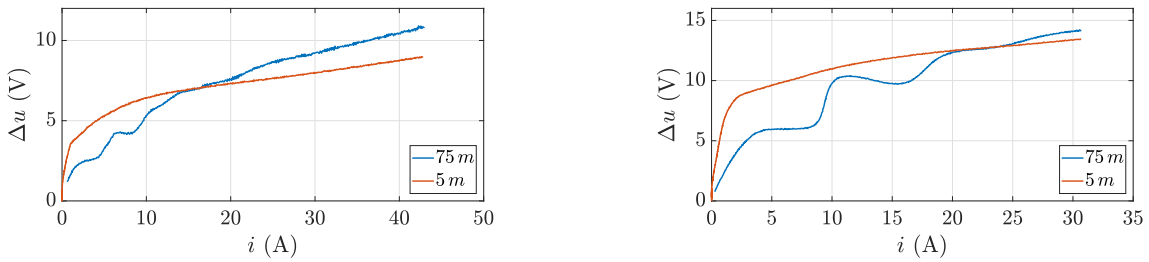

(a) (b)

Figure 3.15: Influence of the cable length on the error voltage Δu. (a) represents the error voltage with a switching frequency of $4\,\mathrm{kHz}$ and (b) represents the error voltage with a switching frequency of $8\,\mathrm{kHz}$.

The measurement results in Fig. 3.15 show that a longer cable (i.e. $75\,\mathrm{m}$ in our case) can

cause a nonlinear behaviour at the low current level, while a shorter cable inherits the identified approximation in Section 3.3.4. At a switching frequency of $4\,\mathrm{kHz}$, the crossing point of the error voltage of the $75\,\mathrm{m}$ cable and the $5\,\mathrm{m}$ cable appears at around $i = 15\,\mathrm{A}$, while at a higher switching frequency ($8\,\mathrm{kHz}$) the crossing point shifts and appears at a larger current (around $i = 23\,\mathrm{A}$). The crossing points denote that the longer cable causes larger error voltage at a higher current level beyond the crossing point. It can be moreover concluded that the switching frequency can also have influence on the error voltage, which is discussed thereafter.

3.3.4.1.4 Switching Frequency The cable resistance is precalculated and denoted as R_c . In Fig. 3.16, three different switching frequencies are compared, namely $4\,\mathrm{kHz}$, $8\,\mathrm{kHz}$ and $16\,\mathrm{kHz}$.

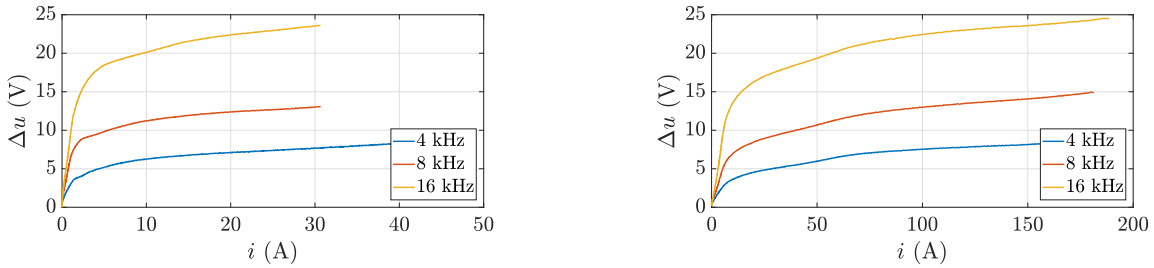

Figure 3.16: Influence of the switching frequency on the error voltage Δu. The cable resistance is precalculated and denotes as R_c. (a) shows the error voltage with a DC-link voltage of $750\,\mathrm{V}$ and $R_c = 36\,\Omega$ and (b) demonstrates the error voltage with a DC-link voltage of $750\,\mathrm{V}$ and $R_c = 280\,\Omega$.

It can be concluded from Fig. 3.16 that a higher switching frequency induces a larger error voltage. Moreover, an increase of the cable resistance will benefit the voltage realization, i.e. a larger cable resistance results in a smaller error voltage at the same current level and the same DC-link voltage.

3.3.4.1.5 DC-Link Voltage Furthermore, the impact from the DC-linkage voltage is investigated. In Fig. 3.17, measurement results of the distorted voltage under two different DC-link voltage, i.e. $560\,\mathrm{V}$ and $750\,\mathrm{V}$, are compared.

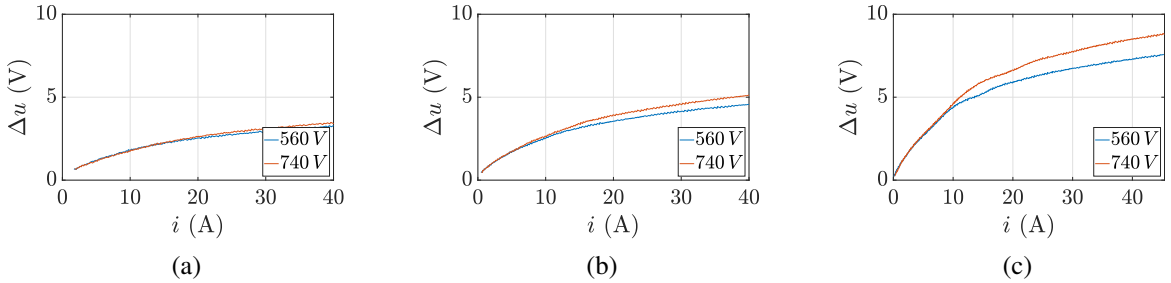

Figure 3.17: Influence of the DC-link voltage on the error voltage Δu. (a) represents the error voltage with a switching frequency of $4\,\mathrm{kHz}$, (b) represents the error voltage with a switching frequency of $8\,\mathrm{kHz}$, (c) shows the error voltage with a switching frequency of $16\,\mathrm{kHz}$.

At a relatively lower switching frequency, i.e. $4\,\mathrm{kHz}$ in Fig. 3.17a, the difference of the distorted voltage resulted from the DC-linkage voltage is smaller than that at a higher switching frequency, which means the DC-link voltage has more significant impact on the error voltage at the high switching frequency. At the same current and the same switching frequency, an increase of the DC-link voltage will cause an increment of the distorted voltage Δu.

3.3.4.1.6 Temperature The characteristics of the inverter are also affected by the temperature. Manufactures normally provide the data sheet of the switching characteristics at various temperatures. The measurements of the error voltage at different temperatures, namely the room temperature, $50\,^{\circ}\mathrm{C}$ and $60\,^{\circ}\mathrm{C}$, have been carried out. The results are presented in Fig. 3.18.

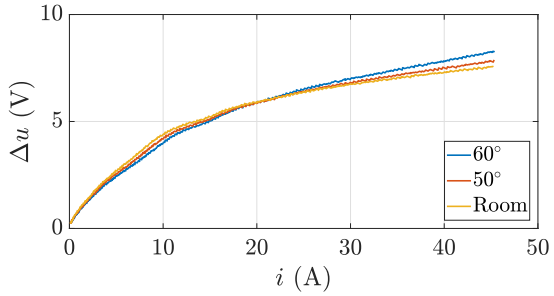

Figure 3.18: Influence of the temperature on the error voltage Δu. The legend *Room* denotes a room temperature around $25\,^{\circ}\mathrm{C}$.

It can be observed from Fig. 3.18 that at low current level (smaller than $20\,\mathrm{A}$), a lower temperature induces a larger error voltage, while at high current level a higher temperature causes a larger error voltage.

3.4 Parameter Estimation with Current Injection

The aforementioned offline determination methods are simple and have lower computational burden. But the offline results have limited capability to capture the real-time behaviour of the electrical parameters, such as the variation caused by the temperature. Moreover, the explicit realization of the offline determination procedures may increase the cost for experimental facilities. Even though the measuring and determining procedures can be completed by the self-commissioning method, which significantly reduces the complexity and the consumed time of the proceedings, extra hardware may still be required and the higher level control mechanism is mandatory. Therefore, the online estimation methods are more suitable for identifying the PMSM in real time and applying the identified results for the precise control. In Section 3.2, the rank deficient problem of the parameter estimation for PMSM is described. In order to achieve the goal of simultaneously estimating all the electrical parameters, a persistent excitation is requested, which can be realized by injecting a varying current. In this section, two methods associating with the current injection are presented, i.e. the square-wave current injection and the sinusoidal current injection. The current is injected on the d-axis, since it has less impact on the torque production, especially for the PMSM with low reluctance, e.g. the surface-mounted PMSM [49].

3.4.1 Current Injection with Square Wave Form

The principle of the square-wave current injection is shown in Fig. 3.19, where the reference of the current and the real trajectory of the current are illustratively presented. The quantities of

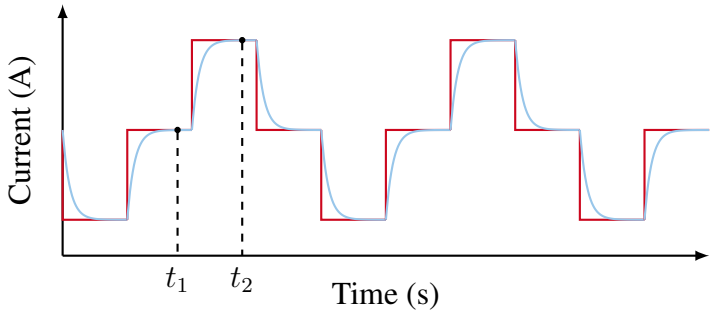

Figure 3.19: The principle of the square-wave injection method. The reference current is shown in red solid line and the real current trajectory is represented in blue solid line.

the PMSM at different operating points, e.g. in Fig. 3.19 at $t = t_1$ and $t = t_2$, are measured and applied to computation of the electrical parameters for the PMSM. The measurements are collected once after the PMSM reaches the steady state, which is defined by that the d-current stays around a new value beyond a certain time period. Therefore, the excitation frequency is chosen to be much lower than the electrical dynamics of the machine in order that the current can reach the steady state at the individual current value. The averaged values of the measurements are subsequently utilized to estimate the electrical parameters. Substitute the available quantities into the linearised voltage equation in the dq reference frame, which is given in (2.19), the corresponding equation set for computing the electrical parameters are shown as

$$\begin{aligned} u_d(t_1) &= R_\mathrm{s}\, i_d(t_1) - \omega_e(t_1) i_q(t_1)\, L_q \,, \\ u_d(t_2) &= R_\mathrm{s}\, i_d(t_2) - \omega_e(t_2)\, i_q(t_2)\, L_q \,, \\ u_q(t_1) &= R_\mathrm{s}\, i_q(t_1) + \omega_e(t_1)\, i_d(t_1)\, L_d + \omega_e(t_1)\, \Psi_\mathrm{m} \,, \\ u_q(t_2) &= R_\mathrm{s}\, i_q(t_2) + \omega_e(t_2)\, i_d(t_2)\, L_d + \omega_e(t_2)\, \Psi_\mathrm{m} \,, \end{aligned} \tag{3.28}$$

where the differential term of the current is omitted, since the steady state of the PMSM is investigated. It can be noticed from (3.28) that the q-axis inductance L_q can only be estimated from the voltage equation of the d-axis. Analogously, the permanent magnet flux linkage Ψ_m and the d-axis inductance L_d can solely be derived from the voltage equation of the q-axis. The stator resistance is required in all equations. The most straightforward strategy to solve (3.28) is to group the two equations of u_d for solving R_s, L_q and the two equations of u_q for solving L_d, Ψ_m. However, if the changing rate of the parameters is taken into consideration, i.e. the inductances vary with the currents, while the stator resistance as well as the permanent magnet flux linkage varies at a much slower rate (variation dominated by the temperature), an approach to separate different updating rate is preferable. A separation of the estimation for different changing rates may reduce the computational burden, since the estimation for parameters of a slower updating rate can be deactivated after their steady state is achieved. However, the computational burden is higher during the transient and the stability can not be guaranteed. Therefore, in this thesis, the computation strategy for estimating the parameter combinations $[R_\mathrm{s},\, L_q]^T$ and $[L_d,\, \Psi_\mathrm{m}]^T$ is chosen. A flow chart to demonstrate the identification strategy is

shown in Fig. 3.20.

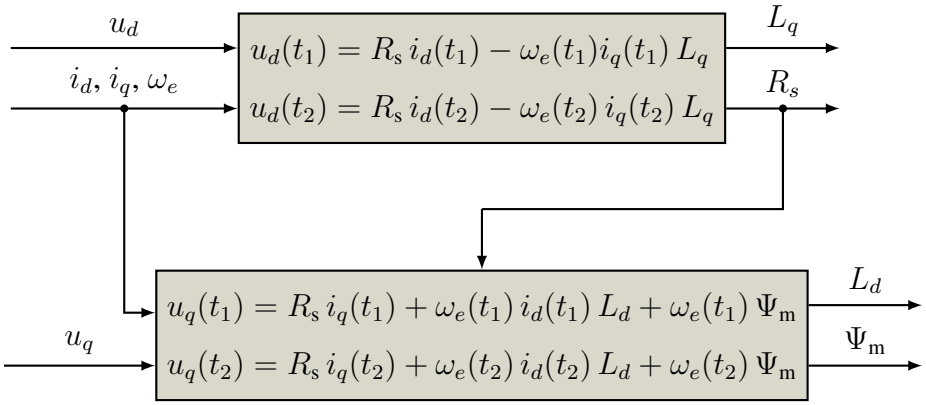

Figure 3.20: The computation mechanism of the current injection method with the square-wave current.

The injected current is defined by the predetermined frequency and amplitude. The injected perturbation is a compromise between the effectiveness of the injected current and the current quality of the PMSM. On the one hand, the injected current has to be as small as possible to minimize the resulted ripples for the motor current as well as for the torque. On the other hand, the injected current has to be large enough to provoke different operating points of the machine. Besides, the frequency of the injected current should satisfy two contradictory requirements, i.e. the frequency should be low enough for the real current to reach the steady state and be high enough to track the parameter variation.

3.4.2 Current Injection with Sinusoidal Wave Form

The square-wave current injection method is simple and has low computational burden. However, as indicated in [108], the square-wave current injection method is infeasible during the transient. Besides, it converges slowly, since only one value set is collected at each current value. Therefore, the sinusoidal current injection was proposed to overcome these drawbacks. A schematic presentation of the sinusoidal current injection method is shown in Fig. 3.21.

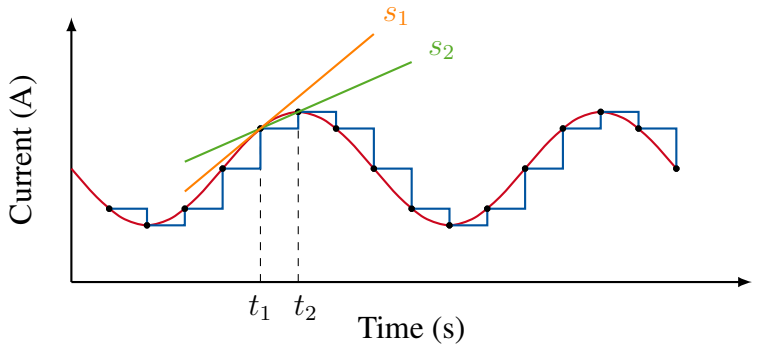

Figure 3.21: The principle of the sinusoidal wave injection method. The reference current is shown in red solid line and the sampled current value at each time instant is represented in blue solid line. The yellow solid line denotes the gradient at the sampling instant $t = t_1$ and the green solid line represents the numerically computed gradient via the forward Euler discretization.

Instead of collecting the information from the steady state, this method creates transients, from which the to be identified parameters are derived accordingly. The equation set for the computation of the identification are given as

$$\begin{aligned}
u_d(t_1) &= R_\mathrm{s}\, i_d(t_1) + L_d \frac{\mathrm{d}}{\mathrm{d}\, t} i_d(t_1) - \omega_e(t_1)\, i_q(t_1)\, L_q \,, \\
u_d(t_2) &= R_\mathrm{s}\, i_d(t_2) + L_d \frac{\mathrm{d}}{\mathrm{d}\, t} i_d(t_2) - \omega_e(t_2)\, i_q(t_2)\, L_q \,, \\
u_q(t_1) &= R_\mathrm{s}\, i_q(t_1) + L_q \frac{\mathrm{d}}{\mathrm{d}\, t} i_q(t_1) + \omega_e(t_1)\, i_d(t_1)\, L_d + \omega_e(t_1)\, \Psi_\mathrm{m} \,, \\
u_q(t_1) &= R_\mathrm{s}\, i_q(t_2) + L_q \frac{\mathrm{d}}{\mathrm{d}\, t} i_q(t_2) + \omega_e(t_2)\, i_d(t_2)\, L_d + \omega_e(t_2)\, \Psi_\mathrm{m} \,.
\end{aligned} \tag{3.29}$$

Moreover, different from the square-wave current injection method, the electrical parameters are coupled in (3.29), which is resulted from the differential terms. The computation of the to be identified parameters need to be carried out with the four equations in (3.29) simultaneously. Because that the equations in (3.29) are valid as an approximation for any time instant, a distortion of the sinusoidal current may have little influence on the identification results. However, the computation of the derivatives becomes critical. As it is shown in Fig. 3.21, the gradient at the time instant t_1 can be computed in a digital control system with the aforementioned forward Euler approximation and represented by s_2, which differs from the real gradient at the time instant t_1 denoted by s_1. Moreover, the computation of the derivatives is sensitive to the measurement noise. In order to tackle these problems, a moving average filter is applied, which integrates the both sides of equations in (3.29) within half period of the sinusoidal signal [108]. As a result, we can have

$$\begin{aligned}
\bar{u}_d(t_1) &= \bar{R}_\mathrm{s}\, \bar{i}_d(t_1) + \bar{L}_d\, \bar{\dot{i}}_d(t_1) - \overline{\omega_e\, i_q}(t_1)\, \bar{L}_q \,, \\
\bar{u}_d(t_2) &= \bar{R}_\mathrm{s}\, \bar{i}_d(t_2) + \bar{L}_d\, \bar{\dot{i}}_\mathrm{d}(t_2) - \overline{\omega_e\, i_q}(t_2)\, \bar{L}_q \,, \\
\bar{u}_q(t_1) &= \bar{R}_\mathrm{s}\, \bar{i}_q(t_1) + \bar{L}_q\, \bar{\dot{i}}_q(t_1) + \overline{\omega_e\, i_d}(t_1)\, \bar{L}_d + \bar{\omega}_e(t_1)\, \bar{\Psi}_\mathrm{m} \,, \\
\bar{u}_q(t_2) &= \bar{R}_\mathrm{s}\, \bar{i}_q(t_2) + \bar{L}_q\, \bar{\dot{i}}_q(t_2) + \overline{\omega_e\, i_d}(t_2)\, \bar{L}_d + \bar{\omega}_e(t_2)\, \bar{\Psi}_\mathrm{m} \,,
\end{aligned} \tag{3.30}$$

where the overline in equation (3.30) denotes the output of the moving average filter for each individual term. The moving average filter for the discrete sequential signal can be given as

$$\bar{x}(t_1) = \frac{1}{N} \sum_{i=0}^{N-1} x(t_1 - i)\, T_{si} \,, \tag{3.31}$$

where N is the ratio between the half period of the injected sinusoidal signal and the sampling period T_{si} of the estimator. Analogously to the square-wave current injection method, the amplitude as well as the frequency of the injected current has a great impact on the estimation results and the control performance. The design parameters are then determined with the help of simulations.

3.4.3 Simulation Results

The aforementioned equations are solved with the recursive least squares method. The details about the RLS are given in Section 3.5.2. In order to find the adequate parameters for the injected current, several simulations are carried out considering various design parameter combinations. The description of the parameter combinations is given in Table 3.3. The injected current is determined by the amplitude A_{in} and the frequency f_{in}. The sinusoidal wave current has one more tuning parameter, i.e. the sampling rate N_{si}, which is defined as the ratio between the sampling frequency of the estimator and the frequency of the injected current. It is worth mentioning that the sampling frequency of the estimator f_{si} is lower than the sampling frequency of the digital control system f_s, through which the computational burden can be significantly reduced. Moreover, the sampling of the estimator can be regarded as a downsampling of the system with the sampling time T_s. The motor parameters of the PMSM II in Table B.3 is employed for the simulations.

Case №	ω_e	P_0	λ	Square		Sinusoidal		
	rad/s (rpm)			A_{in} (A)	f_{in} (Hz)	A_{in} (A)	f_{in}(Hz)	N_{si}
1	200 (1910)	1	0.9	0.072	10	0.072	10	40
2	200 (1910)	1	0.7	0.072	10	0.072	10	40
3	200 (1910)	1	0.5	0.072	10	0.072	10	40
4	200 (1910)	0.1	0.9	0.072	10	0.072	10	40
5	200 (1910)	10	0.9	0.072	10	0.072	10	40
6	100 (955)	1	0.9	0.072	10	0.072	10	40
7	50 (477)	1	0.9	0.072	10	0.072	10	40
8	200 (1910)	1	0.9	0.144	10	0.144	10	40
9	200 (1910)	1	0.9	0.288	10	0.288	10	40
10	200 (1910)	1	0.9	0.72	10	0.72	10	40
11	200 (1910)	1	0.9	0.072	5	0.072	5	40
12	200 (1910)	1	0.9	0.072	20	0.072	20	40
13	200 (1910)	1	0.9	-	-	0.072	10	20
14	200 (1910)	1	0.9	-	-	0.072	10	80
15	200 (1910)	1	0.9	-	-	0.072	10	120

Table 3.3: Description of the cases designed to determine the parameters of the injected current and the solving method.

The tuning parameters in Table 3.3 are explained in the following. P_0 is the initial matrix of the RLS (selected as diagonal matrix) and λ denotes the forgetting factor for the recursive mechanism. The initial value for all testing cases is set to zero. The motor speed for estimation is chosen within the middle-speed range. The simulation of the Case № 1 described in Table 3.3 is conducted for both methods. The simulation results are shown in Fig. 3.22. It can be observed from Fig. 3.22 that the sinusoidal wave current injection method delivers more accurate identification results. Moreover, it converges much faster than the square-wave current injection method. For the purpose of compactness, the rest of the simulation results are summarized as two extracted metrics, i.e. the accuracy and the rate of convergence. The accuracy is evaluated by the absolute error between the estimations and the real values, which is then presented

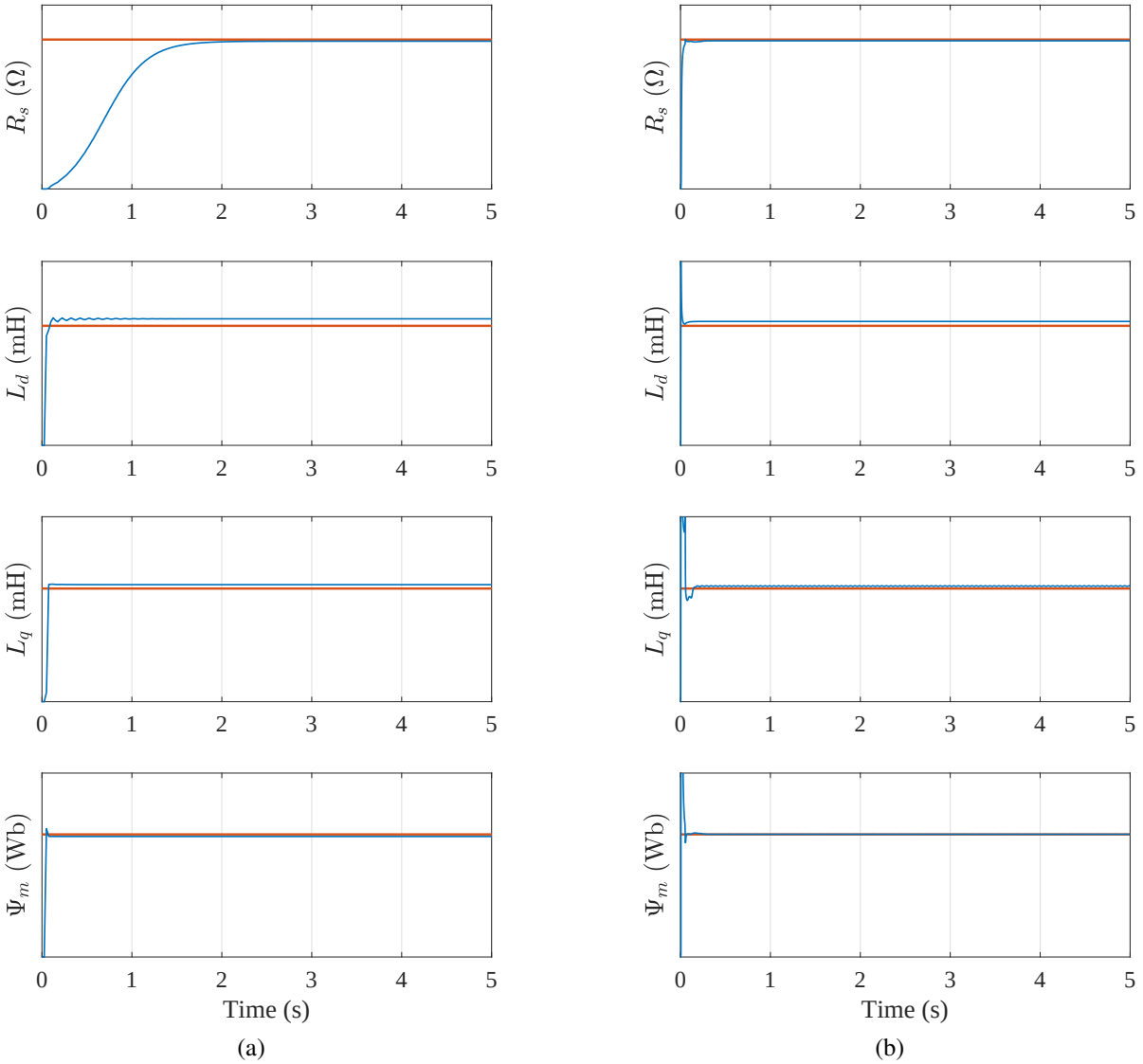

Figure 3.22: Simulation results of the Case № 1 described in Table 3.3, where the reference values are denoted in red and the estimated values are shown in solid blue. (a) shows the simulation results with the square-wave current injection method. (b) represents the simulation results with the sinusoidal wave current injection method.

as a percentage of the corresponding real value. The rate of convergence is given as the time duration from the start of the estimation until the achievement of the end value. The extracted information is summarized and demonstrated in Fig. 3.23 for the square-wave current injection method and in Fig. 3.24 for the sinusoidal wave current injection method.

Several conclusions can be drawn from the simulation results in Fig. 3.23 and Fig. 3.24. First of all, it can be observed that the convergent speed of the sinusoidal wave current injection method is overall much faster than that of the square wave current injection method, which can be explained by the fact that more computations are carried out within one period of the injected sinusoidal current. However, the sinusoidal wave current injection method establishes the estimation problem on a four-dimensional variable basis, while the square wave current injection method handles two two-dimensional variable systems. Therefore, the sinusoidal wave current

injection method expects more computational cost. The first three cases focus on evaluating the influence of the forgetting factor λ on the estimation results. It has impacts on the rate of convergence of the square-wave current injection method and affects the accuracy as well as the rate of convergence of the sinusoidal wave current injection method. The initial matrix P_0 has no impact on the accuracy, but affects the rate of convergence for both methods, i.e. a higher value of P_0 will reduce the convergent time. The choice of the motor speed has slight influence on the estimation accuracy of both methods. From the comparison among cases 8-10, it can be concluded that a larger amplitude of the injected current can accelerate the convergent speed. However, more fluctuation can be observed if a larger current is injected. An increase of the injected current frequency can significantly improve the rate of convergence, which can be clarified by that the increase of the injected current frequency indicates a growth of the updating rate for the estimation.

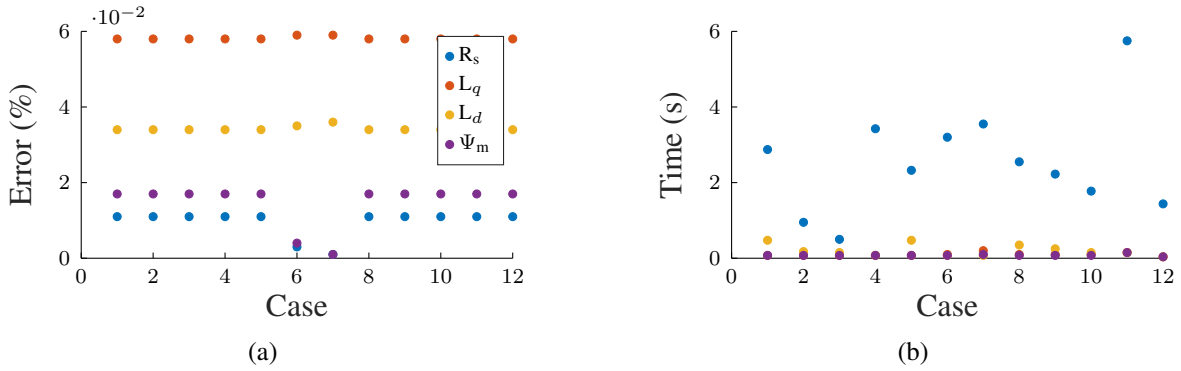

(a) (b)

Figure 3.23: Simulation results of various test cases for the square-wave current injection method. (a) shows the absolute error between the estimated value and the real value, which is shown as a percentage of the real value. (b) denotes the time of convergence.

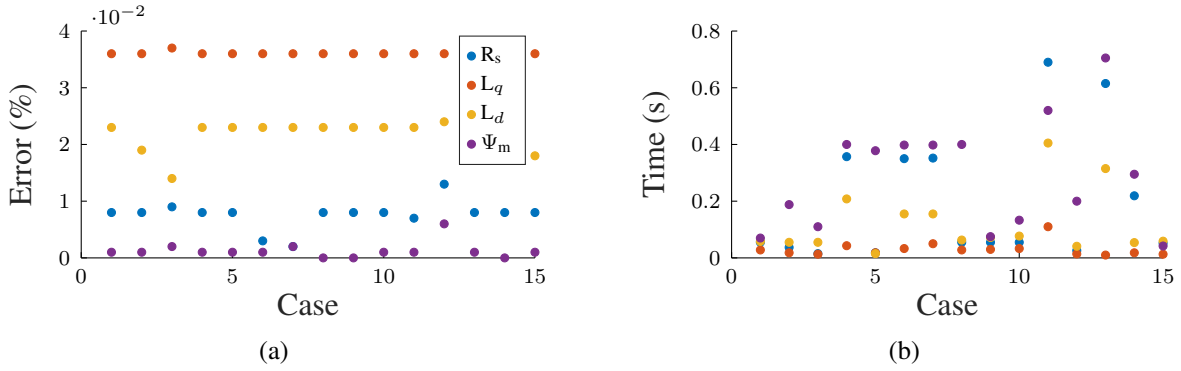

(a) (b)

Figure 3.24: Simulation results of various test cases for the sinusoidal wave current injection method. (a) shows the absolute error between the estimated value and the real value, which is shown as a percentage of the real value. (b) denotes the time of convergence.

3.4.4 Experimental Evaluation

Based on the simulation results, the parameters for the injected current as well as for the RLS are determined. The injected current is then selected with $f_{in} = 10\,\mathrm{Hz}$ and $A_{in} = 0.144\,\mathrm{A}$ for both the sinusoidal current and the square-wave current. These two methods are then implemented on the test bench described in Appendix B.1. In order to demonstrate the influence of the error voltage induced by the VSI nonlinearities, a comparison between the identification results with and without the compensation of the VSI nonlinearities is conducted. The identification method including the compensation of the VSI nonlinearities is denoted in yellow and the one without the compensation is denoted in blue in the following figures. The experimental results for PMSM I are shown in Fig. 3.25 - Fig. 3.28.

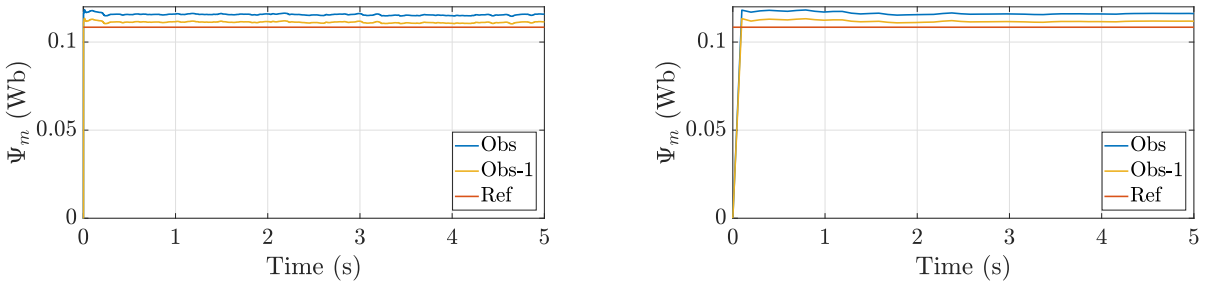

Figure 3.25: Experimental results of estimating Ψ_m by applying the square wave and the sinusoidal wave current injection methods for PMSM I. The identification method including the compensation of the VSI nonlinearities is denoted in yellow and the one without the compensation is denoted in blue. The reference value is represented by red. (a) denotes the identification results of the sinusoidal wave current injection method and (b) shows the results of the square-wave current injection method.

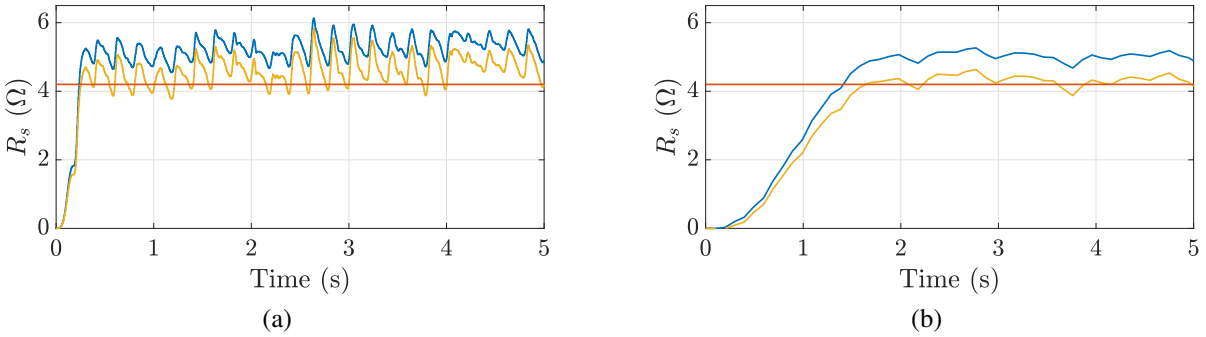

Figure 3.26: Experimental results of estimating R_s by applying the square wave and the sinusoidal wave current injection methods for PMSM I. (a) denotes the identification results of the sinusoidal wave current injection method and (b) shows the results of the square-wave current injection method.

It can be observed from the estimation results that the VSI nonlinearities have a great impact on the estimation of almost all the electrical parameters, i.e. R_s, Ψ_m and L_q. More specifically, the error of estimating Ψ_m with the sinusoidal current injection method and compensation of the distorted voltage is around 2% of the real value, while it is around 7% without compensation. Analogously, if the VSI nonlinear effects are taken into consideration, the estimation error of

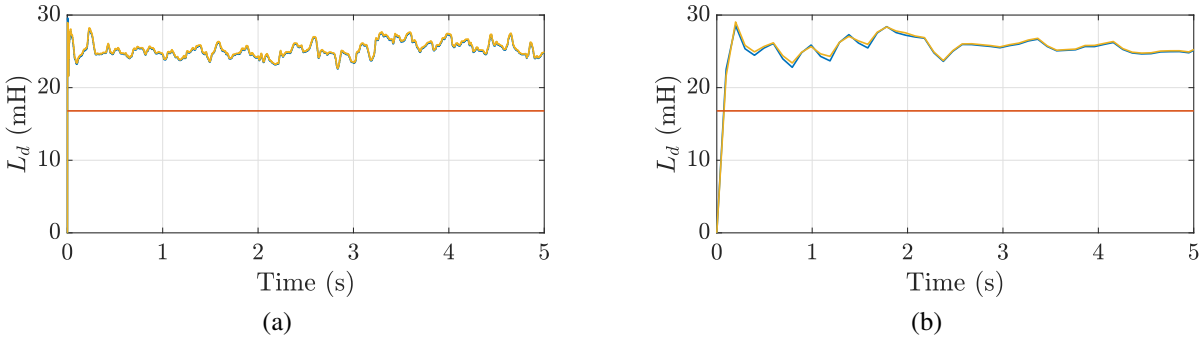

Figure 3.27: Experimental results of estimating L_d by applying the square wave and the sinusoidal wave current injection methods for PMSM I. (a) denotes the identification results of the sinusoidal wave current injection method and (b) shows the results of the square wave current injection method.

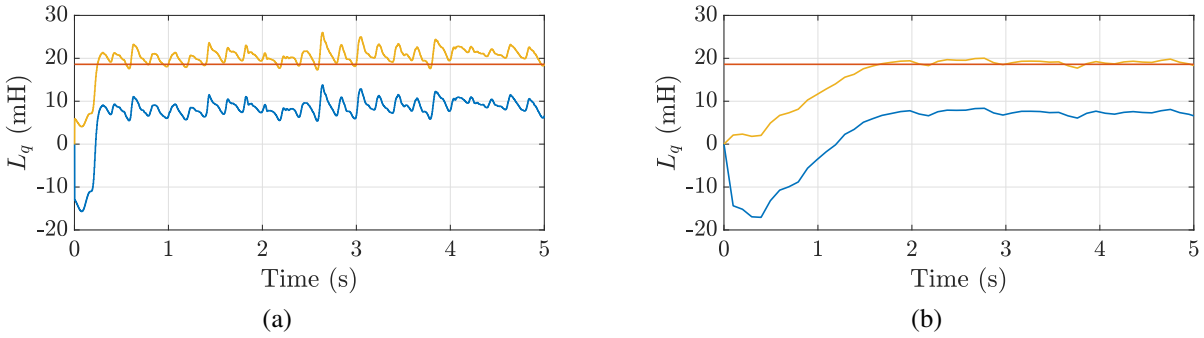

Figure 3.28: Experimental results of estimating L_q by applying the square wave and the sinusoidal wave current injection methods for PMSM I. (a) denotes the identification results of the sinusoidal wave current injection method and (b) shows the results of the square wave current injection method.

R_s and L_q is around 10% and 12%, respectively, while the errors without compensation are more than 50% and 60%, respectively. Moreover, it is worth mentioning that the estimation results with the square-wave current injection method is in general more accurate than that of sinusoidal current injection method, i.e. the results are less fluctuated and demonstrate smaller errors. Nonetheless, this conclusion is in contrast to the conclusions from the simulation results, which may result from that higher noise content and disturbances are expected in the practical implementation. However, the converging speed of the sinusoidal current injection method is much faster than that of the square-wave current injection method, which can be also noticed from the simulation results.

The parameter estimations for the PMSM II with the two current injection methods are furthermore conducted. The corresponding results are shown in Fig. 3.29 - Fig. 3.32.

Similar conclusions to the experimental results of the PMSM I can be drawn from the estimation results of the PMSM II. On the one hand, the square-wave current injection method can provide more accurate identification results. On the other hand, the sinusoidal current injection method reaches the end value faster than the other one. Regarding the impacts of the inverter, the error of estimating Ψ_m with the sinusoidal current injection method and the compensation of the distorted voltage is limited by 1%, while it is around 5% without compensation. The estimation error of R_s considering the VSI is around 10%, which increases to more than 50% of the nominal value when the compensation is omitted. The results of estimating L_q with the

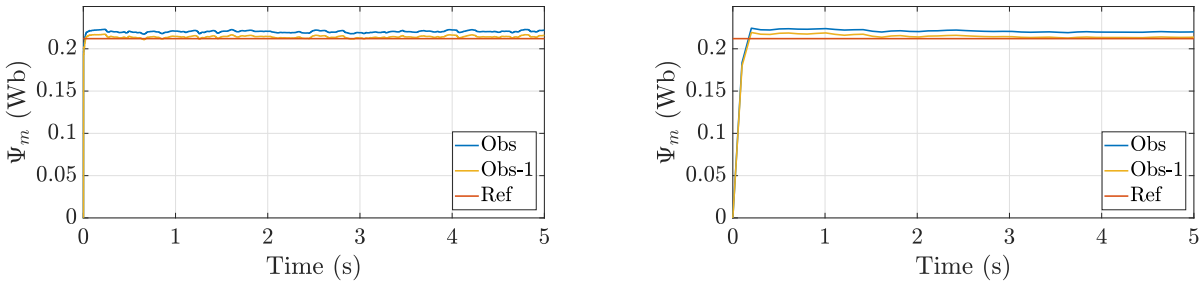

Figure 3.29: Experimental results of estimating Ψ_{m} by applying the square wave and the sinusoidal wave current injection methods for PMSM II. (a) denotes the identification results of the sinusoidal wave current injection method and (b) shows the results of the square wave current injection method.

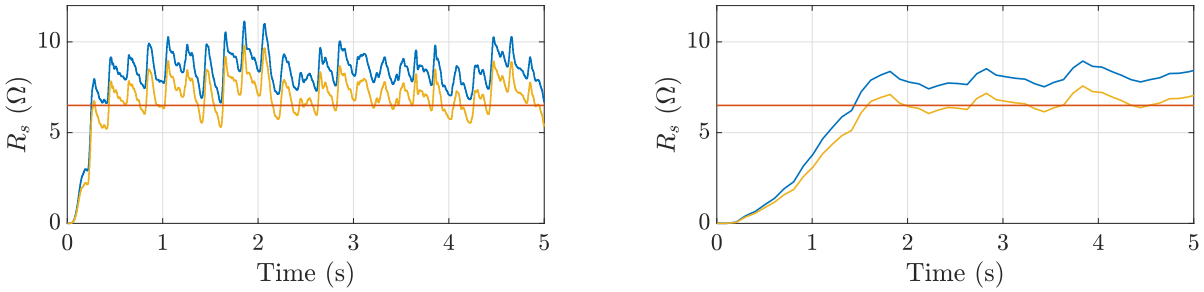

Figure 3.30: Experimental results of estimating R_{s} by applying the square wave and the sinusoidal wave current injection methods for PMSM II. (a) denotes the identification results of the sinusoidal wave current injection method and (b) shows the results of the square wave current injection method.

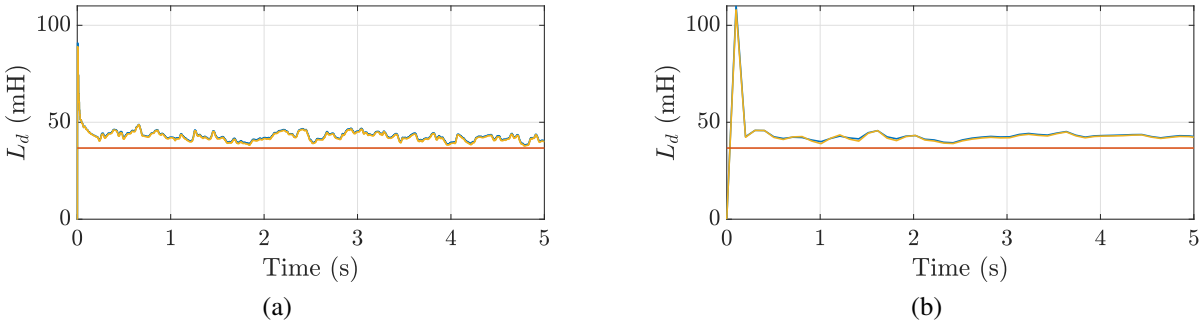

Figure 3.31: Experimental results of estimating L_d by applying the square wave and the sinusoidal wave current injection methods for PMSM II. (a) denotes the identification results of the sinusoidal wave current injection method and (b) shows the results of the square wave current injection method.

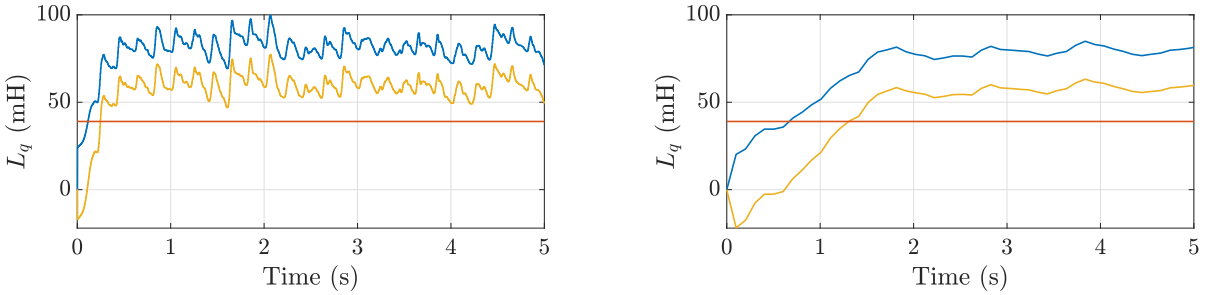

Figure 3.32: Experimental results of estimating L_q by applying the square wave and the sinusoidal wave current injection methods for PMSM II. (a) denotes the identification results of the sinusoidal wave current injection method and (b) shows the results of the square wave current injection method.

compensation is still erroneous, which is around 50%. However, the estimation results of L_q without compensation is even more inaccurate, i.e. with an error of more than 110% of the nominal value.

In order to better analyze the experimental results shown above, the estimation of the parameters is derived from the simplified PMSM model and the values of the estimated parameters are determined such that a set of equations in (3.28) and in (3.29) is satisfied. During the current injection estimation procedure, it is assumed that the injected current has slight impact on the working points, i.e. the inductances L_d and L_q are constant. They can be given as

$$\hat{L}_d = \frac{u_q - \hat{R}_\mathrm{s}\, i_q - \omega_e\, \hat{\Psi}_\mathrm{m}}{\omega_e\, i_d}\,, \tag{3.32}$$

where $u_q = u_q^* - \Delta u_q$. The superscript $\hat{x}$ denotes the estimated quantities.

$$\hat{L}_q = -\frac{u_d - \hat{R}_\mathrm{s}\, i_d}{\omega_e\, i_q}\,, \tag{3.33}$$

where $u_d = u_d^* - \Delta u_d$. Furthermore, the small signal analysis is applied for further investigation. Then, the formulation of $\hat{L}_d$ in (3.32) can be further derived as

$$\mathrm{d}\hat{L}_d = \frac{\partial \hat{L}_d}{\partial \hat{R}_\mathrm{s}}\,\mathrm{d}\hat{R}_\mathrm{s} + \frac{\partial \hat{L}_d}{\partial \hat{\Psi}_\mathrm{m}}\,\mathrm{d}\hat{\Psi}_\mathrm{m} + \frac{\partial \hat{L}_d}{\partial u_q}\,\mathrm{d}u_q\,. \tag{3.34}$$

The equation for L_q can be similarly obtained. Substitute (3.32) into (3.34), it can be given that

$$\mathrm{d}\hat{L}_d = -\frac{i_q}{\omega_e\, i_d}\,\mathrm{d}\hat{R}_\mathrm{s} - \frac{1}{i_d}\,\mathrm{d}\hat{\Psi}_\mathrm{m} + \frac{1}{\omega_e\, i_d}\,\mathrm{d}u_q\,. \tag{3.35}$$

Analogously, the sensitivity equation of $\hat{L}_q$ can be derived from (3.33) as

$$\mathrm{d}\hat{L}_q = \frac{i_d}{\omega_e\, i_q}\,\mathrm{d}\hat{R}_\mathrm{s} - \frac{1}{\omega_e\, i_q}\,\mathrm{d}u_d\,. \tag{3.36}$$

The inductances L_d and L_q can be affected by the estimation error of $\hat{R}_s$. L_d is moreover affected by the estimation of Ψ_m and the accuracy of the compensation, while L_q is influenced

by the accuracy of the compensation. For the conventional FOC of SPMSM, a $i_d = 0$ control is deployed. The amplitude of the injected current is also small. Thus, the term related to the estimation results of the permanent magnet flux linkage Ψ_m in (3.35) may have significant impact on the estimation of L_d. Similar to that, the impact of the estimation of R_s as well as the compensation of the distorted voltage becomes more significant as the i_d approaches $0\,\mathrm{A}$. On the contrary, the term related to $\hat{R}_\mathrm{s}$ in (3.36) may have relatively small impact on the estimation of L_q.

Several conclusions can be drawn from the experimental results above. Firstly, because of the deployed machine model for the estimation, the square-wave current injection provides more stable and accurate results at the steady operation of the PMSM. The sinusoidal current injection method is more severely disturbed by the measurement noise as well as the voltage distortion. The results from the square-wave current injection method can be regarded as a filtered results of the sinusoidal current injection method, if the injected currents have a comparable amplitude and frequency. Furthermore, it can be observed from the experimental results that the L_d is not really affected by the distorted voltage, which contradicts the analysis above that the distorted voltage will also affect the estimation of L_d. However, it may be resulted from that the impact of the distorted voltage is projected onto $\hat{R}_\mathrm{s}$ and $\hat{\Psi}_\mathrm{m}$. The estimated parameter values show difference to the nominal parameter values, which can be explained by that the measurement of the speed and the currents may contain noises and bias. Especially the noises, as demonstrated in Section 2.4, may appear coloured in real applications and therefore affect the estimation results. Moreover, even though the injected current has small amplitudes, it can still affect the actual inductance values, since the inductance is sensitive to the current value, as shown in Section 3.3.2. Besides, it can be noted that the influence from the VSI nonlinear effect is significant. The compensation of the VSI nonlinearities effectively improves the accuracy of the estimation results.

3.5 Online Parameter Estimation

It has been presented previously that the current injection methods can solve the rank deficient problem of the parameter identification for PMSM. However, the current injection, both the square-wave current injection and the sinusoidal-wave current injection, will cause the pulsation in the current loop as well as in the speed control loop. Furthermore, in many applications only the parameters of interest are required for the estimation. Therefore, the online parameter estimation methods are proposed and deployed for online estimating the parameters. They are based on the current dynamics and require no persistent excitement. As analyzed at the beginning of this chapter, up to two electrical parameters can be identified simultaneously, if no persistent excitement is applied. The two parameters can be chosen arbitrarily. However, the conditions for the feasibility need to be satisfied, which are studied in Section 3.2.

The following works are regarded as classifiers for the most used online estimators. Recursive least squares (RLS) is one of the most popular online parameter estimators and has been widely applied because of its simpleness for implementation and the low computational cost. RLS is designed to minimize the weighted linear least square function. As it is indicated in [109], the main drawbacks of RLS are the slow tracking capability and the high prediction error. In [110], a RLS-based online parameter identification method was proposed to improve

the performance of sensorless control of PMSMs. However, the identified parameters differ from the actual values, which may result from the fact that the nonlinearities in PMSM are excluded. Reference [111] applied RLS as an online resistance estimator and employed the offline identified q-axis inductance, in order to improve the accuracy of the position estimation of the interior PMSM at low speed. Model reference adaptive system (MRAS) is also one of the attractive methods for the online estimation problem. In MRAS, the ideal system model is deployed as the adjustable model, where the identified parameters from an adaptive mechanism are fed back to the adjustable model. The adaptive mechanism is so designed that the error between the most recent measurement and the output of the adjustable model is eliminated. Owing to the straightforward implementation and the low computational burden, MRAS is widely applied for the sensorless control of machines, which can be regarded as a variant of the online parameter estimation problem. Reference [112] utilized an improved MRAS for sensorless control of induction motor drives. Authors in [113] implemented MRAS for sensorless control of PMSM and deployed an extended Kalman filter to eliminate the effect from the variation of the permanent magnet flux linkage. Reference [114] applied a novel MRAS approach for the identification of inductances in PMSMs. [115] proposed a MRAS-based estimator to simultaneously estimate the stator resistance and the speed of an induction motor. Thanks to the increasing computational power of the embedded control hardware, more complex algorithms, such as methods from the Kalman-filter family and the moving horizon estimator (MHE), have gained more attentions for the online parameter estimation problem. Extended Kalman filter (EKF) is an extension of the Kalman filter to the nonlinear systems, which linearises the nonlinear propagation function at the current step to predict the system states as well as the covariance and applies the newest measurement to correct the predictions. It has been deployed in many domains. Reference [116] applied EKF to identify the rotor flux linkage of the PMSM in real time. Authors in [117] proposed a symmetric strong tracking EKF to improve the performance of the sensorless control for induction motors. Reference [118] applied EKF for estimating the rotor speed, the rotor/stator flux and the stator currents to improve the performance of the sensorless finite-state predictive torque control. Another promising estimator belonging to the Kalman-filter family is the unscented Kalman filter (UKF), which was proposed in [119] to deal with the drawbacks of EKF, e.g. instability due to the linearisation and biased estimates [120]. Instead of linearising the nonlinear model of the system, UKF uses a set of deterministic samples to approximate the nonlinearity of the system, which can better capture the true mean and the real covariance than EKF [121]. Reference [122] proposed a square-root UKF for the sensorless control of induction motor drives, which aims to improve the low-speed performance and to reduce the computational errors of the UKF. Authors in [123] applied UKF for the nonlinear state estimation and concluded that the UKF is better than EKF considering both robustness and the speed of convergence. It is worth mentioning that EKF and UKF have also been used in electrical systems as a diagnosing mechanism as mentioned in [124–126]. Besides the aforementioned methods, the optimization-problem based method, MHE, has been recently widely utilized in various applications, such as the towed cable system [127], the state of charge estimation for Li-Ion batteries [128] and the sensorless control [129, 130], because of its high dynamic performance and the ability to handle constraints. MHE was firstly proposed in [131] and generally formulated in [132]. Reference [129] has concluded from simulations that MHE has superior performance than MRAS and EKF in the sensorless control application and demonstrated the real-time feasibility on an industrial digital signal processor (DSP).

Some authors moreover proposed data-driven estimators to solve the estimation problem, such as partial swarm optimization [133] and neural network [134]. They will not be discussed in this thesis.

In the following, the estimation of the parameter combination comprising the stator resistance R_s and the permanent magnet flux linkage Ψ_m is selected as an example to investigate the online estimation methods and conduct the corresponding comparisons, since the offline measurement results of them are comparably accurate. The other parameter combinations can be estimated by adjusting the system model accordingly, as long as the related identifiability matrix has full rank, as shown in Section 3.2.

3.5.1 Model Reference Adaptive System

3.5.1.1 Introduction

MRAS implemented for the parameter estimation of PMSM is firstly proposed by [135], where the stator resistance and the magnitude of the flux linkage are simultaneously estimated under the assumption of the constant stator inductance. The general concept behind MRAS is to compare the output of two models that both describe the dynamics of the same variables but in different manners. The error of the outputs is then computed and fed into the adaptive mechanism, which adjusts the model to minimize this error. The block diagram of the MRAS is shown in Fig. 3.33.

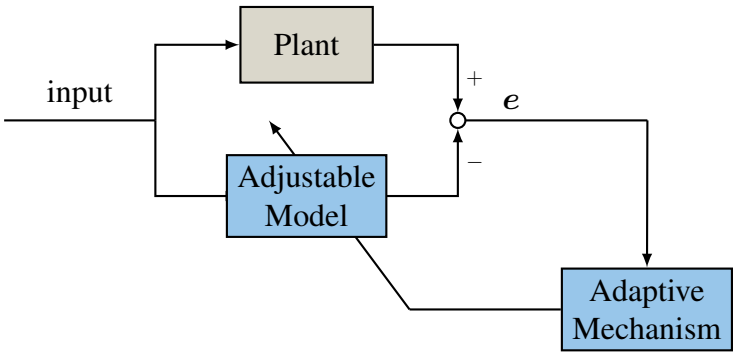

Figure 3.33: Block diagram of the model reference adaptive system.

The adaptive system is so designed that the variations in the operating conditions can be compensated with the basic structure and the explicit measurement, which can further improve the system performance. As shown in Fig. 3.33, the desired performance of the system is represented by the mathematical model of the adjustable model, while the real behaviour of the system is measured. The adjustable model is then modified if its behaviour differs from the real plant. The modification can be finished either by adjusting the parameters of the adjustable model or by generating an additional compensation signal. In the domain of the parameter estimation problem, the first solution is employed.

3.5.1.2 System Analysis

Recall the current dynamic of PMSM in the dq reference frame, which can be compactly written as

$$\frac{\mathrm{d}}{\mathrm{d}t}\boldsymbol{i} = \boldsymbol{A}\,\boldsymbol{i} + \boldsymbol{B}\,\boldsymbol{u} + \boldsymbol{E}\,, \tag{3.37}$$

where

$$\boldsymbol{A} = \begin{bmatrix} -\dfrac{R_\mathrm{s}}{L_d} & \dfrac{\omega_e\, L_q}{L_d} \\ -\dfrac{\omega_e\, L_d}{L_q} & -\dfrac{R_\mathrm{s}}{L_q} \end{bmatrix}\,, \quad \boldsymbol{B} = \begin{bmatrix} \dfrac{1}{L_d} & 0 \\ 0 & \dfrac{1}{L_q} \end{bmatrix}\,, \quad \boldsymbol{E} = \begin{bmatrix} 0 \\ -\dfrac{\Psi_\mathrm{m}\,\omega_e}{L_q} \end{bmatrix}\,. \tag{3.38}$$

The corresponding adjustable estimator can be given as

$$\frac{\mathrm{d}}{\mathrm{d}t}\hat{\boldsymbol{i}} = \hat{\boldsymbol{A}}\,\hat{\boldsymbol{i}} + \boldsymbol{B}\,\boldsymbol{u} + \hat{\boldsymbol{E}} + \boldsymbol{G}\,(\hat{\boldsymbol{i}} - \boldsymbol{i})\,, \tag{3.39}$$

where $\hat{\cdot}$ denotes the observed varaibles and $\boldsymbol{G}$ is the observer gain. $\boldsymbol{G}$ is selected in order to assign poles of the current observer at the specified locations on the complex plane [135]. An convincing gain is chosen as

$$\boldsymbol{G} = k_G \cdot \begin{bmatrix} -\dfrac{R_\mathrm{s}}{L_d} & \dfrac{\omega_e\, L_q}{L_d} \\ -\dfrac{\omega_e\, L_d}{L_q} & -\dfrac{R_\mathrm{s}}{L_q} \end{bmatrix}\,, \tag{3.40}$$

where $k_G = k - 1$ such that the poles of the closed-loop observer are k-times ($k \geq 0$) of those from the PMSM. Moreover, the error dynamic guarantees the stability of the adaptive system.

3.5.1.3 Design of Adaptive Mechanism

As aforementioned, MRAS comprises an adjustable model and an adaptive mechanism. In order to estimate R_s and Ψ_m, the adjustable model is selected as (3.39) and the reference model is given as (3.37). The corresponding error dynamic is given by subtracting (3.39) from (3.37) and can be written as

$$\begin{aligned} \frac{\mathrm{d}}{\mathrm{d}t}\boldsymbol{e} &= (\boldsymbol{A} + \boldsymbol{G})\,\boldsymbol{e} + (\boldsymbol{A} - \hat{\boldsymbol{A}})\,\hat{\boldsymbol{i}} + (\boldsymbol{E} - \hat{\boldsymbol{E}}) \\ &= (\boldsymbol{A} + \boldsymbol{G})\boldsymbol{e} + \zeta\,, \end{aligned} \tag{3.41}$$

where $\boldsymbol{e}$ denotes the error between measurements and the predicted currents. ζ is a nonlinear time-varying term and defined as $\zeta := (\boldsymbol{A} - \hat{\boldsymbol{A}})\,\hat{\boldsymbol{i}} + (\boldsymbol{E} - \hat{\boldsymbol{E}})$. Therefore, the error system consists of a linear time invariant forward term and a nonlinear feedback term [135]. In general, two main theories can be applied for the design of the adaptive mechanism, i.e. the hyperstability of a system by employing the Popov's integral inequality [136] and the Lyapunov stability theory [115, 136]. In this work, the adaptive mechanism is designed to guarantee the hyperstability. The hyperstability is guaranteed under two conditions:

- The linear time invariant forward block is strictly positive real.

- The nonlinear feedback block satisfies Popov's hyperstability criterion.

Based on these two conditions, the adaptive mechanism can be designed. The first condition is satisfied, since the diagonal element of the matrix $\boldsymbol{A}+\boldsymbol{G}$ is negative and the forward transfer matrix is strictly positive real. The Popov's hyperstability inequality is given as [137]

$$\int_0^{t_1} \boldsymbol{e}^T \zeta \,\mathrm{d}t \leq \delta^2, \;\; \forall t_1 \geq 0 \,, \tag{3.42}$$

where δ^2 denotes a finite positive constant. Furthermore, the term $\boldsymbol{e}^T\zeta$ can be expanded as

$$\boldsymbol{e}^T\zeta = \boldsymbol{e}^T \left(\begin{bmatrix} -\dfrac{R_\mathrm{s}-\hat{R}_\mathrm{s}}{L_d} & 0 \\ 0 & -\dfrac{R_\mathrm{s}-\hat{R}_\mathrm{s}}{L_q} \end{bmatrix} \hat{\boldsymbol{i}} + \begin{bmatrix} 0 \\ -\dfrac{\Psi_\mathrm{m}-\hat{\Psi}_\mathrm{m}}{L_q}\,\omega_e \end{bmatrix} \right) . \tag{3.43}$$

Furthermore, (3.43) is equivalent to the equation set as

$$\int_0^{t_1} \boldsymbol{e}^T \begin{bmatrix} -\dfrac{R_\mathrm{s}-\hat{R}_\mathrm{s}}{L_d} & 0 \\ 0 & -\dfrac{R_\mathrm{s}-\hat{R}_\mathrm{s}}{L_q} \end{bmatrix} \hat{\boldsymbol{i}} \,\mathrm{d}t \leq \delta_1^2 \,, \quad \int_0^{t_1} \boldsymbol{e}^T \begin{bmatrix} 0 \\ -\dfrac{\Psi_\mathrm{m}-\hat{\Psi}_\mathrm{m}}{L_q}\omega_e \end{bmatrix} \mathrm{d}t \leq \delta_2^2 \,, \tag{3.44}$$

where δ_1^2 and δ_2^2 are finite positive constants. As a result, the stator resistance R_s and the permanent magnet flux linkage Ψ_m are estimated by integrating the error-related functions with

$$\hat{R}_\mathrm{s} = \int_0^t \Upsilon_R(\boldsymbol{e})\,\mathrm{d}\tau + \hat{R}_\mathrm{s}(0) \,, \quad \hat{\Psi}_\mathrm{m} = \int_0^t \Upsilon_\Psi(\boldsymbol{e})\,\mathrm{d}\tau + \hat{\Psi}_\mathrm{m}(0) \,, \tag{3.45}$$

where $\Upsilon(\boldsymbol{e})$ is an adaptive function of the error $\boldsymbol{e}$. $\hat{R}_\mathrm{s}(0)$ and $\hat{\Psi}_\mathrm{m}(0)$ denote the initial guess of the estimated R_s and Ψ_m. R_s and Ψ_m can be estimated by integrating the corresponding terms given in (3.44). Furthermore, in order to improve the estimation performance, the adaptive mechanisms are designed as a PI-form estimator [135], which are shown in the following

$$\hat{R}_\mathrm{s} = -\left(k_\mathrm{PR} + \frac{k_\mathrm{IR}}{s}\right) \left(e_d \,\frac{\hat{i}_\mathrm{d}}{L_d} + e_q \,\frac{\hat{i}_q}{L_q} \right) \,, \quad \hat{\Psi}_\mathrm{m} = -\left(k_{\mathrm{P}\Psi} + \frac{k_{\mathrm{I}\Psi}}{s}\right) (e_d\,\omega_e) \,. \tag{3.46}$$

It is worth mentioning that in practice a stochastic environment is normally involved. Therefore, high gains in the adaptive loop may exacerbate the influence of the noises.

3.5.1.4 System Stability

The design of the adaptive mechanism is introduced in the former section. The stability of the closed-loop system is studied in the following. The necessary condition of a stable system in the state-space formulation is that the eigenvalues of the system matrix are stable [86]. The error dynamic is given in (3.41). The corresponding system matrix is then given as

$$\boldsymbol{A_e} = k\boldsymbol{A} \,. \tag{3.47}$$

The corresponding eigenvalues $\lambda_{1,2}$ are calculated from the equation

$$\lambda^2 + kR_\mathrm{s}(\frac{1}{L_d} + \frac{1}{L_q})\lambda + \frac{k^2{R_\mathrm{s}}^2}{L_d L_q} + k^2\omega_e^2 = 0\,. \tag{3.48}$$

After solving the (3.48), the eigenvalues are given as

$$\lambda_{1,2} = \frac{-kR_\mathrm{s}(\frac{1}{L_d} + \frac{1}{L_q}) \pm \sqrt{k^2{R_\mathrm{s}}^2(\frac{1}{L_d} + \frac{1}{L_q})^2 - 4(\frac{k^2{R_\mathrm{s}}^2}{L_d L_q} + k^2\omega_e^2)}}{2}\,. \tag{3.49}$$

One of the eigenvalues is obviously negative, the other one satisfies

$$\begin{aligned}\lambda_2 &= \frac{-k\,R_\mathrm{s}\left(\dfrac{1}{L_d} + \dfrac{1}{L_q}\right) + \sqrt{k^2\,{R_\mathrm{s}}^2\left(\frac{1}{L_d} + \dfrac{1}{L_q}\right)^2 - 4\left(\dfrac{k^2{R_\mathrm{s}}^2}{L_d L_q} + k^2\,\omega_e^2\right)}}{2} \\ &< \frac{-k\,R_\mathrm{s}\left(\dfrac{1}{L_d} + \dfrac{1}{L_q}\right) + k\,R_\mathrm{s}\left|\dfrac{1}{L_d} - \dfrac{1}{L_q}\right|}{2} < 0\,.\end{aligned} \tag{3.50}$$

Therefore, the closed-loop system is stable.

3.5.2 Recursive Least Squares

3.5.2.1 Introduction

The method of least squares (LS) was the first method of formulating an optimal estimation from noisy measurements [138]. The RLS method is developed from the LS method. The principle of them is to minimize the squared error between the measured data and their predictions. The main difference between LS and RLS algorithm is that the former one collects a sequence of measurements from the output and the input for the execution of the algorithm, contrarily the latter one executes the algorithm recursively. Therefore, the RLS method allocates less memory comparing to LS. Because of its simplicity, RLS algorithm is pertinent for the online parameter identification and has been applied to the parameter estimation problem in enormous areas. References [110, 111, 139] employed RLS as an efficient method for the parameter estimation of motors. In [140], RLS was implemented as the estimator for the Lithium-Ion batteries. Furthermore, it was utilised for the underwater robotic vehicles in [141]. The LS and RLS share the same characteristic that they compromise the convergence speed of the estimations and the filtering effect.

3.5.2.2 Principles

The LS algorithm is firstly introduced. It is set up for a system defined as

$$\boldsymbol{y} = \boldsymbol{\varphi}^T\boldsymbol{\theta} + \boldsymbol{v}\,, \tag{3.51}$$

where $\boldsymbol{y}$, $\boldsymbol{\varphi}$ and $\boldsymbol{\theta}$ denote the system output, the system matrix and the parameters to be estimated, respectively. $\boldsymbol{v}$ denotes the measurement noise. LS method proceeds for the purpose of

minimizing the objective function J over a certain time horizon $[k-N_e+1,\ k-N_e+2,\ \ldots,\ k]$, where N_e denotes the estimation horizon. The objective function J is defined by

$$J := \sum_{i=k-N_e+1}^{k} \left\| \boldsymbol{y}_i - \boldsymbol{\varphi}_i^T \hat{\boldsymbol{\theta}} \right\|^2 , \tag{3.52}$$

where the subscript i denotes the measurement and the system matrix at the time step i within the estimation horizon, i.e. $i = k - N_e + 1,\ k - N_e + 2,\ \ldots,\ k$. The estimated parameters $\hat{\boldsymbol{\theta}}$ are the minimizing arguments of J and formulated as [138]

$$\hat{\boldsymbol{\theta}} = \arg\min_{\boldsymbol{\theta}} J \ . \tag{3.53}$$

The solution of (3.53) is given according to [138] as

$$\hat{\boldsymbol{\theta}}_k = (\boldsymbol{\Phi}_k^T \boldsymbol{\Phi}_k)^{-1} \boldsymbol{\Phi}_k^T \boldsymbol{Y}_k \ , \tag{3.54}$$

where $\boldsymbol{\Phi}_k := (\boldsymbol{\varphi}_{k-N_e+1},\ \boldsymbol{\varphi}_{k-N_e+2},\ \ldots,\ \boldsymbol{\varphi}_k)^T$ and $\boldsymbol{Y}_k := (\boldsymbol{y}_{k-N_e+1}^T,\ \boldsymbol{y}_{k-N_e+2}^T,\ \ldots,\ \boldsymbol{y}_k^T)^T$. Apparently, $\boldsymbol{\Phi}_k$ and $\boldsymbol{Y}_k$ can be derived from the sequences of the last step $\boldsymbol{\Phi}_{k-1}$ and $\boldsymbol{Y}_{k-1}$ by

$$\boldsymbol{\Phi}_k = \begin{bmatrix} \boldsymbol{\Phi}_{k-1} \\ \boldsymbol{\varphi}_k^T \end{bmatrix} , \quad \boldsymbol{Y}_k = \begin{bmatrix} \boldsymbol{Y}_{k-1} \\ \boldsymbol{y}_k \end{bmatrix} . \tag{3.55}$$

By substituting (3.55) into (3.54), $\hat{\boldsymbol{\theta}}_k$ can be expressed as a function of $\hat{\boldsymbol{\theta}}_{k-1}$, which can be given as

$$\hat{\boldsymbol{\theta}}_k = \hat{\boldsymbol{\theta}}_{k-1} + (\boldsymbol{\Phi}_k^T\, \boldsymbol{\Phi}_k)^{-1} \boldsymbol{\varphi}_k \left(\boldsymbol{y}_k - \boldsymbol{\varphi}_k^T\, \hat{\boldsymbol{\theta}}_{k-1} \right) . \tag{3.56}$$

Since the inversion of matrix $\boldsymbol{\Phi}_k^T\, \boldsymbol{\Phi}_k$ has a high computational cost, the solution from $\hat{\boldsymbol{\theta}}_{k-1}$ with (3.56) has to be further simplified. Firstly, we define a new matrix as $\boldsymbol{P}_k := (\boldsymbol{\Phi}_k^T\, \boldsymbol{\Phi}_k)^{-1}$. Then $\boldsymbol{P}_k$ can be derived from $\boldsymbol{P}_{k-1}$ as

$$\boldsymbol{P}_k = (\boldsymbol{P}_{k-1}^{-1} + \boldsymbol{\varphi}_k \boldsymbol{\varphi}_k^T)^{-1} . \tag{3.57}$$

Furthermore, it can be given that

$$\boldsymbol{P}_k = \boldsymbol{P}_{k-1} - \boldsymbol{P}_{k-1}\, \boldsymbol{\varphi}_k \left(\boldsymbol{\varphi}_k^T\, \boldsymbol{P}_{k-1}\, \boldsymbol{\varphi}_k + \boldsymbol{I} \right)^{-1} \boldsymbol{\varphi}_k\, \boldsymbol{P}_{k-1} . \tag{3.58}$$

Therefore, the RLS algorithm can be written as solving the following matrices [142]

$$\begin{aligned} \hat{\boldsymbol{\theta}}_k &= \hat{\boldsymbol{\theta}}_{k-1} + \boldsymbol{K}_k \left(\boldsymbol{y}_k - \boldsymbol{\varphi}_k^T \hat{\boldsymbol{\theta}}_{k-1} \right) , \\ \boldsymbol{K}_k &= \boldsymbol{P}_{k-1} \boldsymbol{\varphi}_k \left(\boldsymbol{\varphi}_k^T \boldsymbol{P}_{k-1} \boldsymbol{\varphi}_k + \boldsymbol{I} \right)^{-1} , \\ \boldsymbol{P}_k &= (\boldsymbol{I} - \boldsymbol{K}_k \boldsymbol{\varphi}_k^T) \boldsymbol{P}_{k-1} . \end{aligned} \tag{3.59}$$

As a result of the aforementioned computation sequence, the measurements of different time steps have the same impacts on the estimation results. However, considering the variation of the

estimated parameters, the algorithm needs to be modified aiming to encompass more information from the more recent measurements, i.e. to reduce the influence from the past information. The modified RLS algorithm introduces a factor λ into the objective function J as

$$J = \sum_{i=k-N_e+1}^{k} \lambda^{k-i} \left\| \boldsymbol{y}_i - \boldsymbol{\varphi}_i^T \boldsymbol{\theta} \right\|^2 . \tag{3.60}$$

The factor λ is called the forgetting factor or the weighting factor that satisfies $0 < \lambda < 1$. Then the modified RLS algorithm can be formulated as

$$\begin{aligned} \hat{\boldsymbol{\theta}}_k &= \hat{\boldsymbol{\theta}}_{k-1} + \boldsymbol{K}_k \left(\boldsymbol{y}_k - \boldsymbol{\varphi}_k^T \hat{\boldsymbol{\theta}}_{k-1} \right) , \\ \boldsymbol{K}_k &= \boldsymbol{P}_{k-1} \boldsymbol{\varphi}_k \left(\boldsymbol{\varphi}_k^T \boldsymbol{P}_{k-1} \boldsymbol{\varphi}_k + \lambda \boldsymbol{I} \right)^{-1} , \\ \boldsymbol{P}_k &= \frac{1}{\lambda} (\boldsymbol{I} - \boldsymbol{K}_k \boldsymbol{\varphi}_k^T) \boldsymbol{P}_{k-1} . \end{aligned} \tag{3.61}$$

3.5.2.3 Reformulation of RLS for PMSM

With the introduction to the RLS algorithm, the parameter identification problem of PMSM can be formulated accordingly. However, considering different machine states, the steady-state formulation as well as the transient formulation can be both presented.

3.5.2.3.1 Steady State The formulation of RLS for PMSM at the steady state, i.e. $\frac{\mathrm{d}}{\mathrm{d}t}\boldsymbol{i} = \boldsymbol{0}$, is firstly shown, which is given in the following

$$\boldsymbol{y} = \begin{bmatrix} u_{d,\,k} + L_q\, \omega_{e,\,k}\, i_{q,\,k} \\ u_{q,\,k} - L_d\, \omega_{e,\,k}\, i_{d,\,k} \end{bmatrix}, \quad \boldsymbol{\varphi}^{\mathrm{T}} = \begin{bmatrix} i_{d,\,k} & 0 \\ i_{q,\,k} & \omega_{e,\,k} \end{bmatrix}, \quad \boldsymbol{\theta} = \begin{bmatrix} R_{\mathrm{s}} \\ \Psi_{\mathrm{m}} \end{bmatrix} .$$

3.5.2.3.2 Transient Subsequently, the matrices of RLS algorithm for the PMSM during the transient are adjusted. They are given as

$$\boldsymbol{y} = \begin{bmatrix} u_{d,\,k} + L_q\, \omega_{e,\,k}\, i_{q,\,k} - \dfrac{L_d}{T_s} \left(i_{d,\,k+1} - i_{d,\,k} \right) \\ u_{q,\,k} - L_d\, \omega_{e,\,k}\, i_{d,\,k} - \dfrac{L_q}{T_s} \left(i_{q,\,k+1} - i_{q,\,k} \right) \end{bmatrix}, \quad \boldsymbol{\varphi}^{\mathrm{T}} = \begin{bmatrix} i_{d,\,k} & 0 \\ i_{q,\,k} & \omega_{e,\,k} \end{bmatrix}, \quad \theta = \begin{bmatrix} R_{\mathrm{s}} \\ \Psi_{\mathrm{m}} \end{bmatrix} .$$

As mentioned before, the steady-state formulation is simpler and more robust at noisy conditions, which however is not valid during the transient.

3.5.3 Kalman Filter

3.5.3.1 Introduction

KF was firstly proposed in [143] and served as a method utilising the state-space formulation of a linear system to calculate the recursive solution of the linear optimal filtering problem [144].

Analogously to the RLS, the estimation via Kalman filter is derived in an optimum manner, where a cost function is defined for incorrect estimates. The cost function should satisfy two requirements, i.e. it is non-negative and is a non-decreasing function of the estimation error [144]. Kalman filter (KF) provides satisfactory solutions due to the recursive nature and the effective use of the Riccati equation. Moreover, it conducts optimization for achieving the minimum variance of the estimation error and is asymptotically stable [145]. KF has been applied to diverse areas, for example the space- and aircraft domain, the automotive industry, the chemical process industry and the communication networks. The principle of the Kalman filter is to find the optimum estimation $\hat{\boldsymbol{x}}$ of the state variable $\boldsymbol{x}$ according to the cost function J, which is defined as the mean squared error at the current time step k. However, its cost function J is more general than that of the least squares method, where the uncertainty of the initial state and the error of the model are furthermore considered. The principle of the Kalman filter is conceptually introduced in the following.

Recall the system representation in (3.1) and assume the process noise $\boldsymbol{w}_k$ as well as the measurement noise $\boldsymbol{v}_k$ to be additive, white and Gaussian, i.e.

$$E[\boldsymbol{w}_n \boldsymbol{w}_k^T] = \begin{cases} \boldsymbol{Q}_k, & \text{for } n = k \ , \\ \boldsymbol{0}, & \text{for } n \neq k \ , \end{cases} \qquad E[\boldsymbol{v}_n \boldsymbol{v}_k^T] = \begin{cases} \boldsymbol{R}_k, & \text{for } n = k \ , \\ \boldsymbol{0}, & \text{for } n \neq k \ . \end{cases} \tag{3.62}$$

The cost function at the time step k is given as

$$J_k = E[(\boldsymbol{x}_k - \hat{\boldsymbol{x}}_k)(\boldsymbol{x}_k - \hat{\boldsymbol{x}}_k)^T] \ . \tag{3.63}$$

The corresponding solution is derived from (3.63) with the following theorems [146, 147].

Theorem 3.2 (Principle of Orthogonality)
Let the stochastic processes $\boldsymbol{x}_k$ and $\boldsymbol{y}_k$ be of zero means, that is

$$E[\boldsymbol{x}_k] = E[\boldsymbol{y}_k] = \boldsymbol{0} \ , \quad \forall \ k \ .$$

Then:

- *the stochastic processes $\boldsymbol{x}_k$ and $\boldsymbol{y}_k$ are jointly Gaussian; or if the optimal estimate $\hat{\boldsymbol{x}}_k$ is restricted to be a linear function of the observables and the cost function is the mean-squared error,*
- *then the optimum estimate $\hat{\boldsymbol{x}}_k$, given the observables $\boldsymbol{y}_1, \boldsymbol{y}_2, ..., \boldsymbol{y}_k$, is the orthogonal projection of $\boldsymbol{x}_k$ on the space spanned by these observables.*

Theorem 3.3 (Conditioned Mean Estimator)
If the stochastic processes $\boldsymbol{x}_k$ and $\boldsymbol{y}_k$ are jointly Gaussian, then the optimum estimate $\hat{\boldsymbol{x}}$ that minimizes the mean-squared error J_k is the conditional mean estimator with

$$\hat{\boldsymbol{x}} = E[\boldsymbol{x}_k | \ \boldsymbol{y}_1, \boldsymbol{y}_2, ..., \boldsymbol{y}_k] \ .$$

With the aforementioned theorems, the optimal solution regarding the cost function in (3.63) is given by [146, 148, 149]

$$\hat{\boldsymbol{x}}_k = \hat{\boldsymbol{x}}_{k|k-1} + \boldsymbol{K}_k \left(\boldsymbol{y}_k - \boldsymbol{C}_k \, \hat{\boldsymbol{x}}_{k|k-1} \right) \ , \tag{3.64}$$

where $\hat{\boldsymbol{x}}_{k|k-1}$ is a priori estimate of the state, which is available by means of the system model at the time step k. $\boldsymbol{K}_k$ is the so called Kalman gain and can be formulated as

$$\boldsymbol{K}_k = \boldsymbol{P}_k \, \boldsymbol{C}_k^T \, [\boldsymbol{R}_k + \boldsymbol{C}_k \, \boldsymbol{P}_k \, \boldsymbol{C}_k^T]^{-1} \, , \tag{3.65}$$

where

$$\boldsymbol{P}_{k+1} = \boldsymbol{A}_k \, \boldsymbol{P}_k \, \boldsymbol{A}_k^T + \boldsymbol{Q}_k - \boldsymbol{K}_k \, \boldsymbol{C}_k \, \boldsymbol{P}_k \, \boldsymbol{A}_k^T \, . \tag{3.66}$$

It can be observed from (3.65) and (3.66) that the computation of $\boldsymbol{K}_k$ and $\boldsymbol{P}_k$ depends solely on the matrices $\boldsymbol{A}$, $\boldsymbol{C}$ and noise covariance matrices $\boldsymbol{R}$, $\boldsymbol{Q}$. Therefore, $\boldsymbol{K}$ and $\boldsymbol{P}$ can be calculated offline, if the noise covariance matrices $\boldsymbol{R}$, $\boldsymbol{Q}$ can be regarded as constant. For a linear time-invariant (LTI) system, the covariance $\boldsymbol{P}$ converges to a steady-state value, i.e. $\boldsymbol{P}_k = \boldsymbol{P}_{k+1}$. Substitute (3.65) into (3.66) with a defined steady-state value $\boldsymbol{P}$ for $\boldsymbol{P}_k$, we can have the so-called discrete algebraic Riccati equation as

$$\boldsymbol{P} = \boldsymbol{A} \, \boldsymbol{P} \, \boldsymbol{A}^T - \boldsymbol{A} \, \boldsymbol{P} \, \boldsymbol{C}^T [\boldsymbol{R} + \boldsymbol{C} \, \boldsymbol{P} \, \boldsymbol{C}^T]^{-1} \, \boldsymbol{C} \, \boldsymbol{P} \, \boldsymbol{A}^T + \boldsymbol{Q} \, . \tag{3.67}$$

The conditions for uniqueness of the discrete algebraic Riccati equation in (3.67) are [150]:

- $\boldsymbol{A}$ is stable,
- $(\boldsymbol{A}, \, \boldsymbol{C})$ is observable,
- $\boldsymbol{R}$ and $\boldsymbol{Q}$ are positive definite matrices.

As it is indicated in [151] that the Kalman filter shares similarities with the RLS, i.e. $\boldsymbol{x}_{k+1} = \boldsymbol{\theta}_{k+1} = \boldsymbol{\theta}_k$ and $\boldsymbol{y} = \boldsymbol{\varphi}^T \boldsymbol{\theta} + \boldsymbol{v}$. However, the Kalman filter shows advantage over RLS considering that the parameter changes can be easily incorporated and interpreted as the covariance matrix with the Kalman filter.

3.5.3.2 State Augmentation

In general, there are two groups of methods addressing the Kalman filtering with model uncertainties, i. e. the robust Kalman filtering and the adaptive Kalman filtering. The robust Kalman filtering is so designed that a range of model parameters are taken into account. The Kalman gain is computed to minimize the bound on the trace of the state error covariance instead of the trace [152]. The adaptive Kalman filtering can be realized by the bootstrap method as well as the augmentation method. The bootstrap method firstly estimates the parameters based on the nominal values and the estimated parameter from the previous step is applied for estimating the states with the stochastic approximation [153]. The augmentation method combines the to be estimated parameters and the system states as the augmented system vector and derives the estimation for the augmented system based on the measurements [154]. The augmented system is normally nonlinear, even though the nominal system is a linear system. The nonlinear filtering techniques, such as the extended Kalman filter, the unscented Kalman filter and the particle filter, can be applied for such a nonlinear system and simultaneously estimate the states, parameters. Many works have studied the problem of estimating the parameters and the states by augmenting the system state vector, e.g. [80, 155–157], to name but a few. In this thesis, the state augmentation method is deployed. The intuition of the state augmentation is to include

the to be estimated parameters into the state vector. The augmented state vector is denoted by a new state vector $\boldsymbol{z}$, which is given as

$$\boldsymbol{z} = \begin{bmatrix} \boldsymbol{x} \\ \boldsymbol{p} \end{bmatrix} . \tag{3.68}$$

The to be estimated parameters are modelled as stochastic variables with

$$\frac{\mathrm{d}}{\mathrm{d}t}\boldsymbol{p} = \boldsymbol{v}_p , \tag{3.69}$$

where $\boldsymbol{v}_p$ is the zero mean Gaussian noise with a covariance defined as $\boldsymbol{Q}_p$. The system process noise covariance matrix is accordingly augmented as

$$\boldsymbol{Q}_z = \begin{bmatrix} \boldsymbol{Q} & \boldsymbol{0} \\ \boldsymbol{0} & \boldsymbol{Q}_p \end{bmatrix} . \tag{3.70}$$

It is worth mentioning that the augmented system is normally nonlinear, even though the original system is linear, since the to be estimated parameters may be coupled with the system states $\boldsymbol{x}$.

3.5.3.3 Extended Kalman Filter

Since the most systems in practice are nonlinear, the Kalman filter has been further developed to adapt to the nonlinearity. Given the nonlinear system dynamics and the measurement data, the EKF is used to compute the minimum variance estimate of the system state $\boldsymbol{x}$. The principle of the extended Kalman filter is to linearise the nonlinear equations by using the Taylor series expansion around the Kalman filter estimates and conducting the Kalman filter estimates based on the linearised system. Because of its capability to handle the system nonlinearity and the acceptable computational cost, EKF has been used as the standard technique for the recursive nonlinear estimations [144], in works such as [158–160].

EKF extends the Kalman filter through the linearisation around the most recent estimations of the nonlinear dynamical system. It is moreover assumed that the process noise and the measurement noise are mutually uncorrelated. Consider the nonlinear system in the discrete-time domain represented in a general formulation as follows

$$\begin{aligned} \boldsymbol{x}_{k+1} &= F(\boldsymbol{x}_k, \boldsymbol{u}_k) + \boldsymbol{w}_k , \\ \boldsymbol{y}_k &= H(\boldsymbol{x}_k) + \boldsymbol{v}_k , \end{aligned} \tag{3.71}$$

where $\boldsymbol{w}_k$ and $\boldsymbol{v}_k$ are zero mean white Gaussian noises with covariance $\boldsymbol{Q}$ and $\boldsymbol{R}$, respectively. By deploying EKF, the original system stated in (3.71) is then approximated with a first-order Taylor approximation by

$$\begin{aligned} F(\boldsymbol{x}_k, \boldsymbol{u}_k) &\approx F(\boldsymbol{x}_{k-1}, \boldsymbol{u}_{k-1}) + (\boldsymbol{x}_k - \boldsymbol{x}_{k-1})\boldsymbol{F}(\boldsymbol{x}_{k-1}) , \\ H(\boldsymbol{x}_k) &\approx H(\boldsymbol{x}_{k-1}) + (\boldsymbol{x}_k - \boldsymbol{x}_{k-1})\boldsymbol{H}(\boldsymbol{x}_{k-1}) , \end{aligned} \tag{3.72}$$

where $\boldsymbol{F} := \nabla_{\boldsymbol{x}_{k-1}} F$ and $\boldsymbol{H} := \nabla_{\boldsymbol{x}_{k-1}} H$. The calculation $\nabla_{\boldsymbol{x}} f$ denotes the Jacobian of the function f with respect to $\boldsymbol{x}$.

The recursive computation of the EKF is in general same as that of the linear Kalman filter and consists of two steps, i.e. the prediction and the update. The prediction conducts a propagation by using the linear approximation of the nonlinear system. In the update procedure of the EKF, the predictions are corrected based on the most recent measurement. However, for the linear Kalman filter, the matrix $\boldsymbol{P}$ is equivalent to the covariance of the estimation error, which is not valid for the extended Kalman filter, since only the first-order terms are included during the linearisation. Therefore, $\boldsymbol{P}$ is approximately equal to the covariance of the estimation error, if the errors caused by the linearisation are relatively small. Moreover, the state error covariance and the Kalman gain are computed as a closed form in the linear Kalman filter, which can not be realized with EKF. The explicit description of the EKF algorithm is shown below in Algorithm 3.1. The state transition function $\boldsymbol{F}_{k-1}$ is the Jacobian matrix of $F(\hat{\boldsymbol{x}}_{k-1|k-1}, \boldsymbol{u}_{k-1})$ over

Algorithm 3.1 Extended Kalman Filter

Input: $\hat{\boldsymbol{x}}_{k-1}$, $\boldsymbol{P}_{k-1}$, $\boldsymbol{u}_{k-1}$, $\boldsymbol{y}_k$
Output: $\hat{\boldsymbol{x}}_k$, $\boldsymbol{P}_k$

Initialization:

$$\hat{\boldsymbol{x}}_0 = E[\boldsymbol{x}_0] \,,$$
$$\boldsymbol{P}_0 = E[(\boldsymbol{x}_0 - \hat{\boldsymbol{x}}_0)(\boldsymbol{x}_0 - \hat{\boldsymbol{x}}_0)^T] \,,$$

Prediction:

$$\hat{\boldsymbol{x}}_{k|k-1} = F(\hat{\boldsymbol{x}}_{k-1|k-1},\, \boldsymbol{u}_{k-1}) \,,$$
$$\boldsymbol{P}_{k|k-1} = \boldsymbol{F}_{k-1}\boldsymbol{P}_{k-1|k-1}\boldsymbol{F}_{k-1}^T + \boldsymbol{Q}_{k-1} \,,$$

Update:

$$\tilde{\boldsymbol{y}}_k = \boldsymbol{y}_k - h(\hat{\boldsymbol{x}}_{k|k-1}) \,,$$
$$\boldsymbol{S}_k = \boldsymbol{H}_k\, \boldsymbol{P}_{k|k-1}\, \boldsymbol{H}_k^T + \boldsymbol{R}_k \,,$$
$$\boldsymbol{K}_k = \boldsymbol{P}_{k|k-1}\, \boldsymbol{H}_k^T\, \boldsymbol{S}_k^{-1} \,,$$
$$\hat{\boldsymbol{x}}_{k|k} = \hat{\boldsymbol{x}}_{k|k-1} + \boldsymbol{K}_k\, \tilde{\boldsymbol{y}}_k \,,$$
$$\boldsymbol{P}_{k|k} = (\boldsymbol{I} - \boldsymbol{K}_k\, \boldsymbol{H}_k)\, \boldsymbol{P}_{k|k-1} \,.$$

$\hat{\boldsymbol{x}}_{k-1|k-1}$, which is then written as

$$\boldsymbol{F}_{k-1} = \nabla_{\hat{\boldsymbol{x}}} F(\hat{\boldsymbol{x}}_{k-1|k-1}, \boldsymbol{u}_{k-1}) \,. \tag{3.73}$$

Analogously, $\boldsymbol{H}_k$ is defined as

$$\boldsymbol{H}_k = \nabla_{\hat{\boldsymbol{x}}} H(\hat{\boldsymbol{x}}_{k|k-1}) \,. \tag{3.74}$$

However, according to [161], EKF has several drawbacks in spite of its simplicity:

- Instability due to the linearisation around operating points and erroneous parameters.
- Expensive computation of the Jacobian matrices.
- Biased estimates.
- Difficulty of proper selection of the model covariance.

As it is indicated in [144], the EKF-based parameter estimation may lead to satisfying results, but is not robust to large uncertainties in initial parameter estimate and the error covariance matrix if the to be estimated parameter vector has a large dimension. Moreover, the estimation results depend on the initial estimation error covariance matrix and the initial value of the to be estimated parameters.

3.5.3.4 Unscented Kalman Filter

Since EKF contains only the first order information of the Taylor series expansions, the estimations of EKF for highly nonlinear system may converge to erroneous values or even cause instability. Furthermore, the derivation of the Jacobian matrix is nontrivial in many applications. Therefore, estimators such as the UKF and the ensemble KF containing higher order information of Taylor series are proposed. We will just talk about the unscented Kalman filter in this thesis. UKF was firstly proposed in [162], in which it is furthermore compared with the extended Kalman filter for a navigation application and has shown better results than EKF. Further studies, such as [163–165], presented a better performance of UKF over EKF in various applications. The main superiority of UKF over EKF is that UKF has no linearisation procedure for computing the covariance and the estimations. Instead of applying linearisation for the nonlinear function, UKF uses a deterministic sampling approach and propagates through the original nonlinear system. Therefore, UKF can deliver more accurate results than EKF. Moreover, no explicit Jacobian or Hessian calculations are required for the UKF. It is worth mentioning that the computational burden of the UKF is of the same order as the EKF.

The unscented Kalman filter is developed based on the so-called unscented transformation (UT), which is a method for calculating the statics of a small set of specially selected samples through a nonlinear transformation [163]. UT utilizes the instinct that the approximation of a probability distribution is much easier than that of the propagation for a nonlinear system [166]. Let us assume that the mean and the covariance of the system state $\boldsymbol{x}$ are $\bar{\boldsymbol{x}}$ and $\boldsymbol{P_x}$, respectively. UT forms a matrix $\boldsymbol{\mathcal{X}}$ consisting of $2N_x+1$ sigma vectors $\mathcal{X}_i$ with predefined weights W_i , where N_x denotes the dimension of the state vector. They are computed through

$$
\begin{aligned}
\mathcal{X}_0 = &\quad \bar{\boldsymbol{x}} \ , \\
\mathcal{X}_i = &\quad \begin{cases} \bar{\boldsymbol{x}} + (\sqrt{N_x+\lambda}\ \boldsymbol{P}_x^{\frac{1}{2}})_i \ , & i = 1,2,...,N_x \ , \\ \bar{\boldsymbol{x}} - (\sqrt{N_x+\lambda}\ \boldsymbol{P}_x^{\frac{1}{2}})_{i-N_x} \ , & i = N_x+1, N_x+2, ..., 2N_x \ , \end{cases} \\
W_0^m = &\quad \frac{\lambda}{\lambda + N_x} \ , \\
W_0^c = &\quad \frac{\lambda}{\lambda + N_x} + (1 - \alpha^2 + \beta) \ , \\
W_i^m = &\quad W_i^c = \frac{1}{2(N_x+\lambda)}, \quad i = 1,2,...,2N_x \ ,
\end{aligned}
\tag{3.75}
$$

where $\lambda := \alpha^2(N_x + \kappa) - N_x$ is a scaling parameter. The coefficient α determines the spread of the sigma points around the mean value and is commonly set to a small positive value. The coefficient κ is also a scaling parameter, which provides one more degree of freedom to tune the higher order moments of the approximation [163]. Furthermore, κ has the function of reducing the overall prediction errors. β is the parameter incorporating the prior knowledge of the

distribution of $\boldsymbol{x}$. As given in [121], β has the optimal value $\beta = 2$ for Gaussian distributions. $(\sqrt{N_x + \lambda}\ \boldsymbol{P}_x^{\frac{1}{2}})_i$ is the i-th row of the matrix square root. The sigma points are propagated through the output function and construct a new output vector $\mathcal{Y}_i$ by

$$\mathcal{Y}_i = H(\mathcal{X}_i), \quad i = 0,\ 1,\ ...,\ 2N_x\ . \tag{3.76}$$

Furthermore, the mean and the covariance of the output $\boldsymbol{y}$ are approximated with a weighted sample mean and covariance. The mean is computed with the weighted average of the transformed points. Numerically efficient and stable methods, such as Cholesky decomposition, can be used for the square root computation. The covariance is the weighted outer product of the transformed points. The mean and the covariance of the new output vector are given as

$$\bar{\boldsymbol{y}} = \sum_{i=0}^{2N_x} W_i^m \mathcal{Y}_i\ , \quad \boldsymbol{P_{yy}} = \sum_{i=0}^{2N_x} W_i^c (\mathcal{Y}_i - \bar{\boldsymbol{y}})(\mathcal{Y}_i - \bar{\boldsymbol{y}})^T\ . \tag{3.77}$$

Analogously to the extended Kalman filter, the algorithm of UKF consists of two main parts, i.e. the prediction and the correction. The explicit description of the algorithm is given in Algorithm 3.2.

3.5.4 Moving Horizon Estimator

3.5.4.1 Introduction

The moving horizon estimator was firstly presented in [167] as the limited memory filter. However, the exact recursive solutions for a general nonlinear system are intractable in the real-time application, since the problem becomes infinite [168]. Therefore, approximations are required for the nonlinear filters. Authors in [169] proposed a nonlinear unconstrained MHE in 1986. The study in [170] extended this work and provided a systematic formulation of an optimization problem to estimate the system states and the parameters of a nonlinear system. The optimization problem is formulated with the past N_e measurements and aims to minimize the error between the predicted system dynamics and the real measurements. The estimation horizon N_e provides also a compromise between the computational burden and the estimation accuracy. However, as author in [171] has mentioned, the moving horizon estimator is equivalent to the extended Kalman filter as long as solely the most recent measurement is used. The stability problem of MHE has also been intensively investigated, e.g. in [172, 173] for the linear system, in [174, 175] for the nonlinear system and in [176] for the hybrid system.

A general formulation of the MHE optimization problem at the time instant $k = n + N_e - 1$ is given in the following [171]

$$\begin{aligned}
\min_{\boldsymbol{x},\boldsymbol{z},\boldsymbol{p},\boldsymbol{w}} \quad & J_a^k(\boldsymbol{x}_n,\ \boldsymbol{p}_n) + \sum_{j=n}^{k} \|\boldsymbol{y}_j - H(\boldsymbol{x}_j, \boldsymbol{z}_j, \boldsymbol{p}_j)\|_{\boldsymbol{V}_j}^2 + \sum_{j=n}^{k-1} \|\boldsymbol{w}_j\|_{\boldsymbol{W}_j}^2 \\
\text{s. t.} \quad & \boldsymbol{x}_{j+1} = F(\boldsymbol{x}_j, \boldsymbol{z}_j, \boldsymbol{p}_j, \boldsymbol{u}_j) + \boldsymbol{w}_j\ , \\
& \boldsymbol{g}(\boldsymbol{x}_j, \boldsymbol{z}_j, \boldsymbol{p}_j, \boldsymbol{u}_j) = 0\ , \\
& \boldsymbol{x}_j \in \mathbb{X}_j\ , \quad \boldsymbol{z}_j \in \mathbb{Z}_j\ , \quad \boldsymbol{w}_j \in \mathbb{W}_j\ , \quad \boldsymbol{p}_j \in \mathbb{P}\ ,
\end{aligned} \tag{3.78}$$

Algorithm 3.2 Unscented Kalman Filter

Input: $\hat{\boldsymbol{x}}_{k-1}$, $\boldsymbol{P}_{k-1}$, $\boldsymbol{u}_{k-1}$, $\boldsymbol{y}_k$
Output: $\hat{\boldsymbol{x}}_k$, $\boldsymbol{P}_k$

Initialization:

$$\hat{\boldsymbol{x}}_0 = E[\boldsymbol{x}_0] \,,$$
$$\boldsymbol{P}_{x,\,0} = E[(\boldsymbol{x}_0 - \hat{\boldsymbol{x}}_0)(\boldsymbol{x}_0 - \hat{\boldsymbol{x}}_0)^T] \,.$$

Prediction:

$$\boldsymbol{\mathcal{X}}_{k|k-1} = F(\boldsymbol{\mathcal{X}}_{k-1},\ \boldsymbol{u}_{k-1}) \,,$$
$$\hat{\boldsymbol{x}}_{k|k-1} = \sum_{i=0}^{2N_x} W_i^m \, \mathcal{X}_{i,\,k|k-1} \,,$$
$$\boldsymbol{P}_{x,\,k|k-1} = \sum_{i=0}^{2N_x} W_i^c \, (\mathcal{X}_{i,\,k|k-1} - \hat{\boldsymbol{x}}_{k|k-1})(\mathcal{X}_{i,\,k|k-1} - \hat{\boldsymbol{x}}_{k|k-1})^T + \boldsymbol{Q} \,,$$
$$\boldsymbol{\mathcal{Y}}_{k|k-1} = H(\boldsymbol{\mathcal{X}}_{k|k-1}) \,,$$
$$\hat{\boldsymbol{y}}_{k|k-1} = \sum_{i=0}^{2N_x} W_i^m \mathcal{Y}_{i,\,k|k-1} \,.$$

Correction:

$$\boldsymbol{P}_{\boldsymbol{y}_k\boldsymbol{y}_k} = \sum_{i=0}^{2N_x} W_i^c [\mathcal{Y}_{i,\,k|k-1} - \hat{\boldsymbol{y}}_{k|k-1}][\mathcal{Y}_{i,\,k|k-1} - \hat{\boldsymbol{y}}_{k|k-1}]^T + \boldsymbol{R} \,,$$
$$\boldsymbol{P}_{\boldsymbol{x}_k\boldsymbol{y}_k} = \sum_{i=0}^{2N_x} W_i^c [\mathcal{X}_{i,\,k|k-1} - \hat{\boldsymbol{x}}_{k|k-1}][\mathcal{Y}_{i,\,k|k-1} - \hat{\boldsymbol{y}}_{k|k-1}]^T \,,$$
$$\boldsymbol{K}_k = \boldsymbol{P}_{\boldsymbol{x}_k\boldsymbol{y}_k} \boldsymbol{P}_{\boldsymbol{y}_k\boldsymbol{y}_k}^{-1} \,,$$
$$\hat{\boldsymbol{x}}_{k|k} = \hat{\boldsymbol{x}}_{k|k-1} + \boldsymbol{K}_k(\boldsymbol{y}_k - \hat{\boldsymbol{y}}_{k|k-1}) \,,$$
$$\boldsymbol{P}_{x,\,k} = \boldsymbol{P}_{x,\,k|k-1} - \boldsymbol{K}_k \boldsymbol{P}_{\boldsymbol{y}_k\boldsymbol{y}_k} \boldsymbol{K}_k^T \,.$$

where N_e is the estimation horizon, $\boldsymbol{x}$ is the state vector, $\boldsymbol{z}$ is the algebraic state vector, $\boldsymbol{p}$ is the parameter vector. $\mathbb{X}$, $\mathbb{Z}$, $\mathbb{P}$ and $\mathbb{W}$ are constraints on the individual vector. $\|\delta\|_{\boldsymbol{V}}^2$ denotes the squared weighted euclidean norms with the positive definite weighting matrix $\boldsymbol{V}$ and is computed by $\delta^T \boldsymbol{V}^T \boldsymbol{V} \delta$. Weighting matrices $\boldsymbol{V}_j$ and $\boldsymbol{W}_j$ are the square root of $\boldsymbol{R}^{-1}$ and $\boldsymbol{Q}^{-1}$, respectively. They specify the relative contribution of each term in the cost function. For some applications, instead of the ℓ_2 norm, the ℓ_1 norm or the Huber penalty function is employed to improve the robustness of the estimation problem, if outliers and parameter jumps are expected. On the one hand, the constraints is originated from the specific definitions of the variables. On the other hand, the physical as well as the practical limitations can also contribute to the constraints. Particularly, the constraints may increase the estimation performance by excluding the non-physical optima in the nonlinear optimization problem, which is normally non-convex and has several local optima [177]. Moreover, the constraints can also simplify the model. In Fig. 3.34, the principle of the MHE is illustrated, where the estimation is carried out over the estimation window with a finite length and formulated as an optimization problem penalizing

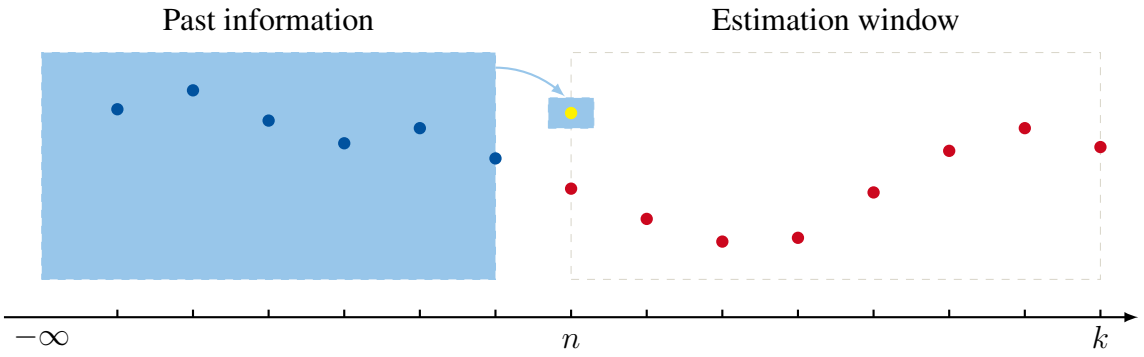

Figure 3.34: Demonstration of the principle of the moving horizon estimation method.

the measurement disturbance and the process disturbance. An additional arrival cost is also included to summarize the accumulated past information, which is denoted by the yellow point in the Fig. 3.34. The underlying optimization problem is solved afterwards with efficient solving methods. Subsequently, the estimation window is shifted at next time step. Meanwhile, the arrival cost is updated. The arrival cost $J_a^k(\boldsymbol{x}_n,\, \boldsymbol{p}_n)$ represent the accumulated past knowledge, which is exactly computed via

$$J_a^k(\boldsymbol{x}_n,\, \boldsymbol{p}_n) = \min_{\boldsymbol{x},\, \boldsymbol{w}} \sum_{j=-\infty}^{n} \|\boldsymbol{y}_j - H(\boldsymbol{x}_j,\, \boldsymbol{z}_j,\, \boldsymbol{p}_j)\|^2_{\boldsymbol{V}_j} + \sum_{j=-\infty}^{n-1} \|\boldsymbol{w}_j\|^2_{\boldsymbol{W}_j} \,. \tag{3.79}$$

The arrival cost J_a^k is essential for the MHE, since it provides the possibility to summarize the past information and transform an unbounded estimation problem into a fixed-size problem. Moreover, the arrival cost strongly affects the stability of MHE [171]. However, the exact computation of arrival cost is intractable. Therefore, a proper choice of the arrival cost approximation is essential for the computational efficiency.

It can be concluded from the formulation in (3.78), MHE is a typical constrained NLP, which can be generally formulated as

$$\begin{aligned} \min_{\boldsymbol{x}} \quad & J(\boldsymbol{x}) \\ \text{s. t.} \quad & \boldsymbol{g}(\boldsymbol{x}) = 0 \,, \\ & \boldsymbol{h}(\boldsymbol{x}) \leq 0 \,. \end{aligned} \tag{3.80}$$

A Lagrangian function is an essential tool to solve a optimization problem with constraints, which provides an equivalent statement of the stationary points from the original optimization problem (3.80) [178], as shown in Section 2.3. It can be given by [179]

$$\mathcal{L}(\boldsymbol{x},\, \boldsymbol{\lambda}_{\boldsymbol{g}},\, \boldsymbol{\lambda}_{\boldsymbol{h}}) = J(\boldsymbol{x}) + \boldsymbol{\lambda}_{\boldsymbol{g}}\, \boldsymbol{g}(\boldsymbol{x}) + \boldsymbol{\lambda}_{\boldsymbol{h}}\, \boldsymbol{h}(\boldsymbol{x}) \,, \tag{3.81}$$

where $\boldsymbol{\lambda}_{\boldsymbol{g}}$ and $\boldsymbol{\lambda}_{\boldsymbol{h}}$ are the Lagrange multipliers. Since the application discussed in this thesis includes only the equalities as constraints, we focus on a special case of NLP, the so-called equality constrained nonlinear programming (ENLP).

3.5.4.2 Solving Methods

The general MHE problem is presented in (3.78), which is an optimization-based estimation problem, more specifically a constrained NLP problem, and strongly depends on the underlying numerical solving schemes. As it is stated in the former chapter, a MHE problem can be solved with SQP methods. In this section, a brief introduction to the SQP is given firstly. Then, the real-time iteration method, which has a relatively low computational cost, is explained to solve the MHE problem in real time. Furthermore, an efficient method is shown to approximately update the arrival cost.

The variants of SQP are introduced in the following, namely the exact Hessian variant, the Newton-Lagrange method and the Quasi-Newton method. Moreover, a special case of Quasi-Newton method called constrained Gauss-Newton method is also presented here, which is suitable for the ENLP problem.

3.5.4.2.1 Exact Hessian Variant Exact Hessian variant denotes the method calculating the Hessian matrix of the Lagrangian function (3.81), which is represented by $\nabla^2_{\boldsymbol{x}}\mathcal{L}$. The cost function is approximated up to second order Taylor series at the current iterate $(\boldsymbol{x}_k,\, \boldsymbol{\lambda}_{\boldsymbol{g},\,k},\, \boldsymbol{\lambda}_{\boldsymbol{h},\,k})$ and given as [32]

$$J(\boldsymbol{x}) \approx \nabla_{\boldsymbol{x}} J(\boldsymbol{x}_k)^T \boldsymbol{x} + \frac{1}{2}(\boldsymbol{x}-\boldsymbol{x}_k)^T\, \nabla^2_{\boldsymbol{x}}\mathcal{L}(\boldsymbol{x}_k,\, \boldsymbol{\lambda}_{\boldsymbol{g},\,k},\, \boldsymbol{\lambda}_{\boldsymbol{h},\,k})\, (\boldsymbol{x}-\boldsymbol{x}_k)\ . \tag{3.82}$$

Moreover, the constraints are also linearised with the first order Taylor series around the current iterate as

$$\begin{aligned} \boldsymbol{g}(\boldsymbol{x}) &\approx \boldsymbol{g}(\boldsymbol{x}_k) + \nabla_{\boldsymbol{x}}\boldsymbol{g}(\boldsymbol{x}_k)(\boldsymbol{x}-\boldsymbol{x}_k)\ , \\ \boldsymbol{h}(\boldsymbol{x}) &\approx \boldsymbol{h}(\boldsymbol{x}_k) + \nabla_{\boldsymbol{x}}\boldsymbol{h}(\boldsymbol{x}_k)(\boldsymbol{x}-\boldsymbol{x}_k)\ . \end{aligned} \tag{3.83}$$

As a result, all nonlinear functions in (3.80) are linearised and can be interpreted as KKT conditions of a QP [32]

$$\begin{aligned} \min_{\boldsymbol{x}} \quad & \nabla_{\boldsymbol{x}} J(\boldsymbol{x}_k)^T \boldsymbol{x} + \frac{1}{2}(\boldsymbol{x}-\boldsymbol{x}_k)^T\, \nabla^2_{\boldsymbol{x}}\mathcal{L}(\boldsymbol{x}_k,\, \boldsymbol{\lambda}_{\boldsymbol{g},\,k},\, \boldsymbol{\lambda}_{\boldsymbol{h},\,k})\, (\boldsymbol{x}-\boldsymbol{x}_k) \\ \text{s. t.} \quad & \boldsymbol{g}(\boldsymbol{x}_k) + \nabla_{\boldsymbol{x}}\boldsymbol{g}(\boldsymbol{x}_k)(\boldsymbol{x}-\boldsymbol{x}_k) = 0\ , \\ & \boldsymbol{h}(\boldsymbol{x}_k) + \nabla_{\boldsymbol{x}}\boldsymbol{h}(\boldsymbol{x}_k)(\boldsymbol{x}-\boldsymbol{x}_k) \leq 0\ . \end{aligned} \tag{3.84}$$

By solving the QP in (3.84), we can get the next iterate $(\boldsymbol{x}_{k+1},\, \boldsymbol{\lambda}_{\boldsymbol{g},\,k+1},\, \boldsymbol{\lambda}_{\boldsymbol{h},\,k+1})$, where $\boldsymbol{x}_{k+1} = \boldsymbol{x}_k + \Delta\boldsymbol{x}_k$. This method is expedient for a system, if the computation of its Hessian matrices is cheap [180]. However, the Hessian matrices tend to be approximated with the inexact Hessian or the Jacobian matrices, since the calculation of the Hessian matrices can be problematic.

3.5.4.2.2 Newton-Lagrange Method Newton-Lagrange method is normally applied for the ENLP. According to [178], a local optimum of the ENLP can be found by solving the equalities

$$\begin{pmatrix} \nabla_{\boldsymbol{x}}\mathcal{L}(\boldsymbol{x},\, \boldsymbol{\lambda}_{\boldsymbol{g}}) \\ \boldsymbol{g}(\boldsymbol{x}) \end{pmatrix} = \boldsymbol{0}\ . \tag{3.85}$$

Therefore, the Lagrangian function includes only the equality constraint $\boldsymbol{g}(\boldsymbol{x})$ is given as

$$\mathcal{L}(\boldsymbol{x},\, \boldsymbol{\lambda}_{\boldsymbol{g}}) = J(\boldsymbol{x}) - \boldsymbol{\lambda}_{\boldsymbol{g}}\, \boldsymbol{g}(x)\ . \tag{3.86}$$

By approximating the term $\nabla_{\boldsymbol{x}}\mathcal{L}(\boldsymbol{x},\, \boldsymbol{\lambda}_{\boldsymbol{g}})$ around the current iterate $(\boldsymbol{x}_k,\, \boldsymbol{\lambda}_{\boldsymbol{g},\,k},\, \boldsymbol{\lambda}_{\boldsymbol{h},\,k})$, the equalities in (3.85) can be linearised as

$$\begin{pmatrix} \nabla^2_{\boldsymbol{x}} J(\boldsymbol{x}_k)(\boldsymbol{x}-\boldsymbol{x}_k) + \nabla_{\boldsymbol{x}} J(\boldsymbol{x}_k) - \nabla_{\boldsymbol{x}}\boldsymbol{g}(\boldsymbol{x}_k)^T(\boldsymbol{\lambda}_{\boldsymbol{g}} - \boldsymbol{\lambda}_{\boldsymbol{g},k}) \\ \boldsymbol{g}(\boldsymbol{x}_k) + \nabla_{\boldsymbol{x}}\boldsymbol{g}(\boldsymbol{x}_k)(\boldsymbol{x}-\boldsymbol{x}_k) \end{pmatrix} = \boldsymbol{0}\,. \tag{3.87}$$

Furthermore, the equations in (3.87) can be reformulated as the KKT system as

$$\begin{pmatrix} \nabla^2_{\boldsymbol{x}} J(\boldsymbol{x}_k) & -\boldsymbol{G}_k^T \\ \boldsymbol{G}_k & \boldsymbol{0} \end{pmatrix} \begin{pmatrix} \boldsymbol{x}-\boldsymbol{x}_k \\ \boldsymbol{\lambda}-\boldsymbol{\lambda}_k \end{pmatrix} = \begin{pmatrix} -\nabla_{\boldsymbol{x}} J(\boldsymbol{x}_k) \\ -\boldsymbol{g}(\boldsymbol{x}_k) \end{pmatrix}\,, \tag{3.88}$$

where $\boldsymbol{G}_k := \nabla_{\boldsymbol{x}}\boldsymbol{g}(\boldsymbol{x}_k)$. The system in (3.88) can be solved with a linear solver.

3.5.4.2.3 Quasi-Newton Method Different from the aforementioned methods, the Quasi-Newton method approximates the Hessian matrix and calculates the exact Jacobian matrix of the Lagrangian function in (3.81), which is inspired by the work in [181]. This procedure avoids the computation of the second derivatives and denotes low computational cost.

The Quasi-Newton method calculates the approximation of the Hessian matrix, denoted by $\boldsymbol{H}_J$, satisfying the secant equation $\boldsymbol{H}_J\Delta\boldsymbol{x} = \boldsymbol{\gamma}$, where

$$\boldsymbol{\gamma} = \nabla_{\boldsymbol{x}}\mathcal{L}(\boldsymbol{x}_{k+1},\, \boldsymbol{\lambda}_{\boldsymbol{g},\,k+1},\, \boldsymbol{\lambda}_{\boldsymbol{h},\,k+1}) - \nabla_{\boldsymbol{x}}\mathcal{L}(\boldsymbol{x}_k,\, \boldsymbol{\lambda}_{\boldsymbol{g},\,k+1},\, \boldsymbol{\lambda}_{\boldsymbol{h},\,k+1})\,.$$

Furthermore, $\boldsymbol{H}_J$ is updated utilising the BFGS method, which is given by [182]

$$\boldsymbol{H}_{J,\,k+1} = \boldsymbol{H}_{J,\,k} + \frac{\boldsymbol{\gamma}\boldsymbol{\gamma}^T}{\boldsymbol{\gamma}^T\Delta\boldsymbol{x}} - \frac{\boldsymbol{H}_{J,\,k}\Delta\boldsymbol{x}\Delta\boldsymbol{x}^T\boldsymbol{H}_{J,\,k}}{\Delta\boldsymbol{x}^T\boldsymbol{H}_{J,\,k}\Delta\boldsymbol{x}}\,. \tag{3.89}$$

3.5.4.2.4 Constrained (Generalized) Gauss-Newton Method As a special case of the Quasi-Newton method, the constrained Gauss-Newton method is applied for the problem with a cost function consisting of the sum of squares. It can be written in a general form as

$$J(\boldsymbol{x}) = \frac{1}{2}\|\boldsymbol{f}(\boldsymbol{x})\|_2^2\,. \tag{3.90}$$

The Hessian matrix can be approximated by the product of the Jacobian matrices at the current iterate as

$$\nabla^2_{\boldsymbol{x}} J(\boldsymbol{x}_k) \approx \nabla_{\boldsymbol{x}}\boldsymbol{f}(\boldsymbol{x}_k)^T\nabla_{\boldsymbol{x}}\boldsymbol{f}(\boldsymbol{x}_k)\,. \tag{3.91}$$

As a result, (3.87) is then approximated as

$$\begin{pmatrix} \boldsymbol{F}_k^T\boldsymbol{F}_k(\boldsymbol{x}-\boldsymbol{x}_k) + \boldsymbol{F}_k^T f(\boldsymbol{x}_k) - \boldsymbol{G}_k^T(\boldsymbol{\lambda}_{\boldsymbol{g}} - \boldsymbol{\lambda}_{\boldsymbol{g},k}) \\ \boldsymbol{g}(\boldsymbol{x}_k) + \boldsymbol{G}_k(\boldsymbol{x}-\boldsymbol{x}_k) \end{pmatrix} = \boldsymbol{0}\,, \tag{3.92}$$

where

$$\boldsymbol{F}_k := \nabla_{\boldsymbol{x}}\boldsymbol{f}(\boldsymbol{x}_k)\,,$$
$$\boldsymbol{G}_k := \nabla_{\boldsymbol{x}}\boldsymbol{g}(\boldsymbol{x}_k)\,.$$

The corresponding KKT system can be as

$$\begin{pmatrix} \boldsymbol{F}_k^T\boldsymbol{F}_k & -\boldsymbol{G}_k^T \\ \boldsymbol{G}_k & \boldsymbol{0} \end{pmatrix} \begin{pmatrix} \boldsymbol{x}-\boldsymbol{x}_k \\ \boldsymbol{\lambda}-\boldsymbol{\lambda}_k \end{pmatrix} = \begin{pmatrix} -\boldsymbol{F}_k^T\,\boldsymbol{f}(\boldsymbol{x}_k) \\ -\boldsymbol{g}(\boldsymbol{x}_k) \end{pmatrix}\,, \tag{3.93}$$

Since the constrained Gauss-Newton method is a special case of the Quasi-Newton method, it shows moreover computational advantage.

3.5.4.3 Real-Time Solution

Authors in [183] summarized the methods for solving the generic NLP. In this paper, the inequality constraints are omitted, since they are not really hit during the optimization and can heavily increase the computational burden. Therefore, the optimization problem in (3.78) is then simplified as an equality constrained NLP and solved with the generalized Gauss-Newton method. Redefine all variables of (3.78) into a new variable $\boldsymbol{z}_k$, which is can be written as

$$\boldsymbol{z}_k := \begin{pmatrix} \boldsymbol{x}_n, & \boldsymbol{w}_n, & \boldsymbol{x}_{n+1}, & \boldsymbol{w}_{n+1}, & \cdots, & \boldsymbol{x}_{k-1}, & \boldsymbol{w}_{k-1}, & \boldsymbol{x}_k \end{pmatrix}^T . \tag{3.94}$$

As a result, the optimization problem in (3.78) can be written in a compact form as

$$\begin{aligned} \min_{\boldsymbol{z}_k} \quad & \|J(\boldsymbol{z}_k)\|_2^2 \\ \text{s. t.} \quad & F(\boldsymbol{z}_k) = \boldsymbol{0} \, . \end{aligned} \tag{3.95}$$

The solution of (3.95) can be transformed into solving the root finding problem of

$$\begin{pmatrix} \nabla \mathcal{L}(\boldsymbol{z}_k, \, \boldsymbol{\lambda}) \\ F(\boldsymbol{z}_k) \end{pmatrix} = \boldsymbol{0} \, , \tag{3.96}$$

where $\mathcal{L}$ is the Lagrangian function and given by

$$\mathcal{L}(\boldsymbol{z}_k, \, \boldsymbol{\lambda}) := \|J(\boldsymbol{z}_k)\|_2^2 - \boldsymbol{\lambda}^T F(\boldsymbol{z}_k) \, . \tag{3.97}$$

The cost function and the equality constraint in (3.96) can be linearised using the generalized Gaussian-Newton method around the current iteration value $\boldsymbol{z}_k^i$. It is then rewritten as

$$\begin{pmatrix} (\nabla_{\boldsymbol{z}} J)^T \nabla_{\boldsymbol{z}} J & -(\nabla_{\boldsymbol{z}} F)^T (\boldsymbol{z}_k) \\ (\nabla_{\boldsymbol{z}} F)^T & \boldsymbol{0} \end{pmatrix} \begin{pmatrix} \Delta \boldsymbol{z}_k^* \\ \Delta \boldsymbol{\lambda}_k^* \end{pmatrix} = \begin{pmatrix} -(\nabla_{\boldsymbol{z}} J)^T J \\ -F \end{pmatrix} . \tag{3.98}$$

The solution to equations in (3.98) denotes the increment of the next iterate, which is computed with $\boldsymbol{z}_k^{i+1} = \boldsymbol{z}_k^i + \Delta \boldsymbol{z}_k^*$. The problem in (3.95) is then solved with (3.98) recursively until a pre-specified convergence criterion is satisfied. However, the conventional generalized Gaussian-Newton method is not suitable for the real-time implementation. Instead of solving the QP problem in (3.98) repeatedly, the real-time iteration (RTI) approach reduces the computational burden of solving the optimization problem to one single generalized Gaussian-Newton iteration [171]. The convergence of this approach was guaranteed with an appropriate initialization [184].

3.5.4.4 Approximation of the Arrival Cost

As described afore, the arrival cost includes all the prior information and plays an important role for stabilizing the MHE. It works analogously to the terminal cost in the MPC problem, which limits the MHE problem to a fixed-size problem [185]. However, an exact computation of the arrival cost is intractable. There are several techniques to approximate the arrival cost. One alternative is to use the first-order Taylor expansion around the past estimations. The other possibility is to use a particle filter and the MHE smoothing to update the arrival cost [186].

In this thesis, we approximate the arrival cost as a quadratic term by implementing the method presented in [171]. The arrival cost is then transformed into a recursive procedure. Consider the arrival cost over the increased interval $[n-1,\, n]$ and assume that the solution $\bar{\boldsymbol{x}}_n$ from the last interval is already obtained. Then it can be seen that

$$J_a^k(\boldsymbol{x}_n,\, \boldsymbol{p}_n) \approx \text{const} + \left\| \begin{matrix} \boldsymbol{x}_n - \bar{\boldsymbol{x}}_n \\ \boldsymbol{p}_n - \bar{\boldsymbol{p}}_n \end{matrix} \right\|_{\boldsymbol{P}_n}^2 , \tag{3.99}$$

where $\bar{\boldsymbol{x}}_n$, $\bar{\boldsymbol{p}}_n$ denotes the initial state of the MHE problem and $\boldsymbol{P}_n$ is the weighting matrix of the arrival cost. They are derived by shifting the horizon from $n-1$ to n and summarizing the information within this one step. Apparently, the constant part of $J_a^k(\boldsymbol{x}_n,\, \boldsymbol{p}_n)$ has no impact on the optimization. Then, the arrival cost over the estimation window $[n+1,\, k+1]$ can be calculated from the solution of MHE problem of the previous interval $[n,\, k]$ by substituting the linearised system dynamic and the linearised output function into the new quadratic function as

$$\begin{aligned} J_a^{k+1}(\boldsymbol{x}_{n+1}, \boldsymbol{p}_{n+1}) &\approx \text{const} + \left\| \begin{matrix} \boldsymbol{x}_{n+1} - \bar{\boldsymbol{x}}_{n+1} \\ \boldsymbol{p}_{n+1} - \bar{\boldsymbol{p}}_{n+1} \end{matrix} \right\|_{\boldsymbol{P}_{n+1}}^2 \\ &\approx \text{const} + \left\| \begin{matrix} \boldsymbol{P}_n \begin{pmatrix} \boldsymbol{x}_n - \bar{\boldsymbol{x}}_n \\ \boldsymbol{p}_n - \bar{\boldsymbol{p}}_n \end{pmatrix} \\ \boldsymbol{V}_n(\boldsymbol{y}_n - \tilde{h} - \boldsymbol{H}_x\, \boldsymbol{x}_n - \boldsymbol{H}_p\, \boldsymbol{p}_n) \\ \boldsymbol{W}_n \begin{pmatrix} \boldsymbol{x}_{n+1} - \tilde{x} - \boldsymbol{X}_x\, \boldsymbol{x}_n - \boldsymbol{X}_p\, \boldsymbol{p}_n \\ \boldsymbol{p}_{n+1} - \boldsymbol{p}_n \end{pmatrix} \end{matrix} \right\|_2^2 , \end{aligned} \tag{3.100}$$

where

$$\begin{aligned} \boldsymbol{H}_x &:= \frac{\mathrm{d}H(n+1; \boldsymbol{x}^*(n),\, \boldsymbol{p}^*)}{\mathrm{d}\boldsymbol{x}_(n)} , & \tilde{x} &:= F(n+1; x^*(n),\, \boldsymbol{p}^*) - \boldsymbol{X}_x\, \boldsymbol{x}^*(n) - \boldsymbol{X}_p\, \boldsymbol{p}^* , \\ \boldsymbol{H}_p &:= \frac{\mathrm{d}H(n+1; \boldsymbol{x}^*(n),\, \boldsymbol{p}^*)}{\mathrm{d}\boldsymbol{p}} , & \tilde{h} &:= H(n+1; x^*(n), \boldsymbol{p}^*) - \boldsymbol{H}_x\, \boldsymbol{x}^*(n) - \boldsymbol{H}_p\, \boldsymbol{p}^* . \\ \boldsymbol{X}_x &:= \frac{\mathrm{d}F(n+1; \boldsymbol{x}^*(n),\, \boldsymbol{p}^*)}{\mathrm{d}\boldsymbol{x}(n)} , & \boldsymbol{X}_p &:= \frac{\mathrm{d}F(n+1; \boldsymbol{x}^*(n),\, \boldsymbol{p}^*)}{\mathrm{d}\boldsymbol{p}} . \end{aligned}$$

The arrival cost in (3.100) is thereby transformed into an analytically solvable optimization problem $\mathcal{P}_a$, which can be written as

$$\mathcal{P}_a := \min_{\boldsymbol{x}_n,\, \boldsymbol{p}_n} \left\| \begin{matrix} \boldsymbol{P}_n \begin{pmatrix} \boldsymbol{x}_n - \bar{\boldsymbol{x}}_n \\ \boldsymbol{p}_n - \bar{\boldsymbol{p}}_n \end{pmatrix} \\ \boldsymbol{V}_n(\boldsymbol{y}_n - \tilde{h} - \boldsymbol{H}_x \boldsymbol{x}_n - \boldsymbol{H}_p \boldsymbol{p}_n) \\ \boldsymbol{W}_n \begin{pmatrix} \boldsymbol{x}_{n+1} - \tilde{x} - \boldsymbol{X}_x \boldsymbol{x}_n - \boldsymbol{X}_p \boldsymbol{p}_n \\ \boldsymbol{p}_{n+1} - \boldsymbol{p}_n \end{pmatrix} \end{matrix} \right\|_2^2 . \tag{3.101}$$

It can be solved by using QR-factorization [171]. As a result, the optimization problem $\mathcal{P}_a$ can be compactly written as

$$\mathcal{P}_a = \min_{\boldsymbol{x}_n,\, \boldsymbol{p}_n} \left\| \begin{pmatrix} \rho_1 \\ \rho_2 \\ \rho_3 \end{pmatrix} + \begin{pmatrix} \boldsymbol{R}_{11} & \boldsymbol{R}_{12} \\ \boldsymbol{0} & \boldsymbol{R}_{22} \\ \boldsymbol{0} & \boldsymbol{0} \end{pmatrix} \begin{pmatrix} \boldsymbol{x}_n \\ \boldsymbol{p}_n \\ \boldsymbol{x}_{n+1} \\ \boldsymbol{p}_{n+1} \end{pmatrix} \right\|_2^2 = \left\| \rho_3 \right\|_2^2 + \left\| \rho_2 + \boldsymbol{R}_{22} \begin{pmatrix} \boldsymbol{x}_{n+1} \\ \boldsymbol{p}_{n+1} \end{pmatrix} \right\|_2^2 . \tag{3.102}$$

The solution of (3.101) is then obtained by comparing (3.101) with (3.102) and given as

$$\boldsymbol{P}_{n+1} = \boldsymbol{R}_{22} \ , \quad \begin{pmatrix} \bar{\boldsymbol{x}}_{n+1} \\ \bar{\boldsymbol{p}}_{n+1} \end{pmatrix} = -\boldsymbol{R}_{22}^{-1}\, \rho_2 \ . \tag{3.103}$$

It is worth mentioning that the reference [132] established the relationship between the MHE and the Kalman filter for the nonlinear system in (3.1) as follows.

Theorem 3.4
Let the initial value of the system state $\boldsymbol{x}_0$ and the disturbances $\boldsymbol{w}_i$, $\boldsymbol{v}_i$ be uncorrelated Gaussian sequences. Their mean value and covariance are given as $\boldsymbol{x}_0 \sim \mathcal{N}(\bar{\boldsymbol{x}}_0,\, \boldsymbol{P}_0)$, $\boldsymbol{w}_i \sim \mathcal{N}(\boldsymbol{0},\, \boldsymbol{Q})$ and $\boldsymbol{v}_i \sim \mathcal{N}(\boldsymbol{0},\, \boldsymbol{R})$. If the arrival cost is chosen as the approximation

$$J_a^k(\boldsymbol{x}_n) = \left\| \hat{\boldsymbol{x}}_n - \bar{\boldsymbol{x}}_n \right\|_{\boldsymbol{P}_n}^2 \ , \tag{3.104}$$

where $\bar{\boldsymbol{x}}_n$ denotes the optimal MHE estimate at step n given the measurement sequence $\boldsymbol{Y} = [\boldsymbol{y}_0^T, \cdots, \boldsymbol{y}_{n-1}^T]$ and the covariance matrix $\boldsymbol{P}_n$ is updated by the Riccati equation

$$\boldsymbol{P}_{k+1} = \boldsymbol{Q} + \boldsymbol{F}_k\, \boldsymbol{P}_k\, \boldsymbol{A}_k^T - \boldsymbol{F}_k\, \boldsymbol{P}_k\, \boldsymbol{H}_k^T\, (\boldsymbol{H}_k\, \boldsymbol{P}_k\, \boldsymbol{H}_k^T + \boldsymbol{R})^{-1}\, \boldsymbol{H}_k\, \boldsymbol{P}_k\, \boldsymbol{F}_k^T \ ,$$

then the estimation results obtained by the MHE is for $k - n = 1$ equivalent to the estimation results derived by an EKF.

It is worth mentioning that the Theorem 3.4 is also valid for all $k - n \geq 1$ of the linear system.

3.5.5 Data-based Approaches

Besides the recursive nonlinear estimators, data-based approaches have been applied as the estimators. Reference [187] presented a clustering technique to realize the online identification of electric vehicle (EV) and hybrid electric vehicle (HEV). The author claims that this technique can identify all electrical parameters simultaneously with a low computational complexity. In [188], a neural network (NN) approach was implemented to online estimate the electrical parameters of the nonsalient-pole PMSM. Furthermore, authors in [134] used the same NN method to estimate the rotor flux linkage and the stator winding resistance of PMSM with the consideration of the VSI nonlinearity. This approach was validated on several motors and showed good performance. Reference [189] implemented NN for estimating parameters of PMSM at the steady state. Besides aforementioned methods, the particle swarm optimization (PSO) has been likewise widely implemented for the parameter estimations. Reference [190]

used PSO for evaluating parameters as well as tuning the controller for the electrical motor drives. The VSI nonlinearity was included by [191], which also simultaneously estimated all electrical parameters. Furthermore, authors in [191] compared various PSO algorithms and claimed that a dynamic particle swarm optimization with learning strategy has the best performance. However, the data-based approaches are out of the scope of this work. More details can be found in corresponding references.

3.5.6 Experimental Evaluation

In this section, the experimental results for evaluating the previously introduced methods are presented. The Test Bench B.1 is utilized for validating the estimation methods. The comparison is conducted with following tests: the steady-state performance test, the speed-step test and the load-step test. Moreover, the accuracy of the estimation results is evaluated with the absolute value of the mean error and the root mean squared error (RMSE). They are represented as the percentage of the nominal values. The tracking ability of the methods is also investigated. The variation of the estimated parameters, i.e. the permanent magnet flux linkage Ψ_m and the stator resistance R_s, is approximated by their individual temperature model. The temperature models are introduced in Chapter 2.4, where the temperature is measured with the temperature sensor. The PMSMs are controlled with FOC, where the coefficients of the controller are tuned before the tests and remain unchanged during the experimental evaluation.

3.5.6.1 Steady-State Performance

The steady state performance is evaluated with the constant speed test. Two PMSMs, i.e. PMSM I and PMSM II, were tested with various speed values. But because of the limitation of space, only the results of one operating point are shown. The experimental results of the steady-state performance are shown in Fig. 3.35 and Fig. 3.36. The initial value of all estimations are set to zero. The parameters of the estimators are so tuned that the estimation results are stable and comparatively satisfying.

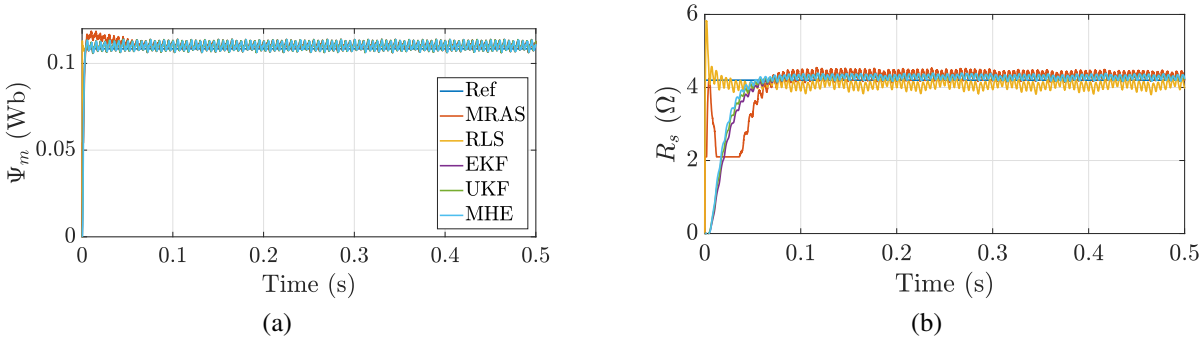

Figure 3.35: Experimental results of the PMSM I: the constant-speed profile. The PMSM run at 1000 rpm. (a) shows the estimated permanent flux linkage $\hat{\Psi}_\mathrm{m}$. (b) presents the estimated stator resistance $\hat{R}_\mathrm{s}$.

Fig. 3.35 shows the experimental results of the PMSM I. It can be noted that the RLS is the fastest one converging from zero to the end value. EKF, UKF and MHE have almost the same rate of convergence. At identifying the resistance, RLS shows conspicuous overshoot

at the beginning of the identification procedure, but converges very fast, while MRAS is the slowest one. Moreover, a nonlinear trajectory of the estimated resistance can be observed from MRAS, which is probably caused by the nonlinearity of the adaptive mechanism. A noticeable steady-state offset can be observed from RLS. The estimation results of RLS and MRAS are more disturbed than the other three methods. On the contrary, RLS has the least noisy results at identifying the permanent magnet flux linkage. At the beginning of estimating Ψ_m, MRAS has an overshoot of about 20% of the nominal value, while the other four methods steadily converge to the end value.

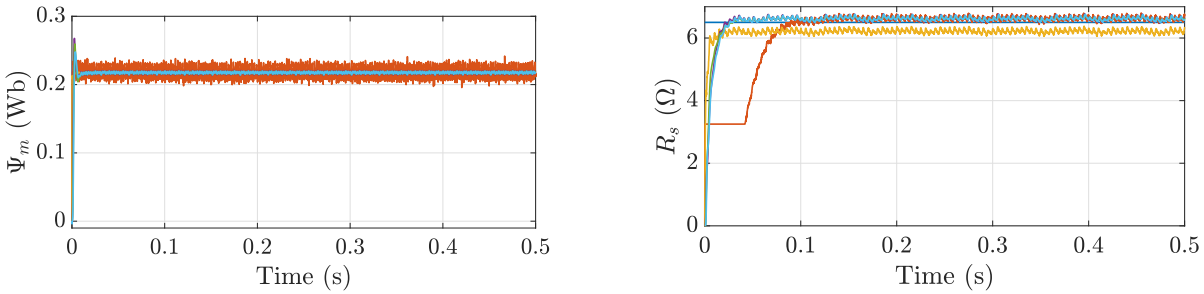

Figure 3.36: Experimental results of the PMSM II: the constant-speed profile. The PMSM run at $1000\,\mathrm{rpm}$. (a) shows the estimated permanent flux linkage $\hat{\Psi}_\mathrm{m}$. (b) demonstrates the estimated stator resistance $\hat{R}_\mathrm{s}$.

Another steady-state performance test was conducted with the PMSM II. The corresponding results are shown in Fig. 3.36. Similar to the previous test, RLS converges the fastest. However, at identifying R_s, RLS shows no overshoot anymore, but its steady-state offset is more evident than the result of PMSM I, which amounts up to $4.6\,\%$ of the nominal value. EKF, UKF and MHE have similar performance. The results of them nearly overlap with each other. Nonetheless, the convergent rate of UKF is slightly faster than the other two methods. At identifying the permanent magnet flux linkage, RLS outperforms the other four methods in terms of the rate of convergence and the accuracy. MRAS is apparently more disturbed than the other four methods.

3.5.6.2 Performance under Speed Step

The dynamic performance under the speed changing is a criterion to evaluate the performance of the estimator, since the speed of the PMSM may change during the operation. The performance is assessed by applying a speed step from $500\,\mathrm{rpm}$ to $1000\,\mathrm{rpm}$ on the PMSM II at $t = 0\,\mathrm{s}$. Because of the limitation of experimental facilities as well as of the space, the speed step test was conducted only with the PMSM II, while the load step test was conducted only with the PMSM I. The experimental results of the speed-step test are shown in Fig. 3.37, where the transient behaviour is furthermore zoomed in and demonstrated in the figures.

It can be noted from Fig. 3.37 that for estimating Ψ_m, the results of MRAS are heavily disturbed and show a conspicuous overshoot during the transient. analogous to the steady-state test, RLS exceeds the other four estimators by showing less overshoot after the step and less noisy result. Regarding the estimation results of R_s, MRAS, EKF, UKF and MHE reach the new steady state within $20\,\mathrm{ms}$ after the speed step, while RLS needs more than $50\,\mathrm{ms}$ to converge.

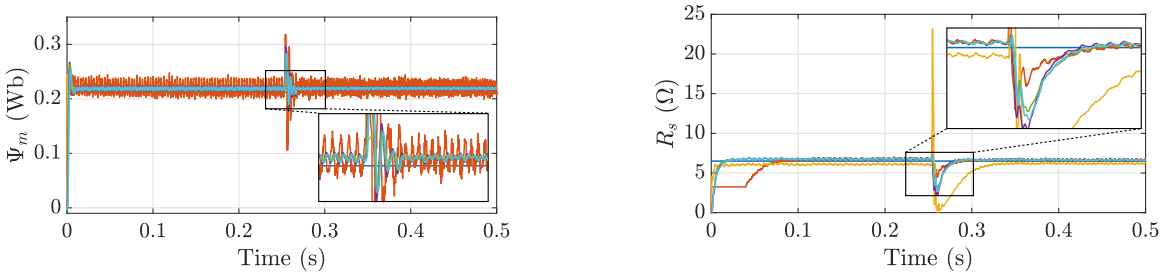

(a) (b)

Figure 3.37: Experimental results of the PMSM II under the test of a speed-step profile. (a) shows the estimated permanent flux linkage $\hat{\Psi}_\mathrm{m}$. (b) presents the estimated stator resistance $\hat{R}_\mathrm{s}$.

MRAS surpasses EKF, UKF and MHE in terms of the stability during the transient. Moreover, a conspicuous strike can be observed from RLS at $t = 0.25\,\mathrm{s}$, when the speed step was applied. Its steady-state offset can still be noticed after the speed step. It is worth mentioning that all estimators obtained more accurate estimations after the speed step, which can be explained by the fact that the steady state of PMSM is the worst scenario for the parameter estimation problem and the speed step creates a transient for the PMSM, which can be regarded as an excitement for the current loop and provides more information of the dynamic behaviour. Particularly, the steady-state offset of the estimated value of RLS has reduced by $50\,\%$ of the nominal value.

3.5.6.3 Performance under Torque Step

Furthermore, the algorithms are tested with a load step on PMSM I, since the addition of a load torque occurs often during the operation of the PMSM. 50% of the rated torque was added to the PMSM I at $t = 0.25\,\mathrm{s}$ through the load machine that is identical to the PMSM I. The corresponding estimation results are shown in Fig. 3.38.

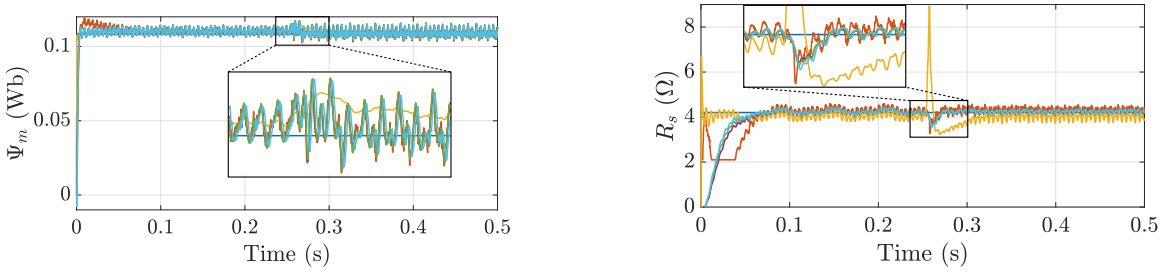

(a) (b)

Figure 3.38: Experimental results of the PMSM I under the test with a load step profile. (a) presents the estimated results of the permanent flux linkage Ψ_m. (b) shows the estimated results of the stator resistance R_s.

At estimating Ψ_m, RLS performs still the best in terms of the ripple of the results and the transient performance. MRAS, EKF, UKF and MHE perform almost the same. At estimating the stator resistance, the results of RLS is most disturbed and a strike can be observed from RLS at the step occurrence. Similar to the speed-step test, RLS converges more slowly than the other four methods. MRAS gives more overshoot and is more noisy than EKF, UKF and MHE.

EKF outperforms slightly UKF and MHE in terms of the rate of convergence.

3.5.6.4 Evaluation of the Accuracy

The evaluation of the estimation accuracy is carried out by computing the absolute value of the mean error and the RMSE, of which the computing formulations are given in (3.105) and (3.106), respectively. They are presented as a percentage of the nominal values.

$$\text{Mean} = \left| \frac{\sum_{i=1}^{N_n}(\hat{p}-p)}{N_n} \cdot \frac{1}{p} \right| \cdot 100\% \tag{3.105}$$

$$\text{RMSE} = \sqrt{\frac{\sum_{i=1}^{N_n}(\hat{p}-p)^2}{N_n}} \cdot \frac{1}{p} \cdot 100\% \tag{3.106}$$

where p denotes the nominal value of the to be estimated parameters and $\hat{p}$ is the estimation results. N_n represents the number of the collected measurements. The computation results are shown in Fig. 3.39 and Fig. 3.40, where the label *Test 1* denotes the PMSM I with the constant speed, the label *Test 2* denotes the PMSM I with the load step test, the label *Test 3* denotes the PMSM II with constant speed and the label *Test 4* denotes the PMSM II with the speed step profile. The measurements are collected at the steady state after the step, if a step is applied.

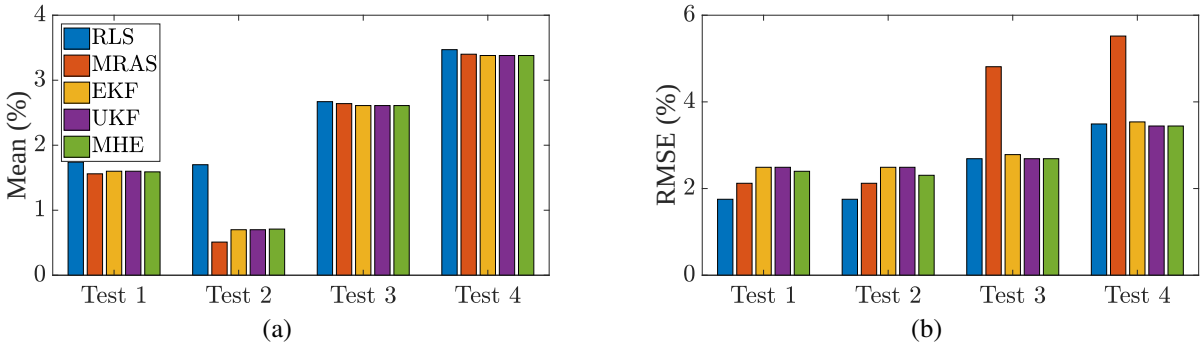

Figure 3.39: Estimation errors of the permanent magnet flux linkage Ψ_m. (a) presents the absolute value of the mean error that is defined in (3.105). (b) shows the RMSE computed via (3.106).

The estimation results in Fig. 3.39 provides several conclusions. At identifying Ψ_m, RLS delivers as good results as EKF, UKF and MHE in most tests, except in *Test 2*. MRAS has the most disturbed results fir PMSM II, while the ripple of its results for PMSM I is even smaller than that of MHE. However, EKF, UKF and MHE still perform the best. Minor differences can be observed among them that MHE is slightly more accurate and more robust to the noises than the other two methods. Moreover, from Fig. 3.40, it can be concluded that RLS delivers results with an obvious steady-state offset, nearly 3% in *Test 1*, over 4% in the other three test cases. Moreover, it has the noisiest result in all tests. MRAS performs much worse than EKF, UKF and MHE for the PMSM I, but it gives similar results regarding the ripple and the end value accuracy to the three methods in some test cases. EKF, UKF and MHE have almost the same performance. They can deliver the results with an error below 2.5%.

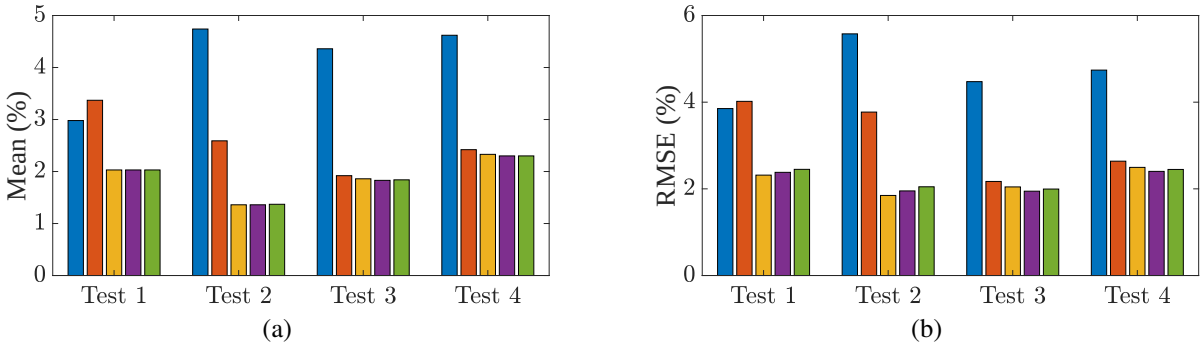

Figure 3.40: Estimation errors of the stator resistance R_s. (a) shows the absolute value of the mean error that is defined in (3.105). (b) demonstrates the value of RMSE that is defined in (3.106).

3.5.6.5 Tracking Ability

The performance of the individual estimation method is furthermore evaluated for the tracking ability. As it is introduced in Chapter 2.4, the to be estimated parameters, i.e. Ψ_m and R_s, change mainly because of the temperature. Their variations can be simplified as a linear function of the temperature with the corresponding temperature coefficients, which are shown in (2.58) and (2.59). Therefore, the tracking ability test is conducted by changing the machine temperature, which rose from the room temperature, i.e. $25\,^\circ\mathrm{C}$, to around $45\,^\circ\mathrm{C}$. The reference value of the to be estimated parameters are computed using the simplified linear temperature models of R_s and Ψ_m. The experimental results are shown in Fig. 3.41.

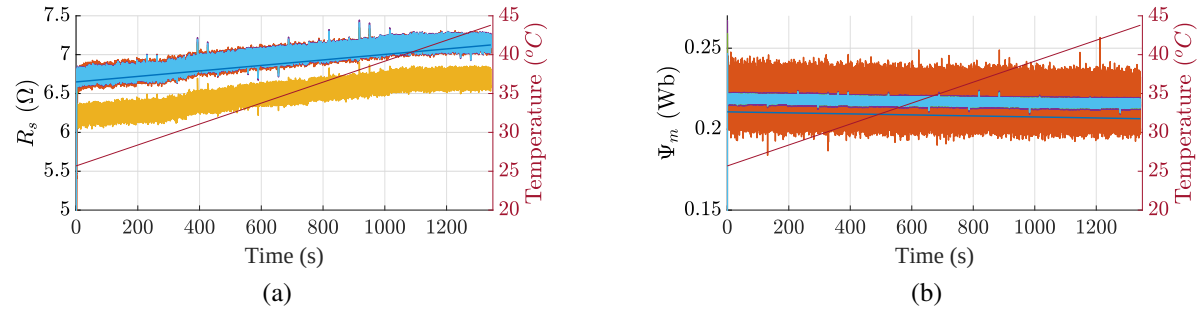

Figure 3.41: Experimental results of the PMSM II under temperature variation. (a) demonstrates the estimated stator resistance $\hat{R}_\mathrm{s}$. (b) presents the estimated permanent flux linkage $\hat{\Psi}_\mathrm{m}$.

As it is shown in Fig. 3.41, all estimators have tracked the parameter variations. Their performance is similar to the steady state performance in terms of the accuracy and the robustness against noise.

3.5.6.6 Influence of Working Points

The working points can also have impacts on the estimation performance. Therefore, further experiments to study the influence of the rotor speed on the estimators were conducted. The PMSM II was engaged and controlled under various speed values ranging from $100\,\mathrm{rpm}$ to $2000\,\mathrm{rpm}$. The measurements were collected at the steady state of diverse speed values. The

corresponding errors regarding the evaluation criteria are computed and presented in Fig. 3.42 and Fig. 3.43 for Ψ_{m} and R_{s}, respectively.

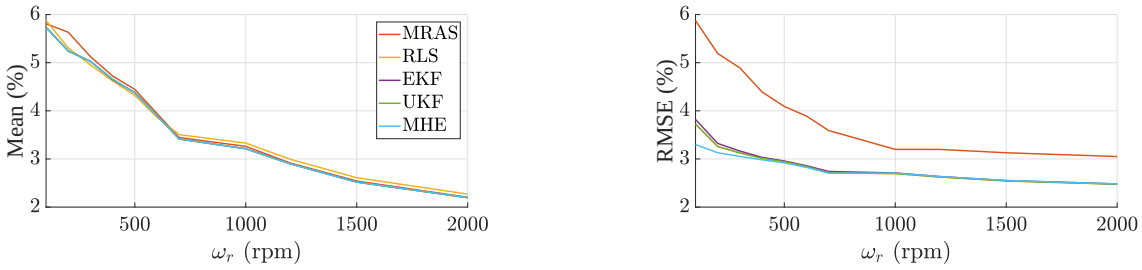

Figure 3.42: Experimental results of $\hat{\Psi}_{\mathrm{m}}$ in relation to the machine rotor speed. (a) presents the absolute value of the mean error defined in (3.105). (b) shows the RMSE value defined in (3.106).

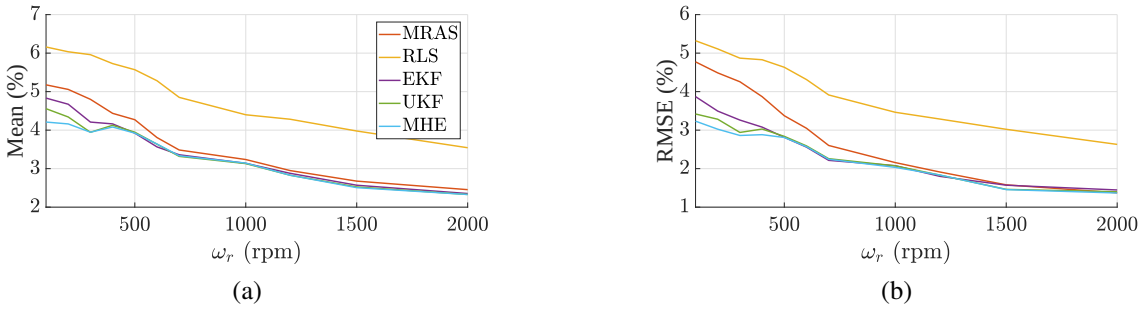

Figure 3.43: Experimental results of $\hat{R}_{\mathrm{s}}$ in relation to the machine rotor speed. (a) shows the absolute value of the mean error defined in (3.105). (b) demonstrates the RMSE defined in (3.106).

These results show that MHE outperforms the other estimators especially in the low-speed region. EKF and UKF have analogous performance, while UKF is slightly better than EKF in terms of the accuracy as well as the robustness against noise. The performance of MRAS deteriorates at the low-speed area, which may result from the sensitivity of MRAS to noises. Analogous to the former tests, RLS has delivered the biased results. In general, the speed has a great impact on the estimation results. The estimators perform worse at the low-speed region. This is an expected conclusion mainly because of the fact that in the low-speed region the signal-to-noise ratio is higher and the voltage distortions caused by the converters are more evident. Even though the error voltage caused by the nonlinear effects of the VSI is compensated, the accuracy of the compensation is limited and other uncertainties also exists in the drive system.

3.5.6.7 Computational Effort

The computational effort is evaluated by the metric of the execution time on the Renesas microprocessor. The execution time of each online estimation method is collected and summarized in Table 3.4.

As it is shown in Table 3.4, MRAS has the least computational burden, since it deploys solely the simple PI technique. RLS has more computational cost than MRAS because of the matrix

Table 3.4: Execution time on the embedded system

Algorithm	Execution time		
	Average	Maximal	Minimal
RLS	3.14 µs	9 µs	3 µs
MRAS	1.05 µs	7 µs	1 µs
EKF	14.55 µs	26 µs	13 µs
UKF	30.33 µs	41 µs	28 µs
MHE (N=5)	279.02 µs	285 µs	274 µs

computations in the algorithm. MHE has the highest computational cost with a horizon length of five. The computational cost will be reduced if the horizon length is shortened. But due to the computation of solving the optimization problem enclosing in the MHE, the computational cost remains higher than the other methods.

3.5.6.8 Summary

Based on the aforementioned experimental results and the corresponding evaluating analysis, the advantages and disadvantages of the online estimation methods are summarized. In this thesis, five criteria are selected to represent their performance, i.e. accuracy, computational burden, rate of the convergence, robustness and memory allocation.

3.5.6.8.1 Accuracy The accuracy is the most important criterion of the parameter estimation, especially for the high precise control, since the parameter mismatch can cause steady-state offset or even cause instability of the whole system, as shown in Chapter 2. The accuracy is summarized based on the overall estimation results of the estimation methods in various tests.

3.5.6.8.2 Computational Burden The estimation methods are implemented on the embedded systems and the computational burden is critical there, particularly for the low-budget applications. The execution time on the embedded system is taken as the indicator of the computational cost. Even though the computational burden depends on the solving approaches of the individual method, e.g. solving approaches for the matrix inversion, the execution time measured in former section is based on the condition that the basic computations are the same.

3.5.6.8.3 Rate of the Convergence The convergent rate indicates the dynamic performance of the estimators, especially for the dynamic and precise control of the drive system. For example, the parameters with fast changing rate, e.g. the inductances, require a relatively fast convergence rate, in order that the changes of the parameters can be tracked accurately.

3.5.6.8.4 Robustness In practical applications, many uncertainties and disturbances can be expected during the identification procedure. Therefore, the capability of the estimator to deliver accurate results under the existence of the disturbances and uncertainties is essential for its performance in practice.

3.5.6.8.5 Memory Allocation The memory required for an algorithm is determined by the nature of the data, i.e. structure or sparsity and the implementation of the algorithm. In general, a storage of a matrix requires a memory allocation of at least the number of non-zero elements. The memory is critical for resource limited applications. In general, less memory allocation is preferred.

The evaluations of all estimation methods are illustrated in a radar map regarding the individual criterion.

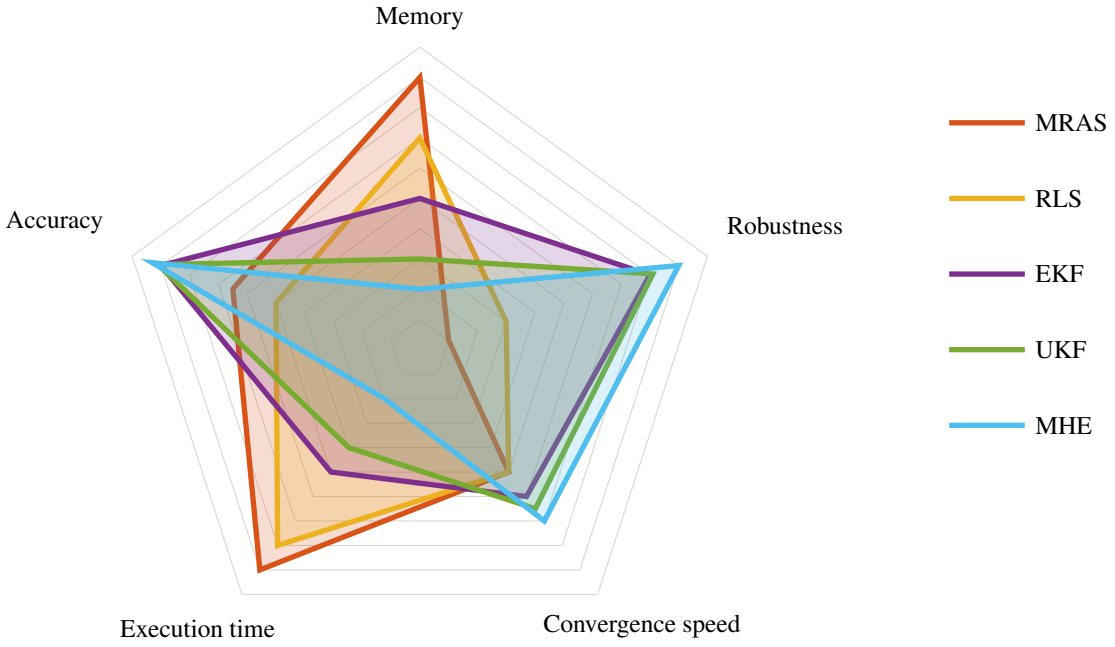

Figure 3.44: A summary of the characteristics of individual estimation method regarding diverse criteria.

Several remarks can be concluded from the theoretical studies as well as the experimental results. RLS is simple to implement and has very low computational burden. But the forgetting factor is the only tuning parameter of the algorithm. Therefore, the implementation of RLS is a trade-off between the robustness to noises and the dynamic performance. Besides, it may deliver biased estimates. MRAS has simple structure, easy implementation and the lowest computational burden among the five methods. But it works within limited bandwidth and is sensitive to noise. Besides, the finely tuning of MRAS is time consuming and the formulation for multiple parameters is complex. EKF, UKF and MHE show similar performance for the online parameter estimation of PMSM. UKF and MHE are slightly better than EKF in terms of accuracy and robustness to noises. However, the tuning of UKF is more complicated than EKF and MHE, although suggestions about the choice of tuning parameters according to the distribution of samples was given in [121]. MHE outperforms EKF and UKF, especially in the low-speed region. Moreover, it shows advantages in tuning the estimator and including the constraints. But the computational burden is much higher, which can be reduced by shortening the estimation horizon. However, this drawback still should be taken into consideration, particularly for applications with limited computational resources. However, the nonlinearities of converter and the inductances were approximated and incorporated into the estimation problem. The performance of estimators may deteriorate, if the nonlinearities of converter or the other pa-

rameters are unknown. Moreover, in the low-speed region, the estimators perform much worse or may even fail. In general, the higher computational burden brings more accuracy, while the computational power is limited by the hardware configuration. These results can be served as a reference for further researches on implementing or developing online estimators.

3.6 Online Parameter Estimation Considering VSI Nonlinearities

The former presented online parameter estimation methods proceed with a relatively accurate compensation of the nonlinear effects of VSI. However, on the one hand, in many applications an accurate compensation of the VSI nonlinearities is not always available. On the other hand, as demonstrated in former sections, the compensation of the distorted voltage caused by the VSI nonlinear effects has a great impact on the identification results. Therefore, in this section, an effective approach is proposed, by which the VSI nonlinear effect and the parameters can be identified simultaneously.

3.6.1 Problem Formulation

The reference voltages are conventionally applied for the online parameter estimation problem in VSI-fed PMSM systems. However, due to the high-frequency switching inverters, the difference between the referred voltage $\boldsymbol{u}^*$ and the actually applied voltage $\boldsymbol{u}$ is considerable. Their difference can be represented by $\Delta\boldsymbol{u}$, i.e. $\Delta\boldsymbol{u} := \boldsymbol{u}^* - \boldsymbol{u}$, which is then simplified from (2.75) and given by [86]

$$\begin{bmatrix}\Delta u_d \\ \Delta u_d\end{bmatrix} = \begin{bmatrix}u_d^* - u_d \\ u_q^* - u_q\end{bmatrix} = U_{dead} \cdot \boldsymbol{T}_{dq}(\theta_e)\,[\text{sgn}(i_a),\ \text{sgn}(i_b),\ \text{sgn}(i_c)]^T\,, \tag{3.107}$$

where Δu_d and Δu_q are the disturbance voltages in the d- and q-axis, respectively. The term $(\mathcal{F}_d,\ \mathcal{F}_q)^T$ is employed to represent the multiplication of the last two terms in (3.107) and can be updated at each step. (3.107) is then compactly written as

$$\big(\Delta u_d,\quad \Delta u_d\big)^T = U_{dead} \cdot (\mathcal{F}_d,\ \mathcal{F}_q)^T\,. \tag{3.108}$$

U_{dead} is the approximation of the VSI nonlinearities and can be given as

$$U_{dead} = \frac{T_{dead} + T_{on} - T_{off}}{T_c}(U_{dc} - U_{ce} + U_d) + \frac{U_{ce} - U_d}{U_{dc}}U_{\text{ref}} + \frac{U_{ce} + U_d}{2}\,, \tag{3.109}$$

where T_{dead}, T_{on} and T_{off} are the dead time, the turn-on time and the turn-off time of the active switches, respectively. T_{cs} is the carrier period of the pulse-width modulation (PWM). U_{ce} is the on-state voltage drop of the active switch and U_d is the forward voltage drop of the freewheeling diode. U_{dc} is the DC-link voltage. U_{ref} is the reference voltage delivered from the current controller. The second term in (3.109) is normally neglected because U_{dc} is much larger than $U_{ce} - U_d$. Therefore, in some applications, U_{dead} can be approximated as

$$U_{dead} = \frac{T_{dead} + T_{on} - T_{off}}{T_c}(U_{dc} - U_{ce} + U_d) + \frac{U_{ce} + U_d}{2}\,. \tag{3.110}$$

By substituting the U_{dead} into the function of the parameter estimation problem, the current model of the PMSM can be compactly rewritten as

$$\begin{aligned} \frac{\mathrm{d}}{\mathrm{d}\,t}\boldsymbol{x} &= f(\boldsymbol{x},\boldsymbol{u})\ , \\ \boldsymbol{y} &= h(\boldsymbol{x},\boldsymbol{u})\ , \end{aligned} \tag{3.111}$$

where $\boldsymbol{u} := \left(u_d^*,\ u_q^*\right)^T$, $\boldsymbol{y} := \left(i_d,\ i_q\right)^T$ and $\boldsymbol{x} := \left(i_d,\ i_q,\ p_1,\ p_2,\ U_{dead}\right)^T$. p_1 and p_2 denote two arbitrary electrical parameters of PMSM, which satisfy the simultaneous identification condition introduced in former section. The variation of p_1, p_2 and U_{dead} is assumed to be zero during one sampling period, since the variation of parameters are much slower than that of the currents. The extended system function f is then given as

$$f = \begin{bmatrix} -\dfrac{R_\mathrm{s}}{L_d} i_d + \dfrac{L_q}{L_d}\cdot\omega_e\cdot i_q + \dfrac{u_d^* - U_{dead}\cdot\mathcal{F}_d}{L_d} \\ -\dfrac{R_\mathrm{s}}{L_q} i_q - \dfrac{L_d}{L_q}\cdot\omega_e\cdot i_d + \dfrac{u_q^* - U_{dead}\cdot\mathcal{F}_q}{L_q} - \dfrac{\Psi_\mathrm{m}}{L_q}\omega_e \\ \mathbf{0} \end{bmatrix}\ , \tag{3.112}$$

where $\mathbf{0} \in \mathbb{R}^{3\times 1}$. The system disturbance as well as the measurement noise is then included into the model and the system model is therefore reformulated and can be transformed into the discrete-time domain, which gives

$$\begin{aligned} \boldsymbol{x}_{k+1} &= F_k(\boldsymbol{x}_k,\boldsymbol{u}_k) + \boldsymbol{w}_k\ , \\ \boldsymbol{y}_k &= H(\boldsymbol{x}_k) + \boldsymbol{v}_k\ , \end{aligned} \tag{3.113}$$

where $\boldsymbol{w}_k$ denotes the system disturbance and $\boldsymbol{v}_k$ represents the measurement noise. The function F_k is given by

$$F_k = \begin{bmatrix} \left(1 - \dfrac{R_{\mathrm{s},\,k}}{L_d}\,T_\mathrm{s}\right) i_{d,\,k} + \dfrac{L_q}{L_d}\,\omega_{e,\,k}\,i_{q,\,k}\,T_\mathrm{s} + \dfrac{u_{d,\,k}^* - U_{dead,\,k}\cdot\mathcal{F}_{d,\,k}}{L_d}\,T_s \\ \left(1 - \dfrac{R_{\mathrm{s},\,k}}{L_q}\,T_s\right) i_{q,\,k} - \dfrac{L_d}{L_q}\,\omega_{e,\,k}\,i_{d,\,k}\,T_\mathrm{s} + (\dfrac{u_{q,\,k}^* - U_{dead,\,k}\cdot\mathcal{F}_{q,\,k}}{L_\mathrm{q}} - \dfrac{\Psi_{\mathrm{m},\,k}}{L_q}\,\omega_{\mathrm{e},\,k})\,T_\mathrm{s} \\ R_{\mathrm{s},\,k} \\ \Psi_{\mathrm{m},\,k} \\ U_{dead,\,k} \end{bmatrix}\ , \tag{3.114}$$

where the stator resistance and the permanent magnet flux linkage are still employed as the to be estimated parameters.

3.6.2 EKF and DEKF based estimator

3.6.2.1 Dual Extended Kalman Filter

The dual extended Kalman filter is a further development of EKF for the simultaneous state and parameter estimation [80]. It has two separate filters running concurrently, which divides

the estimation problem of a nonlinear system into two separate, less strongly nonlinear problems [192]. Moreover, DEKF provides the possibility to switch off the parameter estimator, which could consequently increase the performance of the state estimation and reduce the computational burden. For the online parameter estimation problem of PMSM, two concurrent filters are implemented, a state filter that estimates the current dynamics, and a parameter filter that estimates two electrical parameters of interest as well as the VSI nonlinearity U_{dead}. The working principle of DEKF is illustrated in Fig. 3.45. The system model of DEKF for the

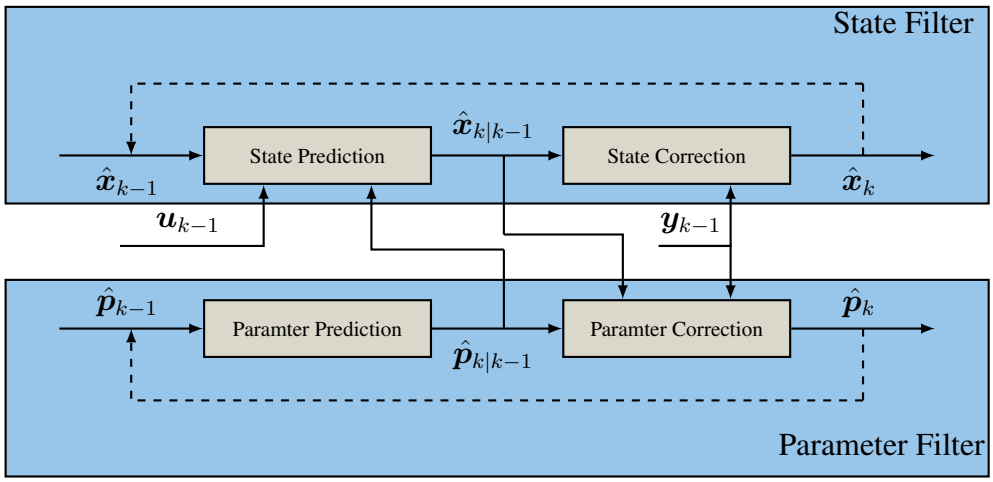

Figure 3.45: Structure of a dual extended Kalman filter.

parameter identification problem of PMSM is given as

$$\begin{aligned} \boldsymbol{x}_{k+1} &= F_k(\boldsymbol{x}_k,\, \boldsymbol{p}_k,\, \boldsymbol{u}_k) + \boldsymbol{w}_{x,\,k}\ , \\ \boldsymbol{p}_{k+1} &= \boldsymbol{p}_k + \boldsymbol{w}_{p,\,k}\ , \\ \boldsymbol{y}_k &= H(\boldsymbol{x}_k) + \boldsymbol{v}_k\ , \end{aligned} \tag{3.115}$$

where $\boldsymbol{x} := \left(i_d,\, i_q\right)^T$ and $\boldsymbol{p} := \left(p_1,\, p_2,\, U_{dead}\right)^T$. Analogous to EKF, each filter of DEKF computes the results in two steps [193]. The principle of the DEKF is shown in Algorithm 3.3. where

$$\boldsymbol{F}_{x,\,k-1} = \frac{\partial F(\hat{\boldsymbol{x}}_{k-1|k-1},\, \hat{\boldsymbol{p}}_{k|k-1}, \boldsymbol{u}_{k-1})}{\partial \hat{\boldsymbol{x}}}\ , \quad \boldsymbol{H}_{x,\,k} = \frac{\partial H(\hat{\boldsymbol{x}}_{k|k-1})}{\partial \hat{\boldsymbol{x}}}\ .$$

Furthermore, $\boldsymbol{R}_x = \boldsymbol{R}_p$, since the same output vector is used. $\boldsymbol{Q}_x$ and $\boldsymbol{Q}_p$ denote the covariances of $\boldsymbol{w}_{x,\,k}$ and $\boldsymbol{w}_{p,\,k}$, respectively. $\boldsymbol{H}_{p,\,k} = \mathrm{d}H(\hat{\boldsymbol{x}}_{k|k-1})/\mathrm{d}\hat{\boldsymbol{p}}$ is the complete derivative of the parameters respected to the output function. The calculation of $\boldsymbol{H}_{p,\,k}$ uses the recurrent derivatives since the output function H is only a function of system states $\boldsymbol{x}$. The complete computation of $\boldsymbol{H}_{p,\,k}$ is given in (3.116).

$$\begin{aligned} \boldsymbol{H}_{p,\,k} &= \frac{\mathrm{d}H(\hat{\boldsymbol{x}}_{k|k-1})}{\mathrm{d}\hat{\boldsymbol{p}}} = \frac{\partial H(\hat{\boldsymbol{x}}_{k|k-1})}{\partial \hat{\boldsymbol{p}}} + \frac{\partial H(\hat{\boldsymbol{x}}_{k|k-1})}{\partial \hat{\boldsymbol{x}}} \frac{\mathrm{d}\hat{\boldsymbol{x}}_{k|k-1}}{\mathrm{d}\hat{\boldsymbol{p}}}\ , \\ \frac{\mathrm{d}\hat{\boldsymbol{x}}_{k|k-1}}{\mathrm{d}\hat{\boldsymbol{p}}} &= \frac{\partial F(\hat{\boldsymbol{x}}_{k-1|k-1},\, \hat{\boldsymbol{p}}_{k-1|k-1},\, \boldsymbol{u}_{k-1})}{\partial \hat{\boldsymbol{p}}} + \frac{\partial F(\hat{\boldsymbol{x}}_{k-1|k-1},\, \hat{\boldsymbol{p}}_{k-1|k-1},\, \boldsymbol{u}_{k-1})}{\partial \hat{\boldsymbol{x}}} \frac{\mathrm{d}\hat{\boldsymbol{x}}_{k-1|k-1}}{\mathrm{d}\hat{\boldsymbol{p}}}\ , \\ \frac{\mathrm{d}\hat{\boldsymbol{x}}_{k-1|k-1}}{\mathrm{d}\hat{\boldsymbol{p}}} &= \frac{\mathrm{d}\hat{\boldsymbol{x}}_{k-1|k-2}}{\mathrm{d}\hat{\boldsymbol{p}}} - \boldsymbol{K}_{x,\,k-1} \frac{\mathrm{d}H(\hat{\boldsymbol{x}}_{k-1|k-2})}{\mathrm{d}\hat{\boldsymbol{p}}}\ . \end{aligned} \tag{3.116}$$

Algorithm 3.3 Dual Extended Kalman Filter

Input: $\hat{\boldsymbol{x}}_{k-1}$, $\hat{\boldsymbol{p}}_{k-1}$, $\boldsymbol{P}_{x,\,k-1}$, $\boldsymbol{P}_{p,\,k-1}$, $\boldsymbol{u}_{k-1}$, $\boldsymbol{y}_k$
Output: $\hat{\boldsymbol{x}}_k$, $\hat{\boldsymbol{p}}_k$, $\boldsymbol{P}_{x,\,k}$, $\boldsymbol{P}_{p,\,k}$

Initialization:

$$\hat{\boldsymbol{x}}_0 = E[\boldsymbol{x}_0]\ ,$$
$$\boldsymbol{P}_0 = E[(\boldsymbol{x}_0 - \hat{\boldsymbol{x}}_0)(\boldsymbol{x}_0 - \hat{\boldsymbol{x}}_0)^T]\ ,$$

Prediction:

$$\hat{\boldsymbol{p}}_{k|k-1} = \hat{\boldsymbol{p}}_{k-1|k-1}$$
$$\boldsymbol{P}_{p,\,k|k-1} = \boldsymbol{P}_{p,\,k-1|k-1} + \boldsymbol{Q}_p$$
$$\hat{\boldsymbol{x}}_{k|k-1} = F(\hat{\boldsymbol{x}}_{k-1|k-1},\ \hat{\boldsymbol{p}}_{k|k-1},\ \boldsymbol{u}_{k-1})$$
$$\boldsymbol{P}_{x,\,k|k-1} = \boldsymbol{F}_{x,\,k-1}\boldsymbol{P}_{x,\,k-1|k-1}\boldsymbol{F}_{x,\,k-1}^T + \boldsymbol{Q}_x$$

Update:

$$\tilde{\boldsymbol{y}}_k = \boldsymbol{y}_k - H(\hat{\boldsymbol{x}}_{k|k-1})$$
$$\boldsymbol{S}_k = \boldsymbol{H}_{x,\,k}\boldsymbol{P}_{x,\,k|k-1}\boldsymbol{H}_{x,\,k}^T + \boldsymbol{R}_x$$
$$\boldsymbol{K}_k = \boldsymbol{P}_{x,\,k|k-1}\boldsymbol{H}_{x,\,k}^T\boldsymbol{S}_k^{-1}$$
$$\hat{\boldsymbol{x}}_{k|k} = \hat{\boldsymbol{x}}_{k|k-1} + \boldsymbol{K}_k\,\tilde{\boldsymbol{y}}_k$$
$$\boldsymbol{P}_{x,\,k|k} = (\boldsymbol{I} - \boldsymbol{K}_k\,\boldsymbol{H}_{x,\,k})\boldsymbol{P}_{x,\,k|k-1}$$
$$\boldsymbol{K}_{p,\,k} = \boldsymbol{P}_{p,\,k|k-1}\boldsymbol{H}_{p,\,k}^T(\boldsymbol{H}_{p,\,k}\boldsymbol{P}_{p,\,k|k-1}\boldsymbol{H}_{p,\,k}^T + \boldsymbol{R}_p)^{-1}$$
$$\boldsymbol{P}_{p,\,k|k} = (\boldsymbol{I} - \boldsymbol{K}_{p,\,k}\boldsymbol{H}_{p,\,k})\boldsymbol{P}_{p,\,k|k-1}$$
$$\hat{\boldsymbol{p}}_{k|k} = \hat{\boldsymbol{p}}_{k|k-1} + \boldsymbol{K}_{p,\,k}\,\tilde{\boldsymbol{y}}_k$$

The EKF and DEKF are then implemented on the embedded system and validated.

3.6.3 Experimental Evaluation

Same as the previous section, the permanent magnet flux linkage Ψ_m and the stator resistance R_s are selected as the to be estimated parameter combination for implementing and validating the proposed parameter estimators. The experimental results of the proposed methods are compared with EKF without VSI-nonlinearities compensation. The superiority of proposed methods is revealed.

3.6.3.1 Performance under Constant Speed

The first test is conducted with the PMSM running at a constant speed. The PMSM run from the standstill until the constant speed at $1000\,\mathrm{rpm}$. The initial values of the online parameter estimators were set to zero. The measurement noise covariance $\boldsymbol{R}$ was selected as identity matrix and the process noise covariance matrix of individual method was set as diagonal matrix such that the diagonal elements were of an order of approximately 10% of the corresponding actual values for the system states, since the system model is more reliable than the real-time measurement. The process noise covariances were further refined via trial-and-error method. The identified results of the parameters are shown in Fig. 3.46.

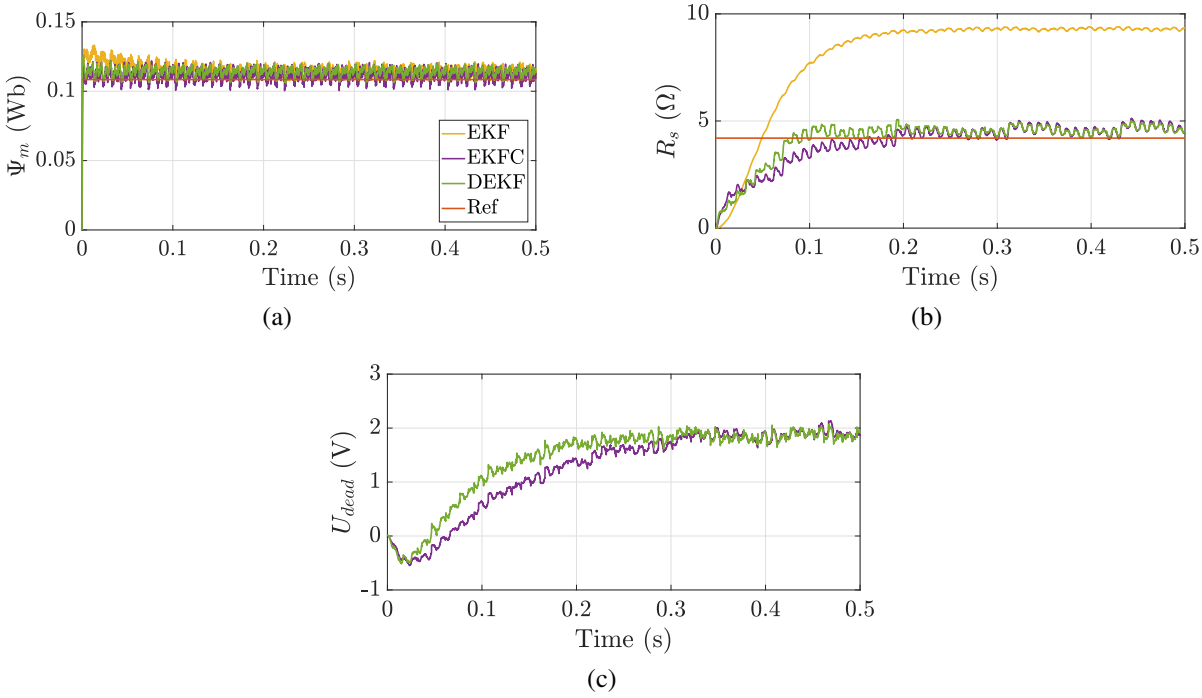

Figure 3.46: Estimated parameters of PMSM with the constant speed. Offline measured value is shown in red. EKF without VSI-nonlinearity compensation is in purple. EKF with VSI-nonlinearity consideration is presented in green and denoted with EKFC. DEKF is shown in blue. (a) The estimated stator resistance $\hat{R}_\mathrm{s}$. (b) The estimated permanent flux linkage $\hat{\Psi}_\mathrm{m}$. (c) The estimated VSI nonlinearities $\hat{U}_{dead}$.

As it is shown in Fig. 3.46, EKF without VSI nonlinearity compensation with an estimated resistance value of $9.5428\,\Omega$ has magnificent offset at the steady state from the nominal value $4.2\,\Omega$ ($4.35\,\Omega$ from the offline measurement). The estimated stator resistance of EKF with compensation ($4.6751\,\Omega$) and the estimated value of DEKF ($4.4457\,\Omega$) are much more accurate, where DEKF is slightly better than EKF with compensation. The convergence speeds of EKF with compensation and DEKF are almost the same. The slight differences can be observed at the steady state of estimation results of Ψ_m in Fig. 3.46, where DEKF delivers the value $0.1129\,\mathrm{Wb}$, EKF with compensation converges to $0.1155\,\mathrm{Wb}$ and EKF without compensation has the value $0.1138\,\mathrm{Wb}$. However, EKF without compensation shows more overshoot at the beginning of the estimations than EKF with compensation and DEKF. Furthermore, the estimated $\hat{\Psi}_\mathrm{m}$ of DEKF is least noisy. It is conspicuous to be mentioned that the VSI nonlinearities has more impact on the identification of R_s than Ψ_m, which can be explained by the fact that the term $\Psi_\mathrm{m}\,\omega_e$ in the dynamic model of i_q is much larger than the other terms and the voltage level of U_{dead} is similar to that of u_d. The estimation results $\hat{R}_\mathrm{s}$ and $\hat{U}_{dead}$ moreover contain the suppressed noises and harmonics from current measurements. Fig. 3.46 shows that the VSI nonlinearity U_{dead} can be observed simultaneously with electrical parameters by implementing the proposed methods.

3.6.3.2 Performance under Speed Step

Moreover, a speed-step test was also carried out to test the transient performance of the proposed estimators. The PMSM was given a speed step from $500\,\mathrm{rpm}$ to $1000\,\mathrm{rpm}$ at the time instant $t = 0.25\,\mathrm{s}$. The estimation results are shown in Fig. 3.47. As it is shown in Fig. 3.47, EKF

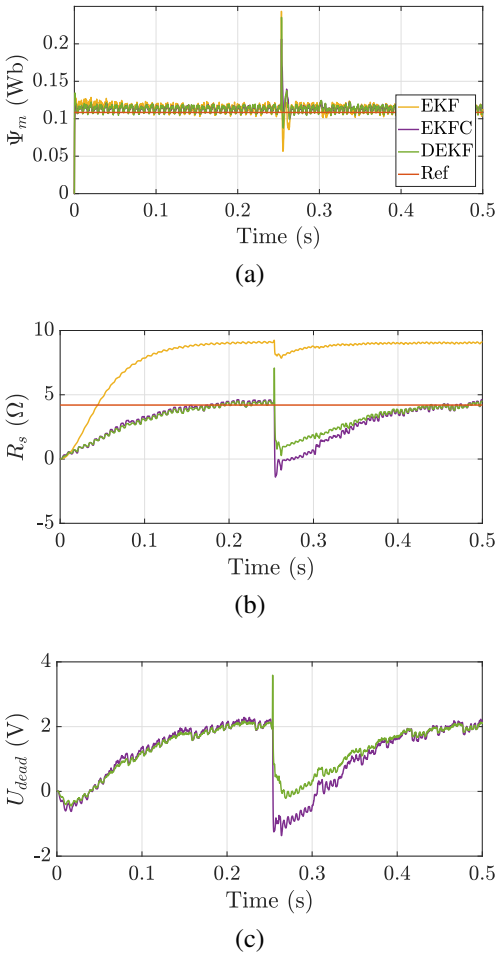

Figure 3.47: Estimated parameters of PMSM with the speed-step profile. (a) The estimated stator resistance $\hat{R}_\mathrm{s}$. (b) The estimated permanent flux linkage $\hat{\Psi}_\mathrm{m}$. (c) The estimated value of the VSI nonlinearity $\hat{U}_{dead}$.

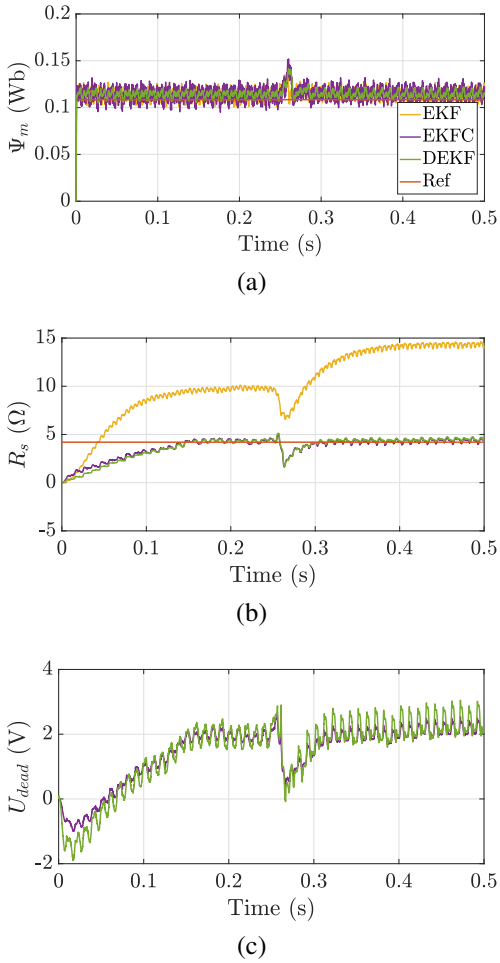

Figure 3.48: Estimation results for PMSM tested with the load-step profile. (a) The estimated stator resistance $\hat{R}_\mathrm{s}$. (b) The estimated permanent flux linkage $\hat{\Psi}_\mathrm{m}$. (c) The estimated VSI nonlinearity $\hat{U}_{dead}$.

without compensation converges after the speed step within $80\,\mathrm{ms}$, while the proposed EKF with compensation and DEKF reached the new steady state within $200\,\mathrm{ms}$, which may result from the parameter tuning of the estimators. Comparing to EKF with compensation, DEKF has less overshoot during the transient. Besides, EKF without compensation reacted faster than the proposed methods, but the estimation result $\hat{R}_\mathrm{s}$ ($9.4783\,\Omega$) still lies far from the nominal value. The actual value of R_s stays constant during the speed test, since the speed test lasts only a short time, so that the temperature of the PMSM remains constant. Otherwise, the temperature model should be involved. From the Fig. 3.47, it can be seen that similar to the constant speed test the estimation results from the three estimators have just slight differences. They all converge to the new steady state within a relatively short time. However, DEKF has the least overshoot during the transient.

3.6.3.3 Performance under Load Step

Furthermore, the proposed methods and EKF without VSI nonlinearity compensation were tested with a load-step profile. 50% of the rated torque was added at $t = 0.25\,\mathrm{s}$ to the PMSM under test. The parameters of estimators are so selected that the element of the covariance matrix respecting to the U_{dead} is relatively larger, since the load step would cause an increase of currents and has larger influence on the VSI nonlinearity than the electrical parameters. The corresponding experimental results are shown in Fig. 3.48.

It can be concluded from Fig. 3.48b and Fig. 3.48c that the load step accelerates the convergence speed for observing the stator resistance $\hat{R}_\mathrm{s}$ and VSI nonlinearity $\hat{U}_{dead}$. However, the load step results in an even larger steady-state error of estimation results from EKF without compensation. It can be elucidated by the fact that the VSI nonlinearities vary with the operation points, especially with the currents. However, the relationship between the VSI nonlinearities and the currents is nonlinear, which has been studied in former sections. A load step will introduce a current change and further influence the VSI nonlinearities. Moreover, the corresponding offline measured characteristics of L_d and L_q need to be implemented into the estimation process. The proposed two estimators are robust to the load step of the PMSM.

3.6.3.4 Estimation Accuracy

The summarization of the estimation results from the experiments are shown in Table 3.5, Fig. 3.49 and Fig. 3.50. The results presented in Table 3.5 are the mean value of the steady-state values after changes, i.e. the results of the speed-step test and the load-step test are collected at the steady state after the step. Fig. 3.49 and Fig. 3.50 present the errors of the proposed methods and EKF without compensation, where the mean error and the root-mean-square-error are computed correspondingly and respectively presented. To visualize the errors of the estimation methods, the absolute value of the mean error and the RMSE are computed and plotted in Fig. 3.49 and Fig. 3.50, respectively.

Table 3.5: Mean value of the estimation results at the steady state

	R_s (Ω)			Ψ_m (Wb)		
	Constand speed	Speed step	Load step	Constand speed	Speed step	Load step
EKF	9.5428	9.4783	13.7050	0.1133	0.1130	0.1147
EKFC	4.6751	4.3853	4.3670	0.1136	0.1145	0.1144
DEKF	4.4457	4.4936	4.4906	0.1135	0.1143	0.1143

The identification results of the three methods on permanent magnet flux linkage Ψ_m are very similar. However, slight differences can be observed in the figures. For estimating Ψ_m, EKF without compensation performs slightly better than the EKF with compensation and DEKF considering the mean error under the constant-speed and the speed-step condition, which can be concluded from Fig. 3.49a. The mean value of DEKF is most accurate under the load-step condition. It is shown in Fig. 3.50a that DEKF is less disturbed than the other two methods at the constant-peed and load-step test, while EKF with compensation performs the best at the

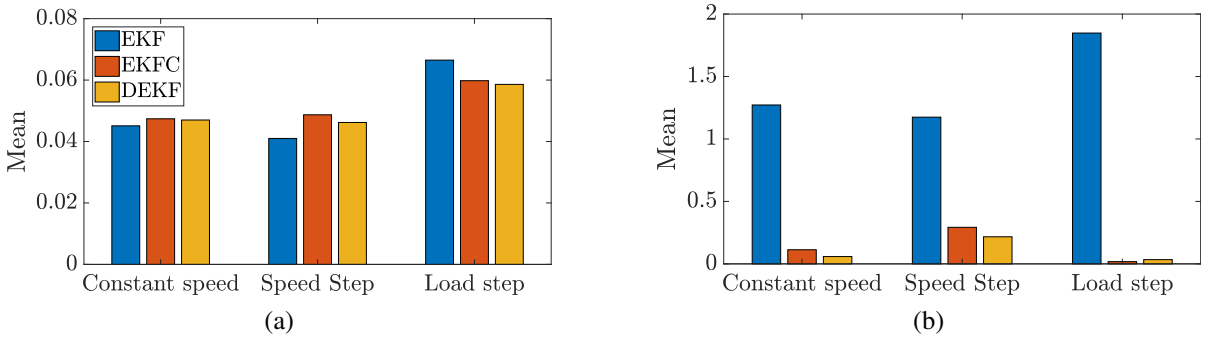

Figure 3.49: The absolute value of the mean error for estimated parameters. (a) The absolute mean error of the estimated Ψ_{m}. (b) The absolute mean error of the estimated R_{s}.

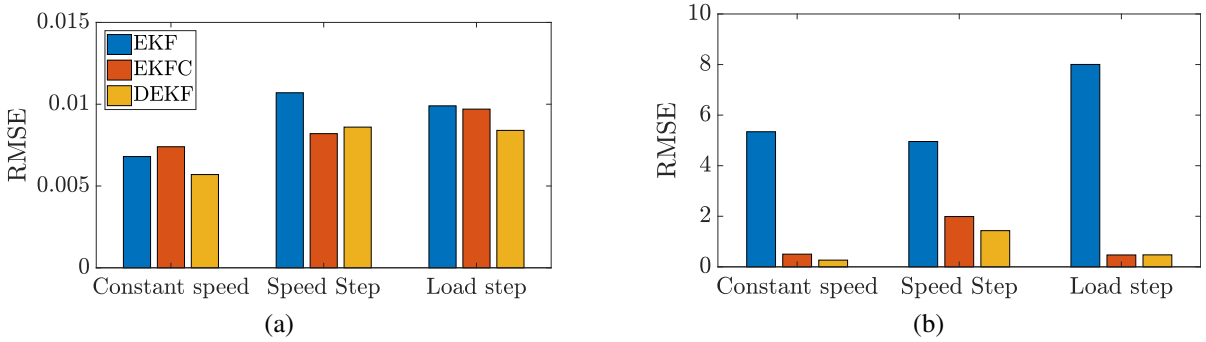

Figure 3.50: The root mean squared error (RMSE) of the estimated results. (a) The absolute mean error of the estimated Ψ_{m}. (b) The absolute mean error of the estimated R_{s}.

speed-step test. It is worth mentioning that since no filter for the measured currents nor for the measured speed was deployed, the noises and the harmonics of the speed and the current would affect the results. Although the Kalman filter is able to weaken the influence of noises, the ability is limited to a certain level. Therefore, the mean values of the estimated results from the proposed methods are close to the nominal values, but fluctuations on the trajectories of estimations can be evidently observed. An obvious improvement by implementing proposed methods for estimating stator resistance R_{s} is presented in Fig. 3.49b and Fig. 3.50b. Moreover, the estimation result of DEKF is less noisy than that of EKF with compensation, which can be concluded from Fig. 3.50b.

3.6.3.5 Sensitivity to Initial Values

The Kalman-filter-based parameter estimators depend on the estimations from previous steps and the extended Kalman filter linearises the system propagation function. Therefore, the initial value of the estimators are essential for the convergence of the estimated values. In this section, the proposed methods are tested with the same experimental data as in the constant-speed test, but the initial guesses of parameters are altered. The initial value of the system states in estimators is shown as a percentage of the nominal values and presented with various colours in Fig. 3.51 and Fig. 3.52.

Fig. 3.51 and Fig. 3.52 show the results of EKF with compensation and dual EKF running with six different initial guesses, which vary from 0% to 200% with an interval of 40% of the

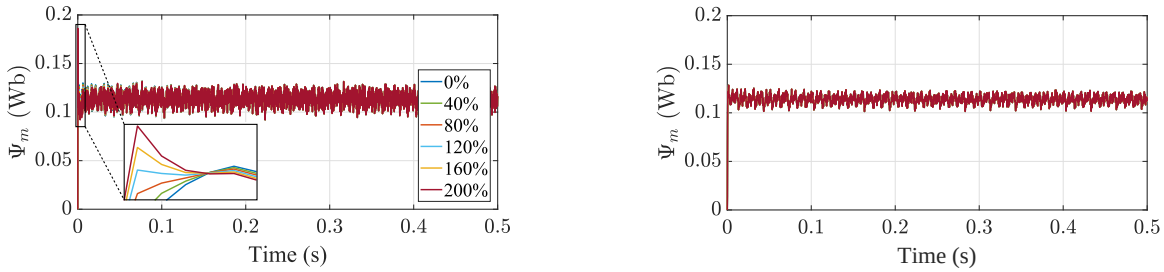

Figure 3.51: Initial value sensitivity test of EKF with compensation and dual EKF for estimating the permanent magnet flux linkage Ψ_m. (a) The estimated permanent magnet flux linkage $\hat{\Psi}_\mathrm{m}$ by EKF with compensation for various different initial values. (b) The estimated permanent magnet flux linkage $\hat{\Psi}_\mathrm{m}$ by dual EKF for various different initial values.

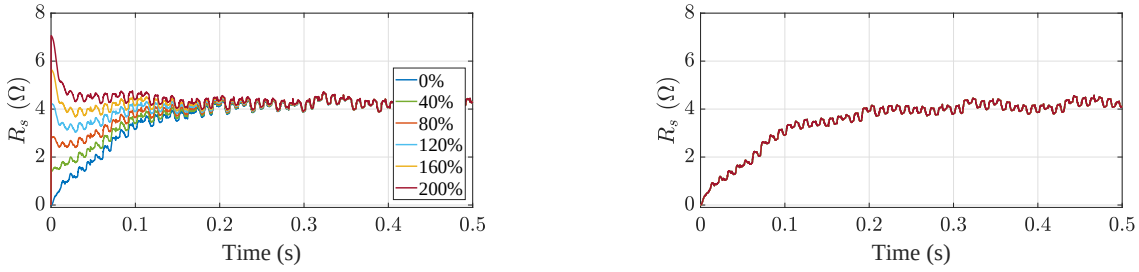

Figure 3.52: Initial value sensitivity test of EKF with compensation and dual EKF for estimating the stator resistance R_s. (a) The estimated stator resistance R_s by EKF with compensation for various different initial values. (b) The estimated stator resistance R_s by dual EKF for various different initial values.

nominal values, respectively. The estimation on R_s is more affected by the initial values than the estimation on Ψ_m. The steady-state values are not affected by the initial value, but the convergence speeds are heavily influenced, i.e. the EKF with compensation converges faster, if the initial condition is closer to the real value. A similar phenomenon can be observed at estimating Ψ_m. However, DEKF is robust to the initial value variation, which can be concluded from the Fig. 3.51b and the Fig. 3.52b. The trajectories of estimating R_s and Ψ_m with various initial values overlap with each other.

3.6.3.6 Computational Cost

The computational cost of the three estimation methods is compared based on the execution times, i.e. the average execution time, the maximal execution time as well as the minimal execution time. The algorithms run on a Renesas SH7750R with an internal clock 240 MHz, as it is shown in Appendix B.1. The execution times are summarized in Table 3.6.

EKF without compensation is the fastest algorithm, since the dimension of the state vector and of the covariance matrix in this algorithm is the least. DEKF is the slowest. Besides, the computation of $\boldsymbol{H}_{p,\,k}$ in DEKF is complicated and the computation results need to be stored for the next step. However, due to the features of DEKF, the parameter filter can be deactivated at the steady state, which will significantly reduce the computational effort.

Table 3.6: Execution time

Algorithm	Execution time		
	Average	Maximal	Minimal
EKF	18.8 µs	21 µs	18 µs
EKFC	29.1 µs	39 µs	27 µs
DEKF	32 µs	43 µs	30 µs

3.6.3.7 Conclusions

In this section two general formulations of Kalman-filter-based online parameter estimators are proposed. By including the VSI nonlinearity as a system state into the PMSM current model, the accuracy of estimation results was significantly improved. An obvious improvement can be observed at identifying the stator resistance. Furthermore, the proposed methods are more robust to the noises than the conventional EKF estimator. The proposed EKF-based estimator has less computational effort compared to the proposed DEKF-based estimator, but the convergence speed of it is more sensitive to the initial guesses. DEKF-based estimator is robust to the initial value of states and has better performance in terms of the quality of estimation results. Moreover, it is possible to deactivate the parameter filter of DEKF, which can significantly reduce the computational burden.

3.7 Summary

The varying conditions of PMSM impair the performance of the controllers or even cause machine instability, which has been discussed in previous chapter. In this chapter, the observability of the PMSM is firstly examined, where the observability matrix derived from local observability theory for the nonlinear system is verified. Several conclusions can be drawn after the examination, e.g. the identifiability of the parameter combinations is related to the operating points, up to two electrical parameters can be simultaneously identified if no persistence excitement is applied. Furthermore, the offline determination procedures for the individual electrical parameters are introduced. The corresponding experimental results for the PMSMs in Appendix B.1 are presented and discussed. Subsequently, the methods with the current injection, which are normally utilised at the start-up or also online, are introduced, where two variants, namely with square-wave current injection and with sinusoidal current injection, are presented and compared with corresponding experimental results. The square-wave current injection method can achieve less noisy identification results, while the sinusoidal current injection method converges faster and can capture the transient of the PMSM. Nonetheless, the current injection method may affect the control performance of PMSM and cause pulsation. A promising way to overcome these problems is to implement an online electrical parameter estimator. In this chapter, five online estimation methods are presented and compared, namely RLS, MRAS, EKF, UKF and MHE. Generally speaking, a higher computational cost can benefit the estimation results in terms of accuracy. However, the estimation method should be selected based on the requirement of the accuracy and the available computational resources. Moreover, their advantages

and disadvantages have also been concluded and summarized in this chapter. The nonlinear effects of VSI have a great impact on the estimation results, since instead of the real terminal voltage the command voltage is normally employed for the estimation. Therefore, an estimation model including the VSI nonlinearities is investigated. Two estimators are proposed to eliminate the influence of the VSI nonlinearities. Their effectiveness has been verified with experimental results.

Part III

CONTROLLER OPTIMIZATION

CHAPTER 4

Continuous-Control-Set Model Predictive Control

4.1 Introduction

The utilization of predictions can achieve high-performance control, which meanwhile is able to complete complex tasks and ensures the satisfaction of the operational constraints for various applications. By reason that the control approaches are deployed on an embedded system and computed in a discrete-time manner, the underlying finite-horizon predictive control problem with the corresponding constraints creates a sequence of inputs by formulating and solving the optimization problem N_p steps into the future. The optimization problem is called constrained finite time optimal control and N_p is its prediction horizon. This control method has gained significant popularity in the area of power electronics and electrical drives during the last decades and has been comprehensively studied in the literature [194–196], to name but a few. The optimal control and the optimal estimation, e.g. the estimation procedure mentioned in previous chapter, can be regarded as dual problems [146]. For the LTI system the Kalman filter is normally applied for estimation and the linear quadratic regulator (LQR) is used as the controller. Both of them are propagated by the Riccati recursion. More specifically, the Riccati recursion of LQR runs backwards and the one of Kalman filter runs forward. Many similarities can be observed between the moving horizon estimator and the model predictive control. However, the duality relationship between them are more complicated because of the constraints and system dynamics. Different from the Lagrangian duality, which is introduced in Section 2.3, duality in system theory is more vague and indicates that a estimation problem can be interpreted as a control problem. The ultimate goal of the optimal control is to find a control law that minimizes certain objectives over an infinite horizon, which furthermore subjects to the system model and the constraints. Normally, the objective of the model predictive control is defined as a quadratic function by

$$J(\boldsymbol{x}, \boldsymbol{u}) = \sum_{k=0}^{\infty} \|\boldsymbol{x}_k\|^2_{\boldsymbol{Q}_k} + \sum_{k=0}^{\infty} \|\boldsymbol{u}_k\|^2_{\boldsymbol{R}_k} \,, \tag{4.1}$$

where $\boldsymbol{Q}$ and $\boldsymbol{R}$ are the weighting matrices served for the objective design. In some applications, the $\mathcal{L}_1$ or $\mathcal{L}_\infty$ norm is also utilized. Analogously to the MHE, the infinite control horizon problem can be transformed by an equivalent finite control horizon problem as

$$\begin{aligned} \min_{\mathbf{U}} \quad & J = \sum_{k=0}^{N-1} \|\boldsymbol{x}_k\|^2_{\boldsymbol{Q}_k} + \sum_{j=0}^{N} \|\boldsymbol{u}_k\|^2_{\boldsymbol{R}_k} + J_t \\ \text{s. t.} \quad & \boldsymbol{x}_{j+1} = F(\boldsymbol{x}_j,\, \boldsymbol{p}_j,\, \boldsymbol{u}_j) + \boldsymbol{w}_j \,, \\ & \boldsymbol{x}_j \in \mathbb{X}_j \,, \\ & \boldsymbol{u}_j \in \mathbb{U}_j \,, \end{aligned} \tag{4.2}$$

where J_t denotes the terminal cost. In [197], an approximation of the terminal cost J_t is proposed to guarantee the asymptotic stability for the linear system without disturbances, which assumes that the system can be controlled with a LQR afterwards. The corresponding approximated terminal cost is given as

$$J_t = \|\boldsymbol{x}_N\|^2_{\boldsymbol{P}_N} \,, \tag{4.3}$$

where $\boldsymbol{P}_N$ denotes the solution to the corresponding LQR discrete Riccati equation. As it is introduced in Section 2.3, the receding horizon policy is applied in MPC, where only the first element of the optimal control input sequence is applied. At next sampling time, the underlying CFTOC is repeatedly solved with the updated measurements over the shifted time window.

4.2 Continuous-Control-Set Model Predictive Control

Based on the fundamental knowledge of MPC, a widely applied control method, i.e. continuous-control-set model predictive control, is introduced as follows. The CCS-MPC specifies the constraints as convex, which include the state constraints as well as the input constraints. The computed solutions are further fed into the modulator, which generates the switching signals via PWM or SVM, which is introduced in Section 2.2. In this section, the classic CCS-MPC for PMSM current control is investigated, including the set-up of the control problem, the constraints, the solving of the optimization problem and the implementation.

4.2.1 Control Problem

The control problem of the current control for a PMSM can be formulated in the dq reference frame as well as in the $\alpha\beta$ reference frame. In this section, the formulation in the dq reference frame is introduced, since it has been deployed in most applications. The objective of the current control problem is to manipulate the three-phase voltage of the PMSM such that the stator currents precisely track the predefined reference values. The reference value for the inner loop, i.e. the current control loop, is determined normally by the outer control loops, if a cascaded control structure is deployed. Meanwhile, the output voltage is restricted by penalizing the voltage value with a weighting factor. The current controller predicts the system behaviour based on the system model given in the Section 4.2.2 and the most recent measurements of the current. The optimization problem is so designed that the object function, the system model and the constraints are included. A special case of the CCS-MPC is the so-called deadbeat

control, where the prediction horizon is limited to one and the constraints of the optimization problem are omitted. Moreover, the penalization on the control input voltage is also disregarded. Therefore, the deadbeat control can realize zero steady-state error under the condition that the investigated system model is error-free. Furthermore, it has the advantages such like minimum rise time and minimum settling time. However, the control input voltage is relatively high without the corresponding penalization.

4.2.2 System Model

The conventional CCS-MPC for PMSM is set up in the dq reference frame, in order to simplify the control problem. Recall the system model of the current control loop in the continuous-time domain can be obtained as

$$\begin{bmatrix} \frac{\mathrm{d}}{\mathrm{dt}} i_d \\ \frac{\mathrm{d}}{\mathrm{dt}} i_q \end{bmatrix} = \begin{bmatrix} -\frac{R_\mathrm{s}}{L_d} & \frac{L_q}{L_d}\,\omega_\mathrm{e} \\ -\frac{L_d}{L_q}\,\omega_{\mathrm{e},k} & -\frac{R_\mathrm{s}}{L_q} \end{bmatrix} \begin{bmatrix} i_d \\ i_q \end{bmatrix} + \begin{bmatrix} \frac{1}{L_d} & 0 \\ 0 & \frac{T_\mathrm{s}}{L_q} \end{bmatrix} \begin{bmatrix} u_d \\ u_q \end{bmatrix} + \begin{bmatrix} 0 \\ -\frac{\Psi_\mathrm{m}}{L_q}\,\omega_\mathrm{e} \end{bmatrix} . \tag{4.4}$$

The continuous model in (4.4) can be further discretized via the methods mentioned in Section 2.3.4.2. In this thesis, the Euler method is deployed, since the sampling frequency is relatively high and the discrete-time model via the Euler method is usually sufficiently accurate [24]. The discrete model of the current loop for PMSM in (4.4) at $t = k\,T_\mathrm{s}$ can be given as

$$\begin{bmatrix} i_{d,\,k+1} \\ i_{q,\,k+1} \end{bmatrix} = \begin{bmatrix} 1 - \frac{R_\mathrm{s}}{L_d}\,T_\mathrm{s} & \frac{L_q}{L_d}\,\omega_{e,\,k}\,T_\mathrm{s} \\ -\frac{L_d}{L_q}\,\omega_{e,\,k}\,T_\mathrm{s} & 1 - \frac{R_\mathrm{s}}{L_q}\,T_\mathrm{s} \end{bmatrix} \begin{bmatrix} i_{d,\,k} \\ i_{q,\,k} \end{bmatrix} + \begin{bmatrix} \frac{T_\mathrm{s}}{L_d} & 0 \\ 0 & \frac{T_\mathrm{s}}{L_q} \end{bmatrix} \begin{bmatrix} u_{d,\,k} \\ u_{q,\,k} \end{bmatrix} + \begin{bmatrix} 0 \\ -\frac{\Psi_\mathrm{m}}{L_q}\,\omega_{e,\,k}\,T_\mathrm{s} \end{bmatrix} \tag{4.5}$$

For the purpose of compactness, the discrete-time system model is written as

$$\begin{aligned} \boldsymbol{x}_{k+1} &= \boldsymbol{A}_k\,\boldsymbol{x}_k + \boldsymbol{B}_k\,\boldsymbol{u}_k + \boldsymbol{E}_k \\ \boldsymbol{y}_k &= \boldsymbol{C}_k\,\boldsymbol{x}_k \end{aligned} \tag{4.6}$$

where $\boldsymbol{x} = [i_d,\, i_q]^T$, $\boldsymbol{u} = [u_d,\, u_q]^T$ and $\boldsymbol{y} = [i_d,\, i_q]^T$.

4.2.3 Optimization Problem

The current control problem with CCS-MPC at the time step k can be generally regarded as a tracking problem and mapped into the cost function. Including the system constraints, the resulting optimization problem for the current control $\mathcal{P}_c$ is then given in the following

$$\begin{aligned} \min_{\mathbf{U}_k} \quad & J = \sum_{j=k}^{k+N_p-1} \|\boldsymbol{y}_r - \boldsymbol{C}\,\boldsymbol{x}_{j+1}\|^2_{\boldsymbol{Q}} + \sum_{j=k}^{k+N_p-1} \|\boldsymbol{u}_j\|^2_{\boldsymbol{R}} \\ \text{s. t.} \quad & \boldsymbol{x}_{j+1} = \boldsymbol{A}_j\,\boldsymbol{x}_j + \boldsymbol{B}_j\,\boldsymbol{u}_j + \boldsymbol{E}_j\,, \quad j = k,\, k+1\,\cdots,\, k+N_p-1\,, \\ & \boldsymbol{x}_j \in \mathbb{X}_j\,, \\ & \boldsymbol{u}_j \in \mathbb{U}_j\,, \end{aligned} \tag{4.7}$$

where $\boldsymbol{y}_r$ denotes the target reference. N_p is the prediction horizon. The first term of the cost function quadratically penalizes the prediction error over the prediction horizon. The second term penalizes the output effort. $\boldsymbol{Q}$ and $\boldsymbol{R}$ are weighting matrices that adjust the trade-off between the tracking accuracy and the output voltage. $\mathbb{X}_j$ and $\mathbb{U}_j$, which denote the constraints on the system states and the control inputs respectively, are omitted, since they are not really violated during the simulation and the experiment. The computation result with a given initial state $\boldsymbol{x}_k$ is a control sequence $\mathbf{U}_k := [\boldsymbol{u}_k^T,\, \boldsymbol{u}_{k+1}^T,\, \ldots,\, \boldsymbol{u}_{k+N_p-1}^T]^T$, i.e.

$$\begin{aligned} \mathbf{U}_k \quad &:= \arg\min_{\mathbf{U}_k} J \,, \\ \text{s. t.} \quad &\boldsymbol{x}_{j+1} = \boldsymbol{A}_j\, \boldsymbol{x}_j + \boldsymbol{B}_j\, \boldsymbol{u}_j + \boldsymbol{E}_j \,, \quad j = k,\, k+1 \cdots,\, k+N_p-1 \,. \end{aligned} \tag{4.8}$$

By employing the receding horizon policy the first element of $\mathbf{U}_k$, i.e. $\boldsymbol{u}_k$, will be applied to the system. As a special case of MPC, the deadbeat control omits the system states limitation $\mathbb{X}_j$ and the constraint on the control inputs $\mathbb{U}_j$ in (4.7). Moreover the penalization on control input is also excluded. Therefore, the deadbeat control has the advantage of simpleness as well as low computational burden at the sacrifice of the stability and the control performance.

The optimal control voltage is obtained by solving the optimization problem $\mathcal{P}_c$ in (4.7). The solution depends on the the most recent measurement, the previous solution and the eventual current reference. Normally, the current reference value is regarded as constant over the prediction horizon.

4.2.4 Implementation

After the optimization problem $\mathcal{P}_c$ in (4.7) is designed, it is then implemented on the digital control platform to realize the control of the PMSM drive system. As introduced previously, there are many efficient numerical methods to solve the optimization problem. The solving of the problem $\mathcal{P}_c$ is relatively simple, since the constraints except the system dynamics are omitted. The propagation of the system state $\boldsymbol{x}$ at the time step j can be given as a function of initial values $\boldsymbol{x}_k$ and the control sequence $\mathbf{U}$ as follows

$$\boldsymbol{x}_{j+1} = \boldsymbol{A}^{j+1-k}\, \boldsymbol{x}_k + [\boldsymbol{A}^{j-k}\boldsymbol{B},\, \cdots,\, \boldsymbol{B}]\, \mathbf{U} + \sum_{i=0}^{j-k} \boldsymbol{A}^i\, \boldsymbol{E} \,. \tag{4.9}$$

Let $\boldsymbol{Y}$ denote the sequence of the outputs over the prediction horizon N_p from the step k, i.e. $\boldsymbol{Y} := [\boldsymbol{y}_{k+1}^T,\, \cdots,\, \boldsymbol{y}_{k+N_p}^T]^T$. It can be written as

$$\boldsymbol{Y} = \boldsymbol{\Pi}\, \boldsymbol{x}_n + \boldsymbol{\Lambda}\, \mathbf{U} + \boldsymbol{\Sigma} + \boldsymbol{\Omega}\, \hat{\boldsymbol{\varepsilon}}_n \,, \tag{4.10}$$

where

$$\boldsymbol{\Pi} = \begin{pmatrix} \boldsymbol{CA} \\ \boldsymbol{CA}^2 \\ \vdots \\ \boldsymbol{CA}^{N_p} \end{pmatrix},\, \boldsymbol{\Lambda} = \begin{pmatrix} \boldsymbol{CB} & 0 & \ldots & 0 \\ \boldsymbol{CAB} & \boldsymbol{CB} & \ddots & 0 \\ \vdots & \vdots & \ddots & \vdots \\ \boldsymbol{CA}^{N_p-1}\boldsymbol{B} & \boldsymbol{CA}^{N_p-2}\boldsymbol{B} & \ldots & \boldsymbol{CB} \end{pmatrix}, \boldsymbol{\Sigma} = \begin{pmatrix} \boldsymbol{CE} \\ \boldsymbol{CAE} + \boldsymbol{CE} \\ \vdots \\ \sum_{i=0}^{N_p-1} \boldsymbol{CA}^i\, \boldsymbol{E} \end{pmatrix} . \tag{4.11}$$

By substituting (4.10) into the cost function J, the solution to the CFTOC problem $\mathcal{P}_c$ can be obtained by solving the root finding problem as

$$\nabla_{\mathbf{U}} J = \mathbf{0} \, . \tag{4.12}$$

The solution $\mathbf{U}$ can be simply obtained as

$$\mathbf{U} = \left(\boldsymbol{\Lambda}^T \, \mathcal{Q} \, \boldsymbol{\Lambda} + \mathcal{R}\right)^{-1} \boldsymbol{\Lambda}^T \, \mathcal{Q} \left(\boldsymbol{Y}_r - \boldsymbol{\Pi} \, \boldsymbol{x}_k - \boldsymbol{\Sigma}\right) , \tag{4.13}$$

where $\mathcal{Q} := \boldsymbol{I}^{N_p} \otimes \boldsymbol{Q}$, $\mathcal{R} := \boldsymbol{I}^{N_p} \otimes \boldsymbol{R}$ and $\boldsymbol{Y}_r := \boldsymbol{I}^{N_p} \otimes \boldsymbol{y}_r$. Symbol $\otimes$ denotes the Kronecker product of two matrices. By deploying the receding horizon policy, the control voltage is given as

$$\boldsymbol{u}_k = [\mathbf{1}, \, \mathbf{0}, \cdots , \, \mathbf{0}] \, \mathbf{U} \, . \tag{4.14}$$

The control voltage $\boldsymbol{u}_k$ is then delivered to the modulator and further transformed as the switching signals for the inverter. Besides the aforementioned real-time solution of the optimization problem $\mathcal{P}_c$, the multi-parametric programming [198] can be applied. It solves the optimization problem $\mathcal{P}_c$ offline and therefore transforms the online solving of the optimization problem into a online searching problem. The multi-parametric programming divides the parameter spaces into several convex polytopes, in which a individual piecewise affine control law is contained. However, the offline calculation time and the number of polytopes increase exponentially with the prediction horizon by applying the multi-parametric programming.

4.3 Robust Continuous Control Set MPC

As mentioned previously, the parameter of PMSM drive system is time-varying and diverse disturbances can be encountered during the operation, which deteriorates the performance of the PMSM drive system or even causes instability. For instance, the stator resistance as well as the permanent magnet flux linkage changes with the variation of the temperature and the inductances are related to the currents. More details have been demonstrated in Chapter 2.4. All parameters can have impact on the control performance. However, the identification of all parameters may increase the computational burden significantly. As concluded in [68], various external disturbances, such as the load torque and the measurement errors, are crucial for the control of PMSMs. Moreover, the digital delay is inevitable in the real-time control [199, 200]. The digital delay has a great impact on the control accuracy, especially for the drive system sampled with a relatively low sampling frequency. On the one hand, over- and under-compensation may introduce more errors. On the other hand, the accurate compensation of the digital delay requires additional measurements. In order to tackle these problems, many researches have been carried out to improve the stability and the performance of MPC under the parameter variations and the existence of disturbances. Authors in [201] considered the worst case of the corresponding CFTOC problem and solved the minimization problem with the prerequisite of the worst control condition of the plant, which can be obtained by computing the maximization problem. Therefore, this method is also called min-max MPC. It is designed in order that the controller can maintain stability and meet the specified performance requirement under the existence of disturbances and uncertainties. It means that the controller synthesis must satisfy the given specifications for all possible uncertainty realizations [202]. Other than the min-max

MPC, the satisfaction of the controller synthesis under all possible circumstances can be realized by bounding the disturbance within certain functions or constants [202, 203]. In [203], a Lyapunov-based MPC was proposed, where the stability of PMSM drive system is guaranteed via the additional Lyapunov-function-based constraint. Furthermore, authors in [202] improved its performance by considering the dead time and adjusting the Lyapunov function accordingly. The robust control strategies are comparatively conservative and have to more or less sacrifice the nominal performance so that the overall robustness can be guaranteed. Even though methods are proposed to adjust the control Lyapunov function in real operation [202], which aims to relax their conservatism, the computational burden of the robust control strategies is still one of the main concerns [204]. Besides the robust MPC, other modification of the controller can be also implemented to deal with the disturbances and uncertainties. In [204, 205], an integral mechanism was employed to eliminate the constant or slowly varying disturbance. Besides the direct modification of the controller, the deployment of a disturbance observer can improve the stability as well as the control performance. As indicated in [68], the disturbance estimation and attenuation methods, which can be regarded as a trade-off between the dynamic response and the robustness, provide a promising performance. Many works have implemented disturbance observers to deal with the model uncertainties and the external disturbances. Reference [206] applied an extended state observer for the speed regulation problem of PMSM. Reference [207] employed the fuzzy approach as the torque observer. The selection of the disturbance observers depends on the requirements of the application and the available computational resources. Various disturbance observers have been studied and implemented, the reduced order disturbance observer [208], the proportional disturbance observer [209], the adaptive disturbance observer [63,210], the recursive-least-square-based disturbance observer [211] and the neural-network-based disturbance observer [48], to name but a few.

4.3.1 Control Problem

In order to tackle the aforementioned problems, a generalized observer-based robust control strategy is proposed for the predictive current control of PMSM, aiming to eliminate the influence of the parameter variation and the external disturbances and to track the given reference precisely. The lumped disturbance is estimated by the extended state observer, which is further fed into the current controller with the augmented system model. The control voltage is then computed based on the augmented system model. The overall robust control strategy is illustrated in Fig. 4.1. The robust predictive current control (RPCC) in Fig. 4.1 denotes the observer-based robust control strategy for the current control of the PMSM drive system. The output voltage is given as $\boldsymbol{u}^*$ and the terminal voltage of the PMSM is denoted by $\boldsymbol{u}$. Their difference, i.e. the error voltage, is denoted by $\Delta\boldsymbol{u}$ and defined as $\Delta\boldsymbol{u} = \boldsymbol{u}^* - \boldsymbol{u}$. The system model for the controller as well as for the observer is augmented with the lumped disturbances. The controller predicts the system states based on the estimated values of the current as well as of the disturbance and minimizes the control objectives.

4.3.2 System Model

Different from the model deployed in the predictive current control by CCS-MPC in Section 4.2, the robust predictive current control strategy employs the augmented model including the term

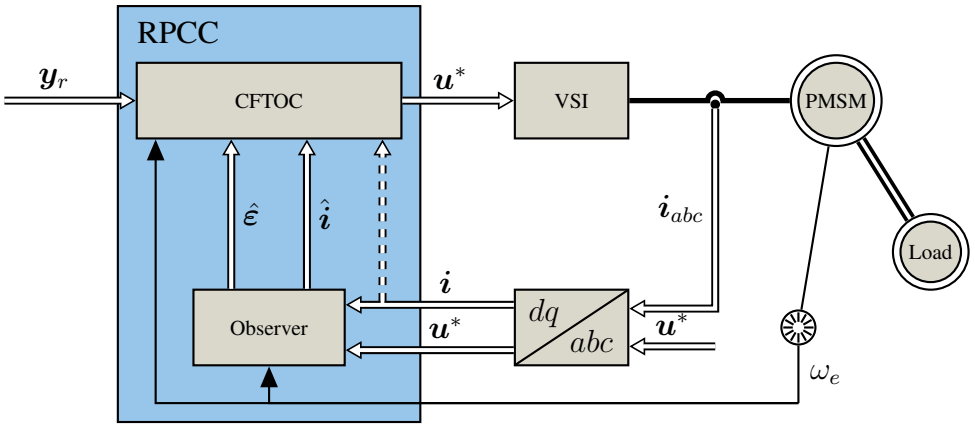

Figure 4.1: The block diagram of the robust CCS-MPC for the PMSM.

of the disturbances. The conventional CCS-MPC utilizes the system model in (4.5) with the command voltage $\boldsymbol{u}^*$ as the control input, since the terminal voltage is normally not measured and is different from the command voltage $\boldsymbol{u}^*$. However, because of the parameter mismatches and the disturbances, the real model of PMSM differs from the ideal model in (4.5). Therefore, the nominal system in (4.5) can be augmented with a lumped disturbance as

$$\begin{bmatrix} i_{d,\,k+1} \\ i_{q,\,k+1} \end{bmatrix} = \begin{bmatrix} 1 - \dfrac{R_\mathrm{s}}{L_d} T_\mathrm{s} & \dfrac{L_q}{L_d} \omega_{e,\,k} T_\mathrm{s} \\ -\dfrac{L_d}{L_q} \omega_{e,\,k} T_\mathrm{s} & 1 - \dfrac{R_\mathrm{s}}{L_q} T_\mathrm{s} \end{bmatrix} \begin{bmatrix} i_{d,\,k} \\ i_{q,\,k} \end{bmatrix} + \begin{bmatrix} \dfrac{T_\mathrm{s}}{L_d} & 0 \\ 0 & \dfrac{T_\mathrm{s}}{L_q} \end{bmatrix} \begin{bmatrix} u^*_{d,\,k} \\ u^*_{q,\,k} \end{bmatrix} + \begin{bmatrix} 0 \\ -\dfrac{\Psi_\mathrm{m}}{L_q} \omega_{e,\,k} T_\mathrm{s} \end{bmatrix} + \begin{bmatrix} \varepsilon_{d,\,k} \\ \varepsilon_{q,\,k} \end{bmatrix} , \tag{4.15}$$

where $\varepsilon_{d,\,k}$ and $\varepsilon_{q,\,k}$ denote the disturbance and unmodeled uncertainties in d- and q-axis, respectively. The system model in (4.15) can be compactly written as

$$\boldsymbol{x}_{k+1} = \boldsymbol{A}_k \, \boldsymbol{x}_k + \boldsymbol{B}_k \, \boldsymbol{u}^*_k + \boldsymbol{E}_k + \boldsymbol{\varepsilon}_k \, , \tag{4.16}$$

where $\boldsymbol{\varepsilon}_k := [\varepsilon_{d,\,k},\, \varepsilon_{q,\,k}]^T$ includes the effects resulted from the parameter variation and the non-periodic disturbances. As it is shown in (4.16), the disturbance term $\boldsymbol{\varepsilon}$ is similar to the term $\boldsymbol{E}$ for the current control, since they are regarded as constant for the system state $\boldsymbol{x}$ at the next time instant.

In order to estimate the disturbances, the augmented system in (4.16) is extended with two more system states, i.e. $\boldsymbol{\varepsilon}_k$, of which the dynamics can be given as $\varepsilon_{d,\,k+1} = \varepsilon_{d,\,k}$ and $\varepsilon_{q,\,k+1} = \varepsilon_{q,\,k}$. Subsequently, the augmented system can be extended and rewritten as

$$\begin{pmatrix} \hat{\boldsymbol{x}}_{k+1} \\ \hat{\boldsymbol{\varepsilon}}_{k+1} \end{pmatrix} = \begin{pmatrix} \boldsymbol{A}_k & \boldsymbol{I} \\ \boldsymbol{0} & \boldsymbol{I} \end{pmatrix} \begin{pmatrix} \hat{\boldsymbol{x}}_k \\ \hat{\boldsymbol{\varepsilon}}_k \end{pmatrix} + \begin{pmatrix} \boldsymbol{B}_k \\ \boldsymbol{0} \end{pmatrix} \boldsymbol{u}^*_k + \begin{pmatrix} \boldsymbol{E}_k \\ \boldsymbol{0} \end{pmatrix} , \tag{4.17}$$

which can be compactly reformulated as

$$\begin{pmatrix} \hat{\boldsymbol{x}}_{k+1} \\ \hat{\boldsymbol{\varepsilon}}_{k+1} \end{pmatrix} = \boldsymbol{A}^a_k \begin{pmatrix} \hat{\boldsymbol{x}}_k \\ \hat{\boldsymbol{\varepsilon}}_k \end{pmatrix} + \boldsymbol{B}^a_k \, \boldsymbol{u}^*_k + \boldsymbol{E}^a_k \, . \tag{4.18}$$

The system model in (4.16) is then employed for the CCS-MPC and the system model in (4.18) is used for the estimation.

4.3.3 Optimization Problem

The estimation can be realized with the methods mentioned in Chapter 3. After obtaining the estimation results of the disturbance term $\hat{\boldsymbol{\varepsilon}}$ and the system state $\hat{\boldsymbol{x}}$, the CFTOC problem in (4.2) can be reformulated by replacing the nominal system $\boldsymbol{x}_{j+1} = \boldsymbol{A}_j\boldsymbol{x}_j + \boldsymbol{B}_j\boldsymbol{u}_j + \boldsymbol{E}_j$ with the augmented system $\boldsymbol{x}_{j+1} = \boldsymbol{A}_k\boldsymbol{x}_j + \boldsymbol{B}_j\boldsymbol{u}_j^* + \boldsymbol{E}_j + \boldsymbol{\varepsilon}_j$ in (4.16), which propagates with the initial value $\boldsymbol{x}_k = \hat{\boldsymbol{x}}_k$ and $\boldsymbol{\varepsilon}_k = \hat{\boldsymbol{\varepsilon}}_k$. The CFTOC problem $\mathcal{P}_r$ for the proposed robust control strategy can be written by modifying the optimization problem $\mathcal{P}_c$ in (4.2) as

$$\begin{aligned} \min_{\mathbf{U}} \quad & \sum_{j=k}^{k+N_p-1} \|\boldsymbol{y}_r - \boldsymbol{C}\,\boldsymbol{x}_{j+1}\|_{\mathbf{Q}}^2 + \|\boldsymbol{u}_j\|_{\mathbf{R}}^2 \\ \text{s. t.} \quad & \boldsymbol{x}_{j+1} = \boldsymbol{A}\boldsymbol{x}_j + \boldsymbol{B}\boldsymbol{u}_j^* + \boldsymbol{E} + \boldsymbol{\varepsilon}_j\,, \quad j = k,\, k+1\,\cdots,\, k+N_p-1\,. \end{aligned} \tag{4.19}$$

Analogously to the CFTOC problem $\mathcal{P}_c$, the computation result with a given initial state $\boldsymbol{x}_k$ is a control sequence $\mathbf{U}_k := [\boldsymbol{u}_k^{*T},\, \boldsymbol{u}_{k+1}^{*T},\, \ldots,\, \boldsymbol{u}_{k+N_p-1}^{*T}]^T$, i.e.

$$\begin{aligned} \mathbf{U} \quad & := \arg\min_{\mathbf{U}_k} J \\ \text{s. t.} \quad & \boldsymbol{x}_{j+1} = \boldsymbol{A}_j\,\boldsymbol{x}_j + \boldsymbol{B}_j\,\boldsymbol{u}_j^* + \boldsymbol{E}_j + \boldsymbol{\varepsilon}_j\,, \quad j = k,\, k+1\,\cdots,\, k+N_p-1\,. \end{aligned} \tag{4.20}$$

After obtaining the control sequence $\mathbf{U}_k$, the receding horizon policy is applied and the first element of the sequence is deployed.

4.3.4 Implementation

The propagation of the system state $\boldsymbol{x}$ at the time step j can be given as a function of the initial values $\boldsymbol{x}_k = \hat{\boldsymbol{x}}_k$, $\boldsymbol{\varepsilon}_k = \hat{\boldsymbol{\varepsilon}}_k$ and the control sequence $\mathbf{U}_k$ as follows

$$\boldsymbol{x}_{j+1} = \boldsymbol{A}^{j+1-k}\,\hat{\boldsymbol{x}}_n + [\boldsymbol{A}^{j-k}\boldsymbol{B},\,\cdots,\,\boldsymbol{B}]\,\mathbf{U}_k + \sum_{i=0}^{j-k}\boldsymbol{A}^i\,\boldsymbol{E} + \sum_{i=0}^{j-k}\boldsymbol{A}^i\,\boldsymbol{I}\,\hat{\boldsymbol{\varepsilon}}_k\,. \tag{4.21}$$

The sequence of the outputs over the prediction horizon N_p from the step k can be reformulated as

$$\boldsymbol{Y} = \boldsymbol{\Pi}\,\hat{\boldsymbol{x}}_k + \boldsymbol{\Lambda}\,\mathbf{U}_k + \boldsymbol{\Sigma} + \boldsymbol{\Omega}\,\hat{\boldsymbol{\varepsilon}}_k\,. \tag{4.22}$$

Then, the optimization problem $\mathcal{P}_r$ can be analogously solved with the root finding method. The solution is given as

$$\mathbf{U}_k = (\boldsymbol{\Lambda}^T\mathcal{Q}\boldsymbol{\Lambda} + \mathcal{R})^{-1}\boldsymbol{\Lambda}^T\mathcal{Q}(\boldsymbol{Y}_r - \boldsymbol{\Pi}\,\hat{\boldsymbol{x}}_k - \boldsymbol{\Sigma} - \boldsymbol{\Omega}\,\hat{\boldsymbol{\varepsilon}}_k)\,, \tag{4.23}$$

where the intermediate matrices $\boldsymbol{\Pi}$, $\boldsymbol{\Lambda}$ and $\boldsymbol{\Sigma}$ are same as (4.11) and $\boldsymbol{\Omega}$ is given as

$$\boldsymbol{\Omega} = \begin{pmatrix} \boldsymbol{C}\boldsymbol{I} \\ \boldsymbol{C}\boldsymbol{A}\boldsymbol{I} + \boldsymbol{C}\boldsymbol{I} \\ \vdots \\ \sum_{i=0}^{N_p-1}\boldsymbol{C}\boldsymbol{A}^i\,\boldsymbol{I} \end{pmatrix}. \tag{4.24}$$

Analogously, only the first element of the control sequence is then delivered to the modulator.

4.3.5 Stability Analysis

Applying the observer with the extended system model and the current controller to the PMSM drive system constructs a closed loop system. The stability of the whole control structure need to be examined, since the observer error can deteriorate the closed-loop stability. Prior to the examination of the output-feedback nonlinear model predictive control (NMPC), several definition need to be introduced.

Definition 4.1 (Asymptotic Stable [212])
Consider a LTI system given as

$$\begin{aligned} \boldsymbol{x}_{k+1} &= \boldsymbol{A}\,\boldsymbol{x}_k\ , \\ \boldsymbol{y}_k &= \boldsymbol{C}\,\boldsymbol{x}_k\ . \end{aligned} \tag{4.25}$$

The system is asymptotically stable, i.e. $\boldsymbol{x} \to \mathbf{0}$, if and only if any eigenvalue λ of the matrix $\boldsymbol{A}$ satisfies $|\lambda| < 1$.

Definition 4.2 (K-function [212])
A function $\alpha(\cdot)$ is a $\mathcal{K}$-function if it is continuous, strictly increasing and $\alpha(0) = 0$.

Definition 4.3 ($\mathcal{K}_\infty$-function [212])
A function $\gamma(\cdot)$ is a $\mathcal{K}_\infty$-function if it is a $\mathcal{K}$-function and $\gamma(s) \to +\infty$ as $s \to +\infty$.

Definition 4.4 ($\mathcal{KL}$-function [212])
A function $\beta(\cdot,\,\cdot) : \mathbb{R} \times \mathbb{Z} \to \mathbb{R}$ is a $\mathcal{KL}$-function if for each fixed $t \geq 0$, $\beta(\cdot,\,t)$ is of class $\mathcal{K}$, for each fixed $s \geq 0$, $\beta(s,\,\cdot)$ is decreasing. Moreover $\beta(s,\,t) \to 0$ as $t \to \infty$.

Consider a to be controlled system is nonlinear time invariant and can be written in the discrete domain-time as

$$x_{k+1} = f(x_k,\,u_k,\,d_k,\,w_k)\ , \tag{4.26}$$

where x and u denote the system state and control input, respectively. d and w represent the external disturbances and the model mismatches, respectively. The system output is given as

$$y_k = h(x_k,\,u_k)\ .$$

The following assumptions about the system are stated before the analysis.

Assumption 4.1 ([212])

- *System* (4.26) *has an equilibrium point at the origin, i.e. $f(0,\,0,\,0,\,0) = 0$*
- *The system state x and the control input u satisfy the constraint $\mathbb{Z}$, i.e. $(x_k,\,u_k) \in \mathbb{Z}$, where $\mathbb{Z} \subset \mathbb{R}^{N_x+N_u}$ is closed and contains the origin in its interior.*
- *The model uncertainty w is given as $w_k = w_{\eta,\,k}\,\eta(x_k,\,u_k)$ for all $k \geq 0$, where η is a known function that is continuous and contains the origin in its interior. $w_{\eta,\,k}$ is exogenous signal and satisfies $w_{\eta,\,k} \in \mathbb{W}_\eta$, where $\mathbb{W}_\eta$ is a compact set.*
- *The disturbance d fulfils $d \in \mathbb{D}$ for all $k \geq 0$, where $\mathbb{D}$ is a known compact set and contains the origin.*
- *The system state is measurable at each sampling instant.*

If the system is controlled by a certain control law $u_k = \kappa(x_k)$, then the closed-loop system can be given as

$$x_{k+1} = f_\kappa(x_k,\, d_k,\, w_k)\;, \tag{4.27}$$

where $f_\kappa(x_k,\, d_k,\, w_k) := f(x_k,\, \kappa(x_k),\, d_k,\, w_k)$. The nominal system without the disturbances d and the model mismatches w is given as $\bar{f}_\kappa(x) := \bar{f}(x, \kappa(x))$. The state at the time instant k, which has an initial value of x_0 and the control input $u = \kappa(x)$, is denoted as $\phi_\kappa(k,\, x_0,\, \boldsymbol{d},\, \boldsymbol{w})$ for the real system and $\bar{\phi}_\kappa(k,\, x_0) := \phi_\kappa(k,\, x_0,\, 0,\, 0)$ for the nominal system. $\boldsymbol{d}$ is the sequence of the disturbances and is given as $\boldsymbol{d} := [d_0,\, d_1,\, \cdots]$. Analogously, $\boldsymbol{w}$ is defined as $\boldsymbol{w} := [w_0,\, w_1,\, \cdots]$.

Definition 4.5 (Lyapunov Function [212])
A function $J : \mathbb{R}^n \to \mathbb{R}$ is a Lyapunov function of the nominal system $\bar{x}_{k+1} = f_\kappa(\bar{x}_k)$ if there are three $\mathcal{K}_\infty$-functions, γ_1, γ_2, γ_3 such that $\gamma_1(|x|) \leq J(x) \leq \gamma_2(|x|)$ and $J(\bar{f}_\kappa(x)) - J(x) \leq \gamma_3(|x|)$.

Definition 4.6 (Asymptotically Stable [212])
The nominal system with the controller $u = \kappa(x)$, i.e. $\bar{x}_{k+1} = \bar{f}_\kappa(\kappa(x))$ is globally asymptotically stable, if there exists a $\mathcal{KL}$-function β such that $|\bar{\phi}_\kappa(i,\, x_0)| \leq \beta(|x_0|,\, i)$.

Definition 4.7 (Input to State Stable [212])
The nominal system with the controller $u = \kappa(x)$, i.e. $\bar{x}_{k+1} = \bar{f}_\kappa(\kappa(x))$ is globally input-to-state stable if there exist a $\mathcal{KL}$-function β and a $\mathcal{K}$-function α such that for all initial state x_0 and the sequence of the disturbance d,

$$|\bar{\phi}_\kappa(i,\, x_0,\, \boldsymbol{d})| \leq \beta(|x_0|,\, i) + \alpha(\|\boldsymbol{d}_{i-1}\|)\;.$$

It is worth mentioning that the input-to-state stability of a system comprises the nominal system stability and the uniformly bounded uncertainties.

Definition 4.8 (Input-to-State practically Stable [212])
Suppose Assumption 4.1 is satisfied for system (4.26). The system (4.26) is said to be input-to-state practical stable in a set $\mathcal{X}_r$ with respect to d if $\mathcal{X}_r$ is a robust positively invariant set for the system (4.26) and there are a $\mathcal{K}$ function α, a $\mathcal{KL}$ function β and a constant $c \geq 0$ such that

$$\phi_\kappa(i,\, x_0,\, \boldsymbol{d},\, \boldsymbol{w}) \leq\; \beta(|x_0|,\, i) + \alpha(\|\boldsymbol{d}_{i-1}\|) +\; c\;, \tag{4.28}$$

for all $x_0 \in \mathcal{X}_r$, where $\mathcal{X}_r$ includes the origin as an interior point.

The stability analysis of the state-feedback NMPC have been intensively studied in the literatures such as [197, 212], which is based on the assumption that the states of the system are measurable. However, the integration of an observer into the control loop impedes the analysis of the closed-loop stability. Several works have been conducted to evaluate the system stability with an observer. Reference [213] employed a fast high-gain observer to obtain the stability for a robust NMPC with vanishing perturbations. The non-vanishing model mismatches were included in [214], where the controller was designed in the discrete-time domain. In this thesis, the nonlinear system with the model mismatches and the disturbances is considered. The corresponding system dynamic is given in (4.16) and can be compactly represented by $\boldsymbol{x}_{k+1} = F(\boldsymbol{x}_k,\, \boldsymbol{u}_k,\, \boldsymbol{\varepsilon}_k)$, where $\boldsymbol{\varepsilon} \in \mathbb{E}$ and $\mathbb{E}$ is a compact set.

Assumption 4.2
The initial observer error is bounded by a positive constant ϵ_0, i.e. $|\hat{\boldsymbol{x}}_0 - \boldsymbol{x}_0| \leq \epsilon_0$.

The cost function at the step k of the CFTOC problem $\mathcal{P}_r$ in (4.19) is a function of $\boldsymbol{x}_k$, $\boldsymbol{\varepsilon}_k$ and $\mathbf{U}_k$. It can be then written as $J(\boldsymbol{x}_k,\, \mathbf{U}_k,\, \boldsymbol{\varepsilon}_k)$. The difference of two adjacent cost functions can be decomposed as

$$\begin{aligned} &J(\boldsymbol{x}_{k+1}) - J(\boldsymbol{x}_k) = J(F(\boldsymbol{x}_k,\, \boldsymbol{u}_k,\, \boldsymbol{\varepsilon}_k)) - J(\boldsymbol{x}_k) \\ =&J(F(\hat{\boldsymbol{x}}_k\, \boldsymbol{u}_k, \hat{\boldsymbol{\varepsilon}}_k)) - J(\hat{\boldsymbol{x}}_k) + J(\hat{\boldsymbol{x}}_k) + J(F(\boldsymbol{x}_k\, \boldsymbol{u}_k, \boldsymbol{\varepsilon}_k)) - J(\boldsymbol{x}_k) - J(F(\hat{\boldsymbol{x}}_k\, \boldsymbol{u}_k, \hat{\boldsymbol{\varepsilon}}_k)) \,, \end{aligned} \tag{4.29}$$

where $F(\boldsymbol{x}_k,\, \boldsymbol{u}_k,\, \boldsymbol{\varepsilon}_k) = \boldsymbol{A}_k\, \boldsymbol{x}_k + \boldsymbol{B}_k\, \boldsymbol{u}_k + \boldsymbol{E}_k + \boldsymbol{\varepsilon}_k$, which is asymptotically stable. Therefore there is a $\mathcal{K}$-function α_1 that

$$J(F(\hat{\boldsymbol{x}}_k\, \boldsymbol{u}_k, \hat{\boldsymbol{\varepsilon}}_k)) - J(\hat{\boldsymbol{x}}_k) \leq -\alpha_1(|\hat{\boldsymbol{x}}_k|) \,, \tag{4.30}$$

where the $\mathcal{K}$-function is defined in [212]. Moreover as it is indicated in [212], there exists a $\mathcal{K}$-function α_2 that satisfies

$$J(\hat{\boldsymbol{x}}_k) - J(\boldsymbol{x}_k) \leq \alpha_2(|\hat{\boldsymbol{x}}_k - \boldsymbol{x}_k|) \,. \tag{4.31}$$

Since $\boldsymbol{\varepsilon}$ contains the model uncertainties, the system propagation function in (4.16) is uniform continuous in $\boldsymbol{\varepsilon}$ for all $\boldsymbol{x} \in \mathbb{X}$ and $\boldsymbol{u} \in \mathbb{U}$, $\mathcal{K}$-functions α_3 and α_4 can be found to satisfy

$$\begin{aligned} J(F(\boldsymbol{x}_k,\, \boldsymbol{u}_k,\, \boldsymbol{\varepsilon}_k)) - J(F(\hat{\boldsymbol{x}}_k,\, \boldsymbol{u}_k,\, \hat{\boldsymbol{\varepsilon}}_k)) &\leq \alpha_2(|F(\boldsymbol{x}_k,\, \boldsymbol{u}_k,\, \boldsymbol{\varepsilon}_k) - F(\hat{\boldsymbol{x}}_k,\, \boldsymbol{u}_k,\, \hat{\boldsymbol{\varepsilon}}_k)|) \\ &\leq \alpha_2 \circ (\alpha_3(|\hat{\boldsymbol{x}}_k - \boldsymbol{x}_k|) + \alpha_4(|\hat{\boldsymbol{\varepsilon}}_k - \boldsymbol{\varepsilon}_k|)) \,, \end{aligned} \tag{4.32}$$

where $\alpha_2 \circ \alpha_3(\cdot) := \alpha_2(\alpha_3(\cdot))$. Substitute (4.30), (4.31) and (4.32) into (4.29), it can be obtained that

$$J(F(\boldsymbol{x}_k,\, \boldsymbol{u}_k,\, \boldsymbol{\varepsilon}_k)) - J(\boldsymbol{x}_k) \leq -\alpha_1(|\hat{\boldsymbol{x}}_k|) + \alpha_2(|\hat{\boldsymbol{x}}_k - \boldsymbol{x}_k|) + \alpha_2 \circ (\alpha_3(|\hat{\boldsymbol{x}}_k - \boldsymbol{x}_k|) + \alpha_4(|\boldsymbol{\varepsilon}_k|)) \,. \tag{4.33}$$

The closed-loop system need to be robustly stable for the initial state of the observer with $|\hat{\boldsymbol{x}}_0 - \boldsymbol{x}_0| \leq \epsilon_0$ and the propagations, i.e. $|\hat{\boldsymbol{x}}_k - \boldsymbol{x}_k| \leq \bar{\epsilon} + \alpha_o(\|\varepsilon_{k-1}\|)$, where $\bar{\epsilon}$ is a positive constant and α_o is a $\mathcal{K}$-function. They are defined to guarantee that the behaviour of the estimation error $\boldsymbol{e}_k = \boldsymbol{x}_k - \hat{\boldsymbol{x}}_k$ satisfies

$$|\boldsymbol{e}_k| \leq a\, |\boldsymbol{e}_0|\, b^{-k} + \alpha_o(\|\varepsilon_{k-1}\|) \,, \tag{4.34}$$

when $|\boldsymbol{e}_0| \leq \epsilon_0$, where a, ϵ_0 are positive constants and $b > 1$.

Then, the closed-loop system is input-to-state stable with the bounded initial observer error ϵ_0, i.e. $|\hat{\boldsymbol{x}}_0 - \boldsymbol{x}_0| \leq \epsilon_0$ and ϵ_0 is a positive constant, and the disturbance set $\mathbb{E}$ with $\boldsymbol{\varepsilon} \in \mathbb{E}$ is sufficient small. The first condition is guaranteed by the design of the arrival cost in MHE [175] and the proper choose of initial values of EKF [215]. Moreover, the cost function need to be a Lyapunov function for the closed-loop nominal system.

4.4 Simulation Results

Simulations aiming to investigate the impacts of the parameter mismatches on the CCS-MPC have been conducted. The weighting factor $\boldsymbol{R}$ in $\mathcal{P}_r$ is omitted and the prediction horizon N_p

is chosen as one for comparing the proposed RPCC with the conventional deadbeat control. The ratio indicating the parameter mismatch is represented with the coefficient r_p defined as a percentage of the nominal parameter value, i.e.

$$r_p = \frac{p_c}{p_m} \times 100\% \,, \tag{4.35}$$

where p_c is the value of the parameter applied in the controller and p_m is the nominal value of the motor parameter. In the subsequent investigations, the value of the parameters in the current control is modified accordingly for the purpose of verifying the control performance under the parameter mismatch. Moreover, various parameter variations with different load conditions, i.e. 0%, 50% and 100% of the rated torque, are assessed. The mean error of the control performance is computed as

$$e_i = \frac{\|\boldsymbol{i} - \boldsymbol{i}^*\|_2}{I_N} \,, \tag{4.36}$$

where $\boldsymbol{i}^*$ denotes the current reference vector given in the dq domain. The black dots in the following figures demonstrate the actual computed error e_i, while the surface are fitted with the spline interpolation that introduced in Section. 3.3.2.1.

4.4.1 The Impact from the Stator Resistance

Firstly, the simulation is conducted to study the impact from the parameter mismatch of the stator resistance R_s . The parameter varies from 50% to 150% of the nominal value, with a 10% of the nominal value as the step. The load condition changes from 0% to 100% with a step 10% of the rated torque. The tracking error e_i defined in (4.36) of the simulation results are shown in Fig. 4.2.

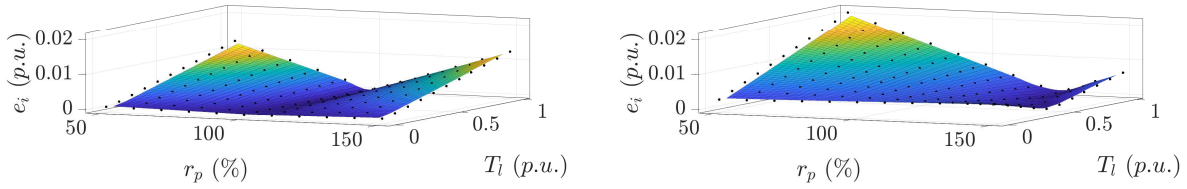

Figure 4.2: The steady state error e_i caused by the parameter mismatch of R_s for the CCS-MPC with $N_p = 1$ in (a) and with $N_p = 5$ in (b).

As it is shown in Fig. 4.2, the influence of R_s is roughly symmetric for the deadbeat control regarding the rate of the parameter variation. Moreover, a higher load will lead to a higher control error under the parameter variation of R_s. For the CCS-MPC with a longer prediction horizon, the error is unsymmetrical in terms of the variation rate. The reduction of the stator resistance will cause more tracking error than its increase. Regarding the influence of the load condition, the conclusion is similar to the deadbeat control, i.e. the variation of the stator resistance will cause a higher control error at a higher load condition. Therefore, for both the deadbeat control and the CCS-MPC with $N_p = 5$, the largest resulted error appears at the full-load condition.

4.4.2 The Impact from the Inductance

The influence of the inductances is simulated. The corresponding simulation results to investigate the parameter variation of L_d and L_q are shown in Fig. 4.3 and in Fig. 4.4, respectively.

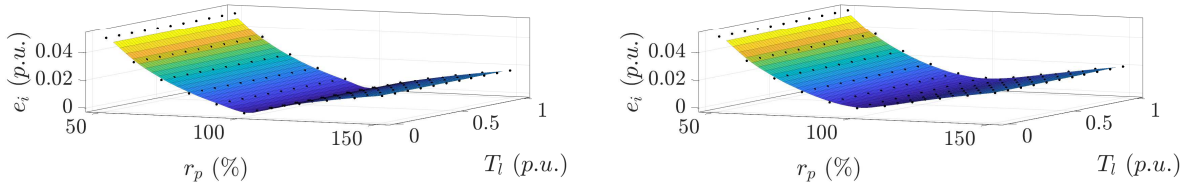

(a) (b)

Figure 4.3: The steady state error e_i caused by the parameter mismatch of L_d for the CCS-MPC with $N_p = 1$ in (a) and with $N_p = 5$ in (b).

Several conclusions can be drawn from the simulation results. Fig. 4.3 shows that a reduction of L_d value has a larger impact on the tracking performance than its increase, i.e. it can cause larger tracking error. The impact of the parameter mismatch from L_d is slightly affected by the load condition. These conclusions can be applied for both deadbeat control and the CCS-MPC with a prediction horizon of $N_p = 5$.

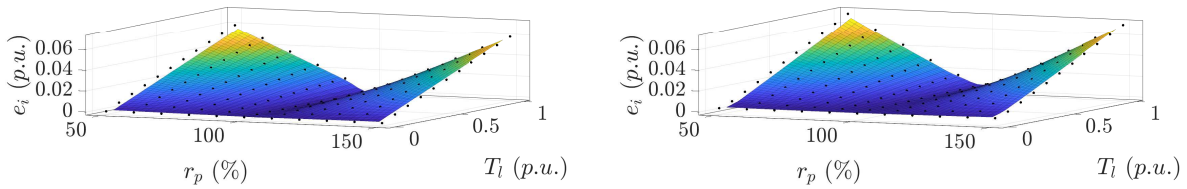

(a) (b)

Figure 4.4: The steady state error e_i caused by the parameter mismatch of L_q for the CCS-MPC with $N_p = 1$ in (a) and with $N_p = 5$ in (b).

The effects from the parameter mismatch of L_q differs from those of L_d. Fig. 4.4 shows that the load torque has a great impact on the error current e_i caused by the parameter mismatch of L_q , i.e. a higher load torque causes a higher error. The effects of the L_q variation is symmetric regarding to r_p . There are few differences between the influences of the parameter L_q variation on the deadbeat control and on the CCS-MPC.

4.4.3 The Impact from the Permanent Magnet Flux Linkage

The impact of the permanent magnet flux linkage is simulated and the corresponding simulation results are shown in Fig. 4.5.

It can be concluded from the Fig. 4.5 that the impact from the permanent magnet flux linkage is symmetrical regarding the rate of the variation, which is valid for both the deadbeat control and the CCS-MPC. The load has little impact on the tracking error. Furthermore, comparing to the other three electrical parameters, the permanent magnet flux linkage induces the largest

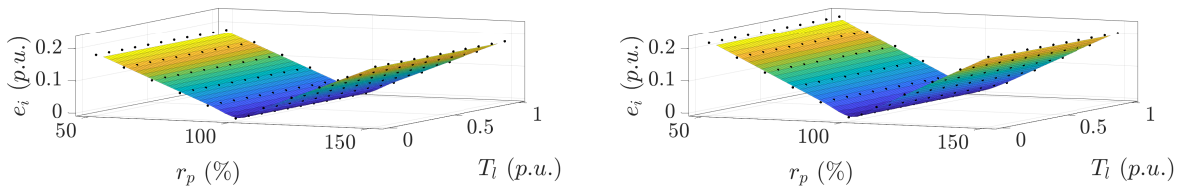

Figure 4.5: The steady state error e_i caused by the parameter mismatch of Ψ_{m} for the CCS-MPC with $N_p = 1$ in (a) and with $N_p = 5$ in (b).

tracking error under the same rate of parameter variation and the same load condition. It may be resulted from that the term related to the permanent magnet flux linkage in (4.5) can be regarded as a constant disturbance, which directly causes the offset for the control result if it is not perfectly compensated, while the other three parameters are related to the system characteristics and have more effects on the system behaviours, such as the system stability and the system dynamics.

It is worth mentioning that the parameter variation of the aforementioned electrical parameters can cause more tracking errors for the CCS-MPC than for the deadbeat control, which can be explained by the fact that the error of the model is accumulated as the prediction grows. Therefore, a larger tracking error can be observed under the control of the CCS-MPC as the prediction horizon increases.

4.5 Experimental Results

The proposed observer-based robust predictive current control strategy was implemented on a dSPACE real-time system that described in Appendix B.2. Several experimental scenarios are designed. The corresponding experiments have been carried out to investigate the behaviour of the proposed method and to compare it with the classical predictive current control. Firstly, the performances at the steady state with various situations of the parameter mismatches are compared, namely the parameter mismatch of R_{s}, L_d, L_q and Ψ_{m}, for both the deadbeat control and the CCS-MPC with a prediction horizon of three. The experiments are furthermore conducted with the proposed robust current controller. Moreover, as it is shown in the simulations, the load condition can affect the control performance under the parameter mismatch. Therefore, several load conditions are investigated via experiments. Subsequently, the comparison is conducted under the existence of the encoder error. The digital delay can also affect the control performance, particularly for the embedded system with a relatively low sampling frequency. Therefore, the control performances without digital-delay compensation and under an inaccurate digital-delay compensation are furthermore investigated. At last, the conclusions can be drawn accordingly.

4.5.1 Comparison of the Deadbeat Control and the RPCC under the Parameter Mismatch

The experiments have been firstly conducted for the PMSM drive system controlled with the deadbeat control method. These experiments aiming to evaluate the performance under the parameter mismatches were carried out through the same pattern, i.e. r_p reduces to 50% at $t = 2\,\mathrm{s}$ and increases to 200% at $t = 4\,\mathrm{s}$. The EKF as well as the MHE is deployed as the disturbance observer for estimating the current and the disturbance.

4.5.1.1 Performance under the Variation of L_d

The influence from the parameter mismatch of L_d is firstly investigated. The experimental results are shown in Fig. 4.6 for the no load condition, in Fig. 4.7 for a load of 50% of the rated torque and in Fig. 4.8 for the full load condition.

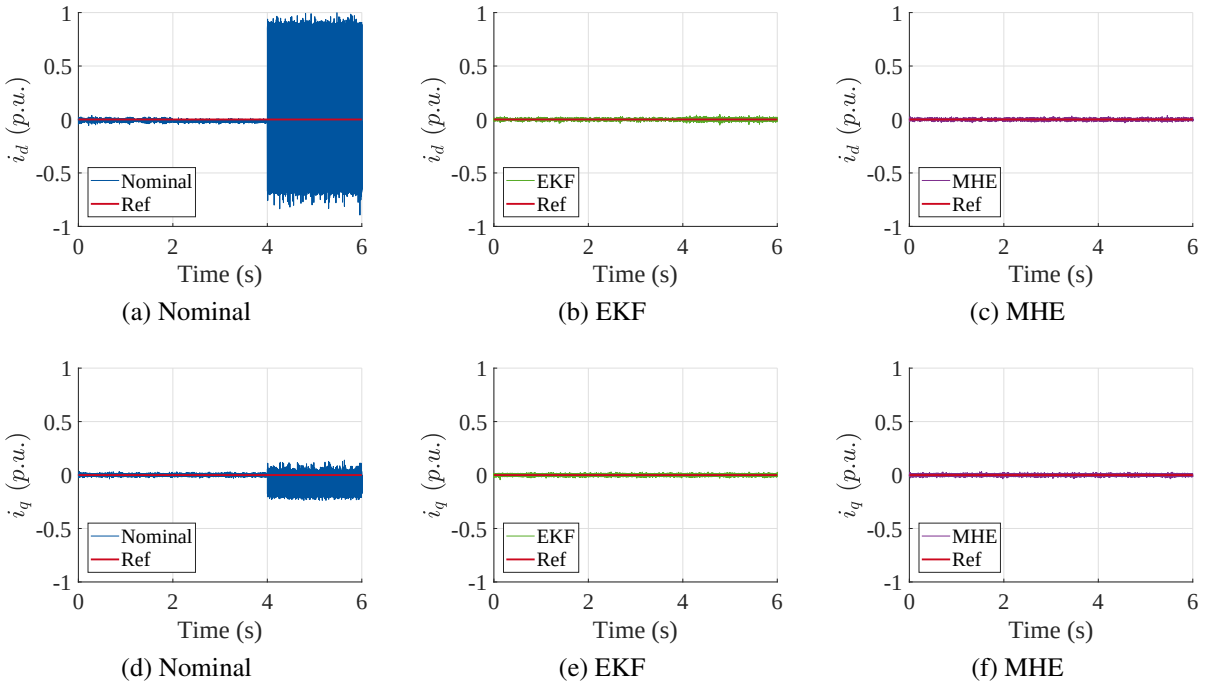

(a) Nominal (b) EKF (c) MHE

(d) Nominal (e) EKF (f) MHE

Figure 4.6: Comparison of the deadbeat control and the RPCC under the parameter mismatch of L_d and no load condition. (a) and (d) denote the experimental results with the deadbeat control. (b) and (e) are the results with the RPCC deploying EKF. (c) and (f) represent the experimental results with the RPCC employing MHE.

Fig. 4.6 shows that from $t = 4\,\mathrm{s}$, i.e. the variation of L_d to $r_p = 200\%$, severe oscillation (up to the rated current value) can be noted for the deadbeat control. More ripples can be observed at $r_p = 50\%$ than the nominal condition. On the contrary, the current loop controlled with the robust predictive control strategy, both with the EKF and with the MHE, remains stable and reveals accurate tracking results under the parameter variation of L_d.

Similar phenomenon can be observed with a 50% of the rated torque as the load, i.e. the closed-loop system of the current control exhibits instability at $r_p = 200\%$, where an oscillation with an amplitude of the rated current can be observed. Moreover, at the parameter mismatch

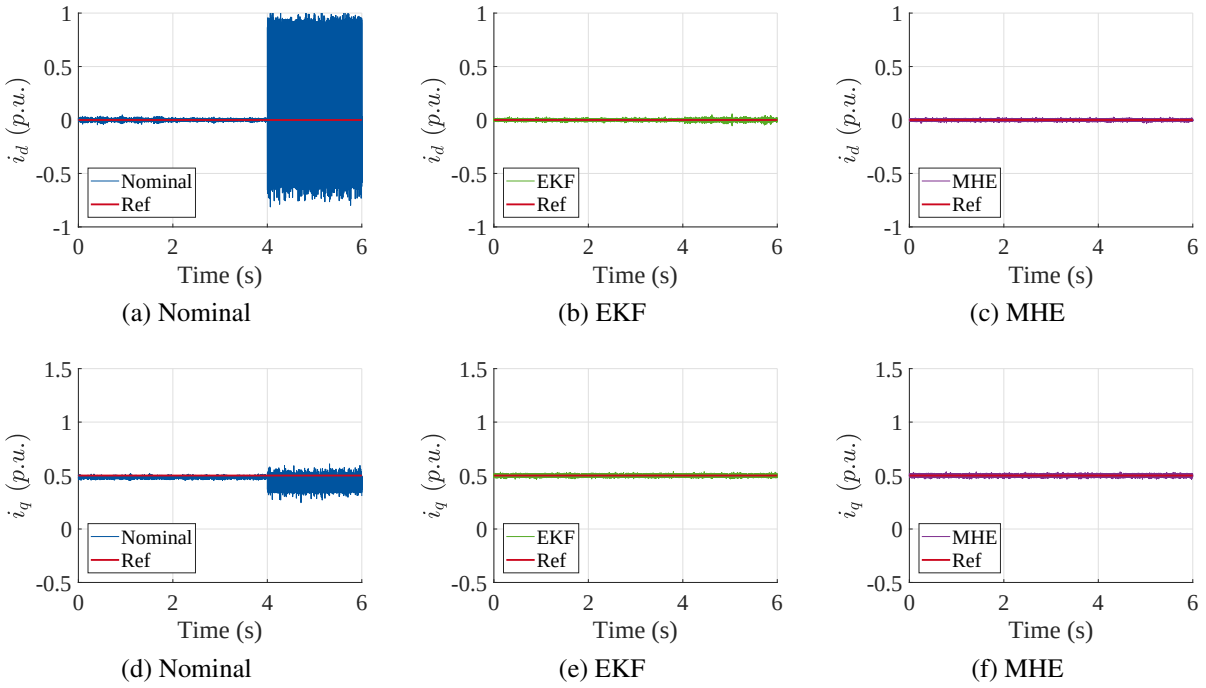

Figure 4.7: Comparison of the deadbeat control and the RPCC under the parameter mismatch of L_d and 50% of the rated torque as the load. (a) and (d) denote the experimental results with the deadbeat control. (b) and (e) are the results with the RPCC deploying EKF. (c) and (f) represent the experimental results with the RPCC employing MHE.

of $r_p = 50\%$, more ripples than no load condition is noted. The RPCC with EKF as well as MHE can both track the current reference accurately. Moreover, the system stability with the RPCC is not affected by the variation of L_d.

The deadbeat control demonstrates analogous phenomenon at the parameter mismatch of L_d under the full-load condition to the other load conditions. Nonetheless, at the full-load condition, higher values of the oscillated current can be noticed in Fig. 4.8. It can be concluded from the previous experiments that the parameter mismatch of L_d changes the system characteristics and can cause conspicuous ripples or even the system instability. However, the implementation of the robust control strategy, either with the EKF or the MHE, improves the robustness of the closed-loop system significantly and reduces the noises as well as ripples contained in the currents.

4.5.1.2 Performance under the Variation of L_q

Subsequently, the influence from the parameter mismatch of L_q is investigated. The experimental results under no load condition are shown in Fig. 4.9. In comparison with the experimental results in Fig. 4.6, it can be seen that the parameter mismatch of L_q has less effect on the system characteristics than that of L_d, i.e. the current loop can remain stable under the parameter mismatch of L_q. However, obvious ripples can be observed. More specifically the parameter mismatch of L_q causes a ripple up to 20% of I_N in q-axis. On the contrary, the proposed RPCC can track the reference accurately and remains stable.

Because of the limitation of the space, the transient performance of 50% load condition is

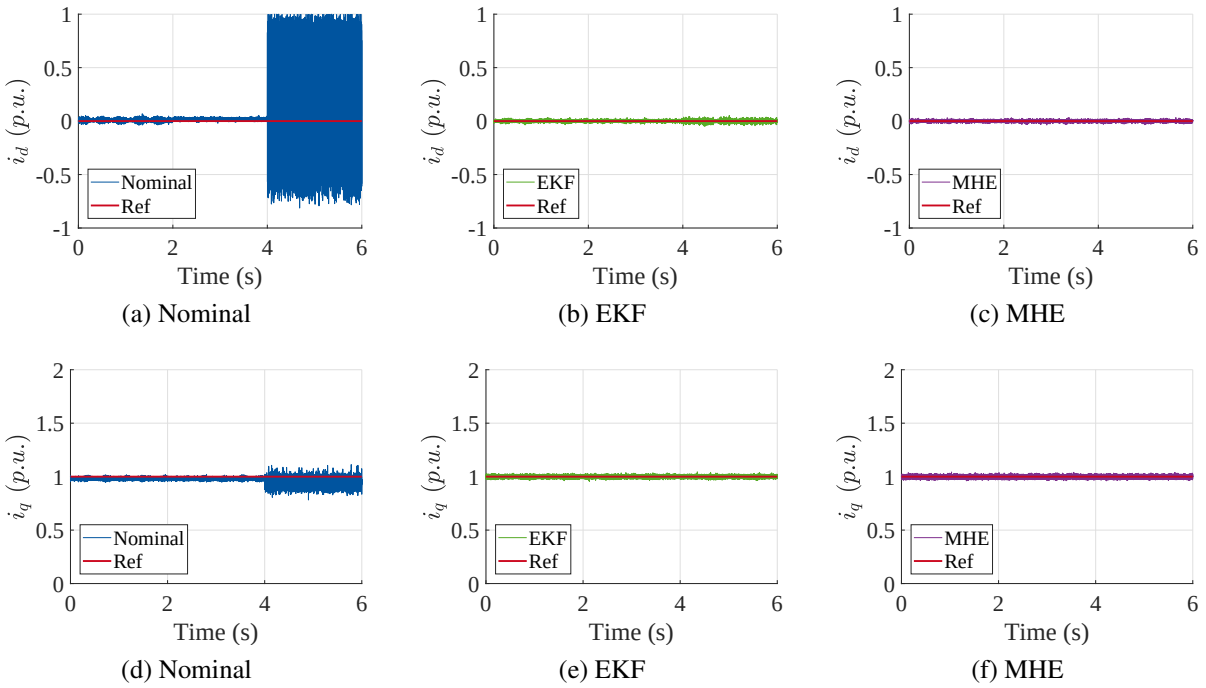

Figure 4.8: Comparison of the deadbeat control and the RPCC under the parameter mismatch of L_d and full load condition. (a) and (d) denote the experimental results with the deadbeat control. (b) and (e) are the results with the RPCC deploying EKF. (c) and (f) represent the experimental results with the RPCC employing MHE.

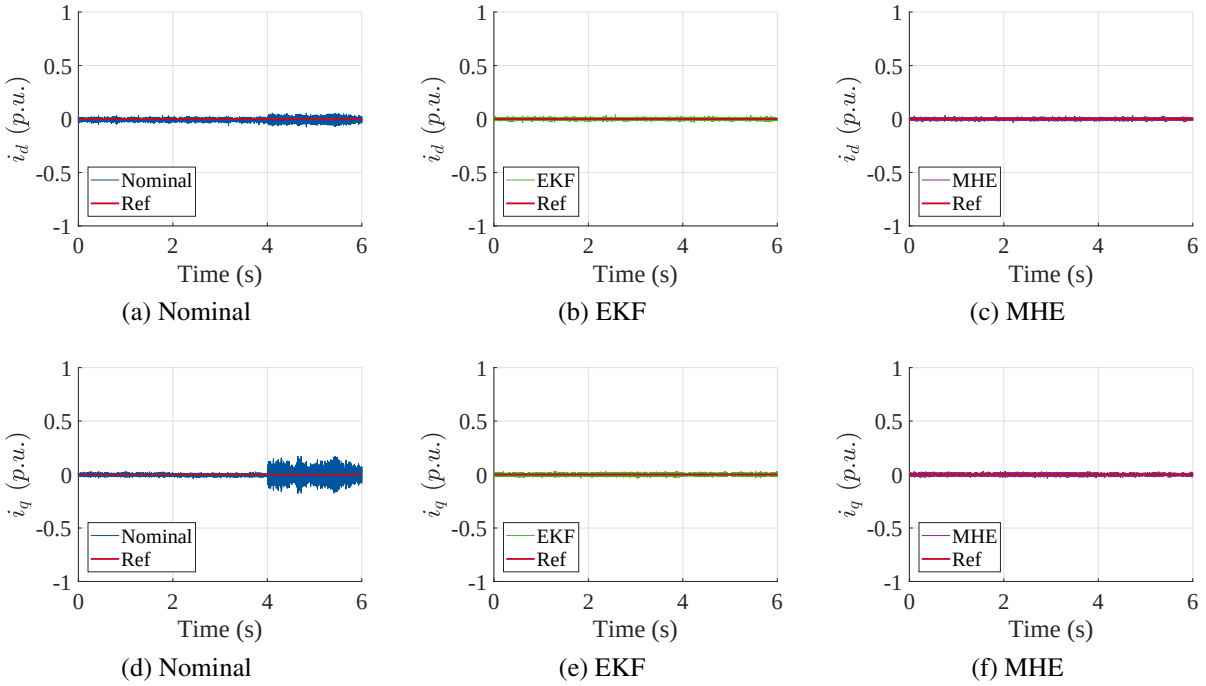

Figure 4.9: Comparison of the deadbeat control and the RPCC under the parameter mismatch of L_q and no load condition.

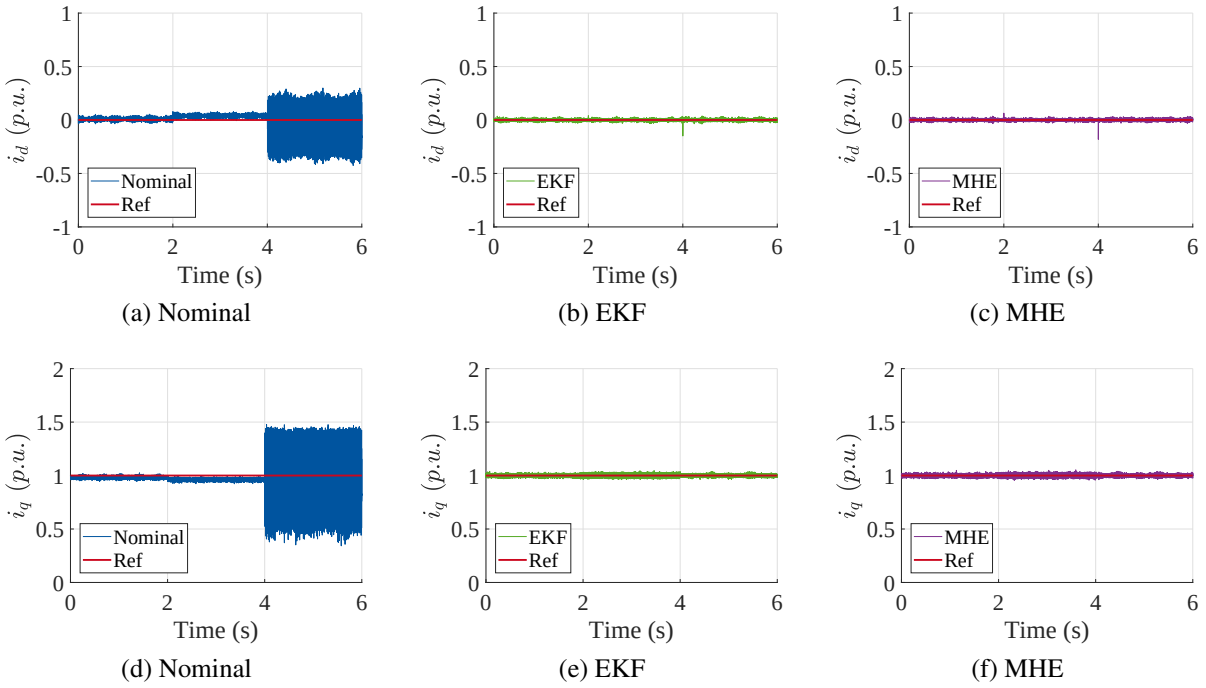

Figure 4.10: Comparison of the deadbeat control and the RPCC under the parameter mismatch of L_q and full load condition.

omitted. The experimental results are shown in Fig. 4.10. The reduction of L_q, i.e. $r_p = 50\%$ causes a steady-state offset for i_d and i_q, which can be noticed at the full-load condition. Under a load of 50% of the rated torque, the deadbeat control reveals unstable behaviour when $r_p = 200\%$. Same behaviour can be observed under the full load, where the oscillations at $r_p = 200\%$ with full load is much higher than that with 50% of the rated torque as load. It is worth mentioning that the parameter mismatch of L_d mainly causes the oscillations in d-current, which has an amplitude of almost the rated current, while the parameter mismatch of L_q causes the oscillations mainly in q-axis, which may be up to $1.5\, I_N$. Moreover, the parameter mismatch of L_d induces the ripples in q-axis current, which can be up to 25% of the rated current. The parameter mismatch of L_q also causes ripples in d-axis. Their amplitude depends on the load condition. As it is shown in (4.5), the coupling between i_d and i_q reflects the instability of one axis on the other axis. But the induced impact is limited to a certain degree. Therefore, the oscillation in the q-axis caused by the L_d variation remains unchanged, even though the load condition is varied, while the oscillation in d-axis caused by the L_q variation varies with the load condition. In general, the inductances, namely L_d and L_q, have both significant impacts on the system characteristics and affect the closed-loop stability.

4.5.1.3 Performance under the Variation of R_s

The control performance of the deadbeat control and of the proposed RPCC is further investigated under the variation of R_s. The experimental results are shown in Fig. 4.11 and Fig. 4.12. Comparing to the experimental results of the previous scenarios, i.e. the parameter mismatches of L_d and L_q, it can be noticed that the parameter mismatch of the stator resistance has less impact on the deadbeat control. Neither unstable system behaviour nor obvious steady-state

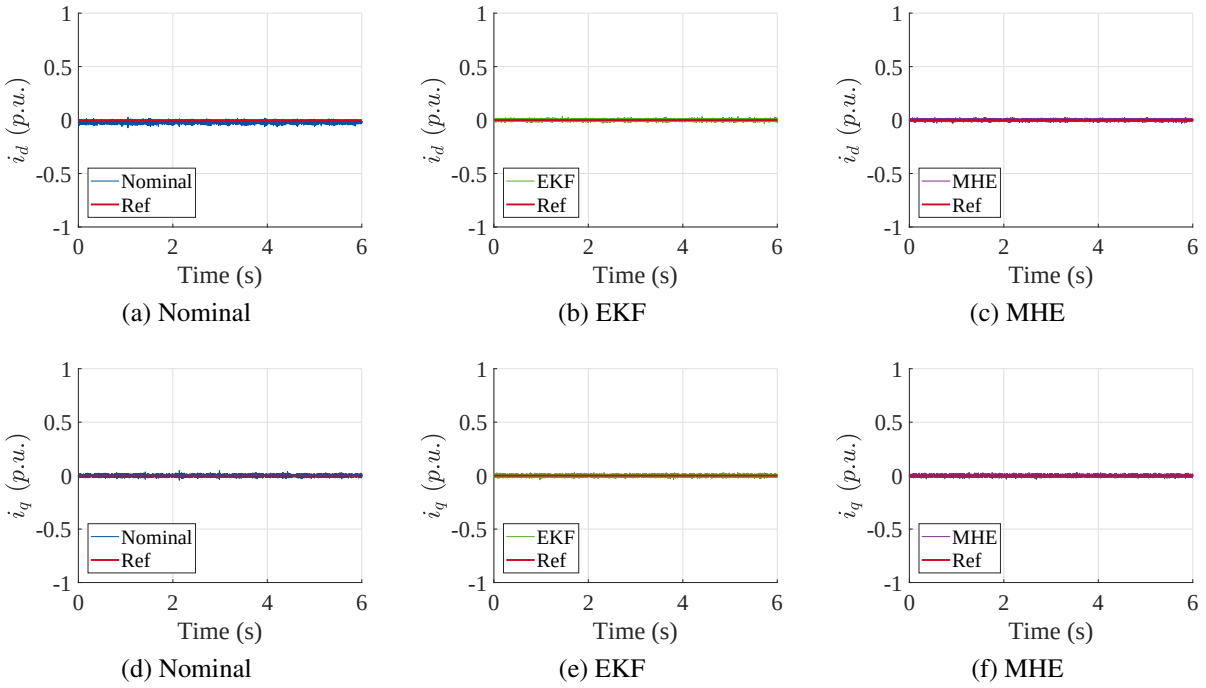

(a) Nominal (b) EKF (c) MHE

(d) Nominal (e) EKF (f) MHE

Figure 4.11: Comparison of the deadbeat control and the RPCC under the parameter mismatch of R_s and no load condition.

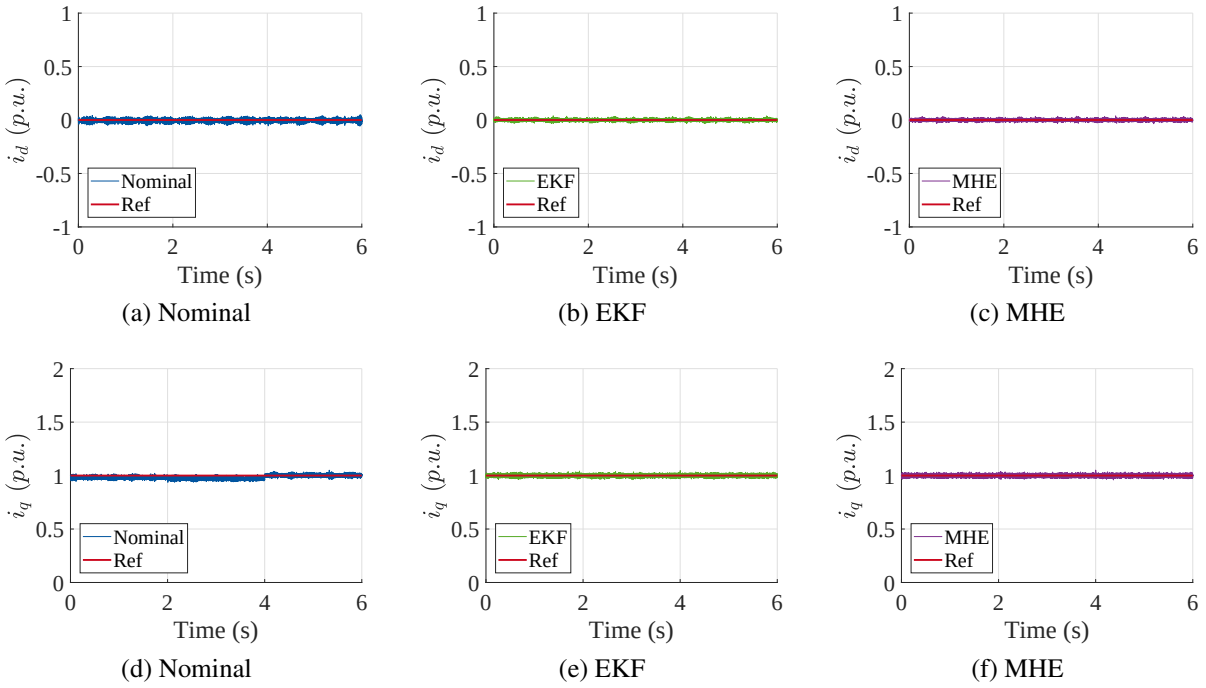

(a) Nominal (b) EKF (c) MHE

(d) Nominal (e) EKF (f) MHE

Figure 4.12: Comparison of the deadbeat control and the RPCC under the parameter mismatch of R_s and full load condition.

offset can be observed from the experimental results with no-load condition in Fig. 4.11 and full-load condition in Fig. 4.12. However, the parameter mismatch of R_s can deteriorates the control performance at a higher load condition, where tracking error as well as higher ripples can be noted. In contrast, the proposed RPCC remains stable and accurate under the variation of R_s.

4.5.1.4 Performance under the Variation of Ψ_m

At last, the control performance under the variation of the permanent magnet flux linkage Ψ_m is investigated. The corresponding results are shown in Fig. 4.13 and Fig. 4.14. As it is shown

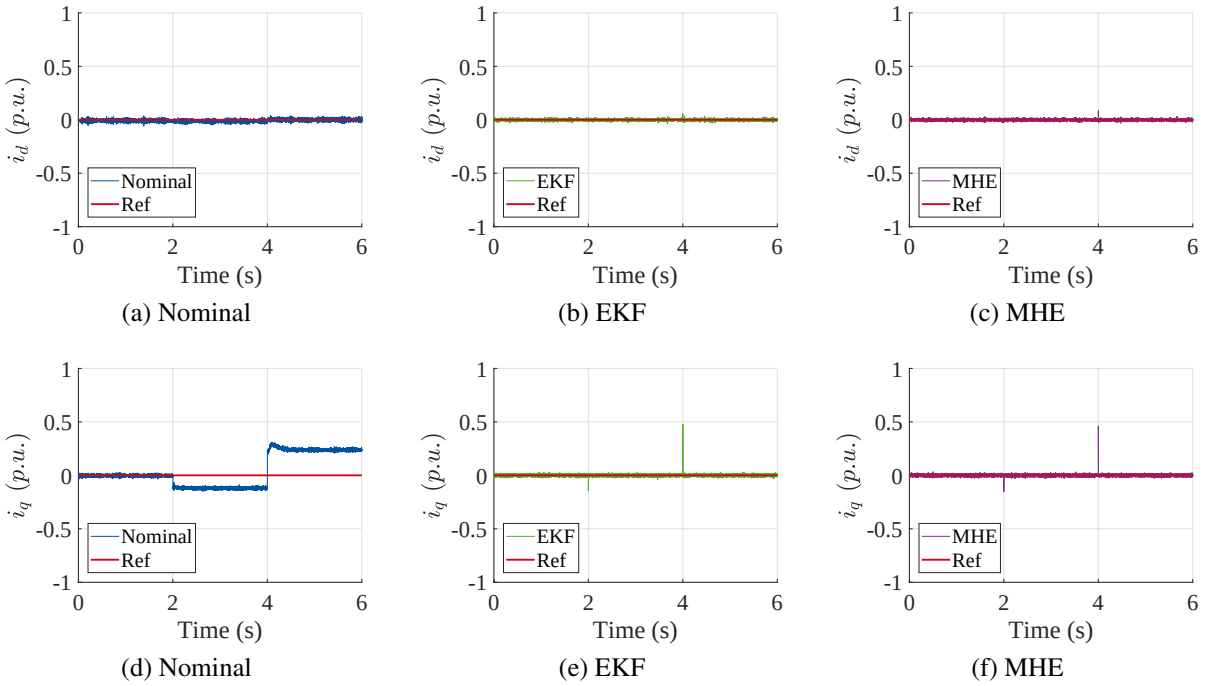

Figure 4.13: Comparison of the deadbeat control and the RPCC under the parameter mismatch of Ψ_m and no load condition.

in Fig.4.13, the variation of Ψ_m causes an evident steady-state error for the current of q-axis. A steady-state offset around 15% of I_N at $r_p = 50\%$ and an offset up to 25% of I_N at $r_p = 200\%$ can be observed under the control of the conventional deadbeat control, while RPCC effectively eliminates the influence of the parameter mismatch of Ψ_m. During the transient of the parameter variation, i.e. at $t = 2\,\mathrm{s}$ and at $t = 4\,\mathrm{s}$, an overshoot can be noted under the control of RPCC. Moreover, the overshoot of i_q is much higher than that of i_d.

An analogous steady-state offset can be observed with 50% of the rated torque as the load and also with full-load condition. Particularly, the experimental results of the full-load condition are shown in the Fig. 4.14. Comparing to the no-load condition, higher ripples can be noticed with a heavier load, both in d-axis and q-axis. Conversely, the proposed RPCC eliminates the steady-state error. Nonetheless, similar to the no-load condition, overshoots can be noted at the transient of the parameter variation.

Several conclusions can be drawn after comparing the experimental results of the parameter

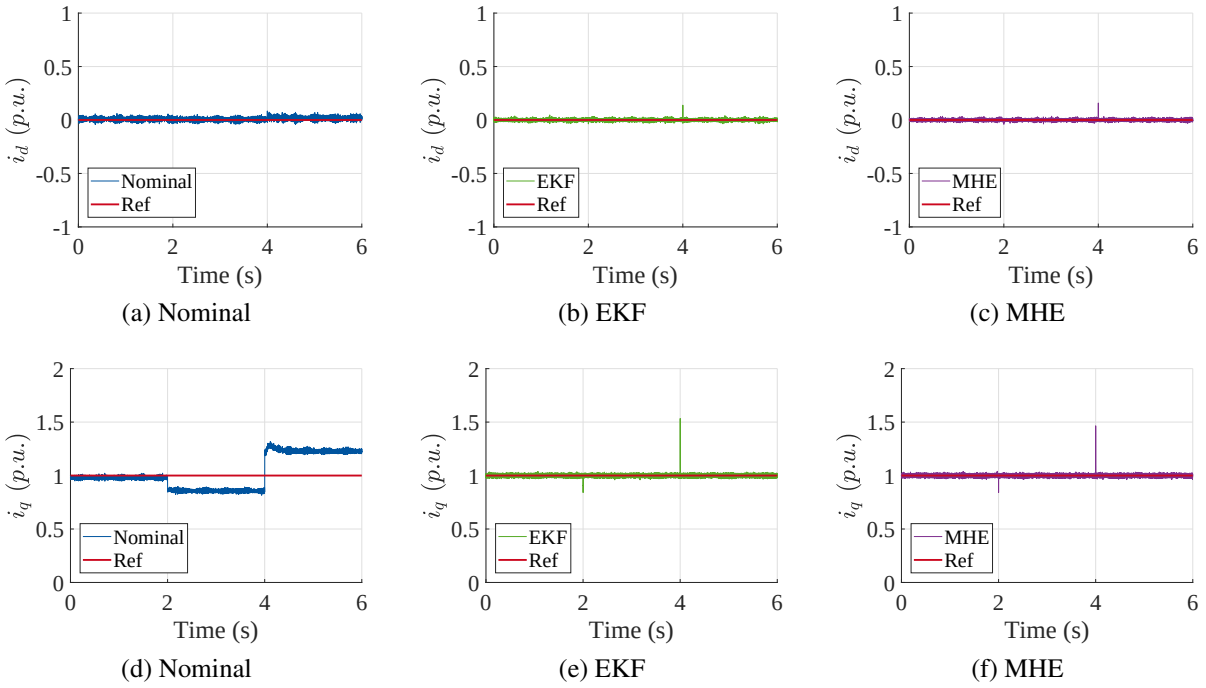

(a) Nominal (b) EKF (c) MHE

(d) Nominal (e) EKF (f) MHE

Figure 4.14: Comparison of the deadbeat control and the RPCC under the parameter mismatch of Ψ_m and full load condition.

variation of Ψ_m under different load conditions. Firstly, the permanent magnet flux linkage has little effect on the system stability, but its mismatch can cause an evident tracking error for the deadbeat control. Moreover, a higher load torque may result in a larger current ripple. The proposed RPCC eliminates the steady-state error. However, an obvious overshoot during the transient of the parameter variation can be noted in q-axis, if the RPCC is deployed. It may be resulted from the tuning of the parameters for the observers, i.e. the covariance matrices of the system noise and of the measurement noise, since the estimator is so tuned that the variation can be tracked quickly. Therefore, the estimator is rather aggressive. It should be pointed out that the overall performance of MHE is practically the same as that of EKF. Thus, it should be sufficient to deploy EKF as the disturbance observer to compensate the effects from the parameter mismatches and the disturbances as well as to improve the system robustness, the control performance for the PMSM drive system.

4.5.1.5 Summary of the Steady-State Error

In order to better visualize the steady-state error and compare them more perceptually, the control performance is evaluated by the absolute value of the error, which is defined by employing

$$e_{i_d,\,i_q} = \frac{|i_{d,\,q} - i^*_{d,\,q}|}{I_N}\,, \tag{4.37}$$

where $i^*_{d,\,q}$ denotes the current reference value given for the d-axis or the q-axis. Regarding various parameter mismatches and load conditions, the computational results are presented in histograms and demonstrated in Fig. 4.15 - Fig. 4.18.

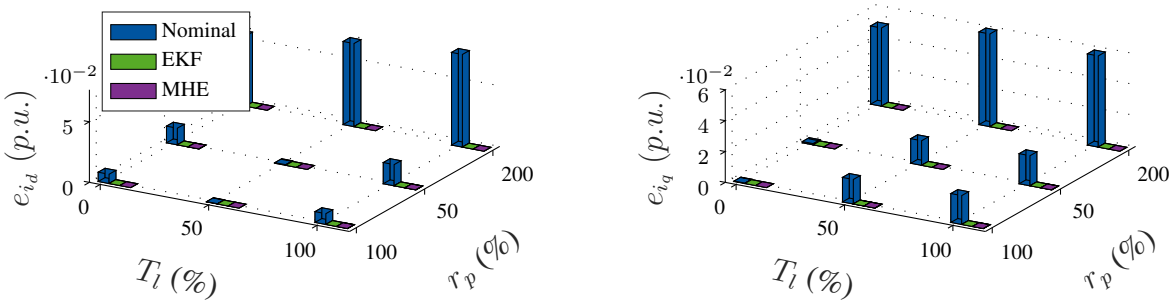

(a) (b)

Figure 4.15: Comparison between the proposed RPCC with MHE/ EKF as the disturbance observer and the conventional deadbeat control under the variation of L_d.

It can be noticed from the Fig. 4.15 that the proposed RPCC with the observers, i.e. either EKF or MHE, outperforms the conventional deadbeat control under the variation of L_d with and without load. The variation of L_d causes instability for the deadbeat control at $r_p = 200\%$, which can be seen from Fig. 4.6, Fig. 4.7 and Fig. 4.8. Moreover, it evokes a steady-state error of around 6% of the rated current. The aforementioned problems are nonetheless tackled by implementing the RPCC strategy. The improvements generated by the two different disturbance observers are almost the same.

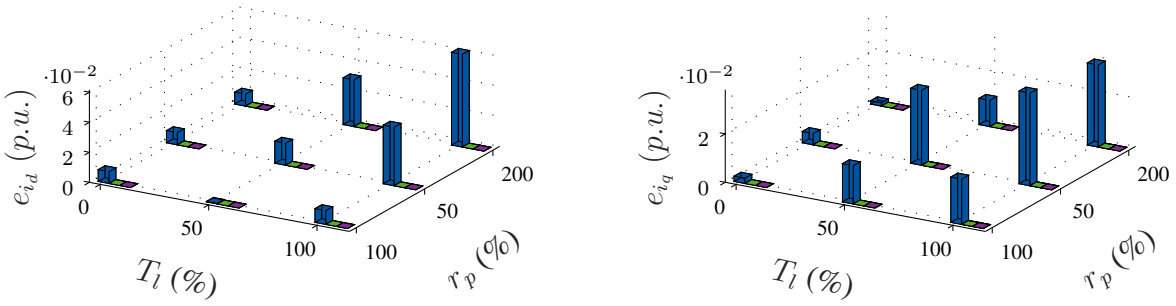

(a) (b)

Figure 4.16: Comparison between the proposed RPCC with MHE as well as EKF as the disturbance observer and the conventional deadbeat control under the variation of L_q.

Comparing to the variation of L_d, the variation of L_q has less influence on the closed-loop stability. However, fierce oscillations can still be observed at $r_p = 200\%$, while the mean error is abnormally reduced compared with the nominal situation. On the contrary, the proposed RPCC delivers better control performance, in terms of the tracking accuracy and the system robustness. The rate of the impact caused by the parameter mismatch of L_d depends more on r_p , i.e. the rate of the parameter variation, while the impacts evoked by the parameter mismatch of L_q hinges more on the load condition.

The influence of the parameter mismatch of Ψ_m is summarized in Fig. 4.17. As given in (4.16), Ψ_m in the matrix $\boldsymbol{E}$ affects the steady-state performance of the current control. An evident steady-state offset can be found under the Ψ_m variation with the conventional deadbeat control, which can amount to 20% of the rated current. The relatively small error of i_d at $r_p =$

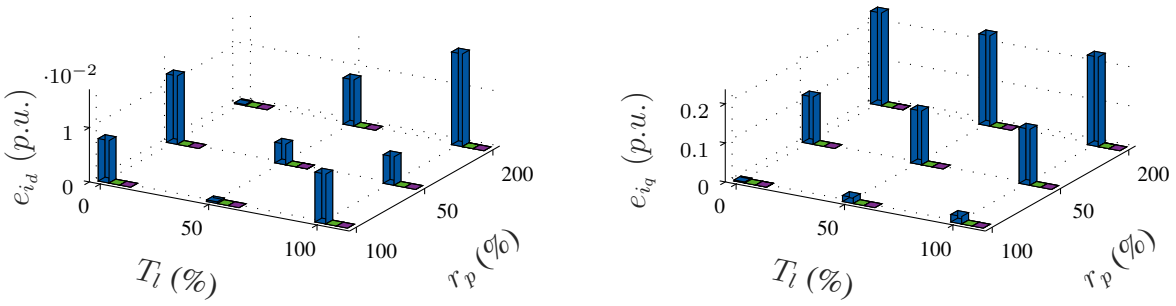

(a) (b)

Figure 4.17: Comparison between the proposed RPCC with MHE/ EKF as the disturbance observer and the conventional deadbeat control under the variation of Ψ_{m}.

200% and no-load condition can be explained by that the error induced in i_q may compensate the original disturbances. A larger error is observed in q-axis, which is dependent on the rate of parameter variation and the load condition.

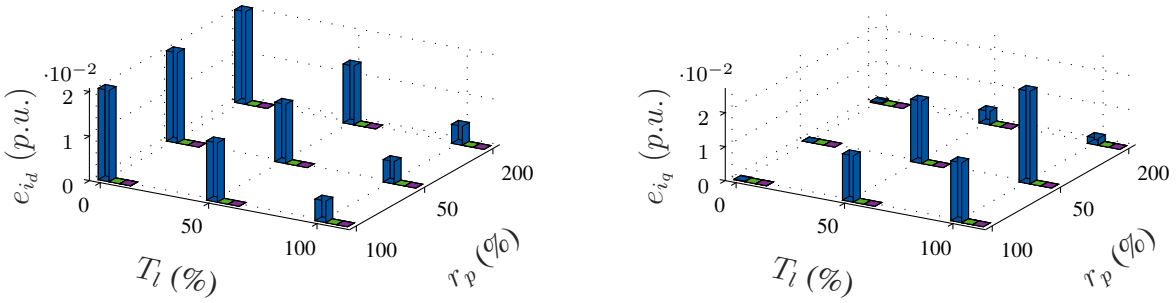

(a) (b)

Figure 4.18: Comparison between the proposed RPCC with MHE/EKF as the observer and the conventional deadbeat control under the variation of R_{s}.

Comparing to the other parameters, R_{s} has the least influence on the control performance, in term of the mean error and the ripple, which can be observed in Fig. 4.18. The largest steady-state error can be found at no-load condition, which is up to 2% of the rated current value.

It can be summarised that the employment of MHE and EKF into the framework of the proposed robust predictive current control have slight difference for estimating the model uncertainties that is resulted from the parameter variation, and also for compensating the disturbances. This conclusion can be explained by the fact that the rate of the parameter variation is relatively slow and the propagation of the augmented system model for the PMSM can be captured by the linearisation conducted by the EKF. The parameter variation of inductances affects the system characteristics and can cause instability of the closed-loop system, while the variation of the permanent magnet flux linkage induces an evident steady-state error, which is dependent on the rate of the parameter variation and the load condition. The stator resistance has the least influence on the accuracy of the tracking performance as well as the closed-loop stability. The implementation of the proposed RPCC effectively eliminates the steady-state error and improves the closed-loop stability. More specifically, the closed-loop system reveals

stable under the various parameter mismatches and accurately tracks the reference.

4.5.2 Comparison of the CCS-MPC and the RPCC under the Parameter Mismatch

Moreover, the proposed RPCC is compared with the conventional CCS-MPC and the CCS-MPC with an output compensation, which is realized by $\boldsymbol{u}_k + \boldsymbol{B}^{-1}\hat{\boldsymbol{\varepsilon}}_k$. Due to the limitation of the computational power, in some applications the implementation of the CCS-MPC is realized by computing the explicit solution offline. Then, the solution $\boldsymbol{u}_k$ is searched online from the offline computational results and applied to the modulator. In this case, the estimated disturbance can not be directly included into the CFTOC problem. Therefore, the compensation can only be executed by compensating the control voltage with the term $\boldsymbol{B}^{-1}\hat{\boldsymbol{\varepsilon}}_k$. However, it can be predicted that the compensation of the disturbance term for the command voltage instead of including it into the optimization problem can result in a no-optimal solution. The prediction horizon of the conventional CCS-MPC, CCS-MPC with an output compensation and RPCC is set to be $N_p = 3$ in the following investigations. On the purpose of compactness, only the dynamic response to the parameter variation of L_d and Ψ_m is shown in the following, since the results of L_q is relatively similar to that of L_d and R_s has only slight influence on the control performance. Nonetheless, the steady-state error of all kinds of parameter mismatches are computed and summarized in histograms, analogously to the deadbeat control performance evaluation. Since little difference between the estimating performances of EKF and MHE can be found, as it is indicated in the previous section, the EKF is selected as the disturbance observer for the long prediction horizon current control in the following.

4.5.2.1 Performance under the Variation of L_d

Firstly, the control performances of the conventional CCS-MPC, CCS-MPC with the compensation and the proposed RPCC are investigated under the parameter variation of L_d . The experimental results are shown in Fig. 4.19.

Comparing to the control performance of the deadbeat control, which is shown in Fig. 4.8, the control of the CCS-MPC remains stable, even when the L_d changes to 200% of the nominal value. It is worth mentioning that a small steady-state offset of i_q can be observed, also at the state without parameter mismatch, which can be explained by the fact that the parameter values deployed in controller are directly obtained from the manufacturer's data sheet and may differ from the real parameter values. Moreover, the digital delay has also impact on the control performance, for which the implemented digital-delay compensation may be inaccurate. However, the implementation of the RPCC eliminates the tracking error effectively. Furthermore, little difference can be noted between the CCS-MPC with the output compensation and the RPCC. More specifically, RPCC is slightly better than the CCS-MPC regarding the tracking accuracy, especially for the q current.

4.5.2.2 Performance under the Variation of Ψ_m

The performance evaluation of the deadbeat control indicates the significance of the parameter mismatch of Ψ_m on the tracking accuracy. Its impact on the CCS-MPC is furthermore studied.

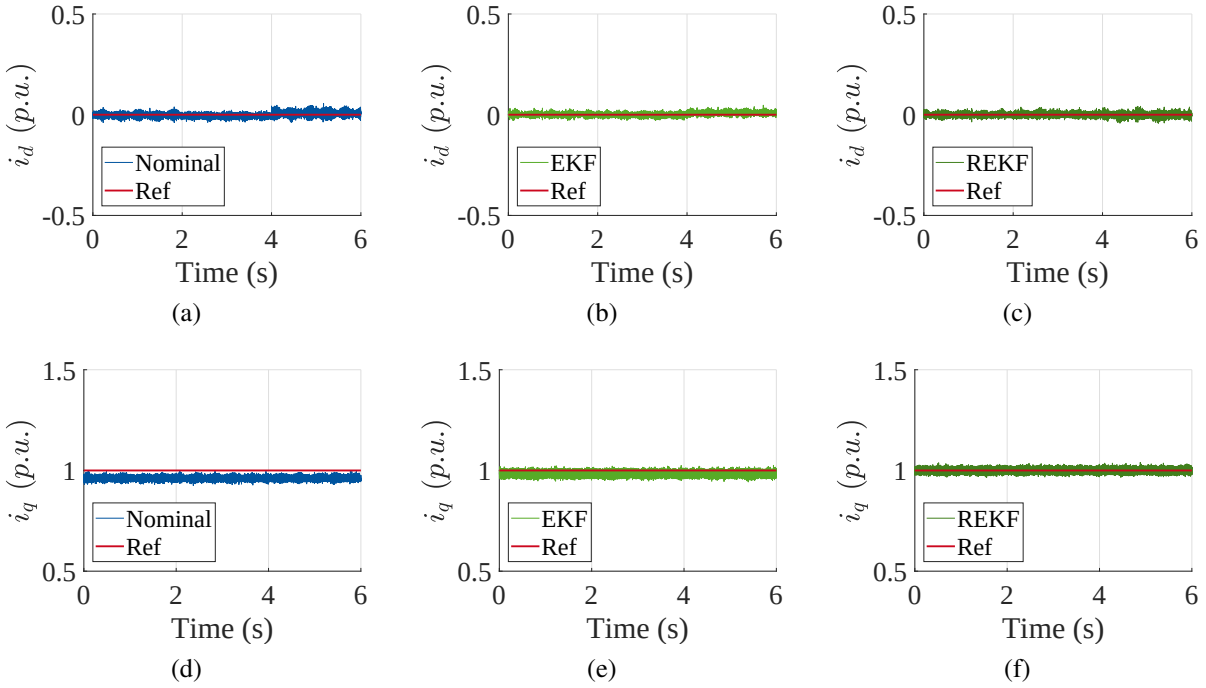

Figure 4.19: Comparison of the proposed RPCC to the conventional CCS-MPC as well as CCS-MPC with the output compensation under the parameter mismatch of L_d and full-load condition. (a) and (d) denote the experimental results with the CCS-MPC. (b) and (e) are the currents controlled by the CCS-MPC with the output compensation. (c) and (f) represent the experimental results with the RPCC employing EKF. The conventional CCS-MPC is denoted by blue, CCS-MPC with the output compensation is presented by light green and the proposed RPCC with EKF is shown in dark green.

The corresponding experimental results are shown in Fig. 4.20.

Because that the prediction error resulting from the parameter mismatch of the permanent magnet flux linkage accumulates as the prediction horizon grows, a larger tracking error compared to the deadbeat control, which can amount around to 30% of the rated current, can be observed under the control of CCS-MPC at the full-load condition with $r_p = 200\%$. The output compensation for CCS-MPC can eliminates the offset to a certain level. Nonetheless, a small steady-state error can still be noticed at $r_p = 200\%$, when the output compensation is applied. However, as mentioned in [216], an overall optimization is required for the CCS-MPC. The inclusion of the disturbance term into the optimization problem, as in RPCC, shows significant improvement of the control performance in terms of the tracking accuracy. The RPCC effectively cancels the steady-state error. However, both CCS-MPC with the output compensation and RPCC reveal an overshoot at the time instant of the parameter variation, which is analogous to the deadbeat control and may be caused by the parameter selection of the estimators.

4.5.2.3 Summary of the Steady-State Error

The absolute values of the mean errors regarding i_d and i_q are computed, summarized in Fig. 4.21 - Fig. 4.24.

As it is shown in Fig. 4.21, the respective errors of the currents in d-axis and q-axis show different dependence on the load condition. However, it can be noticed that the steady-state

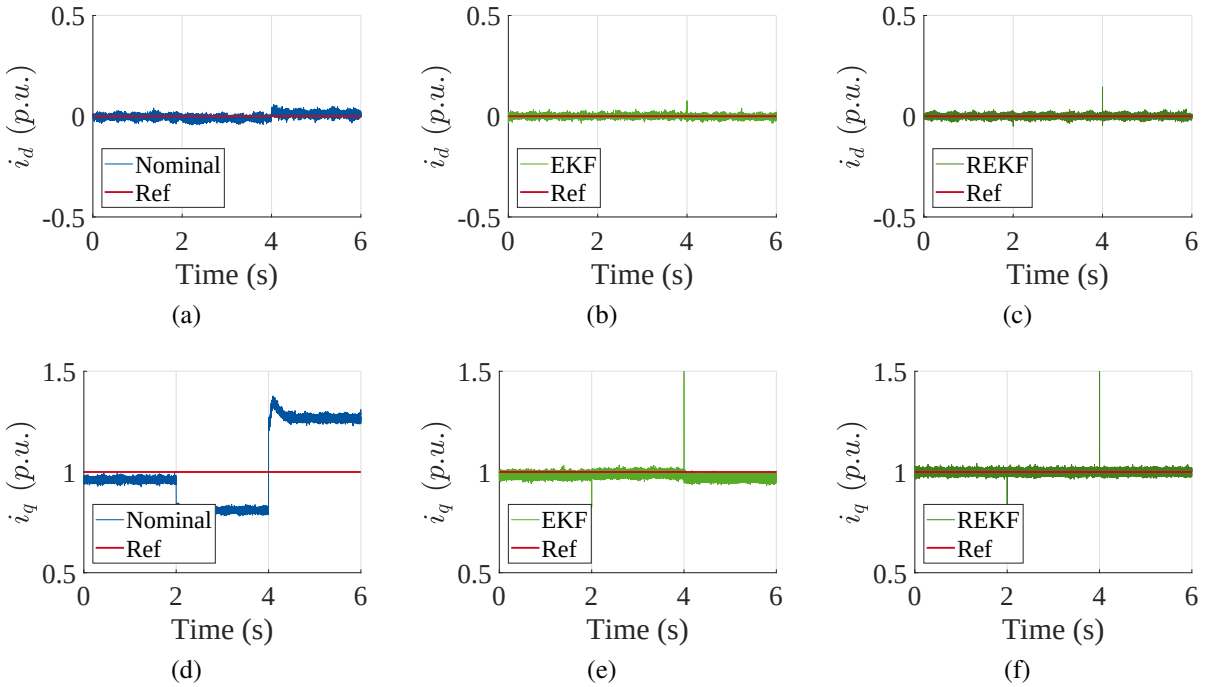

Figure 4.20: Comparison among the proposed RPCC, the conventional CCS-MPC as well as CCS-MPC with the output compensation under the parameter mismatch of Ψ_m and full-load condition. (a) and (d) denote the experimental results with the deadbeat control. (b) and (e) are the currents controlled by the CCS-MPC with the output compensation. (c) and (f) represent the experimental results with the RPCC employing EKF.

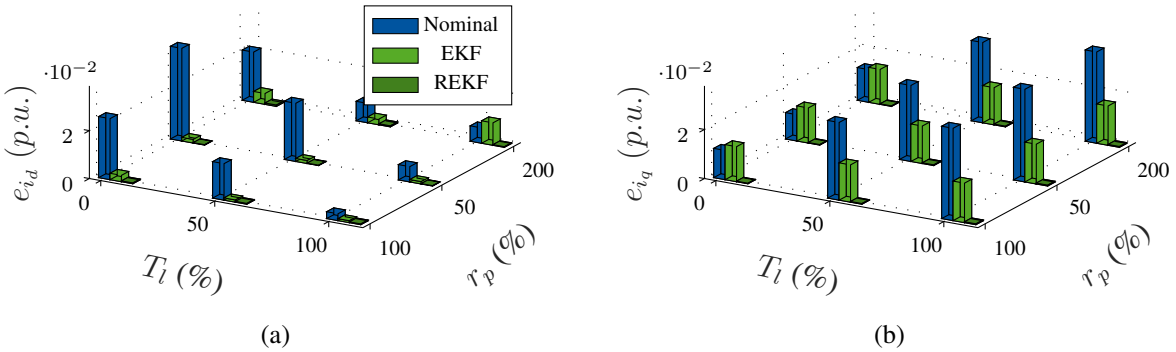

Figure 4.21: Comparison among the proposed RPCC, the conventional CCS-MPC and the CCS-MPC with the output compensation under the variation of L_d. The conventional CCS-MPC is denoted by blue, CCS-MPC with the output compensation is presented by light green and the proposed RPCC with EKF is shown in dark green.

error amplitude, i.e. $|\boldsymbol{e}_i|$, is relatively constant regarding T_l. A reduction of L_d can cause a larger tracking error than an increase of L_d. The output compensation improves the tracking accuracy in the most test cases. Nonetheless, it deteriorates the control performance comparing to the conventional CCS-MPC in some cases, e.g. i_d at $r_p = 200\%$, the full-load condition as well as i_q at the no-load condition. The proposed RPCC effectively eliminates the steady-state errors.

The steady-state errors under the parameter variation of L_q are computed and summarized in Fig. 4.22. In general, the parameter variation of L_q can induce larger steady-state errors than L_d,

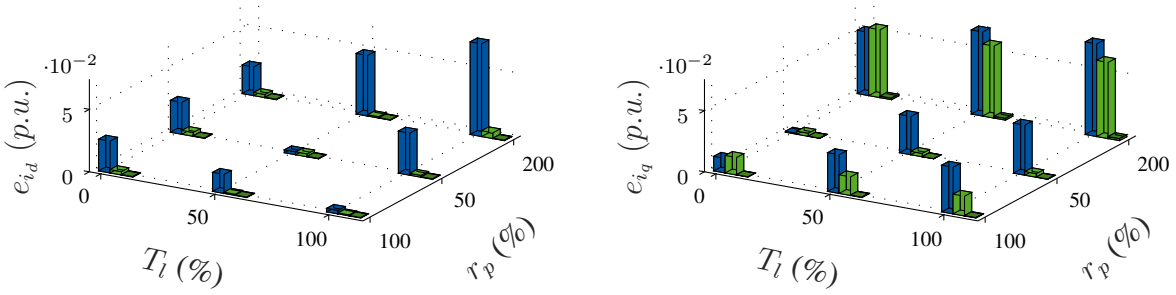

(a) (b)

Figure 4.22: Comparison of the proposed RPCC and the conventional CCS-MPC as well as CCS-MPC with output compensation under the variation of L_q.

both in d-axis and q-axis. More specifically, L_d can induce a steady-state error of approximately 3% of the rated current, while L_q results in an error of up to 8% of the rated current. Its impact depends on the load condition as well as the rate of the variation. The output compensation of CCS-MPC significantly reduces the tracking error in d-axis, while it affects the tracking performance of i_q irrelevantly for the most test scenarios. On the contrary, the proposed RPCC effectively redresses the errors of i_d and i_q.

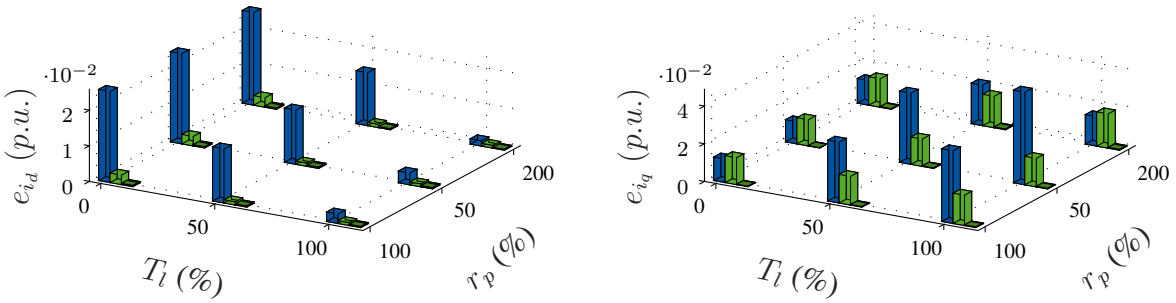

(a) (b)

Figure 4.23: Comparison of the proposed RPCC and the conventional CCS-MPC as well as CCS-MPC with output compensation under the variation of R_s.

In Fig. 4.23, the impacts from the parameter mismatch of R_s are demonstrated. Similar phenomenon to the deadbeat control can be noticed. The output compensation efficaciously eliminates the tracking error of i_d, but reduces the error of i_q only to a certain level or even aggravates the tracking performance in some test cases. The feedforward compensation can

only realize the suboptimum solution for the current control, while the proposed RPCC disposes of the error and reveals the system stability, as presented in Fig. 4.23.

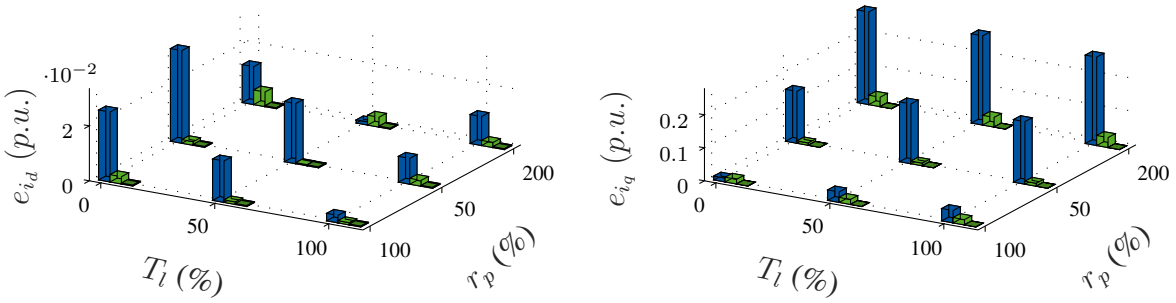

(a) (b)

Figure 4.24: Comparison of the proposed RPCC and the conventional CCS-MPC as well as CCS-MPC with output compensation under the variation of Ψ_m.

From Fig. 4.24, it can be noted that the permanent magnet flux linkage Ψ_m can induce a larger steady-state error for the CCS-MPC than that for the deadbeat control, which can be explained by the fact that the permanent magnet flux linkage Ψ_m contributes to the offset term of the control loop and the induced error is accumulated as the prediction horizon increases. Therefore, the parameter mismatch of the permanent magnet flux linkage Ψ_m can cause larger steady-state errors at most working points. For example, the parameter mismatch of Ψ_m induces a steady-state error of more than 30% of the rated current under the control of the CCS-MPC, which is around 25% under the deadbeat control. An output compensation can significantly reduce the error. However, the steady-state errors can still be noticed. After employing the RPCC, the errors are efficiently eliminated.

In summary, the CCS-MPC is more stable than the deadbeat control, while it demonstrates larger tracking errors under the same parameter mismatches. The reason can be traced back to the fact that the effect of the disturbance accumulates with the increase of the prediction horizon N_p. The output compensation of CCS-MPC can mitigate the impacts of the parameter mismatches to a certain level. But in some cases, depending on the rate of the parameter mismatch and the load condition, the compensation can over-/under-compensate the error and therefore deteriorates the control performance. However, the proposed RPCC outperforms the other two methods and minimizes the effects resulted from the parameter mismatches.

4.5.3 Performance under Encoder Error

Furthermore, the experiment of simulating the encoder error was carried out. An offset is added to the encoder signal. The offset is arbitrary and selected as the biased value at the rotor alignment. Accordingly, the experimental results are shown in Fig. 4.25. The PMSM run at a constant speed of $1500\,\mathrm{rpm}$, where the proposed RPCC was activated at $t = 1\,\mathrm{s}$.

As it is shown in Fig. 4.25, the conventional CCS-MPC fails to track the reference under the existence of an encoder error. An tracking error of around 130% of the rated current can be observed in the q-axis. However, the proposed RPCC effectively compensates the encoder error, i.e. the steady-state error has been cancelled after activating the RPCC. Moreover, it can

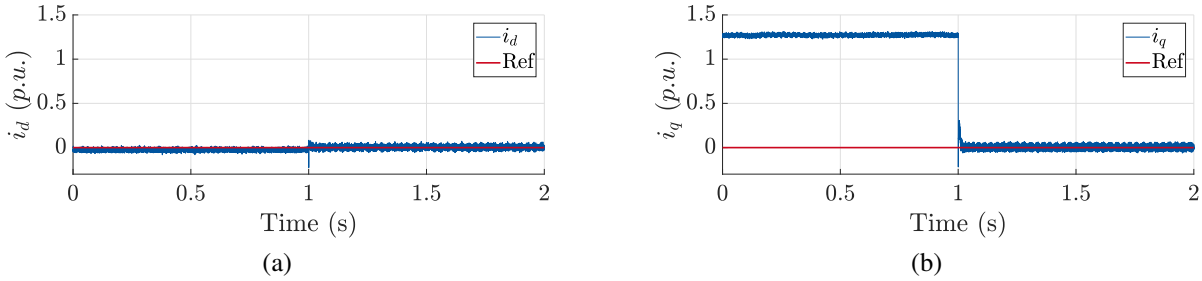

Figure 4.25: Comparison between the CCS-MPC and the proposed RPCC under the encoder error. (a) represents the measurements of i_d and (b) shows the results of i_q.

be concluded that the proposed RPCC can be activated smoothly during the control process and has little effect on the system stability. A small overshoot can be observed at the activation of the RPCC, which is around 15% of the rated current. However, it can be reduced by tuning the parameters of the disturbance observer.

4.5.4 Performance under Inaccurate Digital Delay Compensation

4.5.4.1 High Sampling Frequency

The digital delay is inevitable in the drive system. Normally $1.5\,T_s$ is compensated for the control algorithm to eliminate the influence from the digital delay [24]. In Fig. 4.26, the experimental results of the conventional CCS-MPC without the digital delay compensation is presented. Experimental results of CCS-MPC with a digital delay compensation of $1.5\,T_s$ and the proposed RPCC are shown in Fig. 4.27 and Fig. 4.28, respectively. A load step of 100% of the rated torque was added at $t = 1.5\,\mathrm{s}$.

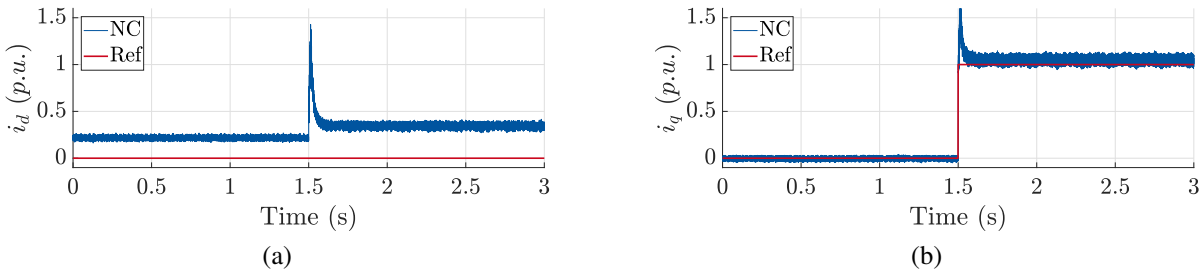

Figure 4.26: The experimental results of the conventional CCS-MPC without digital delay compensation, where the legend 'NC' denotes the corresponding measured currents.

Fig. 4.26 shows that the digital delay mainly causes the steady-state error in the d-axis. Moreover, conspicuous overshoots at the insertion of the load step can be observed both in the d- and the q-axis, which amount to 130% of the rated current in d-axis and 110% of the rated current in q-axis. At no-load condition, the tracking error of i_d accounts for around 25% of I_N. It increases to 40% of the rated current after a load of 100% rated torque is applied.

In Fig. 4.27, a compensation of $1.5\,T_s$ is applied to the PMSM drive system to realize the digital delay compensation. It can be noticed that at the no-load condition, the steady-state error caused by the digital delay is effectively eliminated. However, at $1.5\,\mathrm{s}$, a full load is added

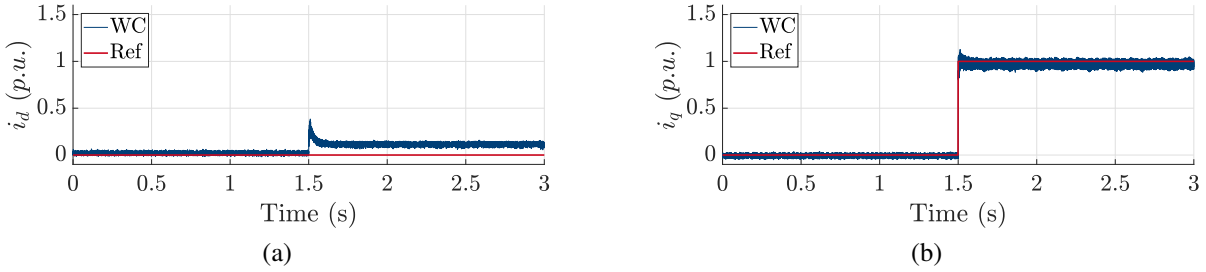

Figure 4.27: The experimental results of the conventional CCS-MPC with a digital delay compensation of $1.5\,T_s$, where the legend 'WC' denotes the corresponding measured currents.

to the PMSM, a tracking error around 15% of the rated current can be noted in the d-axis. By deploying a constant digital delay compensation, the conspicuous overshoot observed in Fig. 4.26 has been dramatically reduced to approximately 25% of I_N in the d-axis and almost fully eliminated in the q-axis.

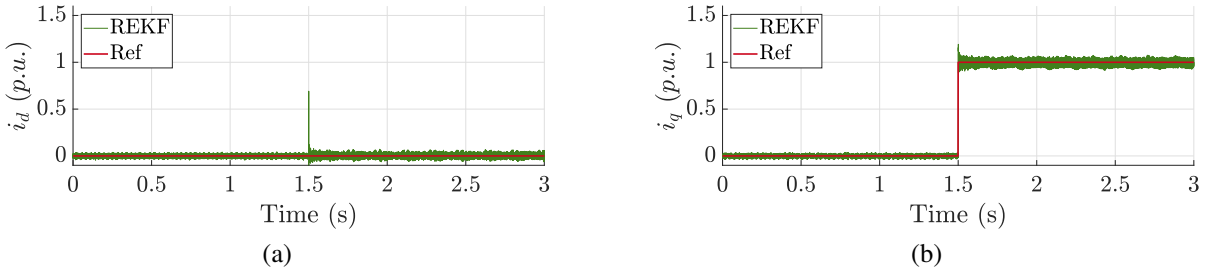

Figure 4.28: The experimental results of the proposed RPCC. The legend 'REKF' denotes the measured currents with RPCC, where EKF is deployed as the observer.

The proposed RPCC is also tested under the existence of the digital delay. The experimental results are shown in Fig. 4.28. The steady-state errors, both in no-load condition and full-load condition, are eliminated by implementing the proposed RPCC. However, it can be noticed that an overshoot of more than 50% of I_N in the d-axis is generated at the load step, which has a relatively high amplitude but a short duration time. This may be resulted from the parameter choice of the EKF, which is so tuned that EKF is relatively aggressive and can react to the disturbance fast. The overshoot noted in Fig. 4.28 can be reduced by tuning the EKF parameters.

4.5.4.2 Low Sampling Frequency

The implemented discretization method in this thesis is the Euler approach. A relatively low sampling frequency impairs the approximation of the discrete-time system to the continuous-time system. Therefore, the digital delay is more crucial for the control with a lower sampling frequency. CCS-MPC and RPCC are furthermore tested with a sampling time of $T_s = 500\,\mu\text{s}$. The PMSM run at $2000\,\text{rpm}$ for this test.

With a larger sampling time and a higher speed, the digital delay is more critical for the control performance of CCS-MPC, i.e. a larger error can be observed at the steady state. It can be observed from Fig. 4.29 that the steady-state error of i_d amounts around 80% of I_N with a sampling frequency of $2\,\text{kHz}$ and under no load, which is much higher than the error at the same

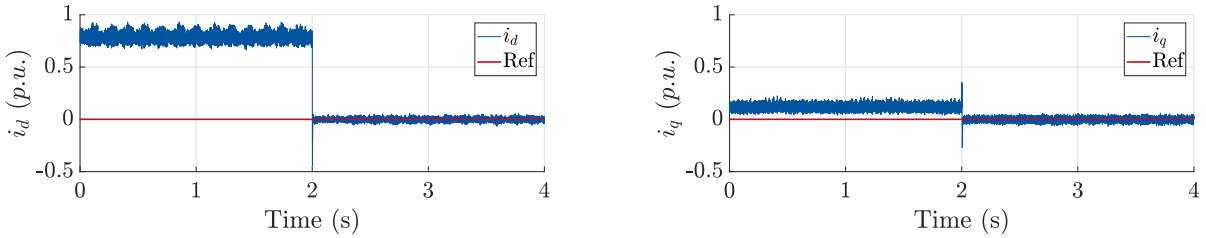

(a) I_d (b) I_q

Figure 4.29: Comparison between the CCS-MPC and the proposed RPCC with a sampling time of $T_s = 500$ µs. The proposed RPCC is activated at $t = 2$ s

condition but with a higher sampling frequency of $10\,\mathrm{kHz}$, which is 25% of the rated current. A small bias can be noted in the q-axis, which is around 10% of I_N. However, after activation of the proposed RPCC, the errors are eliminated. It is worth mentioning that the implementation of the RPCC also reduces the current ripples and therefore improves the current quality.

4.5.5 Summary

In this section, an observer-based robust predictive current control scheme is proposed. This scheme is generally formulated and applicable to any AC drive system. It has been proved to be input-to-state stable, if several prerequisites are satisfied, i.e. the cost function of the corresponding CFTOC problem is a Lyapunov function for the closed-loop nominal system, the initial observer error is bounded and the system propagation function is uniformly continuous in disturbance domain. The effectiveness of the proposed robust predictive current control is verified with experimental results under various scenarios, i.e. the parameter mismatches, the encoder error and the inaccurate digital compensation. The proposed control strategy can be smoothly activated and causes slight overshoot. Therefore, it outperforms conventional predictive controllers, i.e. the deadbeat control and the CCS-MPC at the steady state as well as during the transient. Moreover, because of the filtering effect along with the EKF and MHE, high order harmonics can be attenuated to a certain level. However, due to the limited bandwidth of the observers, the filtering effects have less impact on the low order harmonics.

4.6 Conclusion

The basic concepts of the continuous-control-set model predictive control are firstly reviewed in the first part of this chapter. The CCS-MPC is a powerful approach to synthesize controllers for the constrained systems. However, the synthesis of the CCS-MPC relies on the knowledge of the controlled system. The existence of the model uncertainties and the disturbances impairs the control performance of the CCS-MPC or even cause instability of the closed-loop system, which has been verified by the simulations and experiments. Unfortunately, designing a MPC under these circumstances is challenging in general. Many paradigms, such as the robust MPC and the stochastic MPC, have been proposed to deal with the uncertainties and the disturbances. In this chapter, a disturbance observer is implemented to eliminate the error caused by the parameter mismatches and the disturbances. It can be regarded as a compromise between the

dynamic performance and the robustness, which can provide satisfactory tracking performance and has acceptable computational cost. The proposed control strategy can be extended to other AC drive systems. The inclusion of an observer into the close-loop system affects the system behaviour. Therefore, the closed-loop stability is furthermore investigated, which is proved to be input-to-state stable under the satisfaction of several conditions. The proposed robust predictive current control scheme has shown its effectiveness against parameter mismatches and disturbances, such as the measurement error of the encoder and the digital delay of an embedded system, via the implementation on the embedded system and the corresponding experimental results. However, the low-order harmonics can not be eliminated by implementing the disturbance observer due to the limited bandwidth of the estimator. The attenuation of the low-order harmonics is discussed in the Chapter. 6.

CHAPTER 5

Finite-Control-Set Model Predictive Control

5.1 Introduction

The finite-control-set model predictive control (FCS-MPC) was proposed to inherit the discrete nature of the inverter. Different from the continuous-control-set MPC, FCS-MPC is conceptually simple, has straightforward implementation as well as fast dynamic response and requires less computational resources, if a short prediction horizon is applied [24]. Moreover, since the switching signals of the inverter are directly computed through FCS-MPC, no modulator is required in the FCS-MPC framework [2]. Because of the aforementioned advantages of FCS-MPC, many applications have implemented it to realize the control of power converter. In [217], the FCS-MPC was implemented for a three-phase two-level inverter. In [218], it was applied for a three-phase neutral-point-clamped inverter and in [219] for H-Bridge inverters. Moreover, it has been deployed for different control objects. Authors in [66] implemented the FCS-MPC for the torque control of the induction machines. In [220], it was employed for the speed control for the PMSM and IM and in [97] for the current control of the PMSM. In FCS-MPC, the possible switching states are taken into consideration in the optimization problem. Analogously to CCS-MPC, the underlying optimization problem is a trade-off problem between the reference tracking and the output effort. In the FCS-MPC scheme, the penalization on the command output is replaced by the switching effort.

One of the main drawbacks of FCS-MPC is the high computational burden of solving the underlying optimization problem with a long prediction horizon or when the converter under control, such as modular multi-level converter (MMC), has a large number of switching states, since the problem is in these cases NP-hard, i.e. the computational complexity increases exponentially with the prediction horizon and the voltage level of the inverter [221]. In many applications, the prediction horizon is consequently chosen to be one, aiming to enable the deployment of FCS-MPC in real time. However, the multi-step FCS-MPC shows excellent performance for example for the high-order inverter to cover the oscillation period during the filter resonance. Therefore, many researches focusing on reducing the computational burden

of the long horizon FCS-MPC have been carried out. In [222], the multistep FCS-MPC problem is formulated as an integer least square problem, which can be solved efficiently by using the sphere decoding algorithm. Authors in [223] presented a variable switching point predictive control method with the extended prediction horizon. It shows that the torque ripple and the total harmonic distortion of the current are significantly reduced with a longer prediction horizon. Besides the works focusing on the control algorithms, the efficient implementation of FCS-MPC on real-time control platforms has also been studied. Reference [224] presented an efficient FPGA implementation of FCS-MPC for the flying-capacitor converters and reference [225] implemented a long-horizon FCS-MPC with the sphere decoder on a FPGA. In this chapter, the multi-step FCS-MPC for the current loop, which is also called the multi-step predictive direct current control (MPDCC), is deployed to realize the current control of the PMSM drive system. The multi-step FCS-MPC solves the optimization problem of the current control by reconstructing the optimization problem and applying specific solving algorithm. Then, it employs the receding horizon policy to realize the control. This solution of the FCS-MPC distinguishes itself from other FCS-MPC methods, such as the enumeration-based FCS-MPC and the extrapolation-based FCS-MPC.

As it is indicated in [226], the performance of FCS-MPC is also affected by the parameter mismatches. In this chapter, the principle of the FCS-MPC is introduced firstly, which is followed by the introduction to the MPDCC. The optimization problem, the associated implementation and the solving method are furthermore elaborated. Besides, the influences of the parameter mismatch problem on the FCS-MPC are studied. An improvement of the control performance under the parameter mismatches is proposed by deploying the disturbance observer into the control scheme. Moreover, a special case of PMSM is discussed, i.e. SPMSM. Because of the symmetry of its matrices in the state-space formulation, the MPDCC problem can be simplified by allocating some heavy computations offline, which significantly reduces the online computational burden. Moreover, the effectiveness of implementing the proposed robust solution is shown with the experimental results and compared with the classic FCS-MPC. The corresponding conclusions can be drawn for both the one-step solution and the multi-step solution.

5.2 Finite-Control-Set Model Predictive Control

5.2.1 Control Problem

The control problem of the current loop of a PMSM with the deployment of the FCS-MPC is analogous to that of CCS-MPC. The control problem can be formulated either in the dq reference frame or in the $\alpha\beta$ reference frame. In this thesis, a general formulation in the dq reference frame is firstly given, which is followed by a computational efficient solution in the $\alpha\beta$ reference frame for a special case of PMSM, i.e. SPMSM. The objective function includes two terms, the penalization on the current tracking quality and the penalization on the switching effort. Their weightings in the objective function are tuned by a tuning parameter λ_u, which is appended to the term penalizing the switching effort. In [221], the key elements for the design of the FCS-MPC are mentioned and explicitly analysed via simulations, e.g. the choice of the norm and the tuning of the penalty. As mentioned in Chapter 4, $\mathcal{L}_1$-or $\mathcal{L}_\infty$-norm can

also be used in the objective function. $\mathcal{L}_1$-norm has even the computational advantage over the most applied $\mathcal{L}_2$-norm. Nonetheless, on the one hand, the $\mathcal{L}_1$-norm can result in a performance degradation or even cause the instability of the closed-loop system if $\lambda_u \neq 0$. On the other hand, the stability is guaranteed at $\lambda_u = 0$, while an increase of the switching losses can be prognosticated. Furthermore, the choice of the tuning parameter has a great impact on the control performance. One of the most important criteria to evaluate the control performance of FCS-MPC is the TDD or THD. Their relationships are discussed later in this section via the simulations.

5.2.2 System Model

As it is mentioned previously in this section, the system models of the dq reference frame and of the $\alpha\beta$ reference frame are deployed for the further discussions. Therefore, in order to differentiate the two system models, superscript S is employed to denote the system model in the $\alpha\beta$ reference frame and superscript R represents the dq reference frame. Recall the mathematical model of the PMSM in the dq reference frame, which is given as

$$\begin{aligned} u_d &= R_\mathrm{s}\, i_d + \frac{\mathrm{d}\Psi_d}{\mathrm{d}t} - \omega_\mathrm{e}\Psi_q \,, \\ u_q &= R_\mathrm{s}\, i_q + \frac{\mathrm{d}\Psi_q}{\mathrm{d}t} + \omega_\mathrm{e}\Psi_d \,, \end{aligned} \tag{5.1}$$

where

$$\begin{aligned} \Psi_d &= L_d\, i_d + \Psi_\mathrm{m} \,, \\ \Psi_q &= L_q\, i_q \,. \end{aligned} \tag{5.2}$$

As a result the system model of PMSM in the dq reference frame can be discretized and rewritten in the compact form as follows

$$\begin{aligned} \boldsymbol{x}^R_{k+1} &= \boldsymbol{A}^R \boldsymbol{x}^R_k + \boldsymbol{B}^R \boldsymbol{u}^R_k + \boldsymbol{E}^R \,, \\ \boldsymbol{y}^R_k &= \boldsymbol{C} \boldsymbol{x}^R_k \,, \end{aligned} \tag{5.3}$$

where $\boldsymbol{x}^R := [i_d,\, i_q]^T$, $\boldsymbol{u}^R := [u_d,\, u_q]^T$ and $\boldsymbol{y}^R := [i_d,\, i_q]^T$.

By deploying the inverse Park transformation in (2.11), the system model of the current loop in the $\alpha\beta$ reference frame can be given as follows

$$\begin{bmatrix} u_\alpha \\ u_\beta \end{bmatrix} = \begin{bmatrix} R_\mathrm{s} - 2\omega_e L_{\alpha\beta} & \omega_e L_\alpha - \omega_e L_\beta \\ \omega_e L_\alpha - \omega_e L_\beta & R_\mathrm{s} + 2\omega_e L_{\beta\alpha} \end{bmatrix} \begin{bmatrix} i_\alpha \\ i_\beta \end{bmatrix} + \begin{bmatrix} L_\alpha & L_{\alpha\beta} \\ L_{\beta\alpha} & L_\beta \end{bmatrix} \begin{bmatrix} \dfrac{\mathrm{d}i_\alpha}{\mathrm{d}t} \\ \dfrac{\mathrm{d}i_\beta}{\mathrm{d}t} \end{bmatrix} + \omega_e\, \Psi_\mathrm{m} \begin{bmatrix} -\sin(\theta_e) \\ \cos(\theta_e) \end{bmatrix} \,, \tag{5.4}$$

where

$$L_\alpha = L_0 + L_1 \cos(2\theta_e) \,, \quad L_\beta = L_0 - L_1 \cos(2\theta_e) \,, \quad L_{\alpha\beta} = L_{\beta\alpha} = L_1 \sin(2\theta_e) \,, \tag{5.5}$$

and

$$L_0 = \frac{L_d + L_q}{2} \,, \quad L_1 = \frac{L_d - L_q}{2} \,. \tag{5.6}$$

For the SPMSM, the current dynamics in (5.4) can be simplified with $L_d = L_q = L_0$ as

$$\begin{bmatrix} u_\alpha \\ u_\beta \end{bmatrix} = \begin{bmatrix} R_\mathrm{s} & 0 \\ 0 & R_\mathrm{s} \end{bmatrix} \begin{bmatrix} i_\alpha \\ i_\beta \end{bmatrix} + \begin{bmatrix} L_0 & 0 \\ 0 & L_0 \end{bmatrix} \begin{bmatrix} \dfrac{\mathrm{d}i_\alpha}{\mathrm{d}t} \\ \dfrac{\mathrm{d}i_\beta}{\mathrm{d}t} \end{bmatrix} + \omega_e \, \Psi_\mathrm{m} \begin{bmatrix} -\sin(\theta_e) \\ \cos(\theta_e) \end{bmatrix} . \tag{5.7}$$

Analogously to the dq model presented in (5.3), the system model in the $\alpha\beta$ reference frame is discretized and compactly written as

$$\begin{aligned} \boldsymbol{x}^S_{k+1} &= \boldsymbol{A}^S \boldsymbol{x}^S_k + \boldsymbol{B}^S \boldsymbol{u}^S_k + \boldsymbol{E}^S_k \, , \\ \boldsymbol{y}^S_k &= \boldsymbol{C} \boldsymbol{x}^S_k \, , \end{aligned} \tag{5.8}$$

The vectors are defined as $\boldsymbol{x}^S := [i_\alpha, \, i_\beta]^T$, $\boldsymbol{u}^S := [u_\alpha, \, u_\beta]^T$ and $\boldsymbol{y}^S := [i_\alpha, \, i_\beta]^T$.

5.2.3 Optimization Problem

The most applied FCS-MPC for PMSM is the one-step variant, which indicates that the prediction horizon is chosen as one. The values of the objective function regarding the eight possible switching states are computed and compared. The candidate yielding the minimum cost is then selected as the solution. For a long-horizon control problem, the computational burden of the aforementioned enumeration solving method increases exponentially with the prediction horizon. In this thesis, the sphere decoding algorithm is implemented to tackle this problem, more specifically, to reduce the online computational cost [24].

The current control problem realized with the FCS-MPC at the time step k is formulated as an optimization problem $\mathcal{P}_f$, which can be given in the dq reference frame as [227]

$$\begin{aligned} \min_{\mathbf{U}_k} \quad & J = \sum_{j=k}^{k+N_p-1} \| \boldsymbol{y}_r - \boldsymbol{C} \, \boldsymbol{x}^R_{j+1} \|_2^2 + \lambda_u \| \boldsymbol{u}_{abc,\,j} - \boldsymbol{u}_{abc,\,j-1} \|_2^2 \\ \text{s. t.} \quad & \boldsymbol{x}^R_{j+1} = \boldsymbol{A}^R \, \boldsymbol{x}^R_j + \boldsymbol{B}^R \, \boldsymbol{T}_{dq,\,j} \, \boldsymbol{u}_{abc,\,j} + \boldsymbol{E}^R \, , \\ & \boldsymbol{u}_{abc,\,j} \in \mathbb{V} \times \mathbb{V} \times \mathbb{V} \, , \end{aligned} \tag{5.9}$$

where $\boldsymbol{u}_{abc} := [u_a, \, u_b, \, u_c]^T$ denotes the voltage of the three phases. The voltage constraint $\mathbb{V}$ is given in (2.23) for the two-level VSI. The symbol $\times$ denotes the Cartesian product. $\boldsymbol{T}_{dq}$ represents the Park transformation in (2.11). $\mathbf{U}_k$ denotes the control sequence and can be given as $\mathbf{U}_k := [\boldsymbol{u}^T_{abc,\,k}, \, \boldsymbol{u}^T_{abc,\,k+1}, \, \ldots, \, \boldsymbol{u}^T_{abc,\,k+N_p-1}]^T$, which can be denoted as

$$\begin{aligned} \mathbf{U}^*_k \quad & := \arg\min_{\mathbf{U}_k} J \\ \text{s. t.} \quad & \boldsymbol{x}^R_{j+1} = \boldsymbol{A}^R \, \boldsymbol{x}^R_j + \boldsymbol{B}^R \, \boldsymbol{T}_{dq,\,j} \, \boldsymbol{u}_{abc,\,j} + \boldsymbol{E}^R, \quad j = k, \, k+1 \cdots, \, k+N_p-1 \, , \\ & \mathbf{U}_k \in \mathcal{V} \times \cdots \times \mathcal{V} \, . \end{aligned} \tag{5.10}$$

where $\mathcal{V} := \mathbb{V} \times \mathbb{V} \times \mathbb{V}$. The solution of the aforementioned CFTOC problem $\mathcal{P}_f$ depends on the initial state vector $\boldsymbol{x}_k$, the previously chosen switch state $\boldsymbol{u}_{abc,\,k-1}$ and the reference value. Employing the receding horizon policy, only the first element of $\mathbf{U}^*_k$ is applied to the VSI at the time instant k. At the next time instant, i.e. $t = k+1$, the optimization problem $\mathcal{P}_f$ over a shifted prediction window from $k+1$ to $k+N_p$ is formulated. The solving procedure conducted at the preceding step k is then repeated accordingly.

5.2.4 Implementation

The most straightforward solving method for the optimization problem $\mathcal{P}_f$ is the exhaustive enumeration method, where the set of admissible switching sequences $\mathbf{U}_k$ is enumerated and the cost function is evaluated for each individual switching state. The procedure to conduct the enumeration for $N_p = 1$ is described in the following.

Algorithm 5.1 Enumeration Algorithm

Input: $\boldsymbol{x}_k$, $\boldsymbol{u}_{abc,\,k-1}$, $\mathbb{V}$, N_p, J^*
Output: $\boldsymbol{u}_{abc,\,k}$
  for $\boldsymbol{u}_{abc,i} \in \mathbb{V} \times \mathbb{V} \times \mathbb{V}$ **do**
    if $J_i < J^*$ **then**
      $\boldsymbol{u}_{abc,\,k} = \boldsymbol{u}_{abc,\,i}$
      $J^* = J_i$
    end if
  end for

For a relatively long prediction horizon, all possible switching states over the horizon N_p should be evaluated, which means that the cost function needs to be evaluated 2^{3N_p} times. It is obviously impractical in real-time applications. Therefore, the sphere-decoding algorithm is implemented in this thesis to reduce the computational burden of the long-horizon FCS-MPC. Based on the system model in (5.9), the state vector at the sampling time instant $j+1$ can be written as a function of the initial value $\boldsymbol{x}_k^R$ and the control sequence $\mathbf{U}_k$ in the following

$$\boldsymbol{x}_{j+1} = (\mathbf{A}^R)^{j+1-k}\,\boldsymbol{x}_k + [(\mathbf{A}^R)^{j-k}\,\mathbf{B}^R\,\mathbf{T}_{dq,\,k},\,\cdots,\,\mathbf{B}^R\,\mathbf{T}_{dq,\,j}]\,\mathbf{U}_k + \sum_{i=0}^{j-k}(\mathbf{A}^R)^i\,\mathbf{E}^R\,, \tag{5.11}$$

where $\mathbf{T}_{dq,\,i}$ is computed with the corresponding rotor angle $\theta_{e,\,i}$ at the step i via (2.11). The sequence of the output over the prediction horizon N_p from the time step k is denoted with $\mathbf{Y} := [\boldsymbol{y}_{k+1}^T,\,\cdots,\,\boldsymbol{y}_{k+N_p}^T]^T$, which can be rewritten as

$$\mathbf{Y}^R = \mathbf{\Pi}^R\,\boldsymbol{x}_k^R + \mathbf{\Lambda}^R\,\mathbf{U}_k + \mathbf{\Sigma}^R\,\boldsymbol{E}^R, \tag{5.12}$$

where

$$\mathbf{\Pi}^R = \begin{bmatrix} \boldsymbol{C}\boldsymbol{A}^R \\ \boldsymbol{C}(\boldsymbol{A}^R)^2 \\ \vdots \\ \boldsymbol{C}(\boldsymbol{A}^R)^{N_p} \end{bmatrix}, \quad \mathbf{\Sigma}^R = \begin{bmatrix} \boldsymbol{C}\boldsymbol{I} \\ \boldsymbol{C}\boldsymbol{A}^R + \boldsymbol{C}\boldsymbol{I} \\ \vdots \\ \boldsymbol{C}(\boldsymbol{A}^R)^{N_p-1} + \boldsymbol{C}(\boldsymbol{A}^R)^{N_p-2} + \ldots + \boldsymbol{C}\boldsymbol{I} \end{bmatrix},$$

$$\mathbf{\Lambda}^R = \begin{bmatrix} \boldsymbol{C}\boldsymbol{B}^R\mathbf{T}_{dq,\,k} & \mathbf{0} & \cdots & \mathbf{0} \\ \boldsymbol{C}\boldsymbol{A}^R\boldsymbol{B}^R\mathbf{T}_{dq,\,k} & \boldsymbol{C}\boldsymbol{B}^R\mathbf{T}_{dq,\,k+1} & \cdots & \mathbf{0} \\ \vdots & \vdots & \ddots & \vdots \\ \boldsymbol{C}(\boldsymbol{A}^R)^{N_p-1}\boldsymbol{B}^R\mathbf{T}_{dq,\,k} & \boldsymbol{C}(\boldsymbol{A}^R)^{N_p-2}\boldsymbol{B}^R\mathbf{T}_{dq,\,k+1} & \cdots & \boldsymbol{C}\boldsymbol{B}^R\mathbf{T}_{dq,\,k+N_p-1} \end{bmatrix}. \tag{5.13}$$

Substitute the formulation of the output sequence $\mathbf{Y}$ in (5.12) into the cost function in (5.9) yielding

$$J = \|\boldsymbol{\Pi}^R \boldsymbol{x}_k^R + \boldsymbol{\Lambda}^R \mathbf{U}_k + \boldsymbol{\Sigma}^R \boldsymbol{E}^R - \mathbf{Y}_r\|_2^2 + \lambda_u \|\boldsymbol{S}\mathbf{U}_k - \boldsymbol{\delta}\boldsymbol{u}_{abc,\,k-1}\|_2^2 \tag{5.14}$$

where the matrices $\boldsymbol{S}$ and $\boldsymbol{\delta}$ are given as

$$\boldsymbol{S} = \begin{bmatrix} \boldsymbol{I} & \mathbf{0} & \dots & \mathbf{0} \\ -\boldsymbol{I} & \boldsymbol{I} & \dots & \mathbf{0} \\ \mathbf{0} & -\boldsymbol{I} & \dots & \mathbf{0} \\ \vdots & \vdots & & \vdots \\ \mathbf{0} & \mathbf{0} & \dots & \boldsymbol{I} \end{bmatrix}, \quad \boldsymbol{\delta} = \begin{bmatrix} \boldsymbol{I} \\ \mathbf{0} \\ \mathbf{0} \\ \vdots \\ \mathbf{0} \end{bmatrix}. \tag{5.15}$$

In (5.14), $\boldsymbol{x}_k$ and $\boldsymbol{u}_{abc,\,k-1}$ are already available at establishing the optimization problem $\mathcal{P}_f$. The cost function can be reformulated to separate the $\mathbf{U}_k$ related term and the unrelated term, which can be established as

$$J = \theta_k + 2\boldsymbol{\Theta}_k^T \mathbf{U}_k + \|\mathbf{U}_k\|_{\boldsymbol{H}_t}^2 , \tag{5.16}$$

where

$$\begin{aligned} \theta_k :=& \|\mathbf{Y}_r - \boldsymbol{\Pi}^R \boldsymbol{x}_k^R - \boldsymbol{\Sigma}^R \boldsymbol{E}^R\|_2^2 + \lambda_u \|\boldsymbol{\delta}\, \boldsymbol{u}_{abc,\,k-1}\|_2^2 , \\ \boldsymbol{\Theta}_k :=& \big((\mathbf{Y}_r - \boldsymbol{\Pi}^S \boldsymbol{x}_k^R - \boldsymbol{\Sigma}^R \boldsymbol{E}^R)^T \boldsymbol{\Lambda}^R - \lambda_u (\boldsymbol{\delta}\, \boldsymbol{u}_{abc,\,k-1})^T \boldsymbol{S}\big)^T , \\ \boldsymbol{H}_t :=& (\boldsymbol{\Lambda}^R)^T \boldsymbol{\Lambda}^R + \lambda_u \boldsymbol{S}^T \boldsymbol{S} . \end{aligned}$$

The squared form related to $\mathbf{U}_k$ can be derived from (5.16) as

$$J = (\mathbf{U}_k + \boldsymbol{H}_t^{-1}\boldsymbol{\Theta}_k)^T \boldsymbol{H}_t (\mathbf{U}_k + \boldsymbol{H}_t^{-1}\boldsymbol{\Theta}_k) + J_c(\boldsymbol{x}_k^R,\, \boldsymbol{u}_{abc,\,k-1}) , \tag{5.17}$$

where $J_c(\boldsymbol{x}_k^R,\, \boldsymbol{u}_{abc,\,k-1})$ denotes the term only related to $\boldsymbol{x}_k^R$, $\boldsymbol{u}_{abc,\,k-1}$ and can be regarded as a constant at solving $\mathcal{P}_f$. Obviously, regardless of the constraint $\boldsymbol{u}_{abc,\,j} \in \mathbb{V} \times \mathbb{V} \times \mathbb{V}$, the optimization problem $\mathcal{P}_f$ can be solved analogously to CCS-MPC, i.e. by solving the root finding problem of

$$\nabla_{\mathbf{U}_k} J = \mathbf{0} . \tag{5.18}$$

Thus, the unconstrained solution at the time step k can be given as

$$\mathbf{U}_{unc} = -\boldsymbol{H}_t^{-1}\boldsymbol{\Theta}_k , \tag{5.19}$$

which can be substituted into (5.17) and gives

$$J = (\mathbf{U}_k - \mathbf{U}_{unc})^T \boldsymbol{H}_t (\mathbf{U}_k - \mathbf{U}_{unc}) + J_c . \tag{5.20}$$

The matrix $\boldsymbol{H}_t$ is positive definite and symmetric, if a positive λ_u is applied in the cost function. As a result, it can be decomposed with the Cholesky decomposition as

$$\boldsymbol{H}^{-1}\boldsymbol{H}^{-T} = \boldsymbol{H}_t^{-1} . \tag{5.21}$$

By substituting (5.21) into (5.20), the solution to the optimization problem can be written as

$$\mathbf{U}^* = \arg\min_{\mathbf{U}_k} \|\boldsymbol{H}\mathbf{U}_k - \boldsymbol{H}\,\mathbf{U}_{unc}\|_2^2\,, \tag{5.22}$$

subject to $\mathbf{U}_k \in \mathcal{V} \times \cdots \times \mathcal{V}$.

The optimization problem $\mathcal{P}_f$ can be sorted into the category of the mixed-integer quadratic programming (MIQP) problem. Branch-and-bound is a classic method for solving this problem, which is based on avoiding exploring the entire feasible set in most cases when all possible solutions are enumerated [228]. The branching decides which subproblem to solve and the bounding uses these subproblems to compute lower bounds of the optimal cost. The applied sphere decoding algorithm is built on the branch-and-bound techniques, which is introduced, explained and improved in several works, such as [229, 230]. In contrast to other algorithms, sphere decoder restricts the search region to a certain sphere of a radius d around the given vector, which reduces the complexity of solving the optimization problem. Besides, the prospective complexity is polynomial or often roughly cubic. The principle of the algorithm is to iteratively evaluate the candidate switching sequences whether they lie inside the sphere consisting of the radius $\rho_k > 0$ and the center $\boldsymbol{H}\,\mathbf{U}_{unc}$, i.e.

$$\|\boldsymbol{H}\mathbf{U}_k - \mathbf{U}_{unc}^H\|_2 \leq\ \rho_k\,, \tag{5.23}$$

where $\mathbf{U}_{unc}^H = \boldsymbol{H}\,\mathbf{U}_{unc}$ and find the lattice point $\mathbf{U}_k$ within the sphere. Actually, the optimal solution $\mathbf{U}_k^*$ is the lattice point that has the shortest Euclidean distance to the sphere center. As previously stated, the sphere decoding algorithm adopts the notion of branch-and-band technique, where the branching is conducted by considering admissible single-phase switch states $\mathbb{V}$ and bounding is realized by assessing the solutions with the predefined radius ρ_k of the sphere [24].

Thanks to the characteristics of the matrix $\boldsymbol{H}$, i.e. lower triangular, the inequality (5.23) can be reformulated as

$$\rho_k \geq (u_{1,\,k}^H -\ h_{1,\,1}\,u_{1,\,k})^2 + (u_{2,\,k}^H -\ h_{2,\,1}\,u_{1,\,k} -\ h_{2,\,2}\,u_{2,\,k})^2 + \cdots\,, \tag{5.24}$$

where $u_{i,\,k}^H$ is the i-th element of $\mathbf{U}_{unc}^H$. $u_{i,\,k}$ represents the i-th element of $\mathbf{U}_k$ and $h_{i,\,j}$ denotes the i-th row, j-th column of $\boldsymbol{H}$. It is worth mentioning that the optimal solution of the integer least square problem in (5.23) is sequentially determined. Each branch and node of the search tree has corresponding physical meanings, where the branch denotes the two possibilities of the switching state at corresponding node. Let the searching procedure start from the first level and search firstly the left branch. One step after, the updated Euclidean distance ρ_1 is given by

$$\rho_1^2 := (u_{1,\,k}^H - h_{1,\,1}\,u_{1,\,k})^2\,. \tag{5.25}$$

Then, the value ρ_1 is compared with the sphere radius ρ_0, if the condition $\rho_0^2 \geq \rho_1^2$ holds, the searching process continues to the next level, likewise firstly to the left side. The updated Euclidean distance has an extra term $u_{2,\,k}^H -\ h_{2,\,1}\,u_{1,\,k} -\ h_{2,\,2}\,u_{2,\,k}$ in comparison to ρ_1^2 and is formed as

$$\rho_1^2 + (u_{2,\,k}^H -\ h_{2,\,1}\,u_{1,\,k} -\ h_{2,\,2}\,u_{2,\,k})^2\,. \tag{5.26}$$

The distance is updated until the leaf of the search tree is reached, which can be represented by ρ_3^2, so far the first possible switching sequence is verified. Then, the new Euclidean distance ρ^2

is defined by ρ_3^2, which denotes a new shrinking sphere compared with the one with radius ρ_0. This methods is also known as the shrinking-radius strategy. Then, the second node of the third level is explored, which obviously denotes a larger value compared with ρ_3^2, i.e. the right node of third level lies out of the sphere with radius ρ. Analogously, the other nodes are beyond the sphere defined by the radius $\rho = \rho_3$, i.e. these nodes denote only the non-optimal solutions. As a result, the search tree is pruned. Because of the characteristic of the integer least-squares (ILS) problem, the sphere decoding algorithm distinguishes itself from the conventional enumeration algorithm, which will run through all the nodes included in the tree. Since the sphere decoding algorithm is widely used and researched in communication field, there are various methods for further reducing the complexity, such as the nulling canceling decoding in [231], Schnorr-Euchner sphere decoding in [232] and [233] as well as lattice reduction method in [234], which is based on fundamentals from [235] and LLL reduction method from [236]. Readers can refer to these works for details. Another important parameter to be determined prior to the optimization is the initial value of ρ_k, which should be large enough to ensure the existence of the solution set and meanwhile be small enough to bound as few candidate switching sequences a priori as possible. As it is proposed in [24], an initial radius based on the educated guess is deployed, which is computed by shifting the most recent solution $\mathbf{U}_{k-1}^*$ and repeating the last switching states $\boldsymbol{u}_{abc,\,k-1+N_p-1}$, i.e. $\rho_0 = \|\boldsymbol{H}\mathbf{U}_{0,\,k} - \mathbf{U}_{unc}^H\|_2$ where

$$\mathbf{U}_{0,\,k} = \begin{bmatrix} \mathbf{0} & \boldsymbol{I} & \mathbf{0} & \cdots & \mathbf{0} \\ \mathbf{0} & \mathbf{0} & \boldsymbol{I} & \ddots & \vdots \\ \vdots & \ddots & \ddots & \ddots & \mathbf{0} \\ \mathbf{0} & \mathbf{0} & \cdots & \mathbf{0} & \boldsymbol{I} \\ \mathbf{0} & \mathbf{0} & \cdots & \mathbf{0} & \boldsymbol{I} \end{bmatrix} \mathbf{U}_{k-1}^* \,. \tag{5.27}$$

The complete sphere decoding algorithm is shown in Algorithm 5.2.

Algorithm 5.2 Sphere Decoding Algorithm

function $\mathbf{U}^* = \mathbf{SpD}(i,\ \rho_0,\ \mathbf{U}_{unc}^H,\ \epsilon)$
for $\boldsymbol{u} \in \mathcal{V}$ **do**
  $\boldsymbol{u}_{i,\,k} = \boldsymbol{u}$
  $\rho^2 = \|\boldsymbol{u}_{i,\,k}^H - \boldsymbol{h}_{i,\,1:i}\,\boldsymbol{u}_{i,\,k}\|_2^2 + \epsilon^2$
  if $\rho^2 \leq \rho_0^2$ **then**
    if $i < 3N_p$ **then**
      $\mathbf{SpD}(i+1,\ \rho_0,\ \mathbf{U}_{unc}^H,\ \epsilon)$
    else
      $\mathbf{U}^* = \mathbf{U}$
      $\rho_0^2 = \rho^2$
    end if
  end if
end for
end function

5.3 Observer-Enhanced FCS-MPC

It has been mentioned in Section 4.3 that the parameter mismatches and the disturbances have a great impact on the control performance. Simulations as well as experiments have been further carried out to verify the influence from the uncertainties and disturbances on the continuous-control-set MPC. Different from the CCS-MPC, FCS-MPC includes the discrete nature of the VSI into the optimization problem, which impedes the analysis and the quantification of the influences. In this section, the analysis with the aid of the simulations is carried out. However, because of the discrete characteristic of the FCS-MPC, the model uncertainties and the disturbances not necessarily affect the solution. Therefore, the probability of the selection of the non-optimal solution is shown via the simulations. The aforementioned MPDCC problem is formulated in the dq reference frame, the solving of the underlying optimization problem follows the procedure introduced in Section 5.2.4. The matrix $\boldsymbol{H}_t$, which defines the searching space, needs to be computed individually at each sampling instant, since the matrix $\boldsymbol{\Lambda}^R$ contains the Park transformations based on the current as well as the subsequent rotor position. It aggravates the computational burden of FCS-MPC as the prediction horizon increases. Considering the characteristics of SPMSM, the FCS-MPC can be formulated in the $\alpha\beta$ reference domain, which reduces the computational burden of the optimization problem by allocating part of the matrices computation offline. Furthermore, the effects of the parameter mismatch on the permanent magnet synchronous motor drive system with the FCS-MPC as the current controller is comprehensively simulated in this section and their quantitative assessment is also given. In order to improve the control performance, the external disturbance is then estimated with the moving horizon estimator and included into the current control problem. The effectiveness of the proposed method is validated with experiments.

5.3.1 Control Problem

An observed-based robust direct current control scheme is proposed for the PMSM drive system. In this section, the moving horizon estimator is chosen to realize the estimation of the disturbance as well as the currents. The other estimators, such as EKF and UKF, can be implemented analogously.

The control structure of the proposed observed-enhanced FCS-MPC is shown in Fig. 5.1. The estimator is set up in the dq reference frame, while the current controller is formulated in the $\alpha\beta$ domain. It is worth mentioning, if instead of SPMSM a general PMSM is of interest, the control problem formulation in the $\alpha\beta$ reference frame has few advantage over the formulation in dq reference frame. In this case, the FCS-MPC should be established in the dq reference frame.

5.3.2 System Model

In the framework of the proposed observer-enhanced direct current control, two system models are deployed, i.e. the current dynamic formulation in the dq reference frame in (5.3) and that in the $\alpha\beta$ reference frame in (5.8). The observer is constructed in the dq reference frame, which is based on the fact that the state-space formulation given in (5.7) is a special case of PMSM, i.e. SPMSM, and its matrices, e.g. $\boldsymbol{E}^S$ (also $\boldsymbol{A}^S$ and $\boldsymbol{B}^S$ for other types of PMSM), are related to

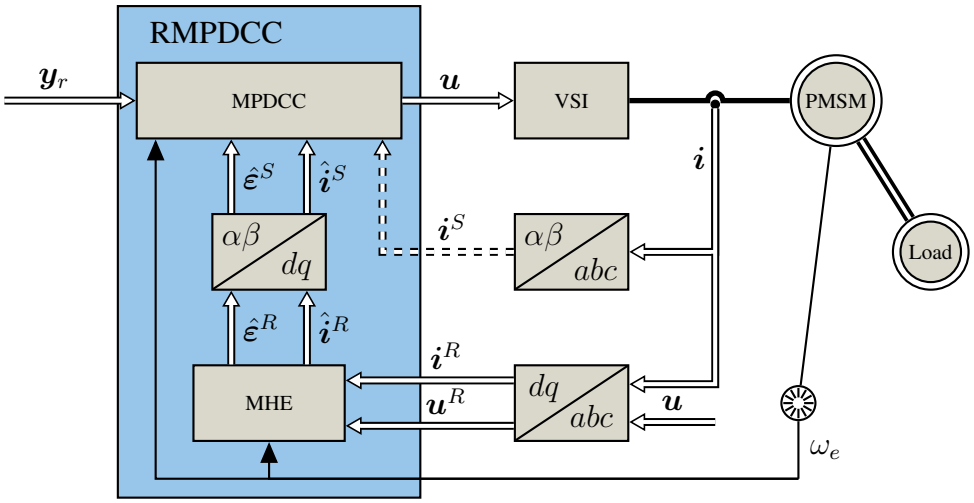

Figure 5.1: Whole control structure FCS PMSM

the electrical rotor position θ_e. Therefore, the matrices of the observer, especially for the case of a long estimation horizon, need to be separately computed and updated at each sampling time instant if the estimation problem is established in the $\alpha\beta$ reference frame. As a result, the estimation is computationally expensive and requires additional computations as well as memories. Nonetheless, the controller is formulated in the $\alpha\beta$ domain for the SPMSM. For the other types of machine, of which the symmetry of the matrix is not valid, a formulation of the current controller in the dq reference frame is recommended. Considering the system state-space of SPMSM in (5.7), the matrix $\boldsymbol{H}_t$ required for the FCS-MPC can be then computed offline.

5.3.3 Optimization Problem

In this section, two optimization problems are elaborated, i.e. the CFTOC problem $\mathcal{P}_f$ and the MHE-based estimation problem $\mathcal{P}_e$. The moving horizon estimator is implemented to estimate the disturbance caused by the unmodelled uncertainties, e.g. the parameter mismatches and the disturbances. The MHE is formulated in the dq reference frame and employs the incremental computation, which is sensitive to the initial value and the parameter selections. However, it has computational advantages over the MHE formulated in (3.78). The associating optimization problem $\mathcal{P}_e$ at the time step $k = n + N_e - 1$ over an estimation horizon of N_e can be written as [171]

$$\begin{aligned} \min_{\boldsymbol{x},\,\boldsymbol{\varepsilon}} \quad & J_{obs} = \sum_{j=n}^{k} \|\boldsymbol{y}_j^R - \boldsymbol{C}\hat{\boldsymbol{x}}_j^R\|_{\mathbf{Q}}^2 + \sum_{j=n}^{k-1} \|\Delta\hat{\boldsymbol{\varepsilon}}_j^R\|_{\mathbf{R}}^2 \\ \text{s.t.} \quad & \hat{\boldsymbol{x}}_{j+1}^R = \boldsymbol{A}^R\hat{\boldsymbol{x}}_j^R + \boldsymbol{B}^R\boldsymbol{u}_j^R + \boldsymbol{E}^R + \hat{\boldsymbol{\varepsilon}}_j^R \,, \\ & \hat{\boldsymbol{\varepsilon}}_{j+1}^R = \hat{\boldsymbol{\varepsilon}}_n^R + \Delta\hat{\boldsymbol{\varepsilon}}_j^R \,. \end{aligned} \tag{5.28}$$

The optimization problem $\mathcal{P}_e$ in (5.28) is then reformulated into a matrix formulation after substitute the system state-space formulation into the cost function. The cost function is then rewritten as

$$J_{obs} = (\mathbf{Y}^R - \mathbf{Y}^R)^T \mathcal{Q} \, (\mathbf{Y}^R - \hat{\mathbf{Y}}^R) + (\Delta\hat{\boldsymbol{\mathcal{E}}}^F)^T \mathcal{R} \, \Delta\hat{\boldsymbol{\mathcal{E}}}^R \,, \tag{5.29}$$

where $\mathbf{Y}^R$ is the sequence of the measurements, which can be written as $\mathbf{Y}^R := [\boldsymbol{y}_n^T,\, \boldsymbol{y}_{n+1}^T,\, \ldots,\, \boldsymbol{y}_k^T]^T$. $\Delta\hat{\boldsymbol{\mathcal{E}}}$ is the sequence of the disturbance increment over the estimating horizon, which can be written as $\Delta\hat{\boldsymbol{\mathcal{E}}} := [\Delta\hat{\boldsymbol{\varepsilon}}_n^T,\, \Delta\hat{\boldsymbol{\varepsilon}}_{n+1}^T,\, \ldots,\, \Delta\hat{\boldsymbol{\varepsilon}}_k^T]^T$ and $\hat{\mathbf{Y}}$ is the sequence of the estimation on the output variables, which is defined as $\hat{\mathbf{Y}} := [\hat{\boldsymbol{y}}_n^T,\, \hat{\boldsymbol{y}}_{n+1}^T,\, \ldots,\, \hat{\boldsymbol{y}}_k^T]^T$. $\hat{\mathbf{Y}}$ can be further written as a function of the initial value of the estimated state $\hat{\boldsymbol{x}}_n$, the control sequence $\mathbf{U}$ and the estimated disturbance $\hat{\boldsymbol{\varepsilon}}_n$ as

$$\hat{\mathbf{Y}}^R = \boldsymbol{\Pi}^R\, \hat{\boldsymbol{x}}_n^R + \boldsymbol{\Lambda}^R\, \mathbf{U}^R + \boldsymbol{\Sigma}^R\, (\boldsymbol{E}^R + \hat{\boldsymbol{\varepsilon}}_n^R) + \boldsymbol{\Phi}^R \Delta\hat{\boldsymbol{\mathcal{E}}}^R\,, \tag{5.30}$$

where $\boldsymbol{\Pi}^R$ and $\boldsymbol{\Sigma}^R$ share the same structure as in (5.12). $\boldsymbol{\Lambda}^R$ and $\boldsymbol{\Phi}^R$ are given as

$$\boldsymbol{\Phi}^R = \begin{bmatrix} \boldsymbol{CI} & \mathbf{0} & \ldots & \mathbf{0} \\ \boldsymbol{CA}^R & \boldsymbol{CI} & \ldots & \mathbf{0} \\ \vdots & \vdots & \ddots & \vdots \\ \boldsymbol{C}(\boldsymbol{A}^R)^{N_e-1} & \ldots & \ldots & \boldsymbol{CI} \end{bmatrix},\ \boldsymbol{\Lambda}^R = \begin{bmatrix} \boldsymbol{CB}^R & \mathbf{0} & \ldots & \mathbf{0} \\ \boldsymbol{CA}^R\boldsymbol{B}^R & \boldsymbol{CB}^R & \ldots & \mathbf{0} \\ \vdots & \vdots & \ddots & \vdots \\ \boldsymbol{C}(\boldsymbol{A}^R)^{N_e-1}\boldsymbol{B}^R & \boldsymbol{C}(\boldsymbol{A}^R)^{N_e-2}\boldsymbol{B}^R & \ldots & \boldsymbol{CB}^R \end{bmatrix}.$$

The problem $\mathcal{P}_e$ can be solved by solving the root-finding problem

$$\nabla_{\Delta\hat{\boldsymbol{\mathcal{E}}}^R} J_{obs} = \mathbf{0}\,. \tag{5.31}$$

By substituting (5.30) into (5.29) the solution of (5.31) can be derived as

$$\Delta\hat{\boldsymbol{\mathcal{E}}}^R = ((\boldsymbol{\Phi}^R)^T\, \mathcal{Q}\, \boldsymbol{\Phi}^R + \mathcal{R})^{-1} (\boldsymbol{\Phi}^R)^T \mathcal{Q}\, \boldsymbol{\xi} \tag{5.32}$$

where

$$\boldsymbol{\xi} = \boldsymbol{Y}^R - \boldsymbol{\Pi}^R\, \hat{\boldsymbol{x}}_n^R - \boldsymbol{\Lambda}^R\, \boldsymbol{U}^R - \boldsymbol{\Sigma}^R\, (\boldsymbol{E}^R + \hat{\boldsymbol{\varepsilon}}_n^R) \tag{5.33}$$

After obtaining the estimating results $\hat{\boldsymbol{x}}^R$ and $\hat{\boldsymbol{\varepsilon}}^R$ from MHE, the inverse Park transformation is deployed to transform the quantity from the dq reference frame to the $\alpha\beta$ reference frame. The current control problem in (5.9) need to be reformulated into the $\alpha\beta$ reference frame, which is then given as

$$\begin{aligned} \min_{\mathbf{U}_k} \quad & J = \sum_{j=k}^{k+N_p-1} \|\boldsymbol{y}_r - \boldsymbol{C}\, \hat{\boldsymbol{x}}_{j+1}^S\|_2^2 + \lambda_u \|\boldsymbol{u}_{abc,\,j} - \boldsymbol{u}_{abc,\,j-1}\|_2^2 \\ \text{s. t.} \quad & \hat{\boldsymbol{x}}_{j+1}^S = \boldsymbol{A}^S\, \hat{\boldsymbol{x}}_j^S + \boldsymbol{B}^S\, \boldsymbol{T}_{\alpha\beta}\, \boldsymbol{u}_{abc,\,j} + \boldsymbol{E}_j^S + \hat{\boldsymbol{\varepsilon}}_j^S\,, \\ & \boldsymbol{u}_{abc,\,j} \in \mathbb{V} \times \mathbb{V} \times \mathbb{V}\,. \end{aligned} \tag{5.34}$$

5.3.4 Implementation

The solution and implementation of the problem $\mathcal{P}_f$ in (5.34) is given in the following. Analogously to the solving procedure for the classic FCS-MPC in (5.9), the objective function of (5.34) can be reformulated as

$$J = \theta_k + 2(\boldsymbol{\Theta}_k)^T \mathbf{U}_k + \|\mathbf{U}_k\|_{\boldsymbol{H}_t}^2 \tag{5.35}$$

where

$$\begin{aligned}\theta_k :=& \|\mathbf{Y}_r - \boldsymbol{\Pi}^S\,\hat{\boldsymbol{x}}_k^S - \boldsymbol{\Phi}^S\,\boldsymbol{T}\,(\boldsymbol{E}^R + \hat{\boldsymbol{\varepsilon}}_k^R)\|_2^2 + \lambda_u \|\boldsymbol{\delta}\boldsymbol{u}_{abc,k-1}\|_2^2\,,\\ \boldsymbol{\Theta}_k :=& ((\mathbf{Y}_r - \boldsymbol{\Pi}^S\,\hat{\boldsymbol{x}}_k^S - \boldsymbol{\Phi}^S\,\boldsymbol{T}\,(\boldsymbol{E}^R + \hat{\boldsymbol{\varepsilon}}_k^R))^T\,\boldsymbol{\Lambda}^S - \lambda_u(\boldsymbol{\delta}\boldsymbol{u}_{abc,k-1})^T\boldsymbol{S})^T\,,\\ \boldsymbol{H}_t :=& (\boldsymbol{\Lambda}^S)^T\boldsymbol{\Lambda}^S + \lambda_u\,\boldsymbol{S}^T\boldsymbol{S}\,,\end{aligned}$$

where $\mathbf{Y}_r$ denotes the N_p replicates of $\boldsymbol{y}_r$. The matrices $\boldsymbol{S}$, $\boldsymbol{\delta}$ are presented in (5.15). The matrices $\boldsymbol{\Pi}^S$, $\boldsymbol{\Phi}^S$, $\boldsymbol{\Lambda}^S$ and $\boldsymbol{T}$ are given in the following as

$$\boldsymbol{\Pi}^S = \begin{bmatrix} \boldsymbol{C}\boldsymbol{A}^S \\ \boldsymbol{C}(\boldsymbol{A}^S)^2 \\ \vdots \\ \boldsymbol{C}(\boldsymbol{A}^S)^{N_p} \end{bmatrix},\ \boldsymbol{\Phi}^S = \begin{bmatrix} \boldsymbol{C}\boldsymbol{I} & \mathbf{0} & \dots & \mathbf{0} \\ \boldsymbol{C}\boldsymbol{A}^S & \boldsymbol{C}\boldsymbol{I} & \dots & \mathbf{0} \\ \vdots & \vdots & \ddots & \vdots \\ \boldsymbol{C}(\boldsymbol{A}^S)^{N_p-1} & \dots & \dots & \boldsymbol{C}\boldsymbol{I} \end{bmatrix},\ \boldsymbol{T} = \begin{bmatrix} \boldsymbol{T}_{dq,\,k}^{-1} \\ \boldsymbol{T}_{dq,\,k+1}^{-1} \\ \vdots \\ \boldsymbol{T}_{dq,\,k+N_p-1}^{-1} \end{bmatrix},$$

$$\boldsymbol{\Lambda}^S = \begin{bmatrix} \boldsymbol{C}\boldsymbol{B}^S\boldsymbol{T}_{\alpha\beta} & \mathbf{0} & \dots & \mathbf{0} \\ \boldsymbol{C}\boldsymbol{A}^S\boldsymbol{B}^S\boldsymbol{T}_{\alpha\beta} & \boldsymbol{C}\boldsymbol{B}^S\boldsymbol{T}_{\alpha\beta} & \dots & \mathbf{0} \\ \vdots & \vdots & \ddots & \vdots \\ \boldsymbol{C}(\boldsymbol{A}^S)^{N_p-1}\boldsymbol{B}^S\boldsymbol{T}_{\alpha\beta} & \dots & \dots & \boldsymbol{C}\boldsymbol{B}^S\boldsymbol{T}_{\alpha\beta} \end{bmatrix}.$$

Similarly to the nominal MPDCC in [227], the solution to the optimization problem in (5.35) can be computed via the Algorithm 5.2 and rewritten more compactly as

$$\mathbf{U}^* = \arg\min_{\mathbf{U}_k} \|\boldsymbol{H}\mathbf{U}_k - \mathbf{U}_{unc}^H\|_2^2\,. \tag{5.36}$$

It is worth mentioning that the matrices $\boldsymbol{\Pi}^S$, $\boldsymbol{\Phi}^S$ and $\boldsymbol{\Lambda}^S$ can be computed offline, since they are only related to the system matrix $\boldsymbol{A}^S$, the input matrix $\boldsymbol{B}^S$, the output matrix $\boldsymbol{C}$ and the Clarke transformation matrix $\boldsymbol{T}_{\alpha\beta}$, which are time invariant. Therefore, the computation of the intermediate matrices $\boldsymbol{H}_t$ and $\boldsymbol{H}$ is then allocated offline, which reduces the online computational burden significantly. After constructing the optimization problem, the problem in (5.34) is then solved with the Algorithm 5.2.

5.3.5 Simulation Results

5.3.5.1 Parameter Design

Firstly, the simulations to demonstrate the impact from the design parameter of the FCS-MPC on the control performance have been carried out. The investigated system is a two-level inverter drive system with a PMSM operated at the rated speed and the full-load condition. The sampling frequency f_s is chosen as $10\,\mathrm{kHz}$. The first simulation for investigating the performance of FCS-MPC in terms of the THD related to the switching frequencies was carried out for prediction horizons $N_p = 1, 3, 5, 10$. The simulation results are presented in Fig. 5.2a. The second simulation was conducted to study the relationship between the weighting factor λ_u and the switching frequencies, where the prediction horizon N_p was selected of the values 1, 3, 5 and 10. The simulation results are shown in Fig. 5.2b.

It can be observed from the Fig. 5.2 that under the same switching frequencies FCS-MPC with diverse prediction horizons delivers similar THDs. Nonetheless, differences can still be

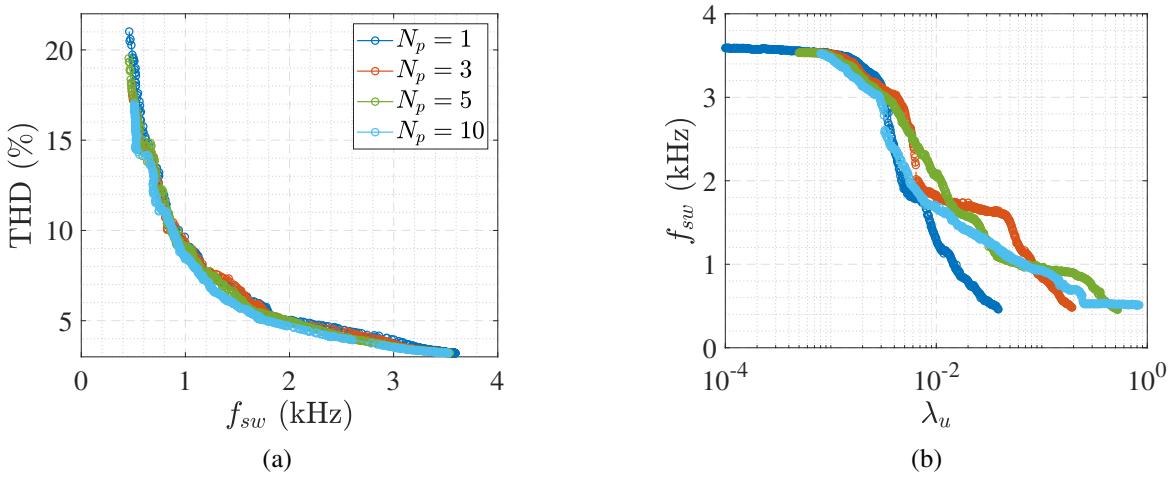

Figure 5.2: The impacts of the design parameters on the performance of the FCS-MPC with the prediction horizons $N_p = 1,\ 3,\ 5,\ 10$ and $f_s = 10\,\mathrm{kHz}$.

noticed that FCS-MPC benefits from a longer prediction horizon, since a smaller THD can be obtained with a longer prediction horizon under the same switching frequency. Moreover, the trade-off between the penalization on the switching effort and the tracking accuracy can be tuned by the design parameter λ_u. The same λ_u can result in different switching frequencies, if distinct prediction horizon is applied.

5.3.5.2 Influence of Parameter Mismatch

Furthermore, several simulations have been conducted to study the effects of the parameter mismatches on the solutions of the problem (5.9) and the control performance of FCS-MPC. The FCS-MPC is designed with the switching frequency around $1.5\,\mathrm{kHz}$. The difference between the solutions to the problem in (5.9) with and without the parameter mismatch of Ψ_m is shown in the Fig. 5.3. In order to differ the optimization problems in (5.9) for the nominal system and the system with the parameter mismatch, $\bar{\mathcal{P}}_f$ and $\mathcal{P}_f$ are deployed to represent them, respectively. The unconstrained solutions $\bar{\mathbf{U}}_{unc}$ and $\mathbf{U}_{unc}$ have slight difference, as presented in Fig. 5.3. It shows that the parameter mismatch of Ψ_m can result in a non-optimal solution of $\mathbf{U}_{unc}$ for the optimization problem. The sphere determined by the $\bar{\mathbf{U}}_{unc}$ as the circle center, denoted by the blue surface is shifted from the sphere determined by $\mathbf{U}_{unc}$ and $\mathbf{U}^*$ in green. Besides, their volumes are also unequal. This conclusion is not necessarily true for all working points of the PMSM drive system. The optimal solution can still be obtained even under the parameter mismatches in some working points. In spite of the narrow difference between the unconstrained solutions $\bar{\mathbf{U}}_{unc}$ and $\mathbf{U}_{unc}$, the distinct final solutions, i.e. $\mathbf{U}^*$ and $\bar{\mathbf{U}}^*$, are selected for $\bar{\mathbf{U}}_{unc}$ and $\mathbf{U}_{unc}$, as observed in Fig. 5.3. Subsequently, the probability of choosing the non-optimal solution because of the parameter mismatch is investigated through simulations.

5.3.5.3 Probability

The mixed-integer characteristic of FCS-MPC impedes the quantification of errors caused by the uncertainties and the disturbances. The first step to study the influence of the parameter

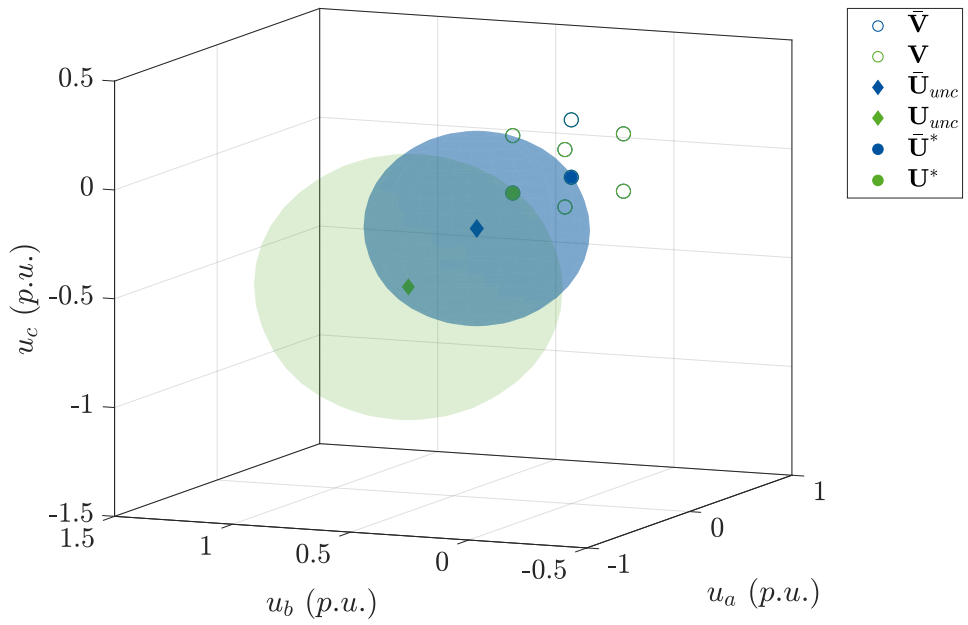

Figure 5.3: Comparison of the solutions of optimization problem in (5.9) between the scenarios with and without the parameter mismatch of Ψ_{m}. The hollow circles denote the all the switching candidates $\boldsymbol{V}$. The filled diamonds represent the unconstrained solution $\mathbf{U}_{unc}$ and the filled circles depict the solution $\mathbf{U}^*$. The superscript $\bar{\cdot}$ denotes the quantities in nominal system without the parameter mismatch, which is shown in blue. The quantities in the disturbed system are presented in green.

mismatches on the solutions to the optimization problem $\mathcal{P}_f$ is to investigate the probability of acquiring the optimal solutions under the existence of various parameter mismatches. In order to study the incidence of the non-optimal solutions, simulations over the admissible region of i_α and i_β, regarding different parameter variations, have been conducted. On the one hand, the solution of the FCS-MPC is the control sequence $\mathbf{U}^*$ over the prediction horizon N_p. On the other hand, the receding horizon policy of MPC implements only the first element of the control sequence into the plant. Therefore, the impacts of the parameter mismatches on these two quantities, i.e. $\mathbf{U}^*$ and $\boldsymbol{u}^*_{abc}$, are investigated. Moreover, the prediction horizon N_p is an essential design parameter for the FCS-MPC. Therefore, the probability distribution of different prediction horizons varying from $N_p = 1$ to $N_p = 10$ has been evaluated. The simulations were conducted in various operating points ranging from the no-load condition to the full-load condition with a step of 10% of the rated torque. The results are summarized and shown in Fig. 5.4 - Fig. 5.7.

The simulation results of $r_p = 50\%$ and of $r_p = 200\%$ for the FCS-MPC of choosing a non-optimal solution $\mathbf{U}$ are presented in Fig. 5.4 and in Fig. 5.5, respectively.

The probability of choosing the non-optimal control sequence increases as the prediction horizon N_p grows, as observed from Fig. 5.4 and Fig. 5.5, which can be explained by the fact that the model error accumulates over the prediction horizon. However, it can be noticed that the probability $\mathbf{P}$ is not linearly related to the prediction horizon. This phenomenon is more obvious at the parameter mismatch of R_{s}. Besides, at the parameter mismatch of L_s, a jump of $\mathbf{P}$ can be noted at $N_p = 2$ for the situation of $r_p = 50\%$ and at $N_p = 3$ for the situation of $r_p = 200\%$. The dependence of the incidence probability is furthermore related to the varied parameter. Moreover, different parameters and different rate of changes have various impacts

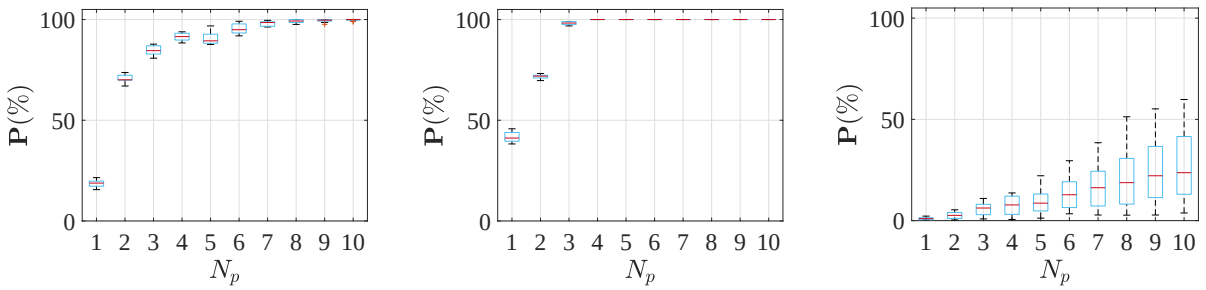

Figure 5.4: Probability distribution of choosing different $\mathbf{U}$ to nominal condition considering various parameter variations. (a) denotes the influence of $r_{L_s} = 50\%$. (b) represents the effects from Ψ_m with a ratio of 50%. (c) shows the influence of $r_{R_s} = 50\%$.

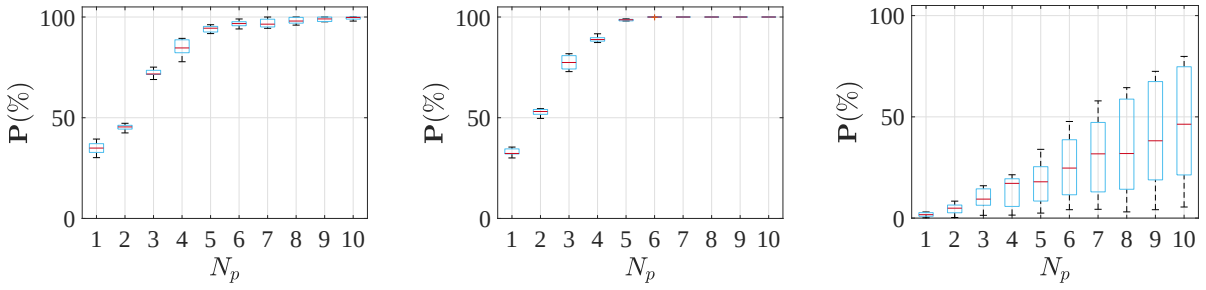

Figure 5.5: Probability distribution of choosing different $\mathbf{U}$ to nominal condition considering various parameter variations. (a) denotes the influence of $r_{L_s} = 200\%$. (b) represents the effects from Ψ_m with a ratio of 200%. (c) shows the influence of $r_{R_s} = 200\%$.

on the probability of the occurrence of the non-optimal solutions. The parameter mismatch of Ψ_m reaches the $\mathbf{P} = 100\%$ at $N_p = 5$, while the parameter mismatch of R_s shows apparently less impact.

However, considering the receding horizon policy employed in the FCS-MPC, only the first element of $\mathbf{U}^*$ is implemented in the current control loop, i.e. $\boldsymbol{u}^*_{abc,\,k}$. A non-optimal solution of the control sequence $\mathbf{U}^*$ is not necessarily equivalent to a non-optimal solution $\boldsymbol{u}^*_{abc,\,k}$ for the plant. Therefore, simulations regarding the probability of choosing the non-optimal solutions $\boldsymbol{u}^*_{abc,\,k}$ have been conducted. The investigation of $r_p = 50\%$ and of $r_p = 200\%$ for the FCS-MPC choosing different solutions $\boldsymbol{u}^*_{abc,\,k}$ are presented in Fig. 5.6 and in Fig. 5.7, respectively.

It can be observed from the Fig. 5.6 and the Fig. 5.7 that the probability of the choice of the non-optimal switching states for the implementation as a control input into the plant is in general heavily dependent on the varied parameters, i.e. the permanent magnet flux linkage Ψ_m induces the highest probability of obtaining the non-optimal solution, which is followed by the inductance, while the stator resistance has the least effect on the solution to the optimization problem. This conclusion can be traced back to the impacts of the parameter mismatches on the CCS-MPC in Chapter 4, since the unconstrained solution $\mathbf{U}_{unc}$ is equivalent to the optimal solution of the optimization problem $\mathcal{P}_c$ in (4.7) under the modification of the weighting matri-

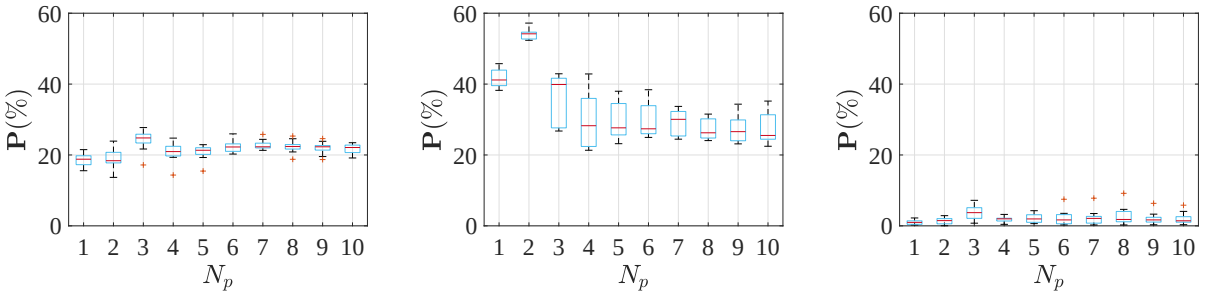

(a) (b) (c)

Figure 5.6: Probability distribution of choosing different $\boldsymbol{u}_{abc}$ to the nominal condition considering various parameter variations. (a) denotes the influence of $r_{L_s} = 50\%$. (b) represents the effects from Ψ_m with a ratio of 50%. (c) shows the influence of $r_{R_s} = 50\%$.

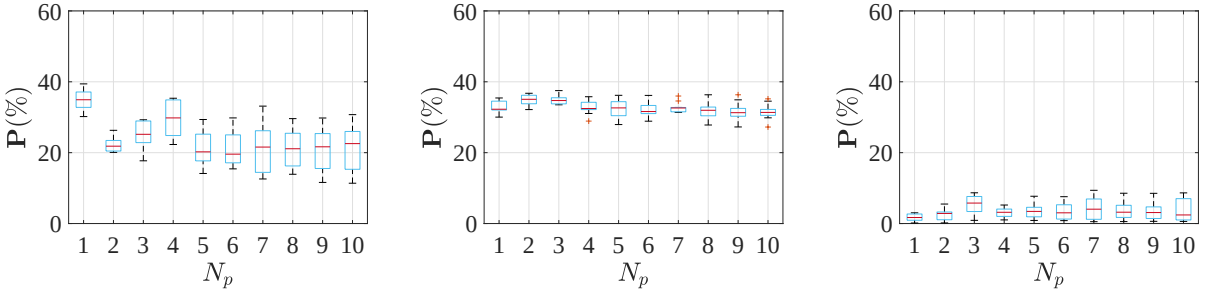

(a) (b) (c)

Figure 5.7: Probability distribution of choosing different $\boldsymbol{u}_{abc}$ to the nominal condition considering various parameter variations. (a) denotes the influence of $r_{L_s} = 200\%$. (b) represents the effects from Ψ_m with a ratio of 200%. (c) shows the influence of $r_{R_s} = 200\%$.

ces $\boldsymbol{Q}$ and $\boldsymbol{R}$, so that they are scalar matrices, i.e. $\boldsymbol{Q} = q\,\mathbf{I}$ and $\mathbf{R} = r\,\mathbf{I}$, and satisfy $r/q = \lambda_u$. The permanent magnet flux linkage Ψ_m has the most impact on the CCS-MPC, as indicated in Section. 4.4. Its impact further reflects on the FCS-MPC. Analogously, the impact of the stator resistance on the CCS-MPC is the least. It causes the least probability of the incidence of the non-optimal solutions for the FCS-MPC. It is worth mentioning that the FCS-MPC is more robust against the variation of the inductance than CCS-MPC. More specifically, FCS-MPC can remain stable under a severe variation of the inductance.

5.3.5.4 Tracking Error

Subsequently, the tracking errors of the FCS-MPC regarding the effects of the parameter mismatch in the PMSM are studied via the simulations. The ratio r_p is applied to indicate the scenario of the parameter mismatch. The tracking error at the steady state is quantified by the intermediate quantity e_i, which is defined in (4.36). The measured current is collected and averaged at the steady state over a filtering time span. The FCS-MPC with $N_p = 1$ and $N_p = 5$ are studied individually, since both designing parameters of the FCS-MPC are applied in the ensuing experiments. Different working points are considered during the simulations. The black dots in the figures demonstrate the actual computed error e_i in the simulations, while the surface are fitted with the spline interpolation that introduced in Section 3.3.2.1. The simulation results

regarding the parameter R_s are shown in Fig. 5.8.

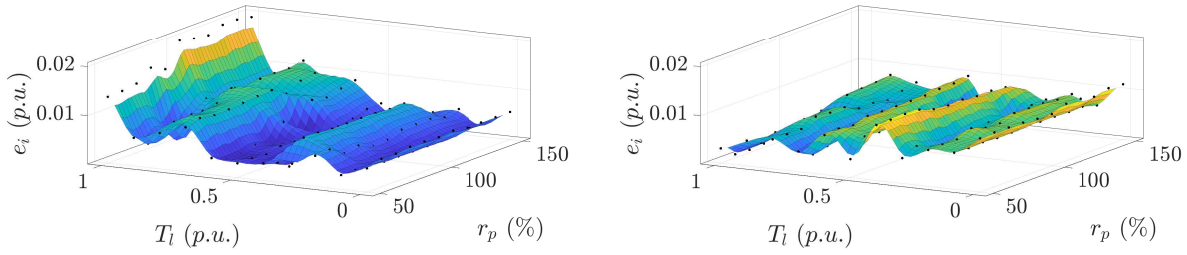

(a) (b)

Figure 5.8: The steady state error e_i caused by the parameter mismatch of R_s for the MPDCC with $N_p = 1$ in (a) and with $N_p = 5$ in (b).

Comparing the Fig. 5.8 to the Fig. 4.2, the continuous relationships between r_p and e_i as well as between T_l and e_i from the CCS-MPC are no longer valid for the FCS-MPC. However, their amplitude levels of the error are comparable, i.e. e_i remains several percent of the rated current I_N. The fitted maps in Fig. 5.8 show obvious differences of e_i under the control with $N_p = 1$ and $N_p = 5$. More specifically, the most severe error under the control of $N_p = 1$ appears at the full-load condition, while it occurs at the no-load condition with $N_p = 5$.

Further investigations about the influence of the inductance L_s on the tracking performance of FCS-MPC is shown in Fig. 5.9.

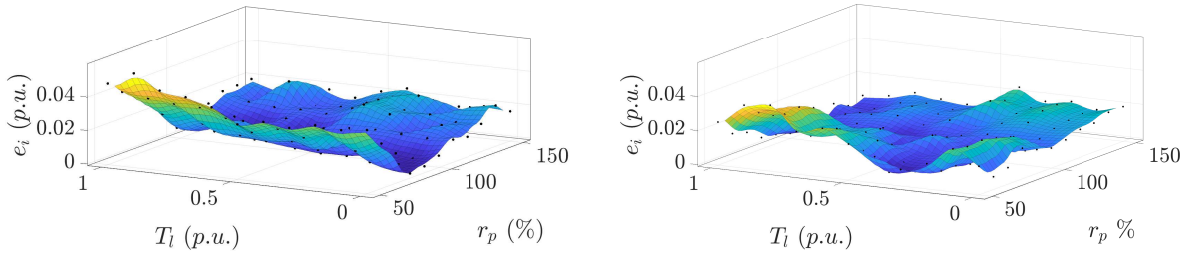

(a) (b)

Figure 5.9: The steady state error e_i caused by the parameter mismatch of L_s for the MPDCC with $N_p = 1$ in (a) and with $N_p = 5$ in (b).

At $N_p = 1$, the relationship between r_p and e_i as well as between T_l and e_i is similar to that of CCS-MPC, i.e. the error grows as the rate of the mismatch increases and the load has little impact on the tracking performance. However, it can be noticed that the least tracking error resulted from the L_s mismatch is not aligned with the line of $r_p = 100\%$, which is shifted to around $r_p = 80\%$. Moreover, the error map of $N_p = 5$ is nonlinear to both T_l and r_p .

Finally, the impact from the parameter variation of Ψ_m is studied with the simulation results presented in Fig. 5.10. The parameter Ψ_m has the similar impact on the FCS-MPC to that on the CCS-MPC. The tracking error has the minimal value if the parameter Ψ_m applied in the controller exactly matches the motor parameter. Moreover, the load condition has diminutive impacts on the tracking error, i.e. at the same r_p the MPDCC demonstrates almost the same tracking error under diverse load conditions. It is worth mentioning that e_i is quasi symmetric

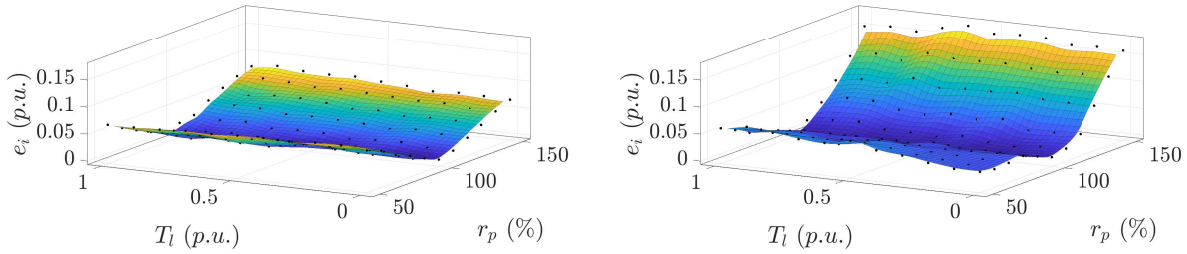

Figure 5.10: The steady state error e_i caused by the parameter mismatch of Ψ_m for the MPDCC with $N_p = 1$ in (a) and with $N_p = 5$ in (b).

about the $r_p = 100\%$ at $N_p = 1$, while larger error can be observed at $r_p = 150\%$ than at $r_p = 50\%$ for $N_p = 5$.

Several conclusions can be drawn from the simulation results. Firstly, the stator resistance has the least impact on the control performance of MPDCC. The influence from the parameter variation of R_s and L_s is not linear regarding the operating points. On the contrary, the parameter variation of Ψ_m is nearly linear to the load torque. For a certain load torque, the steady state error is linearly dependent on the rate of the parameter variation on Ψ_m. Moreover, Ψ_m causes more steady -state error than R_s and L_s. Furthermore, it can be observed in the Fig. 5.10a and the Fig. 5.10b that the parameter mismatch of Ψ_m causes more steady state error for the MPDCC with $N_p = 5$ than for the MPDCC with $N_p = 1$. For the one-step MPDCC, the variation of Ψ_m, in a range from $r_p = 50\%$ to $r_p = 150\%$, can result in a steady-state error up to 8% of the rated current. Nonetheless, it can cause a steady-state error for MPDCC with $N_p = 5$ up to almost 15% of the rated value, which is however less than its impact on the CCS-MPC.

5.3.6 Experimental Results

In order to analyse the impacts of the parameter mismatches on the MPDCC and validate the proposed observer-enhanced control strategy, which eliminates the tracking error resulted from the parameter mismatches and improves the system performance, in terms of the robustness and the tracking accuracy, the corresponding experiments have been carried out on the Test Bench B.2. The currents and the switching frequencies under the nominal condition and under diverse parameter mismatches have been recorded. Furthermore, the dynamic behaviours of the classic MPDCC and the enhanced MPDCC can be observed from the applied load step during the experiments. Besides, the total demand harmonics are computed and compared. The experimental results as well as the computational results are demonstrated accordingly.

5.3.6.1 Performance under Nominal Condition

Firstly, the performance of both methods are tested under the nominal condition, i.e. with the nominal parameters of the PMSM listed in Table. B.6. A load step from 0% to 50% of the rated torque is added at $t = 2$ s and another load step from 50% to full load is applied at $t = 4$ s. The PMSM run at $2000\,\mathrm{rpm}$. The experimental results of the test with one-step FCS-MPC are shown in Fig. 5.11.

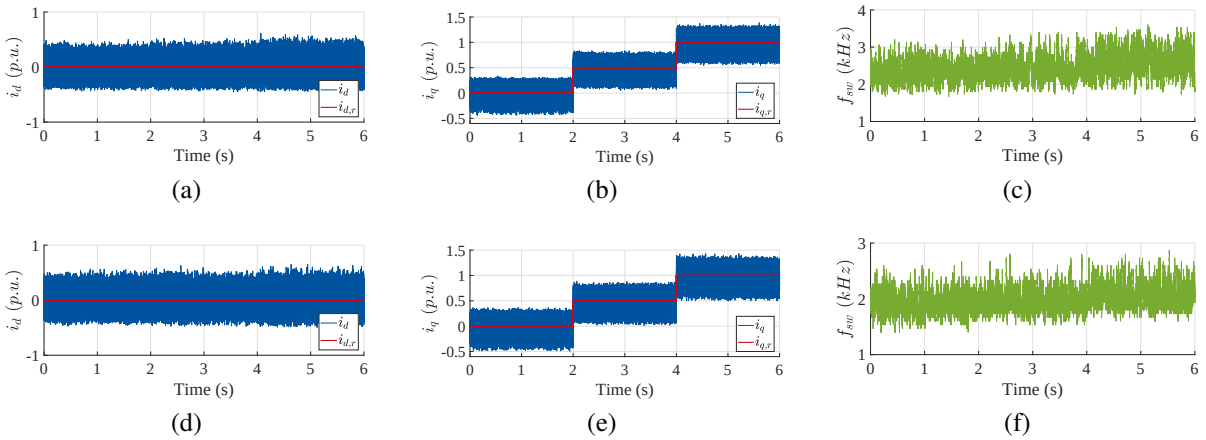

Figure 5.11: Comparison between the RMPDCC and MPDCC with $N_p = 1$ under the nominal condition. (a)-(c) denote the performance of MPDCC and (d)-(f) represent the control performance of the proposed RMPDCC. (a) and (d) denote the tracking performance of d-current. (b) and (e) represent the tracking performance of q-current. (c) and (f) are the switching frequencies.

The further tests for MPDCC and the proposed RMPDCC with $N_p = 5$ have been carried out in the nominal condition. The experimental results are shown in Fig. 5.12 accordingly. It can be observed from Fig. 5.11 that the MPDCC and RMPDCC yield similar performance

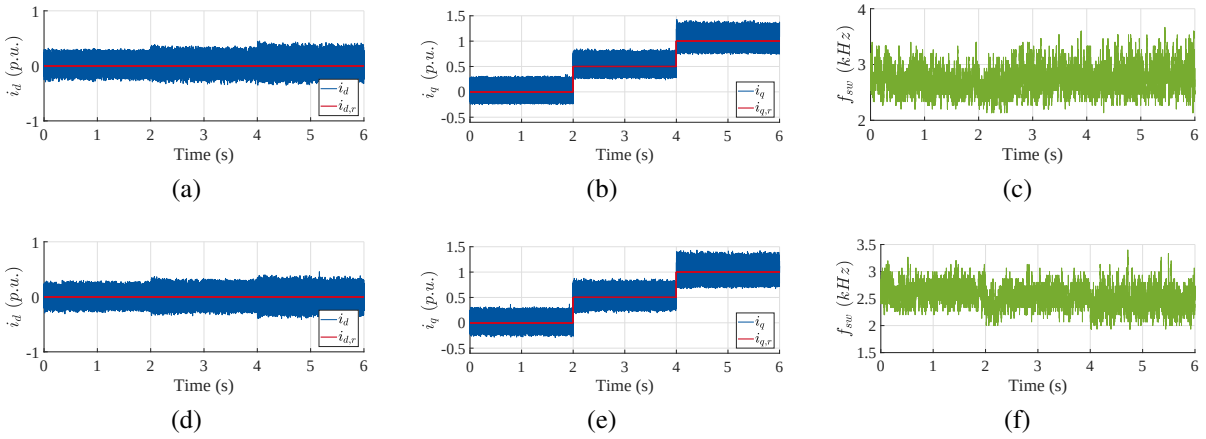

Figure 5.12: Comparison between the RMPDCC and MPDCC with $N_p = 5$ under the nominal condition. (a)-(c) denote the performance of MPDCC and (d)-(f) represent the control performance of the proposed RMPDCC.

under the nominal condition with $N_p = 1$. In Fig. 5.12 similar conclusion can be drawn. However, a smaller current ripple during the steady state under the control with RMPDCC is worth mentioning. The control with $N_p = 5$ has smaller current ripples than the control with $N_p = 1$ for MPDCC, where the comparable switching frequencies are employed. Moreover, the RMPDCC can reach the new steady state faster than the MPDCC.

5.3.6.2 Performance under the Variation of Ψ_m

The second validating scenario is the parameter variation of the permanent magnet flux linkage Ψ_m. The experiments with $r_p = 50\%$ and $r_p = 150\%$ have been conducted respectively. The

experimental results of $r_p = 50\%$ for $N_p = 1$ and $N_p = 5$ are presented in Fig. 5.13 and Fig. 5.14, respectively.

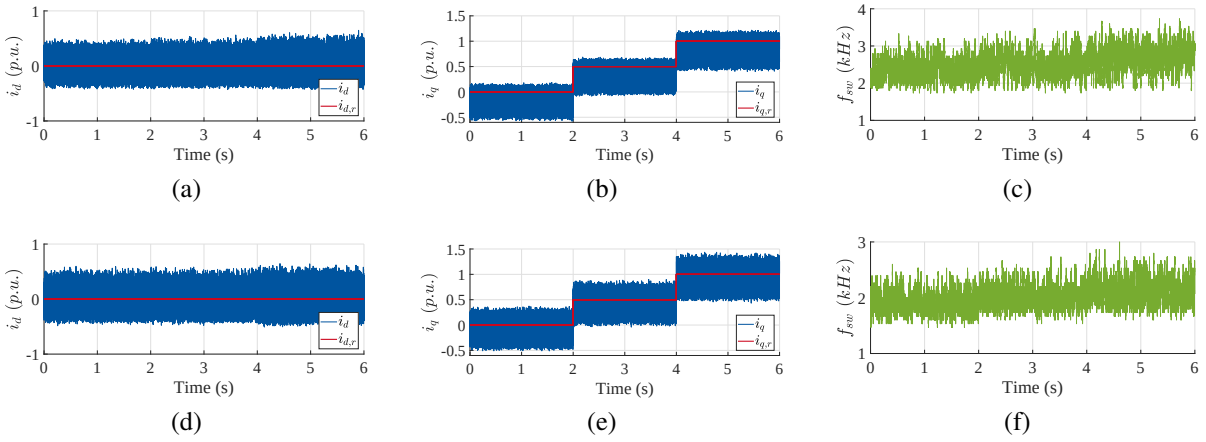

Figure 5.13: Comparison between the RMPDCC and MPDCC with $N_p = 1$ under the parameter mismatch of Ψ_m with $r_p = 50\%$. (a)-(c) denote the performance of MPDCC and (d)-(f) represent the control performance of the proposed RMPDCC.

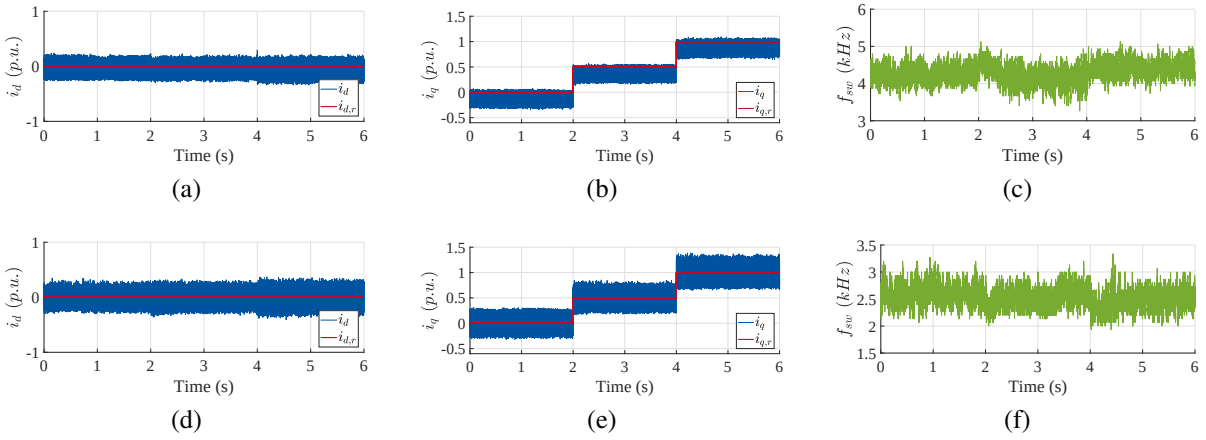

Figure 5.14: Comparison between the RMPDCC and MPDCC with $N_p = 5$ under the parameter mismatch of Ψ_m with $r_p = 50\%$. (a)-(c) denote the performance of MPDCC and (d)-(f) represent the control performance of the proposed RMPDCC.

It can be noted from Fig. 5.13 and Fig. 5.14 that the decrease of the Ψ_m value generates a negative steady-state offset for the current of q-axis, which amounts to around 25% of the rated current. An obvious improvement can be observed at the steady state by implementing the proposed RMPDCC, i.e. the steady-state error caused by the decrease of Ψ_m is mitigated.

The experimental results of $r_p = 150\%$ for $N_p = 1$ and $N_p = 5$ are presented in Fig. 5.15 and Fig. 5.16, respectively. Similar to the previous observation, an increase of the Ψ_m value can also result in a steady-state error for MPDCC. In Fig. 5.15 and Fig. 5.16 the current in q-axis reached the current limit at $t = 4$ s and triggered the over-current protection mechanism of the drive system. On the contrary, RMPDCC tracked the reference accurately and retained the control performance under the parameter mismatch of Ψ_m. Even though the current under

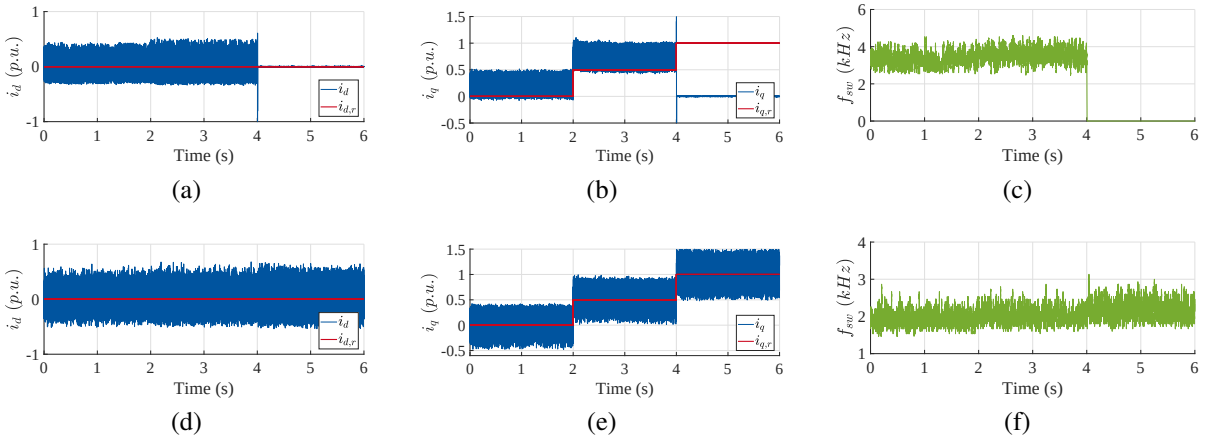

Figure 5.15: Comparison between the RMPDCC and MPDCC with $N_p = 1$ under the parameter mismatch of Ψ_m with $r_p = 150\%$. (a)-(c) denote the performance of MPDCC and (d)-(f) represent the control performance of the proposed RMPDCC.

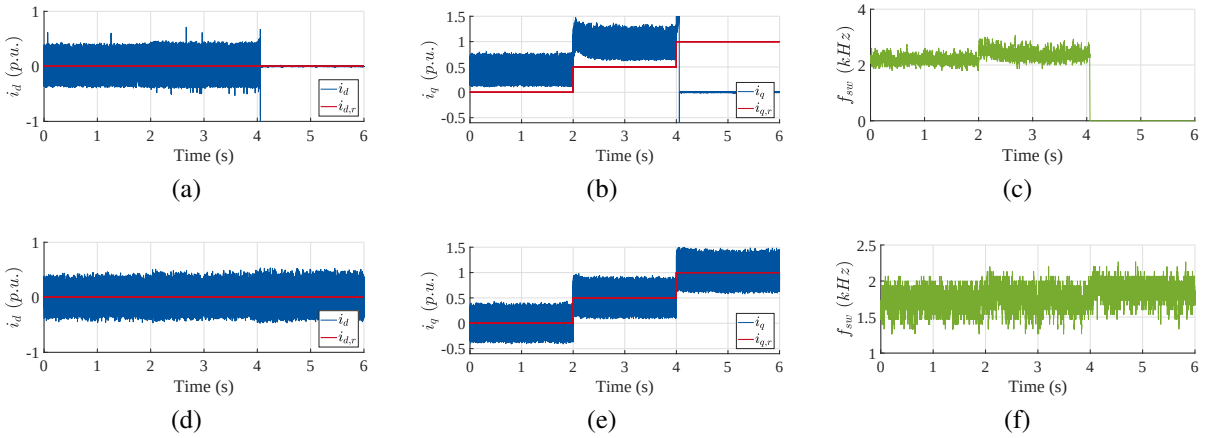

Figure 5.16: Comparison between the RMPDCC and MPDCC with $N_p = 5$ under the parameter mismatch of Ψ_m with $r_p = 150\%$. (a)-(c) denote the performance of MPDCC and (d)-(f) represent the control performance of the proposed RMPDCC.

the control of the MPDCC stays within the current limits before $t = 4\,\mathrm{s}$, an obvious offset can be observed, which is around 25% of the rated current. Moreover, the MPDCC with a longer prediction horizon demonstrates a larger steady-state offset under the parameter mismatch of Ψ_m. More specifically, an offset of around 25% of the rated current at $N_p = 1$ and an offset of around 45% of I_N at $N_p = 5$ are noticeable, which complies with the conclusions drawn from the simulation results. However, the deployment of the proposed RMPDCC can eliminate the errors effectively. Moreover, the switching frequency remains quasi constant under various load conditions, if the RMPDCC is employed.

5.3.6.3 Performance under the Variation of L_s

MPDCC and RMPDCC are further tested under the parameter mismatch of L_s. $r_p = 50\%$ and $r_p = 150\%$ are tested individually. The experimental results are shown in Fig. 5.17, Fig. 5.18 and Fig. 5.19, Fig. 5.20, respectively.

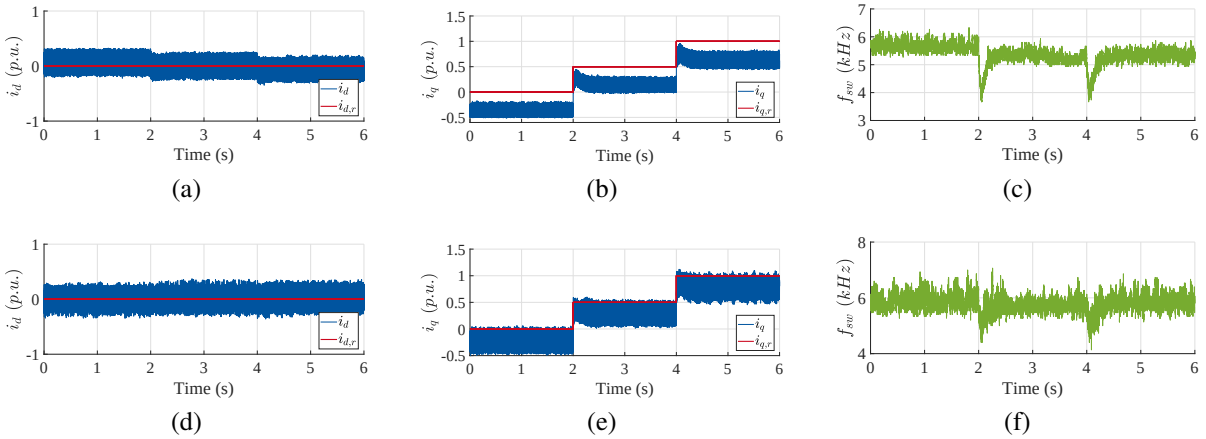

Figure 5.17: Comparison between the RMPDCC and MPDCC with $N_p = 1$ under the parameter mismatch of L_s with $r_p = 50\%$. (a)-(c) denote the performance of MPDCC and (d)-(f) represent the control performance of the proposed RMPDCC.

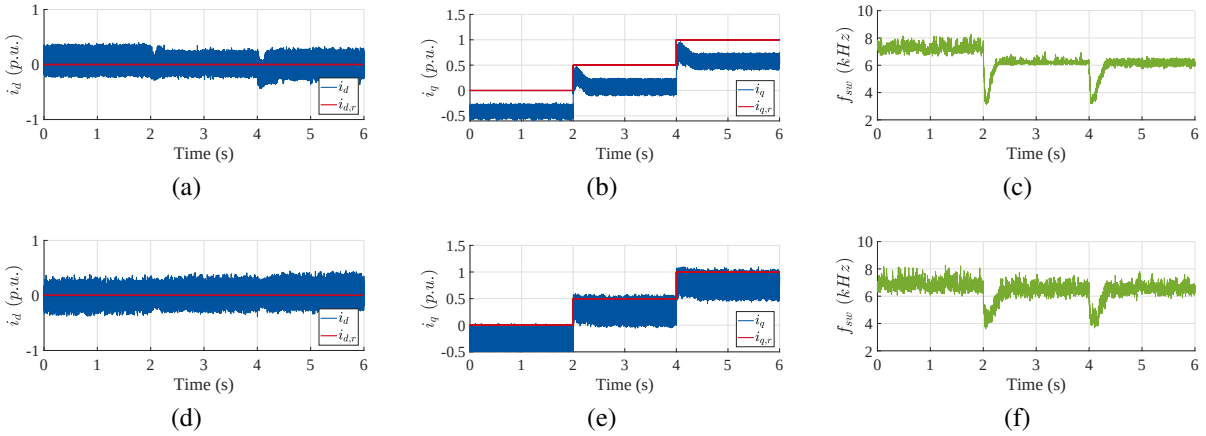

Figure 5.18: Comparison between the RMPDCC and MPDCC with $N_p = 5$ under the parameter mismatch of L_s with $r_p = 50\%$. (a)-(c) denote the performance of MPDCC and (d)-(f) represent the control performance of the proposed RMPDCC.

In Fig. 5.17 and Fig. 5.18, a more obvious steady-state error than the control of the MPDCC under the variation of Ψ_m can be observed at $r_p = 50\%$, i.e. an offset of around 35% of the rated current at $N_p = 1$ and an offset of around 35% of I_N with no load, 45% of I_N with full load at $N_p = 5$ can be noted. The controller with $N_p = 5$ has a larger error than the one with $N_p = 1$. Moreover, the switching frequency is heavily influenced by the variation of L_s. It worth mentioning that under the $r_p = 50\%$ of L_s variation, the RMPDCC demonstrates also small steady-state offset, which is much smaller than the offset of MPDCC. The performances for the situation of the parameter mismatch of L_s and $r_p = 150\%$ are shown in Fig. 5.19 and in Fig. 5.20.

Steady state errors can also be observed under the variation of L_s and $r_p = 150\%$. However, the errors are much smaller than the former test scenario, where the change of L_s is set to $r_p = 50\%$. The drive system reached the current limit at the full load under $r_p = 150\%$. The investigations on the impacts from the stator resistance variation are omitted, since its effects are relatively low.

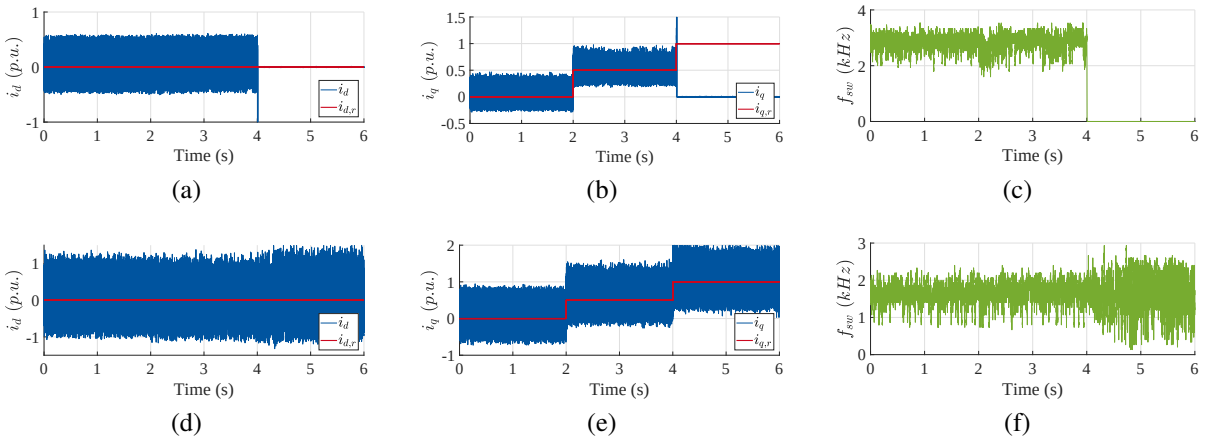

Figure 5.19: Comparison between the RMPDCC and MPDCC with $N_p = 1$ under the parameter mismatch of L_s with $r_p = 150\%$. (a)-(c) denote the performance of MPDCC and (d)-(f) represent the control performance of the proposed RMPDCC.

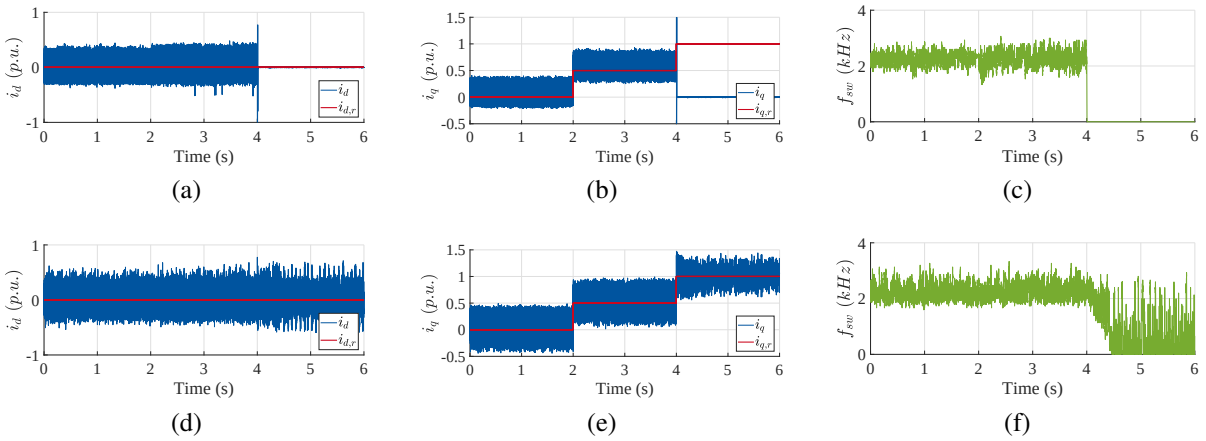

Figure 5.20: Comparison between the RMPDCC and MPDCC with $N_p = 5$ under the parameter mismatch of L_s with $r_p = 150\%$. (a)-(c) denote the performance of MPDCC and (d)-(f) represent the control performance of the proposed RMPDCC.

5.3.6.4 Total Demand Harmonics

The TDDs of the MPDCC and of the RMPDCC are furthermore computed, since the total demand distortion is one of the important performance metrics to evaluate the control methods. The TDD is computed via

$$\mathrm{TDD} = \frac{1}{\sqrt{2}\, I_N} \sqrt{\sum_{j \neq 1} i_{s,j}^2}\,, \tag{5.37}$$

where j denotes the order of the current harmonics. As it is shown in former section, the stator resistance has slight impact on the control performance. Therefore, only the TDD under the parameter mismatches of Ψ_m and L_s are computed and demonstrated. The results are shown in Fig. 5.21 and Fig. 5.22, where Fig. 5.21 shows the results from the parameter variation of Ψ_m and Fig. 5.22 represents the results under the variation of L_s . The switching frequencies are also affected by the parameter mismatches, as shown in preceding experiments. The current metrics

are heavily dependent on the switching frequencies. Therefore, the MPDCC is furthermore tuned to operate with a comparable switching frequency as the RMPDCC at the respective scenario. The currents under the control of corresponding MPDCC are also measured, of which the TDD is computed. The corresponding TDDs are computed and presented.

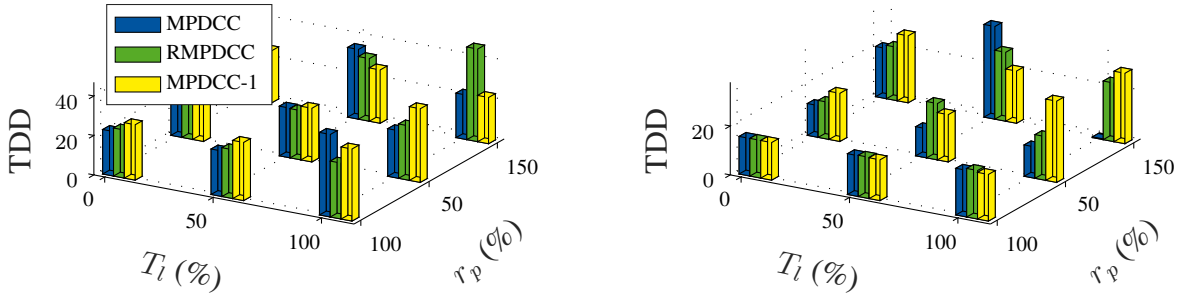

Figure 5.21: Comparison of the TDD under the parameter mismatch of Ψ_{m}, where the blue and the green denote the TDD with switching frequencies shown in previous testing scenarios of MPDCC and the proposed RMPDCC, respectively. The yellow represents the TDD of MPDCC with the mean switching frequency same as that of the RMPDCC in respective test scenarios. (a) denotes the control of $N_p = 1$ and (b) shows the results from the control of $N_p = 5$.

Fig. 5.21 shows that the proposed RMPDCC yields smaller TDD than the MPDCC at most test cases. However, for some test scenarios, e.g. $r_p = 150\%$ and $T_l = 100\%$ at $N_p = 1$, a contrast phenomenon can be observed. It may be explained by the fact that the performance of the observer degrades under the control of MPDCC because that the measured currents are heavily disturbed by the harmonics (comparing to the control results of CCS-MPC). Analogously to

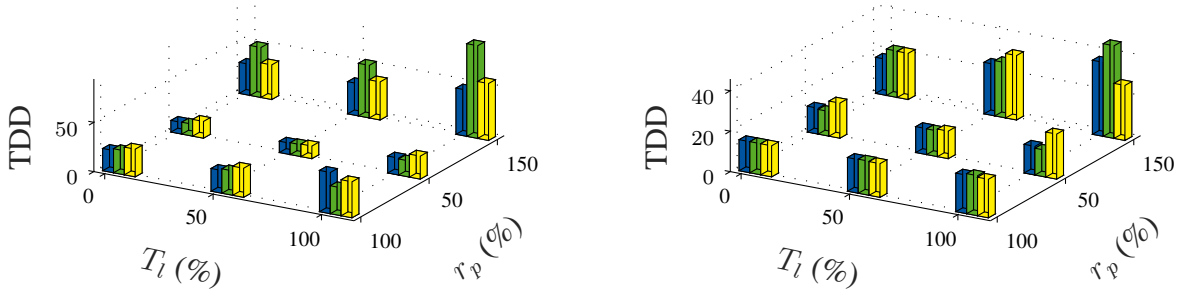

Figure 5.22: Comparison of the TDD under the parameter mismatch of L_{s}. (a) and (b) represent the results from the current control of $N_p = 1$ and $N_p = 5$, respectively.

the observations in Fig. 5.21, in Fig. 5.22 it can be noticed that the RMPDCC outperforms the MPDCC at most test cases. However, it shows higher TDD value at some test scenarios. Besides, it can be concluded from the computation results that a long prediction horizon benefits the MPDCC in terms of the current ripple, since a smaller TDD can be noticed at $N_p = 5$ under the same load condition and with the comparable switching frequencies. Moreover, the proposed RMPDCC yields smaller TDD than the MPDCC for the most cases. However, MPDCC

outperforms RMPDCC in terms of the harmonics content at some cases. But RMPDCC eliminates the steady-state offsets effectively.

5.4 Conclusion

In this chapter, the FCS-MPC based current controller is developed for the PMSM drive system. More specifically, the one-step solution as well as the controller with a long prediction horizon is introduced. Depending on the applications, i.e. the dynamic requirement and the available computational power, either the enumeration method or the sphere decoding algorithm can be implemented to solve the underlying mixed-integer optimization problem. As it is shown in this chapter, the deployment of the sphere decoding algorithm reduces the computational burden of the control problem with a long prediction horizon and enables a real-time application of the MPDCC. Furthermore, thanks to the symmetry of the matrices for the SPMSM, some proportion of the heavy computations can be allocated to the offline preparation, which reduces the online computational burden. However, analogous to the continuous-control-set MPC, FCS-MPC also suffers from the parameter mismatches and the disturbances. Although it is more robust against these effects, an improvement needs to be proposed to tackle this problem. In this chapter, a disturbance observer is deployed into the FCS-MPC framework. Its effectiveness has been validated via experiments at various working points. Moreover, the real-time feasibility of the MPDCC and the RMPDCC of up to $10\,\mathrm{kHz}$ sampling rate is demonstrated by experiments, where a prediction horizon of $N_p = 5$ can be realised.

CHAPTER 6

Attenuation of the Periodic Disturbance

6.1 Introduction

In Chapter 4 and Chapter 5, an observer-based robust solution to eliminate the unmodelled uncertainties and the disturbances has been introduced and verified via experiments. However, because of the capability limitation of the observer, the periodic disturbance, such as the nonlinear effects of the VSI and the flux harmonics, remains in the PMSM drive system and may result in performance degradation of the PMSM drive system, such as the current distortion as well as the torque pulsation [56]. As indicated in [237], FOC as well as MPC is sufficient for the control purpose, if the disturbances are non-periodic, or if the frequency of the disturbance is lower than the bandwidth of the controlled plant. In this chapter, the principle of the promising methods are introduced to compensate the $6i$-th order harmonics that are resulted from the VSI nonlinear effects, where $i \in \mathbb{Z}$, since they heavily influence the parameter identification results as well as the control performance. The compensation targeting other harmonics can be deployed analogously. The most intuitive perspective is to combine the method of VSI nonlinear effect estimation proposed in Section 3.6 and the disturbance estimation method discussed in Section 4.3. However, after examination of the observability, it can be concluded that the disturbance $\boldsymbol{\varepsilon}$ and the VSI nonlinearities U_{dead} can not be estimated simultaneously. Therefore, an auspicious method is proposed in this chapter to tackle this problem. Firstly, the state-of-the-art compensation methods dealing with the periodic disturbances are introduced as a start point of this chapter, where they are roughly categorized. Subsequently, the most applied methods among them are introduced and compared in details, i.e. the offline method, the adaptive solution [238], the resonant control [204] and the repetitive control [239]. Furthermore, a fractional-repetitive-control (FRPC) based periodic disturbance attenuation method is presented in this chapter. The proposed method solves the problem encountered in the practical implementation, when the ratio between the period of the periodic signals and the sampling time is non-integer. Moreover, since the compensating voltage is varying with the rotor speed in terms of the frequency, a speed-dependent FRPC is derived to adjust the delay time of the FRPC ac-

cordingly. The parameter determination of the proposed FRPC-based approach is completed via simulations. Besides, it is compared with the state-of-the-art methods through experiments.

As it is shown in Section 2.4, the nonlinearities of the inverter comprises mainly the dead time, the turn-on/-off time of the power switches, the voltage drops of the switches as well as of the freewheeling diodes and the parasitic effects. With the analysis performed in [57, 59, 106], methods for mitigating the impacts of the VSI nonlinearities have been developed both in academia and in industry. In general, they can be categorized into two families: the elimination/minimization of the nonlinear effects of the VSI and the compensation of the distorted voltage. They differ on the basis of the engaging component, i.e. the elimination/minimization occurs in the modulator or the VSI, while the compensation is carried out before the modulation. The elimination/minimization for the VSI-nonlinearities is normally accomplished by modifying the switching strategy. In [240], the reference wave of the PWM was modified and a logic circuit was applied to mitigate the dead time. Reference [241] eliminated the dead-time effect by shifting the pulse by the dead-time in each PWM cycle. Reference [242] included furthermore the effects of the non-ideal DC-link voltage and the switching delay. However, precise current sensors is needed to detect the current polarity for the elimination. Reference [243] proposed a digital modulator with a single switch commutation technique to omit the insertion of the dead time and adopts a sufficient threshold for the current polarity detection. Instead of detecting the phase current polarity, [244] and [245] employed detecting circuits to determine the current polarity of the freewheeling diode and [246] used the information of the reference current to achieve this goal. Reference [247] adjusted the switching frequency according to the amplitude of the reference voltages and minimized the harmonics of the output voltage. Besides the dead-time effect, [248] included the voltage drops, [249] considered the influence of the turn-on/turn-off time and [54] mitigated against the effects of the snubber and the parasitic capacitance. Various PWM strategies [250–254] as well as many modified topologies [255–258] have also been proposed to eliminate the dead time. However, the elimination/minimization methods mainly focuses on excluding the dead-time effect with the averaged value and the other time-varying VSI nonlinearities are hardly considered. They require commonly the additional circuit for the modulation or aiding the switching strategy. Moreover, even though they are simple and fast, their application to devices with slow control update rate, e.g. GTO, would be inadequate and the integration of other VSI nonlinearities may increase the design complexity.

On the other hand, the compensating method can be easily adapted to an arbitrary system and the inclusion of VSI nonlinearities is straightforward. The compensating voltage $\Delta \boldsymbol{u}$ can be either applied at the output of the controller as a compensation signal or directly computed in the controller as an additional control output. The first category applies the offline or online determined compensating voltage at the output of the controller and delivers the sum of controller output with this compensating signal to the modulator. The second category analyzes the characteristics of the VSI nonlinearities and applies adequate control techniques to improve the performance against this disturbance. With respect to the determination of the compensating voltage, numerous methods have been proposed. They can be roughly sorted into following categories: the curve-fitting method [55, 56, 259–264], the average-value-based method [62, 107, 265–267], the observer/ filter-based method [88, 209, 238, 268–271], the real-time measurement method [272–274] and the modification of controllers [203, 239, 275–279]. Their principles are briefly introduced as follows.

6.1.1 The Curve-Fitting Method

The curve-fitting method executes experiments and measurements to obtain the datasets of the distorted voltage that can be regarded as a function of the phase current or other obtainable signals, e.g. the reference voltage. The method furthermore adopts certain curves or a look-up table (LUT) to approximate the sustained characteristics. The offline measurements can be obtained at the start-up [263] or by an offline self-commissioning procedure [259]. The measurements can be further modelled as a piecewise linear function [280, 281], a linear saturated function [259, 263], a logarithmic function [260], a piecewise nonlinear function [107, 261, 282, 283], a support vector regression model [55], a trapezoidal function [264] or saved as a LUT [56, 106, 262, 284], which will be interpolated as well as extrapolated online during operation. The accuracy of the compensation varies as the complexity of the chosen approximating function changes. In general, the curve-fitting method is relatively accurate. But the offline measuring procedure is time consuming and each VSI need to be determined individually. Besides, the influence from the environmental conditions, such as the temperature and the humidity, is excluded.

6.1.2 The Average-Value-Based Method

The average-value-based method explicitly analyzes the VSI nonlinearities and models the error based on the VSI characteristics as an average value, which is computed as the voltage-second error within one PWM period, as shown in Fig. 2.22. The average value is then fed forward to compensate the reference voltage and delivered together as a sum to the modulator.

Depending on the application as well as the requirement for the accuracy of the compensation voltage, different elements of the VSI nonlinearities are selected and included into the computation of the average value. The dead time is normally regarded as a constant. The turn-on/-off time and the voltage drops can be obtained from the manufacturers' data sheets. In [64, 285], only the dead time is taken into consideration, which is regarded as a constant and compensates the reference voltage by segmenting the current domain. Reference [267,286] included both the dead time and the voltage drops. And in [265] the zero-current clamping phenomenon was addressed. Besides the dead time and voltage drops, works such as [62,287] included furthermore the turn-on/-off time of the VSI. Instead of comprehensively computing the average value, [266] included the dead time and used a coefficient to approximate the non-ideal switching characteristics. The average-value-based method is simple but the compensation performance is limited, since the average value is calculated based on certain constant values from the manufacturers' data sheets in most cases.

6.1.3 The Filter-Based Method

The main effect of the VSI nonlinearities is causing the increase of the odd harmonic content in the phase current [238] as well as in the phase voltage [104]. The analysis of the corresponding harmonics provides another perspective for compensating the VSI nonlinearities. Based on the analysis conducted in Section 2.4.2, the currents i_d and i_q considering the nonlinear effect of

the VSI can be expanded with Fourier analysis and written as [238]

$$
\begin{aligned}
i_d &= A_I \left[-\sin\theta - \sum_{n=6\,k}^{\infty} \frac{\sin(n\,\theta_e - (n-1)\,\theta)}{n-1} + \sum_{n=6\,k}^{\infty} \frac{\sin(n\,\theta_e - (n+1)\,\theta)}{n+1} \right], \\
i_q &= A_I \left[-\cos\theta + \sum_{n=6\,k}^{\infty} \frac{\cos(n\,\theta_e - (n-1)\,\theta)}{n-1} - \sum_{n=6\,k}^{\infty} \frac{\cos(n\,\theta_e - (n+1)\,\theta)}{n+1} \right],
\end{aligned}
\tag{6.1}
$$

where $k = 1, 2, 3, \cdots$ and A_I is the amplitude of the current. θ_e is the electrical angle of the rotor and θ is related to the load power factor.

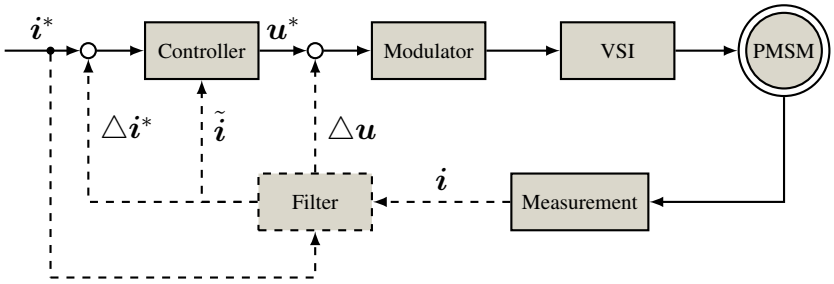

Figure 6.1: Block diagram of the filter-based method.

As it is shown in Fig. 6.1, there are several strategies to insert the compensation signals that are computed based on the filter. In [238], the compensating voltage $\Delta \boldsymbol{u}$ is generated by minimizing the sixth harmonic of the currents with a tuning factor for the design of the convergence rate. Analogously, reference [288] separated the fundamental component as well as the harmonics of the currents and voltages. The compensating voltage $\Delta \boldsymbol{u}$ was computed based on the harmonic model. Reference [104] adopted the adaptive-linear-neuron-based method to solve the optimization problem of minimizing the harmonics. Instead of generating the compensating voltage, it is also applicable to modify the reference current with $\Delta \boldsymbol{i}^*$. In [268], the reference current $\boldsymbol{i}^*$ was modified by analyzing the harmonics. The resulting reference current corrector $\Delta \boldsymbol{i}^*$ was computed based on the analysis. Reference [270] corrected the reference current by extracting the low-frequency component of the current error $\boldsymbol{e}_i := \boldsymbol{i}^* - \boldsymbol{i}$ and computing the current error corrector Δi^* as the integral of $\boldsymbol{e}_i$. Reference [269] applied an adaptive first-order infinite-impulse-response (IIR) filter to filter out the harmonics of the current $\boldsymbol{i}$ and delivered the filtered current $\tilde{\boldsymbol{i}}$ to the controller. The coefficients of the IIR is tuned with a high-pass filter and the corresponding adaptation algorithm. Works, such as [103, 289], applied a proportional controller over the harmonics. More specifically, reference [289] deployed an adaptive notch filter and reference [103] applied an all-pass-based adaptive band-pass filter to estimate the 6-th order of the current harmonics. Authors in [103] considered furthermore the DC bias of the distorted voltage, which is related to the current vector angle, and compensated the voltage distortion with $\Delta \boldsymbol{u}$ through the average-value method. The filter-based method is straightforward, but the filter system need to be properly tuned and the filtering of multiple harmonics aggravates the design complexity of the filter.

6.1.4 The Observer-Based Method

Besides the aforementioned methods, the observer-based method can also be implemented to compensate the distorted voltage. The observer-based method incorporates the error voltage induced by the VSI nonlinearities into the system dynamics with $\boldsymbol{u}_k = \boldsymbol{u}_k^* - \Delta\boldsymbol{u}$. Therefore, the system dynamics in dq reference frame is correspondingly reformulated as

$$\begin{aligned} \boldsymbol{x}_{k+1} &= F(\boldsymbol{x}_k, \Delta\boldsymbol{u}, \boldsymbol{u}_k^*) \,, \\ \boldsymbol{y}_k &= H(\boldsymbol{x}_k) \,. \end{aligned} \tag{6.2}$$

The principle of the observer-based method, which is shown in Fig. 6.2, is to minimize the measurements $\boldsymbol{y}_k$ and the predicted system states $\boldsymbol{x}_k$ from the last step, either by directly extending the system model with the to be estimated parameters [63, 208, 211, 271], or by deriving the error voltage as a function of the reconstructed physical quantities [88, 290].

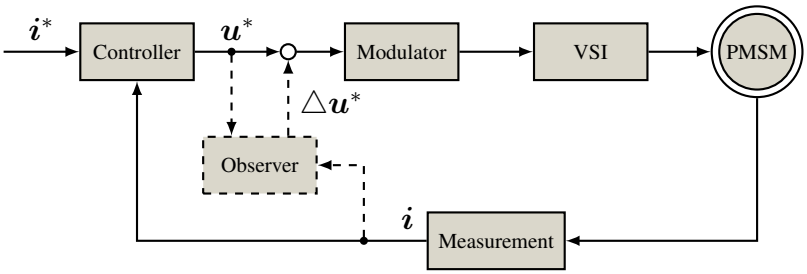

Figure 6.2: Structure diagram of the observer-based method.

Depending on the solving methods of the minimization problem, there are several alternatives to be applied as the disturbance observer: reduced-order disturbance observer [208], first-order disturbance observer [290], adaptive disturbance observer [63, 210, 271, 281], vectorial disturbance observer [88], recursive-least-square-based disturbance observer [211], Kalman filter-based disturbance observer [291], neural-network-based disturbance observer [48] and particle-swarm-optimization-based disturbance observer [133, 292], etc. Many of them require an accurate knowledge of the machine parameters, since the prediction as well as the quantity reconstruction is based on the machine models. Nonetheless, the adaptive disturbance observer [63, 210] and the solutions proposed in [48, 133, 292] are stated to be robust against the machine parameter variation. But they need several operating points to solve the optimization problem and are more computational expensive than the other methods. The tuning of the adaptive disturbance observer is however burdensome.

6.1.5 The Real-Time Measurement Method

The real-time measurement method, presented in Fig. 6.3, originates from the intuition of directly measuring the terminal voltage $\boldsymbol{u}$ and comparing the measurements with the reference voltage $\boldsymbol{u}^*$. Many works have been conducted to realize the real-time measurement method. Reference [272] designed a circuit to measure the volt-second value of the error voltage by integrating the terminal voltage over the dead-time interval. Authors in [273] measured the actual applied duty cycle and compared it with the command duty cycle to compute the compensating time. In [293], the actual output voltage with additional measurements of phase current

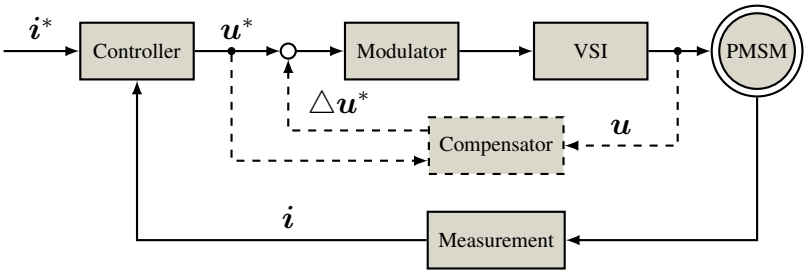

Figure 6.3: Block diagram of the real-time measurement method.

and DC-link voltage is estimated. Reference [274] employed the terminal voltage to compute the compensation time as well as to detect the current polarity. The real-time measurement method is independent of the topology and characteristics of the power devices. Furthermore, the method from this category is relatively efficient, simple for the computation and provides the possibility of eliminating the influence from the current sensor for the current polarity detection. However, the additional hardware is required for the measurements. Besides, the compensated value is one step delayed.

6.1.6 Modification of the Controller

The principle of modifying the controller for reducing the effects of VSI nonlinearities is to solve a general robust tracking problem, i.e. tracking the reference enduring the existence of disturbance with considerable amount. The most methods are derived from the internal model principle, which is widely deployed due to its simplicity and straightforward implementation [294]. The internal model principle was developed in the late 1970s and utilized in the chemical industries [295]. The concept of the internal model principle is to deploy an internal model of the exogenous disturbances in the feedback system and actively reject the disturbances.

The two-degrees-of-freedom control (2DOFC) is a method based on the internal principle and well developed. Its block diagram is shown in Fig. 6.4, where $\mathcal{L}$ denotes the set-point filter and $\mathcal{Q}$ is the disturbance rejection gain.

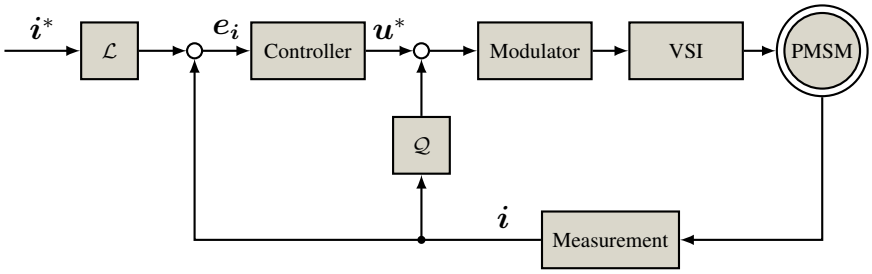

Figure 6.4: Block diagram of general two-degrees-of-freedom control.

Reference [296] used the 2DOFC scheme to compensate the dead-time effect by regulating the error of currents e_i. The two-degrees-of-freedom control method provides more freedom for the control problem, while the design and the parameter selection are relatively complicated.

The resonant control (RSC) is another method derived from the internal model principle, which has a high gain around the resonant frequency and therefore is able to track or reject a sinusoidal signal of a certain frequency [297]. Since the implementation of the ideal reso-

nant is difficult, a quasi-resonant controller is normally deployed. Its transfer function G_{RSC} is designed as a second-order system and expressed as

$$G_{\mathrm{RSC}}(\omega_d) = \frac{2\,K_{\mathrm{RSC}}\,\omega_c\,s}{s^2 + 2\,\omega_c\,s + \omega_d^2}\,, \tag{6.3}$$

where K_{RSC} denotes the resonant coefficient, ω_d is the resonant frequency and ω_c is the cutoff frequency [278]. The structure diagram of the general RC is shown in Fig. 6.5, where the G_Σ denotes the multi-resonant controllers (MRC), which consists of several parallel quasi-resonant controllers, i.e. $G_\Sigma = \sum_{i=1,2,3,\ldots} G_{\mathrm{RSC}}(\omega_i)$. G_1 is an augmented controller and is set as $G_1 = 1$

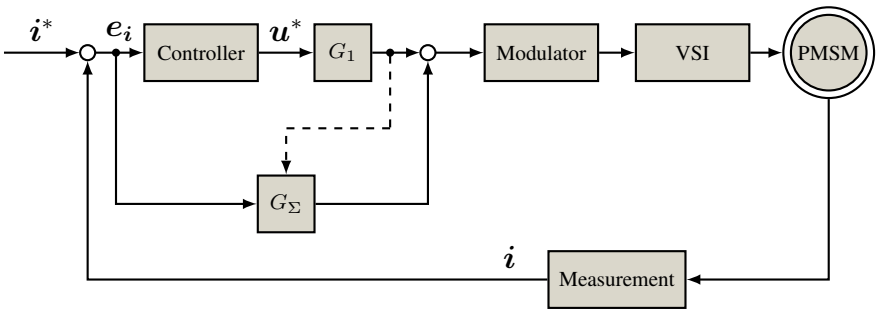

Figure 6.5: Block diagram of general resonant control.

for the traditional resonant control.

As it is explained previously in (6.1), the VSI nonlinearities causes $6\,i$-th order ($i = 1, 2, 3, \ldots$) harmonics in i_d and i_q, among which the sixth order harmonic is dominant. Reference [278] compensated the VSI nonlinearities by applying a RSC with resonant frequency of six times rotor frequency due to the fact that the 6th-order harmonic dominates in harmonic components. Authors in [298] considered both 6th- and 12th-order harmonic and combined RSC with 2DOFC to further improve the tracking and disturbance rejection capability of the proposed method. In several works, the augmented controller G_1 is designed as an integral term to suppress the constant disturbance, i.e. $G_1 = \frac{1}{s}$. For example, works in [204] and [205] combined MPC and the resonant controller. More specifically, in [204] the MPC is developed over an incremental system model to eliminate the constant disturbance and the resonant controller is designed to suppress the 6th-order harmonic. However, the cascaded combination of MPC and resonant controllers degrades the dynamic performance and can cause undesired peak around the resonant frequency in the closed-loop control [205]. Thus, an observer was employed in [205] to estimate the non-periodic disturbance as well as the currents. Furthermore, a vector resonant controller was applied to tackle the problem of the conventional resonant controller.

Another alternative deduced from the internal model principle is the repetitive control, which shares the same structure with the iterative learning control [299]. Therefore, they are treated as the equals and abbreviated as RPC in this thesis. They are also able to track or reject periodic signals. The structure of a general repetitive control as well as the iterative learning control scheme is shown in Fig. 6.6. In Fig. 6.6, $\mathcal{L}$ represents the learning function/control gain, $\mathcal{Q}$ is the filter and T_p is the repetition period. In [61], the RPC was applied in the angle domain of the induction motor. Works, such as [239, 279], applied a fractional RPC to solve the problem that the performance of the RPC degrades, if the time delay steps T_p is non-integer. Reference [300] improved the closed-loop system robustness for the VSI-nonlinearities compensation problem

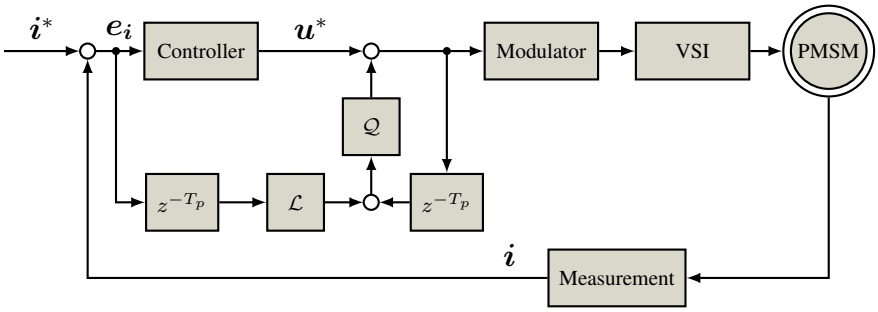

Figure 6.6: Block diagram of the repetitive control/ the iterative learning control.

by integrating a finite impulse response moving average filter that limits the gain of the RPC and also empowers the controller to suppress the target disturbances. In [301], RPC associated with a sliding mode observer to realize the sensorless control of the PMSM.

After analyzing and comparing the principle of the RPC and RSC, it is noticeable that RPC is equivalent to combining infinite resonant controller in all frequencies. Therefore, the RPC can reject all harmonics, but is dynamically slow, while the resonant control has fast dynamic, but works on a single frequency [302].

Besides the internal model principle based methods, the robust control method is also widely applied to deal with the disturbances, which is designed in order that the controller can maintain stability and meet specified performance with the existence of plant uncertainties and external disturbances. However, the robust control method has few effect on the elimination of the periodic disturbances.

Moreover, works based on the analysis on the characteristics of the VSI nonlinearities can be found in [210, 275–277], to name but only a few. Reference [275] applied the PI technique over the difference between the referred voltage and the DC-link voltage to control the DC-link voltage, which derived from the conclusion that the error voltage can be largely reduced if the ratio between the command output voltage and the DC-link voltage is well controlled. Authors in [276] proposed a compensation strategy in the angle domain, which is based on the conclusion that the integral of the current error generates the sixth order harmonic, and cancelled it with the PI technique. Reference [210] applied a similar technique to compensate the VSI nonlinearities and moreover implemented an adaptive controller to cancel the effects from the machine parameter variation. Authors in [277] applied an all-pass filter to compute the instantaneous angle and the magnitude of the zero-axis current and implemented a zero-axis current regulator to eliminate the harmonics.

6.2 State-of-the-Art Methodologies

In the preceding section, the general categorization of the compensation methods for the VSI nonlinear effects is introduced. Subsequently, the state-of-the-art approaches are selected and introduced in this section, where their principles as well as implementations are demonstrated accordingly. The following methods are chosen for the investigations and the further implementations, the offline average-value-based method, the adaptive harmonic filtering method, the resonant control method and the repetitive control method, since they have been widely applied and have particular advantages as well as disadvantages.

6.2.1 Offline Average-Value-Based Method

As introduced prior, the most simple and straightforward method is to employ the relationship between the nonlinear effect of the VSI and the error voltage, where U_{dead} is approximated with the values from the data sheet, which is provided by the manufacture. Recall the approximation of U_{dead} from (3.109) as

$$U_{dead} = \frac{T_{dead} + T_{on} - T_{off}}{T_c}(U_{dc} - U_{ce} + U_d) + \frac{U_{ce} - U_d}{U_{dc}} U_{\text{ref}} + \frac{U_{ce} + U_d}{2} \,, \tag{6.4}$$

as explained in Section 2.4.2, the error voltage caused by the VSI nonlinearities can be represented by a function of U_{dead}, θ_e and the currents direction in (3.107), i.e. $\Delta \boldsymbol{u} = U_{dead} \cdot (\mathcal{F}_d,\ \mathcal{F}_q)^T$, where

$$\begin{bmatrix} \mathcal{F}_d \\ \mathcal{F}_q \end{bmatrix} = \boldsymbol{T}_{dq}(\theta_e) \begin{bmatrix} \text{sgn}(i_a) \\ \text{sgn}(i_b) \\ \text{sgn}(i_c) \end{bmatrix} \,. \tag{6.5}$$

Different from the proposed method in Section 3.6, where the value of U_{dead} is estimated and adjusted in real time. The compensating voltage here is computed with the help of the offline obtained value via (6.4) and the online computed value with (6.5).

6.2.2 Adaptive Harmonic Filtering

The adaptive periodic disturbance filtering method is based on the analysis of the harmonics and eliminates them by adjusting the amplitude of the compensation signal. The VSI nonlinearities causes the $6i$-th harmonics for the drive system. As it is described in Section 2.4.2, the error voltage in the three-phase stationary reference frame can be transformed into the two-phase dq reference frame as

$$\begin{bmatrix} \Delta u_d \\ \Delta u_q \end{bmatrix} = \boldsymbol{T}_{dq} \begin{bmatrix} \Delta u_a \\ \Delta u_b \\ \Delta u_c \end{bmatrix} = A_U \begin{bmatrix} -\sin\gamma - \sum_{n=6i}^{\infty} \left(\dfrac{\sin(n\,\theta_e + (n-1)\,\gamma)}{n-1} + \dfrac{\sin(n\,\theta_e + (n+1)\,\gamma)}{n+1} \right) \\ \cos\gamma - \sum_{n=6i}^{\infty} \left(\dfrac{\cos(n\,\theta_e + (n-1)\,\gamma)}{n-1} - \dfrac{\cos(n\,\theta_e + (n+1)\,\gamma)}{n+1} \right) \end{bmatrix} \tag{6.6}$$

where $A_U = \frac{4\,U_{dead}}{\pi}$, $i = 1,\, 2,\, 3,\, \ldots$, and $\gamma = \theta_{\boldsymbol{i}} - \frac{\pi}{2}$ denotes the angle between the current vector and the q-axis. It can be concluded from the aforementioned formulation of $\Delta \boldsymbol{u}$ that the VSI nonlinearities can be compensated by eliminating the fundamental as well as the $6i$-th harmonics. Moreover, authors in [103] mentioned that the higher order harmonics with $i \geq 2$ have less effect on the voltage distortion. Therefore, an elimination of the sixth harmonic is sufficient to compensate the distorted voltage. Then, the problem of compensating the distorted voltage becomes the filtering of the sixth harmonic, which is realized by a simple second-order all-pass-based adaptive bandpass filter [103]. Its center frequency is dependent on the rotor angular speed, i.e. ω_e. The application of the second-order all-pass filter independently facilitates the control of the bandpass frequency and the bandwidth [103]. The transfer function of the bandpass filter given in z domain can be written as

$$G_{bp}(z) = \frac{1 - G_a(z)}{2} \,, \tag{6.7}$$

where $G_a(z)$ denotes the transfer function of the second-order all-pass filter, which employs the framework of the second-order lattice Gray–Markel all-pass filter and can be given as

$$G_a(z) = \frac{k_2 + k_1\,(1 + k_2)\,z^{-1} + z^{-2}}{1 + k_1\,(1 + k_2)\,z^{-1} + k_2\,z^{-2}}\,, \tag{6.8}$$

where k_1 determines the center frequency of the filter and gives

$$k_1 = -\cos\omega_{bo}\,. \tag{6.9}$$

The frequency ω_{bo} denotes the center frequency of the filter. The coefficient k_2 controls the bandwidth through

$$k_2 = \frac{1 - \tan(B_b)}{1 + \tan(B_b)}\,, \tag{6.10}$$

where B_b represents the bandwidth of the filter, which directly represents the distance from the pole to the unity-circle. The characteristics of the bandpass filter can be determined by choosing adequate coefficients k_1 and k_2. More specifically, the center frequency ω_{bo} of the bandpass filter is defined by the coefficient k_1, which is related to the rotor angular speed, and the bandwidth is determined by specifying the value of the coefficient k_2. In terms of cancelling the VSI nonlinear effects, the center frequency is selected as the $6k$-th harmonics of the PMSM, i.e.

$$\omega_{bo} = 6\,k\,\omega_e\,T_s\,, \tag{6.11}$$

where $k \in \mathbb{Z}^+$, ω_e denotes the electrical rotor angular speed of PMSM and T_s is the sampling time. If the elimination of the sixth harmonic is sufficient to compensate the VSI nonlinearities, as stated in [103], then i is chosen as $i = 1$.

After obtaining the sixth order harmonic, a simple proportional type feedforward compensator via (6.6) is applied, i.e. $\Delta\boldsymbol{u}_c = K_a\,\Delta\boldsymbol{u}$, where $\Delta\boldsymbol{u}$ is given in (6.6). The amplitude A_U in (6.6) is an approximation, which is in practice time varying. Therefore, a K_a is applied to adjust the amplitude of the compensating voltage $\Delta\boldsymbol{u}_c$. The method proposed in [238] is deployed to online adjust the amplitude of the compensation voltage, which gives

$$\begin{aligned} K_{a,\,i+1} &= K_{a,\,i} + \delta_{k,\,i}\,, \\ \delta_{k,\,i} &= -\alpha_k\,\delta_{k,\,i-1}\,\mathrm{sgn}(K_{a,\,i} - K_{a,\,i-1})\,\mathrm{sgn}(\Sigma_{a,\,i} - \Sigma_{a,\,i-1})\,, \end{aligned} \tag{6.12}$$

where α_k denotes the converging coefficient and $\Sigma_{a,\,i}$ represents the accumulation of the sixth harmonic over half the period.

6.2.3 Resonant Control

The concept of internal models plays an essential role in the regulation problem, which estimates the development of the disturbance by simulating the system response. In this thesis, two methods derived from the internal model principle, i.e. the resonant control and the repetitive control, are introduced and compared. The resonant control can track sinusoidal references of arbitrary frequencies with zero steady-state error [303]. Derived from the internal model principle, the resonant controller embeds the poles of the open-loop transfer function into the forward

path between the reference and the output. The transfer function of an ideal resonant controller can be given in Laplace domain as [204]

$$G_{\mathrm{RSC}}(s) = \frac{K_{\mathrm{RSC}}\, s}{s^2 + \omega_d^2}\,, \tag{6.13}$$

where K_{RSC} denotes the resonant coefficient and ω_d represents the resonant angular frequency, i.e. the frequency of the periodic signals. This assures the perfect tracking or eliminating the components rotating at the resonant frequency ω_d when the RSC controller is implemented in the closed-loop. Nonetheless, the ideal resonant controller is difficult to implement in practice and demonstrates poor frequency robustness. Moreover, because of the narrow band and the infinite gain, the discretization is essential for the resonant controllers. A small frequency deviation may even result in a significant performance degradation of the proportional resonant controllers [304]. Therefore, instead of the ideal resonant controller, the quasi-resonant controller is normally deployed to realize the periodic disturbance attenuation, as mentioned previously. The transfer function of the quasi-resonant controller has been introduced and given in (6.3). If more than one single frequency need to be cancelled, the quasi-resonant controllers of the individual frequency need to be parallel constructed, which can be written as

$$G_{\Sigma}(s) = \sum_i \frac{K_{\mathrm{RSC,\,i}}\, \omega_c\, s}{s^2 + 2\,\omega_c\, s + \omega_{d,\,i}^2}\,, \tag{6.14}$$

where $\omega_{d,\,i}$ denote the resonant angular frequency of interest.

6.2.4 Repetitive Control

Besides the resonant control, the repetitive control is also based on the internal model principle and aims to realize an asymptotic tracking as well as rejection of periodic signals. It requires only the knowledge of the period time and was originally designed in the continuous time domain. The repetitive control (RPC) shows superior performance when the periodic signals contains infinite number of harmonics, e.g. the square wave, over the finite dimensional controllers, for example the resonant control. The repetitive control is employed in a feedforward manner, if the periodic signals can be predetermined [305]. The conventional repetitive controller consists of a repetitive control gain K_{RPC} and a delay term, which is defined by the delay time T_d [299, 305]. The delay time T_d is selected equivalently to the disturbance signals. The delay mechanism is normally realized by a memory loop and constitutes a periodic signal generator. The block diagram of a conventional repetitive control is shown in Fig. 6.7, where the controller is demonstrated in z-domain. The RPC can be integrated into the system regarding

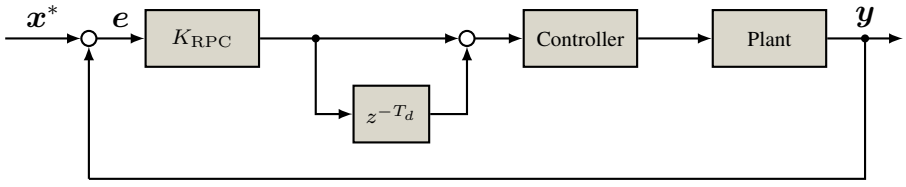

Figure 6.7: Principle of the conventional repetitive control.

different architectures, namely the series approach and the plug-in (parallel) approach. In this

thesis, the plug-in architecture is deployed to compensate the nonlinear effects of the VSI, since the plug-in type RPC can be inserted into the control loop without affecting the performance of the existing controller [306].

However, the repetitive control requires an exact knowledge of the period time of the periodic signals, which is equivalent to the known constant period time or can be obtained through accurately measurement in real-time.

6.3 Speed-Adaptive Fractional Repetitive Control

As mentioned formerly, the repetitive controller was proposed to track or reject the periodic signals in a wide field of researches and applications, such as manufacturing processes, hard disk drives and chemical processes [306]. A guarantee of the performance for the conventional repetitive control is the accurate knowledge of the periodic signals. However, the practical application faces the problem that the periodic frequency varies during the operation and the to be controlled system is in general uncertain. Moreover, the implementation of the conventional repetitive control on a digital control platform evokes normally a non-integer ratio between the period of the periodic signals and the sampling time, which dramatically degrades the performance of the repetitive controller. Furthermore, in the context of the attenuating the periodic disturbance for the electric drive system, the disturbance is varying in terms of the frequency. Therefore, a speed-adaptive fractional repetitive control strategy is proposed to tackle these problems.

6.3.1 System Description

The VSI nonlinearities can be considered as a repetitive signal, which propagates with a frequency of $6\,f_e$. f_e is the fundamental frequency of the PMSM, i.e. $f_e = \omega_e/(2\,\pi)$. Therefore, the time delay can be computed in a discrete manner as a multiples of the sampling time as

$$N_s = \frac{\pi}{3\,\omega_e\,T_s}\,, \tag{6.15}$$

where N_s represents the number of the delayed time period, ω_e denotes the electrical angular speed and T_s is the sampling time. However, the ratio N_s is normally a fraction. For example, a common working condition, the rated condition with $\omega_e = 100\pi\,\mathrm{rad/s}$ and $T_s = 10\,\mathrm{kHz}$, the ratio is obviously a fraction. Therefore, it can be concluded from (6.15) that the ratio N_s, on the one hand, can be a fractional number. On the other hand, it is time varying and depends on the electrical motor speed ω_e. The ratio N_s is normally rounded and the nearest integer is applied for the delay mechanism, as it is shown in [300]. But this approximation degrades the disturbance attenuation performance, since the high control gains shift away from the targeted harmonic frequencies [279]. A simulation is conducted to demonstrate this phenomenon. In Fig. 6.8, the frequency response of the conventional RPC under two scenarios is shown, i.e. N_s is a integer, which is represented with N^*, and N_s is a fraction, of which the integer part is represented by N.

It can be noted from the Fig. 6.8 that the gains at the target frequencies decrease significantly, when the delay step N_s is a non-integer. Besides, the conventional RPC has infinite gain at

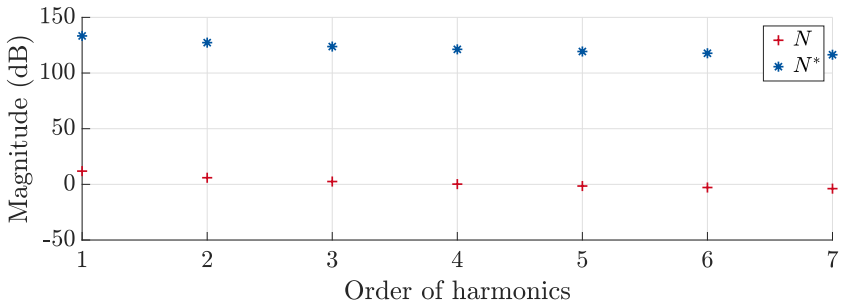

Figure 6.8: Frequency response comparison between the conventional RPC with N_s as an integer and a non-integer. The situation, where the ratio N_s is an integer, is represented by the legend N^* and in blue star, where the non-integer ratio N_s is given by the legend N and in red plus.

frequencies of $2\,i\,\pi/T_d$ ($i = 0,\ 1,\ 2,\ ...$), which can cause the system too sensitive to the certain frequencies and has a great impact on the stability of the closed-loop system [299]. Moreover, based on the prior analysis that the delay time T_d is related to the electrical angular speed ω_e , the RPC may evoke undesired peak around the frequencies of $2\,i\,\pi/T_d$ and reduces the stability margin with increase of the angular speed.

To tackle these problems, a plug-in fractional RPC with a moving horizon average filter is proposed to eliminate the disturbance caused by the VSI nonlinearities and to guarantee that

$$\lim_{i\to\infty} \boldsymbol{e}_{\boldsymbol{i}}^{d} = \mathbf{0} \in \mathbb{R}^{N_x \times 1}\,, \tag{6.16}$$

where $\boldsymbol{e}_{\boldsymbol{i}}^{d}$ denotes the error caused by the VSI nonlinearities. The block diagram presenting the predictive current control with the proposed speed-adaptive fractional repetitive control (FRPC) compensation mechanism is give in Fig. 6.9. The proposed speed-adaptive FRPC method is im-

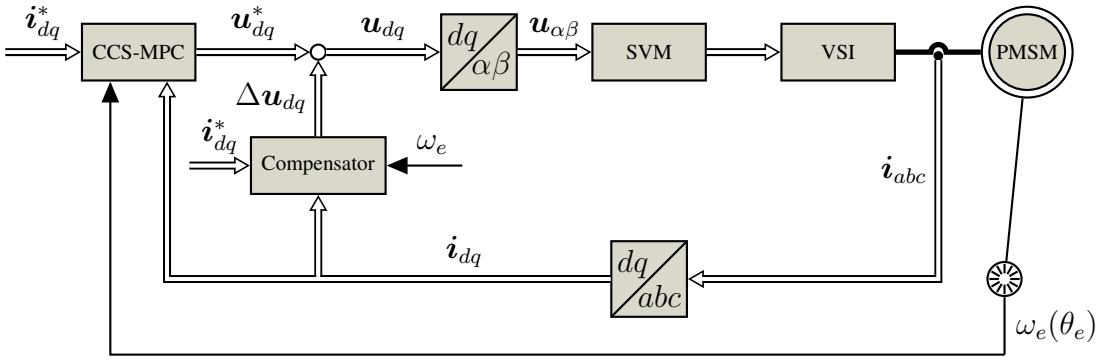

Figure 6.9: The control block diagram of the predictive current control with the proposed compensation method, where the compensator is realized with speed-adaptive fractional repetitive control.

plemented as a compensator, which compensates the distorted voltage in a plug-in manner. The model predictive current control is realized with the CCS-MPC or the deadbeat control, of which the details are described in Chapter 4. The reference current $\boldsymbol{i}^*$ as well as the measurements $\boldsymbol{i}$ are firstly transformed into the dq reference frame and then fed into the compensator. More specifically, the block diagram of the proposed compensation strategy is shown in Fig. 6.10.

The gain K_{RPC} is the gain of the fractional repetitive controller. The filter L is normally selected as a zero-phase low-pass filter to deal with the fact that the RPC has high gains at

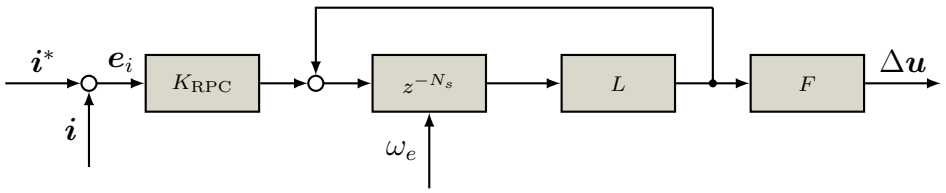

Figure 6.10: Structure of the plug-in repetitive control strategy.

the disturbance related frequencies and therefore may induce instability. In this thesis, a zero-phase moving average filter is implemented [300] and enhances the robustness of the closed-loop system [307]. The filter F denotes a linear-phase lead filter, which is applied to stabilize the overall closed-loop system. It is a zero-phase-error tracking controller and can be designed with methods mentioned in [308], of which the coefficients can be determined with experiments [309]. The transfer function of the plug-in RPC presented in Fig. 6.10 can be written as

$$G_{\mathrm{FRPC}}(z) = \frac{U_c(z)}{E(z)} = K_{\mathrm{RPC}} \frac{z^{-N_s} L(z)}{1 - z^{-N_s} L(z)} F(z) \, . \tag{6.17}$$

The poles of $G_{\mathrm{FRPC}}(z)$ are located at the frequencies $2i\pi f_d$, where f_d is the fundamental frequency of the periodic disturbance. In the context of eliminating the VSI nonlinear effects, f_d is defined as $f_d := 6\, f_e$, where $i \in \mathbb{Z}$. Therefore, the transfer function $G_{\mathrm{FRPC}}(z)$ has an infinite amplitude at the frequencies $2i\pi f_d$ if $L(z) = 1$, which indicates that the RPC can achieve zero steady-state error for the harmonics below the Nyquist frequency if $L(z) = 1$ and N_s is an integer. The stability of RPC can be guaranteed by the design of the feedback gain, as indicated in [310]. However, in practical applications, the non-integer delayed time step N_s is more often encountered. In order to tackle the problem, a technique to handle the fractional delay element is deployed, which approximates the fractional delay by a Lagrange-interpolation-based finite-impulse-response filter. The employed filter handling the fractional delay costs only limited computational resources and is one of the easiest methods to design a fractional delay filter [311]. It is suitable for the online tuning of the fractional delay [311], since the filter on the one hand is simple to implement, on the other hand provides high accuracy for the approximations. The delay z^{-N_s} can be split by the Lagrange-interpolation-based finite-impulse-response filter, i.e. a N_1-th order FIR filter as [312]

$$z^{-N_s} \simeq z^{-N_s^*} \sum_{k=0}^{N_1} m(k) z^{-k} \, , \tag{6.18}$$

where N_s^* is the integer part of N_s and N_1 is an integer, which is selected during the filter design and indicates the accuracy of the approximation. $m(k)$ is so designed that the error between the term on the right hand side and the term on the left hand side of (6.18) is minimized. As it is stated in [313], the coefficients $m(k)$ can be obtained by employing the Lagrange interpolation as follows

$$m(k) = \prod_{j=0,\, j\neq k}^{N_1} \frac{N_s^+ - j}{k - j} \, , \text{ for } k = 0, 1, ...N_1 \, , \tag{6.19}$$

where N_s^+ is the fractional part of N_s and N_1 is the order of the FIR filter, as it is shown in (6.18). The accuracy of the FIR filter in (6.18) is improved with the increase of N_1. A simple linear

interpolation of z^{-N_s} is obtained with $N_1 = 1$. The approximation conducted in (6.18) leaves a remainder R for the fractional delay, which can be derived by subtracting the approximation from the fractional delay and deploying the properties of the Lagrange interpolation as [239]

$$R = z^{-N_s^+} - \sum_{k=0}^{N_1} m(k) z^{-k} = \frac{\delta^{-N_s^+ - N_1} \prod_{i=0}^{N_1 - 1} (-N_s^+ - i)}{(N_1 + 1)!} \prod_{i=0}^{N_1} (N_s^+ - i) \,, \tag{6.20}$$

where $\delta \in [T_{s,k},\, T_{s,k+1}]$. It can be concluded from the formulation of the remainder R that an increase of N_1 improves the accuracy of the approximation in (6.18). Furthermore, the transfer function of the fractional repetitive control can be further rewritten by substituting the formulation of the FIR filter for the fractional delay in (6.18) as

$$G_{\mathrm{FRPC}}(z) = K_{\mathrm{RPC}} \frac{z^{-N_s^*} \sum_{k=0}^{N_1} m(k) z^{-k}\, L(z)}{1 - z^{-N_s^*} \sum_{k=0}^{N_1} m(k) z^{-k}\, L(z)}\, F(z) \,, \tag{6.21}$$

which turns into a repetitive controller with $N_s^+ = 0$. The integer component N_s^* and the fractional term N_s^+ change with the rotor speed and the sampling frequency, where the sampling frequency is normally constant for an implementation of the control for the PMSM drive system on an embedded system.

6.3.2 Parameter Design

After obtaining the general form of the fractional repetitive controller in (6.21), the parameters of (6.21) need to be designed properly, in order to eliminate the periodic disturbances and realize the precise control. First of all, the parameter of the FIR filter for approximating the fractional delay is investigated, i.e. the order of the filter N_1. The simulations of the frequency response considering various values of the parameter N_1 have been carried out, where the target frequencies are $480\,\mathrm{Hz}$ and its multiples. The corresponding results are shown in Fig. 6.11.

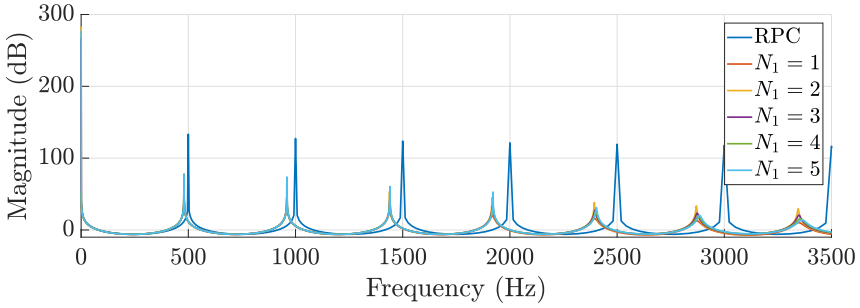

Figure 6.11: Frequency response of the FRPC designed with various values of the parameter N_1, which represents the order of the Lagrange-interpolation-based FIR filter.

In Fig. 6.11, it can be observed that the FRPC can accurately suppress the signals at the designed frequencies, while the conventional RPC shifted the control gain on the frequency domain. The gain of the conventional RPC is relatively large at the frequency of $500\,\mathrm{Hz}$ and its multiples, while it is significantly reduced at the target frequency $480\,\mathrm{Hz}$ and its multiples. It is worth mentioning that the gain reduction of the conventional RPC is even worse in higher frequency region.

In order to demonstrate the frequency response of the respective filter with different parameter selections, the gains at the harmonic frequencies, which consider $480\,\mathrm{Hz}$ as the fundamental frequency, are collected and presented in the relation to the harmonic order in Fig. 6.12.

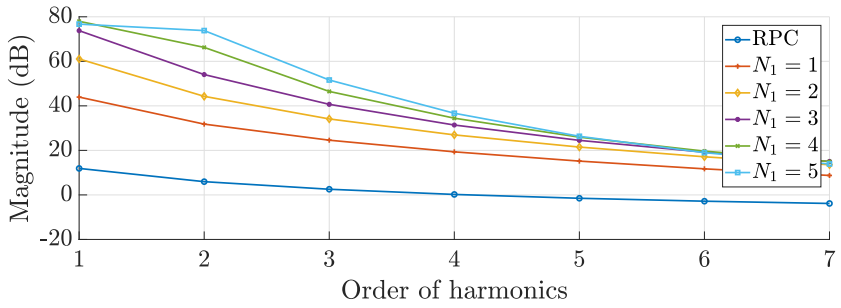

Figure 6.12: Frequency response of different values of the parameter N_1 as a relation to the harmonic order.

Obviously, the gain reduction of the conventional RPC at the target frequencies is significant. Consequently, the rejection ability of the conventional RPC is dramatically reduced. Because of the principle of the fractional repetitive control, the gain at the target frequencies is reduced and yet large enough. An increase on the order of the Lagrange-interpolation-based FIR filter can result in a higher gain at the target frequencies, which furthermore delivers a more accurate approximation and improves the disturbance rejection performance. However, the computational burden is increased accordingly.

The moving average filter $L(z)$ is utilized to guarantee the system stability by limiting the control gain of the repetitive control as finite and yet large enough at the target frequencies to suppress the periodic disturbance [309]. Moreover, it can realize the functionality of a low-pass filter and demonstrates zero phase shift. The formulation of a general moving average filter can be given as

$$L(z) = \frac{\sum_{j=0}^{N_2} \alpha_j z^j + \sum_{j=1}^{N_2} \alpha_j z^{-j}}{2\sum_{j=1}^{N_2} \alpha_j + \alpha_0}\,, \tag{6.22}$$

where $\alpha_j > 0$ with $j = 0,\, 1,\, \cdots,\, N_2$. The determination of the parameter N_2 and the coefficients α_j depends on various factors, e.g. the phase delay, the gains and the current measurement noise. For a causal FIR filter, the phase delay increases as the filter length N_2 gets longer. Nonetheless, the FIR filter in (6.22) can achieve zero phase delay. The simulations to study the frequency response of the FIR filter given in (6.22) have been carried out in terms of the different parameter selections of N_2. The corresponding results are shown in Fig. 6.13.

It can be concluded from the Fig. 6.13 that a larger value of N_2 can lead to a smaller gain at the target frequencies, which however improves the robustness of the closed-loop system [314]. A first-order filter with $N_2 = 1$ is normally sufficient for the practical applications, as claimed in [309]. Once the order of the moving average filter is determined, the weighting allocating coefficients α_j are studied subsequently. Simulations for investigating the relationship between α_0 and the gain at the target frequencies have been carried, of which the results are shown in Fig. 6.14 correspondingly.

A larger α_0 enlarges the passband of the filter $L(z)$, while a smaller value of α_0 brings a wider stability range for the gain K_{RPC} [309]. As it is indicated in [315], the lowest noise is obtained when all the input samples are treated equally. Moreover, it can be observed that $\|L(z)\| \to 1$

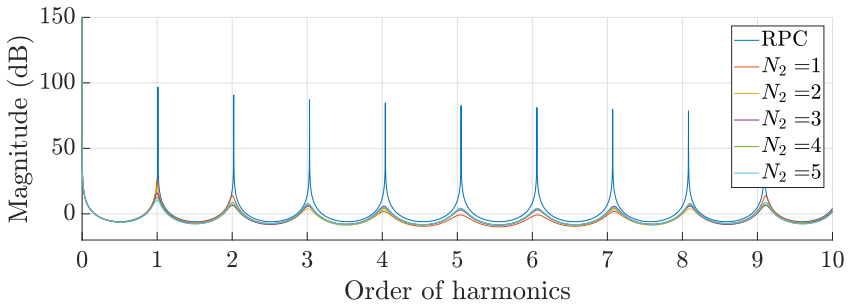

Figure 6.13: Frequency response of different parameter selections of N_2 for the FRPC, which is represented as a function of the harmonic orders.

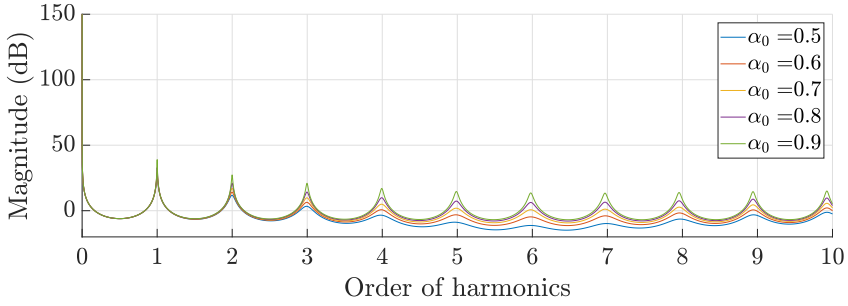

Figure 6.14: Frequency response of different parameter design of α_0 for the FRPC filter.

at low frequencies and $\|L(z)\| \rightarrow 0$ at high frequencies. Therefore, the parameter design of $L(z)$ can be regarded as a tradeoff between the tracking ability and the system robustness [316]. Since the moving average filter $L(z)$ has no extra phase displacement, its phase characteristics is zero.

Moreover, the original closed current loop demonstrates the system delay and phase shift. Therefore, the implementation of a phase lead filter $F(z)$ is encouraged to realize the zero-phase-shift compensation [309]. The phase lead filter can be chosen as a stable inversion of the current dynamics, which can be generally written as [317]

$$F(z) = \frac{z^{N_3} A(z^{-1}) B^u(z^{-1})}{B^a(z^{-1}) B^u(1)} \,, \tag{6.23}$$

where N_3 represents the delay of the system, $B^u(z^{-1})$ and $B^a(z^{-1})$ denote the unstable zeros and stable zeros of the plant, respectively. $A(z^{-1})$ includes poles of the plant. $B^u(1)$ is the scaling factor of the steady state control gain of the controller. However, the inverse of the system is normally unavailable due to various uncertainties and disturbances [309]. But the value of the parameter N_3 can be determined via experiments [309].

After applying the plug-in speed-adaptive FRPC into the current control loop, the overall control law $\boldsymbol{u}$ at step k from Fig. 6.9 is then given as:

$$\boldsymbol{u}_k = \boldsymbol{u}_k^* + \Delta \boldsymbol{u}_k \,, \tag{6.24}$$

where $\boldsymbol{u}_k^*$ is the control voltage computed from the predictive controller and the $\Delta \boldsymbol{u}_k$ denotes the compensating voltage obtained from the proposed plug-in speed-adaptive FRPC. As a result,

the transfer function of the plug-in speed-adaptive FRPC is summarized as

$$G_{\mathrm{FRPC}}(z) = \frac{U_c(z)}{E(z)} = K_{\mathrm{RPC}} \frac{z^{-N_s} L(z)}{1 - z^{-N_s} L(z)} F(z) \,, \tag{6.25}$$

where z^{-N_s}, L and F can be realized with (6.18), (6.22) and (6.23), respectively.

In the discrete-time domain, the delay z^{-1} is realized by implementing the buffer stack. Its length is determined by the delay time and the sampling time. The buffer stack is updated at each sampling instant. More specifically, the stack is shifted by one element and the most recent data is enclosed.

6.3.3 Stability Analysis

After determining the aforementioned parameters of FRPC with the help of simulations and experiments, the control gain K_{RPC} needs to be assigned. It denotes the trade-off between the stability robustness and the steady-state performance [318]. A proper selection of the control gain K_{RPC} enables a decrease of the non-harmonic components [319]. The transfer function of the closed-loop system regardless of the controllers can be written as

$$G_{cp}(z) = \frac{G_p(z)}{1 + G_p(z)} \,, \tag{6.26}$$

where $G_p(z)$ denotes the transfer function of the system, i.e. the current loop of the PMSM. After deploying the plug-in speed-adaptive FRPC, the transfer function of the reference $Y_r(z)$ and the disturbance $D_s(z)$ to the system output or measurement $Y(z)$ can be derived as [309]

$$\frac{Y(z)}{Y_r(z)} = \frac{\left[1 - L(z)\, z^{-N_s} (1 - K_{\mathrm{RPC}}\, F(z))\right] G_{cp}(z)}{1 - L(z)\, z^{-N_s} (1 - K_{\mathrm{RPC}}\, F(z)\, G_{cp}(z))} \,, \tag{6.27}$$

and

$$\frac{Y(z)}{D_s(z)} = \frac{1 - L(z)\, z^{-N_s}}{1 + G_p(z)} \cdot \frac{1}{1 - L(z)\, z^{-N_s} (1 - K_{\mathrm{RPC}}\, F(z)\, G_{cp}(z))} \,, \tag{6.28}$$

respectively. The error transfer function of the FRPC-based compensation mechanism can be given as

$$\frac{E(z)}{Y_r(z) - D_s(z)} = \frac{(1 + G_p(z))^{-1} \left(1 - z^{-N_s}\, L(z)\right)}{1 - z^{-N_s}\, L(z)\, (1 - K_{\mathrm{RPC}}\, F(z)\, G_{cp}(z))} \,. \tag{6.29}$$

As a result, the stability of the closed-loop system controlled by the FRPC is asymptotically stable as long as the following two conditions are satisfied: the closed-loop feedback system $G_{cp}(z)$ is stable and the roots of the denominator, i.e. $1 - z^{-N_s} L(z)\, (1 - K_{\mathrm{RPC}} F(z)\, G_{cp}(z))$, are inside the unit circle, which gives

$$|1 - K_{\mathrm{RPC}}\, F(z)\, G_{cp}(z)| < |L(z)|^{-1} \left| \sum_{k=0}^{N_1} m(k) z^{-k} \right|^{-1} \,, \; \forall z = e^{j\omega},\, 0 < \omega < \frac{\pi}{T_s} \,. \tag{6.30}$$

The first condition is equivalent to the statement that the roots of $\left(1 + G_p(z)\right)^{-1}$ are inside the unit circle, which is same as the conventional repetitive control method. The second stability

criterion is almost equivalent to the consideration of the conventional repetitive control within the passband of the fractional delay filter in (6.18), i.e. $\left|\sum_{k=0}^{N_1} m(k)z^{-k}\right| \to 1$. Furthermore, if the bandwidth of the moving average filter $L(z)$ is smaller than the bandwidth of the fractional delay filter, it can be obtained that $|L(z)|\left|\sum_{k=0}^{N_1} m(k)z^{-k}\right| \to 1$. Then the second condition in (6.30) can be simplified as a more conservative condition as

$$|1 - K_{\mathrm{RPC}}\, F(z)\, G_{cp}(z)| < 1\ . \tag{6.31}$$

If the applied phase lead filter $F(z)$ can achieve zero-phase compensation, the synthesis of the plug-in speed-adaptive FRPC is similar to that of the conventional repetitive controller [309]. If the frequency of the reference signal $y_r(t)$ and the disturbance $d_s(t)$ approaches $\omega_i = 2i\pi\, f_d$, where $i = 0,\, 1,\, 2,\, ...,\, N_s^*$ ($N_s^* = \lfloor N_s \rfloor$), then $z^{-N_s} = 1$. Consequently, if the overall closed-loop system is asymptotically stable, the error $E(z)$ can be derived from (6.29) with the assumption $L(z) = 1$ as

$$\lim_{\omega \to \omega_i} \|E(z)\| = 0,\ \forall \omega_i\ , \tag{6.32}$$

which denotes that for any periodic reference signal with a frequency less than the Nyquist frequency, a zero steady-state tracking error can be guaranteed even under the existence of the model uncertainties. It can be concluded from the inequality in (6.30) that the choice of the parameters for $F(z)$ and K_{RPC} is coupled.

Let $M_{G_{cp}}$ and $\theta_{G_{cp}}$ represent the magnitude characteristics and the phase characteristics of $G_{cp}(z)$, respectively, i.e. $G_{cp}(j\omega) = M_{G_{cp}}(\omega)e^{j\theta_{G_{cp}}(\omega)}$. Analogously, $F(z)$ has the frequency characteristics $F(j\omega) = M_F(\omega)e^{j\theta_F(\omega)}$, where $M_F(\omega)$ and $e^{j\theta_F(\omega)}$ denote its magnitude and phase, respectively. Substitute the magnitude characteristics as well as the phase characteristics of $G_{cp}(z)$ and $F(z)$ into (6.31), it can be obtained that

$$|1 - K_{\mathrm{RPC}}\, M_{G_{cp}}(\omega) M_F(\omega)\, e^{j\theta_{G_{cp}}(\omega) + j\theta_F(\omega)}| < 1\ . \tag{6.33}$$

The phase lead filter $F(z)$ is deployed to realize the zero-phase compensation and normally is designed in practice as

$$F(z) = z^{N_3}\ . \tag{6.34}$$

As a result, the inequality (6.33) can be simplified as

$$|1 - K_{\mathrm{RPC}}\, M_{G_{cp}}(\omega)\, e^{j(\theta_{G_{cp}}(\omega) + N_3\, \omega)}| < 1\ . \tag{6.35}$$

Therefore, it can be derived from (6.30) that [320]

$$0 < K_{\mathrm{RPC}} < \frac{2}{M_{G_{cp}}}\ . \tag{6.36}$$

Thus, if $F(z)$ yields a zero-phase compensation for the closed-loop system, the stability range of the gain K_{RPC} will be $0 < K_{\mathrm{RPC}} < \frac{2}{M_{G_{cp}}}$.

It is worth mentioning that the conditions are sufficient to guarantee the closed-loop stability, which however has been claimed to be close to the necessary ones in practice [321]. Moreover, works such as [322] and [306] provide the guidelines for designing the repetitive controllers.

6.4 Experimental Evaluation

Subsequent to the explicit introduction and analysis of the overall system behaviour and the stability issue, the proposed speed-adaptive FRPC is implemented on the laboratory facility described in Appendix B.2. The proposed method is firstly tested at the steady state, in order to compare with the state-of-the-art methods mentioned previously, namely the offline average-value-based method, the adaptive harmonic filtering method and the resonant controller. Subsequently, the proposed method has been tested under the parameter mismatch of L_d, L_q and Ψ_{m}. The performance under the parameter mismatch of R_{s} is not investigated, since its influence is almost ignorable. At last, the dynamic performance of the proposed FRPC is evaluated under a load step.

6.4.1 Steady State Performance

First of all, the steady-state performance in terms of the harmonics elimination are evaluated for all methods with an analysis of the harmonic content of the three-phase current up to 13-th order. The working point of the PMSM is chosen as the rated speed and the no-load condition. The computation results of the harmonic contents are shown in Table. 6.1. Moreover, their sum is also computed and shown in Table 6.1 under the denotation named **HD**.

Table 6.1: Harmonic analysis

	5th	7th	11th	13th	HD
CCS-MPC	5.48%	2.07%	0.14%	0.19%	7.88%
Offline	4.59%	1.02%	0.43%	0.59%	6.63%
AHF	5.12%	1.24%	0.08%	0.11%	6.55%
RSC	3.29%	0.77%	0.06%	0.08%	4.20%
FRPC	3.60%	0.73%	0.10%	0.14%	4.57%

In Table 6.1, the term *Offline* represents the offline average-value-based method and the *AHF* denotes the adaptive harmonic filtering method. It can be observed from the computational results in Table 6.1 that the predictive current control yields a harmonic distortion up to 13-th order of almost 8% of the fundamental amplitude and the implementation of the disturbance observer introduced in Chapter 4 has little effect on the harmonic elimination, since the disturbance observer mainly focuses on the constant-like disturbance and has effect on the noises. Although the deployed disturbance observer, e.g. the derivatives of the Kalman filter and the MHE, has the ability to filter out the measurement noises and the system noises, their bandwidth is however limited. Moreover, they have little effects on the low-order harmonics. After implementing the offline average-value-based method, of which the values are obtained from the manufacturer's data sheet, has reduced the harmonic content (up to 13-th harmonic) to 6.63%. An obvious reduction of the 5-th and 7-th harmonic can be observed, while the 11-th and the 13-th harmonics have been increased significantly. The adaptive harmonic filtering has reduced the harmonic content by 1.33% and the values of all harmonics have declined. The

resonant controllers outperforms the other three methods, which reduced the harmonic content to 4.2%. However, multiple resonant controllers need to be implemented to eliminate individual harmonic content. The system under the control of the proposed FRPC can achieve a harmonic distortion of 4.57%, which reduced the harmonic distortion of the CCS-MPC by 42% and shows better performance than the offline average-value-based method and the adaptive harmonic filtering method.

6.4.2 Parameter Variation of L_d

The proposed method can furthermore eliminate the steady-state error caused by the parameter mismatches to a certain level. The first test scenario is the parameter variation of the inductance in the d-axis. The PMSM runs at the rated speed and has no load. L_d has increased by 20% in the CCS-MPC. The corresponding experimental results are shown in Fig. 6.15. The proposed speed-adaptive FRPC is activated at $t = 0\,\mathrm{s}$. Analogously, an reduction of the parameter L_d in

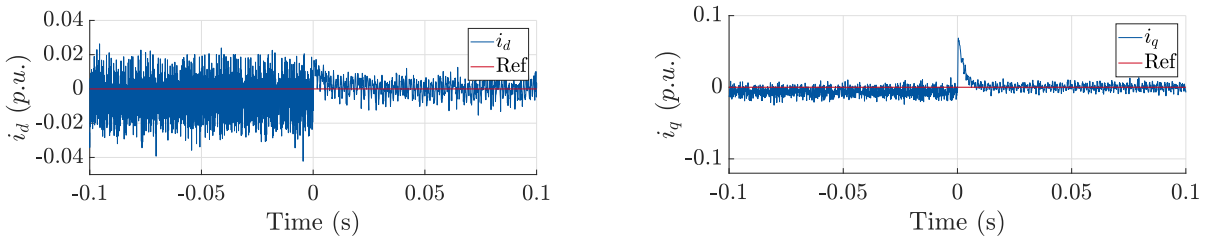

Figure 6.15: The control performance of the predictive current control and the proposed harmonic elimination strategy under the parameter mismatch of L_d with $r_p = 120\%$. The speed-adaptive FRPC is activated at $t = 0\,\mathrm{s}$.

the controller is also investigated, i.e. $r_p = 80\%$. The corresponding experimental results are shown in Fig. 6.16.

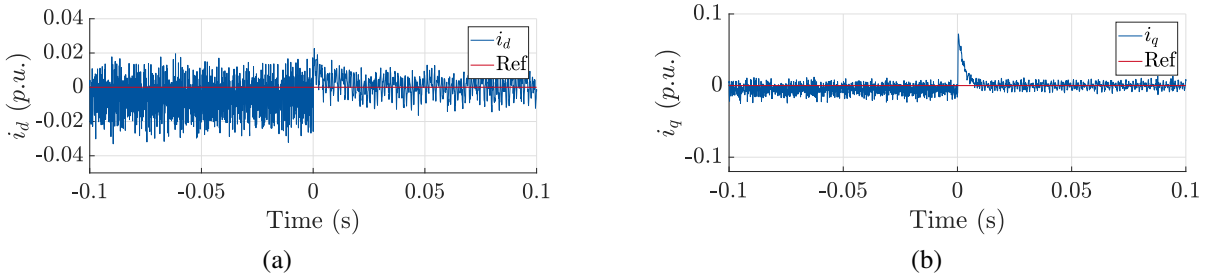

Figure 6.16: The control performance of the predictive current control and the proposed harmonic elimination strategy under the parameter mismatch of L_d with $r_p = 80\%$. The speed-adaptive FRPC is activated at $t = 0\,\mathrm{s}$.

It can be concluded from Fig. 6.15 and Fig. 6.16 that the proposed FRPC-enhanced CCS-MPC eliminates the harmonics significantly, especially for the d-axis current. After activating the proposed method, the system converges to the new steady state within $10\,\mathrm{ms}$. The variation of the inductance L_d causes small steady-state offsets in d- and q-axis, which are cancelled by activating the FRPC at $t = 0\,\mathrm{s}$.

6.4.3 Parameter Variation of L_q

The control performance under the parameter mismatch of the L_q is furthermore investigated. Similar to the former test scenario, experiments simulating the increase as well as the reduction of L_q have been carried out. The experimental results are shown in Fig. 6.17 and Fig. 6.18, respectively.

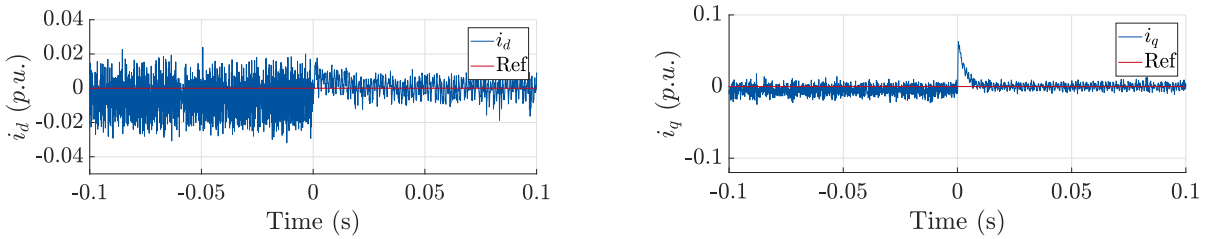

(a) (b)

Figure 6.17: The control performance of the predictive current control and the proposed harmonic elimination strategy under the parameter mismatch of L_q with $r_p = 120\%$. The speed-adaptive FRPC is activated at $t = 0\,\mathrm{s}$.

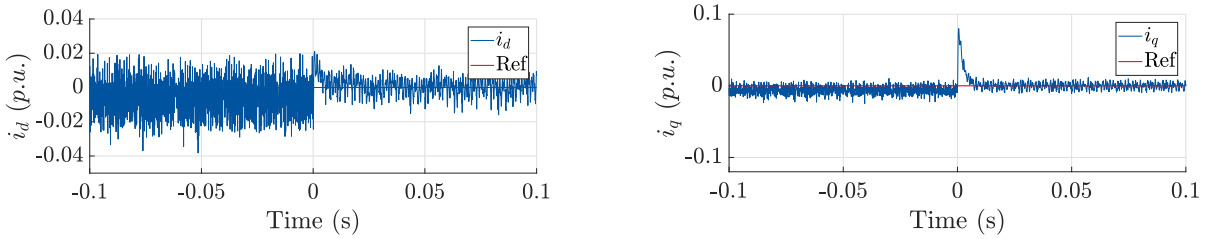

(a) I_d (b) I_q

Figure 6.18: The control performance of the predictive current control and the proposed harmonic elimination strategy under the parameter mismatch of L_q with $r_p = 80\%$. The speed-adaptive FRPC is activated at $t = 0\,\mathrm{s}$.

Similar conclusions to the test scenario of L_d variation can be drawn from Fig. 6.17 and Fig. 6.18 that the proposed strategy reduce the harmonic content significantly and cancelled the small steady-state error of CCS-MPC under the parameter mismatch of L_q.

6.4.4 Parameter Variation of Ψ_m

As it has been studied in Chapter 4, the parameter mismatch of the permanent magnet flux linkage Ψ_m can cause the most steady-state offset among all electrical parameters. The control performance under the parameter variation of Ψ_m is then furthermore studied with the experiments on the increase and the reduction of Ψ_m. The corresponding experimental results are shown in Fig. 6.19 and Fig. 6.20.

It can be observed from Fig. 6.19 that a conspicuous steady-state offset can be observed in the q-axis before $t = 0\,\mathrm{s}$, which is however reduced by integrating the FRPC-based compensation mechanism. A small steady-state offset can also be observed in the d-axis, which has been cancelled after $t = 0\,\mathrm{s}$ as well. In Fig. 6.20, a larger steady-state offset is observed in q-axis than the test scenario presented in Fig. 6.19, where $r_p = 120\%$. The error can be reduced to a

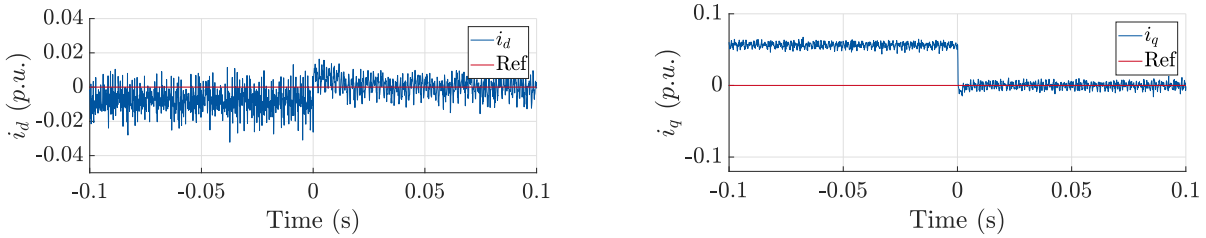

Figure 6.19: The control performance of the predictive current control and the proposed harmonic elimination strategy under the parameter mismatch of Ψ_{m}, where $r_p = 120\%$. The speed-adaptive FRPC is activated at $t = 0\,\mathrm{s}$.

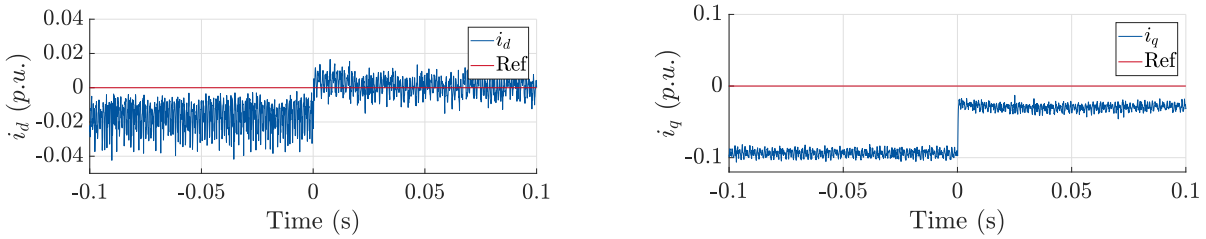

Figure 6.20: The control performance of the predictive current control and the proposed harmonic elimination strategy under the parameter mismatch of Ψ_{m}, where $r_p = 80\%$. The speed-adaptive FRPC is activated at $t = 0\,\mathrm{s}$.

certain level by activating the FRPC at $t = 0\,\mathrm{s}$, while the tracking error in d-axis is effectively eliminated. Consequently, the capability of the proposed FRPC-based control strategy to eliminate the steady-state error caused by the parameter mismatch is limited, which means that it can improve the robustness of the closed-loop system against the model uncertainties to a certain degree. Severe parameter variation may still have observable impacts on the tracking accuracy. An increase of the control gain K_{RPC} can increase the tracking ability, but it is nonetheless limited by the stability criterion.

It is worth mentioning that the different parameter mismatches altered the harmonic content, i.e. the parameter variation of the inductances induces a severer harmonic distortion than the variation of the permanent magnet flux linkage. The reason to this observation can be traced back to the fact stated in Chapter 2 that the parameter mismatch of the inductances influences the system characteristics, while the parameter mismatch of the Ψ_{m} results in a steady-state error.

6.4.5 Dynamic Performance

Furthermore, the dynamic performance of the proposed harmonic cancellation strategy is tested and compared with the CCS-MPC. A load step of the full load is added to the PMSM at $t = 0\,\mathrm{s}$. The corresponding results are shown in Fig. 6.21 and Fig. 6.22, respectively.

It can be noted from Fig. 6.21 that the increase of the load condition impairs the control performance of the predictive current control, i.e. more obvious voltage distortion caused by the VSI can be observed in the d-axis and a conspicuous steady-state offset can be observed in the q-axis after the insertion of the load step. Moreover, an overshoot of more than 5% of the rated

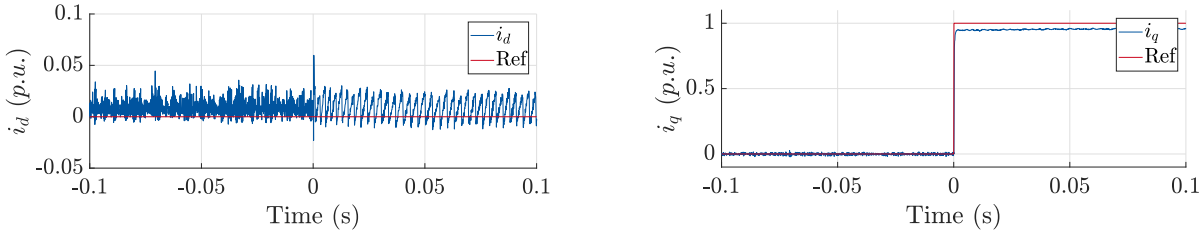

Figure 6.21: Dynamic performance of the CCS-MPC. A load step of the full load is added at $t = 0\,\mathrm{s}$.

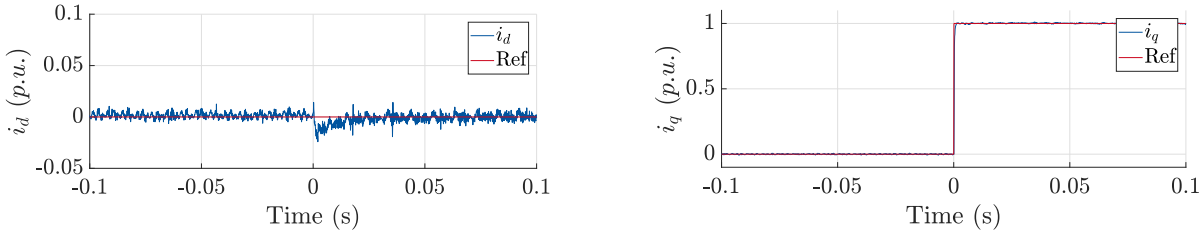

Figure 6.22: Dynamic performance of the proposed harmonics elimination strategy. A load step of the full load is added at $t = 0\,\mathrm{s}$.

current appeared during the transient. A significant improvement of the control performance can be realized by employing the proposed speed-adaptive FRPC, which is shown in Fig. 6.22. The harmonic contents of the d-current have been significantly reduced. Furthermore, the overshoot during the transient has decreased to around 2% of the rated current. It is worth mentioning that the dynamic of the d-current is affected, which is slower than the classical predictive current control. Nonetheless, the dynamic of q-current is hardly affected and the steady-state error after the load step has been eliminated effectively. Moreover, the current quality of i_q in terms of the ripples has also been improved.

6.5 Conclusion

In this chapter, the attenuation of the periodic disturbances is addressed. More specially, the voltage distortion problem raised by the nonlinear effects of the VSI is discussed. Firstly, the state-of-the-art approaches dealing with the VSI nonlinearities are introduced. Subsequently, the offline average-value-based method, the adaptive harmonic filtering, the resonant control and the repetitive control are elaborated in detail. However, the promising repetitive control method suffers from the problem of fractional ratio between the target frequency and the sampling frequency, which significantly degrades the performance of eliminating the periodic disturbance. Therefore, the speed-adaptive fractional-repetitive-control-enhanced predictive current control is proposed to tackle the aforementioned problem, where a plug-in architecture is employed. The proposed method can effectively eliminate the current harmonics caused by the nonlinear effect of VSI. Its performance in terms of eliminating the harmonics outperforms the offline averaged value method and the adaptive harmonic filtering method, while it is slightly worse than the resonant controllers. Nonetheless, the resonant controller is designed for a single

target frequency, which means that the compensation of the distorted voltage requires multiple parallel resonant controllers. Moreover, the proposed strategy can improve the system robustness against the parameter variation to a certain level. A significant improvement of the current tracking ability can be noticed at the full-load condition, where the VSI nonlinear effect is dominant.

Part IV

CONCLUSIONS AND OUTLOOKS

CHAPTER 7

Conclusions and Outlook

In this work, two problems are investigated, i.e. the parameter identification and the controller optimization. First, the investigation of the parameter identification of the PMSM drive system was carried out. More specifically, both offline identification procedures and online estimation methods for the electrical parameters and the VSI nonlinear effects have been addressed. Second, the control problems with the continuous-control-set MPC and the finite-control-set MPC under the existence of the model uncertainties and the disturbances have been studied. The control performance has been improved in terms of the tacking ability and the robustness against model uncertainties, disturbances. These two focuses of this thesis were addressed separately in Part II and Part III.

7.1 Conclusions

7.1.1 Part II: Parameter Identification

One of the main objectives in this part is to refine the offline determination procedures for the electrical parameters of the PMSM and the nonlinear effects of the inverter. Based on the simplified and the general formulation of the current dynamics for the PMSM, the important electrical parameters for describing the PMSM current dynamics can be identified respectively. Moreover, because of the non-ideal behaviour of the inverter, the nonlinear effects of the VSI were furthermore analysed and identified as the distorted voltage at the machine terminal. The offline determination procedures are accurate and employ simple computation methodology. However, the design of the procedure is normally sophisticated and requires extra equipment or hardware to realize the measurement. Even though the self-commissioning strategy can be implemented to complete the procedures, the high-level control logic is still required. Moreover, an accurate modelling of the parameter values requests the establishment of a multi-dimensional relationship. For example, the inductance of the PMSM is primarily related to the temperature and the

current, which is also affected by the humidity and the material characteristics. Therefore, the online estimation can better capture the real-time variation of the parameters. The identifiability of the parameter combinations have been studied and is regarded as the prerequisite for the online estimator implementation. Numerous estimation methods have been proposed and applied in the industry and also academia to achieve the goal of estimating the parameters during the operation. The model reference adaptive system employs the PI technique to guarantee the hyperstability of the closed-loop system. It is simple and has low computational burden. However, it is sensitive against the noises and the tuning of the PI coefficient is burdensome. The recursive least squares method is the first method of formulating an optimal estimation from noisy measurements in a recursive manner. It has also relatively low computational burden and is easy to implement. But the implementation of the recursive least squares method is a tradeoff between the robustness to the noises and the dynamic performance. As the experimental results showed, it may deliver biased estimates. Two variants from the Kalman-filter family were also investigated, i.e. the extended Kalman filter and the unscented Kalman filter. The extended Kalman filter linearised the nonlinear system constructed during the parameter estimation problem, while the unscented Kalman filter applied scattered sample points to interpret the nonlinearity. They involve the measurement noise and the process noise in the problem formulation. Thus, they are relatively accurate and dynamic in the practical application, but has high computational cost. An optimization based estimator, the moving horizon estimator, has also been investigated. It is normally preferred for the problem with constraints and requiring high dynamic response. The parameter estimation problem is generally formulated in the context of the moving horizon estimator, where the solving methods were systematically introduced and elaborated. These methods have been implemented and tested under various scenarios. Their performances were summarized in terms of the accuracy, the computational burden, the dynamic response, the robustness and the memory allocation. In summary, the complexity of the estimation method benefits the accuracy of the results. However, the computational power is limited by the hardware configuration. The methods have individual advantages and disadvantages. Thus, the choice of the proper estimator depends on the requirements of the application. As addressed in the context of offline determination procedures, the nonlinear effect of the inverter has a significant impact on the parameter estimation, which is therefore approximated and included into the system model. As a result, the nonlinear effect of the inverter can be estimated concurrently with the machine parameters. Furthermore, a dual extended Kalman filter was applied to realize the estimation. Because of the separation of the state estimation and the parameter estimation within the framework of the dual Kalman filter, the computational burden can be significantly reduced by deactivating the parameter estimator.

7.1.2 Part III: Controller Optimization

This part concentrates on the optimization of the predictive current control of the PMSM drive system under the existence of uncertainties and disturbances. Based on the theoretical analysis and experimental investigations about the uncertainties and disturbances in the PMSM drive system, their impacts on the control performance are furthermore studied. Because that the model predictive control is set up based on the system dynamics, its sensitivity to the system model accuracy is rather higher than FOC. The uncertainties as well as the disturbances can result in steady-state error, harmonic content or even cause instability. This problem was firstly

addressed for the continuous-control-set MPC, where the deadbeat control is regarded as a special case of the CCS-MPC. The problem resulted from the parameter mismatches, the encoder error and the digital delay were investigated via the experiments. It can be concluded that in the PMSM drive system, the permanent magnet flux linkage causes mainly the steady-state error, while the inductances can affect the stability of the closed-loop system. The impact from the stator resistance is almost ignorable. A disturbance observer was implemented to estimate the currents and the disturbances. The estimates were then fed into the underlying optimization problem of CCS-MPC, which is tasked to find the optimum of the control problem based on the augmented PMSM current model. The stability of the overall control strategy was addressed, which is proven to be input-to-state stable, if several conditions are satisfied. Moreover, the proposed control strategy is generally formulated and can be applied to an arbitrary drive system. Analogously, the conclusion about the system stability can be mapped to other drive system. Different from CCS-MPC, finite-control-set MPC inherits the discrete nature of the inverter. Therefore, it demonstrates higher robustness against the uncertainties and disturbances, but it is still affected. The influence of the parameter mismatch was analysed and quantified with several designed simulations. An observer was likewise applied to improve the performance of the FCS-MPC. In order to reduce the computational burden of FCS-MPC, a problem formulation in the $\alpha\beta$ domain was proposed for a special PMSM, SPMSM. Thanks to the symmetry of the related matrices, the major part of the heavy computations involving in the FCS-MPC can be allocated offline, which significantly reduces the online computational burden. Furthermore, the disturbances can increase the harmonic content of the current as well as the speed. The periodic disturbances produced by the VSI nonlinear effects were subsequently emphasized. The most straightforward intuition is to combine the aforementioned parameter estimator and the disturbance observer. Nonetheless, after examining the extended system model with the terms related to the VSI nonlinearity and the disturbance, it can be noticed that they are not simultaneously observable. Therefore, a speed-adaptive fractional-repetitive-control based compensation scheme was proposed, which aims to cancel the $6i$-th harmonics with $i \in \mathbb{Z}$. The effectiveness was validated and compared with state-of-the-art methods.

7.2 Outlook

Chapter 3 introduces the offline as well as the online parameter identification methods, which offers several potential directions for future research. Firstly, the comparison and discussion are based on the PMSM drive system. It would be interesting to study if the conclusions can be derived from other electrical drive systems. Theoretically, the algorithm and the principle of the determination procedures should be independently of the machine and the inverter type. Nonetheless, a further validation and research would be beneficial. Furthermore, several assumptions are made before constructing the machine model. Although the omitted terms, e.g. the core losses, are normally neglected in the drive modelling. They can have impacts on the parameter identifications and estimations. Thus, a further investigation including the losses of the PMSM is worth engaging.

In the Chapter 4, the problems encountered in the framework of the continuous-control-set MPC have been addressed and tackled via the proposed robust control strategy, where a disturbance estimator is employed. The closed-loop system stability are unifying verified. Nonethe-

less, the conditions to guarantee the stability was validated in the context of the extended Kalman filter and the moving horizon estimator. An extended validation of the theory with other estimators could be an interesting research direction. Moreover, the robust control strategy can be applied to an arbitrary electrical drive system. A verification on the other systems, besides the PMSM drive system, would be useful for the application of the proposed theory.

Chapter 5 provides researching results about the performance improvement of the finite-control-set MPC. As the analysis suggests, the uncertainties and the disturbances not necessarily cause the performance deterioration of the FCS-MPC. To the author's knowledge, this problem has not been explored yet in the literature. Therefore, a possible research direction would be improving the control performance of the FCS-MPC based on the probability, especially for the long horizon solution with a receding horizon implementation.

Chapter 6 presented an adaptive compensation strategy for the inverter invoked harmonics. However, the design process requires multiple simulations and even experiments. Therefore, a promising improving potential is to deploy self-learning process to determine the parameters and realize accurate elimination of the harmonic content, which meanwhile guarantees the closed-loop stability.

APPENDIX A

List of Abbreviations

2DOFC two-degrees-of-freedom control

AC alternating current

CCS-MPC continuous-control-set model predictive control

CFTOC constrained finite time optimal control

DC direct current

DEKF dual extended Kalman filter

DSP digital signal processor

DTC direct torque control

EKF extended Kalman filter

EMF electro-motive force

ENLP equality constrained nonlinear programming

EV electric vehicle

FCS-MPC finite-control-set model predictive control

FFT fast Fourier transform

FOC field oriented control

FPGA field-programmable gate array

FRPC fractional repetitive control

HEV hybrid electric vehicle

IGBT insulated gate bipolar transistor

IIR infinite-impulse-response

ILS integer least-squares

IM induction machine

IP interior point

IPMSM interior permanent-magnet synchronous machine

KF Kalman filter

KKT Karush-Kuhn-Tucker

LQR linear quadratic regulator

LS least squares

LTI linear time-invariant

LTV linear time-variant

LUT look-up table

MHE moving horizon estimator

MIP mixed-integer programming

MIQP mixed-integer quadratic programming

MMC modular multi-level converter

MOSFET metal oxide semiconductor field effect transistor

MPC model predictive control

MPDCC multi-step predictive direct current control

MRAS model reference adaptive system

MTPA maximum torque per ampere

MTPV maximum torque per voltage

NeFeB Neodymium

NLP nonlinear programming

NMPC nonlinear model predictive control

NN neural network

NTI nonlinear time-invariant

OPP optimized pulse patterns

PI proportional-integral

PID proportional-integral-derivative

PLC programmable logic controller

PMSM permanent-magnet synchronous machine

PSO particle swarm optimization

PWM pulse width modulator

QP quadratic programming

RC resistor-capacitor

RLC resistor-inductor-capacitor

RLS recursive least squares

RMSE root mean squared error

RPC repetitive control

RSC resonant control

RTI real-time iteration

SmCo Samarium-Cobalt

SPMSM surface permanent-magnet synchronous machine

SQP sequential quadratic programming

SSFR standstill frequency response

SVM space vector modulator

TDD total demand distortion

THD total harmonic distortion

UKF unscented Kalman filter

UT unscented transformation

VSI voltage source inverter

APPENDIX B

Test Bench Data

B.1 IndraDrive

The first test bench consists of a real-time embedded drive system, including control unit and two-level inverters, and two permanent magnet synchronous machines.

B.1.1 Embedded System

The embedded system is a product from Bosch Rexroth AG, the IndraDrive Cs. It is equipped with a microprocessor, i.e. Renesas SH7750R, which is running at $240\,\mathrm{MHz}$. The inverter SKiiP 36NAB126V1 comes from SEMIKRON with the characteristics listed in Table B.1. The position is measured with single-turn absolute encoder from HIPERFACE.

B.1.2 Two-Level Inverter

The characteristics of the two-level VSI from the data sheet are shown in the following.

Table B.1: Characteristics of VSI (from data sheet)

Parameter	Symbol	Value
Turn-on time	T_{on}	$80\,\mathrm{ns}$
Turn-off time	T_{off}	$390\,\mathrm{ns}$
Switch control dead time	T_{dead}	$2\,\mu\mathrm{s}$
Voltage drop of the active switch ($25\,^{\circ}\mathrm{C}$)	U_{ce}	$1.2\,\mathrm{V}$
Voltage drop of the freewheeling diode ($25\,^{\circ}\mathrm{C}$)	U_d	$1.5\,\mathrm{V}$

B.1.3 Machines

The parameters from the data sheets of the PMSMs, i.e. PMSM I is a servo motor with MSK040B-0600-NN-M1-UG1-NNNN from Bosch Rexroth and PMSM II is MSK050B-0300-NN-M2-UG0-RNNN, are given in Table B.2 and Table B.3.

Table B.2: Parameters of the PMSM I

Parameter	Symbol	Value
Rated current	I_N	$2.2\,\mathrm{A}$
Rated speed	w_{mN}	$7500\,\mathrm{rpm}$
Rated torque	T_N	$1.7\,\mathrm{N\,m}$
Number of pole pairs	n_p	4
Nominal permanent flux	Ψ_m	$0.108\,\mathrm{Wb}$
Nominal phase resistance	R_s	$4.2\,\Omega$
Nominal d-axis inductance	L_d	$16.8\,\mathrm{mH}$
Nominal q-axis inductance	L_q	$18.6\,\mathrm{mH}$

Table B.3: Parameters of the PMSM II

Parameter	Symbol	Value
Rated current	I_N	$2\,\mathrm{A}$
Rated speed	w_{mN}	$4700\,\mathrm{rpm}$
Rated torque	T_N	$3\,\mathrm{N\,m}$
Number of pole pairs	n_p	4
Nominal permanent flux	Ψ_m	$0.212\,\mathrm{Wb}$
Nominal phase resistance	R_s	$6.5\,\Omega$
Nominal d-axis inductance	L_d	$36.7\,\mathrm{mH}$
Nominal q-axis inductance	L_q	$39\,\mathrm{mH}$

B.2 dSPACE-based System

The dSPACE-based system consists of a dSPACE system as the control unit and a product from SEW-Eurodrive with the number MDX-60A as the inverter. The dSPACE real-time system comprising a 4-core $3.5\,\mathrm{GHz}$ Intel XEON E3V6 processor and a FPGA from Xilinx Kintex-7 family. The PMSM is driven by the SEW MDX-60A and coupled with an induction machine.

B.2.1 Two-Level Inverter

The inverter applied in the SEW MDX-60A is SEMIKRON SKiiP 35NAB12T4V1, of which the parameters from the data sheet are given in Table B.4.

Table B.4: Characteristics of VSI

Parameter	Symbol	Value
Turn-on time	T_{on}	$60\,\mathrm{ns}$
Turn-off time	T_{off}	$370\,\mathrm{ns}$
Switch control dead time	T_{dead}	$1.4\,\mu\mathrm{s}$
Voltage drop of the active switch (25 °C)	U_{ce}	$1.85\,\mathrm{V}$ -$2.1\,\mathrm{V}$
Voltage drop of the freewheeling diode (25 °C)	U_d	$2.22\,\mathrm{V}$-$2.54\,\mathrm{V}$

B.2.2 Machines

The parameters of the IM and the PMSM are shown in Table B.5 and Table B.6, respectively.

Table B.5: Parameters of the Induction Machine

Parameter	Symbol	Value
Synchronous frequency	f_N	$50\,\mathrm{Hz}$
Rated current	I_N	$8.5\,\mathrm{A}$
Power factor	$\cos(\varphi)$	0.86
Nominal speed	ω_{mN}	$2830\,\mathrm{rpm}$
Number of pole pairs	n_p	1
Stator resistance	R_s	$2.1294\,\Omega$
Rotor resistance	R_r	$2.2773\,\Omega$
Stator inductance	L_s	$350.47\,\mathrm{mH}$
Rotor inductance	L_r	$350.47\,\mathrm{mH}$
Mutual inductance	L_m	$340.42\,\mathrm{mH}$
Inertia	J	$0.002\,\mathrm{kg\,m^2}$

Table B.6: Parameters of the PMSM

Parameter	Symbol	Value
Rated current	I_N	$6.3\,\mathrm{A}$
Rated speed	w_{mN}	$3000\,\mathrm{rpm}$
Rated torque	T_N	$10.5\,\mathrm{N\,m}$
Number of pole pairs	n_p	3
Nominal permanent flux	Ψ_m	$0.26\,\mathrm{Wb}$
Nominal phase resistance	R_s	$0.95\,\Omega$
Nominal d-axis inductance	L_d	$9.6\,\mathrm{mH}$
Nominal q-axis inductance	L_q	$9.6\,\mathrm{mH}$

Bibliography

[1] S. B. Niku, *Introduction to Robotics: Analysis, Control, Applications*. John Wiley & Sons, 2011.

[2] J. Rodriguez and P. Cortes, *Predictive Control of Power Converters and Electrical Drives*. Wiley-IEEE Press, 2012.

[3] S. Guru and H. R. Hiziroglu, *Electric Machinery and Transformers*. Oxford University Press, 2001.

[4] G. Müller and B. Ponick, *Theorie Elektrischer Maschinen*. John Wiley & Son Ltd, 2009.

[5] J. Pyrhonen, V. Hrabovcova, and R. Semken, *Electrical Machine Drives Control: An Introduction*. Wiley, 2004.

[6] G. Muller and B. Ponick, *Grundlagen Elektrischer Maschinen*. Wiley, 2015.

[7] J. Si, S. He, W. Cao, X. Xu, and G. Feng, "Electromagnetic characteristics analysis of surface-mounted and interior hybrid PMSM based on equivalent magnetic circuit method," in *2014 17th International Conference on Electrical Machines and Systems (ICEMS)*, Oct 2014, pp. 1125–1131.

[8] H. I. Park, J. Y. Choi, K. H. Jeong, and S. K. Cho, "Comparative analysis of surface-mounted and interior permanent magnet synchronous motor for compressor of air-conditioning system in electric vehicles," in *2015 9th International Conference on Power Electronics and ECCE Asia (ICPE-ECCE Asia)*, June 2015, pp. 1700–1705.

[9] P. Campbell, *Permanent magnet materials and their application*. Cambridge University Press, 1996.

[10] D. Schröder, *Elektrische Antriebe Regelung von Antriebssystemen*. Springer, 2001.

[11] R. Fischer, *Elektrische Maschinen*. Hanser, 2006.

[12] B. Stumberger, G. Stumberger, D. Dolinar, A. Hamler, and M. Trlep, "Evaluation of saturation and cross-magnetization effects in interior permanent-magnet synchronous motor," *IEEE Trans. Ind. Appl.*, vol. 39, no. 5, pp. 1264–1271, 2003.

[13] R. Unbehauen, *Grundlagen der Elektrotechnik I Allgemeine Grundlagen, lineare Netzwerke, stationäres Verhalten*. Springer Verlag, 1999.

[14] T. Frenzke, *Geberlose DrehmomentRegelung für permanentmagneterregte Synchronmaschinen in der Bahntraktion*. Shaker, 2009.

[15] G. Dajaku, *Model Predictive Control of High Power Converters and Industrial Drives*. Shaker, 2006.

[16] "IEEE guide for test procedures for synchronous machines," *IEEE Std 115-2009 (Revision of IEEE Std 115-1995)*, pp. 1–219, May 2010.

[17] P. L. Dandeno *et al.*, "Experience with standstill frequency response (SSFR) testing and analysis of salient pole synchronous machines," *IEEE Trans. Energy Convers.*, vol. 14, no. 4, pp. 1209–1217, Dec 1999.

[18] G. Wang *et al.*, "Self-commissioning of permanent magnet synchronous machine drives at standstill considering inverter nonlinearities," *IEEE Trans. Power Electron.*, vol. 29, no. 12, pp. 6615–6627, 2014.

[19] N. Mohan, T. M. Undeland, and W. P. Robbins, *Power Electronics*. John Wiley & Sons, 2003.

[20] S. Boyd and L. Vandenberghe, *Convex optimization*. Cambridge University Press, 2010.

[21] J. Holtz, "Pulsewidth modulation-a survey," *IEEE Trans. Ind. Electron.*, vol. 39, no. 5, pp. 410–420, 1992.

[22] A. Kumar and D. Chatterjee, "A survey on space vector pulse width modulation technique for a two-level inverter," in *2017 National Power Electronics Conference (NPEC)*, 2017, pp. 78–83.

[23] A. Edpuganti and A. K. Rathore, "A survey of low switching frequency modulation techniques for medium-voltage multilevel converters," *IEEE Trans. Ind. Appl.*, vol. 51, no. 5, pp. 4212–4228, 2015.

[24] T. Geyer, *Electromagnetic and thermal modeling of highly utilized PM machines*. Wiley, 2016.

[25] D. G. Holmes and T. A. Lipo, *Pulse Width Modulation for Power Converters: Principles and Practice (IEEE Press Series on Power Engineering)*. Wiley-IEEE Press, 2003.

[26] N. Celanovic and D. Boroyevich, "A fast space-vector modulation algorithm for multilevel three-phase converters," *IEEE Trans. Ind. Appl.*, vol. 37, no. 2, pp. 637–641, 2001.

[27] Y. Nesterov and A. Nemirovskii, *Interior-Point Polynomial Algorithms in Convex Programming*. Society for Industrial and Applied Mathematics, 1994.

[28] R. Fletcher, "A General Quadratic Programming Algorithm," *IMA Journal of Applied Mathematics*, vol. 7, no. 1, pp. 76–91, 02 1971.

[29] Y. E. Nesterov, "A method for solving the convex programming problem with convergence rate $\mathcal{O}(1/k^2)$," *Dokl. Akad. Nauk SSSR*, vol. 269, pp. 543–547, 1983.

[30] M. R. Garey and D. S. Johnson, *Computers and intractability: A guide to the theory of NP-completeness*. W. H. Freeman and Company, 1979.

[31] C. A. Floudas, *Nonlinear and Mixed-Integer Optimization: Fundamentals and Applications*, ser. Topics in Chemical Engineering. Oxford University Press, USA, 1995.

[32] M. Diehl, H. J. Ferreau, and N. Haverbeke, *Efficient numerical methods for nonlinear MPC and moving horizon estimation*. Berlin, Heidelberg: Springer Berlin Heidelberg, 2009, pp. 391–417.

[33] P. Cortes, M. P. Kazmierkowski, R. M. Kennel, D. E. Quevedo, and J. Rodriguez, "Predictive control in power electronics and drives," *IEEE Trans. Ind. Electron.*, vol. 55, no. 12, pp. 4312–4324, 2008.

[34] F. Blaschke, "The principle of field orientation as applied to the new transvector closed-loop control system for rotating machines," *Siemens Review*, vol. 39, no. 12, pp. 217–220, 1972.

[35] I. Takahashi and T. Noguchi, "A new quick-response and high-efficiency control strategy of an induction motor," *IEEE Trans. Ind. Appl.*, vol. IA-22, no. 5, pp. 820–827, 1986.

[36] F. Wang, "Model predictive torque control for electrical drive systems with and without an encoder," Ph.D. dissertation, Technical University of Munich, 2014.

[37] G. S. Buja and M. P. Kazmierkowski, "Direct torque control of PWM inverter-fed AC motors - a survey," *IEEE Trans. Ind. Electron.*, vol. 51, no. 4, pp. 744–757, Aug 2004.

[38] J. Holtz and S. Stadtfeld, "Field-oriented control by forced motor currents in a voltage fed inverter drive," *IFAC Proceedings Volumes*, vol. 16, no. 16, pp. 103 – 110, 1983, 3rd IFAC Symposium on Control in Power Electronics and Electrical Drives, Lausanne, Switzerland, 12-14 September, 1983.

[39] P. Mutschler, "A new speed-control method for induction motors," ser. PCIM Europe: International Intelligent Motion Conference Nürnberg, Januar 1998.

[40] S. Vazquez, J. Rodriguez, M. Rivera, L. G. Franquelo, and M. Norambuena, "Model predictive control for power converters and drives: advances and trends," *IEEE Trans. Ind. Electron.*, vol. 64, no. 2, pp. 935–947, 2017.

[41] S. Kouro, P. Cortes, R. Vargas, U. Ammann, and J. Rodriguez, "Model predictive control - a simple and powerful method to control power converters," *IEEE Trans. Ind. Electron.*, vol. 56, no. 6, pp. 1826–1838, 2009.

[42] J. H. Lee, "Model predictive control: review of the three decades of development," *International Journal of Control, Automation and Systems*, vol. 9, no. 3, pp. 415–424, 2011.

[43] W. Leonhard, *Control of Electrical Drives*. Springer, 1996.

[44] J. C. Butcher, *Numerical Methods for Ordinary Differential Equations*. Wiley, 2008.

[45] J. Lemmens, P. Vanassche, and J. Driesen, "PMSM drive current and voltage limiting as a constraint optimal control problem," *IEEE Journal of Emerging and Selected Topics in Power Electronics*, vol. 3, no. 2, pp. 326–338, 2015.

[46] S. Choi *et al.*, "Fault diagnosis techniques for permanent magnet AC machine and drives - a review of current state of the art," *IEEE Trans. Transport. Electrific.*, vol. 4, no. 2, pp. 444–463, June 2018.

[47] J. Yu, P. Shi, H. Yu, B. Chen, and C. Lin, "Approximation-based discrete-time adaptive position tracking control for interior permanent magnet synchronous motors," *IEEE Trans. Cybern.*, vol. 45, no. 7, pp. 1363–1371, July 2015.

[48] K. Liu and Z. Q. Zhu, "Online estimation of the rotor flux linkage and voltage-source inverter nonlinearity in permanent magnet synchronous machine drives," *IEEE Trans. Power Electron.*, vol. 29, no. 1, pp. 418–427, 2014.

[49] S. J. Underwood and I. Husain, "Online parameter estimation and adaptive control of permanent-magnet synchronous machines," *IEEE Trans. Ind. Electron.*, vol. 57, no. 7, pp. 2435–2443, July 2010.

[50] H. Li and Y. Shen, "Thermal analysis of the permanent-magnet spherical motor," *IEEE Trans. Energy Convers.*, vol. 30, no. 3, pp. 991–998, 2015.

[51] T. Sebastian, "Temperature effects on torque production and efficiency of PM motors using NdFeB magnets," *IEEE Trans. Ind. Appl.*, vol. 31, no. 2, pp. 353–357, 1995.

[52] R. Skomski and J. M. D. Coey, *Permanent Magnetism*. Institute of Physics Bristol, 1999.

[53] N. Bedetti, S. Calligaro, and R. Petrella, "Self-commissioning of inverter dead-time compensation by multiple linear regression based on a physical model," *IEEE Trans. Ind. Appl.*, vol. 51, no. 5, pp. 3954–3964, 2015.

[54] Z. Zhang and L. Xu, "Dead-time compensation of inverters considering snubber and parasitic capacitance," *IEEE Trans. Power Electron.*, vol. 29, no. 6, pp. 3179–3187, 2014.

[55] C. Choi and J. Seok, "Compensation of zero-current clamping effects in high-frequency-signal-injection-based sensorless PM motor drives," *IEEE Trans. Ind. Appl.*, vol. 43, no. 5, pp. 1258–1265, 2007.

[56] A. R. Munoz and T. A. Lipo, "On-line dead-time compensation technique for open-loop PWM-VSI drives," *IEEE Trans. Power Electron.*, vol. 14, no. 4, pp. 683–689, 1999.

[57] J. W. Choi and S. K. Sul, "Inverter output voltage synthesis using novel dead time compensation," *IEEE Trans. Power Electron.*, vol. 11, no. 2, pp. 221–227, 1996.

[58] T. Liu, R. Ning, T. T. Y. Wong, and Z. J. Shen, "Modeling and analysis of SiC MOSFET switching oscillations," *IEEE Journal of Emerging and Selected Topics in Power Electronics*, vol. 4, no. 3, pp. 747–756, 2016.

[59] X. Ding *et al.*, "Analytical and experimental evaluation of SiC-inverter nonlinearities for traction drives used in electric vehicles," *IEEE Trans. Veh. Technol.*, vol. 67, no. 1, pp. 146–159, 2018.

[60] D. Wang, P. Zhang, Y. Jin, M. Wang, G. Liu, and M. Wang, "Influences on output distortion in voltage source inverter caused by power devices' parasitic capacitance," *IEEE Trans. Power Electron.*, vol. 33, no. 5, pp. 4261–4273, 2018.

[61] L. Ben-Brahim, "On the compensation of dead time and zero-current crossing for a PWM-inverter-controlled AC servo drive," *IEEE Trans. Ind. Electron.*, vol. 51, no. 5, pp. 1113–1118, 2004.

[62] J. W. Choi and S. K. Sul, "Inverter output voltage synthesis using novel dead time compensation," *IEEE Trans. Power Electron.*, vol. 11, no. 2, pp. 221–227, March 1996.

[63] Hag-Wone Kim, Myung-Joong Youn, Kwan-Yuhl Cho, and Hyun-Soo Kim, "Nonlinearity estimation and compensation of PWM VSI for PMSM under resistance and flux linkage uncertainty," *IEEE Trans. Control Syst. Technol.*, vol. 14, no. 4, pp. 589–601, 2006.

[64] T. Sukegawa, K. Kamiyama, K. Mizuno, T. Matsui, and T. Okuyama, "Fully digital, vector-controlled PWM VSI-fed AC drives with an inverter dead-time compensation strategy," *IEEE Trans. Ind. Appl.*, vol. 27, no. 3, pp. 552–559, 1991.

[65] H. Abu-Rub, J. Guzinski, Z. Krzeminski, and H. A. Toliyat, "Predictive current control of voltage-source inverters," *IEEE Trans. Ind. Electron.*, vol. 51, no. 3, pp. 585–593, 2004.

[66] H. Miranda, P. Cortes, J. I. Yuz, and J. Rodriguez, "Predictive torque control of induction machines based on state-space models," *IEEE Trans. Ind. Electron.*, vol. 56, no. 6, pp. 1916–1924, 2009.

[67] W. Qian, S. K. Panda, and J.-X. Xu, "Torque ripple minimization in PM synchronous motors using iterative learning control," *IEEE Trans. Power Electron.*, vol. 19, no. 2, pp. 272–279, March 2004.

[68] J. Yang, W. Chen, S. Li, L. Guo, and Y. Yan, "Disturbance/Uncertainty estimation and attenuation techniques in PMSM drives - a survey," *IEEE Trans. Ind. Electron.*, vol. 64, no. 4, pp. 3273–3285, 2017.

[69] Z. Q. Zhu, S. Ruangsinchaiwanich, and D. Howe, "Synthesis of cogging torque waveform from analysis of a single stator slot," in *IEEE International Conference on Electric Machines and Drives, 2005.*, 2005, pp. 125–130.

[70] S.-K. Chung, H.-S. Kim, C.-G. Kim, and M.-J. Youn, "A new instantaneous torque control of PM synchronous motor for high-performance direct-drive applications," *IEEE Trans. Power Electron.*, vol. 13, no. 3, pp. 388–400, 1998.

[71] C. Xia, B. Ji, and Y. Yan, "Smooth speed control for low-speed high-torque permanent-magnet synchronous motor using proportional–integral–resonant controller," *IEEE Trans. Ind. Electron.*, vol. 62, no. 4, pp. 2123–2134, 2015.

[72] D. W. Chung and S. K. Sul, "Analysis and compensation of current measurement error in vector-controlled AC motor drives," *IEEE Trans. Ind. Appl.*, vol. 34, no. 2, pp. 340–345, 1998.

[73] T. Schlicksbier, H. J. Gevatter, and U. Grünhaupt, *Handbuch der Mess- und Automatisierungstechnik in der Produktion*. Springer-Verlag, 2006.

[74] S. N. Vukosavic and M. R. Stojic, "Suppression of torsional oscillations in a high-performance speed servo drive," *IEEE Trans. Ind. Electron.*, vol. 45, no. 1, pp. 108–117, 1998.

[75] H. Olsson, K. Astrom, C. Canudas de Wit, M. Gafvert, and P. Lischinsky, "Friction models and friction compensation," *European Journal of Control*, vol. 4, no. 3, pp. 176 – 195, 1998.

[76] W. C. Carter, "Mechanical factors affecting electrical drive performance," *IEEE Trans. Ind. Gen. Appl.*, vol. IGA-5, no. 3, pp. 282–290, 1969.

[77] H. Eldeeb, C. M. Hackl, L. Horlbeck, and J. Kullick, "A unified theory for optimal feed-forward torque control of anisotropic synchronous machines," *International Journal of Control*, vol. 91, no. 10, pp. 2273–2302, 2018.

[78] M. Preindl and S. Bolognani, "Optimal state reference computation with constrained MTPA criterion for PM motor drives," *IEEE Trans. Power Electron.*, vol. 30, no. 8, pp. 4524–4535, 2015.

[79] J. Umland and M. Safiuddin, "Magnitude and symmetric optimum criterion for the design of linear control systems: What is it and how does it compare with the others?" *Industry Applications, IEEE Transactions on*, vol. 26, pp. 489 – 497, 06 1990.

[80] E. A. Wan and A. T. Nelson, "Dual Kalman filtering methods for nonlinear prediction, smoothing, and estimation," *Advances in Neural Information Processing Systems*, vol. 9, 1997.

[81] J. B. N. A. O. Demerdash *et al.*, "Characterization of induction motors in adjustable-speed drives using a time-stepping coupled finite-element state-space method including experimental validation," *IEEE Transaction Industry Application*, vol. 35, no. 790–802, 1996.

[82] P. L. Dandeno *et al.*, "Experience with standstill frequency response (SSFR) testing and analysis of salient pole synchronous machines," *IEEE Trans. Energy Convers.*, vol. 14, no. 4, pp. 1209–1217, Dec 1999.

[83] T. L. Vandoorn *et al.*, "Generation of multisinusoidal test signals for the identification of synchronous-machine parameters by using a voltage-source inverter," *IEEE Trans. Ind. Electron.*, vol. 57, no. 1, pp. 430–439, Jan 2010.

[84] A. K. S.I. Moon, "Estimation of induction machine parameters from standstill time-domain data," *IEEE Transaction Industry Application*, vol. 30, no. 1609–1615, 1994.

[85] A. R. Munoz and T. A. Lipo, "On-line dead-time compensation technique for open-loop PWM-VSI drives," *IEEE Trans. Power Electron.*, vol. 14, no. 4, pp. 683–689, July 1999.

[86] H. S. Kim, H. T. Moon, and M. J. Youn, "On-line dead-time compensation method using disturbance observer," *IEEE Trans. Power Electron.*, vol. 18, no. 6, pp. 1336–1345, Nov 2003.

[87] N. Urasaki, T. Senjyu, K. Uezato, and T. Funabashi, "Adaptive dead-time compensation strategy for permanent magnet synchronous motor drive," *IEEE Trans. Energy Convers.*, vol. 22, no. 2, pp. 271–280, June 2007.

[88] S. Kim, W. Lee, M. Rho, and S. Park, "Effective dead-time compensation using a simple vectorial disturbance estimator in PMSM drives," *IEEE Trans. Ind. Electron.*, vol. 57, no. 5, pp. 1609–1614, 2010.

[89] D. Liang, J. Li, R. Qu, and W. Kong, "Adaptive second-order sliding-mode observer for PMSM sensorless control considering VSI nonlinearity," *IEEE Trans. Power Electron.*, vol. 33, no. 10, pp. 8994–9004, Oct 2018.

[90] M. Li, J. Chiasson, M. Bodson, and L. Tolbert, "Observability of speed in an induction motor from stator currents and voltages," in *Proceedings of the 44th IEEE Conference on Decision and Control*, 2005, pp. 3438–3443.

[91] S. Nalakath, M. Preindl, and A. Emadi, "Online multi-parameter estimation of interior permanent magnet motor drives with finite control set model predictive control," *IET Electric Power Applications*, vol. 11, no. 5, pp. 944–951, 2017.

[92] E. Laroche, E. Sedda, and C. Durieu, "Methodological insights for online estimation of induction motor parameters," *IEEE Trans. Control Syst. Technol.*, vol. 16, no. 5, pp. 1021–1028, 2008.

[93] R. Hermann and A. Krener, "Nonlinear controllability and observability," *IEEE Trans. Autom. Control*, vol. 22, no. 5, pp. 728–740, Oct 1977.

[94] P. Vaclavek, P. Blaha, and I. Herman, "AC drive observability analysis," *IEEE Trans. Ind. Electron.*, vol. 60, no. 8, pp. 3047–3059, 2013.

[95] Y. Inoue, Y. Kawaguchi, S. Morimoto, and M. Sanada, "Performance improvement of sensorless IPMSM drives in a low-speed region using online parameter identification," *IEEE Trans. Ind. Appl.*, vol. 47, no. 2, pp. 798–804, 2011.

[96] S. D. Wilson, G. W. Jewell, and P. G. Stewart, "Resistance estimation for temperature determination in PMSMs through signal injection," in *IEEE International Conference on Electric Machines and Drives, 2005.*, 2005, pp. 735–740.

[97] M. Preindl and S. Bolognani, "Model predictive direct torque control with finite control set for PMSM drive systems, part 1: maximum torque per ampere operation," *IEEE Trans. Ind. Informat.*, vol. 9, no. 4, pp. 1912–1921, 2013.

[98] H. Noack, *Freiformkurven und flächen in CADSystemen: Vorlesung*. Hamburg, 2009.

[99] R. Arcangéli, M. Silanes, L. María, and J. Torrens, *Multidimensional Minimizing Splines: Theory and Applications*. Springer, 2004.

[100] M. Seilmeier, S. Ebersberger, and B. Piepenbreier, "HF test current injection-based self-sensing control of PMSM for low- and zero-speed range using two-degree-of-freedom current control," *IEEE Trans. Ind. Appl.*, vol. 51, no. 3, pp. 2268–2278, 2015.

[101] S. L. Kellner and B. Piepenbreier, "General PMSM dq-model using optimized interpolated absolute and differential inductance surfaces," in *2011 IEEE International Electric Machines Drives Conference (IEMDC)*, 2011, pp. 212–217.

[102] G. Goertzel, "An algorithm for the evaluation of finite trigonometric series," *The American Mathematical Monthly*, vol. 65, no. 1, pp. 34–35, 1958.

[103] S. Kim and S. Park, "Compensation of dead-time effects based on adaptive harmonic filtering in the vector-controlled AC motor drives," *IEEE Trans. Ind. Electron.*, vol. 54, no. 3, pp. 1768–1777, 2007.

[104] T. Qiu, X. Wen, and F. Zhao, "Adaptive-linear-neuron-based dead-time effects compensation scheme for PMSM drives," *IEEE Trans. Power Electron.*, vol. 31, no. 3, pp. 2530–2538, 2016.

[105] J. Reill, *Lagegeberlose Regelung für ein accelerometergestütztes, hochdynamisches Roboterantriebssystem mit permanenterregtem Synchronmotor*. Dissertation, Friedrich Alexander Universität, Erlangen, 2010.

[106] Y. Wang, W. Xie, X. Wang, and D. Gerling, "A precise voltage distortion compensation strategy for voltage source inverters," *IEEE Trans. Ind. Electron.*, vol. 65, no. 1, pp. 59–66, 2018.

[107] R. J. Kerkman, D. Leggate, D. W. Schlegel, and C. Winterhalter, "Effects of parasitics on the control of voltage source inverters," *IEEE Trans. Power Electron.*, vol. 18, no. 1, pp. 140–150, 2003.

[108] Q. Liu and K. Hameyer, "A fast online full parameter estimation of a PMSM with sinusoidal signal injection," in *2015 IEEE Energy Conversion Congress and Exposition (ECCE)*, Sep. 2015, pp. 4091–4096.

[109] Wen-Chun Yu and Neng-Yih Shih, "Bi-loop recursive least squares algorithm with forgetting factors," *IEEE Signal Processing Letters*, vol. 13, no. 8, pp. 505–508, 2006.

[110] S. Ichikawa, M. Tomita, S. Doki, and S. Okuma, "Sensorless control of permanent-magnet synchronous motors using online parameter identification based on system identification theory," *IEEE Trans. Ind. Electron.*, vol. 53, no. 2, pp. 363–372, April 2006.

[111] Y. Inoue, Y. Kawaguchi, S. Morimoto, and M. Sanada, "Performance improvement of sensorless IPMSM drives in a low-speed region using online parameter identification," *IEEE Trans. Ind. Appl.*, vol. 47, no. 2, pp. 798–804, March 2011.

[112] A. Pal, S. Das, and A. K. Chattopadhyay, "An improved rotor flux space vector based MRAS for field-oriented control of induction motor drives," *IEEE Trans. Power Electron.*, vol. 33, no. 6, pp. 5131–5141, 2018.

[113] Y. Shi, K. Sun, L. Huang, and Y. Li, "Online identification of permanent magnet flux based on extended Kalman filter for IPMSM drive with position sensorless control," *IEEE Trans. Ind. Electron.*, vol. 59, no. 11, pp. 4169–4178, 2012.

[114] K. Wiedmann and A. Mertens, "Self-sensing control of PM synchronous machines including online system identification based on a novel MRAS approach," in *3rd IEEE International Symposium on Sensorless Control for Electrical Drives (SLED 2012)*, 2012, pp. 1–8.

[115] S. A. Davari, F. Wang, and R. M. Kennel, "Robust deadbeat control of an induction motor by stable MRAS speed and stator estimation," *IEEE Trans. Ind. Informat.*, vol. 14, no. 1, pp. 200–209, 2018.

[116] X. Xiao, C. Chen, and M. Zhang, "Dynamic permanent magnet flux estimation of permanent magnet synchronous machines," *IEEE Trans. Appl. Supercond.*, vol. 20, no. 3, pp. 1085–1088, 2010.

[117] Z. Yin, G. Li, Y. Zhang, and J. Liu, "Symmetric-strong-tracking-extended-Kalman-filter-based sensorless control of induction motor drives for modeling error reduction," *IEEE Trans. Ind. Informat.*, vol. 15, no. 2, pp. 650–662, 2019.

[118] M. Habibullah and D. D. Lu, "A speed-sensorless FS-PTC of induction motors using extended Kalman filters," *IEEE Trans. Ind. Electron.*, vol. 62, no. 11, pp. 6765–6778, 2015.

[119] S. J. Julier, J. K. Uhlmann, and H. F. Durrant-Whyte, "A new approach for filtering nonlinear systems," in *Proceedings of 1995 American Control Conference - ACC'95*, vol. 3, 1995, pp. 1628–1632 vol.3.

[120] B. Akin, U. Orguner, and A. Ersak, "A comparative study on Kalman filtering techniques designed for state estimation of industrial AC drive systems," in *Proceedings of the IEEE International Conference on Mechatronics, 2004. ICM'04.*, 2004, pp. 439–445.

[121] E. A. Wan and R. Van Der Merwe, "The unscented Kalman filter for nonlinear estimation," in *Proceedings of the IEEE 2000 Adaptive Systems for Signal Processing, Communications, and Control Symposium,*, 2000, pp. 153–158.

[122] S. Jafarzadeh, C. Lascu, and M. S. Fadali, "Square root unscented Kalman filters for state estimation of induction motor drives," *IEEE Trans. Ind. Appl.*, vol. 49, no. 1, pp. 92–99, 2013.

[123] R. Kandepu, B. Foss, and L. Imsland, "Applying the unscented Kalman filter for nonlinear state estimation," *Journal of Process Control*, vol. 18, no. 7, pp. 753 – 768, 2008.

[124] N. Tudoroiu, M. Zaheeruddin, V. Cretu, and E. R. Tudoroiu, "IMM-UKF versus frequency analysis [past and present]," *IEEE Industrial Electronics Magazine*, vol. 4, no. 3, pp. 7–18, Sept 2010.

[125] S. Simani, "Identification and fault diagnosis of a simulated model of an industrial gas turbine," *IEEE Trans. Ind. Informat.*, vol. 1, no. 3, pp. 202–216, Aug 2005.

[126] A. Akrad, M. Hilairet, and D. Diallo, "Design of a fault-tolerant controller based on observers for a PMSM drive," *IEEE Trans. Ind. Electron.*, vol. 58, no. 4, pp. 1416–1427, April 2011.

[127] L. Sun, J. D. Castagno, J. D. Hedengren, and R. W. Beard, "Parameter estimation for towed cable systems using moving horizon estimation," *IEEE Trans. Aerosp. Electron. Syst.*, vol. 51, no. 2, pp. 1432–1446, 2015.

[128] J. Shen, J. Shen, Y. He, and Z. Ma, "Accurate state of charge estimation with model mismatch for Li-Ion batteries: A joint moving horizon estimation approach," *IEEE Trans. Power Electron.*, vol. 34, no. 5, pp. 4329–4342, 2019.

[129] D. Frick, A. Domahidi, M. Vukov, S. Mariéthoz, M. Diehl, and M. Morari, "Moving horizon estimation for induction motors," in *3rd IEEE International Symposium on Sensorless Control for Electrical Drives (SLED 2012)*, 2012, pp. 1–6.

[130] F. Toso, D. Da Rù, and S. Bolognani, "A moving horizon estimator for the speed and rotor position of a sensorless PMSM drive," in *2017 IEEE International Symposium on Sensorless Control for Electrical Drives (SLED)*, 2017, pp. 109–114.

[131] K. R. Muske, J. B. Rawlings, and J. H. Lee, "Receding horizon recursive state estimation," in *1993 American Control Conference*, 1993, pp. 900–904.

[132] J. H. L. D. G. Robertson and J. B. Rawlings, "A moving horizon based approach for least-squares estimation," *AIChE Journal*, vol. 42, no. 2209–2224, 1996.

[133] Z. Liu *et al.*, "Parameter estimation for VSI-fed PMSM based on a dynamic PSO with learning strategies," *IEEE Trans. Power Electron.*, vol. 32, no. 4, pp. 3154–3165, 2017.

[134] K. Liu and Z. Q. Zhu, "Position-offset-based parameter estimation using the adaline nn for condition monitoring of permanent-magnet synchronous machines," *IEEE Trans. Ind. Electron.*, vol. 62, no. 4, pp. 2372–2383, April 2015.

[135] K. H. Kim *et al.*, "Parameter estimation and control for permanent magnet synchronous motor drive using model reference adaptive technique," in *Proceedings of IECON '95 - 21st Annual Conference on IEEE Industrial Electronics*, vol. 1, 1995, pp. 387–392 vol.1.

[136] P. Cao, X. Zhang, and S. Yang, "A unified-model-based analysis of MRAS for online rotor time constant estimation in an induction motor drive," *IEEE Trans. Ind. Electron.*, vol. 64, no. 6, pp. 4361–4371, 2017.

[137] F. Chun-bo, "Extension of V.M. Popov's hyperstability theory and its application in adaptive system design," *IFAC Proceedings Volumes*, vol. 14, no. 2, pp. 177 – 182, 1981, 8th IFAC World Congress on Control Science and Technology for the Progress of Society, Kyoto, Japan, 24-28 August 1981.

[138] L. Ljung, *System identification theory for the user*. Prentice Hall, 1999.

[139] Y. Xu, N. Parspour, and U. Vollmer, "Torque ripple minimization using online estimation of the stator resistances with consideration of magnetic saturation," *IEEE Trans. Ind. Electron.*, vol. 61, no. 9, pp. 5105–5114, Sept 2014.

[140] A. Guha and A. Patra, "Online estimation of the electrochemical impedance spectrum and remaining useful life of Lithium-Ion batteries," *IEEE Trans. Instrum. Meas.*, vol. 67, no. 8, pp. 1836–1849, Aug 2018.

[141] G. C. Karras, P. Marantos, C. P. Bechlioulis, and K. J. Kyriakopoulos, "Unsupervised online system identification for underwater robotic vehicles," *IEEE Journal of Oceanic Engineering*, pp. 1–22, 2018.

[142] T. S. Lennart Ljung, *Theory and Practice of Recursive Identification*. MIT Press (MA), 1987.

[143] R. E. Kalman, "A new approach to linear filtering and prediction problems," *Journal of Basic Engineering*, vol. 82, pp. 35–45, 1960.

[144] S. Haykin, *Kalman filtering and neural networks*. John Wiley and Sons, 2001.

[145] H. W. Sorenson, "Least-squares estimation: from Gauss to Kalman," *IEEE Spectrum*, vol. 7, no. 7, pp. 63–68, 1970.

[146] R. Kalman, "A new approach to linear filtering and prediction problems," *Transactions of the ASME–Journal of Basic Engineering*, vol. 82, no. 35-45, 1960.

[147] H. L. V. Trees, *Detection, Estimation, and Modulation Theory: Radar-Sonar Signal Processing and Gaussian Signals in Noise*. Melbourne, FL, USA: Krieger Publishing Co., Inc., 1992.

[148] M. S. Grewal and A. P. Andrews, *Kalman Filtering: Theory and Practice with MATLAB*, 4th ed. Wiley-IEEE Press, 2014.

[149] F. L. Lewis, *Optimal Estimation With an Introduction to Stochastic Control Theory*. New York, NY, USA: John Wiley & Sons, Inc., 1986.

[150] T. Kailath, "Lectures on wiener and Kalman filtering," *International Centre for Mechanical Sciences (Courses and Lectures)*, vol. 140, 1981.

[151] E. Ikonen and K. Najim, *Advanced process identification and control*. Marcel Dekker, Inc, 2002.

[152] Lihua Xie, Yeng Chai Soh, and C. E. de Souza, "Robust Kalman filtering for uncertain discrete-time systems," *IEEE Trans. Autom. Control*, vol. 39, no. 6, pp. 1310–1314, 1994.

[153] H. El-Sherief and N. Sinha, "Bootstrap estimation of parameters and states of linear multivariable systems," *IEEE Trans. Autom. Control*, vol. 24, no. 2, pp. 340–343, 1979.

[154] R. E. Kopp and R. J. Orford, "Linear regression applied to system identification for adaptive control systems," *AIAA Journal*, vol. 1, no. 10, p. 2300–2306, 1979.

[155] P. S. Maybeck, *Combined state and parameter estimation for on-line applications*. PhD thesis, Massachusetts Institute of Technology, 1972.

[156] X. R. L. Y. Bar-Shalom and T. Kirubarajan, *Estimation with Applications to Tracking and Navigation*. John Wiley and Sons, 2001.

[157] S. Zhong and A. Abur, "Combined state estimation and measurement calibration," *IEEE Trans. Power Syst.*, vol. 20, no. 1, p. 458–465, 2005.

[158] L.-C. Zai, C. L. DeMarco, and T. A. Lipo, "An extended Kalman filter approach to rotor time constant measurement in PWM induction motor drives," *IEEE Trans. Ind. Appl.*, vol. 28, no. 1, pp. 96–104, Jan 1992.

[159] J. K. Ji and S. K. Sul, "Kalman filter and LQ based speed controller for torsional vibration suppression in a 2-mass motor drive system," *IEEE Trans. Ind. Electron.*, vol. 42, no. 6, pp. 564–571, Dec 1995.

[160] K. Szabat and T. Orlowska-Kowalska, "Performance improvement of industrial drives with mechanical elasticity using nonlinear adaptive Kalman filter," *IEEE Trans. Ind. Electron.*, vol. 55, no. 3, pp. 1075–1084, March 2008.

[161] B. Akin, U. Orguner, and A. Ersak, "State estimation of induction motor using unscented Kalman filter," in *Proceedings of 2003 IEEE Conference on Control Applications, 2003. CCA 2003.*, vol. 2, June 2003, pp. 915–919 vol.2.

[162] S. J. Julier, J. K. Uhlmann, and H. F. Durrant-Whyte, "A new approach for filtering nonlinear systems," in *American Control Conference, Proceedings of the 1995*, vol. 3, Jun 1995, pp. 1628–1632 vol.3.

[163] S. J. Julier and J. K. Uhlmann, "New extension of the Kalman filter to nonlinear systems," in *AeroSense'97*. International Society for Optics and Photonics, 1997, pp. 182–193.

[164] S. Julier, J. Uhlmann, and H. F. Durrant-Whyte, "A new method for the nonlinear transformation of means and covariances in filters and estimators," *IEEE Trans. Autom. Control*, vol. 45, no. 3, pp. 477–482, Mar 2000.

[165] S. J. Julier and J. K. Uhlmann, "Unscented filtering and nonlinear estimation," *Proceedings of the IEEE*, vol. 92, no. 3, pp. 401–422, 2004.

[166] J. K. Uhlmann, S. J. Julier, and M. Csorba, "Nondivergent simultaneous map building and localization using covariance intersection," *Proc. SPIE*, vol. 3087, pp. 2–11, 1997.

[167] A. H. Jazwinski, "Limited memory optimal filtering," *IEEE Trans. Autom. Control*, vol. 13, p. 558–563, 1968.

[168] H. J. Kushner, "On the differential equations satisfied by conditional probability densities of Markov processses," *SIAM Journal of Control*, vol. 2, no. 106, 1964.

[169] S. S. Jang, B. Joseph, and H. Mukai, "Comparison of two approaches to on-line parameter and state estimation of nonlinear systems," *Ind. Eng. Chem. Proc. Des. Dev.*, vol. 25, no. 809-814, 1986.

[170] K. R. Muske, J. B. Rawlings, and J. H. Lee, "Receding horizon recursive state estimation," in *1993 American Control Conference*, June 1993, pp. 900–904.

[171] P. Kühl, M. Diehl, T. Kraus, J. P. Schlöder, and H. Bock, "A real-time algorithm for moving horizon state and parameter estimation," vol. 35, pp. 71–83, 01 2011.

[172] A. Alessandri, M. Baglietto, and G. Battistelli, "Receding-horizon estimation for discrete-time linear systems," *IEEE Trans. Autom. Control*, vol. 48, no. 473-478, 2003.

[173] C. V. Rao, J. Rawlings, and J. H. Lee, "Constrained linear state estimation-a moving horizon approach," *Automatica*, vol. 37, no. 1619–1628, 2001.

[174] A. Alessandri, M. Baglietto, and G. Battistelli, "Moving-horizon state estimation for nonlinear discrete-time systems: New stability results and approximation schemes," *Automatica*, vol. 44, no. 1753-1765, 2008.

[175] C. V. Rao, J. Rawlings, and D. Mayne, "Constrained state estimation for nonlinear discrete-time systems: Stability and moving horizon approximations," *IEEE Trans. Autom. Control*, vol. 48, no. 246–258, 2003.

[176] D. Mignone, G. Ferrari-Trecate, and M. Morari, "Moving horizon estimation for hybrid systems." *IEEE Trans. Autom. Control*, vol. 47, no. 1663–1676, 2002.

[177] E. L. Haseltine and J. B. Rawlings, "Critical evaluation of extended Kalman filtering and moving horizon estimation," *Ind. Eng. Chem. Res.*, vol. 44, no. 2451–2460, 2005.

[178] I. M. Bomze, V. F. Demyanov, R. Fletcher, and T. Terlaky, *Nonlinear Optimization*. New York: Springer, 2010.

[179] R. Fletcher, *Practical Methods of Optimization; (2Nd Ed.)*. New York, NY, USA: Wiley-Interscience, 1987.

[180] M. Diehl, H. Bock, J. P. Schlöder, R. Findeisen, Z. Nagy, and F. Allgöwer, "Real-time optimization and nonlinear model predictive control of processes governed by differential-algebraic equations," *Journal of Process Control*, vol. 12, no. 4, pp. 577 – 585, 2002.

[181] M. J. D. Powell, "A fast algorithm for nonlinearly constrained optimization calculations," in *Numerical Analysis*, G. A. Watson, Ed. Berlin, Heidelberg: Springer Berlin Heidelberg, 1978, pp. 144–157.

[182] J. Nocedal and S. J. Wright, *Numerical Optimization*, 2nd ed. New York, NY, USA: Springer, 2006.

[183] M. Diehl, J. Ferreau, and N. Haverbeke, *Efficient Numerical Methods for Nonlinear MPC and Moving Horizon Estimation*, 05 2009, vol. 384, pp. 391–417.

[184] A. Wynn, M. Vukov, and M. Diehl, "Convergence guarantees for moving horizon estimation based on the real-time iteration scheme," *IEEE Trans. Autom. Control*, vol. 59, no. 8, pp. 2215–2221, 2014.

[185] C. V. Rao, J. B. Rawlings, and D. Q. Mayne, "Constrained state estimation for nonlinear discrete-time systems: stability and moving horizon approximations," *IEEE Trans. Autom. Control*, vol. 48, no. 2, pp. 246–258, Feb 2003.

[186] J. Rawlings and M. Rajamani, "A hybrid approach for state estimation: combining moving horizon estimation and particle filtering," in *Sandia CSRI Workshop – Large-Scale Inverse Problems and Quantification of Uncertainty*, September 2007.

[187] H. Khreis, A. Deflorio, W. L. Lee, and B. Schmuelling, "Experimental evaluation of online parameter identification method based on cluster technique for EV and HEV," in *2016 19th International Conference on Electrical Machines and Systems (ICEMS)*, Nov 2016, pp. 1–6.

[188] K. Liu, Q. Zhang, J. Chen, Z. Q. Zhu, and J. Zhang, "Online multiparameter estimation of nonsalient-pole PM synchronous machines with temperature variation tracking," *IEEE Trans. Ind. Electron.*, vol. 58, no. 5, pp. 1776–1788, May 2011.

[189] M. Calvo and O. P. Malik, "Synchronous machine steady-state parameter estimation using neural networks," *IEEE Trans. Energy Convers.*, vol. 19, no. 2, pp. 237–244, June 2004.

[190] M. Calvini, M. Carpita, A. Formentini, and M. Marchesoni, "PSO-based self-commissioning of electrical motor drives," *IEEE Trans. Ind. Electron.*, vol. 62, no. 2, pp. 768–776, Feb 2015.

[191] Z. H. Liu *et al.*, "Parameter estimation for VSI-fed PMSM based on a dynamic PSO with learning strategies," *IEEE Trans. Power Electron.*, vol. 32, no. 4, pp. 3154–3165, April 2017.

[192] A. Popovici, P. Zaal, and D. Pool, "Dual extended Kalman filter for the identification of time-varying human manual control behavior," 05 2017.

[193] E. Wan and A. Nelson, *Dual extended Kalman filter methods*. John Wiley & Sons, Ltd, 2001, ch. 5.

[194] J. M. Maciejowski, *Predictive control: with constraints*. Pearson Education, 2002.

[195] J. B. Rawlings and D. Q. Mayne, *Model predictive control: Theory and design*. Nob Hill Pub, 2009.

[196] F. Borrelli, A. Bemporad, and M. Morari, *Predictive Control for Linear and Hybrid Systems*. Cambridge University Press, 2017.

[197] C. R. D. Q. Mayne, J. B. Rawlings and P. Scokaert, "Constrained model predictive control: stability and optimality," *Automatica*, vol. 36, no. 789–814, 2000.

[198] M. Kvasnica, P. Grieder, and M. Baotić, "Multi-Parametric Toolbox (MPT)," 2004. [Online]. Available: http://control.ee.ethz.ch/~mpt/

[199] C. M. Wolf, M. W. Degner, and F. Briz, "Analysis of current sampling errors in PWM VSI drives," *IEEE Trans. Ind. Appl.*, vol. 51, no. 2, pp. 1551–1560, 2015.

[200] L. Jarzebowicz, "Errors of a linear current approximation in high-speed PMSM drives," *IEEE Trans. Power Electron.*, vol. 32, no. 11, pp. 8254–8257, 2017.

[201] A. Bemporad and M. Morari, "Robust model predictive control: a survey," in *Robustness in identification and control*, A. Garulli and A. Tesi, Eds. London: Springer London, 1999, pp. 207–226.

[202] T. Barisa, S. Iles, D. Sumina, and J. Matusko, "Model predictive direct current control of a permanent magnet synchronous generator based on flexible Lyapunov function considering converter dead time," *IEEE Trans. Ind. Appl.*, vol. 54, no. 3, pp. 2899–2912, 2018.

[203] M. Preindl, "Robust control invariant sets and Lyapunov-based MPC for IPM synchronous motor drives," *IEEE Trans. Ind. Electron.*, vol. 63, pp. 1–1, 06 2016.

[204] Z. Zhou, C. Xia, Y. Yan, Z. Wang, and T. Shi, "Disturbances attenuation of permanent magnet synchronous motor drives using cascaded predictive-integral-resonant controllers," *IEEE Trans. Power Electron.*, vol. 33, no. 2, pp. 1514–1527, 2018.

[205] Z. Song and F. Zhou, "Observer-based predictive vector-resonant current control of permanent magnet synchronous machines," *IEEE Trans. Power Electron.*, vol. 34, no. 6, pp. 5969–5980, 2019.

[206] H. Liu and S. Li, "Speed control for PMSM servo system using predictive functional control and extended state observer," *IEEE Trans. Ind. Electron.*, vol. 59, no. 2, pp. 1171–1183, 2012.

[207] H. H. Choi, N. T. Vu, and J. Jung, "Design and implementation of a takagi-sugeno fuzzy speed regulator for a permanent magnet synchronous motor," *IEEE Trans. Ind. Electron.*, vol. 59, no. 8, pp. 3069–3077, 2012.

[208] Hyun-Soo Kim, Hyung-Tae Moon, and Myung-Joong Youn, "On-line dead-time compensation method using disturbance observer," *IEEE Trans. Power Electron.*, vol. 18, no. 6, pp. 1336–1345, 2003.

[209] T. J. Summers and R. E. Betz, "Dead-time issues in predictive current control," *IEEE Trans. Ind. Appl.*, vol. 40, no. 3, pp. 835–844, 2004.

[210] D. Park and K. Kim, "Parameter-independent online compensation scheme for dead time and inverter nonlinearity in IPMSM drive through waveform analysis," *IEEE Trans. Ind. Electron.*, vol. 61, no. 2, pp. 701–707, 2014.

[211] G. Feng, C. Lai, K. Mukherjee, and N. C. Kar, "Current injection-based online parameter and VSI nonlinearity estimation for PMSM drives using current and voltage DC components," *IEEE Trans. Transport. Electrific.*, vol. 2, no. 2, pp. 119–128, 2016.

[212] D. Limon *et al.*, *Input-to-State Stability: A Unifying Framework for Robust Model Predictive Control*. Berlin, Heidelberg: Springer Berlin Heidelberg, 2009, pp. 1–26.

[213] R. Findeisen, L. Imsland, F. Allgöwer, and B. Foss, "Output feedback stabilization of constrained systems with nonlinear predictive control," *International Journal of Robust and Nonlinear Control*, vol. 13, pp. 211 – 227, 02 2003.

[214] L. Magni and R. Scattolini, *Robustness and Robust Design of MPC for Nonlinear Discrete-Time Systems*. Berlin, Heidelberg: Springer Berlin Heidelberg, 2007, pp. 239–254.

[215] F. Alonge, T. Cangemi, F. D'Ippolito, A. Fagiolini, and A. Sferlazza, "Convergence analysis of extended Kalman filter for sensorless control of induction motor," *IEEE Trans. Ind. Electron.*, vol. 62, no. 4, pp. 2341–2352, 2015.

[216] O. Wallscheid and E. F. B. Ngoumtsa, "Investigation of disturbance observers for model predictive current control in electric drives," *IEEE Trans. Power Electron.*, vol. 35, no. 12, pp. 13 563–13 572, 2020.

[217] J. Rodriguez *et al.*, "Predictive current control of a voltage source inverter," *IEEE Trans. Ind. Electron.*, vol. 54, no. 1, pp. 495–503, 2007.

[218] R. Vargas, P. Cortes, U. Ammann, J. Rodriguez, and J. Pontt, "Predictive control of a three-phase neutral-point-clamped inverter," *IEEE Trans. Ind. Electron.*, vol. 54, no. 5, pp. 2697–2705, 2007.

[219] P. Cortés, A. Wilson, S. Kouro, J. Rodriguez, and H. Abu-Rub, "Model predictive control of multilevel cascaded H-bridge inverters," *IEEE Trans. Ind. Electron.*, vol. 57, no. 8, pp. 2691–2699, 2010.

[220] E. Fuentes, D. Kalise, J. Rodríguez, and R. M. Kennel, "Cascade-free predictive speed control for electrical drives," *IEEE Trans. Ind. Electron.*, vol. 61, no. 5, pp. 2176–2184, 2014.

[221] P. Karamanakos and T. Geyer, "Guidelines for the design of finite control set model predictive controllers," *IEEE Trans. Power Electron.*, vol. 35, no. 7, pp. 7434–7450, 2020.

[222] T. Geyer and D. E. Quevedo, "Multistep finite control set model predictive control for power electronics," *IEEE Trans. Power Electron.*, vol. 29, no. 12, pp. 6836–6846, 2014.

[223] I. Alevras, P. Karamanakos, S. Manias, and R. Kennel, "Variable switching point predictive torque control with extended prediction horizon," in *2015 IEEE International Conference on Industrial Technology (ICIT)*, 2015, pp. 2352–2357.

[224] T. J. Vyncke, S. Thielemans, and J. A. Melkebeek, "Finite-set model-based predictive control for flying-capacitor converters: cost function design and efficient FPGA implementation," *IEEE Trans. Ind. Informat.*, vol. 9, no. 2, pp. 1113–1121, 2013.

[225] T. Dorfling, H. du Toit Mouton, T. Geyer, and P. Karamanakos, "Long-horizon finite-control-set model predictive control with nonrecursive sphere decoding on an FPGA," *IEEE Trans. Power Electron.*, vol. 35, no. 7, pp. 7520–7531, 2020.

[226] H. A. Young, M. A. Perez, and J. Rodriguez, "Analysis of finite-control-set model predictive current control with model parameter mismatch in a three-phase inverter," *IEEE Trans. Ind. Electron.*, vol. 63, no. 5, pp. 3100–3107, 2016.

[227] T. Geyer and D. E. Quevedo, "Multistep direct model predictive control for power electronics - part 1: algorithm," in *2013 IEEE Energy Conversion Congress and Exposition*, 2013, pp. 1154–1161.

[228] A. Bemporad, D. Mignone, and M. Morari, "An efficient branch and bound algorithm for state estimation and control of hybrid systems," in *1999 European Control Conference (ECC)*, 1999, pp. 557–562.

[229] U. Fincke and M. Pohst, "Improved methods for calculating vectors of short length in a lattice, including a complexity analysis," in *Mathematics of computation*, vol. 44, no. 170, 1985, pp. 463–471.

[230] M. O. Damen, K. Abed-Meraim, and M. S. Lemdani, "Further results on the sphere decoder," in *Proceedings. 2001 IEEE International Symposium on Information Theory (IEEE Cat. No.01CH37252)*, 2001, pp. 333–.

[231] G. J. Foschini, "Layered space-time architecture for wireless communication in a fading environment when using multi-element antennas," *Bell labs technical journal*, vol. 1, no. 2, pp. 41–59, 1996.

[232] E. Agrell, T. Eriksson, A. Vardy, and K. Zeger, "Closest point search in lattices," *IEEE Trans. Inf. Theory*, vol. 48, no. 8, pp. 2201–2214, 2002.

[233] A. M. Chan and I. Lee, "A new reduced-complexity sphere decoder for multiple antenna systems," in *IEEE International Conference on Communications, 2002. ICC 2002.*, vol. 1. IEEE, 2002, pp. 460–464.

[234] X.-W. Chang, J. Wen, and X. Xie, "Effects of the LLL reduction on the success probability of the Babai point and on the complexity of sphere decoding," *IEEE Trans. Inf. Theory*, vol. 59, no. 8, pp. 4915–4926, 2013.

[235] H. Cohen, *A course in computational algebraic number theory*. Springer Science & Business Media, 2013, vol. 138.

[236] A. K. Lenstra, H. W. Lenstra, and L. Lovász, "Factoring polynomials with rational coefficients," *Mathematische Annalen*, vol. 261, no. 4, pp. 515–534, 1982.

[237] L. Wang, C. T. Freeman, S. Chai, and E. Rogers, "Predictive-repetitive control with constraints: from design to implementation," *Journal of Process Control*, vol. 23, no. 7, pp. 956 – 967, 2013. [Online]. Available: http://www.sciencedirect.com/science/article/pii/S0959152413000619

[238] H. Zhao, Q. M. J. Wu, and A. Kawamura, "An accurate approach of nonlinearity compensation for VSI inverter output voltage," *IEEE Trans. Power Electron.*, vol. 19, no. 4, pp. 1029–1035, 2004.

[239] Z. Zou, K. Zhou, Z. Wang, and M. Cheng, "Frequency-adaptive fractional-order repetitive control of shunt active power filters," *IEEE Trans. Ind. Electron.*, vol. 62, no. 3, pp. 1659–1668, 2015.

[240] S. G. Jeong and M. H. Park, "The analysis and compensation of dead-time effects in PWM inverters," *IEEE Trans. Ind. Electron.*, vol. 38, no. 2, pp. 108–114, 1991.

[241] D. Leggate and R. Kerkman, "Pulse-based dead-time compensator for PWM voltage inverters," *Industrial Electronics, IEEE Transactions on*, vol. 1, pp. 191 – 197, 05 1997.

[242] M. Pande, H. Jin, and G. Joos, "Modulated integral control technique for compensating switch delays and nonideal DC buses in voltage-source inverters," *IEEE Trans. Ind. Electron.*, vol. 44, no. 2, pp. 182–190, 1997.

[243] C. Attaianese, V. Nardi, and G. Tomasso, "A novel SVM strategy for VSI dead-time-effect reduction," *IEEE Trans. Ind. Appl.*, vol. 41, no. 6, pp. 1667–1674, 2005.

[244] L. Chen and F. Z. Peng, "Dead-time elimination for voltage source inverters," *IEEE Trans. Power Electron.*, vol. 23, no. 2, pp. 574–580, 2008.

[245] Y. Lin and Y. Lai, "Dead-time elimination of PWM-controlled inverter/converter without separate power sources for current polarity detection circuit," *IEEE Trans. Ind. Electron.*, vol. 56, no. 6, pp. 2121–2127, 2009.

[246] K. M. Cho, W. S. Oh, Y. T. Kim, and H. J. Kim, "A new switching strategy for pulse width modulation (PWM) power converters," *IEEE Trans. Ind. Electron.*, vol. 54, no. 1, pp. 330–337, 2007.

[247] A. C. Oliveira, C. B. Jacobina, and A. M. N. Lima, "Improved dead-time compensation for sinusoidal PWM inverters operating at high switching frequencies," *IEEE Trans. Ind. Electron.*, vol. 54, no. 4, pp. 2295–2304, 2007.

[248] D. Lee and J. Ahn, "A simple and direct dead-time effect compensation scheme in PWM-VSI," *IEEE Trans. Ind. Appl.*, vol. 50, no. 5, pp. 3017–3025, 2014.

[249] L. Schirone, M. Macellari, and F. Pellitteri, "Predictive dead time controller for GaN-based boost converters," *IET Power Electronics*, vol. 10, no. 4, pp. 421–428, 2017.

[250] D. De and V. Ramanarayanan, "A DC-to-three-phase-AC high-frequency link converter with compensation for nonlinear distortion," *IEEE Trans. Ind. Electron.*, vol. 57, no. 11, pp. 3669–3677, 2010.

[251] H. A. Attia, T. K. S. Freddy, H. S. Che, W. P. Hew, and A. H. El Khateb, "Confined band variable switching frequency pulse width modulation (CB-VSF PWM) for a single-phase inverter with an LCL filter," *IEEE Trans. Power Electron.*, vol. 32, no. 11, pp. 8593–8605, 2017.

[252] B. Liu, R. Ren, E. A. Jones, F. Wang, D. Costinett, and Z. Zhang, "A modulation compensation scheme to reduce input current distortion in GaN-based high switching frequency three-phase three-level Vienna-type rectifiers," *IEEE Trans. Power Electron.*, vol. 33, no. 1, pp. 283–298, 2018.

[253] L. Rovere, A. Formentini, G. L. Calzo, P. Zanchetta, and T. Cox, "Zero-sequence voltage elimination for dual-fed common DC-link open-end winding PMSM high-speed starter-generator-part II: deadtime hysteresis control of zero-sequence current," *IEEE Trans. Ind. Appl.*, vol. 55, no. 6, pp. 7813–7821, 2019.

[254] Z. Shen and D. Jiang, "Dead-time effect compensation method based on current ripple prediction for voltage-source inverters," *IEEE Trans. Power Electron.*, vol. 34, no. 1, pp. 971–983, 2019.

[255] R. W. De Doncker and J. P. Lyons, "The auxiliary resonant commutated pole converter," in *Conference Record of the 1990 IEEE Industry Applications Society Annual Meeting*, 1990, pp. 1228–1235 vol.2.

[256] J. Salmon, J. Ewanchuk, and A. M. Knight, "PWM inverters using split-wound coupled inductors," *IEEE Trans. Ind. Appl.*, vol. 45, no. 6, pp. 2001–2009, 2009.

[257] M. Tariq *et al.*, "Reliability, dead-time, and feasibility analysis of a novel modular tankless ZCS inverter for more electric aircraft," *IEEE Trans. Transport. Electrific.*, vol. 3, no. 4, pp. 843–854, 2017.

[258] J. M. Schellekens, H. Huisman, J. L. Duarte, M. A. M. Hendrix, and E. A. Lomonova, "An analysis of the highly linear transfer characteristics of dual-buck converters," *IEEE Trans. Ind. Electron.*, vol. 65, no. 6, pp. 4681–4690, 2018.

[259] J. Holtz and J. Quan, "Sensorless vector control of induction motors at very low speed using a nonlinear inverter model and parameter identification," *IEEE Trans. Ind. Appl.*, vol. 38, no. 4, pp. 1087–1095, 2002.

[260] S. Bolognani and M. Zigliotto, "Self-commissioning compensation of inverter non-idealities for sensorless AC drives applications," in *2002 International Conference on Power Electronics, Machines and Drives (Conf. Publ. No. 487)*, 2002, pp. 30–37.

[261] A. Cichowski and J. Nieznanski, "Self-tuning dead-time compensation method for voltage-source inverters," *IEEE Power Electronics Letters*, vol. 3, no. 2, pp. 72–75, 2005.

[262] S. R. Minshull, C. M. Bingham, D. A. Stone, and M. P. Foster, "Compensation of non-linearities in diode-clamped multilevel converters," *IEEE Trans. Ind. Electron.*, vol. 57, no. 8, pp. 2651–2658, 2010.

[263] G. Pellegrino, P. Guglielmi, E. Armando, and R. I. Bojoi, "Self-commissioning algorithm for inverter nonlinearity compensation in sensorless induction motor drives," *IEEE Trans. Ind. Appl.*, vol. 46, no. 4, pp. 1416–1424, 2010.

[264] Y. Park and S. Sul, "Implementation schemes to compensate for inverter nonlinearity based on trapezoidal voltage," *IEEE Trans. Ind. Appl.*, vol. 50, no. 2, pp. 1066–1073, 2014.

[265] J. W. Choi and S. K. Sul, "A new compensation strategy reducing voltage/current distortion in PWM VSI systems operating with low output voltages," *IEEE Trans. Ind. Appl.*, vol. 31, no. 5, pp. 1001–1008, 1995.

[266] X. Yu, M. W. Dunnigan, and B. W. Williams, "Phase voltage estimation of a PWM VSI and its application to vector-controlled induction machine parameter estimation," *IEEE Trans. Ind. Electron.*, vol. 47, no. 5, pp. 1181–1184, 2000.

[267] J. Holtz and Juntao Quan, "Drift- and parameter-compensated flux estimator for persistent zero-stator-frequency operation of sensorless-controlled induction motors," *IEEE Trans. Ind. Appl.*, vol. 39, no. 4, pp. 1052–1060, 2003.

[268] S. G. Jeong and M. H. Woo, "DSP-based active power filter with predictive current control," *IEEE Trans. Ind. Electron.*, vol. 44, no. 3, pp. 329–336, 1997.

[269] J. Luukko and K. Rauma, "Open-loop adaptive filter for power electronics applications," *IEEE Trans. Ind. Electron.*, vol. 55, no. 2, pp. 910–917, 2008.

[270] P. Wipasuramonton, Z. Q. Zhu, and D. Howe, "Predictive current control with current-error correction for PM brushless AC drives," *IEEE Trans. Ind. Appl.*, vol. 42, no. 4, pp. 1071–1079, 2006.

[271] N. Urasaki, T. Senjyu, K. Uezato, and T. Funabashi, "Adaptive dead-time compensation strategy for permanent magnet synchronous motor drive," *IEEE Trans. Energy Convers.*, vol. 22, no. 2, pp. 271–280, 2007.

[272] J. Jung and K. Nam, "A PI-type dead-time compensation method for vector-controlled GTO inverters," *IEEE Trans. Ind. Appl.*, vol. 34, no. 3, pp. 452–457, 1998.

[273] W. Dafang, Y. Bowen, Z. Cheng, Z. Chuanwei, and Q. ji, "A feedback-type phase voltage compensation strategy based on phase current reconstruction for ACIM drives," *IEEE Trans. Power Electron.*, vol. 29, no. 9, pp. 5031–5043, 2014.

[274] G. Liu, D. Wang, Y. Jin, M. Wang, and P. Zhang, "Current-detection-independent dead-time compensation method based on terminal voltage A/D conversion for PWM VSI," *IEEE Trans. Ind. Electron.*, vol. 64, no. 10, pp. 7689–7699, 2017.

[275] Y. A. Kwon and S. K. Kim, "A high-performance strategy for sensorless induction motor drive using variable link voltage," *IEEE Trans. Power Electron.*, vol. 22, no. 1, pp. 329–332, 2007.

[276] S. Hwang and J. Kim, "Dead time compensation method for voltage-fed PWM inverter," *IEEE Trans. Energy Convers.*, vol. 25, no. 1, pp. 1–10, 2010.

[277] J. Hwang and H. Wei, "The current harmonics elimination control strategy for six-leg three-phase permanent magnet synchronous motor drives," *IEEE Trans. Power Electron.*, vol. 29, no. 6, pp. 3032–3040, 2014.

[278] H. S. Che, E. Levi, M. Jones, W. Hew, and N. A. Rahim, "Current control methods for an asymmetrical six-phase induction motor drive," *IEEE Trans. Power Electron.*, vol. 29, no. 1, pp. 407–417, 2014.

[279] T. Liu and D. Wang, "Parallel structure fractional repetitive control for PWM inverters," *IEEE Trans. Ind. Electron.*, vol. 62, no. 8, pp. 5045–5054, 2015.

[280] R. Sepe and J. Lang, "Inverter nonlinearities and discrete-time vector current control," *Industry Applications, IEEE Transactions on*, vol. 30, pp. 62 – 70, 02 1994.

[281] M. A. Herran, J. R. Fischer, S. A. Gonzalez, M. G. Judewicz, and D. O. Carrica, "Adaptive dead-time compensation for grid-connected PWM inverters of single-stage PV systems," *IEEE Trans. Power Electron.*, vol. 28, no. 6, pp. 2816–2825, 2013.

[282] T. Mannen and H. Fujita, "Dead-time compensation method based on current ripple estimation," *IEEE Trans. Power Electron.*, vol. 30, no. 7, pp. 4016–4024, 2015.

[283] H. Kim, Y. Kwon, S. Chee, and S. Sul, "Analysis and compensation of inverter nonlinearity for three-level T-type inverters," *IEEE Trans. Power Electron.*, vol. 32, no. 6, pp. 4970–4980, 2017.

[284] H. Ge, Y. Miao, B. Bilgin, B. Nahid-Mobarakeh, and A. Emadi, "Speed range extended maximum torque per ampere control for pm drives considering inverter and motor nonlinearities," *IEEE Trans. Power Electron.*, vol. 32, no. 9, pp. 7151–7159, 2017.

[285] A. Somani, R. K. Gupta, K. K. Mohapatra, and N. Mohan, "On the causes of circulating currents in PWM drives with open-end winding AC machines," *IEEE Trans. Ind. Electron.*, vol. 60, no. 9, pp. 3670–3678, 2013.

[286] F. Blaabjerg and J. K. Pedersen, "An ideal PWM-VSI inverter using only one current sensor in the DC-link," in *1994 Fifth International Conference on Power Electronics and Variable Speed Drives*, 1994, pp. 458–464.

[287] S. Wang, W. Song, J. Ma, J. Zhao, and X. Feng, "Study on comprehensive analysis and compensation for the line current distortion in single-phase three-level NPC converters," *IEEE Trans. Ind. Electron.*, vol. 65, no. 3, pp. 2199–2211, 2018.

[288] L. Padmavathi and P. A. Janakiraman, "Self-tuned feed-forward compensation for harmonic reduction in single-phase low-voltage inverters," *IEEE Trans. Ind. Electron.*, vol. 58, no. 10, pp. 4753–4762, 2011.

[289] Y. Fan, Q. Zhang, W. Wang, and X. Zhou, "Speed regulation system of a flux-modulated permanent-magnet in-wheel motor based on sliding mode control and adaptive notch filter," *IEEE Trans. Energy Convers.*, vol. 33, no. 4, pp. 2183–2190, 2018.

[290] T. Hoshino and J. Itoh, "Output voltage correction for a voltage source type inverter of an induction motor drive," *IEEE Trans. Power Electron.*, vol. 25, no. 9, pp. 2440–2449, 2010.

[291] X. Li and R. Kennel, "General formulation of Kalman-filter based online parameter identification methods for VSI-fed PMSM," *IEEE Trans. Ind. Electron.*, pp. 1–1, 2020.

[292] Z. Liu *et al.*, "Parameter estimation for VSI-fed pmsm based on a dynamic PSO with learning strategies," *IEEE Trans. Power Electron.*, vol. 32, no. 4, pp. 3154–3165, 2017.

[293] A. Lewicki, "Dead-time effect compensation based on additional phase current measurements," *IEEE Trans. Ind. Electron.*, vol. 62, no. 7, pp. 4078–4085, 2015.

[294] M. Morari, "Internal model control - theory and applications," *IFAC Proceedings Volumes*, vol. 16, no. 21, pp. 1–18, 1983, 5th International IFAC/IMEKO Conference on the Instrumentation and Automation in the Paper, Rubber, Plastics and Polymerisation Industries, Antwerp, Belgium, 11-13 October.

[295] B. A. Francis and W. M. Wonham, "Internal model principle in control theory," *Automatica*, vol. 12, pp. 457–465, 1976.

[296] N. Hur, K. Nam, and S. Won, "A two-degrees-of-freedom current control scheme for deadtime compensation," *IEEE Trans. Ind. Electron.*, vol. 47, no. 3, pp. 557–564, 2000.

[297] D. N. Zmood and D. G. Holmes, "Stationary frame current regulation of PWM inverters with zero steady-state error," *IEEE Trans. Power Electron.*, vol. 18, no. 3, pp. 814–822, 2003.

[298] Z. Pan *et al.*, "Combined resonant controller and two-degree-of-freedom PID controller for PMSLM current harmonics suppression," *IEEE Trans. Ind. Electron.*, vol. 65, no. 9, pp. 7558–7568, 2018.

[299] Y. Wang, F. Gao, and F. J. Doyle, "Survey on iterative learning control, repetitive control, and run-to-run control," *Journal of Process Control*, vol. 19, no. 10, pp. 1589 – 1600, 2009.

[300] Z. Tang and B. Akin, "Suppression of dead-time distortion through revised repetitive controller in PMSM drives," *IEEE Trans. Energy Convers.*, vol. 32, no. 3, pp. 918–930, 2017.

[301] Y. Wang, Y. Xu, and J. Zou, "ILC-based voltage compensation method for PMSM sensorless control considering inverter nonlinearity and sampling current DC bias," *IEEE Trans. Ind. Electron.*, vol. 67, no. 7, pp. 5980–5989, 2020.

[302] M. Rashed, C. Klumpner, and G. Asher, "Repetitive and resonant control for a single-phase grid-connected hybrid cascaded multilevel converter," *IEEE Trans. Power Electron.*, vol. 28, no. 5, pp. 2224–2234, 2013.

[303] A. G. Yepes *et al.*, "Effects of discretization methods on the performance of resonant controllers," *IEEE Trans. Power Electron.*, vol. 25, no. 7, pp. 1692–1712, 2010.

[304] X. Yuan, W. Merk, H. Stemmler, and J. Allmeling, "Stationary-frame generalized integrators for current control of active power filters with zero steady-state error for current harmonics of concern under unbalanced and distorted operating conditions," *Industry Applications, IEEE Transactions on*, vol. 38, pp. 523 – 532, 04 2002.

[305] M. Steinbuch, "Repetitive control for systems with uncertain period-time," *Automatica*, vol. 38, no. 12, pp. 2103 – 2109, 2002.

[306] X. Jiang and H. Hong, "Analysis and design of the plug-in type repetitive control system based on steady-state residual convergence ratio," *International Journal of Advanced Robotic Systems*, vol. 16, no. 3, p. 1729881419850977, 2019.

[307] K. Zhou *et al.*, "Zero-phase odd-harmonic repetitive controller for a single-phase PWM inverter," *IEEE Trans. Power Electron.*, vol. 21, no. 1, pp. 193–201, 2006.

[308] M. Tomizuka, "Zero Phase Error Tracking Algorithm for Digital Control," *Journal of Dynamic Systems, Measurement, and Control*, vol. 109, no. 1, pp. 65–68, 03 1987.

[309] B. Zhang, D. Wang, K. Zhou, and Y. Wang, "Linear phase lead compensation repetitive control of a CVCF PWM inverter," *IEEE Trans. Ind. Electron.*, vol. 55, no. 4, pp. 1595–1602, 2008.

[310] R. W. Longman, "Iterative learning control and repetitive control for engineering practice," *International Journal of Control*, vol. 73, no. 10, pp. 930–954, 2000.

[311] W. Lee, L. Caccetta, and V. Rehbock, "Optimal design of all-pass variable fractional-delay digital filters," *Circuits and Systems I: Regular Papers, IEEE Transactions on*, vol. 55, pp. 1248 – 1256, 07 2008.

[312] T. I. Laakso, V. Valimaki, M. Karjalainen, and U. K. Laine, "Splitting the unit delay [FIR/all pass filters design]," *IEEE Signal Processing Magazine*, vol. 13, no. 1, pp. 30–60, 1996.

[313] V. Välimäki, "Discrete-time modeling of acoustic tubes using fractional delay filters," Ph.D. dissertation, Helsinki University of Technology, 1995.

[314] C. Cosner, G. Anwar, and M. Tomizuka, "Plug in repetitive control for industrial robotic manipulators," in *Proceedings., IEEE International Conference on Robotics and Automation*, 1990, pp. 1970–1975 vol.3.

[315] S. W. Smith, *The Scientist & Engineer's Guide to Digital Signal Processing*. California Technical Publishing, 1999.

[316] K. Zhou and D. Wang, "Digital repetitive controlled three-phase PWM rectifier," *IEEE Trans. Power Electron.*, vol. 18, no. 1, pp. 309–316, 2003.

[317] K. Zhou, Y. Yang, F. Blaabjerg, and D. Wang, "Optimal selective harmonic control for power harmonics mitigation," *IEEE Trans. Ind. Electron.*, vol. 62, no. 2, pp. 1220–1230, 2015.

[318] R. C. Lee and M. C. Smith, "Robustness and trade-offs in repetitive control," *Automatica*, vol. 34, no. 7, pp. 889 – 896, 1998.

[319] T. Inoue, "Practical repetitive control system design," in *29th IEEE Conference on Decision and Control*, 1990, pp. 1673–1678 vol.3.

[320] Y. Ye and D. Wang, "Better robot tracking accuracy with phase lead compensated ILC," in *2003 IEEE International Conference on Robotics and Automation (Cat. No.03CH37422)*, vol. 3, 2003, pp. 4380–4385 vol.3.

[321] G. Ramos and R. Costa-Castelló, "Comparison of different repetitive control architectures: synthesis and comparison. application to VSI converters," *Electronics*, vol. 7, p. 446, 12 2018.

[322] W. S. Chang, I. H. Suh, and T. W. Kim, "Analysis and design of two types of digital repetitive control systems," *Automatica*, vol. 31, no. 5, pp. 741 – 746, 1995.